

Third Edition

The Circuits and Filters Handbook

Edited by
Wai-Kai Chen

A microscopic view of a circuit board component, showing a central square chip with a textured surface, surrounded by various soldered connections and traces on a blue-tinted substrate.

 **CRC Press**
Taylor & Francis Group

The Circuits and Filters Handbook

Third Edition

Feedback, Nonlinear, and Distributed Circuits

Edited by

Wai-Kai Chen



CRC Press
Taylor & Francis Group

Feedback, Nonlinear, and Distributed Circuits

The Circuits and Filters Handbook

Third Edition

Edited by

Wai-Kai Chen

Fundamentals of Circuits and Filters

Feedback, Nonlinear, and Distributed Circuits

Analog and VLSI Circuits

Computer Aided Design and Design Automation

Passive, Active, and Digital Filters

The Circuits and Filters Handbook
Third Edition

Feedback, Nonlinear, and Distributed Circuits

Edited by

Wai-Kai Chen

University of Illinois
Chicago, U. S. A.



CRC Press

Taylor & Francis Group

Boca Raton London New York

CRC Press is an imprint of the
Taylor & Francis Group, an **informa** business

CRC Press
Taylor & Francis Group
6000 Broken Sound Parkway NW, Suite 300
Boca Raton, FL 33487-2742

© 2009 by Taylor & Francis Group, LLC
CRC Press is an imprint of Taylor & Francis Group, an Informa business

No claim to original U.S. Government works
Printed in the United States of America on acid-free paper
10 9 8 7 6 5 4 3 2 1

International Standard Book Number-13: 978-1-4200-5881-9 (Hardcover)

This book contains information obtained from authentic and highly regarded sources. Reasonable efforts have been made to publish reliable data and information, but the author and publisher cannot assume responsibility for the validity of all materials or the consequences of their use. The authors and publishers have attempted to trace the copyright holders of all material reproduced in this publication and apologize to copyright holders if permission to publish in this form has not been obtained. If any copyright material has not been acknowledged please write and let us know so we may rectify in any future reprint.

Except as permitted under U.S. Copyright Law, no part of this book may be reprinted, reproduced, transmitted, or utilized in any form by any electronic, mechanical, or other means, now known or hereafter invented, including photocopying, microfilming, and recording, or in any information storage or retrieval system, without written permission from the publishers.

For permission to photocopy or use material electronically from this work, please access www.copyright.com (<http://www.copyright.com/>) or contact the Copyright Clearance Center, Inc. (CCC), 222 Rosewood Drive, Danvers, MA 01923, 978-750-8400. CCC is a not-for-profit organization that provides licenses and registration for a variety of users. For organizations that have been granted a photocopy license by the CCC, a separate system of payment has been arranged.

Trademark Notice: Product or corporate names may be trademarks or registered trademarks, and are used only for identification and explanation without intent to infringe.

Library of Congress Cataloging-in-Publication Data

Feedback, nonlinear, and distributed circuits / edited by Wai-Kai Chen.

p. cm.

Includes bibliographical references and index.

ISBN-13: 978-1-4200-5881-9

ISBN-10: 1-4200-5881-9

1. Electronic circuits. 2. Electric circuits, Nonlinear. I. Chen, Wai-Kai, 1936- II. Title.

TK7867.N627 2009

621.3815--dc22

2008048115

Visit the Taylor & Francis Web site at
<http://www.taylorandfrancis.com>

and the CRC Press Web site at
<http://www.crcpress.com>

Contents

Preface	vii
Editor-in-Chief	ix
Contributors	xi

SECTION I Feedback Circuits

1 Feedback Amplifier Theory	1-1
<i>John Choma, Jr.</i>	
2 Feedback Amplifier Configurations	2-1
<i>John Choma, Jr.</i>	
3 General Feedback Theory	3-1
<i>Wai-Kai Chen</i>	
4 Network Functions and Feedback	4-1
<i>Wai-Kai Chen</i>	
5 Measurement of Return Difference	5-1
<i>Wai-Kai Chen</i>	
6 Multiple-Loop Feedback Amplifiers	6-1
<i>Wai-Kai Chen</i>	

SECTION II Nonlinear Circuits

7 Qualitative Analysis	7-1
<i>Martin Hasler</i>	
8 Synthesis and Design of Nonlinear Circuits	8-1
<i>Angel Rodríguez-Vázquez, Manuel Delgado-Restituto, Jose L. Huertas, and F. Vidal</i>	
9 Representation, Approximation, and Identification	9-1
<i>Guanrong Chen</i>	

10	Transformation and Equivalence	10-1
	<i>Wolfgang Mathis</i>	
11	Piecewise-Linear Circuits and Piecewise-Linear Analysis	11-1
	<i>Joos Vandewalle and Lieven Vandenberghe</i>	
12	Simulation	12-1
	<i>Erik Lindberg</i>	
13	Cellular Neural Networks and Cellular Wave Computers	13-1
	<i>Tamás Roska, Ákos Zarándy, and Csaba Rekeczky</i>	
14	Bifurcation and Chaos	14-1
	<i>Michael Peter Kennedy</i>	

SECTION III Distributed Circuits

15	Transmission Lines	15-1
	<i>Thomas Koryu Ishii</i>	
16	Multiconductor Transmission Lines	16-1
	<i>Daniël De Zutter and Luc Martens</i>	
17	Time and Frequency Domain Responses	17-1
	<i>Luc Martens and Daniël De Zutter</i>	
18	Distributed RC Networks	18-1
	<i>Vladimír Székely</i>	
19	Synthesis of Distributed Circuits	19-1
	<i>Thomas Koryu Ishii</i>	
Index	IN-1

Preface

The purpose of this book is to provide in a single volume a comprehensive reference work covering the broad spectrum of feedback amplifier design; analysis, synthesis, and design of nonlinear circuits; their representation, approximation, identification, and simulation; cellular neural networks; multiconductor transmission lines; and analysis and synthesis of distributed circuits. It also includes the design of multiple-loop feedback amplifiers. This book is written and developed for the practicing electrical engineers and computer scientists in industry, government, and academia. The goal is to provide the most up-to-date information in the field.

Over the years, the fundamentals of the field have evolved to include a wide range of topics and a broad range of practice. To encompass such a wide range of knowledge, this book focuses on the key concepts, models, and equations that enable the design engineer to analyze, design, and predict the behavior of feedback amplifiers, nonlinear and distributed systems. While design formulas and tables are listed, emphasis is placed on the key concepts and theories underlying the processes.

This book stresses fundamental theories behind professional applications and uses several examples to reinforce this point. Extensive development of theory and details of proofs have been omitted. The reader is assumed to have a certain degree of sophistication and experience. However, brief reviews of theories, principles, and mathematics of some subject areas are given. These reviews have been done concisely with perception.

The compilation of this book would not have been possible without the dedication and efforts of Professors Leon O. Chua and Thomas Koryu Ishii, and most of all the contributing authors. I wish to thank them all.

Wai-Kai Chen

Editor-in-Chief



Wai-Kai Chen is a professor and head emeritus of the Department of Electrical Engineering and Computer Science at the University of Illinois at Chicago. He received his BS and MS in electrical engineering at Ohio University, where he was later recognized as a distinguished professor. He earned his PhD in electrical engineering at the University of Illinois at Urbana–Champaign.

Professor Chen has extensive experience in education and industry and is very active professionally in the fields of circuits and systems. He has served as a visiting professor at Purdue University, the University of Hawaii at Manoa, and Chuo University in Tokyo, Japan. He was the editor-in-chief of the *IEEE Transactions on Circuits and Systems, Series I and II*, the president of the IEEE Circuits and Systems Society, and is the founding editor and the editor-in-chief of the *Journal of Circuits, Systems and Computers*.

He received the Lester R. Ford Award from the Mathematical Association of America; the Alexander von Humboldt Award from Germany; the JSPS Fellowship Award from the Japan Society for the Promotion of Science; the National Taipei University of Science and Technology Distinguished Alumnus Award; the Ohio University Alumni Medal of Merit for Distinguished Achievement in Engineering Education; the Senior University Scholar Award and the 2000 Faculty Research Award from the University of Illinois at Chicago; and the Distinguished Alumnus Award from the University of Illinois at Urbana–Champaign. He is the recipient of the Golden Jubilee Medal, the Education Award, and the Meritorious Service Award from the IEEE Circuits and Systems Society, and the Third Millennium Medal from the IEEE. He has also received more than a dozen honorary professorship awards from major institutions in Taiwan and China.

A fellow of the Institute of Electrical and Electronics Engineers (IEEE) and the American Association for the Advancement of Science (AAAS), Professor Chen is widely known in the profession for the following works: *Applied Graph Theory* (North-Holland), *Theory and Design of Broadband Matching Networks* (Pergamon Press), *Active Network and Feedback Amplifier Theory* (McGraw-Hill), *Linear Networks and Systems* (Brooks/Cole), *Passive and Active Filters: Theory and Implements* (John Wiley), *Theory of Nets: Flows in Networks* (Wiley-Interscience), *The Electrical Engineering Handbook* (Academic Press), and *The VLSI Handbook* (CRC Press).

Contributors

Guanrong Chen

Department of Electronic
Engineering
City University of
Hong Kong
Hong Kong, China

Wai-Kai Chen

Department of Electrical and
Computer Engineering
University of Illinois
Chicago, Illinois

John Choma, Jr.

Ming Hsieh Department of
Electrical Engineering
University of Southern
California, Los Angeles
Los Angeles, California

Leon O. Chua

Department of Electrical
Engineering and Computer
Sciences
University of California,
Berkeley
Berkeley, California

Manuel Delgado-Restituto

National Center of
Microelectronics
Bureau of Science and
Technology
Seville, Spain

Daniël De Zutter

Department of Information
Technology
Ghent University
Ghent, Belgium

Martin Hasler

Laboratory of Nonlinear Systems
Swiss Federal Institute of
Technology
Lausanne, Switzerland

Jose L. Huertas

National Center of
Microelectronics
Bureau of Science and
Technology
Seville, Spain

Thomas Koryu Ishii

Department Electrical and
Computer Engineering
Marquette University
Milwaukee, Wisconsin

Michael Peter Kennedy

Department of Microelectronic
Engineering
University College Cork
Cork, Ireland

Erik Lindberg

Department of Information
Technology
Technical University of
Denmark
Lyngby, Denmark

Luc Martens

Department of Information
Technology
Ghent University
Ghent, Belgium

Wolfgang Mathis

Department of Electrical
Engineering and Information
Technology
University of Hanover
Hanover, Germany

Csaba Rekeczky

Eutecus Inc.
Berkeley, California
and
Pázmány Péter Catholic
University
Budapest, Hungary

Angel Rodríguez-Vázquez

Electronics and Electromagnetism
University of Seville
Seville, Spain

Tamás Roska

Computer and Automation
Research Institute
Hungarian Academy of Sciences
Budapest, Hungary
and
Department of Information
Technology
Pázmány Péter Catholic
University
Budapest, Hungary

Vladimír Székely

Department of Electron Devices
Budapest University of
Technology and Economics
Budapest, Hungary

Lieven Vandenberghe

Electrical Engineering
Department
University of California, Los
Angeles
Los Angeles, California

Joos Vandewalle

Department of Electrical
Engineering
Catholic University of Leuven
Leuven, Belgium

F. Vidal

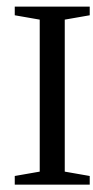
Department of Electronics
University of Málaga
Málaga, Spain

Ákos Zarándy

Computer and Automation
Research Institute
Hungarian Academy of Sciences
Budapest, Hungary

and

Pázmány Péter Catholic
University
Budapest, Hungary



Feedback Circuits

Wai-Kai Chen

University of Illinois at Chicago

1	Feedback Amplifier Theory <i>John Choma, Jr.</i>	1-1
	Introduction • Methods of Analysis • Signal Flow Analysis • Global Single-Loop Feedback • Pole Splitting Open-Loop Compensation • Summary • References	
2	Feedback Amplifier Configurations <i>John Choma, Jr.</i>	2-1
	Introduction • Series–Shunt Feedback Amplifier • Shunt–Series Feedback Amplifier • Shunt–Shunt Feedback Amplifier • Series–Series Feedback Amplifier • Dual-Loop Feedback • Summary • References	
3	General Feedback Theory <i>Wai-Kai Chen</i>	3-1
	Introduction • Indefinite-Admittance Matrix • Return Difference • Null Return Difference • References	
4	Network Functions and Feedback <i>Wai-Kai Chen</i>	4-1
	Blackman’s Formula • Sensitivity Function	
5	Measurement of Return Difference <i>Wai-Kai Chen</i>	5-1
	Blecher’s Procedure • Impedance Measurements • References	
6	Multiple-Loop Feedback Amplifiers <i>Wai-Kai Chen</i>	6-1
	Multiple-Loop Feedback Amplifier Theory • Return Different Matrix • Null Return Difference Matrix • Transfer-Function Matrix and Feedback • Sensitivity Matrix • Multiparameter Sensitivity • References	

1

Feedback Amplifier Theory

1.1	Introduction	1-1
1.2	Methods of Analysis.....	1-2
1.3	Signal Flow Analysis	1-4
1.4	Global Single-Loop Feedback.....	1-6
	Driving-Point I/O Resistances • Diminished Closed-Loop Damping Factor • Frequency Invariant Feedback Factor • Frequency Variant Feedback Factor (Compensation)	
1.5	Pole Splitting Open-Loop Compensation	1-11
	Open-Loop Amplifier • Pole Splitting Analysis	
1.6	Summary.....	1-16
	References.....	1-17

John Choma, Jr.
University of Southern California

1.1 Introduction

Feedback, whether intentional or parasitic, is pervasive of all electronic circuits and systems. In general, feedback is comprised of a subcircuit that allows a fraction of the output signal of an overall network to modify the effective input signal in such a way as to produce a circuit response that can differ substantially from the response produced in the absence of such feedback. If the magnitude and relative phase angle of the fed back signal decreases the magnitude of the signal applied to the input port of an amplifier, the feedback is said to be *negative* or degenerative. On the other hand, *positive* (or regenerative) feedback, which gives rise to oscillatory circuit responses, is the upshot of a feedback signal that increases the magnitude of the effective input signal. Because negative feedback produces stable circuit responses, the majority of all intentional feedback architectures is degenerative [1,2]. However, parasitic feedback incurred by the energy storage elements associated with circuit layout, circuit packaging, and second-order high-frequency device phenomena often degrades an otherwise degenerative feedback circuit into either a potentially regenerative or severely underdamped network.

Intentional degenerative feedback applied around an analog network produces four circuit performance benefits. First, negative feedback desensitizes the gain of an open-loop amplifier (an amplifier implemented without feedback) with respect to variations in circuit element and active device model parameters. This desensitization property is crucial in view of parametric uncertainties caused by aging phenomena, temperature variations, biasing perturbations, and nonzero fabrication and manufacturing tolerances. Second, and principally because of the foregoing desensitization property, degenerative feedback reduces the dependence of circuit responses on the parameters of inherently nonlinear active devices, thereby reducing the total harmonic distortion evidenced in open loops. Third, negative feedback

broadbands the dominant pole of an open-loop amplifier, thereby affording at least the possibility of a closed-loop network with improved high-frequency performance. Finally, by modifying the driving-point input and output impedances of the open-loop circuit, negative feedback provides a convenient vehicle for implementing voltage buffers, current buffers, and matched interstage impedances.

The disadvantages of negative feedback include gain attenuation, a closed-loop configuration that is disposed to potential instability, and, in the absence of suitable frequency compensation, a reduction in the open-loop gain-bandwidth product (GBP). In uncompensated feedback networks, open-loop amplifier gains are reduced in almost direct proportion to the amount by which closed-loop amplifier gains are desensitized with respect to open-loop gains. Although the 3 dB bandwidth of the open-loop circuit is increased by a factor comparable to that by which the open-loop gain is decreased, the closed-loop GBP resulting from uncompensated degenerative feedback is never greater than that of the open-loop configuration [3]. Finally, if feedback is incorporated around an open-loop amplifier that does not have a dominant pole [4], complex conjugate closed-loop poles yielding nonmonotonic frequency responses are likely. Even positive feedback is possible if substantive negative feedback is applied around an open-loop amplifier for which more than two poles significantly influence its frequency response.

Although the foregoing detail is common knowledge deriving from Bode's pathfinding disclosures [5], most circuit designers remain uncomfortable with analytical procedures for estimating the frequency responses, I/O impedances, and other performance indices of practical feedback circuits. The purposes of this section are to formulate systematic feedback circuit analysis procedures and ultimately, to demonstrate their applicability to six specific types of commonly used feedback architectures. Four of these feedback types, the series-shunt, shunt-series, shunt-shunt, and series-series configurations, are single-loop architectures, while the remaining two types are the series-series/shunt-shunt and series-shunt/shunt-series dual-loop configurations.

1.2 Methods of Analysis

Several standard techniques are used for analyzing linear feedback circuits [6]. The most straightforward of these entails writing the Kirchhoff equilibrium equations for the small-signal model of the entire feedback system. This analytical tack presumably leads to the idealized feedback circuit block diagram abstracted in Figure 1.1. In this model, the circuit voltage or current response, X_R , is related to the source current or voltage excitation, X_S , by

$$G_d \triangleq \frac{X_R}{X_S} = \frac{G_o}{1 + fG_o} \equiv \frac{G_o}{1 + T} \quad (1.1)$$

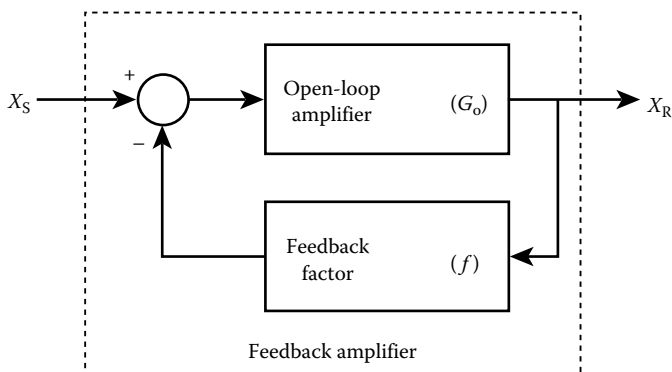


FIGURE 1.1 Block diagram model of a feedback network.

where

G_{cl} is the closed-loop gain of the feedback circuit

f , the feedback factor, is the proportion of circuit response fed back for antiphase superposition with the source signal

G_o represents the open-loop gain

The product fG_o is termed the loop gain T .

Equation 1.1 demonstrates that, for loop gains with magnitudes that are much larger than one, the closed-loop gain collapses to $1/f$, which is independent of the open-loop gain. To the extent that the open-loop amplifier, and not the feedback subcircuit, contains circuit elements and other parameters that are susceptible to modeling uncertainties, variations in the fabrication of active and passive elements, and nonzero manufacturing tolerances, large loop gain achieves a desirable parametric desensitization. Unfortunately, the determination of G_o and f directly from the Kirchhoff relationships is a nontrivial task, especially because G_o is rarely independent of f in practical electronics. Moreover, Equation 1.1 does not illuminate the manner in which the loop gain modifies the driving-point input and output impedances of the open-loop amplifier.

A second approach to feedback network analysis involves modeling the open loop, feedback, and overall closed-loop networks by a homogeneous set of two-port parameters [7]. When the two-port parameter model is selected judiciously, the two-port parameters for the closed-loop network derive from a superposition of the respective two-port parameters of the open loop and feedback subcircuits. Given the resultant parameters of the closed-loop circuit, standard formulas can then be exploited to evaluate closed-loop values of the circuit gain and the driving-point input and output impedances.

Unfortunately, several limitations plague the utility of feedback network analysis predicated on two-port parameters. First, the computation of closed-loop two-port parameters is tedious if the open-loop configuration is a multistage amplifier, or if multiloop feedback is utilized. Second, the two-loop method of feedback circuit analysis is straightforwardly applicable to only those circuits that implement global feedback (feedback applied from output port to input port). Many single-ended feedback amplifiers exploit only local feedback, wherein a fraction of the signal developed at the output port is fed back to a terminal pair other than that associated with the input port. Finally, the appropriate two-port parameters of the open-loop amplifier can be superimposed with the corresponding parameter set of the feedback subcircuit if and only if the Brune condition is satisfied [8]. This requirement mandates equality between the pre- and postconnection values of the two-port parameters of open loop and feedback cells, respectively. The subject condition is often not satisfied when the open-loop amplifier is not a simple three-terminal two-port configuration.

The third method of feedback circuit analysis exploits Mason's signal flow theory [9–11]. The circuit level application of this theory suffers few of the shortcomings indigenous to block diagram and two-port methods of feedback circuit analysis [12]. Signal flow analyses applied to feedback networks efficiently express I/O transfer functions, driving-point input impedances, and driving-point output impedances in terms of an arbitrarily selected critical or reference circuit parameters, say P .

An implicit drawback of signal flow methods is the fact that unless P is selected to be the feedback factor f , which is not always transparent in feedback architectures, expressions for the loop gain and the open-loop gain of feedback amplifiers are obscure. However, by applying signal flow theory to a feedback circuit model engineered from insights that derive from the results of two-port network analyses, the feedback factor can be isolated. The payoff of this hybrid analytical approach includes a conventional block diagram model of the I/O transfer function, as well as convenient mathematical models for evaluating the closed-loop driving-point input and output impedances. Yet, another attribute of hybrid methods of feedback circuit analysis is its ability to delineate the cause, nature, and magnitude of the feedforward transmittance produced by interconnecting a certain feedback subcircuit to a given open-loop amplifier. This information is crucial in feedback network design because feedforward invariably decreases gain and often causes undesirable phase shifts that can lead to significantly underdamped or unstable closed-loop responses.

1.3 Signal Flow Analysis

Guidelines for feedback circuit analysis by hybrid signal flow methods can be established with the aid of Figure 1.2 [13]. Figure 1.2a depicts a linear network whose output port is terminated in a resistance, R_L . The output signal variable is the voltage V_O , which is generated in response to an input port signal whose Thévenin voltage and resistance are respectively, V_S and R_S . Implicit to the linear network is a current-controlled voltage source (CCVS) Pi_b , with a value that is directly proportional to the indicated network branch current i_b . The problem at hand is the deduction of the voltage gain $G_v(R_S, R_L) = V_O/V_S$, the driving-point input resistance (or impedance) R_{in} , and the driving-point output resistance (or impedance) R_{out} , as explicit functions of the critical transimpedance parameter P . Although the following systematic procedure is developed in conjunction with the diagram in Figure 1.2, with obvious changes in notation, it is applicable to determine any type of transfer relationship for any linear network in terms of any type of reference parameter [14].

1. Set $P = 0$, as depicted in Figure 1.2b, and compute the resultant voltage gain $G_{v_0}(R_S, R_L)$, where the indicated notation suggests an anticipated dependence of gain on source and load resistances. Also, compute the corresponding driving-point input and output resistances R_{in_0} and R_{out_0} , respectively. In this case, the “critical” parameter P is associated with a controlled voltage source. Accordingly, $P = 0$ requires that the branch containing the controlled source be supplanted by a

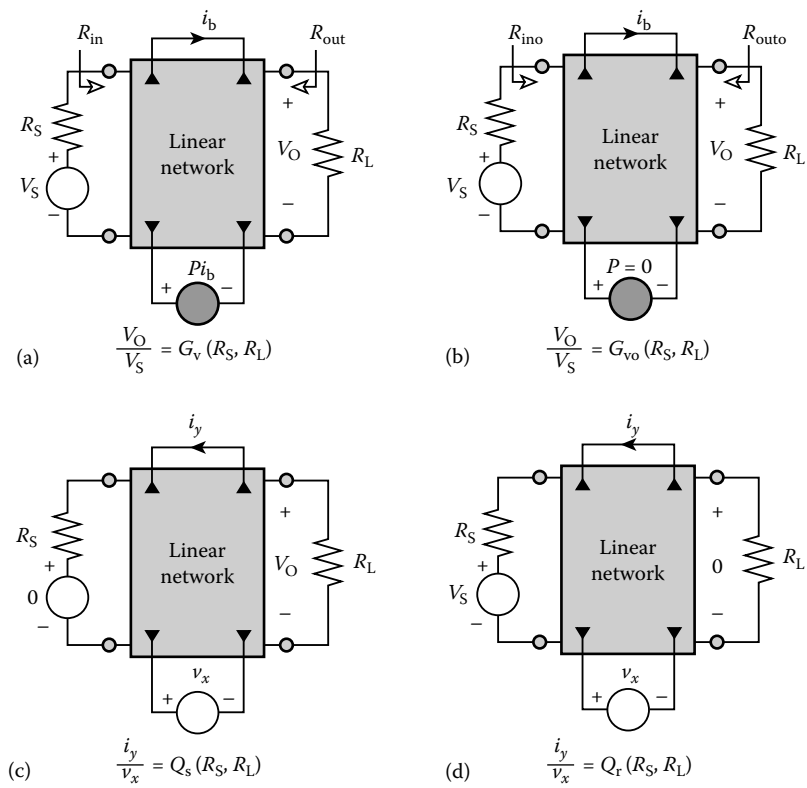


FIGURE 1.2 (a) Linear network with an identified critical parameter P . (b) Model for calculating the $P=0$ value of voltage gain. (c) The return ratio with respect to P is $PQ_s(R_S, R_L)$. (d) The null return ratio with respect to P is $PQ_r(R_S, R_L)$.

short circuit. If, for example, P is associated with a controlled current source, $P=0$ mandates the replacement of the controlled source by an open circuit.

2. Set the Thévenin source voltage V_S to zero, and replace the original controlled voltage source Pi_b by an independent voltage source of symbolic value, v_x . Then, calculate the ratio, i_y/v_x , where, as illustrated in Figure 1.2c, i_y flows in the branch that originally conducts the controlling current i_b . Note, however, that the reference polarity of i_y is opposite to that of i_b . The computed transfer function i_y/v_x is denoted by $Q_s(R_S, R_L)$. This transfer relationship, which is a function of the source and load resistances, is used to determine the *return ratio* $T_s(P, R_S, R_L)$ with respect to parameter P of the original network. In particular,

$$T_s(P, R_S, R_L) = PQ_s(R_S, R_L) \tag{1.2}$$

3. If P is associated with a controlled current source, the controlled generator Pi_b is replaced by a current source of value i_x . If the controlling variable is a voltage, instead of a current, the ratio v_y/v_x is computed, where v_y is the voltage developed across the controlling branch and the polarity is opposite to that of the original controlling voltage.
4. The preceding computational step is repeated, but instead of setting V_S to zero, the output variable, which is the voltage V_O in the present case, is nulled, as indicated in Figure 1.2d. Let the computed ratio i_y/v_x be symbolized as $Q_r(R_S, R_L)$. In turn, the *null return ratio* $T_r(P, R_S, R_L)$, with respect to parameter P is

$$T_r(P, R_S, R_L) = PQ_r(R_S, R_L) \tag{1.3}$$

5. Desired voltage gain $G_v(R_S, R_L)$, of the linear network undergoing study can be shown to be [5,12]

$$G_v(R_S, R_L) = \frac{V_O}{V_S} = G_{vo}(R_S, R_L) \left[\frac{1 + PQ_r(R_S, R_L)}{1 + PQ_s(R_S, R_L)} \right] \tag{1.4}$$

6. Given the function $Q_s(R_S, R_L)$, the driving-point input and output resistances follow straightforwardly from [12]

$$R_{in} = R_{ino} \left[\frac{1 + PQ_s(0, R_L)}{1 + PQ_s(\infty, R_L)} \right] \tag{1.5}$$

$$R_{out} = R_{outo} \left[\frac{1 + PQ_s(R_S, 0)}{1 + PQ_s(R_S, \infty)} \right] \tag{1.6}$$

An important special case entails a controlling electrical variable i_b associated with the selected parameter P that is coincidentally the voltage or current output of the circuit under investigation. In this situation, a factor P of the circuit response is fed back to the port (not necessarily the input port) defined by the terminal pair across which the controlled source is incident. When the controlling variable i_b is the output voltage or current of the subject circuit $Q_r(R_S, R_L)$, which is evaluated under the condition of a nulled network response, is necessarily zero. With $Q_r(R_S, R_L)=0$, the algebraic form of Equation 1.4 is identical to that of Equation 1.1, where the loop gain T is the return ratio with respect to parameter P ; that is,

$$PQ_s(R_S, R_L)|_{Q_r(R_S, R_L)=0} = T \tag{1.7}$$

Moreover, a comparison of Equation 1.4 to Equation 1.1 suggests that $G_v(R_S, R_L)$ symbolizes the closed-loop gain of the circuit, $G_{vo}(R_S, R_L)$ represents the corresponding open-loop gain, and the circuit feedback factor f is

$$f = \frac{PQ_s(R_S, R_L)}{G_{vo}(R_S, R_L)} \tag{1.8}$$

1.4 Global Single-Loop Feedback

Consider the global feedback scenario illustrated in Figure 1.3a, in which a fraction P of the output voltage V_O is fed back to the voltage-driven input port. Figure 1.3b depicts the model used to calculate the return ratio $Q_s(R_S, R_L)$, where, in terms of the branch variables in the schematic diagram, $Q_s(R_S, R_L) = v_y/v_x$. An inspection of this diagram confirms that the transfer function v_y/v_x is identical to the $P = 0$ value of the gain V_O/V_S , which derives from an analysis of the structure in Figure 1.3a. Thus, for global voltage feedback in which a fraction of the output voltage is fed back to a voltage-driven input port, $Q_s(R_S, R_L)$ is the open-loop voltage gain; that is, $Q_s(R_S, R_L) = G_{vo}(R_S, R_L)$. It follows from Equation 1.8 that the feedback factor f is identical to the selected critical parameter P . Similarly, for the global current feedback architecture of Figure 1.4a, a fraction P of the output current, I_O , is fed back to the current-driven input port $f = P$. As implied by the model of Figure 1.4b, $Q_s(R_S, R_L) \equiv G_{io}(R_S, R_L)$, the open-loop current gain.

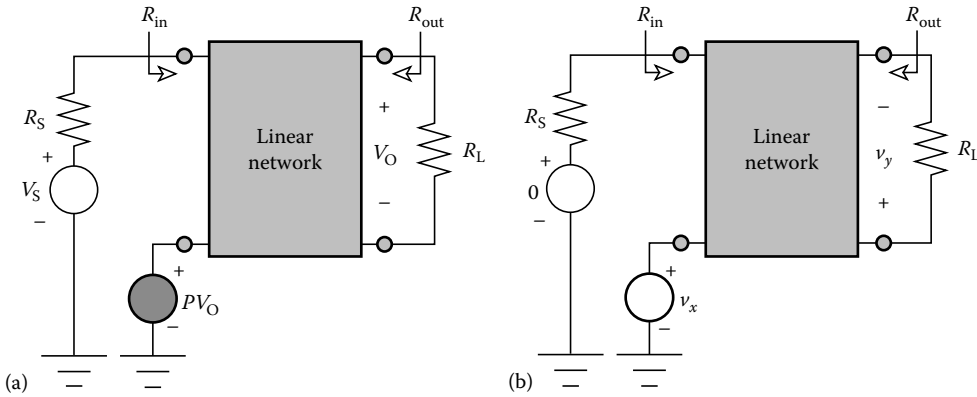


FIGURE 1.3 (a) Voltage-driven linear network with global voltage feedback. (b) Model for the calculation of loop gain.

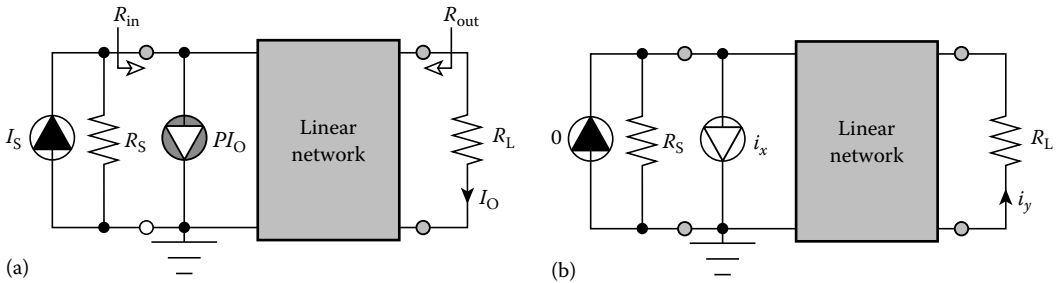


FIGURE 1.4 (a) Current-driven linear network with global current feedback. (b) Model for the calculation of loop gain.

1.4.1 Driving-Point I/O Resistances

Each of the two foregoing circuit architectures has a closed-loop gain where the algebraic form mirrors (Equation 1.1). It follows that for sufficiently large loop gain (equal to either $PG_{vo}(R_S, R_L)$ or $PG_{io}(R_S, R_L)$), the closed-loop gain approaches $(1/P)$ and is therefore desensitized with respect to open-loop gain parameters. However, such a desensitization with respect to the driving-point input and output resistances (or impedances) cannot be achieved. For the voltage feedback circuit in Figure 1.3a, $Q_s(\infty, R_L)$, is the $R_S = \infty$ value, $G_{vo}(R_S, R_L)$, of the open-loop voltage gain. This particular open-loop gain is zero, because $R_S = \infty$ decouples the source voltage from the input port of the amplifier. On the other hand, $Q_s(0, R_L)$ is the $R_S = 0$ value, $G_{vo}(0, R_L)$, of the open-loop voltage gain. This gain is at least as large as $G_{vo}(R_S, R_L)$, since a short-circuited Thévenin source resistance implies lossless coupling of the Thévenin signal to the amplifier input port. Recalling Equation 1.5, the resultant driving-point input resistance of the voltage feedback amplifier is

$$R_{in} = R_{ino}[1 + PG_{vo}(0, R_L)] \geq R_{ino}[1 + PG_{vo}(R_S, R_L)] \quad (1.9)$$

which shows that the closed-loop driving-point input resistance is larger than its open-loop counterpart and is dependent on open-loop voltage gain parameters.

Conversely, the corresponding driving-point output resistance in Figure 1.3a is smaller than the open-loop output resistance and approximately inversely proportional to the open-loop voltage gain. These assertions derive from the facts that $Q_s(R_S, 0)$ is the $R_L = 0$ value of the open-loop voltage gain $G_{vo}(R_S, R_L)$. Because $R_L = 0$ corresponds to the short-circuited load resistance, $G_{vo}(R_S, 0) = 0$. In contrast, $Q_s(R_S, \infty)$, is the $R_L = \infty$ value, $G_{vo}(R_S, \infty)$, of the open-loop gain, which is at least as large as $G_{vo}(R_S, R_L)$. By Equation 1.6,

$$R_{out} = \frac{R_{outo}}{1 + PG_{vo}(R_S, \infty)} \leq \frac{R_{outo}}{1 + PG_{vo}(R_S, R_L)} \quad (1.10)$$

Similarly, the driving-point input and output resistances of the global current feedback configuration of Figure 1.4a are sensitive to open-loop gain parameters. In contrast to the voltage amplifier of Figure 1.3a, the closed loop, driving-point input resistance of current amplifier is smaller than its open-loop value, while the driving-point output resistance is larger than its open-loop counterpart. Noting that the open-loop current gain $G_{io}(R_S, R_L)$ is zero for both $R_S = 0$ (which short circuits the input port), and $R_L = \infty$ (which open circuits the load port), Equations 1.5 and 1.6 give

$$R_{in} = \frac{R_{ino}}{1 + PG_{io}(\infty, R_L)} \quad (1.11)$$

$$R_{out} = R_{outo}[1 + PG_{io}(R_S, 0)] \quad (1.12)$$

1.4.2 Diminished Closed-Loop Damping Factor

In addition to illuminating the driving-point and forward transfer characteristics of single-loop feedback architectures, the special case of global single-loop feedback illustrates the potential instability problems pervasive of almost all feedback circuits. An examination of these problems begins by returning to Equation 1.1 and letting the open-loop gain, G_o , be replaced by the two-pole frequency-domain function,

$$G_o(s) = \frac{G_o(0)}{\left(1 + \frac{s}{p_1}\right)\left(1 + \frac{s}{p_2}\right)} \quad (1.13)$$

where $G_o(0)$ symbolizes the zero-frequency open-loop gain. The pole frequencies p_1 and p_2 in Equation 1.13 are either real numbers or complex conjugate pairs. Alternatively, Equation 1.13 is expressible as

$$G_s(s) = \frac{G_o(0)}{1 + \frac{2\zeta_{ol}}{\omega_{nol}}s + \frac{s^2}{\omega_{nol}^2}} \quad (1.14)$$

where

$$\omega_{nol} = \sqrt{p_1 p_2} \quad (1.15)$$

represents the *undamped natural frequency* of oscillation of the open-loop configuration, and

$$\zeta_{ol} = \frac{1}{2} \left[\sqrt{\frac{p_2}{p_1}} + \sqrt{\frac{p_1}{p_2}} \right] \quad (1.16)$$

is the *damping factor* of the open-loop circuit.

In Equation 1.1, let the feedback factor f be the single left-half-plane zero function,

$$f(s) = f_o \left(1 + \frac{s}{z}\right) \quad (1.17)$$

where

z is the frequency of the real zero introduced by feedback

f_o is the zero-frequency value of the feedback factor

The resultant loop gain is

$$T(s) = f_o \left(1 + \frac{s}{z}\right) G_o(s) \quad (1.18)$$

the zero-frequency value of the loop gain is

$$T(0) = f_o G_o(0) \quad (1.19)$$

and the zero-frequency closed-loop gain $G_{cl}(0)$, is

$$G_{cl}(0) = \frac{G_o(0)}{1 + f_o G_o(0)} = \frac{G_o(0)}{1 + T(0)} \quad (1.20)$$

Upon inserting Equations 1.14 and 1.17 into Equation 1.1, the closed-loop transfer function is determined to be

$$G_{cl}(s) = \frac{G_{cl}(0)}{1 + \frac{2\zeta_{cl}}{\omega_{ncl}}s + \frac{s^2}{\omega_{ncl}^2}} \quad (1.21)$$

where the closed-loop undamped natural frequency of oscillation ω_{ncl} relates to its open-loop counterpart ω_{nol} , in accordance with

$$\omega_{ncl} = \omega_{nol} \sqrt{1 + T(0)} \quad (1.22)$$

Moreover, the closed-loop damping factor ζ_{cl} is

$$\zeta_{cl} = \frac{\zeta_{ol}}{\sqrt{1+T(0)}} + \left[\frac{T(0)}{1+T(0)} \right] \frac{\omega_{ncl}}{2z} = \frac{\zeta_{ol}}{\sqrt{1+T(0)}} + \left[\frac{T(0)}{\sqrt{1+T(0)}} \right] \frac{\omega_{nol}}{2z} \quad (1.23)$$

A frequency invariant feedback factor $f(s)$ applied to the open-loop configuration whose transfer function is given by Equation 1.13 implies an infinitely large frequency, z , of the feedback zero. For this case, Equation 1.23 confirms a closed-loop damping factor that is always less than the open-loop damping factor. Indeed, for a smaller than unity open-loop damping factor (which corresponds to complex conjugate open-loop poles) and reasonable values of the zero-frequency loop gain $T(0)$, $\zeta_{cl} \ll 1$. Thus, constant feedback applied around an underdamped two-pole open-loop amplifier yields a severely underdamped closed-loop configuration. It follows that the closed-loop circuit has a transient step response plagued by overshoot and a frequency response that displays response peaking within the closed-loop passband. Observe that underdamping is likely to occur even in critically damped (identical real open-loop poles) or overdamped (distinct real poles) open-loop amplifiers, which correspond to $\zeta_{ol} = 1$ and $\zeta_{ol} > 1$, respectively, when a large zero-frequency loop gain is exploited.

Underdamped closed-loop amplifiers are not unstable systems, but they are nonetheless unacceptable. From a practical design perspective, closed-loop underdamping predicted by relatively simple mathematical models of the loop gain portend undesirable amplifier responses or even closed-loop instability. The problem is that simple transfer function models invoked in a manual circuit analysis are oblivious to presumably second-order parasitic circuit layout and device model energy storage elements with effects that include a deterioration of phase and gain margins.

1.4.3 Frequency Invariant Feedback Factor

Let the open-loop amplifier be overdamped, such that its real satisfy the relationship

$$p_2 = \kappa^2 p_1 \quad (1.24)$$

If the open-loop amplifier pole p_1 is dominant, κ^2 is a real number that is greater than the magnitude, $|G_o(0)|$, of the open-loop zero-frequency gain, which is presumed to be much larger than one. As a result, the open-loop damping factor in Equation 1.16 reduces to $\zeta_{ol} \approx \kappa/2$. With $\kappa^2 > |G_o(0)| \gg 1$, which formally reflects the *dominant pole approximation*, the 3 dB bandwidth B_{ol} of the open-loop amplifier is given approximately by [15]

$$B_{ol} \approx \frac{\omega_{nol}}{2\zeta_{ol}} = \frac{1}{\frac{1}{p_1} + \frac{1}{p_2}} = \left(\frac{\kappa^2}{\kappa^2 + 1} \right) p_1 \quad (1.25)$$

As expected, Equation 1.25 predicts an open-loop 3 dB bandwidth that is only slightly smaller than the frequency of the open-loop dominant pole.

The frequency, z , in Equation 1.23 is infinitely large if frequency invariant degenerative feedback is applied around an open-loop amplifier. For a critically damped or overdamped closed-loop amplifier, $\zeta_{cl} > 1$. Assuming open-loop pole dominance, this constraint imposes the open-loop pole requirement,

$$\frac{p_2}{p_1} \geq 4[1 + T(0)] \quad (1.26)$$

Thus, for large zero-frequency loop gain, $T(0)$, an underdamped closed-loop response is avoided if and only if the frequency of the nondominant open-loop pole is substantially larger than that of the dominant open-loop pole. Unless frequency compensation measures are exploited in the open loop, Equation 1.26

is difficult to satisfy, especially if feedback is implemented expressly to realize a substantive desensitization of response with respect to open-loop parameters. On the chance that Equation 1.26 can be satisfied, and if the closed-loop amplifier emulates a dominant pole response, the closed-loop bandwidth is, using Equations 1.22, 1.23, and 1.25,

$$B_{cl} \approx \frac{\omega_{ncl}}{2\zeta_{cl}} \approx [1 + T(0)]B_{ol} \approx [1 + T(0)]p_1 \quad (1.27)$$

Observe from Equations 1.26 and 1.27 that the maximum possible closed-loop 3 dB bandwidth is 2 octaves below the minimum acceptable frequency of the nondominant open-loop pole.

Although Equation 1.27 theoretically confirms the broadbanding property of negative feedback amplifiers, the attainment of very large closed-loop 3 dB bandwidths is nevertheless a challenging undertaking. The problem is that Equation 1.26 is rarely satisfied. As a result, the open-loop configuration must be suitably compensated, usually by pole splitting methodology [16–18], to force the validity of Equation 1.26. However, the open-loop poles are not mutually independent, so any compensation that increases p_2 is accompanied by decreases in p_1 . The pragmatic upshot of the matter is that the closed-loop 3 dB bandwidth is not directly proportional to the uncompensated value of p_1 but instead, it is proportional to the smaller, compensated value of p_1 .

1.4.4 Frequency Variant Feedback Factor (Compensation)

Consider now the case where the frequency, z , of the compensating feedback zero is finite and positive. Equation 1.23 underscores the stabilizing property of a left-half-plane feedback zero in that a sufficiently small positive z renders a closed-loop damping factor ζ_{cl} that can be made acceptably large, regardless of the value of the open-loop damping factor ζ_{ol} . To this end, $\zeta_{cl} > 1/\sqrt{2}$ is a desirable design objective in that it ensures a monotonically decreasing closed-loop frequency response. If, as is usually a design goal, the open-loop amplifier subscribes to pole dominance, Equation 1.23 translates the objective, $\zeta_{cl} > 1/\sqrt{2}$, into the design constraint

$$z \leq \frac{\left[\frac{T(0)}{1+T(0)} \right] \omega_{ncl}}{\sqrt{2} - \frac{\omega_{ncl}}{[1+T(0)]B_{ol}}} \quad (1.28)$$

where use is made of Equation 1.25 to cast ζ in terms of the open-loop bandwidth B_{ol} . When the closed-loop damping factor is precisely equal to $1/\sqrt{2}$ a maximally flat magnitude closed-loop response results for which the 3 dB bandwidth is ω_{ncl} . Equation 1.28 can then be cast into the more useful form

$$zG_{cl}(0) = \frac{GBP_{ol}}{\sqrt{2} \left(\frac{GBP_{ol}}{GBP_{cl}} \right) - 1} \quad (1.29)$$

where Equation 1.20 is exploited, GBP_{ol} is the gain-bandwidth product of the open-loop circuit, and GBP_{cl} is the gain-bandwidth product of the resultant closed-loop network.

For a given open-loop gain-bandwidth product GBP_{ol} , a desired low-frequency closed-loop gain, $G_{cl}(0)$, and a desired closed-loop gain-bandwidth product, GBP_{cl} , Equation 1.29 provides a first-order estimate of the requisite feedback compensation zero. Additionally, note that Equation 1.29 imposes an upper limit on the achievable high-frequency performance of the closed-loop configuration. In particular, because z must be positive to ensure acceptable closed-loop damping, Equation 1.29 implies

$$GBP_{ol} > \frac{GBP_{cl}}{\sqrt{2}} \quad (1.30)$$

In effect, Equation 1.30 imposes a lower limit on the required open-loop GBP commensurate with feedback compensation implemented to achieve a maximally flat, closed-loop frequency response.

1.5 Pole Splitting Open-Loop Compensation

Equation 1.26 underscores the desirability of achieving an open-loop dominant pole frequency response in the design of a feedback network. In particular, Equation 1.26 shows that if the ultimate design goal is a closed-loop dominant pole frequency response, the frequency, p_2 , of the nondominant open-loop amplifier pole must be substantially larger than its dominant pole counterpart, p_1 . Even if closed-loop pole dominance is sacrificed as a trade-off for other performance merits, open-loop pole dominance is nonetheless a laudable design objective. This contention follows from Equations 1.16 and 1.23, which combine to suggest that the larger p_2 is in comparison to p_1 , the larger is the open-loop damping factor. In turn, the unacceptably underdamped closed-loop responses that are indicative of small, closed-loop damping factors are thereby eliminated. Moreover, Equation 1.23 indicates that larger, open-loop damping factors impose progressively less demanding restrictions on the feedback compensation zero that may be required to achieve acceptable closed-loop damping. This observation is important because in an actual circuit design setting, small z in Equation 1.23 generally translates into a requirement of a correspondingly large RC time constant, where implementation may prove difficult in monolithic circuit applications.

Unfortunately, many amplifiers, and particularly broadbanded amplifiers, earmarked for use as open-loop cells in degenerative feedback networks, are not characterized by dominant pole frequency responses. The frequency response of these amplifiers is therefore optimized in accordance with a standard design practice known as pole splitting compensation. Such compensation entails the connection of a small capacitor between two high impedance, phase-inverting nodes of the open-loop topology [17,19–21]. Pole splitting techniques increase the frequency p_2 of the uncompensated nondominant open-loop pole to a compensated value, say p_{2c} . The frequency, p_1 , of the uncompensated dominant open-loop pole is simultaneously reduced to a smaller frequency, say p_{1c} . Although these pole frequency translations complement the design requirement implicit to Equations 1.23 and 1.26, they do serve to limit the resultant closed-loop bandwidth, as discussed earlier. As highlighted next, they also impose other performance limitations on the open loop.

1.5.1 Open-Loop Amplifier

The engineering methods, associated mathematics, and engineering trade-offs underlying pole splitting compensation are best revealed in terms of the generalized, phase-inverting linear network abstracted in Figure 1.5. Although this amplifier may comprise the entire open-loop configuration, in the most general case, it is an interstage of the open loop. Accordingly, R_{st} in this diagram is viewed as the Thévenin equivalent resistance of either an input signal source or a preceding amplification stage. The response to the Thévenin driver, V_{st} , is the indicated output voltage, V_i , which is developed across the Thévenin load resistance, R_{lt} , seen by the stage under investigation. Note that the input current conducted by the amplifier is I_s , while the current flowing into the output port of the unit is denoted as I_l . The dashed branch containing the capacitor C_c , which is addressed later, is the pole splitting compensation element.

Because the amplifier under consideration is linear, any convenient set of two-port parameters can be used to model its terminal volt-ampere characteristics. Assuming the existence of the short-circuit admittance, or y parameters,

$$\begin{bmatrix} I_s \\ I_l \end{bmatrix} = \begin{bmatrix} y_{11} & y_{12} \\ y_{21} & y_2 \end{bmatrix} \begin{bmatrix} V_i \\ V_l \end{bmatrix} \quad (1.31)$$

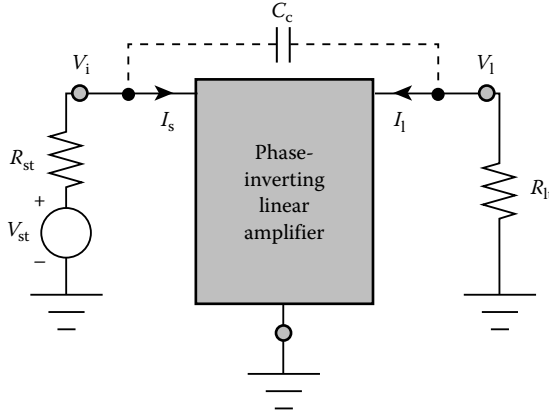


FIGURE 1.5 Linear amplifier for which a pole splitting compensation capacitance C_c is incorporated.

Defining

$$\begin{aligned}
 y_o &\triangleq y_{11} + y_{12} \\
 y_o &\triangleq y_{22} + y_{12} \\
 y_f &\triangleq y_{21} + y_{12} \\
 y_r &\triangleq -y_{12}
 \end{aligned}
 \tag{1.32}$$

Equation 1.31 implies

$$I_s = y_i V_i + y_r (V_i - V_1) \tag{1.33}$$

$$I_l = y_f V_i + y_o V_1 + y_r (V_1 - V_i) \tag{1.34}$$

The last two expressions produce the y -parameter model depicted in Figure 1.6a, in which y_i represents an effective shunt input admittance, y_o is a shunt output admittance, y_f is a forward transadmittance, and y_r reflects voltage feedback intrinsic to the amplifier.

Amplifiers amenable to pole splitting compensation have capacitive input and output admittances; that is, y_i and y_o are of the form

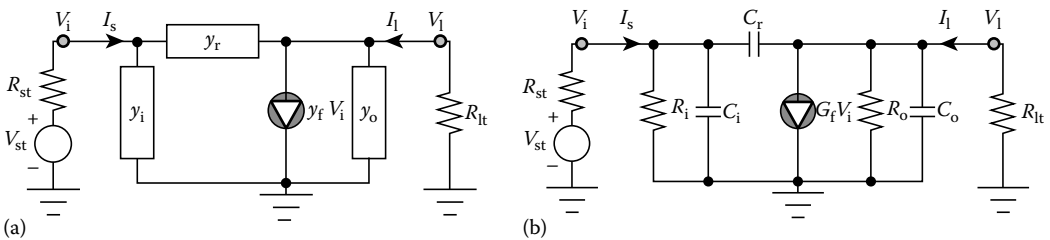


FIGURE 1.6 y -Parameter equivalent circuit of the phase-inverting linear amplifier in Figure 1.5. (b) Approximate form of the model in (a).

$$\begin{aligned} y_i &= \frac{1}{R_i} + sC_i \\ y_o &= \frac{1}{R_o} + sC_o \end{aligned} \quad (1.35)$$

Similarly,

$$\begin{aligned} y_f &= G_f - sC_f \\ y_r &= \frac{1}{R_r} + sC_r \end{aligned} \quad (1.36)$$

In Equation 1.36, the conductance component G_f of the forward transadmittance y_f positive in a phase-inverting amplifier. Moreover, the reactive component $-sC_f$ of y_f produces an *excess phase angle*, and hence, a *group delay*, in the forward gain function. This component, which deteriorates phase margin, can be ignored to first order if the signal frequencies of interest are not excessive in comparison to the upper-frequency limit of performance of the amplifier. Finally, the feedback internal to many practical amplifiers is predominantly capacitive so that the feedback resistance R_r can be ignored. These approximations allow the model in Figure 1.6a to be drawn in the form offered in Figure 1.6b.

It is worthwhile interjecting that the six parameters indigenous to the model in Figure 1.6b need not be deduced analytically from the small-signal models of the active elements embedded in the subject interstage. Instead, SPICE can be exploited to evaluate the y parameters in Equation 1.31 at the pertinent biasing level. Because these y parameters display dependencies on signal frequency, care should be exercised to evaluate their real and imaginary components in the neighborhood of the open loop, 3 dB bandwidth to ensure acceptable computational accuracy at high frequencies. Once the y parameters in Equation 1.31 are deduced by computer-aided analysis, the alternate admittance parameters in Equation 1.23, as well as numerical estimates for the parameters, R_i , C_i , R_o , C_o , C_r , and G_f in Equations 1.35 and 1.36 follow straightforwardly.

1.5.2 Pole Splitting Analysis

An analysis of the circuit in Figure 1.6b produces a voltage transfer function $A_v(s)$ of the form

$$A_v(s) = \frac{V_1(s)}{V_{st}(s)} = A_v(0) \left[\frac{1 - \frac{s}{z_r}}{\left(1 + \frac{s}{p_1}\right)\left(1 + \frac{s}{p_2}\right)} \right] \quad (1.37)$$

Letting

$$R_{||} = R_{it} || R_o \quad (1.38)$$

an inspection of the circuit in Figure 1.6b confirms that

$$A_v(0) = -G_f R_{||} \left(\frac{R_i}{R_i + R_{st}} \right) \quad (1.39)$$

is the zero-frequency voltage gain. Moreover, the frequency, z_r , of the right-half-plane zero is

$$z_r = \frac{G_f}{C_r} \quad (1.40)$$

The lower pole frequency, p_1 , and the higher pole frequency, p_2 , derive implicitly from

$$\frac{1}{p_1} + \frac{1}{p_2} = R_{II}(C_o + C_r) + R_{ss}[C_i + (1 + G_f R_{II})C_r] \tag{1.41}$$

and

$$\frac{1}{p_1 p_2} = R_{ss} R_{II} C_o \left[C_i + \left(\frac{C_o + C_i}{C_o} \right) C_r \right] \tag{1.42}$$

where

$$R_{ss} = R_{st} \triangleq R_I \tag{1.43}$$

Most practical amplifiers, and particularly amplifiers realized in bipolar junction transistor technology, have very large forward transconductance, G_f , and small internal feedback capacitance, C_r . The combination of large G_f and small C_r renders the frequency in Equation 1.40 so large as to be inconsequential to the passband of interest. When utilized in a high-gain application, such as the open-loop signal path of a feedback amplifier, these amplifiers also operate with a large effective load resistance, R_{II} . Accordingly, Equation 1.41 can be used to approximate the pole frequency p_1 as

$$p_1 \approx \frac{1}{R_{ss}[C_i + (1 + G_f R_{II})C_r]} \tag{1.44}$$

Substituting this result into Equation 1.42, the approximate frequency p_2 of the high-frequency pole is

$$p_2 \approx \frac{C_i + (1 + G_f R_{II})C_r}{R_{II} C_o \left[C_i + \left(\frac{C_o + C_i}{C_o} \right) C_r \right]} \tag{1.45}$$

Figure 1.7 illustrates asymptotic frequency responses corresponding to pole dominance and to a two-pole response. Figure 1.7a depicts the frequency response of a dominant pole amplifier, which does not

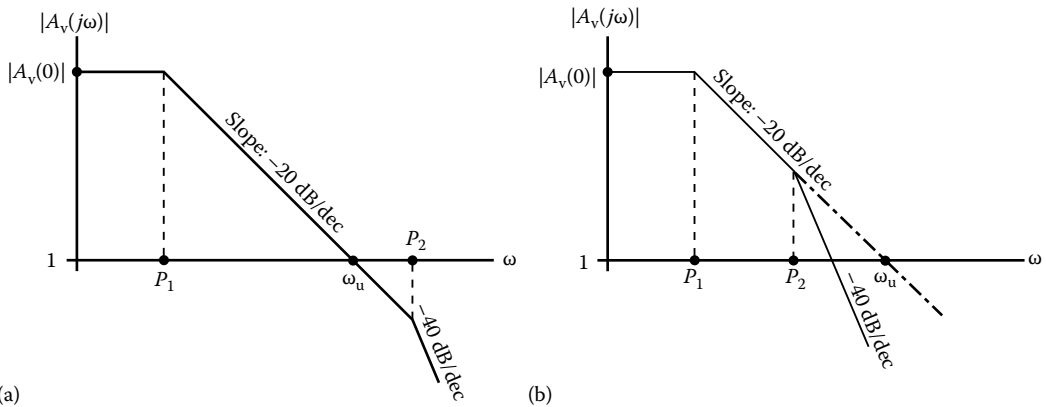


FIGURE 1.7 (a) Asymptotic frequency response for a dominant pole amplifier. Such an amplifier does not require pole splitting compensation because the two lowest frequency amplifier poles, p_1 and p_2 , are already widely separated. (b) Frequency response of an amplifier with high-frequency response that is strongly influenced by both of its lowest frequency poles. The basic objective of pole splitting compensation is to transform the indicated frequency response to a form that emulates that depicted in (a).

require pole splitting compensation. Observe that its high-frequency response is determined by a single pole (p_1 in this case) through the signal frequency at which the gain ultimately degrades to unity. In this interpretation of a dominant pole amplifier, p_2 is not only much larger than p_1 , but is in fact larger than the unity gain frequency, which is indicated as ω_u in the figure. This unity gain frequency, which can be viewed as an upper limit to the useful passband of the amplifier, is approximately, $|A_v(0)|p_1$. To the extent that p_1 is essentially the 3 dB bandwidth when $p_2 \gg p_1$, the unity gain frequency is also the GBP of the subject amplifier. In short, with $|A_v(j\omega_u)| \triangleq 1$, $p_2 \gg p_1$ in Equation 1.37 implies

$$\omega_u \approx |A_v(0)|p_1 \approx \text{GBP} \quad (1.46)$$

The contrasting situation of a response indigenous to the presence of two significant open-loop poles is illustrated in Figure 1.7b. In this case, the higher pole frequency p_2 is smaller than ω_u and hence, the amplifier does not emulate a single-pole response throughout its theoretically useful frequency range. The two critical frequencies, p_1 and p_2 , remain real numbers, and as long as $p_2 \neq p_1$, the corresponding damping factor, is greater than 1. However, the damping factor of the two-pole amplifier (its response is plotted in Figure 1.7b) is nonetheless smaller than that of the dominant pole amplifier. It follows that, for reasonable loop gains, unacceptable underdamping is more likely when feedback is invoked around the two-pole amplifier, as opposed to the same amount of feedback applied around a dominant pole amplifier. Pole splitting attempts to circumvent this problem by transforming the pole conglomeration of the two-pole amplifier into one that emulates the dominant pole situation inferred by Figure 1.7a.

To the foregoing end, append the compensation capacitance C_c between the input and the output ports of the phase-inverting linear amplifier, as suggested in Figure 1.5. With reference to the equivalent circuit in Figure 1.6b, the electrical impact of this additional element is the effective replacement of the internal feedback capacitance C_r by the capacitance sum ($C_r + C_c$). Letting

$$C_p \triangleq C_r + C_c \quad (1.47)$$

it is apparent that Equations 1.40 through 1.42 remain applicable, provided that C_r in these relationships is supplanted by C_p . Because C_p is conceivably significantly larger than C_c , however, the approximate expressions for the resultant pole locations differ from those of Equations 1.44 and 1.45. In particular, a reasonable approximation for the compensated value, say p_{1c} , of the lower pole frequency is now

$$p_{1c} \approx \frac{1}{[R_{II} + (1 + G_f R_{II})R_{ss}]C_p} \quad (1.48)$$

while the higher pole frequency, p_{2c} , becomes

$$p_{2c} \approx \frac{1}{\left(R_{ss} \parallel R_{II} \parallel \frac{1}{G_f}\right)(C_o + C_i)} \quad (1.49)$$

Clearly, $p_{1c} < p_1$ and $p_{2c} > p_2$. Moreover, for large G_f , p_{2c} is potentially much larger than p_{1c} . It should also be noted that the compensated value, say, z_{rc} , of the right-half-plane zero is smaller than its uncompensated value, z_r , because Equation 1.40 demonstrates that

$$z_{rc} = \frac{G_f}{C_p} = z_r \left(\frac{C_r}{C_r + C_c} \right) \quad (1.50)$$

Although z_{rc} can conceivably exert a significant influence on the high-frequency response of the compensated amplifier, the following discussion presumes tacitly that $z_{rc} > p_{2c}$ [2].

Assuming a dominant pole frequency response, the compensated unity gain frequency, ω_{uc} , is, using Equations 1.39, 1.46, and 1.48,

$$\omega_{uc} \approx |A_v(0)|p_{1c} \approx \left(\frac{1}{R_{st}C_p}\right) \left[G_f \left(R_{ss} \parallel R_{ll} \parallel \frac{1}{G_f} \right) \right] \quad (1.51)$$

It is interesting to note that

$$\omega_{uc} < \left(\frac{1}{R_{st}C_p}\right) \quad (1.52)$$

that is, the unity gain frequency is limited by the inverse of the RC time constant formed by the Thévenin source resistance R_{st} and the net capacitance C_p appearing between the input port and the phase inverted output port. The subject inequality comprises a significant performance limitation, for if p_{2c} is indeed much larger than p_{1c} , ω_{uc} is approximately the GBP of the compensated cell. Accordingly, for a given source resistance, a required open-loop gain, and a desired open-loop bandwidth, Equation 1.52 imposes an upper limit on the compensation capacitance that can be exploited for pole splitting purposes.

In order for the compensated amplifier to behave as a dominant pole configuration, p_{2c} must exceed ω_{uc} , as defined by Equation 1.51. Recalling Equation 1.49, the requisite constraint is found to be

$$R_{st}C_p > G_f \left(R_{ss} \parallel R_{ll} \parallel \frac{1}{G_f} \right)^2 (C_o + C_i) \quad (1.53)$$

Assuming $G_f (R_{ss}/R_{ll}) \ll 1$, Equation 1.53 reduces to the useful simple form

$$C_f R_{st} > \frac{C_o + C_i}{C_p} \quad (1.54)$$

which confirms the need for large forward transconductance G_f if pole splitting is to be an effective compensation technique.

1.6 Summary

The use of negative feedback is fundamental to the design of reliable and reproducible analog electronic networks. Accordingly, this chapter documents the salient features of the theory that underlies the efficient analysis and design of commonly used feedback networks. Four especially significant points are postulated in this section.

1. By judiciously exploiting signal flow theory, the classical expression, Equation 1.1, for the I/O transfer relationship of a linear feedback system is rendered applicable to a broad range of electronic feedback circuits. This expression is convenient for design-oriented analysis because it clearly identifies the open-loop gain, G_o , and the loop gain, T . The successful application of signal flow theory is predicated on the requirement that the feedback factor, to which T is proportional and that appears in the signal flow literature as a “critical” or “reference” parameter, can be identified in a given feedback circuit.
2. Signal flow theory, as applied to electronic feedback architectures, proves to be an especially expedient analytical tool because once the loop gain T is identified, the driving-point input and output impedances follow with minimal additional calculations. Moreover, the functional dependence of T on the Thévenin source and terminating load impedances unambiguously brackets the

- magnitudes of the driving point I/O impedances attainable in particular types of feedback arrangements.
3. Damping factor concept is advanced herewith as a simple way of assessing the relative stability of both the open and closed loops of a feedback circuit. The open-loop damping factor derives directly from the critical frequencies of the open-loop gain, while these frequencies and any zeros appearing in the loop gain unambiguously define the corresponding closed-loop damping factor. Signal flow theory is once again used to confirm the propensity of closed loops toward instability unless the open-loop subcircuit functions as a dominant pole network. Also confirmed is the propriety of the common practice of implementing a feedback zero as a means of stabilizing an otherwise potentially unstable closed loop.
 4. Pole splitting as a means to achieve dominant pole open-loop responses is definitively discussed. Generalized design criteria are formulated for this compensation scheme, and limits of performance are established. Of particular interest is the fact that pole splitting limits the GBP of the compensated amplifier to a value that is determined by a source resistance–compensation capacitance time constant.

References

1. J. A. Mataya, G. W. Haines, and S. B. Marshall, IF amplifier using C_c -compensated transistors, *IEEE J. Solid-State Circuits*, SC-3, 401–407, Dec. 1968.
2. W. G. Beall and J. Choma Jr., Charge-neutralized differential amplifiers, *J. Analog Integr. Circuits Signal Process.*, 1, 33–44, Sept. 1991.
3. J. Choma Jr., A generalized bandwidth estimation theory for feedback amplifiers, *IEEE Trans. Circuits Syst.*, CAS-31, 861–865, Oct. 1984.
4. R. D. Thornton, C. L. Searle, D. O. Pederson, R. B. Adler, and E. J. Angelo Jr., *Multistage Transistor Circuits*, New York: John Wiley & Sons, 1965, Chaps. 1 and 8.
5. H. W. Bode, *Network Analysis and Feedback Amplifier Design*, New York: Van Nostrand, 1945.
6. P. J. Hurst, A comparison of two approaches to feedback circuit analysis, *IEEE Trans. Educ.*, 35, 253–261, Aug. 1992.
7. M. S. Ghauri, *Principles and Design of Linear Active Networks*, New York: McGraw-Hill, 1965, pp. 40–56.
8. A. J. Cote Jr. and J. B. Oakes, *Linear Vacuum-Tube and Transistor Circuits*, New York: McGraw-Hill, 1961, pp. 40–46.
9. S. J. Mason, Feedback theory—Some properties of signal flow graphs, *Proc. IRE*, 41, 1144–1156, Sept. 1953.
10. S. J. Mason, Feedback theory—Further properties of signal flow graphs, *Proc. IRE*, 44, 920–926, July 1956.
11. N. Balabanian and T. A. Bickart, *Electrical Network Theory*, New York: John Wiley & Sons, 1969, pp. 639–669.
12. J. Choma Jr., Signal flow analysis of feedback networks, *IEEE Trans. Circuits Syst.*, 37, 455–463, Apr. 1990.
13. J. Choma Jr., *Electrical Networks: Theory and Analysis*, New York: Wiley Interscience, 1985, pp. 589–605.
14. P. J. Hurst, Exact simulation of feedback circuit parameters, *IEEE Trans. Circuits Syst.*, 38, 1382–1389, Nov. 1991.
15. J. Choma Jr. and S. A. Witherspoon, Computationally efficient estimation of frequency response and driving point impedance in wideband analog amplifiers, *IEEE Trans. Circuits Syst.*, 37, 720–728, June 1990.
16. R. G. Meyer and R. A. Blauschild, A wide-band low-noise monolithic transimpedance amplifier, *IEEE J. Solid-State Circuits*, SC-21, 530–533, Aug. 1986.

17. Y. P. Tsividis, Design considerations in single-channel MOS analog integrated circuits, *IEEE J. Solid-State Circuits*, SC-13, 383–391, June 1978.
18. J. J. D’Azzo and C. H. Houppis, *Feedback Control System Analysis and Synthesis*, New York: McGraw-Hill, 1960, pp. 230–234.
19. P. R. Gray and R. G. Meyer, *Analysis and Design of Analog Integrated Circuits*, New York: John Wiley & Sons, 1977, pp. 512–521.
20. P. R. Gray, Basic MOS operational amplifier design—An overview, in *Analog MOS Integrated Circuits*, P. R. Gray, D. A. Hodges, and R.W. Brodersen (Eds.), New York: IEEE, 1980, pp. 28–49.
21. J. E. Solomon, The monolithic op-amp: A tutorial study, *IEEE J. Solid-State Circuits*, SC-9, 314–332, Dec. 1974.

2

Feedback Amplifier Configurations

2.1	Introduction	2-1
2.2	Series–Shunt Feedback Amplifier.....	2-2
	Circuit Modeling and Analysis • Feed-Forward Compensation	
2.3	Shunt–Series Feedback Amplifier.....	2-10
2.4	Shunt–Shunt Feedback Amplifier	2-12
	Circuit Modeling and Analysis • Design Considerations	
2.5	Series–Series Feedback Amplifier.....	2-16
2.6	Dual-Loop Feedback	2-20
	Series–Series/Shunt–Shunt Feedback Amplifier •	
	Series–Shunt/Shunt–Series Feedback Amplifier	
2.7	Summary.....	2-28
	References.....	2-29

John Choma, Jr.
University of Southern California

2.1 Introduction

Four basic types of single-loop feedback amplifiers are available: the series–shunt, shunt–series, shunt–shunt, and series–series architectures [1]. Each of these cells is capable of a significant reduction of the dependence of forward transfer characteristics on the ill-defined or ill-controlled parameters implicit to the open-loop gain; but none of these architectures can simultaneously offer controlled driving-point input and output impedances. Such additional control is afforded only by dual global loops comprised of series and/or shunt feedback signal paths appended to an open-loop amplifier [2,3]. Only two types of global dual-loop feedback architectures are used: the series–series/shunt–shunt feedback amplifier and the series–shunt/shunt–series feedback amplifier.

Although only bipolar technology is exploited in the analysis of the aforementioned four single-loop and two dual-loop feedback cells, all disclosures are generally applicable to metal-oxide-silicon (MOS), heterostructure bipolar transistor (HBT), and III–V compound metal-semiconductor field-effect transistor (MESFET) technologies. All analytical results derive from an application of a hybrid, signal flow/two-port parameter analytical tack. Because the thought processes underlying this technical approach apply to all feedback circuits, the subject analytical procedure is developed in detail for only the series–shunt feedback amplifier.

2.2 Series–Shunt Feedback Amplifier

2.2.1 Circuit Modeling and Analysis

Figure 2.1a depicts the ac schematic diagram (a circuit diagram divorced of biasing details) of a series–shunt feedback amplifier. In this circuit, the output voltage V_O , which is established in response to a single source represented by the Thévenin voltage V_{ST} , and the Thévenin resistance, R_{ST} , is sampled by the feedback network composed of the resistances, R_{EE} and R_F . The sampled voltage is fed back in such a way that the closed-loop input voltage, V_I , is the sum of the voltage, V_{1A} , across the input port of the amplifier and the voltage V_{1F} , developed across R_{EE} in the feedback subcircuit. Because $V_I = V_{1A} + V_{1F}$, the output port of the feedback configuration can be viewed as connected in series with the amplifier input port. On the other hand, output voltage sampling constrains the net load current, I_O , to be the algebraic sum of the amplifier output port current, I_{2A} , and the feedback network input current, I_{2F} . Accordingly, the output topology is indicative of a shunt connection between the feedback subcircuit and the amplifier output port. The fact that voltage is fed back to a voltage-driven input port renders the driving-point input resistance, R_{in} , of the closed-loop amplifier large, whereas the driving-point output resistance, R_{out} , seen by the terminating load resistance, R_{LT} , is small. The resultant closed-loop amplifier

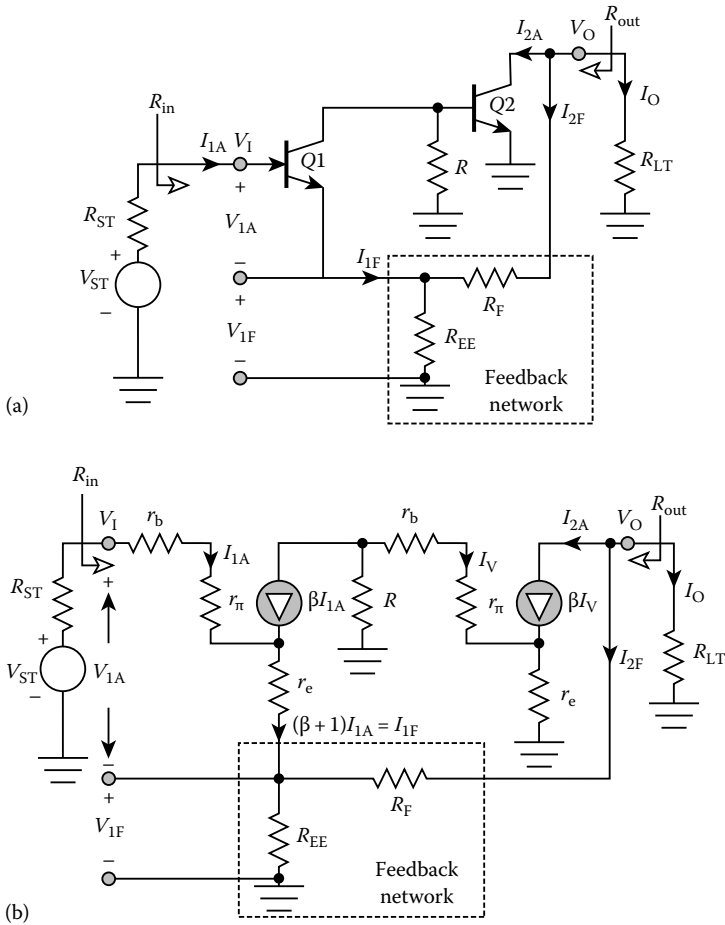


FIGURE 2.1 (a) AC schematic diagram of a bipolar series–shunt feedback amplifier. (b) Low-frequency small-signal equivalent circuit of the feedback amplifier.

is therefore best suited for voltage amplification, in the sense that the closed-loop voltage gain, V_O/V_{ST} , can be made approximately independent of source and load resistances. For large loop gain, this voltage transfer function is also nominally independent of transistor parameters.

Assuming that transistors Q1 and Q2 are identical devices that are biased identically, Figure 2.1b is the applicable low-frequency equivalent circuit. This equivalent circuit exploits the hybrid- π model [4] of a bipolar junction transistor, subject to the proviso that the forward Early resistance [5] used to emulate base conductivity modulation is sufficiently large to warrant its neglect. Because an infinitely large forward Early resistance places the internal collector resistance (not shown in the figure) of a bipolar junction transistor in series with the current-controlled current source, this collector resistance can be ignored as well.

The equivalent circuit of Figure 2.1b can be reduced to a manageable topology by noting that the ratio of the signal current, I_V , flowing into the base of transistor Q2 to the signal current, I_{1A} , flowing into the base of transistor Q1 is

$$\frac{I_V}{I_{1A}} \triangleq -K_\beta = -\frac{\beta R}{R + r_b + r_\pi + (\beta + 1)r_e} = -\frac{\alpha R}{r_{ib} + (1 - \alpha)R} \quad (2.1)$$

where

$$\alpha = \frac{\beta}{\beta + 1} \quad (2.2)$$

is the small-signal, short-circuit common base current gain, and

$$r_{ib} = r_e + \frac{r_\pi + r_b}{\beta + 1} \quad (2.3)$$

symbolizes the short-circuit input resistance of a common base amplifier. It follows that the current source βI_V in Figure 2.1b can be replaced by the equivalent current ($-\beta K_\beta I_{1A}$).

A second reduction of the equivalent circuit in Figure 2.1b results when the feedback subcircuit is replaced by a model that reflects the h -parameter relationships

$$\begin{bmatrix} V_{1F} \\ I_{2F} \end{bmatrix} = \begin{bmatrix} h_{if} & h_{rf} \\ h_{ff} & h_{of} \end{bmatrix} \begin{bmatrix} I_{1F} \\ V_O \end{bmatrix} \quad (2.4)$$

where

$V_{1F}(V_O)$ represents the signal voltage developed across the output (input) port of the feedback subcircuit

$I_{1F}(I_{2F})$ symbolizes the corresponding current flowing into the feedback output (input) port

Although any homogeneous set of two-port parameters can be used to model the feedback subcircuit, h -parameters are the most convenient selection herewith. In particular, the feedback amplifier undergoing study is a series-shunt configuration. The h -parameter equivalent circuit represents its input port as a Thévenin circuit and its output port as a Norton configuration, therefore, the h -parameter equivalent circuit is likewise a series-shunt structure.

For the feedback network at hand, which is redrawn for convenience in Figure 2.2a, the h -parameter equivalent circuit is as depicted in Figure 2.2b. The latter diagram exploits the facts that the short-circuit input resistance h_{if} is a parallel combination of the resistance R_{EE} and R_F , and the open-circuit output conductance h_{of} is $1/(R_{EE} + R_F)$. The open-circuit reverse voltage gain h_{rf} is

$$h_{rf} = \frac{R_{EE}}{R_{EE} + R_F} \quad (2.5)$$

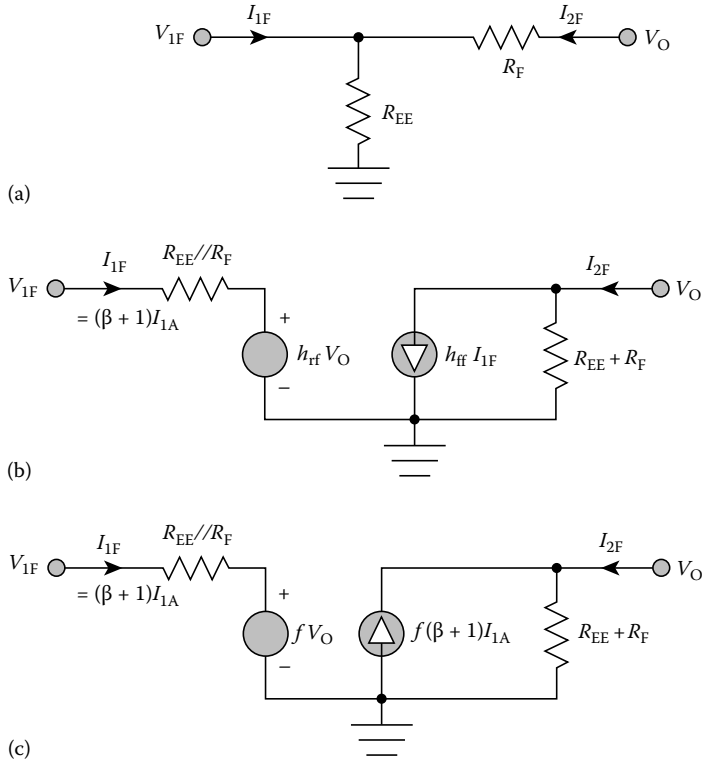


FIGURE 2.2 (a) Feedback subcircuit in the series-shunt feedback amplifier of Figure 2.1a. (b) h -Parameter equivalent circuit of the feedback subcircuit. (c) Alternative form of the h -parameter equivalent circuit.

while the short-circuit forward current gain h_{ff} is

$$h_{ff} = \frac{R_{EE}}{R_{EE} + R_F} = -h_{rf} \quad (2.6)$$

Figure 2.2c modifies the equivalent circuit in Figure 2.2b in accordance with the following two arguments. First, h_{rf} in Equation 2.5 is recognized as the fraction of the feedback subcircuit input signal that is fed back as a component of the feedback subcircuit output voltage, V_{1F} . But this subcircuit input voltage is identical to the closed-loop amplifier output signal V_O . Moreover, V_{1F} superimposes with the Thévenin input signal applied to the feedback amplifier to establish the amplifier input port voltage, V_{1A} . It follows that h_{rf} is logically referenced as a feedback factor, say f , of the amplifier under consideration; that is,

$$h_{rf} = \frac{R_{EE}}{R_{EE} + R_F} \triangleq f \quad (2.7)$$

and by Equation 2.6,

$$h_{ff} = -\frac{R_{EE}}{R_{EE} + R_F} = -f \quad (2.8)$$

Second, the feedback subcircuit output current, I_{1F} , is, as indicated in Figure 2.1b, the signal current, $(\beta + 1)I_{1A}$. Thus, in the model of Figure 2.2b,

$$h_{ff}I_{1F} = -f(\beta + 1)I_{1A} \quad (2.9)$$

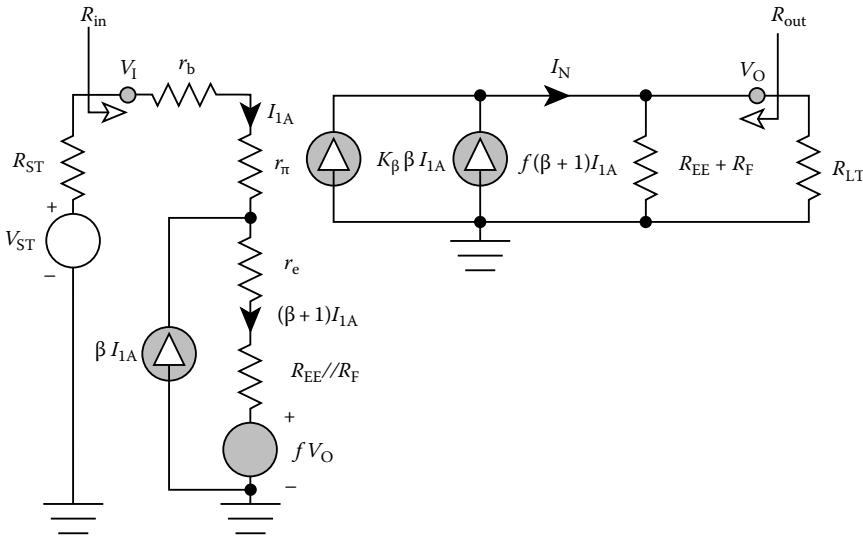


FIGURE 2.3 Modified small-signal model of the series-shunt feedback amplifier.

If the model in Figure 2.2c is used to replace the feedback network in Figure 2.1b the equivalent circuit of the series-shunt feedback amplifier becomes the alternative structure offered in Figure 2.3. In arriving at this model, care has been exercised to ensure that the current flowing through the emitter of transistor Q1 is $(\beta + 1)I_{1A}$. It is important to note that the modified equivalent circuit delivers transfer and driving-point impedance characteristics that are identical to those implicit to the equivalent circuit of Figure 2.1b. In particular, the traditional analytical approach to analyzing a series-shunt feedback amplifier tacitly presumes the satisfaction of the Brune condition [6] to formulate a composite structure where the h -parameter matrix is the sum of the respective h -parameter matrices for the open loop and feedback circuits. In contrast, the model of Figure 2.3 derives from Figure 2.1b without invoking the Brune requirement, which is often not satisfied. It merely exploits the substitution theorem; that is, the feedback network in Figure 2.1b is substituted by its h -parameter representation.

In addition to modeling accuracy, the equivalent circuit in Figure 2.3 boasts at least three other advantages. The first is an illumination of the vehicle by which feedback is implemented in the series-shunt configuration. This vehicle is the voltage-controlled voltage source, fV_O , which feeds back a fraction of the output signal to produce a branch voltage that algebraically superimposes with, and thus modifies, the applied source voltage effectively seen by the input port of the open-loop amplifier. Thus, with $f = 0$, no feedback is evidenced, and the model at hand emulates an open-loop configuration. But even with $f = 0$, the transfer and driving-point impedance characteristics of the resultant open-loop circuit are functionally dependent on the feedback elements, R_{EE} and R_F , because appending the feedback network to the open-loop amplifier incurs additional impedance loads at both the input and the output ports of the amplifier.

The second advantage of the subject model is its revelation of the magnitude and nature of feed-forward through the closed loop. In particular, note that the signal current, I_N , driven into the effective load resistance comprised of the parallel combination of $(R_{EE} + R_F)$ and R_{LT} , is the sum of two current components. One of these currents, $\beta K_\beta I_{1A}$, materializes from the transfer properties of the two transistors utilized in the amplifier. The other current, $f(\beta + 1)I_{1A}$, is the feed-forward current resulting from the bilateral nature of the passive feedback network. In general, negligible feed-forward through the feedback subcircuit is advantageous, particularly in high-frequency signal-processing applications. To this end, the model in Figure 2.3 suggests the design requirement,

$$f \ll \alpha K_\beta \tag{2.10}$$

When the resistance, R , in Figure 2.1a is the resistance associated with the output port of a PNP current source used to supply biasing current to the collector of transistor Q1 and the base of transistor Q2, K_β approaches β , and Equation 2.10 is easily satisfied; however, PNP current sources are undesirable in broadband low-noise amplifiers. In these applications, the requisite biasing current must be supplied by a passive resistance, R , connected between the positive supply voltage and the junction of the Q1 collector and the Q2 base. Unfortunately, the corresponding value of K_β can be considerably smaller than β , with the result that Equation 2.10 may be difficult to satisfy. Circumvention schemes for this situation are addressed later.

A third attribute of the model in Figure 2.3 is its disposition to an application of signal flow theory. For example, with the feedback factor f selected as the reference parameter for signal flow analysis, the open-loop voltage gain $G_{vo}(R_{ST}, R_{LT})$, of the series–shunt feedback amplifier is computed by setting f to zero. Assuming that Equation 2.10 is satisfied, circuit analysis reveals this gain as

$$G_{vo}(R_{ST}, R_{LT}) = \alpha K_\beta \left[\frac{(R_{EE} + R_F) \| R_{LT}}{r_{ib} + (1 - \alpha)R_{ST} + (R_{EE} \| R_F)} \right] \quad (2.11)$$

The corresponding input and output driving-point resistances, R_{ino} and R_{outo} , respectively, are

$$R_{ino} = r_B + r_\pi + (\beta + 1)(r_E + R_{EE} \| R_F) \quad (2.12)$$

and

$$R_{outo} = R_{EE} + R_F \quad (2.13)$$

It follows that the closed-loop gain $G_v(R_{ST}, R_{LT})$ of the series–shunt feedback amplifier is

$$G_v(R_{ST}, R_{LT}) = \frac{G_{vo}(R_{ST}, R_{LT})}{1 + T} \quad (2.14)$$

where the loop gain T is

$$\begin{aligned} T &= fG_{vo}(R_{ST}, R_{LT}) = \left(\frac{R_{EE}}{R_{EE} + R_F} \right) G_{vo}(R_{ST}, R_{LT}) \\ &= \alpha K_\beta \left(\frac{R_{EE}}{R_{EE} + R_F + R_{LT}} \right) \left[\frac{R_{LT}}{r_{ib} + (1 - \alpha)R_{ST} + (R_{EE} \| R_F)} \right] \end{aligned} \quad (2.15)$$

For $T \gg 1$, which mandates a sufficiently large K_β in Equation 2.11, the closed-loop gain collapses to

$$G_v(R_{ST}, R_{LT}) \approx \frac{1}{f} = 1 + \frac{R_F}{R_{EE}} \quad (2.16)$$

which is independent of active element parameters. Moreover, to the extent that $T \gg 1$ the series–shunt feedback amplifier behaves as an ideal voltage-controlled voltage source in the sense that its closed-loop voltage gain is independent of source and load terminations. The fact that the series–shunt feedback network behaves approximately as an ideal voltage amplifier implies that its closed-loop driving-point input resistance is very large and its closed-loop driving-point output resistance is very small. These facts are confirmed analytically by noting that

$$\begin{aligned} R_{in} &= R_{ino}[1 + fG_{vo}(0, R_L)] \approx fR_{ino}G_{vo}(0, R_L) \\ &= \beta K_\beta \left(\frac{R_{EE}}{R_{EE} + R_F + R_{LT}} \right) R_{LT} \end{aligned} \quad (2.17)$$

and

$$R_{out} = \frac{R_{outo}}{1 + fG_{vo}(R_S, \infty)} \approx \frac{R_{outo}}{fG_{vo}(R_S, \infty)} = \left(1 + \frac{R_F}{R_{EE}}\right) \left[\frac{r_{ib} + (1 - \alpha)R_{ST} + R_{EE} \parallel R_F}{\alpha K_\beta}\right] \tag{2.18}$$

To the extent that the interstage biasing resistance, R , is sufficiently large to allow K_β to approach β , observe that R_{in} in Equation 2.17 is nominally proportional to β^2 , while R_{out} in Equation 2.18 is inversely proportional to β .

2.2.2 Feed-Forward Compensation

When practical design restrictions render the satisfaction of Equation 2.10 difficult, feed-forward problems can be circumvented by inserting an emitter follower between the output port of transistor $Q2$ in the circuit diagram of Figure 2.1a and the node to which the load termination and the input terminal of the feedback subcircuit are incident [2]. The resultant circuit diagram, inclusive now of simple biasing subcircuits, is shown in Figure 2.4. The buffer transistor $Q3$ increases the original short-circuit forward current gain, $K_\beta\beta$, of the open-loop amplifier by a factor approaching $(\beta + 1)$, while not altering the feed-forward factor implied by the feedback network in Figure 2.1a. In effect, K_β is increased by a factor of almost $(\beta + 1)$, thereby making Equation 2.10 easy to satisfy. Because of the inherently low output resistance of an emitter follower, the buffer also reduces the driving-point output resistance achievable by the original configuration.

The foregoing contentions can be confirmed through an analysis of the small-signal model for the modified amplifier in Figure 2.4. Such an analysis is expedited by noting that the circuit to the left of the current-controlled current source, $K_\beta\beta I_{1A}$, in Figure 2.3 remains applicable. For zero feedback, it follows that the small-signal current I_{1A} flowing into the base of transistor $Q1$ derives from

$$\left.\frac{I_{1A}}{V_{ST}}\right|_{f=0} = \frac{1 - \alpha}{r_{ib} + (1 - \alpha)R_{ST} + (R_{EE} \parallel R_F)} \tag{2.19}$$

The pertinent small-signal model for the buffered series–shunt feedback amplifier is resultantly the configuration offered in Figure 2.5.

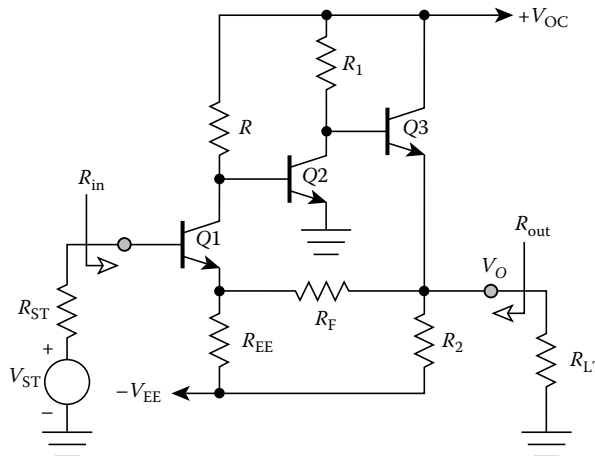


FIGURE 2.4 Series–shunt feedback amplifier that incorporates an emitter follower output stage to reduce the effects of feed-forward through the feedback network.

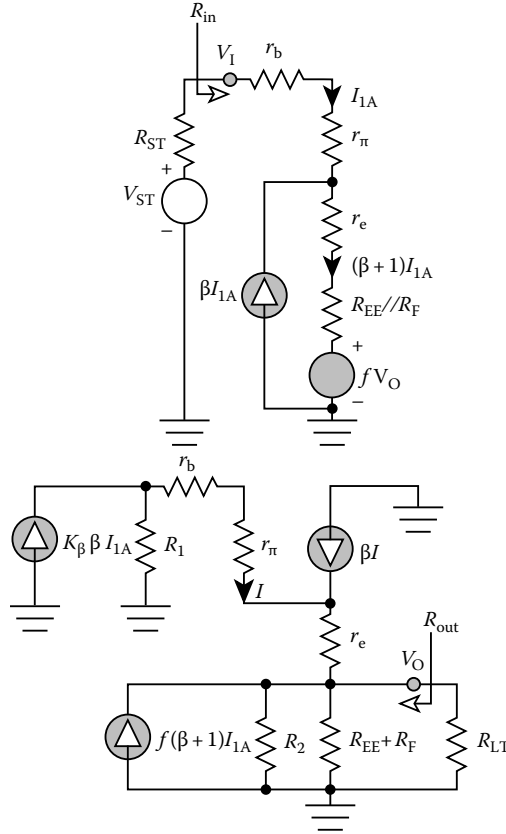


FIGURE 2.5 Small-signal model of the buffered series-shunt feedback amplifier.

Letting

$$R' = R_2 \parallel (R_{EE} + R_F) \parallel R_{LT} \quad (2.20)$$

an analysis of the structure in Figure 2.5 reveals

$$\frac{V_O}{I_{1A}} = (\beta + 1) \left[\frac{R'}{R' + r_{ib} + (1 - \alpha)R_1} \right] \{ \alpha K_\beta R_1 + f[r_{ib} + (1 - \alpha)R_1] \} \quad (2.21)$$

which suggests negligible feed-forward for

$$f \ll \frac{\alpha K_\beta R_1}{r_{ib} + (1 - \alpha)R_1} \quad (2.22)$$

Note that for large R_1 , Equation 2.22 implies the requirement $f \ll \beta K_\beta$, which is easier to satisfy than is Equation 2.10. Assuming the validity of Equations 2.19, 2.21, and 2.22 deliver an open-loop voltage gain, $G_{v_o}(R_{ST}, R_{LT})$, of

$$G_{v_o}(R_{ST}, R_{LT}) = \alpha K_\beta \left[\frac{R'}{r_{ib} + (1 - \alpha)R_{ST} + R_{EE} \parallel R_F} \right] \left[\frac{R_1}{R' + r_{ib} + (1 - \alpha)R_1} \right] \quad (2.23)$$

Recalling Equation 2.1, which demonstrates that K_{β} approaches β for large R , Equation 2.23 suggests an open-loop gain that is nominally proportional to β^2 if R_1 is also large.

Using the concepts evoked by Equations 2.17 and 2.18, the driving-point input and output impedances can now be determined. In a typical realization of the buffered series–shunt feedback amplifier, the resistance, R_2 , in Figure 2.4 is very large because it is manifested as the output resistance of a common base current sink that is employed to stabilize the operating point of transistor Q3. For this situation, and assuming the resistance R_1 is large, the resultant driving-point input resistance is larger than its predecessor input resistance by a factor of approximately $(\beta + 1)$. Similarly, it is easy to show that for large R_1 and large R_2 , the driving-point output resistance is smaller than that predicted by Equation 2.18 by a factor approaching $(\beta + 1)$.

Although the emitter follower output stage in Figure 2.4 all but eliminates feed-forward signal transmission through the feedback network and increases both the driving-point input resistance and output conductance, a potential bandwidth penalty is paid by its incorporation into the basic series–shunt feedback cell. The fundamental problem is that if R_1 is too large, potentially significant Miller multiplication of the base–collector transition capacitance of transistor Q2 materializes. The resultant capacitive loading at the collector of transistor Q1 is exacerbated by large R , which may produce a dominant pole at a frequency that is too low to satisfy closed-loop bandwidth requirements. The bandwidth problem may be mitigated by coupling resistance R_1 to the collector of Q2 through a common base cascode. This stage appears as transistor Q4 in Figure 2.6.

Unfortunately, the use of the common base cascode indicated in Figure 2.6 may produce an open-loop amplifier with transfer characteristics that do not emulate a dominant pole response. In other words, the frequency of the compensated pole established by capacitive loading at the collector of transistor Q1 may be comparable to the frequencies of poles established elsewhere in the circuit, and particularly at the base node of transistor Q1. In this event, frequency compensation aimed toward achieving acceptable closed-loop damping can be implemented by replacing the feedback resistor R_F with the parallel combination of R_F and a feedback capacitance, say C_F , as indicated by the dashed branch in Figure 2.6. The resultant frequency-domain feedback factor $f(s)$ is

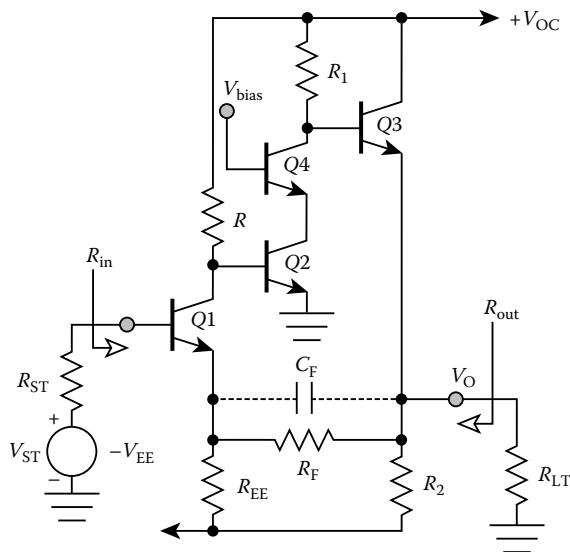


FIGURE 2.6 Buffered series–shunt feedback amplifier with common base cascode compensation of the common emitter amplifier formed by transistor Q2. A feedback zero is introduced by the capacitance C_F to achieve acceptable closed-loop damping.

$$f(s) = f \left[\frac{1 + \frac{s}{z}}{1 + \frac{s}{p}} \right] \tag{2.24}$$

where

f is the feedback factor given by Equation 2.7

z is the frequency of the introduced compensating zero

$$z = \frac{1}{R_F C_F} \tag{2.25}$$

The pole in Equation 2.24 is inconsequential if the closed-loop amplifier bandwidth B_{cl} satisfies the restriction, $fB_{cl}R_FC_F = B_{cl}(R_{EE}||R_F)C_F \ll 1$.

2.3 Shunt-Series Feedback Amplifier

Although the series-shunt circuit functions as a voltage amplifier, the shunt-series configuration (see the ac schematic diagram depicted in Figure 2.7a) is best suited as a current amplifier. In the subject circuit,

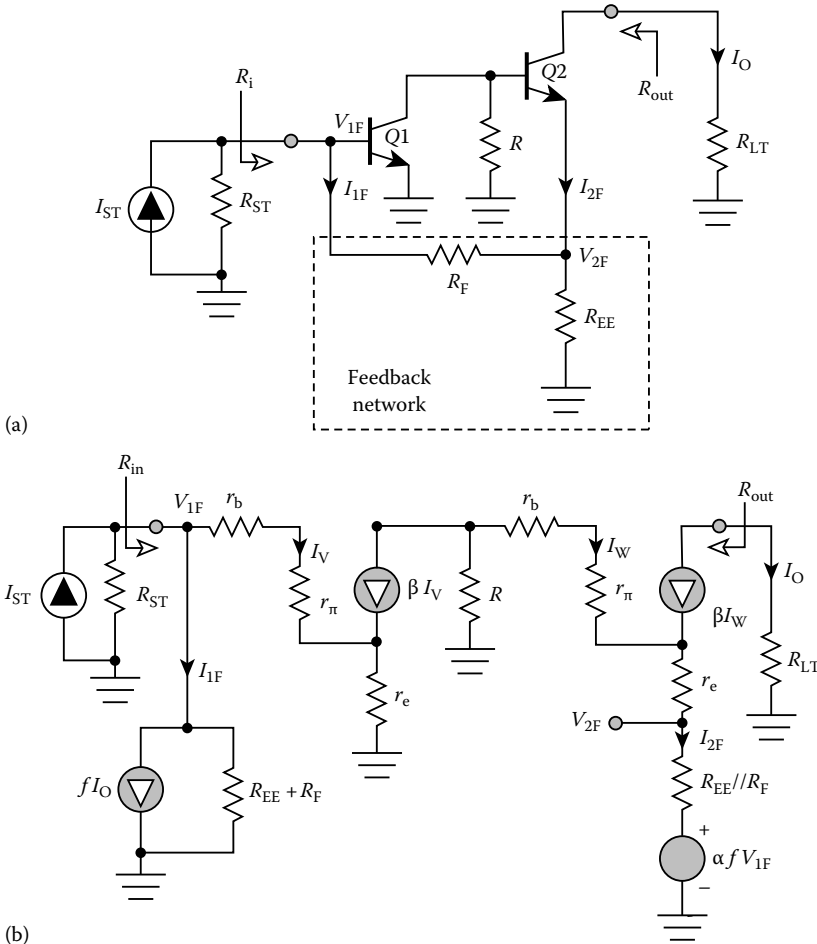


FIGURE 2.7 (a) AC schematic diagram of a bipolar shunt-series feedback amplifier. (b) Low-frequency small-signal equivalent circuit of the feedback amplifier.

the Q2 emitter current, which is a factor of $(1/\alpha)$ of the output signal current, I_O , is sampled by the feedback network formed of the resistances, R_{EE} and R_F . The sampled current is fed back as a current in shunt with the amplifier input port. Because output current is fed back as a current to a current-driven input port, the resultant driving-point output resistance is large, and the driving-point input resistance is small. These characteristics allow for a closed-loop current gain, $G_1(R_{ST}, R_{LT}) = I_O/I_{ST}$, that is relatively independent of source and load resistances and insensitive to transistor parameters.

In the series–shunt amplifier, h -parameters were selected to model the feedback network because the topology of an h -parameter equivalent circuit is, similar to the amplifier in which the feedback network is embedded, a series shunt, or Thévenin–Norton, topology. In analogous train of thought compels the use of g -parameters to represent the feedback network in Figure 2.7a. With reference to the branch variables defined in the schematic diagram,

$$\begin{bmatrix} I_{1F} \\ V_{2F} \end{bmatrix} = \begin{bmatrix} \frac{1}{R_{EE}+R_F} & -\frac{R_{EE}}{R_{EE}+R_F} \\ \frac{R_{EE}}{R_{EE}+R_F} & R_{EE}\|R_F \end{bmatrix} \begin{bmatrix} V_{1F} \\ I_{2F} \end{bmatrix} \quad (2.26)$$

Noting that the feedback network current, I_{2F} , relates to the amplifier output current, I_O , in accordance with

$$I_{2F} = -\frac{I_O}{\alpha} \quad (2.27)$$

and letting the feedback factor, f , be

$$f = \frac{1}{\alpha} \left(\frac{R_{EE}}{R_{EE} + R_F} \right) \quad (2.28)$$

the small-signal equivalent circuit of shunt–series feedback amplifier becomes the network diagrammed in Figure 2.7b. Note that the voltage-controlled voltage source, $\alpha f V_{1F}$, models the feed-forward transfer mechanism of the feedback network, where the controlling voltage, V_{1F} , is

$$V_{1F} = [r_b + r_\pi + (\beta + 1)r_c]I_V = (\beta + 1)r_{ib}I_V \quad (2.29)$$

An analysis of the model in Figure 2.7b confirms that the second-stage, signal-base current I_W relates to the first-stage, signal-base current I_V as

$$\frac{I_W}{I_V} = -\frac{\alpha(R + fr_{ib})}{r_{ib} + R_{EE}\|R_F + (1 - \alpha)R} \quad (2.30)$$

For

$$f \ll \frac{R}{r_{ib}} \quad (2.31)$$

which offsets feed-forward effects,

$$\frac{I_W}{I_V} \approx -\frac{\alpha R}{r_{ib} + R_{EE}\|R_F + (1 - \alpha)R} \triangleq -K_r \quad (2.32)$$

Observe that the constant K_r tends toward β for large R , as can be verified by an inspection of Figure 2.7b.

Using Equation 2.32, the open-loop current gain, found by setting f to zero, is

$$G_{\text{IO}}(R_{\text{ST}}, R_{\text{LT}}) = \frac{I_{\text{O}}}{I_{\text{ST}}} \Big|_{f=0} = \alpha K_{\text{r}} \left\{ \frac{R_{\text{ST}} \parallel (R_{\text{EE}} + R_{\text{F}})}{r_{\text{ib}} + (1 - \alpha) [R_{\text{ST}} \parallel (R_{\text{EE}} + R_{\text{F}})]} \right\} \quad (2.33)$$

and recalling Equation 2.28, the loop gain T is

$$\begin{aligned} T &= f G_{\text{IO}}(R_{\text{ST}}, R_{\text{LT}}) = \frac{1}{\alpha} \left(\frac{R_{\text{EE}}}{R_{\text{EE}} + R_{\text{F}}} \right) G_{\text{IO}}(R_{\text{ST}}, R_{\text{LT}}) \\ &= K_{\text{r}} \left(\frac{R_{\text{EE}}}{R_{\text{EE}} + R_{\text{F}} + R_{\text{ST}}} \right) \left\{ \frac{R_{\text{ST}}}{r_{\text{ib}} + (1 - \alpha) [R_{\text{ST}} \parallel (R_{\text{EE}} + R_{\text{F}})]} \right\} \end{aligned} \quad (2.34)$$

By inspection of the model in Figure 2.7b, the open-loop input resistance, R_{ino} , is

$$R_{\text{ino}} = (R_{\text{EE}} + R_{\text{F}}) [(\beta + 1)r_{\text{ib}}] \quad (2.35)$$

and, within the context of an infinitely large Early resistance, the open-loop output resistance, R_{outo} , is infinitely large.

The closed-loop current gain of the shunt-series feedback amplifier is now found to be

$$G_{\text{I}}(R_{\text{ST}}, R_{\text{LT}}) = \frac{G_{\text{IO}}(R_{\text{ST}}, R_{\text{LT}})}{1 + T} \approx \alpha \left(1 + \frac{R_{\text{F}}}{R_{\text{EE}}} \right) \quad (2.36)$$

where the indicated approximation exploits the presumption that the loop gain T is much larger than one. As a result of the large loop-gain assumption, note that the closed-loop gain is independent of the source and load resistances and is invulnerable to uncertainties and perturbations in transistor parameters. The closed-loop output resistance, which exceeds its open-loop counterpart, remains infinitely large. Finally, the closed-loop driving-point input resistance of the shunt-series amplifier is

$$R_{\text{in}} = \frac{R_{\text{ino}}}{1 + f G_{\text{IO}}(\infty, R_{\text{LT}})} \approx \left(1 + \frac{R_{\text{F}}}{R_{\text{EE}}} \right) \frac{r_{\text{ib}}}{K_{\text{r}}} \quad (2.37)$$

2.4 Shunt-Shunt Feedback Amplifier

2.4.1 Circuit Modeling and Analysis

The ac schematic diagram of the third type of single-loop feedback amplifier, the shunt-shunt triple, is drawn in Figure 2.8a. A cascade interconnection of three transistors Q1, Q2, and Q3, forms the open loop, while the feedback subcircuit is the single resistance, R_{F} . This resistance samples the output voltage, V_{O} , as a current fed back to the input port. Output voltage is fed back as a current to a current-driven input port, so both the driving-point input and output resistances are very small. Accordingly, the circuit operates best as a transresistance amplifier in that its closed-loop transresistance, $R_{\text{M}}(R_{\text{ST}}, R_{\text{LT}}) = V_{\text{O}}/I_{\text{ST}}$, is nominally invariant with source resistance, load resistance, and transistor parameters.

The shunt-shunt nature of the subject amplifier suggests the propriety of y -parameter modeling of the feedback network. For the electrical variables indicated in Figure 2.8a,

$$\begin{bmatrix} I_{1\text{F}} \\ I_{2\text{F}} \end{bmatrix} = \begin{bmatrix} \frac{1}{R_{\text{F}}} & -\frac{1}{R_{\text{F}}} \\ -\frac{1}{R_{\text{F}}} & \frac{1}{R_{\text{F}}} \end{bmatrix} \begin{bmatrix} V_{1\text{F}} \\ V_{\text{O}} \end{bmatrix} \quad (2.38)$$

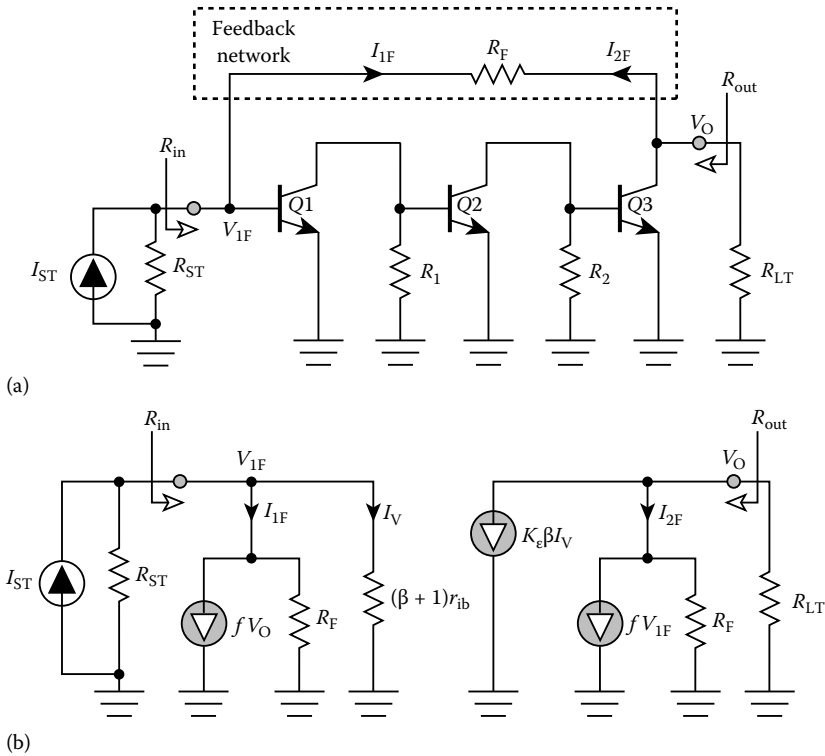


FIGURE 2.8 (a) AC schematic diagram of a bipolar shunt-shunt feedback amplifier. (b) Low-frequency small-signal equivalent circuit of the feedback amplifier.

which implies that a resistance, R_F , loads both the input and the output ports of the open-loop three-stage cascade. The short-circuit admittance relationship in Equation 2.38 also suggests a feedback factor, f , given by

$$f = \frac{1}{R_F} \tag{2.39}$$

The foregoing observations and the small-signal modeling experience gained with the preceding two feedback amplifiers lead to the equivalent circuit submitted in Figure 2.8b. For analytical simplicity, the model reflects the assumption that all three transistors in the open loop have identical small-signal parameters. Moreover, the constant, K_e , which symbolizes the ratio of the signal-base current flowing into transistor Q3 to the signal-base current conducted by transistor Q1, is given by

$$K_e = \left[\frac{\alpha R_1}{r_{ib} + (1 - \alpha)R_1} \right] \left[\frac{\alpha R_2}{r_{ib} + (1 - \alpha)R_2} \right] \tag{2.40}$$

Finally, the voltage-controlled current source, fV_{1F} , accounts for feed-forward signal transmission through the feedback network. If such feed-forward is to be negligible, the magnitude of this controlled current must be significantly smaller than $K_e\beta I_V$, a current that emulates feed-forward through the open-loop amplifier. Noting that the input port voltage, V_{1F} , in the present case remains the same as that specified by Equation 2.29, negligible feed-forward through the feedback network mandates

$$R_F \gg \frac{r_{ib}}{\alpha K_e} \tag{2.41}$$

Because the constant K_e in Equation 2.40 tends toward β^2 if R_1 and R_2 are large resistances, Equation 2.41 is relatively easy to satisfy.

With feed-forward through the feedback network ignored, an analysis of the model in Figure 2.8b provides an open-loop transresistance, $R_{MO}(R_{ST}, R_{LT})$, of

$$R_{MO}(R_{ST}, R_{LT}) = -\alpha K_e \left[\frac{R_F \parallel R_{ST}}{r_{ib}(1 - \alpha)(R_F \parallel R_{ST})} \right] (R_F \parallel R_{LT}) \quad (2.42)$$

while the loop gain is

$$\begin{aligned} T &= fR_{MO}(R_{ST}, R_{LT}) = -\frac{R_{MO}(R_{ST}, R_{LT})}{R_F} \\ &= \alpha K_e \left[\frac{R_{ST}}{R_{ST} + R_F} \right] \left[\frac{R_F \parallel R_{ST}}{r_{ib}(1 - \alpha)(R_F \parallel R_{ST})} \right] \end{aligned} \quad (2.43)$$

For $T \gg 1$, the corresponding closed-loop transresistance $R_M(R_{ST}, R_{LT})$ is

$$R_M(R_{ST}, R_{LT}) = \frac{R_{MO}(R_{ST}, R_{LT})}{1 + T} \approx -R_F \quad (2.44)$$

Finally, the approximate driving-point input and output resistances are, respectively,

$$R_{in} \approx \left(\frac{r_{ib}}{\alpha K_e} \right) \left(1 + \frac{R_F}{R_{LT}} \right) \quad (2.45)$$

$$R_{out} \approx \left[\frac{r_{ib} + (1 - \alpha)(R_F \parallel R_{ST})}{\alpha K_e} \right] \left(1 + \frac{R_F}{R_{ST}} \right) \quad (2.46)$$

2.4.2 Design Considerations

Because the shunt–shunt triple uses three gain stages in the open-loop amplifier, its loop gain is significantly larger than the loop gains provided by either of the previously considered feedback cells. Accordingly, the feedback triple affords superior desensitization of the closed-loop gain with respect to transistor parameters and source and load resistances; but the presence of a cascade of three common emitter gain stages in the open loop of the amplifier complicates frequency compensation and limits the 3 dB bandwidth. The problem is that, although each common emitter stage approximates a dominant pole amplifier, none of the critical frequencies in the cluster of poles established by the cascade interconnection of these units is likely to be dominant. The uncompensated closed loop is therefore predisposed to unacceptable underdamping, thereby making compensation via an introduced feedback zero difficult.

At least three compensation techniques can be exploited to optimize the performance of the shunt–shunt feedback amplifier [3,7–9]. The first of these techniques entail pole splitting of the open-loop interstage through the introduction of a capacitance, C_c , between the base and the collector terminals of transistor Q_2 , as depicted in the ac schematic diagram of Figure 2.9. In principle, pole splitting can be invoked on any one of the three stages of the open loop; but pole splitting of the interstage is most desirable because such compensation of the first stage proves effective only for large source resistance. Moreover, the resultant dominant pole becomes dependent on the source termination. On the other hand, pole splitting of the third stage produces a dominant pole that is sensitive to load termination. In conjunction with pole splitting, a feedback zero can be introduced, if necessary, to increase closed-loop damping by replacing the feedback resistance, R_F , by the parallel combination of R_F and a feedback

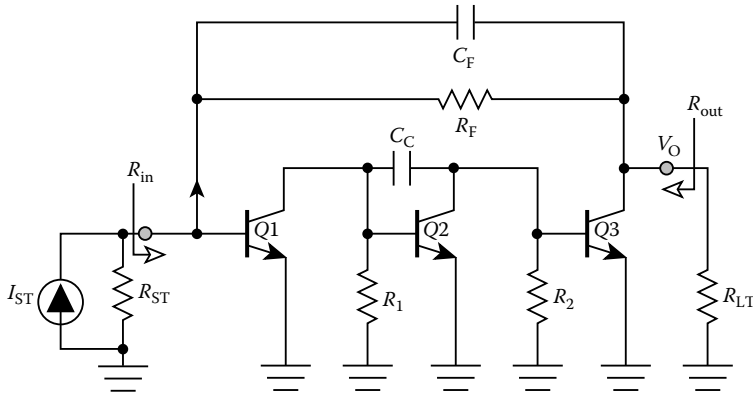


FIGURE 2.9 AC schematic diagram of a frequency-compensated shunt-shunt triple. The capacitance, C_C , achieves open-loop pole splitting, while the capacitance, C_F , implements a compensating feedback network zero.

capacitance, C_F , as illustrated in Figure 2.9. This compensation produces left-half-plane zero in the feedback factor at $s = -(1/R_F)$.

A second compensation method broadbands the interstage of the open-loop amplifier through local current feedback introduced by the resistance, R_X , in Figure 2.10. Simultaneously, the third stage is broadbanded by way of a common base cascode transistor Q4. Because emitter degeneration of the interstage reduces the open-loop gain, an emitter follower (transistor Q5) is embedded between the feedback network and the output port of the open-loop third stage. As in the case of the series-shunt feedback amplifier, the first-order effect of this emitter follower is to increase feed-forward signal transmission through the open-loop amplifier by a factor that approaches $(\beta + 1)$.

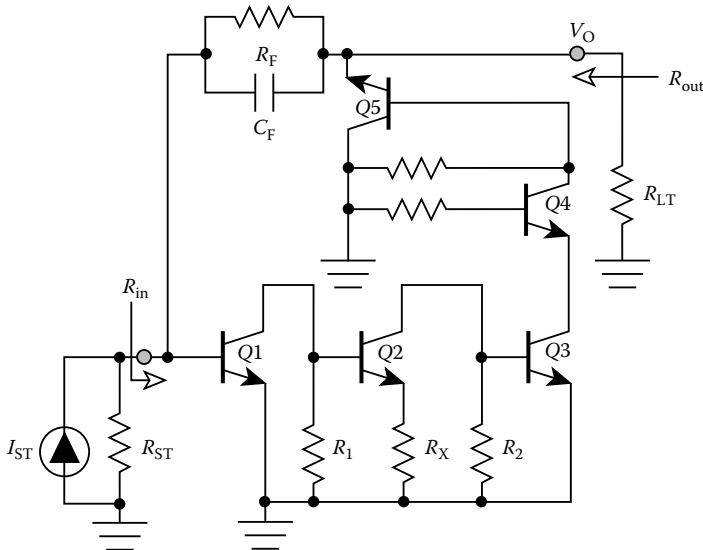


FIGURE 2.10 AC schematic diagram of an alternative compensation scheme for the shunt-shunt triple. Transistor Q2 is broadbanded by the emitter degeneration resistance R_X and transistor Q3 is broadbanded by the common base cascode transistor Q4. The emitter follower transistor, Q5, minimizes feed-forward signal transmission through the feedback network.

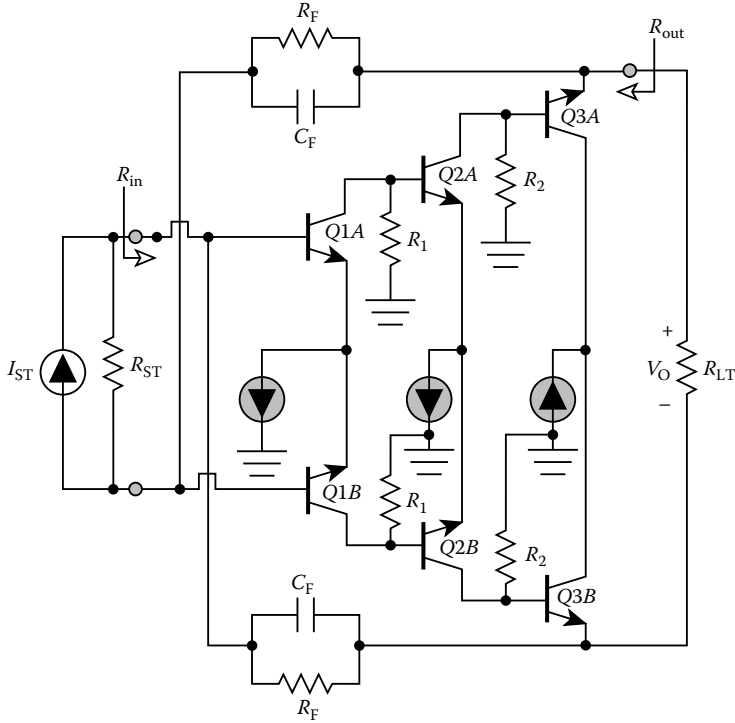


FIGURE 2.11 AC schematic diagram of a differential realization of the compensated shunt-shunt feedback amplifier. The balanced stage boasts improved bandwidth over its single-ended counterpart because of its use of only two high-gain stages in the open loop. The emitter follower pair Q3A and Q3B diminishes feed-forward transmission through the feedback network composed of the shunt interconnection of resistor R_F with capacitor C_F .

A final compensation method is available if shunt-shunt feedback is implemented as the balanced differential architecture (see the ac schematic diagram offered in Figure 2.11). By exploiting the antiphase nature of opposite collectors in a balanced common emitter topology, a shunt-shunt feedback amplifier can be realized with only two gain stages in the open loop. The resultant closed-loop 3 dB bandwidth is invariably larger than that of its three-stage single-ended counterpart, because the open loop is now characterized by only two, as opposed to three, fundamental critical frequencies. Because the forward gain implicit to two amplifier stages is smaller than the gain afforded by three stages of amplification, a balanced emitter follower (transistors Q3A and Q3B) is incorporated to circumvent the deleterious relative effects of feed-forward signal transmission through the feedback network.

2.5 Series-Series Feedback Amplifier

Figure 2.12a is the ac schematic diagram of the series-series feedback amplifier. Three transistors, Q1, Q2, and Q3, are embedded in the open-loop amplifier, while the feedback subcircuit is the wye configuration formed of the resistances R_X , R_Y , and R_Z . Although it is possible to realize series-series feedback via emitter degeneration of a single-stage amplifier, the series-series triple offers substantially more loop gain and thus better desensitization of the forward gain with respect to both transistor parameters and source and load terminations.

In Figure 2.12a, the feedback wye senses the Q3 emitter current, which is a factor of $(1/\alpha)$ of the output signal current I_O . This sampled current is fed back as a voltage in series with the emitter of Q1. Because output current is fed back as a voltage to a voltage-driven input port, both the driving-point input and

output resistances are large. The circuit is therefore best suited as a transconductance amplifier in the sense that for large loop gain, its closed-loop transconductance, $G_M(R_{ST}, R_{LT}) = I_O/V_{ST}$, is almost independent of the source and load resistances.

The series-series topology of the subject amplifier conduces z -parameter modeling of the feedback network. Noting the electrical variables delineated in the diagram of Figure 2.12a,

$$\begin{bmatrix} V_{1F} \\ V_{2F} \end{bmatrix} = \begin{bmatrix} R_X + R_Z & R_Z \\ R_Z & R_Y + R_Z \end{bmatrix} \begin{bmatrix} I_{1F} \\ I_{2F} \end{bmatrix} \tag{2.47}$$

Equation 2.47 suggests that the open-circuit feedback network resistances loading the emitters of transistors Q1 and Q3 are $(R_X + R_Z)$ and $(R_Y + R_Z)$, respectively, and the voltage fed back to the emitter of transistor Q1 is $R_Z I_{2F}$. Because the indicated feedback network current I_{2F} is $(-I_O/\alpha)$, this fed back voltage is equivalent to $(-R_Z I_O/\alpha)$, which suggests a feedback factor, f , of

$$f = \frac{R_Z}{\alpha} \tag{2.48}$$

Finally, the feed-forward through the feedback network if $R_Z I_{1F}$. Because I_{1F} relates to the signal-base current I_V flowing into transistor Q1 by $I_{1F} = (\beta + 1)I_V$, this feed-forward voltage is also expressible

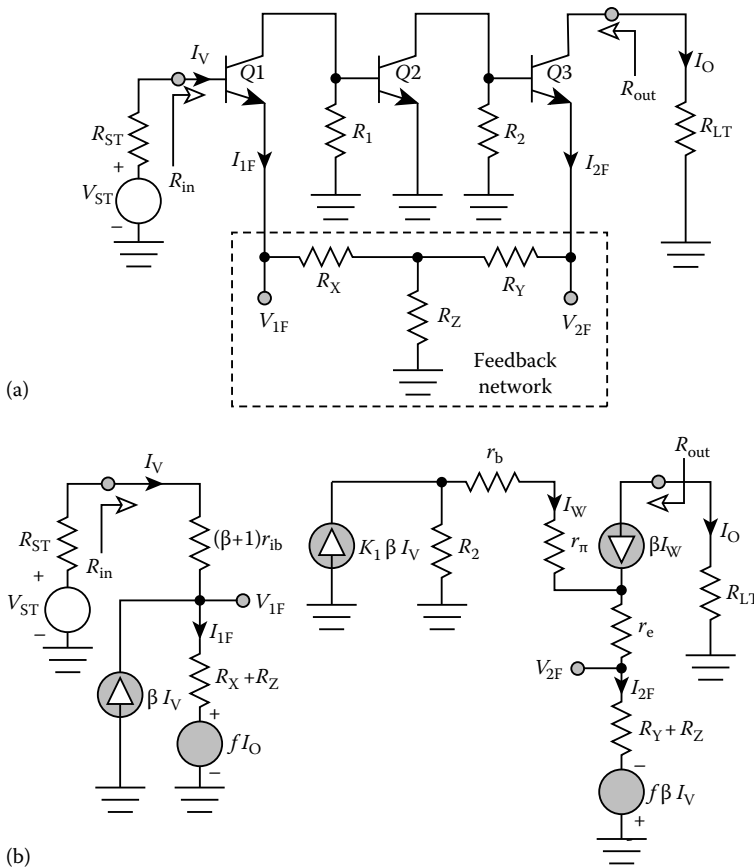


FIGURE 2.12 (a) AC schematic diagram of a bipolar series-series feedback amplifier. (b) Low-frequency, small-signal equivalent circuit of the feedback amplifier.

as $(-f\beta I_V)$. The foregoing observations and the hybrid- π method of a bipolar junction transistor produce the small-signal model depicted in Figure 2.12b. In this model, all transistors are presumed to have identical corresponding small-signal parameters, and the constant, K_1 , is

$$K_1 = \frac{\alpha R_1}{r_{ib} + (1 - \alpha)R_1} \quad (2.49)$$

An analysis of the model of Figure 2.12b confirms that the ratio of the signal current, I_W , flowing into the base of transistor Q3 to the signal-base current, I_V , of transistor Q1 is

$$\frac{I_W}{I_V} = \frac{\alpha K_1 R_2 \left(1 + \frac{f}{K_1 R_2}\right)}{r_{ib} + R_Y + R_Z + (1 - \alpha)R_2} \quad (2.50)$$

This result suggests that feed-forward effects through the feedback network are negligible if $|f| \ll K_1 R_2$, which requires

$$R_Z \ll \alpha K_1 R_2 \quad (2.51)$$

In view of the fact that the constant, K_1 , approaches β for large values of the resistance, R_1 , Equation 2.51 is not a troublesome inequality. Introducing a second constant, K_2 , such that

$$K_2 \triangleq \frac{\alpha R_2}{r_{ib} + R_Y + R_Z + (1 - \alpha)R_2} \quad (2.52)$$

the ratio I_W/I_V in Equation 2.50 becomes

$$\frac{I_W}{I_V} \approx K_1 K_2 \quad (2.53)$$

assuming Equation 2.51 is satisfied.

Given the propriety of Equation 2.50 and using Equation 2.53 the open-loop transconductance, $G_{MO}(R_{ST}, R_{LT})$ is found to be

$$G_{MO}(R_{ST}, R_{LT}) = - \left\{ \frac{\alpha K_1 K_2}{r_{ib} + R_X + R_Z + (1 - \alpha)R_{ST}} \right\} \quad (2.54)$$

and recalling Equation 2.48, the loop gain T is

$$T = - \left(\frac{R_Z}{\alpha} \right) G_{MO}(R_{ST}, R_{LT}) = \frac{K_1 K_2 R_Z}{r_{ib} + R_X + R_Z + (1 - \alpha)R_{ST}} \quad (2.55)$$

It follows that for $T \gg 1$, the closed-loop transconductance is

$$G_M(R_{ST}, R_{LT}) = \frac{G_{MO}(R_{ST}, R_{LT})}{1 + T} \approx - \frac{\alpha}{R_Z} \quad (2.56)$$

The Early resistance is large enough to justify its neglect, so the open loop, and thus the closed-loop, driving-point output resistances are infinitely large. On the other hand, the closed-loop driving-point input resistance R_{in} can be shown to be

$$R_{in} = R_{ino}[1 + fG_{MO}(0, R_{LT})] \approx (\beta + 1)K_1 K_2 R_Z \quad (2.57)$$

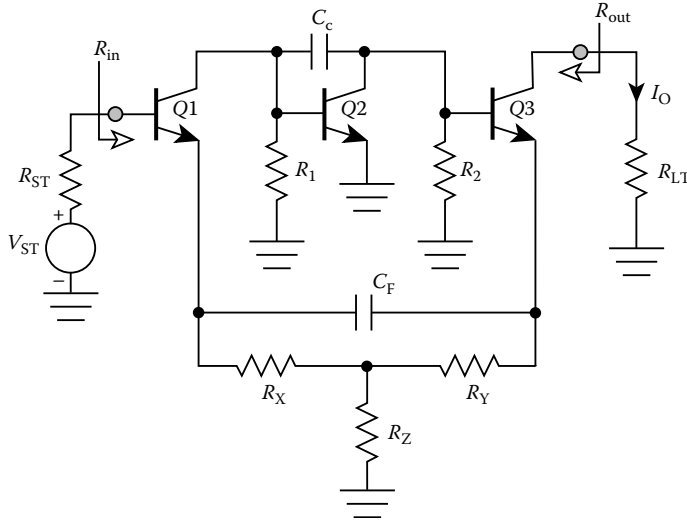


FIGURE 2.13 AC schematic diagram of a frequency-compensated series-series feedback triple. The capacitance, C_c , achieves pole splitting in the open-loop configuration, while the capacitance, C_F , introduces a zero in the feedback factor of the closed-loop amplifier.

Similar to its shunt-shunt counterpart, the series-series feedback amplifier uses three open-loop gain stages to produce large loop gain. However, also similar to the shunt-shunt triple, frequency compensation via an introduced feedback zero is difficult unless design care is exercised to realize a dominant pole open-loop response. To this end, the most commonly used compensation is pole splitting in the open loop, combined, if required, with the introduction of a zero in the feedback factor. The relevant ac schematic diagram appears in Figure 2.13 where the indicated capacitance, C_c , inserted across the base-collector terminals of transistor Q3 achieves the aforementioned pole splitting compensation. The capacitance, C_F , in Figure 2.13 delivers a frequency-dependent feedback factor, $f(s)$ of

$$f(s) = f \left[\frac{1 + \frac{s}{z}}{1 + \frac{s}{z} \left(\frac{R_Z}{R_Z + R_X \parallel R_Y} \right)} \right] \quad (2.58)$$

where the frequency z of the introduced zero derives from

$$\frac{1}{z} = (R_X + R_Y) \left(1 + \frac{R_X \parallel R_Y}{R_Z} \right) C_F \quad (2.59)$$

The corresponding pole in Equation 2.58 is insignificant if the closed-loop amplifier is designed for a bandwidth, B_{cl} that satisfies the inequality, $B_{cl}(R_X + R_Y)C_F \ll 1$.

As is the case with shunt-shunt feedback, an alternative frequency compensation scheme is available if series-series feedback is implemented as a balanced differential architecture. The pertinent ac schematic diagram, inclusive of feedback compensation, appears in Figure 2.14. This diagram exploits the fact that the feedback wye consisting of the resistances, R_X , R_Y , and R_Z as utilized in the single-ended configurations of Figures 2.12a and 2.13 can be transformed into the feedback delta of Figure 2.15. The terminal volt-ampere characteristics of the two networks in Figure 2.15 are identical, provided that the delta subcircuit elements, R_F , R_U , and R_V , are chosen in accordance with

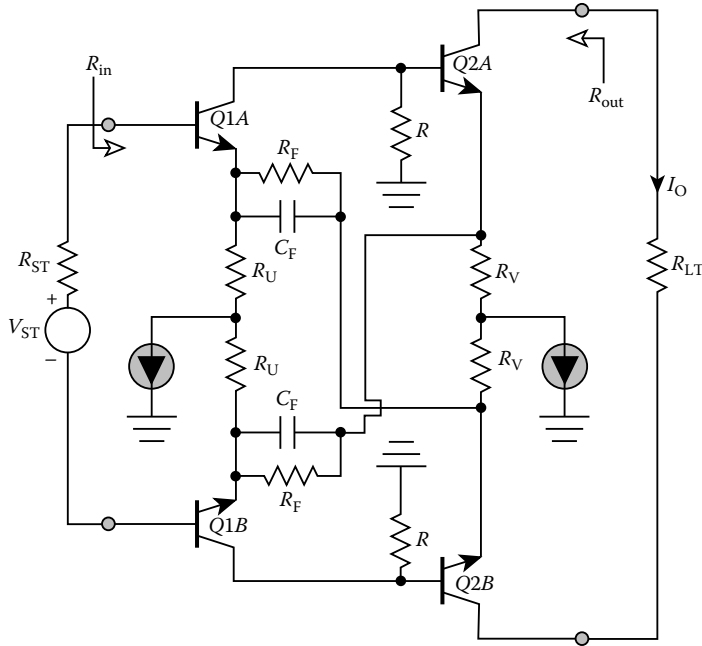


FIGURE 2.14 AC schematic diagram of a balanced differential version of the series-series feedback amplifier. The circuit utilizes only two, as opposed to three, gain stages in the open loop.

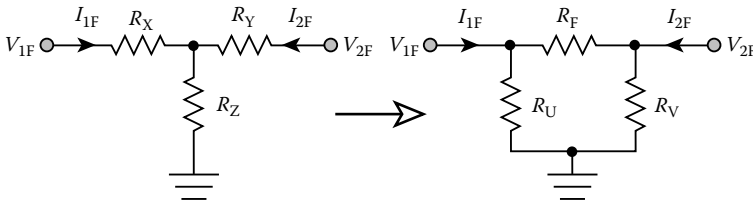


FIGURE 2.15 Transformation of the wye feedback subcircuit used in the amplifier of Figure 2.13 to the delta subcircuit exploited in Figure 2.14. The resistance transformation equations are given by Equations 2.60 through 2.62.

$$R_F = (R_X + R_Y) \left(1 + \frac{R_X || R_Y}{R_Z} \right) \tag{2.60}$$

$$\frac{R_U}{R_F} = \frac{R_Z}{R_Y} \tag{2.61}$$

$$\frac{R_V}{R_F} = \frac{R_Z}{R_X} \tag{2.62}$$

2.6 Dual-Loop Feedback

As mentioned previously, a simultaneous control of the driving-point I/O resistances, as well as the closed-loop gain, mandates the use of dual global loops comprised of series and shunt feedback signal paths. The two global dual-loop feedback architectures are the series-series/shunt-shunt feedback amplifier and the series-shunt/shunt-series feedback amplifier. In Sections 2.6.1 and 2.6.2, both of

these units are studied by judiciously applying the relevant analytical results established earlier for pertinent single-loop feedback architectures. The ac schematic diagrams of these respective circuit realizations are provided, and engineering design considerations are offered.

2.6.1 Series–Series/Shunt–Shunt Feedback Amplifier

Figure 2.16 is a behavioral abstraction of the series–series/shunt–shunt feedback amplifier. Two port z parameters are used to model the series–series feedback subcircuit, for which feed-forward is tacitly ignored and the feedback factor associated with its current-controlled voltage source is f_{ss} . On the other hand, y parameters model the shunt–shunt feedback network, where the feedback factor relative to its voltage-controlled current source is f_{pp} . As in the series–series network, feed-forward in the shunt–shunt subcircuit is presumed negligible. The four-terminal amplifier around which the two feedback units are connected has an open loop (meaning $f_{ss} = 0$ and $f_{pp} = 0$, but with the loading effects of both feedback circuits considered) transconductance of $G_{MO}(R_{ST}, R_{LT})$.

With f_{pp} set to zero to deactivate shunt–shunt feedback, the resultant series–series feedback network is a transconductance amplifier with a closed-loop transconductance, $G_{MS}(R_{ST}, R_{LT})$, is

$$G_{MS}(R_{ST}, R_{LT}) = \frac{I_O}{V_{ST}} = \frac{G_{MO}(R_{ST}, R_{LT})}{1 + f_{ss}G_{MO}(R_{ST}, R_{LT})} \approx \frac{1}{f_{ss}} \tag{2.63}$$

where the loop gain, $f_{ss}G_{MO}(R_{ST}, R_{LT})$, is presumed much larger than one, and the loading effects of both the series–series feedback subcircuit and the deactivated shunt–shunt feedback network are incorporated into $G_{MO}(R_{ST}, R_{LT})$. The transresistance, $R_{MS}(R_{ST}, R_{LT})$, implied by Equation 2.63, which expedites the study of the shunt–shunt component of the feedback configuration, is

$$R_{MS}(R_{ST}, R_{LT}) = \frac{V_O}{I_{ST}} = R_{ST}R_{LT} \frac{I_O}{V_{ST}} \approx \frac{R_{ST}R_{LT}}{f_{ss}} \tag{2.64}$$

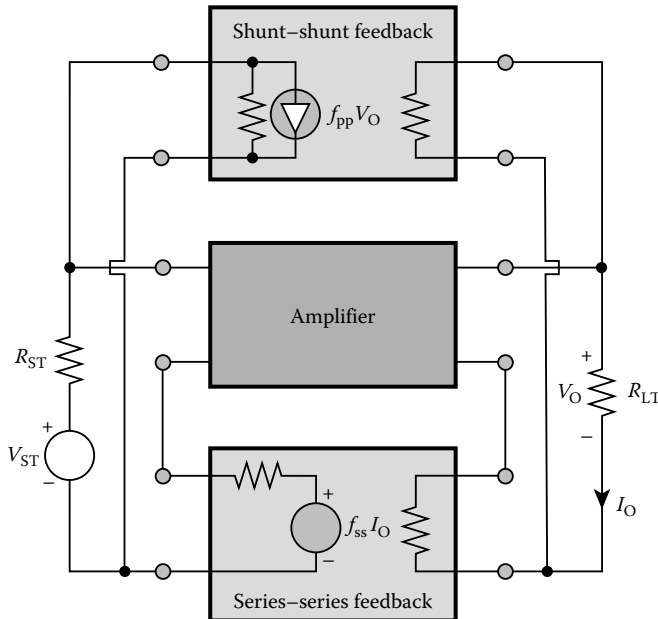


FIGURE 2.16 System-level diagram of a series–series/shunt–shunt dual-loop feedback amplifier. Note that feed-forward signal transmission through either feedback network is ignored.

The series–series feedback input and output resistances R_{ins} and R_{outs} , respectively, are large and given by

$$R_{\text{ins}} = R_{\text{ino}}[1 + f_{\text{ss}}G_{\text{MO}}(0, R_{\text{LT}})] \quad (2.65)$$

and

$$R_{\text{outs}} = R_{\text{outo}}[1 + f_{\text{ss}}G_{\text{MO}}(R_{\text{ST}}, 0)] \quad (2.66)$$

where the zero feedback ($f_{\text{ss}} = 0$ and $f_{\text{pp}} = 0$) values, R_{ino} and R_{outo} , of these driving-point quantities are computed with due consideration given to the loading effects imposed on the amplifier by both feedback subcircuits.

When shunt–shunt feedback is applied around the series–series feedback cell, the configuration becomes a transresistance amplifier. The effective open-loop transresistance is $R_{\text{MS}}(R_{\text{ST}}, R_{\text{LT}})$, as defined by Equation 2.64. Noting a feedback of f_{pp} , the corresponding closed-loop transresistance is

$$R_{\text{M}}(R_{\text{ST}}, R_{\text{LT}}) \approx \frac{\frac{R_{\text{ST}}R_{\text{LT}}}{f_{\text{ss}}}}{1 + f_{\text{pp}}\left(\frac{R_{\text{ST}}R_{\text{LT}}}{f_{\text{ss}}}\right)} \quad (2.67)$$

which is independent of amplifier model parameters, despite the unlikely condition of an effective loop gain $f_{\text{pp}}R_{\text{ST}}R_{\text{LT}}/f_{\text{ss}}$ that is much larger than 1. It should be interjected, however, that Equation 2.67 presumes negligible feed-forward through the shunt–shunt feedback network. This presumption may be inappropriate owing to the relatively low closed-loop gain afforded by the series–series feedback subcircuit. Ignoring this potential problem temporarily, Equation 2.67 suggests a closed-loop voltage gain $A_{\text{V}}(R_{\text{ST}}, R_{\text{LT}})$ of

$$A_{\text{V}}(R_{\text{ST}}, R_{\text{LT}}) = \frac{V_{\text{O}}}{V_{\text{S}}} = \frac{R_{\text{M}}(R_{\text{ST}}, R_{\text{LT}})}{R_{\text{ST}}} \approx \frac{R_{\text{LT}}}{f_{\text{ss}} + f_{\text{pp}}R_{\text{ST}}R_{\text{LT}}} \quad (2.68)$$

The closed-loop, driving-point output resistance R_{out} can be straightforwardly calculated by noting that the open circuit ($R_{\text{LT}} \rightarrow \infty$) voltage gain, A_{VO} , predicted by Equation 2.68 is $A_{\text{VO}} = 1/f_{\text{pp}} R_{\text{ST}}$. Accordingly, Equation 2.68 is alternatively expressible as

$$A_{\text{V}}(R_{\text{ST}}, R_{\text{LT}}) \approx A_{\text{VO}} \left(\frac{R_{\text{LT}}}{R_{\text{LT}} + \frac{f_{\text{ss}}}{f_{\text{pp}}R_{\text{ST}}}} \right) \quad (2.69)$$

Because Equation 2.69 is a voltage divider relationship stemming from a Thévenin model of the output port of the dual-loop feedback amplifier, as delineated in Figure 2.17, it follows that the driving-point output resistance is

$$R_{\text{out}} \approx \frac{f_{\text{ss}}}{f_{\text{pp}}R_{\text{ST}}} \quad (2.70)$$

Observe that, similar to the forward gain characteristics, the driving-point output resistance is nominally insensitive to changes and other uncertainties in open-loop amplifier parameters. Moreover, this output resistance is directly proportional to the ratio $f_{\text{ss}}/f_{\text{pp}}$ of feedback factors. As illustrated in preceding sections, the individual feedback factors, and thus the ratio of feedback factors, is likely to be proportional to a ratio of resistances. In view of the fact that resistance ratios can be tightly controlled in a monolithic fabrication process, R_{out} in Equation 2.70 is accurately prescribed for a given source termination.

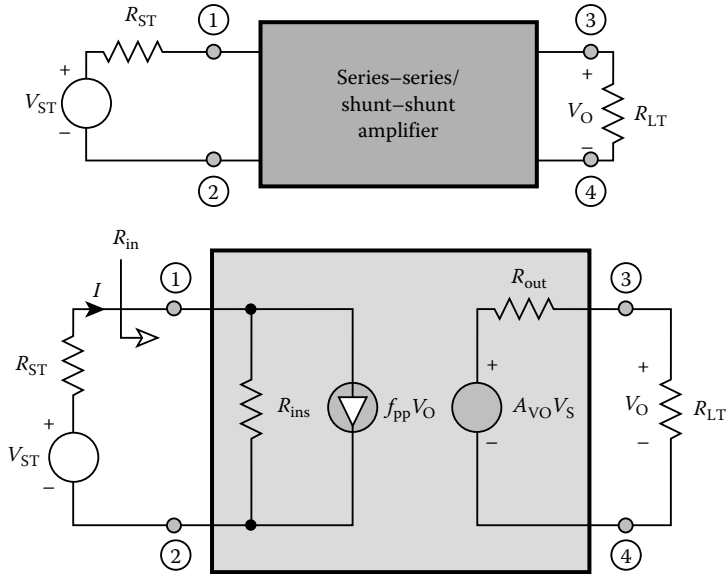


FIGURE 2.17 Norton equivalent input and Thévenin equivalent output circuits for the series-series/shunt-shunt dual-loop feedback amplifier.

The driving-point input resistance R_{in} can be determined from a consideration of the input port component of the system-level equivalent circuit depicted in Figure 2.17. This resistance is the ratio of V_{ST} to I , under the condition of $R_S = 0$. With $R_S = 0$, Equation 2.68 yields $V_O = R_{LT} V_{ST} / f_{ss}$ and thus, Kirchhoff’s voltage law (KVL) applied around the input port of the model at hand yields

$$R_{in} = \frac{R_{ins}}{1 + \frac{f_{pp} R_{LT} R_{ins}}{f_{ss}}} \approx \frac{f_{ss}}{f_{pp} R_{LT}} \tag{2.71}$$

where the “open-loop” input resistance R_{ins} , defined by Equation 2.65, is presumed large. Similar to the driving-point output resistance of the series-series/shunt-shunt feedback amplifier, the driving-point input resistance is nominally independent of open-loop amplifier parameters.

It is interesting to observe that the input resistance in Equation 2.71 is inversely proportional to the load resistance by the same factor (f_{ss}/f_{pp}) that the driving-point output resistance in Equation 2.70 is inversely proportional to the source resistance. As a result,

$$\frac{f_{ss}}{f_{pp}} \approx R_{in} R_{LT} \equiv R_{out} R_{ST} \tag{2.72}$$

Thus, in addition to being stable performance indices for well-defined source and load terminations, the driving-point input and output resistances track one another, despite manufacturing uncertainties and changes in operating temperature that might perturb the individual values of the two feedback factors f_{ss} and f_{pp} .

The circuit property stipulated by Equation 2.72 has immediate utility in the design of wideband communication transceivers and other high-speed signal-processing systems [10–14]. In these and related applications, a cascade of several stages is generally required to satisfy frequency response, distortion, and noise specifications. A convenient way of implementing a cascade interconnection is to force each member of the cascade to operate under the match terminated case of

$R_{ST} = R_{in} = R_{LT} = R_{out} \triangleq R$. From Equation 2.72 match terminated operation demands feedback factors selected so that

$$R = \sqrt{\frac{f_{ss}}{f_{pp}}} \tag{2.73}$$

which forces a match terminated closed-loop voltage gain A_V^* of

$$A_V^* \approx \frac{1}{2f_{pp}R} = \frac{1}{2\sqrt{f_{pp}f_{ss}}} \tag{2.74}$$

The ac schematic diagram of a practical, single-ended series-series/shunt-shunt amplifier is submitted in Figure 2.18. An inspection of this diagram reveals a topology that coalesces the series-series and shunt-shunt triples studied earlier. In particular, the wye network formed of the three resistances, R_X , R_Y , and R_Z , comprises the series-series component of the dual-loop feedback amplifier. The capacitor, C_C , narrowbands the open-loop amplifier to facilitate frequency compensation of the series-series loop through the capacitance, C_{F1} . Compensated shunt feedback of the network is achieved by the parallel combination of the resistance, R_F and the capacitance, C_{F2} . If C_{F1} and C_C combine to deliver a dominant pole series-series feedback amplifier, C_{F2} is not necessary. Conversely, C_{F1} is superfluous if C_{F2} and C_C interact to provide a dominant pole shunt-shunt feedback amplifier. As in the single-ended series-series configuration, transistor $Q3$ can be broadbanded via a common base cascode. Moreover, if feedback through the feedback networks poses a problem, an emitter follower can be inserted at the port to which the shunt feedback path and the load termination are incident.

A low-frequency analysis of the circuit in Figure 2.18 is expedited by assuming high- β transistors having identical corresponding small-signal model parameters. This analysis, which in contrast to the

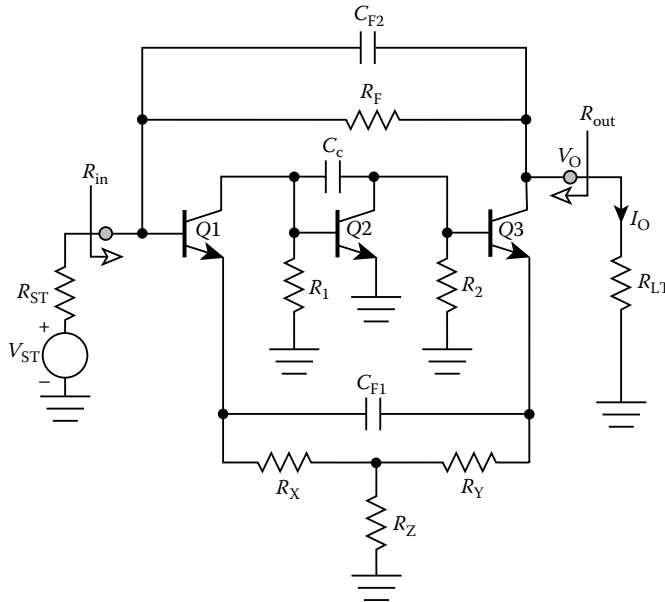


FIGURE 2.18 AC schematic diagram of a frequency-compensated, series-series/shunt-shunt, dual-loop feedback amplifier. The compensation is affected by the capacitances C_{F1} and C_{F2} , while C_C achieves pole splitting in the open-loop amplifier.

simplified behavioral analysis, does not ignore the electrical effects of the aforementioned feed-forward through the shunt–shunt feedback network, yields a voltage gain $A_V(R_{ST}, R_{LT})$, of

$$A_V(R_{ST}, R_{LT}) \approx - \left(\frac{R_{in}}{R_{in} + R_{ST}} \right) \left(\frac{R_{LT}}{R_{LT} + R_F} \right) \left(\frac{\alpha R_F}{R_Z} - 1 \right) \quad (2.75)$$

where the driving-point input resistance of the amplifier R_{in} is

$$R_{in} \approx \frac{R_F + R_{LT}}{1 + \frac{\alpha R_{LT}}{R_Z}} \quad (2.76)$$

The driving-point output resistance R_{out} is

$$R_{out} \approx \frac{R_F + R_{ST}}{1 + \frac{\alpha R_{ST}}{R_Z}} \quad (2.77)$$

As predicted by the behavioral analysis R_{in} , R_{out} , and $A_V(R_{ST}, R_{LT})$, are nominally independent of transistor parameters. Observe that the functional dependence of R_{in} on the load resistance, R_{LT} , is identical to the manner in which R_{out} is related to the source resistance R_{ST} . In particular, $R_{in} \equiv R_{out}$ if $R_{ST} \equiv R_{LT}$. For the match terminated case in which $R_{ST} = R_{in} = R_{LT} = R_{out} \triangleq R$,

$$R \approx \sqrt{\frac{R_F R_Z}{\alpha}} \quad (2.78)$$

The corresponding match terminated voltage gain in Equation 2.75 collapses to

$$A_V^* \approx - \left(\frac{R_F - R}{2R} \right) \quad (2.79)$$

Similar to the series–series and shunt–shunt triples, many of the frequency compensation problems implicit to the presence of three open-loop stages can be circumvented by realizing the series–series/shunt–shunt amplifier as a two-stage differential configuration. Figure 2.19 is the ac schematic diagram of a compensated differential series–series/shunt–shunt feedback dual.

2.6.2 Series–Shunt/Shunt–Series Feedback Amplifier

The only other type of global dual-loop architecture is the series–shunt/shunt–series feedback amplifier; the behavioral diagram appears in Figure 2.20. The series–shunt component of this system, which is modeled by h -parameters, has a negligibly small feed-forward factor and a feedback factor of f_{sp} . Hybrid g -parameters model the shunt–series feedback structure, which has a feedback factor of f_{ps} and a presumably negligible feed-forward factor. The four-terminal amplifier around which the two feedback units are connected has an open loop (meaning $f_{sp} = 0$ and $f_{ps} = 0$, but with the loading effects of both feedback circuits considered) voltage gain of $A_{VO}(R_{ST}, R_{LT})$.

For $f_{ps} = 0$, the series–shunt feedback circuit voltage gain $A_{VS}(R_{ST}, R_{LT})$, is

$$A_{VS}(R_{ST}, R_{LT}) = \frac{V_O}{V_{ST}} = \frac{A_{VO}(R_{ST}, R_{LT})}{1 + f_{sp} A_{VO}(R_{ST}, R_{LT})} \approx \frac{1}{f_{sp}} \quad (2.80)$$

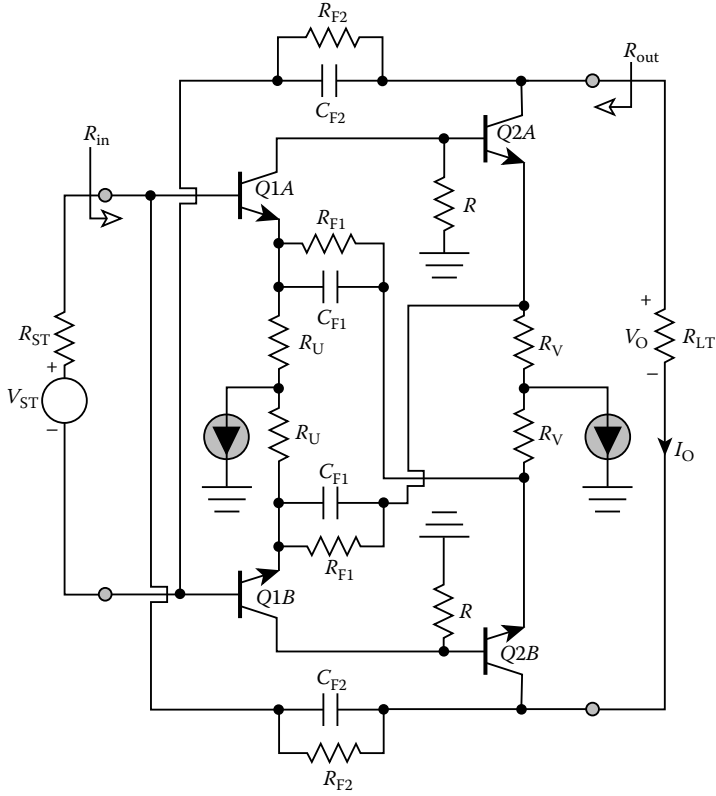


FIGURE 2.19 AC schematic diagram of the differential realization of a compensated series-series/shunt-shunt feedback amplifier.

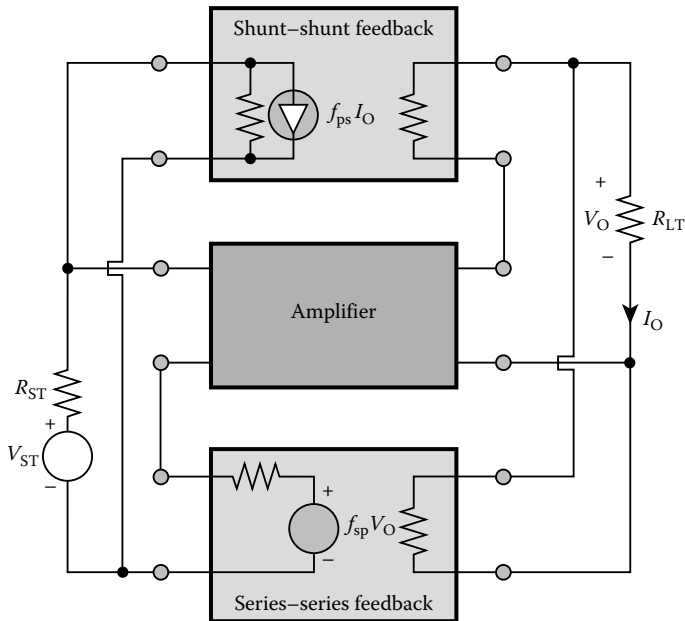


FIGURE 2.20 System-level diagram of a series-shunt/shunt-series, dual-loop feedback amplifier. Note that feed-forward signal transmission through either feedback network is ignored.

where the approximation reflects an assumption of a large loop gain. When the shunt–series component of the feedback amplifier is activated, the dual-loop configuration functions as a current amplifier. Its effective open-loop transfer function is the current gain, $A_{IS}(R_{ST}, R_{LT})$, established by the series–shunt amplifier; namely,

$$A_{IS}(R_{ST}, R_{LT}) = \frac{I_O}{I_{ST}} = \left(\frac{R_{ST}}{R_{LT}} \right) \frac{V_O}{V_{ST}} \approx \frac{R_{ST}}{f_{sp} R_{LT}} \quad (2.81)$$

It follows that the current gain, $A_I(R_{ST}, R_{LT})$, of the closed loop is

$$A_I(R_{ST}, R_{LT}) \approx \frac{\frac{R_{ST}}{f_{sp} R_{LT}}}{1 + f_{ps} \left(\frac{R_{ST}}{f_{sp} R_{LT}} \right)} = \frac{R_{ST}}{f_{sp} R_{LT} + f_{ps} R_{ST}} \quad (2.82)$$

while the corresponding voltage gain, $A_V(R_{ST}, R_{LT})$, assuming negligible feed-forward through the shunt–series feedback network, is

$$A_V(R_{ST}, R_{LT}) = \frac{R_{LT}}{R_{ST}} A_I(R_{ST}, R_{LT}) \approx \frac{R_{LT}}{f_{sp} R_{LT} + f_{ps} R_{ST}} \quad (2.83)$$

Repeating the analytical strategy employed to determine the input and output resistances of the series–series/shunt–shunt configuration, Equation 2.83 delivers a driving-point input resistance of

$$R_{in} \approx \frac{f_{sp} R_{LT}}{f_{ps}} \quad (2.84)$$

and a driving-point output resistance of

$$R_{out} \approx \frac{f_{ps} R_{ST}}{f_{sp}} \quad (2.85)$$

Similar to the forward voltage gain, the driving-point input and output resistances of the series–shunt/shunt–series feedback amplifier are nominally independent of active element parameters. Note, however, that the input resistance is directly proportional to the load resistance by a factor (f_{sp}/f_{ps}) , which is the inverse of the proportionality constant that links the output resistance to the source resistance. Specifically,

$$\frac{f_{sp}}{f_{ps}} = \frac{R_{in}}{R_{LT}} = \frac{R_{ST}}{R_{out}} \quad (2.86)$$

Thus, although R_{in} and R_{out} are reliably determined for well-defined load and source terminations, they do not track one another as well as they do in the series–series/shunt–shunt amplifier. Using Equation 2.86, the voltage gain in Equation 2.83 is expressible as

$$A_V(R_{ST}, R_{LT}) \approx \frac{1}{f_{sp} \left(1 + \sqrt{\frac{R_{out} R_{ST}}{R_{in} R_{LT}}} \right)} \quad (2.87)$$

The simplified ac schematic diagram of a practical series–shunt/shunt–series feedback amplifier appears in Figure 2.21. In this circuit, series–shunt feedback derives from the resistances, R_{EE1} and R_{F1} , and

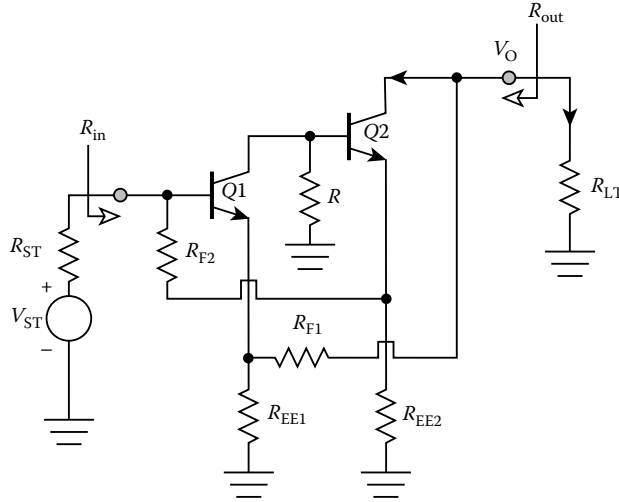


FIGURE 2.21 AC schematic diagram of a series-shunt/shunt-series, dual-loop feedback amplifier.

shunt-series feedback is determined by the resistances, R_{EE2} and R_{F2} . Because this circuit topology merges the series-shunt and shunt-series pairs, requisite frequency compensation, which is not shown in the subject figure, mirrors the relevant compensation schemes studied earlier. Note, however, that a cascade of only two open-loop gain stages renders compensation easier to implement and larger 3 dB bandwidths easier to achieve in the series-series/shunt-shunt circuit, which requires three open-loop gain stages for a single-ended application.

For high- β transistors having identical corresponding small-signal model parameters, a low-frequency analysis of the circuit in Figure 2.21 gives a voltage gain of

$$A_v(R_{ST}, R_{LT}) \approx \left(\frac{\alpha R_{in}}{R_{in} + \alpha R_S} \right) \left(1 + \frac{R_{F1}}{R_{EE1}} \right) \quad (2.88)$$

where the driving-point input resistance, R_{in} , of the subject amplifier is

$$R_{in} \approx \alpha R_{LT} \left(\frac{1 + \frac{R_{F2}}{R_{EE2}}}{1 + \frac{R_{F1}}{R_{EE1}} + \frac{R_{LT}}{R_{EE1} \parallel R_{EE2}}} \right) \quad (2.89)$$

The driving-point output resistance, R_{out} , is

$$R_{out} \approx R_{ST} \left(\frac{1 + \frac{R_{F1}}{R_{EE1}}}{1 + \frac{R_{F2}}{R_{EE2}} + \frac{R_{ST}}{R_{EE1} \parallel R_{EE2}}} \right) \quad (2.90)$$

2.7 Summary

This section documents small-signal performance equations, general operating characteristics, and engineering design guidelines for the six most commonly used global feedback circuits. These observations derive from analyses based on the judicious application of signal flow theory to the small-signal model that results when the subject feedback network is supplanted by an appropriate two-port parameter equivalent circuit.

Four of the six fundamental feedback circuits are single-loop architectures.

1. Series–shunt feedback amplifier functions best as a voltage amplifier in that its input resistance is large, and its output resistance is small. Because only two gain stages are required in the open loop, the amplifier is relatively easy to compensate for acceptable closed-loop damping and features potentially large 3 dB bandwidth. A computationally efficient analysis aimed toward determining loop gain, closed-loop gain, I/O resistances, and the condition that renders feed-forward through the feedback network inconsequential is predicated on replacing the feedback subcircuit with its h -parameter model.
2. Shunt–series feedback amplifier is a current amplifier in that its input resistance is small, and its output resistance is large. Similar to its series–shunt dual, only two gain stages are required in the open loop. Computationally efficient analyses are conducted by replacing the feedback subcircuit with its g -parameter model.
3. Shunt–shunt feedback amplifier is a transresistance signal processor in that both its input and output resistances are small. Although this amplifier can be realized theoretically with only a single open-loop stage, a sufficiently large loop gain generally requires a cascade of three open-loop stages. As a result, pole splitting is invariably required to ensure an open-loop dominant pole response, thereby limiting the achievable closed-loop bandwidth. In addition compensation of the feedback loop may be required for acceptable closed-loop damping. The bandwidth and stability problems implicit to the use of three open-loop gain stages can be circumvented by a balanced differential realization, which requires a cascade of only two open-loop gain stages. Computationally efficient analyses are conducted by replacing the feedback subcircuit with its y -parameter model.
4. Series–series feedback amplifier is a transconductance signal processor in that both its input and output resistances are large. Similar to its shunt–shunt counterpart, its implementation generally requires a cascade of three open-loop gain stages. Computationally efficient analyses are conducted by replacing the feedback subcircuit with its z -parameter model.

The two remaining feedback circuits are dual-loop topologies that can stabilize the driving-point input and output resistances, as well as the forward gain characteristics, with respect to shifts in active element parameters. One of these latter architectures, the series–series/shunt–shunt feedback amplifier, is particularly well suited to electronic applications that require a multistage cascade.

1. Series–series/shunt–shunt feedback amplifier coalesces the series–series architecture with its shunt–shunt dual. It is particularly well suited to applications, such as wideband communication networks, which require match terminated source and load resistances. Requisite frequency compensation and broadbanding criteria mirror those incorporated in the series–series and shunt–shunt single-loop feedback topologies.
2. Series–shunt/shunt–series feedback amplifier coalesces the series–shunt architecture with its shunt–series dual. Although its input resistance can be designed to match the source resistance seen by the input port of the amplifier, and its output resistance can be matched to the load resistance driven by the amplifier, match terminated operating ($R_{in} = R_{ST} = R_{LT} = R_{out}$) is not feasible. Requisite frequency compensation and broadbanding criteria mirror those incorporated in the series–shunt and shunt–series single-loop feedback topologies.

References

1. J. Millman and A. Grabel, *Microelectronics*, 2nd edn., New York: McGraw-Hill, 1987, Chap. 12.
2. A. B. Grebene, *Bipolar and MOS Analog Integrated Circuit Design*, New York: Wiley-Interscience, 1984, pp. 424–432.
3. R. G. Meyer, R. Eschenbach, and R. Chin, A wideband ultralinear amplifier from DC to 300 MHz, *IEEE J. Solid-State Circuits*, SC-9, 167–175, Aug. 1974.

4. A. S. Sedra and K. C. Smith, *Microelectronic Circuits*, New York: Holt, Rinehart Winston, 1987, pp. 428–441.
5. J. M. Early, Effects of space-charge layer widening in junction transistors, *Proc. IRE*, 46, 1141–1152, Nov. 1952.
6. A. J. Cote Jr. and J. B. Oakes, *Linear Vacuum-Tube and Transistor Circuits*, New York: McGraw-Hill, 1961, pp. 40–46.
7. R. G. Meyer and R. A. Blauschild, A four-terminal wideband monolithic amplifier, *IEEE J. Solid-State Circuits*, SC-17, 634–638, Dec. 1981.
8. M. Ohara, Y. Akazawa, N. Ishihara, and S. Konaka, Bipolar monolithic amplifiers for a gigabit optical repeater, *IEEE J. Solid-State Circuits*, SC-19, 491–497, Aug. 1985.
9. M. J. N. Sibley, R. T. Univin, D. R. Smith, B. A. Boxall, and R. J. Hawkins, A monolithic transimpedance preamplifier for high speed optical receivers, *Br. Telecommun. Tech. J.*, 2, 64–66, July 1984.
10. J. F. Kukielka and C. P. Snapp, Wideband monolithic cascadable feedback amplifiers using silicon bipolar technology, *IEEE Microw. Millimeter-Wave Circuits Symp. Dig.*, 2, 330–331, June 1982.
11. R. G. Meyer, M. J. Shensa, and R. Eschenbach, Cross modulation and intermodulation in amplifiers at high frequencies, *IEEE J. Solid-State Circuits*, SC-7, 16–23, Feb. 1972.
12. K. H. Chan and R. G. Meyer, A low distortion monolithic wide-band amplifier, *IEEE J. Solid-State Circuits*, SC-12, 685–690, Dec. 1977.
13. A. Arbel, Multistage transistorized current modules, *IEEE Trans. Circuits Syst.*, CT-13, 302–310, Sept. 1966.
14. A. Arbel, *Analog Signal Processing and Instrumentation*, London: Cambridge University, 1980, Chap. 3.
15. W. G. Beall, New feedback techniques for high performance monolithic wideband amplifiers, Electron. Res. Group, University of Southern California, Tech. Memo., Jan. 1990.

3

General Feedback Theory

Wai-Kai Chen
University of Illinois at Chicago

3.1 Introduction	3-1
3.2 Indefinite-Admittance Matrix	3-1
3.3 Return Difference.....	3-7
3.4 Null Return Difference	3-11
References.....	3-13

3.1 Introduction

In Section 1.2, we used the ideal feedback model to study the properties of feedback amplifiers. The model is useful only if we can separate a feedback amplifier into the basic amplifier $\mu(s)$ and the feedback network $\beta(s)$. The procedure is difficult and sometimes virtually impossible, because the forward path may not be strictly unilateral, the feedback path is usually bilateral, and the input and output coupling networks are often complicated. Thus, the ideal feedback model is not an adequate representation of a practical amplifier. In the remainder of this section, we shall develop Bode's feedback theory, which is applicable to the general network configuration and avoids the necessity of identifying the transfer functions $\mu(s)$ and $\beta(s)$.

Bode's feedback theory [1] is based on the concept of return difference, which is defined in terms of network determinants. We show that the return difference is a generalization of the concept of the feedback factor of the ideal feedback model, and can be measured physically from the amplifier itself. We then introduce the notion of null return difference and discuss its physical significance. Because the feedback theory will be formulated in terms of the first- and second-order cofactors of the elements of the indefinite-admittance matrix of a feedback circuit, we first review briefly the formulation of the indefinite-admittance matrix.

3.2 Indefinite-Admittance Matrix

Figure 3.1 is an n -terminal network N composed of an arbitrary number of active and passive network elements connected in any way whatsoever. Let V_1, V_2, \dots, V_n be the Laplace-transformed potentials measured between terminals $1, 2, \dots, n$ and some arbitrary but unspecified reference point, and let I_1, I_2, \dots, I_n be the Laplace-transformed currents entering the terminals $1, 2, \dots, n$ from outside the network. The network N together with its load is linear, so the terminal current and voltages are related by the equation

$$\begin{bmatrix} I_1 \\ I_2 \\ \vdots \\ I_n \end{bmatrix} = \begin{bmatrix} y_{11} & y_{12} & \cdots & y_{1n} \\ y_{21} & y_{22} & \cdots & y_{2n} \\ \vdots & \vdots & \ddots & \vdots \\ y_{n1} & y_{n2} & \cdots & y_{nn} \end{bmatrix} \begin{bmatrix} V_1 \\ V_2 \\ \vdots \\ V_n \end{bmatrix} + \begin{bmatrix} J_1 \\ J_2 \\ \vdots \\ J_n \end{bmatrix} \quad (3.1)$$

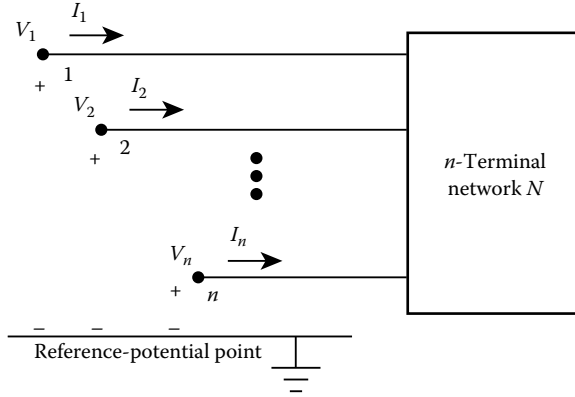


FIGURE 3.1 General symbolic representation of an n -terminal network.

or more succinctly as

$$\mathbf{I}(s) = \mathbf{Y}(s)\mathbf{V}(s) + \mathbf{J}(s) \tag{3.2}$$

where J_k ($k = 1, 2, \dots, n$) denotes the current flowing into the k th terminal when all terminals of N are grounded to the reference point. The coefficient matrix $\mathbf{Y}(s)$ is called the indefinite-admittance matrix because the reference point for the potentials is some arbitrary but unspecified point outside the network. Notice that the symbol $\mathbf{Y}(s)$ is used to denote either the admittance matrix or the indefinite-admittance matrix. This should not create any confusion because the context will tell. In the remainder of this section, we shall deal exclusively with the indefinite-admittance matrix.

We remark that the short-circuit currents J_k result from the independent sources and/or initial conditions in the interior of N . For our purposes, we shall consider all independent sources outside the network and set all initial conditions to zero. Hence, $\mathbf{J}(s)$ is considered to be zero, and Equation 3.2 becomes

$$\mathbf{I}(s) = \mathbf{Y}(s)\mathbf{V}(s) \tag{3.3}$$

where the elements y_{ij} of $\mathbf{Y}(s)$ can be obtained as

$$y_{ij} = \left. \frac{I_i}{V_j} \right|_{v_x=0, x \neq j} \tag{3.4}$$

As an illustration, consider a small-signal equivalent model of a transistor in Figure 3.2. Its indefinite-admittance matrix is found to be

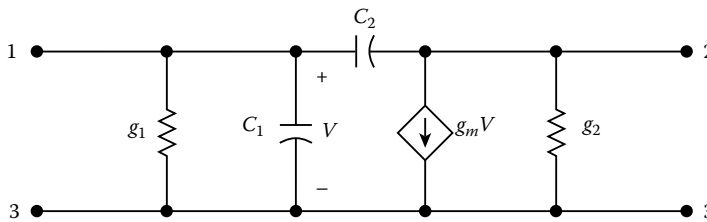


FIGURE 3.2 Small-signal equivalent network of a transistor.

$$\mathbf{Y}(s) = \begin{bmatrix} g_1 + sC_1 + sC_2 & -sC_2 & -g_1 - sC_1 \\ g_m - sC_2 & g_2 + sC_2 & -g_2 - g_m \\ -g_1 - sC_1 - g_m & -g_2 & g_1 + g_2 + g_m + sC_1 \end{bmatrix} \quad (3.5)$$

Observe that the sum of elements of each row or column is equal to zero. The fact that these properties are valid in general for the indefinite-admittance matrix will now be demonstrated.

To see that the sum of the elements in each column of $\mathbf{Y}(s)$ equals zero, we add all n equations of Equation 3.1 to yield

$$\sum_{i=1}^n \sum_{j=1}^n y_{ji} V_i = \sum_{m=1}^n I_m - \sum_{m=1}^n J_m = 0 \quad (3.6)$$

The last equation is obtained by appealing to Kirchhoff's current law for the node corresponding to the reference point. Setting all the terminal voltages to zero except the k th one, which is nonzero, gives

$$V_k \sum_{j=1}^n y_{jk} = 0 \quad (3.7)$$

Because $V_k \neq 0$, it follows that the sum of the elements of each column of $\mathbf{Y}(s)$ equals zero. Thus, the indefinite-admittance matrix is always singular.

To demonstrate that each row sum of $\mathbf{Y}(s)$ is also zero, we recognize that because the point of zero potential may be chosen arbitrarily, the currents J_k and I_k remain invariant when all the terminal voltages V_k are changed by the same but arbitrary constant amount. Thus, if \mathbf{V}_0 is an n -vector, each element of which is $v_0 \neq 0$, then

$$\mathbf{I}(s) - \mathbf{J}(s) = \mathbf{Y}(s)[\mathbf{V}(s) + \mathbf{V}_0] = \mathbf{Y}(s)\mathbf{V}(s) + \mathbf{Y}(s)\mathbf{V}_0 \quad (3.8)$$

which after invoking Equation 3.2 yields that

$$\mathbf{Y}(s)\mathbf{V}_0 = 0 \quad (3.9)$$

or

$$\sum_{j=1}^n y_{ij} = 0, \quad i = 1, 2, \dots, n \quad (3.10)$$

showing that each row sum of $\mathbf{Y}(s)$ equals zero.

Thus, if \mathbf{Y}_{uv} denotes the submatrix obtained from an indefinite-admittance matrix $\mathbf{Y}(s)$ by deleting the u th row and v th column, then the (first order) cofactor, denoted by the symbol Y_{uv} , of the element y_{uv} of $\mathbf{Y}(s)$, is defined by

$$Y_{uv} = (-1)^{u+v} \det \mathbf{Y}_{uv} \quad (3.11)$$

As a consequence of the zero-row-sum and zero-column-sum properties, all the cofactors of the elements of the indefinite-admittance matrix are equal. Such a matrix is also referred to as the equicofactor matrix. If Y_{uv} and Y_{ij} are any two cofactors of the elements of $\mathbf{Y}(s)$, then

$$Y_{uv} = Y_{ij} \quad (3.12)$$

for all $u, v, i,$ and j . For the indefinite-admittance matrix $\mathbf{Y}(s)$ of Equation 3.5 it is straightforward to verify that all of its nine cofactors are equal to

$$Y_{uv} = s^2 C_1 C_2 + s(C_1 g_2 + C_2 g_1 + C_2 g_2 + g_m C_2) + g_1 g_2 \tag{3.13}$$

for $u, v = 1, 2, 3$.

Denote by $\mathbf{Y}_{rp,sq}$ the submatrix obtained from $\mathbf{Y}(s)$ by striking out rows r and s and columns p and q . Then the second-order cofactor, denoted by the symbol $Y_{rp,sq}$ of the elements y_{rp} and y_{sq} of $\mathbf{Y}(s)$ is a scalar quantity defined by the relation

$$Y_{rp,sq} = \text{sgn}(r - s)\text{sgn}(p - q)(-1)^{r+p+s+q} \det \mathbf{Y}_{rp,sq} \tag{3.14}$$

where $r \neq s$ and $p \neq q$, and

$$\text{sgn } u = +1 \quad \text{if } u > 0 \tag{3.15a}$$

$$\text{sgn } u = -1 \quad \text{if } u < 0 \tag{3.15b}$$

The symbols \mathbf{Y}_{uv} and Y_{uv} or $\mathbf{Y}_{rp,sq}$ and $Y_{rp,sq}$ should not create any confusion because one is in boldface whereas the other is italic. Also, for our purposes, it is convenient to define

$$Y_{rp,sq} = 0, \quad r = s \text{ or } p = q \tag{3.16a}$$

or

$$\text{sgn } 0 = 0 \tag{3.16b}$$

This convention will be followed throughout the remainder of this section.

As an example, consider the hybrid-pi equivalent network of a transistor in Figure 3.3. Assume that each node is an accessible terminal of a four-terminal network. Its indefinite-admittance matrix is

$$\mathbf{Y}(s) = \begin{bmatrix} 0.02 & 0 & -0.02 & 0 \\ 0 & 5 \times 10^{-12} s & 0.2 - 5 \times 10^{-12} s & -0.2 \\ -0.02 & -5 \times 10^{-12} s & 0.024 + 105 \times 10^{-12} s & -0.004 - 10^{-10} s \\ 0 & 0 & -0.204 - 10^{-10} s & 0.204 + 10^{-10} s \end{bmatrix} \tag{3.17}$$

The second-order cofactor $Y_{31,42}$ and $Y_{11,34}$ of the elements of $\mathbf{Y}(s)$ of Equation 3.17 are computed as follows:

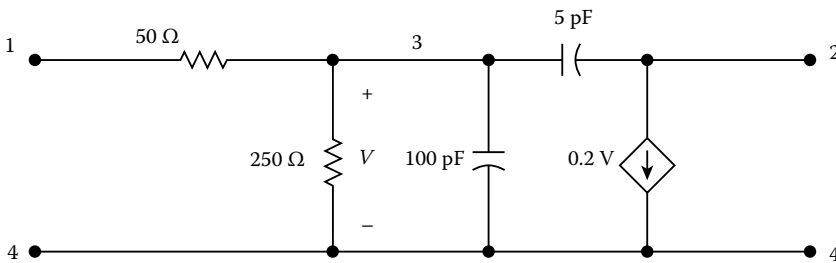


FIGURE 3.3 Hybrid-pi equivalent network of a transistor.

$$Y_{31,42} = \text{sgn}(3 - 4)\text{sgn}(1 - 2)(-1)^{3+1+4+2} \det \begin{bmatrix} -0.02 & 0 \\ 0.2 - 5 \times 10^{-12}s & -0.2 \end{bmatrix}$$

$$= 0.004 \tag{3.18a}$$

$$Y_{11,34} = \text{sgn}(1 - 3)\text{sgn}(1 - 4)(-1)^{1+1+3+4} \det \begin{bmatrix} 5 \times 10^{-12}s & 0.2 - 5 \times 10^{-12}s \\ 0 & -0.204 - 10^{-10}s \end{bmatrix}$$

$$= 5 \times 10^{-12}s(0.204 + 10^{-10}s) \tag{3.18b}$$

The usefulness of the indefinite-admittance matrix lies in the fact that it facilitates the computation of the driving-point or transfer functions between any pair of nodes or from any pair of nodes to any other pair. In the following, we present elegant, compact, and explicit formulas that express the network functions in terms of the ratios of the first- and/or second-order cofactors of the elements of the indefinite-admittance matrix.

Assume that a current source is connected between any two nodes r and s so that a current I_{sr} is injected into the r th node and at the same time is extracted from the s th node. Suppose that an ideal voltmeter is connected from node p to node q so that it indicates the potential rise from q to p , as depicted symbolically in Figure 3.4. Then the transfer impedance, denoted by the symbol $z_{rp,sq}$, between the node pairs rs and pq of the network of Figure 3.4 is defined by the relation

$$z_{rp,sq} = \frac{V_{pq}}{I_{sr}} \tag{3.19}$$

with all initial conditions and independent sources inside N set to zero. The representation is, of course, quite general. When $r = p$ and $s = q$, the transfer impedance $z_{rp,sq}$ becomes the *driving-point impedance* $z_{rr,ss}$ between the terminal pair rs .

In Figure 3.4, set all initial conditions and independent sources in N to zero and choose terminal q to be the reference-potential point for all other terminals. In terms of Equation 3.1, these operations are equivalent to setting $\mathbf{J} = 0$, $V_q = 0$, $I_x = 0$ for $x \neq r, s$ and $I_r = -I_s = I_{sr}$. Because $\mathbf{Y}(s)$ is an equicofactor matrix, the equations of Equation 3.1 are not linearly independent and one of them is superfluous. Let us suppress the s th equation from Equation 3.1, which then reduces to

$$\mathbf{I}_{-s} = \mathbf{Y}_{sq} \mathbf{V}_{-q} \tag{3.20}$$

where \mathbf{I}_{-s} and \mathbf{V}_{-q} denote the subvectors obtained from \mathbf{I} and \mathbf{V} of Equation 3.3 by deleting the s th row and q th row, respectively. Applying Cramer's rule to solve for V_p yields

$$V_p = \frac{\det \tilde{\mathbf{Y}}_{sq}}{\det \mathbf{Y}_{sq}} \tag{3.21}$$

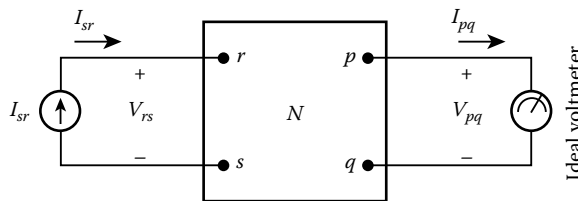


FIGURE 3.4 Symbolic representation for the measurement of the transfer impedance.

where \tilde{Y}_{sq} is the matrix derived from Y_{sq} by replacing the column corresponding to V_p by \mathbf{I}_{-s} . We recognize that \mathbf{I}_{-s} is in the p th column if $p < q$ but in the $(p - 1)$ th column if $p > q$. Furthermore, the row in which I_{sr} appears is the r th row if $r < s$, but is the $(r - 1)$ th row if $r > s$. Thus, we obtain

$$(-1)^{s+q} \det \tilde{Y}_{sq} = I_{sr} Y_{rp,sq} \tag{3.22}$$

In addition, we have

$$\det Y_{sq} = (-1)^{s+q} Y_{sq} \tag{3.23}$$

Substituting these in Equation 3.21 in conjunction with Equation 3.19, we obtain

$$z_{rp,sq} = \frac{Y_{rp,sq}}{Y_{uv}} \tag{3.24}$$

$$z_{rr,ss} = \frac{Y_{rr,ss}}{Y_{uv}} \tag{3.25}$$

in which we have invoked the fact that $Y_{sq} = Y_{uv}$.

The *voltage gain*, denoted by $g_{rp,sq}$ between the node pairs rs and pq of the network of Figure 3.4 is defined by

$$g_{rp,sq} = \frac{V_{pq}}{V_{rs}} \tag{3.26}$$

again with all initial conditions and independent sources in N being set to zero. Thus, from Equations 3.24 and 3.25 we obtain

$$g_{rp,sq} = \frac{z_{rp,sq}}{z_{rr,ss}} = \frac{Y_{rp,sq}}{Y_{rr,ss}} \tag{3.27}$$

The symbols have been chosen to help us remember. In the numerators of Equations 3.24, 3.25, and 3.27, the order of the subscripts is as follows: r , the current injecting node; p , the voltage measurement node; s , the current extracting node; and q , the voltage reference node. Nodes r and p designate the input and output transfer measurement, and nodes s and q form a sort of double datum.

As an illustration, we consider the hybrid- π transistor equivalent network of Figure 3.3. For this transistor, suppose that we connect a 100Ω load resistor between nodes 2 and 4, and excite the resulting circuit by a voltage source V_{14} , as depicted in Figure 3.5. To simplify our notation, let $p = 10^{-9}$ s. The indefinite-admittance matrix of the amplifier is

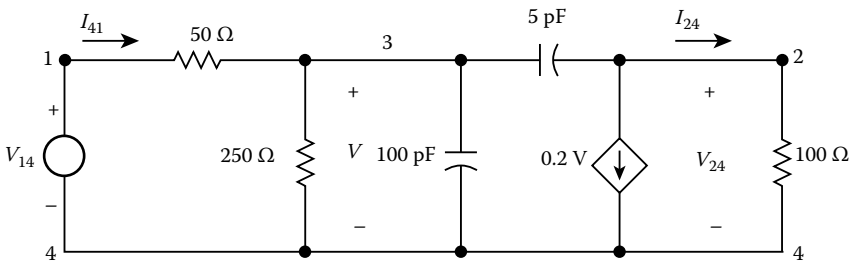


FIGURE 3.5 Transistor amplifier used to illustrate the computation of $g_{rp,sq}$.

$$\mathbf{Y}(s) = \begin{bmatrix} 0.02 & 0 & -0.02 & 0 \\ 0 & 0.01 + 0.005p & 0.2 - 0.005p & -0.21 \\ -0.02 & -0.005p & 0.024 + 0.105p & -0.004 - 0.1p \\ 0 & -0.01 & -0.204 - 0.1p & 0.214 + 0.1p \end{bmatrix} \quad (3.28)$$

To compute the voltage gain $g_{12,44}$, we appeal to Equation 3.27 and obtain

$$g_{12,44} = \frac{V_{24}}{V_{14}} = \frac{Y_{12,44}}{Y_{11,44}} = \frac{p - 40}{5p^2 + 21.7p + 2.4} \quad (3.29)$$

The input impedance facing the voltage source V_{14} is determined by

$$z_{11,44} = \frac{V_{14}}{I_{41}} = \frac{Y_{11,44}}{Y_{44}} = \frac{Y_{11,44}}{Y_{44}} = \frac{50p^2 + 217p + 24}{p^2 + 4.14p + 0.08} \quad (3.30)$$

To compute the current gain defined as the ratio of the current I_{24} in the 100 Ω resistor to the input current I_{41} , we apply Equation 3.24 and obtain

$$\frac{I_{24}}{I_{41}} = 0.01 \frac{V_{24}}{I_{41}} = 0.01 z_{12,44} = 0.01 \frac{Y_{12,44}}{Y_{44}} = \frac{0.1p - 4}{p^2 + 4.14p + 0.08} \quad (3.31)$$

Finally, to compute the transfer admittance defined as the ratio of the load current I_{24} to the input voltage V_{14} , we appeal to Equation 3.27 and obtain

$$\frac{I_{24}}{V_{14}} = 0.01 \frac{V_{24}}{V_{14}} = 0.01 g_{12,44} = 0.01 \frac{Y_{12,44}}{Y_{11,44}} = \frac{p - 40}{500p^2 + 2170p + 240} \quad (3.32)$$

3.3 Return Difference

In the study of feedback amplifier response, we are usually interested in how a particular element of the amplifier affects that response. This element is either crucial in terms of its effect on the entire system or of primary concern to the designer. It may be the transfer function of an active device, the gain of an amplifier, or the immittance of a one-port network. For our purposes, we assume that this element x is the controlling parameter of a voltage-controlled current source defined by the equation

$$I = xV \quad (3.33)$$

To focus our attention on the element x , Figure 3.6 is the general configuration of a feedback amplifier in which the controlled source is brought out as a two-port network connected to a general four-port network, along with the input source combination of I_s and admittance Y_1 and the load admittance Y_2 .

We remark that the two-port representation of a controlled source Equation 3.33 is quite general. It includes the special situation where a one-port element is characterized by its immittance. In this case, the controlling voltage V is the terminal voltage of the controlled current source I , and x become the one-port admittance.

The *return difference* $F(x)$ of a feedback amplifier with respect to an element x is defined as the ratio of the two functional values assumed by the first-order cofactor of an element of its indefinite-admittance matrix under the condition that the element x assumes its nominal value and the condition that the element x assumes the value zero. To emphasize the importance of the feedback element x , we express the

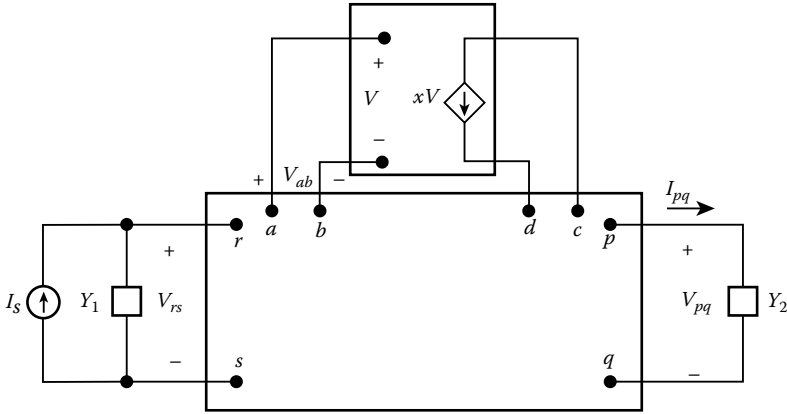


FIGURE 3.6 General configuration of a feedback amplifier.

indefinite-admittance matrix \mathbf{Y} of the amplifier as a function of x , even though it is also a function of the complex-frequency variable s , and write $\mathbf{Y} = \mathbf{Y}(x)$. Then, we have [2]

$$F(x) \equiv \frac{Y_{uv}(x)}{Y_{uv}(0)} \tag{3.34}$$

where

$$Y_{uv}(0) = Y_{uv}(x)|_{x=0} \tag{3.35}$$

The physical significance of the return difference will now be considered. In the network of Figure 3.6, the input, the output, the controlling branch, and the controlled source are labeled as indicated. Then, the element x enters the indefinite-admittance matrix $\mathbf{Y}(x)$ in a rectangular pattern as shown next:

$$\mathbf{Y}(x) = \begin{matrix} & \begin{matrix} a & b & c & d \end{matrix} \\ \begin{matrix} a \\ b \\ c \\ d \end{matrix} & \left[\begin{array}{cccc} & & & \\ & & & \\ x & -x & & \\ -x & x & & \end{array} \right] \end{matrix} \tag{3.36}$$

If in Figure 3.6 we replace the controlled current source xV by an independent current source of $x\text{A}$ and set the excitation current source I_s to zero, the indefinite-admittance matrix of the resulting network is simply $\mathbf{Y}(0)$. By appealing to Equation 3.24, the new voltage V'_{ab} appearing at terminals a and b of the controlling branch is

$$V'_{ab} = x \frac{Y_{da,cb}(0)}{Y_{uv}(0)} = -x \frac{Y_{ca,db}(0)}{Y_{uv}(0)} \tag{3.37}$$

Notice that the current injecting point is terminal d , not c .

The preceding operation of replacing the controlled current source by an independent current source and setting the excitation I_s to zero can be represented symbolically as in Figure 3.7. Observe that the controlling branch is broken off as marked and a 1 V voltage source is applied to the right of the breaking mark. This 1 V sinusoidal voltage of a fixed angular frequency produces a current of $x\text{ A}$ at the controlled

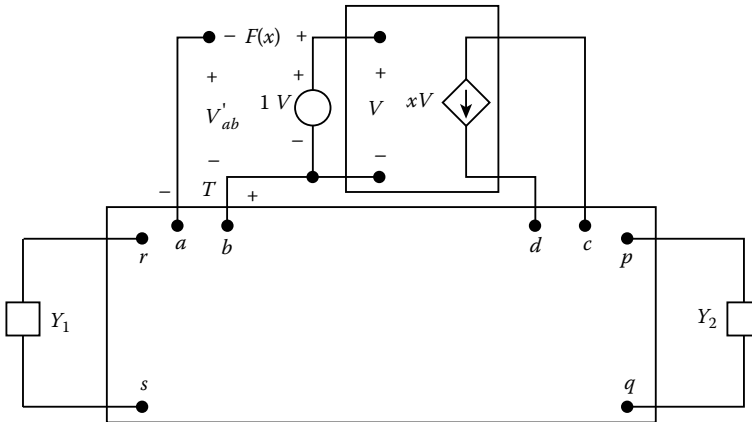


FIGURE 3.7 Physical interpretation of the return difference with respect to the controlling parameter of a voltage-controlled current source.

current source. The voltage appearing at the left of the breaking mark caused by this 1 V excitation is then V'_{ab} as indicated. This returned voltage V'_{ab} has the same physical significance as the loop transmission $\mu\beta$ defined for the ideal feedback model in Chapter 1. To see this, we set the input excitation to the ideal feedback model to zero, break the forward path, and apply a unit input to the right of the break, as depicted in Figure 3.8. The signal appearing at the left of the break is precisely the loop transmission.

For this reason, we introduce the concept of return ratio T , which is defined as the negative of the voltage appearing at the controlling branch when the controlled current source is replaced by an independent current source of x A and the input excitation is set to zero. Thus, the return ratio T is simply the negative of the returned voltage V'_{ab} , or $T = -V'_{ab}$. With this in mind, we next compute the difference between the 1 V excitation and the returned voltage V'_{ab} obtaining

$$\begin{aligned}
 1 - V'_{ab} &= 1 + x \frac{Y_{ca,db}}{Y_{uv}(0)} = \frac{Y_{uv}(0) + xY_{ca,db}}{Y_{uv}(0)} = \frac{Y_{db}(0) + xY_{ca,db}}{Y_{db}(0)} \\
 &= \frac{Y_{db}(x)}{Y_{db}(0)} = \frac{Y_{uv}(x)}{Y_{uv}(0)} = F(x)
 \end{aligned}
 \tag{3.38}$$

in which we have invoked the identities $Y_{uv} = Y_{ij}$ and

$$Y_{db}(x) = Y_{db}(0) + xY_{ca,db}
 \tag{3.39}$$

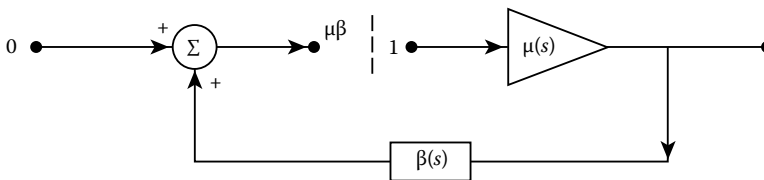


FIGURE 3.8 Physical interpretation of the loop transmission.

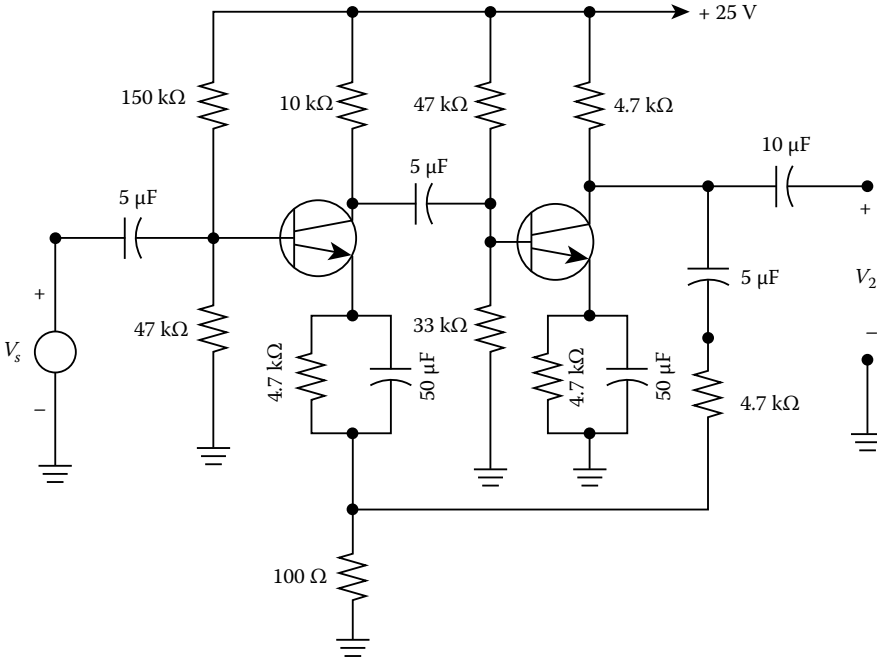


FIGURE 3.9 Voltage-series feedback amplifier together with its biasing and coupling circuitry.

We remark that we write $Y_{ca,db}(x)$ as $Y_{ca,db}$ because it is independent of x . In other words, the return difference $F(x)$ is simply the difference of the 1 V excitation and the returned voltage V'_{ab} as illustrated in Figure 3.7, and hence its name. Because

$$F(x) = 1 + T = 1 - \mu\beta \tag{3.40}$$

we conclude that the return difference has the same physical significance as the feedback factor of the ideal feedback model. The significance of the previous physical interpretations is that it permits us to determine the return ratio T or $-\mu\beta$ by measurement. Once the return ratio is measured, the other quantities such as return difference and loop transmission are known.

To illustrate, consider the voltage-series or the series-parallel feedback amplifier of Figure 3.9. Assume that the two transistors are identical with the following hybrid parameters:

$$h_{ie} = 1.1 \text{ k}\Omega, \quad h_{fe} = 50, \quad h_{re} = h_{oe} = 0 \tag{3.41}$$

After the biasing and coupling circuitry have been removed, the equivalent network is presented in Figure 3.10. The effective load of the first transistor is composed of the parallel combination of the 10, 33, 47, and 1.1 kΩ resistors. The effect of the 150 and 47 kΩ resistors can be ignored; they are included in the equivalent network to show their insignificance in the computation.

To simplify our notation, let

$$\tilde{\alpha}_k = \alpha_k \times 10^{-4} = \frac{h_{fe}}{h_{ie}} = 455 \times 10^{-4}, \quad k = 1, 2 \tag{3.42}$$

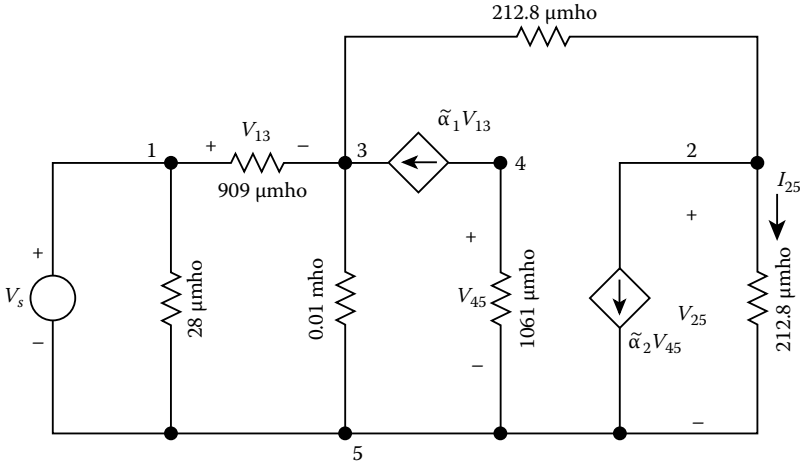


FIGURE 3.10 Equivalent network of the feedback amplifier of Figure 3.9.

The subscript k is used to distinguish the transconductances of the first and the second transistors. The indefinite-admittance matrix of the feedback amplifier of Figure 3.9 is

$$\mathbf{Y} = 10^{-4} \begin{bmatrix} 9.37 & 0 & -9.09 & 0 & -0.28 \\ 0 & 4.256 & -2.128 & \alpha_2 & -2.128 - \alpha_2 \\ -9.09 - \alpha_1 & -2.128 & 111.218 + \alpha_1 & 0 & -100 \\ \alpha_1 & 0 & -\alpha_1 & 10.61 & -10.61 \\ -0.28 & -2.128 & -100 & -10.61 - \alpha_1 & 113.018 + \alpha_1 \end{bmatrix} \quad (3.43)$$

By applying Equation 3.27, the amplifier voltage gain is computed as

$$g_{12,25} = \frac{V_{25}}{V_s} = \frac{V_{12,25}}{V_{11,25}} = \frac{211.54 \times 10^{-7}}{4.66 \times 10^{-7}} = 45.39 \quad (3.44)$$

To calculate the return differences with respect to the transconductances $\tilde{\alpha}_k$ of the transistors, we short circuit the voltage source V_s . The resulting indefinite-admittance matrix is obtained from Equation 3.43 by adding the first row to the fifth row and the first column to the fifth column and then deleting the first row and column. Its first-order cofactor is simply $Y_{11,55}$. Thus, the return differences with respect to $\tilde{\alpha}_k$ are

$$F(\tilde{\alpha}_1) = \frac{Y_{11,55}(\tilde{\alpha}_1)}{Y_{11,55}(0)} = \frac{466.1 \times 10^{-9}}{4.97 \times 10^{-9}} = 93.70 \quad (3.45a)$$

$$F(\tilde{\alpha}_2) = \frac{Y_{11,55}(\tilde{\alpha}_2)}{Y_{11,55}(0)} = \frac{466.1 \times 10^{-9}}{25.52 \times 10^{-9}} = 18.26 \quad (3.45b)$$

3.4 Null Return Difference

In this section, we introduce the notion of null return difference, which is found to be very useful in measurement situations and in the computation of the sensitivity for the feedback amplifiers.

The null return difference $\hat{F}(x)$ of a feedback amplifier with respect to an element x is defined to be the ratio of the two functional values assumed by the second-order cofactor $Y_{rp,sq}$ of the elements of its

indefinite-admittance matrix \mathbf{Y} under the condition that the element x assumes its nominal value and the condition that the element x assumes the value zero where r and s are input terminals, and p and q are the output terminals of the amplifier, or

$$\hat{F}(x) = \frac{Y_{rp,sq}(x)}{Y_{rp,sq}(0)} \quad (3.46)$$

Likewise, the null return ratio \hat{T} , with respect to a voltage-controlled current source $I = xV$, is the negative of the voltage appearing at the controlling branch when the controlled current source is replaced by an independent current source of x A and when the input excitation is adjusted so that the output of the amplifier is identically zero.

Now, we demonstrate that the null return difference is simply the return difference in the network under the situation that the input excitation I_s has been adjusted so that the output is identically zero. In the network of Figure 3.6, suppose that we replace the controlled current source by an independent current source of x A. Then by applying Equation 3.24 and the superposition principle, the output current I_{pq} at the load is

$$I_{pq} = Y_2 \left[I_s \frac{Y_{rp,sq}(0)}{Y_{uv}(0)} + x \frac{Y_{dp,cq}(0)}{Y_{uv}(0)} \right] \quad (3.47)$$

Setting $I_{pq} = 0$ or $V_{pq} = 0$ yields

$$I_s \equiv I_0 = -x \left[\frac{Y_{dp,cq}(0)}{Y_{rp,sq}(0)} \right] \quad (3.48)$$

in which $Y_{dp,cq}$ is independent of x . This adjustment is possible only if a direct transmission occurs from the input to the output when x is set to zero. Thus, in the network of Figure 3.7, if we connect an independent current source of strength I_0 at its input port, the voltage V'_{ab} is the negative of the null return ratio \hat{T} . Using Equation 3.24, we obtain [3]

$$\begin{aligned} \hat{T} &= -V'_{ab} = -x \frac{Y_{da,cb}(0)}{Y_{uv}(0)} - I_0 \frac{Y_{ra,sb}(0)}{Y_{uv}(0)} \\ &= -\frac{x [Y_{da,cb}(0)Y_{rp,sq}(0) - Y_{ra,sb}(0)Y_{dp,cq}(0)]}{Y_{uv}(0)Y_{rp,sq}(0)} \\ &= \frac{x \dot{Y}_{rp,sq}}{Y_{rp,sq}(0)} = \frac{Y_{rp,sq}(x)}{Y_{rp,sq}(0)} - 1 \end{aligned} \quad (3.49)$$

where

$$\dot{Y}_{rp,sq} \equiv \frac{dY_{rp,sq}(x)}{dx} \quad (3.50)$$

This leads to

$$\hat{F}(x) = 1 + \hat{T} = 1 - V'_{ab} \quad (3.51)$$

which demonstrates that the null return difference $\hat{F}(x)$ is simply the difference of the 1 V excitation applied to the right of the breaking mark of the broken controlling branch of the controlled source and

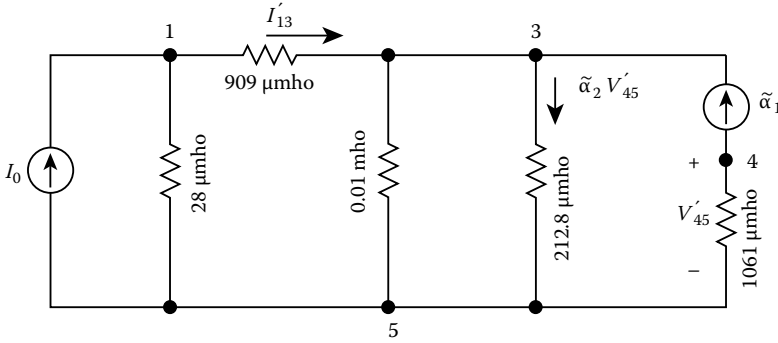


FIGURE 3.11 Network used to compute the null return difference $\hat{F}(\tilde{\alpha}_1)$ by its physical interpretation.

the returned voltage V'_{ab} appearing at the left of the breaking mark under the situation that the input signal I_s is adjusted so that the output is identically zero.

As an illustration, consider the voltage-series feedback amplifier of Figure 3.9, an equivalent network of which is presented in Figure 3.10. Using the indefinite-admittance matrix of Equation 3.43 in conjunction with Equation 3.42, the null return differences with respect to $\tilde{\alpha}_k$ are

$$\hat{F}(\tilde{\alpha}_1) = \frac{Y_{12,55}(\tilde{\alpha}_1)}{Y_{12,55}(0)} = \frac{211.54 \times 10^{-7}}{205.24 \times 10^{-12}} = 103.07 \times 10^3 \quad (3.52a)$$

$$\hat{F}(\tilde{\alpha}_2) = \frac{Y_{12,55}(\tilde{\alpha}_2)}{Y_{12,55}(0)} = \frac{211.54 \times 10^{-7}}{104.79 \times 10^{-10}} = 2018.70 \quad (3.52b)$$

Alternatively, $\hat{F}(\tilde{\alpha}_1)$ can be computed by using its physical interpretation as follows. Replace the controlled source $\tilde{\alpha}_1 V_{13}$ in Figure 3.10 by an independent current source of $\tilde{\alpha}_1$ A. We then adjust the voltage source V_s so that the output current I_{25} is identically zero. Let I_0 be the input current resulting from this source. The corresponding network is presented in Figure 3.11. From this network, we obtain

$$\hat{F}(\tilde{\alpha}_1) = 1 + \hat{T} = 1 - V'_{13} = 1 - \frac{100V'_{35} + \alpha_2 V'_{45} - \alpha_1}{9.09} = 103.07 \times 10^3 \quad (3.53)$$

Likewise, we can use the same procedure to compute the return difference $\hat{F}(\tilde{\alpha}_2)$.

References

1. H. W. Bode, *Network Analysis and Feedback Amplifier Design*, Princeton, NJ: Van Nostrand, 1945.
2. W.-K. Chen, Indefinite-admittance matrix formulation of feedback amplifier theory, *IEEE Trans. Circuits Syst.*, CAS-23, 498–505, 1976.
3. W.-K. Chen, On second-order cofactors and null return difference in feedback amplifier theory, *Int. J. Circuit Theory Appl.*, 6, 305–312, 1978.

4

Network Functions and Feedback

Wai-Kai Chen

University of Illinois at Chicago

4.1 Blackman's Formula.....	4-1
4.2 Sensitivity Function.....	4-6

We now study the effects of feedback on amplifier impedance and gain and obtain some useful relations among the return difference, the null return difference, and impedance functions in general.

Refer to the general feedback configuration of Figure 3.6. Let w be a transfer function. As before, to emphasize the importance of the feedback element x , we write $w = w(x)$. To be definite, let $w(x)$ for the time being be the current gain between the output and input ports. Then, from Equation 3.24 we obtain

$$w(x) = \frac{I_{pq}}{I_s} = \frac{Y_2 V_{pq}}{I_s} = \frac{Y_{rp,sq}(x)}{Y_{uv}(x)} Y_2 \quad (4.1)$$

yielding

$$\frac{w(x)}{w(0)} = \frac{Y_{rp,sq}(x)}{Y_{uv}(x)} \frac{Y_{uv}(0)}{Y_{rp,sq}(0)} = \frac{\hat{F}(x)}{F(x)} \quad (4.2)$$

provided that $w(0) \neq 0$. This gives a very useful formula for computing the current gain:

$$w(x) = w(0) \frac{\hat{F}(x)}{F(x)} \quad (4.3)$$

Equation 4.3 remains valid if $w(x)$ represents the transfer impedance $z_{rp,sq} = V_{pq}/I_s$ instead of the current gain.

4.1 Blackman's Formula

In particular, when $r = p$ and $s = q$, $w(x)$ represents the driving-point impedance $z_{rr,ss}(x)$ looking into the terminals r and s , and we have a somewhat different interpretation. In this case, $F(x)$ is the return difference with respect to the element x under the condition $I_s = 0$. Thus, $F(x)$ is the return difference for the situation when the port where the input impedance is defined is left open without a source and we write $F(x) = F(\text{input open circuited})$. Likewise, from Figure 3.6, $\hat{F}(x)$ is the return difference with respect to x for the input excitation I_s and output response V_{rs} under the condition I_s is adjusted so that V_{rs} is identically zero. Thus, $\hat{F}(x)$ is the return difference for the situation when the port where the input

impedance is defined is short circuited, and we write $\hat{F}(x) = F$ (input short circuited). Consequently, the input impedance $Z(x)$ looking into a terminal pair can be conveniently expressed as

$$Z(x) = Z(0) \frac{F(\text{input short circuited})}{F(\text{input open circuited})} \tag{4.4}$$

This is the well-known Blackman’s formula for computing an active impedance. The formula is extremely useful because the right-hand side can usually be determined rather easily. If x represents the controlling parameter of a controlled source in a single-loop feedback amplifier, then setting $x = 0$ opens the feedback loop and $Z(0)$ is simply a passive impedance. The return difference for x when the input port is short circuited or open circuited is relatively simple to compute because shorting out or opening a terminal pair frequently breaks the feedback loop. In addition, Blackman’s formula can be used to determine the return difference by measurements. Because it involves two return differences, only one of them can be identified and the other must be known in advance. In the case of a single-loop feedback amplifier, it is usually possible to choose a terminal pair so that either the numerator or the denominator on the right-hand side of Equation 4.4 is unity. If $F(\text{input short circuited}) = 1$, $F(\text{input open circuited})$ becomes the return difference under normal operating condition and we have

$$F(x) = \frac{Z(0)}{Z(x)} \tag{4.5}$$

On the other hand, if $F(\text{input open circuited}) = 1$, $F(\text{input short circuited})$ becomes the return difference under normal operating condition and we obtain

$$F(x) = \frac{Z(x)}{Z(0)} \tag{4.6}$$

Example 4.1

The network of Figure 4.1 is a general active RC one-port realization of a rational impedance. We use Blackman’s formula to verify that its input admittance is given by

$$Y = 1 + \frac{Z_3 - Z_4}{Z_1 - Z_2} \tag{4.7}$$

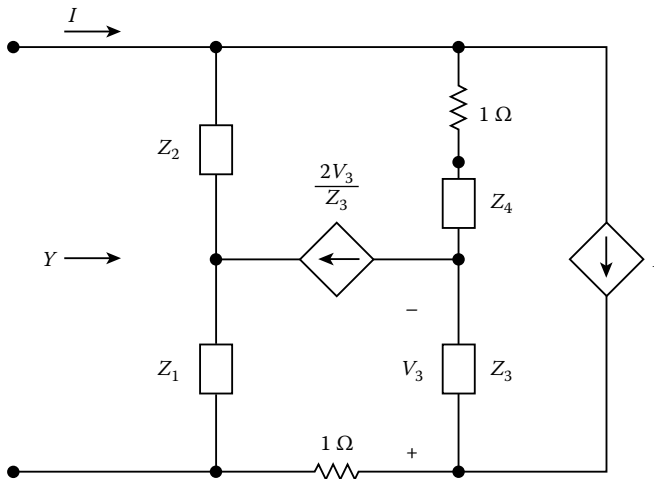


FIGURE 4.1 General active RC one-port realization of a rational function.

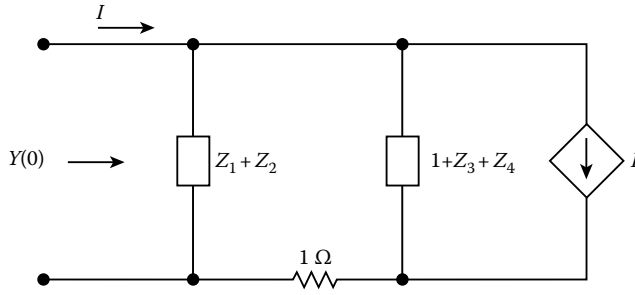


FIGURE 4.2 Network used to compute $Y(0)$.

Appealing to Equation 4.4, the input admittance written as $Y = Y(x)$ can be written as

$$Y(x) = Y(0) \frac{F(\text{input open circuited})}{F(\text{input short circuited})} \tag{4.8}$$

where $x = 2/Z_3$. By setting x to zero, the network used to compute $Y(0)$ is shown in Figure 4.2. Its input admittance is

$$Y(0) = \frac{Z_1 + Z_2 + Z_3 + Z_4 + 2}{Z_1 + Z_2} \tag{4.9}$$

When the input port is open circuited, the network of Figure 4.1 degenerates to that depicted in Figure 4.3. The return difference with respect to x is

$$F(\text{input open circuited}) = 1 - V'_3 = \frac{Z_1 + Z_3 - Z_2 - Z_4}{2 + Z_1 + Z_2 + Z_3 + Z_4} \tag{4.10}$$

where the returned voltage V'_3 at the controlling branch is given by

$$V'_3 = \frac{2(1 + Z_2 + Z_4)}{2 + Z_1 + Z_2 + Z_3 + Z_4} \tag{4.11}$$

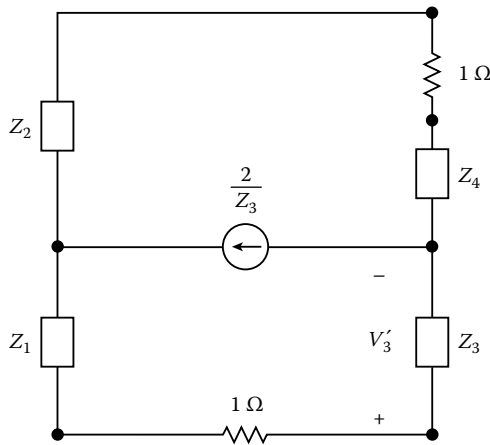


FIGURE 4.3 Network used to compute $F(\text{input open circuited})$.

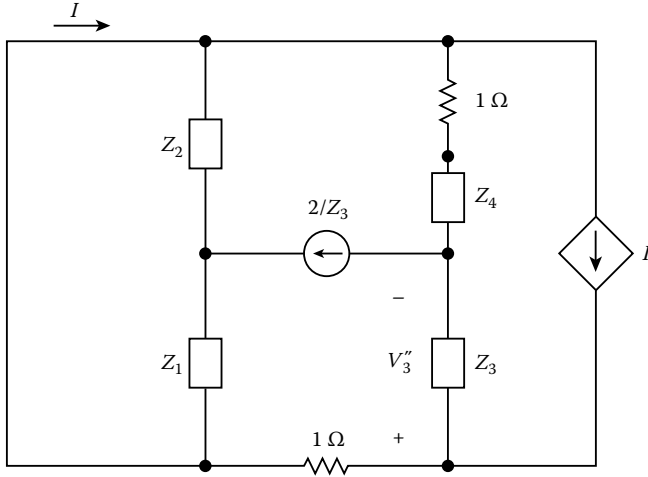


FIGURE 4.4 Network used to compute F (input short circuited).

To compute the return difference when the input port is short circuited, we use the network of Figure 4.4 and obtain

$$F(\text{input short circuited}) = 1 - V_3'' = \frac{Z_1 - Z_2}{Z_1 + Z_2} \tag{4.12}$$

where the return voltage V_3'' at the controlling branch is found to be

$$V_3'' = \frac{2Z_2}{Z_1 + Z_2} \tag{4.13}$$

Substituting Equations 4.9, 4.10, and 4.12 in Equation 4.8 yields the desired result.

$$Y = 1 + \frac{Z_3 - Z_4}{Z_1 - Z_2} \tag{4.14}$$

To determine the effect of feedback on the input and output impedances, we choose the series-parallel feedback configuration of Figure 4.5. By shorting the terminals of Y_2 , we interrupt the feedback loop,

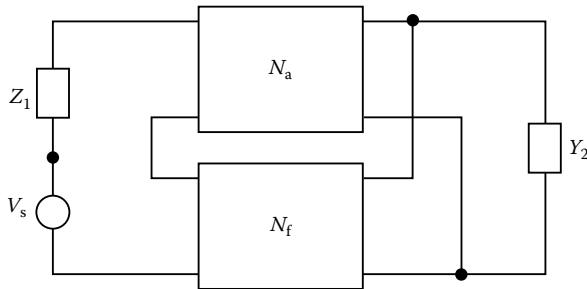


FIGURE 4.5 Series-parallel feedback configuration.

therefore, formula (Equation 4.5) applies and the output impedance across the load admittance Y_2 becomes

$$Z_{\text{out}}(x) = \frac{Z_{\text{out}}(0)}{F(x)} \quad (4.15)$$

demonstrating that the impedance measured across the path of the feedback is reduced by the factor that is the normal value of the return difference with respect to the element x , where x is an arbitrary element of interest. For the input impedance of the amplifier looking into the voltage source V_s of Figure 4.5, by open circuiting or removing the voltage source V_s , we break the feedback loop. Thus, formula (Equation 4.6) applies and the input impedance becomes

$$Z_{\text{in}}(x) = F(x)Z_{\text{in}}(0) \quad (4.16)$$

meaning that the impedance measured in series lines is increased by the same factor $F(x)$. Similar conclusions can be reached for other types of configurations discussed in Chapter 2 by applying Blackman's formula.

Again, refer to the general feedback configuration of Figure 3.6. If $w(x)$ represents the voltage gain V_{pq}/V_{rs} or the transfer admittance I_{pq}/V_{rs} . Then, from Equation 4.27 we can write

$$\frac{w(x)}{w(0)} = \frac{Y_{rp,sq}(x) Y_{rr,ss}(0)}{Y_{rp,sq}(0) Y_{rr,ss}(x)} \quad (4.17)$$

The first term in the product on the right-hand side is the null return difference $\hat{F}(x)$ with respect to x for the input terminals r and s and output terminals p and q . The second term is the reciprocal of the null return difference with respect to x for the same input and output port at terminals r and s . This reciprocal can then be interpreted as the return difference with respect to x when the input port of the amplifier is short circuited. Thus, the voltage gain or the transfer admittance can be expressed as

$$w(x) = w(0) \frac{\hat{F}(x)}{F(\text{input short circuited})} \quad (4.18)$$

Finally, if $w(x)$ denotes the short circuit current gain I_{pq}/I_s as Y_2 approaches infinity, we obtain

$$\frac{w(x)}{w(0)} = \frac{Y_{rp,sq}(x) Y_{pp,qq}(0)}{Y_{rp,sq}(0) Y_{pp,qq}(x)} \quad (4.19)$$

The second term in the product on the right-hand side is the reciprocal of the return difference with respect to x when the output port of the amplifier is short circuited, giving a formula for the short circuit current gain as

$$w(x) = w(0) \frac{\hat{F}(x)}{F(\text{output short circuited})} \quad (4.20)$$

Again, consider the voltage-series or series-parallel feedback amplifier of Figure 3.9 an equivalent network of which is given in Figure 3.10. The return differences $F(\tilde{\alpha}_k)$, the null return differences $\hat{F}(\tilde{\alpha}_k)$ and the voltage gain w were computed earlier in Equations 3.45, 3.52, and 3.44, and are repeated next:

$$F(\tilde{\alpha}_1) = 93.70, \quad F(\tilde{\alpha}_2) = 18.26 \quad (4.21a)$$

$$\hat{F}(\tilde{\alpha}_1) = 103.07 \times 10^3, \quad \hat{F}(\tilde{\alpha}_2) = 2018.70 \quad (4.21b)$$

$$w = \frac{V_{25}}{V_s} = w(\tilde{\alpha}_1) = w(\tilde{\alpha}_2) = 45.39 \quad (4.21c)$$

We apply Equation 4.18 to calculate the voltage gain w , as follows:

$$w(\tilde{\alpha}_1) = w(0) \frac{\hat{F}(\tilde{\alpha}_1)}{F(\text{input short circuited})} = 0.04126 \frac{103.07 \times 10^3}{93.699} = 45.39 \quad (4.22)$$

where

$$w(0) = \frac{Y_{12,55}(\tilde{\alpha}_1)}{Y_{11,55}(\tilde{\alpha}_1)} \Big|_{\tilde{\alpha}_1=0} = \frac{205.24 \times 10^{-12}}{497.41 \times 10^{-11}} = 0.04126 \quad (4.23a)$$

$$F(\text{input short circuited}) = \frac{Y_{11,55}(\tilde{\alpha}_1)}{Y_{11,55}(0)} = \frac{466.07 \times 10^{-9}}{4.9741 \times 10^{-9}} = 93.699 \quad (4.23b)$$

and

$$w(\tilde{\alpha}_2) = w(0) \frac{\hat{F}(\tilde{\alpha}_2)}{F(\text{input short circuited})} = 0.41058 \frac{2018.70}{18.26} = 45.39 \quad (4.24)$$

where

$$w(0) = \frac{Y_{12,55}(\tilde{\alpha}_2)}{Y_{11,55}(\tilde{\alpha}_2)} \Big|_{\tilde{\alpha}_2=0} = \frac{104.79 \times 10^{-10}}{255.22 \times 10^{-10}} = 0.41058 \quad (4.25a)$$

$$F(\text{input short circuited}) = \frac{Y_{11,55}(\tilde{\alpha}_2)}{Y_{11,55}(0)} = \frac{466.07 \times 10^{-9}}{25.52 \times 10^{-9}} = 18.26 \quad (4.25b)$$

4.2 Sensitivity Function

One of the most important effects of negative feedback is its ability to make an amplifier less sensitive to the variations of its parameters because of aging, temperature variations, or other environment changes. A useful quantitative measure for the degree of dependence of an amplifier on a particular parameter is known as the sensitivity. The sensitivity function, written as $\mathcal{S}(x)$, for a given transfer function with respect to an element x is defined as the ratio of the fractional change in a transfer function to the fractional change in x for the situation when all changes concerned are differentially small. Thus, if $w(x)$ is the transfer function, the sensitivity function can be written as

$$\mathcal{S}(x) = \lim_{\Delta x \rightarrow 0} \frac{\Delta w/w}{\Delta x/x} = \frac{x}{w} \frac{\partial w}{\partial x} = x \frac{\partial \ln w}{\partial x} \quad (4.26)$$

Refer to the general feedback configuration of Figure 3.6, and let $w(x)$ represent either the current gain I_{pq}/I_s or the transfer impedance V_{pq}/I_s for the time being. Then, we obtain from Equation 3.24

$$w(x) = Y_2 \frac{Y_{rp,sq}(x)}{Y_{uv}(x)} \quad \text{or} \quad \frac{Y_{rp,sq}(x)}{Y_{uv}(x)} \quad (4.27)$$

As before, we write

$$\dot{Y}_{uv}(x) = \frac{\partial Y_{uv}(x)}{\partial x} \quad (4.28a)$$

$$\dot{Y}_{rp,sq}(x) = \frac{\partial Y_{rp,sq}(x)}{\partial x} \quad (4.28b)$$

obtaining

$$Y_{uv}(x) = Y_{uv}(0) + x\dot{Y}_{uv}(x) \quad (4.29a)$$

$$Y_{rp,sq}(x) = Y_{rp,sq}(0) + x\dot{Y}_{rp,sq}(x) \quad (4.29b)$$

Substituting Equation 4.27 in Equation 4.26, in conjunction with Equation 4.29, yields

$$\begin{aligned} \mathcal{G}(x) &= x \frac{\dot{Y}_{rp,sq}(x)}{Y_{rp,sq}(x)} - x \frac{\dot{Y}_{uv}(x)}{Y_{uv}(x)} = \frac{Y_{rp,sq}(x) - Y_{rp,sq}(0)}{Y_{rp,sq}(x)} - \frac{Y_{uv}(x) - Y_{uv}(0)}{Y_{uv}(x)} \\ &= \frac{Y_{uv}(0)}{Y_{uv}(x)} - \frac{Y_{rp,sq}(0)}{Y_{rp,sq}(x)} = \frac{1}{F(x)} - \frac{1}{\hat{F}(x)} \end{aligned} \quad (4.30)$$

Combining this with Equation 4.3, we obtain

$$\mathcal{G}(x) = \frac{1}{F(x)} \left[1 - \frac{w(0)}{w(x)} \right] \quad (4.31)$$

Observe that if $w(0) = 0$, Equation 4.31 becomes

$$\mathcal{G}(x) = \frac{1}{F(x)} \quad (4.32)$$

meaning that sensitivity is equal to the reciprocal of the return difference. For the ideal feedback model, the feedback path is unilateral. Hence, $w(0) = 0$ and

$$\mathcal{G} = \frac{1}{F} = \frac{1}{1 + T} = \frac{1}{1 - \mu\beta} \quad (4.33)$$

For a practical amplifier, $w(0)$ is usually very much smaller than $w(x)$ in the passband, and $F \approx 1/\mathcal{G}$ may be used as a good estimate of the reciprocal of the sensitivity in the same frequency band. A single-loop feedback amplifier composed of a cascade of common-emitter stages with a passive network providing the desired feedback fulfills this requirements. If in such a structure any one of the transistors fails, the forward transmission is nearly zero and $w(0)$ is practically zero. Our conclusion is that if the failure of any element will interrupt the transmission through the amplifier as a whole to nearly zero, the sensitivity is approximately equal to the reciprocal of the return difference with respect to that element. In the case of driving-point impedance, $w(0)$ is not usually smaller than $w(x)$, and the reciprocity relation is not generally valid.

Now assume that $w(x)$ represents the voltage gain. Substituting Equation 4.27 in Equation 4.26 results in

$$\begin{aligned} \mathcal{G}(x) &= x \frac{\dot{Y}_{rp,sq}(x)}{Y_{rp,sq}(x)} - x \frac{\dot{Y}_{rr,ss}(x)}{Y_{rr,ss}(x)} = \frac{Y_{rp,sq}(x) - Y_{rp,sq}(0)}{Y_{rp,sq}(x)} - \frac{Y_{rr,ss}(x) - Y_{rr,ss}(0)}{Y_{rr,ss}(x)} \\ &= \frac{Y_{rr,ss}(0)}{Y_{rr,ss}(x)} - \frac{Y_{rp,sq}(0)}{Y_{rp,sq}(x)} = \frac{1}{F(\text{input short circuited})} - \frac{1}{\hat{F}(x)} \end{aligned} \quad (4.34)$$

Combining this with Equation 4.18 gives

$$\mathcal{S}(x) = \frac{1}{F(\text{input short circuited})} \left[1 - \frac{w(0)}{w(x)} \right] \tag{4.35}$$

Finally, if $w(x)$ denotes the short circuit current gain I_{pq}/I_s as Y_2 approaches infinity, the sensitivity function can be written as

$$\mathcal{S}(x) = \frac{Y_{pp,qq}(0)}{Y_{pp,qq}(x)} - \frac{Y_{rp,sq}(0)}{Y_{rp,sq}(x)} = \frac{1}{F(\text{output short circuited})} - \frac{1}{\hat{F}(x)} \tag{4.36}$$

which when combined with Equation 4.20 yields

$$\mathcal{S}(x) = \frac{1}{F(\text{output short circuited})} \left[1 - \frac{w(0)}{w(x)} \right] \tag{4.37}$$

We remark that Equations 4.31, 4.35, and 4.39 are quite similar. If the return difference $F(x)$ is interpreted properly, they can all be represented by the single relation Equation 4.31. As before, if $w(0) = 0$, the sensitivity for the voltage gain function is equal to the reciprocal of the return difference under the situation that the input port of the amplifier is short circuited, whereas the sensitivity for the short circuit current gain is the reciprocal of the return difference when the output port is short circuited.

Example 4.2

The network of Figure 4.6 is a common-emitter transistor amplifier. After removing the biasing circuit and using the common-emitter hybrid model for the transistor at low frequencies, an equivalent network of the amplifier is presented in Figure 4.7 with

$$I'_s = \frac{V_s}{R_1 + r_x} \tag{4.38a}$$

$$G'_1 = \frac{1}{R'_1} = \frac{1}{R_1 + r_x} + \frac{1}{r_\pi} \tag{4.38b}$$

$$G'_2 = \frac{1}{R'_2} = \frac{1}{R_2} + \frac{1}{R_c} \tag{4.38c}$$

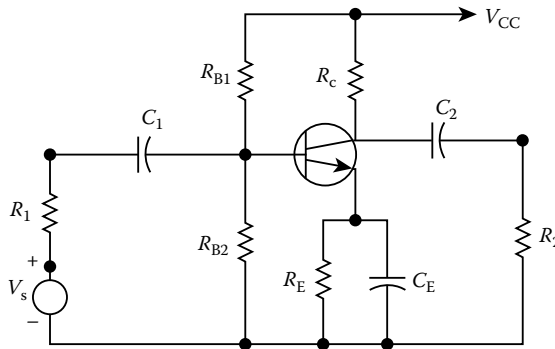
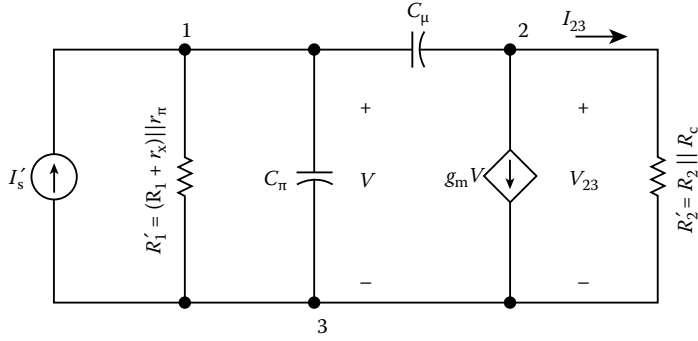


FIGURE 4.6 Common-emitter transistor feedback amplifier.


FIGURE 4.7 Equivalent network of the feedback amplifier of Figure 4.6.

The indefinite admittance matrix of the amplifier is

$$\mathbf{Y} = \begin{bmatrix} G'_1 + sC_\pi + sC_\mu & -sC_\mu & -G'_1 - sC_\pi \\ g_m - sC_\mu & G'_2 + sC_\mu & -G'_2 - g_m \\ -G'_1 - sC_\pi - g_m & -G'_2 & G'_1 + G'_2 + sC_\pi + g_m \end{bmatrix} \quad (4.39)$$

Assume that the controlling parameter g_m is the element of interest. The return difference and the null return difference with respect to g_m in Figure 4.7 with I'_s as the input port and R'_2 as the output port, are

$$F(g_m) = \frac{Y_{33}(g_m)}{Y_{33}(0)} = \frac{(G'_1 + sC_\pi)(G'_2 + sC_\mu) + sC_\mu(G'_2 + g_m)}{(G'_1 + sC_\pi)(G'_2 + sC_\mu) + sC_\mu G'_2} \quad (4.40)$$

$$\hat{F}(g_m) = \frac{Y_{12,33}(g_m)}{Y_{12,33}(0)} = \frac{sC_\mu - g_m}{sC_\mu} = 1 - \frac{g_m}{sC_\mu} \quad (4.41)$$

The current gain I_{23}/I'_s as defined in Figure 4.7, is computed as

$$w(g_m) = \frac{Y_{12,33}(g_m)}{R'_2 Y_{33}(g_m)} = \frac{sC_\mu - g_m}{R'_2 [(G'_1 + sC_\pi)(G'_2 + sC_\mu) + sC_\mu(G'_2 + g_m)]} \quad (4.42)$$

Substituting these in Equations 4.30 or 4.31 gives

$$\mathcal{P}(g_m) = -\frac{g_m(G'_1 + sC_\pi + sC_\mu)(G'_2 + sC_\mu)}{(sC_\mu - g_m)[(G'_1 + sC_\pi)(G'_2 + sC_\mu) + sC_\mu(G'_2 + g_m)]} \quad (4.43)$$

Finally, we compute the sensitivity for the driving-point impedance facing the current source I'_s . From Equation 4.31, we obtain

$$\mathcal{S}(g_m) = \frac{1}{F(g_m)} \left[1 - \frac{Z(0)}{Z(g_m)} \right] = -\frac{sC_\mu g_m}{(G'_1 + sC_\pi)(G'_2 + sC_\mu) + sC_\mu(G'_2 + g_m)} \quad (4.44)$$

where

$$Z(g_m) = \frac{Y_{11,33}(g_m)}{Y_{33}(g_m)} = \frac{G'_2 + sC_\mu}{(G'_1 + sC_\pi)(G'_2 + sC_\mu) + sC_\mu(G'_2 + g_m)} \quad (4.45)$$

5

Measurement of Return Difference

Wai-Kai Chen
University of Illinois at Chicago

5.1 Blecher's Procedure	5-2
5.2 Impedance Measurements	5-4
References	5-7

The zeros of the network determinant are called the natural frequencies. Their locations in the complex-frequency plane are extremely important in that they determine the stability of the network. A network is said to be stable if all of its natural frequencies are restricted to the open left-half side of the complex-frequency plane. If a network determinant is known, its roots can readily be computed explicitly with the aid of a computer if necessary, and the stability problem can then be settled directly. However, for a physical network there remains the difficulty of getting an accurate formulation of the network determinant itself, because every equivalent network is, to a greater or lesser extent, an idealization of the physical reality. As frequency is increased, parasitic effects of the physical elements must be taken into account. What is really needed is some kind of experimental verification that the network is stable and will remain so under certain prescribed conditions. The measurement of the return difference provides an elegant solution to this problem.

The return difference with respect to an element x in a feedback amplifier is defined by

$$F(x) = \frac{Y_{uv}(x)}{Y_{uv}(0)} \tag{5.1}$$

Because $Y_{uv}(x)$ denotes the nodal determinant, the zeros of the return difference are exactly the same as the zeros of the nodal determinant provided that there is no cancellation of common factors between $Y_{uv}(x)$ and $Y_{uv}(0)$. Therefore, if $Y_{uv}(0)$ is known to have no zeros in the closed right-half side of the complex-frequency plane, which is usually the case in a single-loop feedback amplifier when x is set to zero, $F(x)$ gives precisely the same information about the stability of a feedback amplifier as does the nodal determinant itself. The difficulty inherent in the measurement of the return difference with respect to the controlling parameter of a controlled source is that, in a physical system, the controlling branch and the controlled source both form part of a single device such as a transistor, and cannot be physically separated. In the following, we present a scheme that does not require the physical decomposition of a device.

Let a device of interest be brought out as a two-port network connected to a general four-port network as shown in Figure 5.1. For our purposes, assume that this device is characterized by its y parameters, and represented by its y -parameter equivalent two-port network as indicated in Figure 5.2, in which the parameter y_{21} controls signal transmission in the forward direction through the device, whereas y_{12} gives

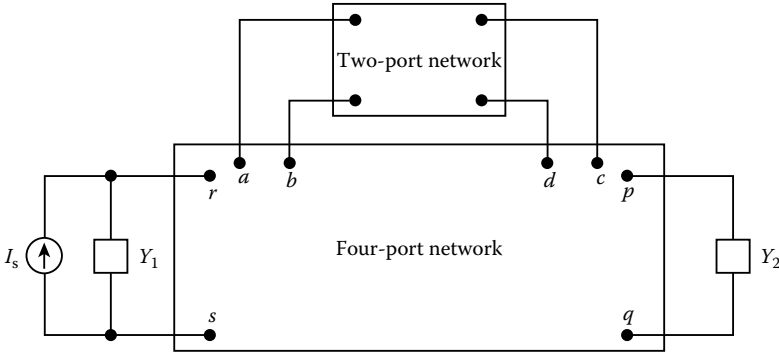


FIGURE 5.1 The general configuration of a feedback amplifier with a two-port device.

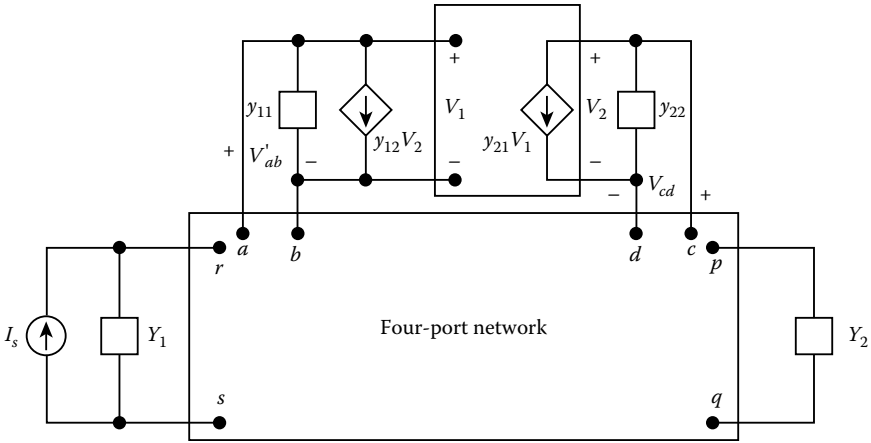


FIGURE 5.2 The representation of a two-port device in Figure 5.1 by its y parameters.

the reverse transmission, accounting for the internal feedback within the device. Our objective is to measure the return difference with respect to the forward short circuit transfer admittance y_{21} .

5.1 Blecher's Procedure [1]

Let the two-port device be a transistor operated in the common-emitter configuration with terminals a , $b=d$, and c representing, respectively, the base, emitter, and collector terminals. To simplify our notation, let $a=1$, $b=d=3$, and $c=2$, as exhibited explicitly in Figure 5.3.

To measure $F(y_{21})$, we break the base terminal of the transistor and apply a 1 V excitation at its input as exhibited in Figure 5.3. To ensure that the controlled current source $y_{21}V_{13}$ drives a replica of what it sees during normal operation, we connect an active one-port network composed of a parallel combination of the admittance y_{11} and a controlled current source $y_{12}V_{23}$ at terminals 1 and 3. The returned voltage V_{13} is precisely the negative of the return ratio with respect to the element y_{21} . If, in the frequency band of interest, the externally applied feedback is large compared with the internal feedback of the transistor, the controlled source $y_{12}V_{23}$ can be ignored. If, however, we find that this internal feedback cannot be ignored, we can simulate it by using an additional transistor, connected as shown in Figure 5.4. This additional transistor must be matched as closely as possible to the one in question. The one-port

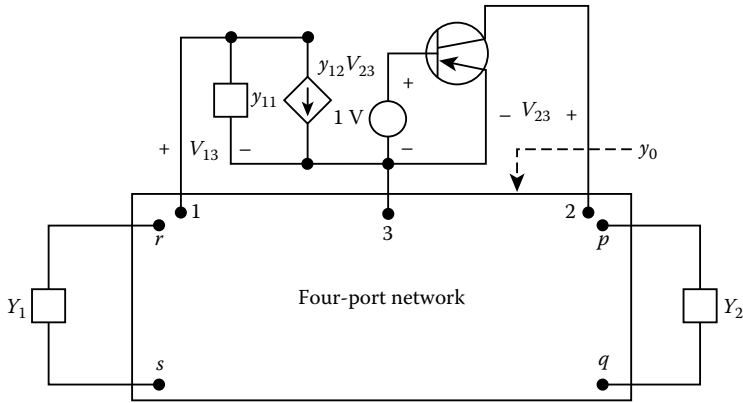


FIGURE 5.3 A physical interpretation of the return difference $F(y_{21})$ for a transistor operated in the common-emitter configuration and represented by its y parameters y_{ij} .

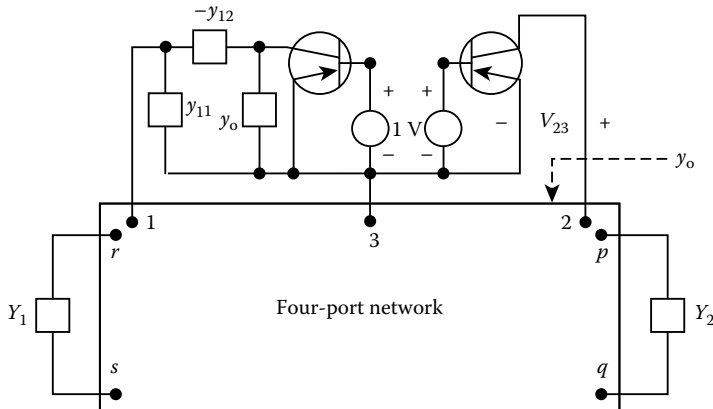


FIGURE 5.4 The measurement of return difference $F(y_{21})$ for a transistor operated in the common-emitter configuration and represented by its y parameters y_{ij} .

admittance y_0 denotes the admittance presented to the output port of the transistor under consideration as indicated in Figures 5.3 and 5.4. For a common-emitter state, it is perfectly reasonable to assume that $|y_0| \gg |y_{12}|$ and $|y_{11}| \gg |y_{12}|$. Under these assumptions, it is straightforward to show that the Norton equivalent network looking into the two-port network at terminals 1 and 3 of Figure 5.4 can be approximated by the parallel combination of y_{11} and $y_{12}V_{23}$, as indicated in Figure 5.3. In Figure 5.4, if the voltage sources have very low internal impedances, we can join together the two base terminals of the transistors and feed them both from a single voltage source of very low internal impedance. In this way, we avoid the need of using two separate sources. For the procedure to be feasible, we must demonstrate the admittances y_{11} and $-y_{12}$ can be realized as the input admittances of one-port RC networks.

Consider the hybrid- π equivalent network of a common-emitter transistor of Figure 5.5, the short circuit admittance matrix of which is found to be

$$\mathbf{Y}_{sc} = \frac{1}{g_x + g_\pi + sC_\pi + sC_\mu} \begin{bmatrix} g_x(g_\pi + sC_\pi + sC_\mu) & -g_x sC_\mu \\ g_x(g_m - sC_\mu) & sC_\mu(g_x + g_\pi + sC_\pi + g_m) \end{bmatrix} \quad (5.2)$$

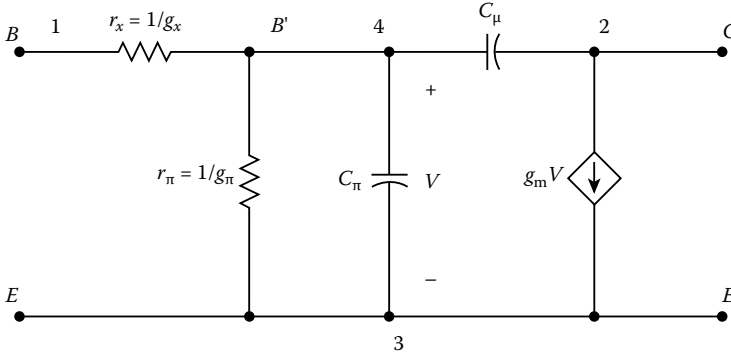


FIGURE 5.5 The hybrid-pi equivalent network of a common-emitter transistor.

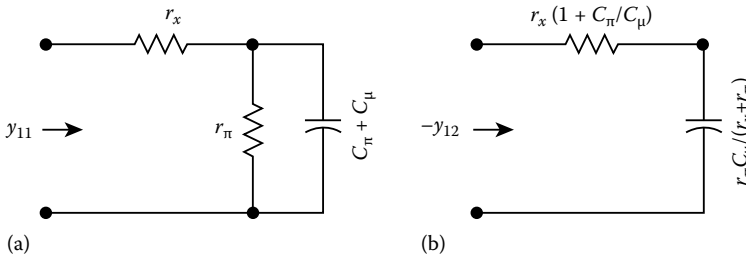


FIGURE 5.6 (a) The realization of y_{11} and (b) the realization of $-y_{12}$.

It is easy to confirm that the admittance y_{11} and $-y_{12}$ can be realized by the one-port networks of Figure 5.6.

5.2 Impedance Measurements

In this section, we show that the return difference can be evaluated by measuring two driving-point impedances at a convenient port in the feedback amplifier [2].

Refer again to the general feedback configuration of Figure 5.2. Suppose that we wish to evaluate the return difference with respect to the forward short circuit transfer admittance y_{21} . The controlling parameters y_{12} and y_{21} enter the indefinite-admittance matrix \mathbf{Y} in the rectangular patterns as shown next:

$$\mathbf{Y}(x) = \begin{matrix} & a & b & c & d \\ \begin{matrix} a \\ b \\ c \\ d \end{matrix} & \left[\begin{array}{cccc} & & y_{12} & -y_{12} \\ & & -y_{12} & y_{12} \\ y_{21} & -y_{21} & & \\ -y_{21} & y_{21} & & \end{array} \right] & & & \end{matrix} \quad (5.3)$$

To emphasize the importance of y_{12} and y_{21} , we again write $Y_{uv}(x)$ as $Y_{uv}(y_{12}, y_{21})$ and $z_{aa,bb}(x)$ as $z_{aa,bb}(y_{12}, y_{21})$. By appealing to Equation 3.25, the impedance looking into terminals a and b of Figure 5.2 is

$$z_{aa,bb}(y_{12}, y_{21}) = \frac{Y_{aa,bb}(y_{12}, y_{21})}{Y_{dd}(y_{12}, y_{21})} \tag{5.4}$$

The return difference with respect to y_{21} is given by

$$F(y_{21}) = \frac{Y_{dd}(y_{12}, y_{21})}{Y_{dd}(y_{12}, 0)} \tag{5.5}$$

Combining these yields

$$\begin{aligned} F(y_{21})z_{aa,bb}(y_{12}, y_{21}) &= \frac{Y_{aa,bb}(y_{12}, y_{21})}{Y_{dd}(y_{12}, 0)} = \frac{Y_{aa,bb}(0, 0)}{Y_{dd}(y_{12}, 0)} \\ &= \frac{Y_{aa,bb}(0, 0)}{Y_{dd}(0, 0)} \frac{Y_{dd}(0, 0)}{Y_{dd}(y_{12}, 0)} = \frac{z_{aa,bb}(0, 0)}{F(y_{12})|_{y_{21}=0}} \end{aligned} \tag{5.6}$$

obtaining a relation

$$F(y_{12})|_{y_{21}=0}F(y_{21}) = \frac{z_{aa,bb}(0, 0)}{z_{aa,bb}(y_{12}, y_{21})} \tag{5.7}$$

among the return differences and the driving-point impedances. $F(y_{12})|_{y_{21}=0}$ is the return difference with respect to y_{12} when y_{21} is set to zero. This quantity can be measured by the arrangement of Figure 5.7. $z_{aa,bb}(y_{12}, y_{21})$ is the driving-point impedance looking into terminals a and b of the network of Figure 5.2. Finally, $z_{aa,bb}(0, 0)$ is the impedance to which $z_{aa,bb}(y_{12}, y_{21})$ reduces when the controlling parameters y_{12} and y_{21} are both set to zero. This impedance can be measured by the arrangement of Figure 5.8. Note that, in all three measurements, the independent current source I_s is removed.

Suppose that we wish to measure the return difference $F(y_{21})$ with respect to the forward transfer admittance y_{21} of a common-emitter transistor shown in Figure 5.2. Then, the return difference $F(y_{12})$ when y_{21} is set to zero, for all practical purposes, is indistinguishable from unity. Therefore, Equation 5.7 reduces to the following simpler form:

$$F(y_{21}) \approx \frac{z_{11, 33}(0, 0)}{z_{11, 33}(y_{12}, y_{21})} \tag{5.8}$$

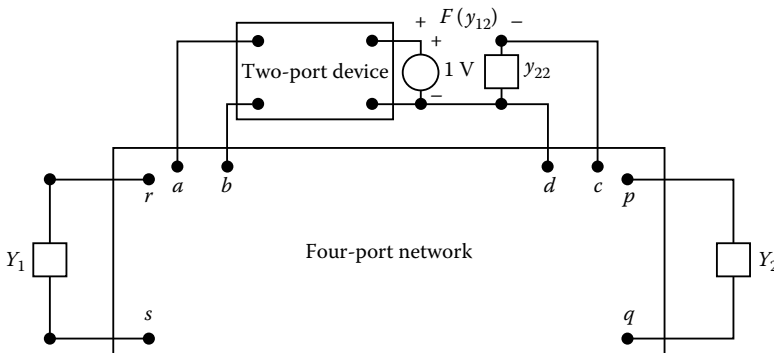


FIGURE 5.7 The measurement of the return difference $F(y_{12})$ with y_{21} set to zero.

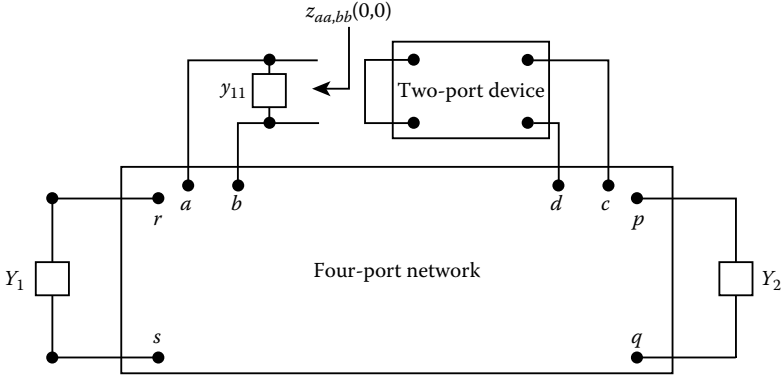


FIGURE 5.8 The measurement of the driving-point impedance $z_{aa,bb}(0, 0)$.

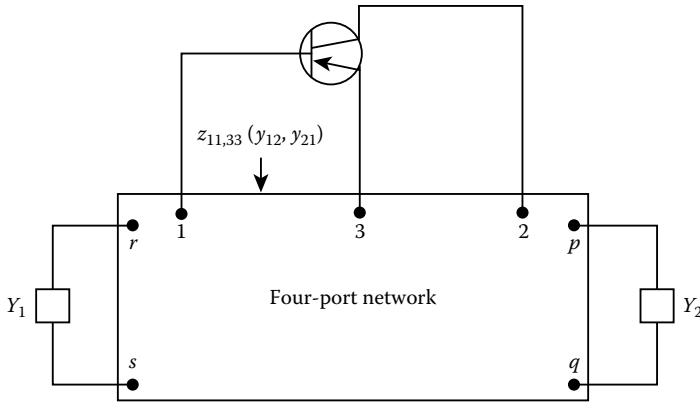


FIGURE 5.9 The measurement of the driving-point impedance $z_{11,33}(y_{12}, y_{21})$.

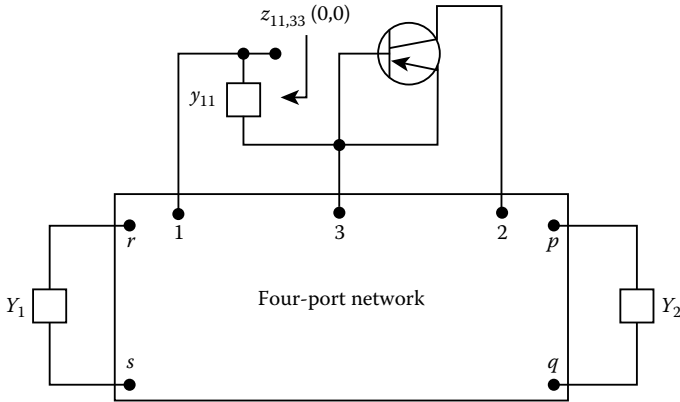


FIGURE 5.10 The measurement of the driving-point impedance $z_{11,33}(0, 0)$.

showing that the return difference $F(y_{21})$ effectively equals the ratio of two functional values assumed by the driving-point impedance looking into terminals 1 and 3 of Figure 5.2 under the condition that the controlling parameters y_{12} and y_{21} are both set to zero and the condition that they assume their nominal values. These two impedances can be measured by the network arrangements of Figures 5.9 and 5.10.

References

1. F. H. Blecher, Design principles for single loop transistor feedback amplifiers, *IRE Trans. Circuit Theory*, CT-4, 145–156, 1957.
2. S. S. Haykin, *Active Network Theory*, Reading, MA: Addison-Wesley, 1970.

6

Multiple-Loop Feedback Amplifiers

6.1	Multiple-Loop Feedback Amplifier Theory	6-1
6.2	Return Different Matrix	6-5
6.3	Null Return Difference Matrix	6-6
6.4	Transfer-Function Matrix and Feedback.....	6-7
6.5	Sensitivity Matrix.....	6-10
6.6	Multiparameter Sensitivity.....	6-14
	References.....	6-17

Wai-Kai Chen

University of Illinois at Chicago

So far, we have studied the single-loop feedback amplifiers. The concept of feedback was introduced in terms of return difference. We found that return difference is the difference between the unit applied signal and the returned signal. The returned signal has the same physical meaning as the loop transmission in the ideal feedback mode. It plays an important role in the study of amplifier stability, its sensitivity to the variations of the parameters, and the determination of its transfer and driving point impedances. The fact that return difference can be measured experimentally for many practical amplifiers indicates that we can include all the parasitic effects in the stability study, and that stability problem can be reduced to a Nyquist plot.

In this section, we study amplifiers that contain a multiplicity of inputs, outputs, and feedback loops. They are referred to as the multiple-loop feedback amplifiers. As might be expected, the notion of return difference with respect to an element is no longer applicable, because we are dealing with a group of elements. For this, we generalize the concept of return difference for a controlled source to the notion of return difference matrix for a multiplicity of controlled sources. For measurement situations, we introduce the null return difference matrix and discuss its physical significance. We demonstrate that the determinant of the overall transfer function matrix can be expressed explicitly in terms of the determinants of the return difference and the null return difference matrices, thereby allowing us to generalize Blackman's formula for the input impedance.

6.1 Multiple-Loop Feedback Amplifier Theory

The general configuration of a multiple-input, multiple-output, and multiple-loop feedback amplifier is presented in Figure 6.1, in which the input, output, and feedback variables may be either currents or voltages. For the specific arrangement of Figure 6.1, the input and output variables are represented by an n -dimensional vector \mathbf{u} and an m -dimensional vector \mathbf{y} as

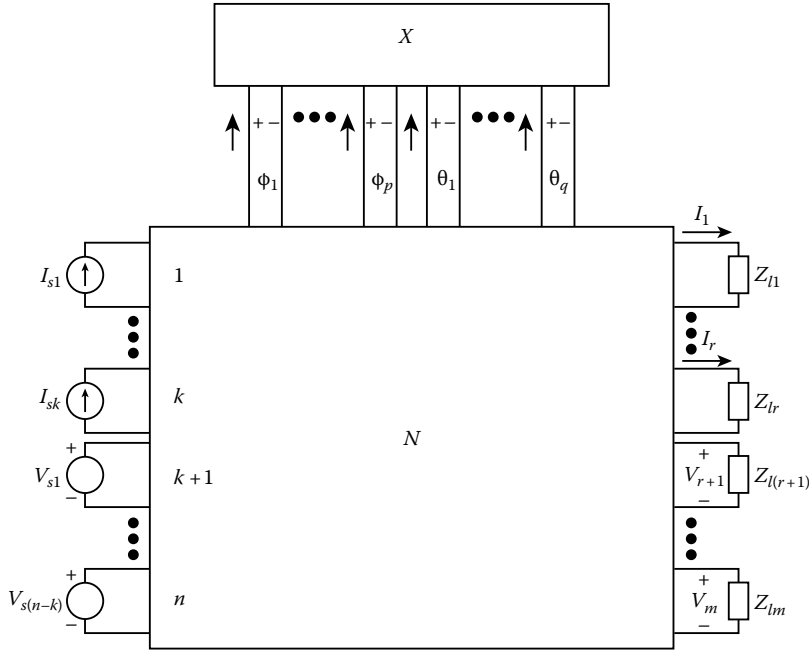


FIGURE 6.1 The general configuration of a multiple-input, multiple-output, and multiple-loop feedback amplifier.

$$\mathbf{u}(s) = \begin{bmatrix} u_1 \\ u_2 \\ \vdots \\ u_k \\ u_{k+1} \\ u_{k+2} \\ \vdots \\ u_n \end{bmatrix} = \begin{bmatrix} I_{s1} \\ I_{s2} \\ \vdots \\ I_{sk} \\ V_{s1} \\ V_{s2} \\ \vdots \\ V_{s(n-k)} \end{bmatrix}, \quad \mathbf{y}(s) = \begin{bmatrix} y_1 \\ y_2 \\ \vdots \\ y_r \\ y_{r+1} \\ y_{r+2} \\ \vdots \\ y_m \end{bmatrix} = \begin{bmatrix} I_1 \\ I_2 \\ \vdots \\ I_r \\ V_{r+1} \\ V_{r+2} \\ \vdots \\ V_m \end{bmatrix} \tag{6.1}$$

respectively. The elements of interest can be represented by a rectangular matrix \mathbf{X} of order $q \times p$ relating the controlled and controlling variables by the matrix equation

$$\Theta = \begin{bmatrix} \theta_1 \\ \theta_2 \\ \vdots \\ \theta_q \end{bmatrix} = \begin{bmatrix} x_{11} & x_{12} & \cdots & x_{1p} \\ x_{21} & x_{22} & \cdots & x_{2p} \\ \vdots & \vdots & \vdots & \vdots \\ x_{q1} & x_{q2} & \cdots & x_{qp} \end{bmatrix} \begin{bmatrix} \phi_1 \\ \phi_2 \\ \vdots \\ \phi_p \end{bmatrix} = \mathbf{X}\Phi \tag{6.2}$$

where the p -dimensional vector Φ is called the controlling vector, and the q -dimensional vector Θ is the controlled vector. The controlled variables θ_k and the controlling variables Φ_k can either be currents or voltages. The matrix \mathbf{X} can represent either a transfer-function matrix or a driving-point function matrix. If \mathbf{X} represents a driving-point function matrix, the vectors Θ and Φ are of the same dimension ($q = p$) and their components are the currents and voltages of a p -port network.

The general configuration of Figure 6.1 can be represented equivalently by the block diagram of Figure 6.2 in which N is a $(p + q + m + n)$ -port network and the elements of interest are exhibited

explicitly by the block \mathbf{X} . For the $(p + q + m + n)$ -port network N , the vectors \mathbf{u} and Θ are its inputs, and the vectors Φ and \mathbf{y} its outputs. Since N is linear, the input and output vectors are related by the matrix equations

$$\Phi = \mathbf{A}\Theta + \mathbf{B}\mathbf{u} \quad (6.3a)$$

$$\mathbf{y} = \mathbf{C}\Theta + \mathbf{D}\mathbf{u} \quad (6.3b)$$

where \mathbf{A} , \mathbf{B} , \mathbf{C} , and \mathbf{D} are transfer-function matrices of orders $p \times q$, $p \times n$, $m \times q$, and $m \times n$, respectively. The vectors Θ and Φ are not independent and are related by

$$\Theta = \mathbf{X}\Phi \quad (6.3c)$$

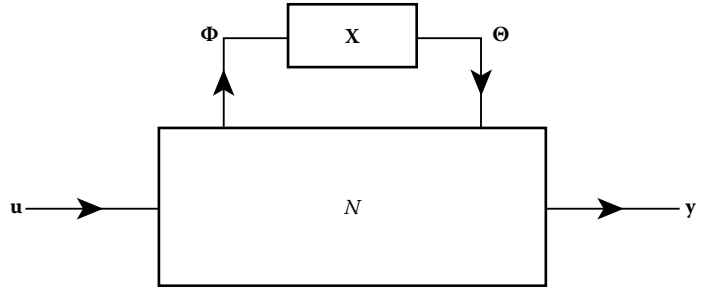


FIGURE 6.2 The block diagram of the general feedback configuration of Figure 6.1.

The relationships among the above three linear matrix equations can also be represented by a matrix signal-flow graph as shown in Figure 6.3 known as the fundamental matrix feedback-flow graph. The overall closed-loop transfer-function matrix of the multiple-loop feedback amplifier is defined by the equation

$$\mathbf{y} = \mathbf{W}(\mathbf{X})\mathbf{u} \quad (6.4)$$

where $\mathbf{W}(\mathbf{X})$ is of order $m \times n$. As before, to emphasize the importance of \mathbf{X} , the matrix \mathbf{W} is written as $\mathbf{W}(\mathbf{X})$ for the present discussion, even though it is also a function of the complex-frequency variable s . Combining the previous matrix equations, the transfer-function matrix is

$$\mathbf{W}(\mathbf{X}) = \mathbf{D} + \mathbf{C}\mathbf{X}(\mathbf{I}_p - \mathbf{A}\mathbf{X})^{-1}\mathbf{B} \quad (6.5a)$$

or

$$\mathbf{W}(\mathbf{X}) = \mathbf{D} + \mathbf{C}(\mathbf{I}_q - \mathbf{X}\mathbf{A})^{-1}\mathbf{X}\mathbf{B} \quad (6.5b)$$

where \mathbf{I}_p denotes the identity matrix of order p . Clearly, we have

$$\mathbf{W}(\mathbf{0}) = \mathbf{D} \quad (6.6)$$

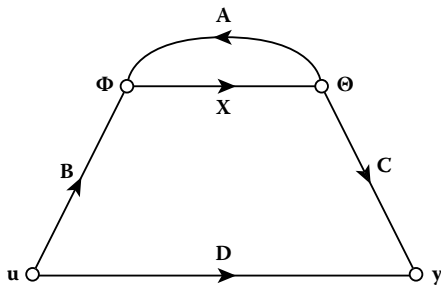


FIGURE 6.3 The fundamental matrix feedback-flow graph.

In particular, when \mathbf{X} is square and nonsingular, Equation 6.5 can be written as

$$\mathbf{W}(\mathbf{X}) = \mathbf{D} + \mathbf{C}(\mathbf{X}^{-1} - \mathbf{A})^{-1}\mathbf{B} \quad (6.7)$$

Example 6.1

Consider the voltage-series feedback amplifier of Figure 3.9. An equivalent network is shown in Figure 6.4 in which we have assumed that the two transistors

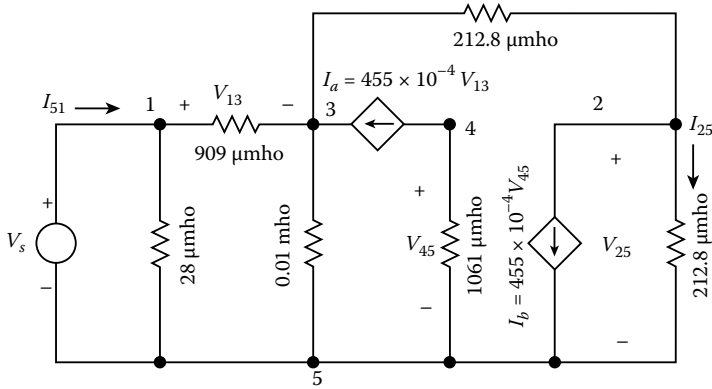


FIGURE 6.4 An equivalent network of the voltage-series feedback amplifier of Figure 3.9.

are identical with $h_{ie} = 1.1 \text{ k}\Omega$, $h_{fe} = 50$, $h_{re} = h_{oe} = 0$. Let the controlling parameters of the two controlled sources be the elements of interest. Then we have

$$\Phi = \begin{bmatrix} I_a \\ I_b \end{bmatrix} = 10^{-4} \begin{bmatrix} 455 & 0 \\ 0 & 455 \end{bmatrix} \begin{bmatrix} V_{13} \\ V_{45} \end{bmatrix} = \mathbf{X}\Phi \tag{6.8}$$

Assume that the output voltage V_{25} and input current I_{51} are the output variables. Then the seven-port network N defined by the variables V_{13} , V_{45} , V_{25} , I_{51} , I_a , I_b , and V_s can be characterized by the matrix equations

$$\begin{aligned} \Phi &= \begin{bmatrix} V_{13} \\ V_{45} \end{bmatrix} = \begin{bmatrix} -90.782 & 45.391 \\ -942.507 & 0 \end{bmatrix} \begin{bmatrix} I_a \\ I_b \end{bmatrix} + \begin{bmatrix} 0.91748 \\ 0 \end{bmatrix} [V_s] \\ &= \mathbf{A}\Phi + \mathbf{B}u \end{aligned} \tag{6.9a}$$

$$\begin{aligned} \mathbf{y} &= \begin{bmatrix} V_{25} \\ I_{51} \end{bmatrix} = \begin{bmatrix} 45.391 & -2372.32 \\ -0.08252 & 0.04126 \end{bmatrix} \begin{bmatrix} I_a \\ I_b \end{bmatrix} + \begin{bmatrix} 0.041260 \\ 0.000862 \end{bmatrix} [V_s] \\ &= \mathbf{C}\Phi + \mathbf{D}u \end{aligned} \tag{6.9b}$$

According to Equation 6.4, the transfer-function matrix of the amplifier is defined by the matrix equation

$$\mathbf{y} = \begin{bmatrix} V_{25} \\ I_{51} \end{bmatrix} = \begin{bmatrix} w_{11} \\ w_{21} \end{bmatrix} [V_s] = \mathbf{W}(\mathbf{X})\mathbf{u} \tag{6.10}$$

Because \mathbf{X} is square and nonsingular, we can use Equation 6.7 to calculate $\mathbf{W}(\mathbf{X})$:

$$\mathbf{W}(\mathbf{X}) = \mathbf{D} + \mathbf{C}(\mathbf{X}^{-1} - \mathbf{A})^{-1} \mathbf{B} = \begin{bmatrix} 45.387 \\ 0.369 \times 10^{-4} \end{bmatrix} = \begin{bmatrix} w_{11} \\ w_{21} \end{bmatrix} \tag{6.11}$$

where

$$(\mathbf{X}^{-1} - \mathbf{A})^{-1} = 10^{-4} \begin{bmatrix} 4.856 & 10.029 \\ -208.245 & 24.914 \end{bmatrix} \tag{6.12}$$

obtaining the closed-loop voltage gain w_{11} and input impedance Z_{in} facing the voltage source V_s as

$$w_{11} = \frac{V_{25}}{V_s} = 45.387, \quad Z_{in} = \frac{V_s}{I_{s1}} = \frac{1}{w_{21}} = 27.1 \text{ k}\Omega \quad (6.13)$$

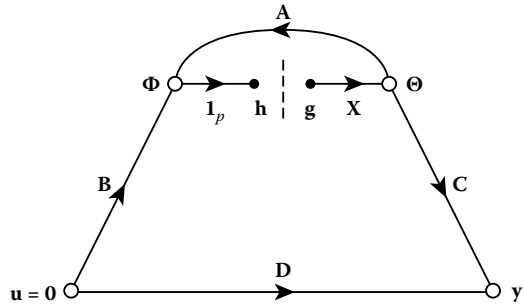


FIGURE 6.5 The physical interpretation of the loop-transmission matrix.

6.2 Return Different Matrix

In this section, we extend the concept of return difference with respect to an element to the notion of return difference matrix with respect to a group of elements.

In the fundamental matrix feedback-flow graph of Figure 6.3, suppose that we break the input of the branch with transmittance X , set the input excitation vector \mathbf{u} to zero, and apply a signal p -vector \mathbf{g} to the right of the breaking mark, as depicted in Figure 6.5. Then the returned signal p -vector \mathbf{h} to the left of the breaking mark is found to be

$$\mathbf{h} = \mathbf{A}\mathbf{X}\mathbf{g} \quad (6.14)$$

The square matrix $\mathbf{A}\mathbf{X}$ is called the loop-transmission matrix and its negative is referred to as the return ratio matrix denoted by

$$\mathbf{T}(\mathbf{X}) = -\mathbf{A}\mathbf{X} \quad (6.15)$$

The difference between the applied signal vector \mathbf{g} and the returned signal vector \mathbf{h} is given by

$$\mathbf{g} - \mathbf{h} = (\mathbf{1}_p - \mathbf{A}\mathbf{X})\mathbf{g} \quad (6.16)$$

The square matrix $\mathbf{1}_p - \mathbf{A}\mathbf{X}$ relating the applied signal vector \mathbf{g} to the difference of the applied signal vector \mathbf{g} and the returned signal vector \mathbf{h} is called the return difference matrix with respect to \mathbf{X} and is denoted by

$$\mathbf{F}(\mathbf{X}) = \mathbf{1}_p - \mathbf{A}\mathbf{X} \quad (6.17)$$

Combining this with Equation 6.15 gives

$$\mathbf{F}(\mathbf{X}) = \mathbf{1}_p + \mathbf{T}(\mathbf{X}) \quad (6.18)$$

For the voltage-series feedback amplifier of Figure 6.4, let the controlling parameters of the two controlled current sources be the elements of interest. Then the return ratio matrix is found from Equations 6.8 and 6.9a

$$\begin{aligned} \mathbf{T}(\mathbf{X}) = -\mathbf{A}\mathbf{X} &= - \begin{bmatrix} -90.782 & 45.391 \\ -942.507 & 0 \end{bmatrix} \begin{bmatrix} 455 \times 10^{-4} & 0 \\ 0 & 455 \times 10^{-4} \end{bmatrix} \\ &= \begin{bmatrix} 4.131 & -2.065 \\ 42.884 & 0 \end{bmatrix} \end{aligned} \quad (6.19)$$

obtaining the return difference matrix as

$$F(X) = I_2 + T(X) = \begin{bmatrix} 5.131 & -2.065 \\ 42.884 & 1 \end{bmatrix} \tag{6.20}$$

6.3 Null Return Difference Matrix

A direct extension of the null return difference for the single-loop feedback amplifier is the null return difference matrix for the multiple-loop feedback networks.

Refer again to the fundamental matrix feedback-flow graph of Figure 6.3. As before, we break the branch with transmittance X and apply a signal p -vector g to the right of the breaking mark, as illustrated in Figure 6.6. We then adjust the input excitation n -vector u so that the total output m -vector y resulting from the inputs g and u is zero. From Figure 6.6, the desired input excitation u is found:

$$Du + CXg = 0 \tag{6.21}$$

or

$$u = -D^{-1}CXg \tag{6.22}$$

provided that the matrix D is square and nonsingular. This requires that the output y be of the same dimension as the input u or $m = n$. Physically, this requirement is reasonable because the effects at the output caused by g can be neutralized by a unique input excitation u only when u and y are of the same dimension. With these inputs u and g , the returned signal h to the left of the breaking mark in Figure 6.6 is computed as

$$h = Bu + AXg = (-BD^{-1}CX + AX)g \tag{6.23}$$

obtaining

$$g - h = (I_p - AX + BD^{-1}CX)g \tag{6.24}$$

The square matrix

$$\begin{aligned} \hat{F}(X) &= I_p + \hat{T}(X) \\ &= I_p - AX + BD^{-1}CX = I_p - \hat{A}X \end{aligned} \tag{6.25}$$

relating the input signal vector g to the difference of the input signal vector g , and the returned signal vector h is called the null return difference matrix with respect to X , where

$$\hat{T}(X) = -AX + BD^{-1}CX = -\hat{A}X \tag{6.26a}$$

$$\hat{A} = A - BD^{-1}C \tag{6.26b}$$

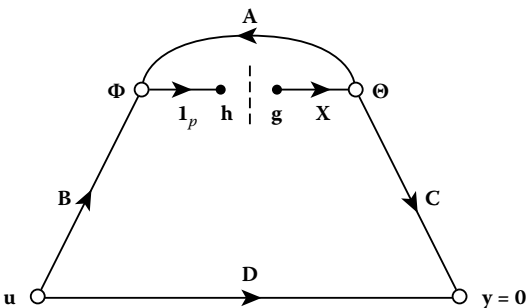


FIGURE 6.6 The physical interpretation of the null return difference matrix.

The square matrix $\hat{T}(X)$ is known as the *null return ratio matrix*.

Example 6.2

Consider again the voltage-series feedback amplifier of Figure 3.9, an equivalent network of which is illustrated in Figure 6.4. Assume that the voltage V_{25} is the output variable. Then from Equation 6.9

$$\begin{aligned}\Phi &= \begin{bmatrix} V_{13} \\ V_{45} \end{bmatrix} = \begin{bmatrix} -90.782 & 45.391 \\ -942.507 & 0 \end{bmatrix} \begin{bmatrix} I_a \\ I_b \end{bmatrix} + \begin{bmatrix} 0.91748 \\ 0 \end{bmatrix} [V_s] \\ &= \mathbf{A}\Phi + \mathbf{B}u\end{aligned}\quad (6.27a)$$

$$\begin{aligned}y &= [V_{25}] = [45.391 \quad -2372.32] \begin{bmatrix} I_a \\ I_b \end{bmatrix} + [0.04126] [V_s] \\ &= \mathbf{C}\Phi + \mathbf{D}u\end{aligned}\quad (6.27b)$$

Substituting the coefficient matrices in Equation 6.26b, we obtain

$$\hat{\mathbf{A}} = \mathbf{A} - \mathbf{B}\mathbf{D}^{-1}\mathbf{C} = \begin{bmatrix} -1, 100.12 & 52, 797.6 \\ -942.507 & 0 \end{bmatrix}\quad (6.28)$$

giving the null return difference matrix with respect to \mathbf{X} as

$$\hat{\mathbf{F}}(\mathbf{X}) = \mathbf{1}_2 - \hat{\mathbf{A}}\mathbf{X} = \begin{bmatrix} 51.055 & -2402.29 \\ 42.884 & 1 \end{bmatrix}\quad (6.29)$$

Suppose that the input current I_{51} is chosen as the output variable. Then, from Equation 6.9b we have

$$y = [I_{51}] = [-0.08252 \quad 0.04126] \begin{bmatrix} I_a \\ I_b \end{bmatrix} + [0.000862] [V_s] = \mathbf{C}\Phi + \mathbf{D}u\quad (6.30)$$

The corresponding null return difference matrix becomes

$$\hat{\mathbf{F}}(\mathbf{X}) = \mathbf{1}_2 - \hat{\mathbf{A}}\mathbf{X} = \begin{bmatrix} 1.13426 & -0.06713 \\ 42.8841 & 1 \end{bmatrix}\quad (6.31)$$

where

$$\hat{\mathbf{A}} = \begin{bmatrix} -2.95085 & 1.47543 \\ -942.507 & 0 \end{bmatrix}\quad (6.32)$$

6.4 Transfer-Function Matrix and Feedback

In this section, we show the effect of feedback on the transfer-function matrix $\mathbf{W}(\mathbf{X})$. Specifically, we express $\det \mathbf{W}(\mathbf{X})$ in terms of the $\det \mathbf{X}(\mathbf{0})$ and the determinants of the return difference and null return difference matrices, thereby generalizing Blackman's impedance formula for a single input to a multiplicity of inputs.

Before we proceed to develop the desired relation, we state the following determinant identity for two arbitrary matrices \mathbf{M} and \mathbf{N} of order $m \times n$ and $n \times m$:

$$\det(\mathbf{1}_m + \mathbf{M}\mathbf{N}) = \det(\mathbf{1}_n + \mathbf{N}\mathbf{M})\quad (6.33)$$

a proof of which may be found in [1,2]. Using this, we next establish the following generalization of Blackman's formula for input impedance.

THEOREM 6.1

In a multiple-loop feedback amplifier, if $\mathbf{W}(\mathbf{0}) = \mathbf{D}$ is nonsingular, then the determinant of the transfer-function matrix $\mathbf{W}(\mathbf{X})$ is related to the determinants of the return difference matrix $\mathbf{F}(\mathbf{X})$ and the null return difference matrix $\hat{\mathbf{F}}(\mathbf{X})$ by

$$\det \mathbf{W}(\mathbf{X}) = \det \mathbf{W}(\mathbf{0}) \frac{\det \hat{\mathbf{F}}(\mathbf{X})}{\det \mathbf{F}(\mathbf{X})} \quad (6.34)$$

PROOF: From Equation 6.5a, we obtain

$$\mathbf{W}(\mathbf{X}) = \mathbf{D} [\mathbf{1}_n + \mathbf{D}^{-1} \mathbf{C} \mathbf{X} (\mathbf{1}_p - \mathbf{A} \mathbf{X})^{-1} \mathbf{B}] \quad (6.35)$$

yielding

$$\begin{aligned} \det \mathbf{W}(\mathbf{X}) &= [\det \mathbf{W}(\mathbf{0})] \det [\mathbf{1}_n + \mathbf{D}^{-1} \mathbf{C} \mathbf{X} (\mathbf{1}_p - \mathbf{A} \mathbf{X})^{-1} \mathbf{B}] \\ &= [\det \mathbf{W}(\mathbf{0})] \det [\mathbf{1}_p + \mathbf{B} \mathbf{D}^{-1} \mathbf{C} \mathbf{X} (\mathbf{1}_p - \mathbf{A} \mathbf{X})^{-1}] \\ &= [\det \mathbf{W}(\mathbf{0})] \det [\mathbf{1}_p - \mathbf{A} \mathbf{X} + \mathbf{B} \mathbf{D}^{-1} \mathbf{C} \mathbf{X}] (\mathbf{1}_p - \mathbf{A} \mathbf{X})^{-1} \\ &= \frac{\det \mathbf{W}(\mathbf{0}) \det \hat{\mathbf{F}}(\mathbf{X})}{\det \mathbf{F}(\mathbf{X})} \end{aligned} \quad (6.36)$$

The second line follows directly from Equation 6.33. This completes the proof of the theorem.

As indicated in Equation 4.4, the input impedance $Z(x)$ looking into a terminal pair can be conveniently expressed as

$$Z(x) = Z(0) \frac{F(\text{input short circuited})}{F(\text{input open circuited})} \quad (6.37)$$

A similar expression can be derived from Equation 6.34 if $\mathbf{W}(\mathbf{X})$ denotes the impedance matrix of an n -port network of Figure 6.1. In this case, $\mathbf{F}(\mathbf{X})$ is the return difference matrix with respect to \mathbf{X} for the situation when the n ports where the impedance matrix are defined are left open without any sources, and we write $\mathbf{F}(\mathbf{X}) = \mathbf{F}(\text{input open-circuited})$. Likewise, $\hat{\mathbf{F}}(\mathbf{X})$ is the return difference matrix with respect to \mathbf{X} for the input port-current vector \mathbf{I}_s and the output port-voltage vector \mathbf{V} under the condition that \mathbf{I}_s is adjusted so that the port-voltage vector \mathbf{V} is identically zero. In other words, $\hat{\mathbf{F}}(\mathbf{X})$ is the return difference matrix for the situation when the n ports, where the impedance matrix is defined, are short-circuited, and we write $\hat{\mathbf{F}}(\mathbf{X}) = \mathbf{F}(\text{input short-circuited})$. Consequently, the determinant of the impedance matrix $\mathbf{Z}(\mathbf{X})$ of an n -port network can be expressed from Equation 6.34 as

$$\det \mathbf{Z}(\mathbf{X}) = \det \mathbf{Z}(\mathbf{0}) \frac{\det \mathbf{F}(\text{input short circuited})}{\det \mathbf{F}(\text{input open circuited})} \quad (6.38) \quad \blacksquare$$

Example 6.3

Refer again to the voltage-series feedback amplifier of Figure 3.9, an equivalent network of which is illustrated in Figure 6.4. As computed in Equation 6.20, the return difference matrix with respect to the two controlling parameters is given by

$$\mathbf{F}(\mathbf{X}) = \mathbf{1}_2 + \mathbf{T}(\mathbf{X}) = \begin{bmatrix} 5.131 & -2.065 \\ 42.884 & 1 \end{bmatrix} \quad (6.39)$$

the determinant of which is

$$\det \mathbf{F}(\mathbf{X}) = 93.68646 \quad (6.40)$$

If V_{25} of Figure 6.4 is chosen as the output and V_s as the input, the null return difference matrix is, from Equation 6.29,

$$\hat{\mathbf{F}}(\mathbf{X}) = \mathbf{1}_2 - \hat{\mathbf{A}}\mathbf{X} = \begin{bmatrix} 51.055 & -2402.29 \\ 42.884 & 1 \end{bmatrix} \quad (6.41)$$

the determinant of which is

$$\det \hat{\mathbf{F}}(\mathbf{X}) = 103,071 \quad (6.42)$$

By appealing to Equation 6.34, the feedback amplifier voltage gain V_{25}/V_s can be written as

$$w(\mathbf{X}) = \frac{V_{25}}{V_s} = w(\mathbf{0}) \frac{\det \hat{\mathbf{F}}(\mathbf{X})}{\det \mathbf{F}(\mathbf{X})} = 0.04126 \frac{103,071}{93.68646} = 45.39 \quad (6.43)$$

confirming Equation 3.44, where $w(\mathbf{0}) = 0.04126$, as given in Equation 6.27b.

Suppose, instead, that the input current I_{s1} is chosen as the output and V_s as the input. Then, from Equation 6.31, the null return difference matrix becomes

$$\hat{\mathbf{F}}(\mathbf{X}) = \mathbf{1}_2 - \hat{\mathbf{A}}(\mathbf{X}) = \begin{bmatrix} 1.13426 & -0.06713 \\ 42.8841 & 1 \end{bmatrix} \quad (6.44)$$

the determinant of which is

$$\det \hat{\mathbf{F}}(\mathbf{X}) = 4.01307 \quad (6.45)$$

By applying Equation 6.34, the amplifier input admittance is obtained as

$$\begin{aligned} w(\mathbf{X}) &= \frac{I_{s1}}{V_s} = w(\mathbf{0}) \frac{\det \hat{\mathbf{F}}(\mathbf{X})}{\det \mathbf{F}(\mathbf{X})} \\ &= 8.62 \times 10^{-4} \frac{4.01307}{93.68646} = 36.92 \mu\text{mho} \end{aligned} \quad (6.46)$$

or 27.1 k Ω , confirming Equation 6.13, where $w(\mathbf{0}) = 862 \mu\text{mho}$ is found from Equation 6.30.

Another useful application of the generalized Blackman's formula (Equation 6.38) is that it provides the basis of a procedure for the indirect measurement of return difference. Refer to the general feedback network of Figure 6.2. Suppose that we wish to measure the return difference $F(y_{21})$ with respect to the forward short circuit transfer admittance y_{21} of a two-port device characterized by its y parameters y_{ij} .

Choose the two controlling parameters y_{21} and y_{12} to be the elements of interest. Then, from Figure 5.2 we obtain

$$\Theta = \begin{bmatrix} I_a \\ I_b \end{bmatrix} = \begin{bmatrix} y_{21} & 0 \\ 0 & y_{12} \end{bmatrix} \begin{bmatrix} V_1 \\ V_2 \end{bmatrix} = \mathbf{X}\Phi \quad (6.47)$$

where I_a and I_b are the currents of the voltage-controlled current sources. By appealing to Equation 6.38, the impedance looking into terminals a and b of Figure 5.2 can be written as

$$z_{aa,bb}(y_{12}, y_{21}) = z_{aa,bb}(0, 0) \frac{\det \mathbf{F} \text{ (input short circuited)}}{\det \mathbf{F} \text{ (input open circuited)}} \quad (6.48)$$

When the input terminals a and b are open-circuited, the resulting return difference matrix is exactly the same as that found under normal operating conditions, and we have

$$\mathbf{F} \text{ (input open circuited)} = \mathbf{F}(\mathbf{X}) = \begin{bmatrix} F_{11} & F_{12} \\ F_{21} & F_{22} \end{bmatrix} \quad (6.49)$$

Because

$$\mathbf{F}(\mathbf{X}) = \mathbf{I}_2 - \mathbf{A}\mathbf{X} \quad (6.50)$$

the elements F_{11} and F_{21} are calculated with $y_{12} = 0$, whereas F_{12} and F_{22} are evaluated with $y_{21} = 0$. When the input terminals a and b are short circuited, the feedback loop is interrupted and only the second row and first column element of the matrix \mathbf{A} is nonzero, and we obtain

$$\det \mathbf{F} \text{ (input short circuited)} = 1 \quad (6.51)$$

Because \mathbf{X} is diagonal, the return difference function $F(y_{21})$ can be expressed in terms of $\det \mathbf{F}(\mathbf{X})$ and the cofactor of the first row and first column element of $\mathbf{F}(\mathbf{X})$:

$$F(y_{21}) = \frac{\det \mathbf{F}(\mathbf{X})}{F_{22}} \quad (6.52)$$

Substituting these in Equation 6.48 yields

$$F(y_{12})|_{y_{21}=0} F(y_{21}) = \frac{z_{aa,bb}(0, 0)}{z_{aa,bb}(y_{12}, y_{21})} \quad (6.53)$$

where

$$F_{22} = 1 - a_{22}y_{12}|_{y_{21}=0} = F(y_{12})|_{y_{21}=0} \quad (6.54)$$

and a_{22} is the second row and second column element of \mathbf{A} . Formula (Equation 6.53) was derived earlier in Equation 5.7 using the network arrangements of Figures 5.7 and 5.8 to measure the elements $F(y_{12})|_{y_{21}=0}$ and $z_{aa,bb}(0,0)$, respectively.

6.5 Sensitivity Matrix

We have studied the sensitivity of a transfer function with respect to the change of a particular element in the network. In a multiple-loop feedback network, we are usually interested in the sensitivity of a transfer function with respect to the variation of a set of elements in the network. This set may include either

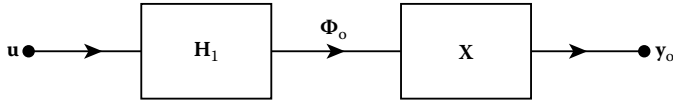


FIGURE 6.7 The block diagram of a multivariable open-loop control system.

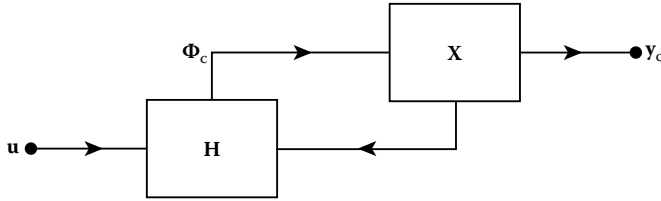


FIGURE 6.8 The general feedback structure.

elements that are inherently sensitive to variation or elements where the effect on the overall amplifier performance is of paramount importance to the designers. For this, we introduce a sensitivity matrix and develop formulas for computing multiparameter sensitivity function for a multiple-loop feedback amplifier [3].

Figure 6.7 is the block diagram of a multivariable open-loop control system with n inputs and m outputs, whereas Figure 6.8 is the general feedback structure. If all feedback signals are obtainable from the output and if the controllers are linear, no loss of generality occurs by assuming the controller to be of the form given in Figure 6.9.

Denote the set of Laplace-transformed input signals by the n -vector \mathbf{u} , the set of inputs to the network \mathbf{X} in the open-loop configuration of Figure 6.7 by the p -vector Φ_o , and the set of outputs of the network \mathbf{X} of Figure 6.7 by the m -vector \mathbf{y}_o . Let the corresponding signals for the closed-loop configuration of Figure 6.9 be denoted by the n -vector \mathbf{u} , the p -vector Φ_c , and the m -vector \mathbf{y}_c , respectively. Then, from Figures 6.7 and 6.9, we obtain the following relations:

$$\mathbf{y}_o = \mathbf{X}\Phi_o \tag{6.55a}$$

$$\Phi_o = \mathbf{H}_1\mathbf{u} \tag{6.55b}$$

$$\mathbf{y}_c = \mathbf{X}\Phi_c \tag{6.55c}$$

$$\Phi_c = \mathbf{H}_2(\mathbf{u} + \mathbf{H}_3\mathbf{y}_c) \tag{6.55d}$$

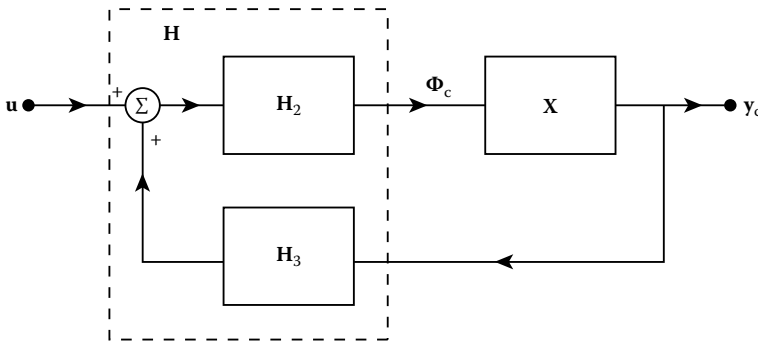


FIGURE 6.9 The general feedback configuration.

where the transfer-function matrices \mathbf{X} , \mathbf{H}_1 , \mathbf{H}_2 , and \mathbf{H}_3 are of order $m \times p$, $p \times n$, $p \times n$, and $n \times m$, respectively. Combining Equation 6.55c and d yields

$$(\mathbf{1}_m - \mathbf{X}\mathbf{H}_2\mathbf{H}_3)\mathbf{y}_c = \mathbf{X}\mathbf{H}_2\mathbf{u} \quad (6.56)$$

or

$$\mathbf{y}_c = (\mathbf{1}_m - \mathbf{X}\mathbf{H}_2\mathbf{H}_3)^{-1}\mathbf{X}\mathbf{H}_2\mathbf{u} \quad (6.57)$$

The closed-loop transfer function matrix $\mathbf{W}(\mathbf{X})$ that relates the input vector \mathbf{u} to the output vector \mathbf{y}_c is defined by the equation

$$\mathbf{y}_c = \mathbf{W}(\mathbf{X})\mathbf{u} \quad (6.58)$$

identifying from Equation 6.57 the $m \times n$ matrix

$$\mathbf{W}(\mathbf{X}) = (\mathbf{1}_m - \mathbf{X}\mathbf{H}_2\mathbf{H}_3)^{-1}\mathbf{X}\mathbf{H}_2 \quad (6.59)$$

Now, suppose that \mathbf{X} is perturbed from \mathbf{X} to $\mathbf{X} + \delta\mathbf{X}$. The outputs of the open-loop and closed-loop systems of Figures 6.7 and 6.9 will no longer be the same as before. Distinguishing the new from the old variables by the superscript $+$, we have

$$\mathbf{y}_o^+ = \mathbf{X}^+\Phi_o \quad (6.60a)$$

$$\mathbf{y}_c^+ = \mathbf{X}^+\Phi_c^+ \quad (6.60b)$$

$$\Phi_c^+ = \mathbf{H}_2(\mathbf{u} + \mathbf{H}_3\mathbf{y}_c^+) \quad (6.60c)$$

where Φ_o remains the same.

We next proceed to compare the relative effects of the variations of \mathbf{X} on the performance of the open-loop and the closed-loop systems. For a meaningful comparison, we assume that \mathbf{H}_1 , \mathbf{H}_2 , and \mathbf{H}_3 are such that when there is no variation of \mathbf{X} , $\mathbf{y}_o = \mathbf{y}_c$. Define the error vectors resulting from perturbation of \mathbf{X} as

$$\mathbf{E}_o = \mathbf{y}_o - \mathbf{y}_o^+ \quad (6.61a)$$

$$\mathbf{E}_c = \mathbf{y}_c - \mathbf{y}_c^+ \quad (6.61b)$$

A square matrix relating \mathbf{E}_o to \mathbf{E}_c is called the **sensitivity matrix** $\mathcal{S}(\mathbf{X})$ for the transfer function matrix $\mathbf{W}(\mathbf{X})$ with respect to the variations of \mathbf{X} :

$$\mathbf{E}_c = \mathcal{S}(\mathbf{X})\mathbf{E}_o \quad (6.62)$$

In the following, we express the **sensitivity matrix** $\mathcal{S}(\mathbf{X})$ in terms of the system matrices \mathbf{X} , \mathbf{H}_2 , and \mathbf{H}_3 .

The input and output relation similar to that given in Equation 6.57 for the perturbed system can be written as

$$\mathbf{y}_c^+ = (\mathbf{1}_m - \mathbf{X}^+\mathbf{H}_2\mathbf{H}_3)^{-1}\mathbf{X}^+\mathbf{H}_2\mathbf{u} \quad (6.63)$$

Substituting Equations 6.57 and 6.63 in Equation 6.61b gives

$$\begin{aligned}
 \mathbf{E}_c &= \mathbf{y}_c - \mathbf{y}_c^+ = [(\mathbf{1}_m - \mathbf{X}\mathbf{H}_2\mathbf{H}_3)^{-1}\mathbf{X}\mathbf{H}_2 - (\mathbf{1}_m - \mathbf{X}^+\mathbf{H}_2\mathbf{H}_3)^{-1}\mathbf{X}^+\mathbf{H}_2]\mathbf{u} \\
 &= (\mathbf{1}_m - \mathbf{X}^+\mathbf{H}_2\mathbf{H}_3)^{-1}\{[\mathbf{1}_m - (\mathbf{X} + \delta\mathbf{X})\mathbf{H}_2\mathbf{H}_3](\mathbf{1}_m - \mathbf{X}\mathbf{H}_2\mathbf{H}_3)^{-1}\mathbf{X}\mathbf{H}_2 - (\mathbf{X} + \delta\mathbf{X})\mathbf{H}_2\}\mathbf{u} \\
 &= (\mathbf{1}_m - \mathbf{X}^+\mathbf{H}_2\mathbf{H}_3)^{-1}[\mathbf{X}\mathbf{H}_2 - \delta\mathbf{X}\mathbf{H}_2\mathbf{H}_3(\mathbf{1}_m - \mathbf{X}\mathbf{H}_2\mathbf{H}_3)^{-1}\mathbf{X}\mathbf{H}_2 - \mathbf{X}\mathbf{H}_2 - \delta\mathbf{X}\mathbf{H}_2]\mathbf{u} \\
 &= -(\mathbf{1}_m - \mathbf{X}^+\mathbf{H}_2\mathbf{H}_3)^{-1}\delta\mathbf{X}\mathbf{H}_2[\mathbf{1}_n + \mathbf{H}_3\mathbf{W}(\mathbf{X})]\mathbf{u}
 \end{aligned} \tag{6.64}$$

From Equations 6.55d and 6.58, we obtain

$$\Phi_c = \mathbf{H}_2[\mathbf{1}_n + \mathbf{H}_3\mathbf{W}(\mathbf{X})]\mathbf{u} \tag{6.65}$$

Because by assuming that $\mathbf{y}_o = \mathbf{y}_c$, we have

$$\Phi_o = \Phi_c = \mathbf{H}_2[\mathbf{1}_n + \mathbf{H}_3\mathbf{W}(\mathbf{X})]\mathbf{u} \tag{6.66}$$

yielding

$$\mathbf{E}_o = \mathbf{y}_o - \mathbf{y}_o^+ = (\mathbf{X} - \mathbf{X}^+)\Phi_o = -\delta\mathbf{X}\mathbf{H}_2[\mathbf{1}_n + \mathbf{H}_3\mathbf{W}(\mathbf{X})]\mathbf{u} \tag{6.67}$$

Combining Equations 6.64 and 6.67 yields an expression relating the error vectors \mathbf{E}_c and \mathbf{E}_o of the closed-loop and open-loop systems by

$$\mathbf{E}_c = (\mathbf{1}_m - \mathbf{X}^+\mathbf{H}_2\mathbf{H}_3)^{-1}\mathbf{E}_o \tag{6.68}$$

obtaining the sensitivity matrix as

$$\mathcal{S}(\mathbf{X}) = (\mathbf{1}_m - \mathbf{X}^+\mathbf{H}_2\mathbf{H}_3)^{-1} \tag{6.69}$$

For small variations of \mathbf{X} , \mathbf{X}^+ is approximately equal to \mathbf{X} . Thus, in Figure 6.9, if the matrix triple product $\mathbf{X}\mathbf{H}_2\mathbf{H}_3$ is regarded as the *loop-transmission matrix* and $-\mathbf{X}\mathbf{H}_2\mathbf{H}_3$ as the *return ratio matrix*, then the difference between the unit matrix and the loop-transmission matrix,

$$\mathbf{1}_m - \mathbf{X}\mathbf{H}_2\mathbf{H}_3 \tag{6.70}$$

can be defined as the *return difference matrix*. Therefore, Equation 6.69 is a direct extension of the sensitivity function defined for a single-input, single-output system and for a single parameter. Recall that in Equation 4.33 we demonstrated that, using the ideal feedback model, the sensitivity function of the closed-loop transfer function with respect to the forward amplifier gain is equal to the reciprocal of its return difference with respect to the same parameter.

In particular, when $\mathbf{W}(\mathbf{X})$, $\delta\mathbf{X}$, and \mathbf{X} are square and nonsingular, from Equations 6.55a, 6.55b, and 6.58, 6.61 can be rewritten as

$$\mathbf{E}_c = \mathbf{y}_c - \mathbf{y}_c^+ = [\mathbf{W}(\mathbf{X}) - \mathbf{W}^+(\mathbf{X})]\mathbf{u} = -\delta\mathbf{W}(\mathbf{X})\mathbf{u} \tag{6.71a}$$

$$\mathbf{E}_o = \mathbf{y}_o - \mathbf{y}_o^+ = [\mathbf{X}\mathbf{H}_1 - \mathbf{X}^+\mathbf{H}_1]\mathbf{u} = -\delta\mathbf{X}\mathbf{H}_1\mathbf{u} \tag{6.71b}$$

If \mathbf{H}_1 is nonsingular, \mathbf{u} in Equation 6.71b can be solved for and substituted in Equation 6.71a to give

$$\mathbf{E}_c = \delta \mathbf{W}(\mathbf{X}) \mathbf{H}_1^{-1} (\delta \mathbf{X})^{-1} \mathbf{E}_o \quad (6.72)$$

As before, for meaningful comparison, we require that $\mathbf{y}_o = \mathbf{y}_c$ or

$$\mathbf{X} \mathbf{H}_1 = \mathbf{W}(\mathbf{X}) \quad (6.73)$$

From Equation 6.72, we obtain

$$\mathbf{E}_c = \delta \mathbf{W}(\mathbf{X}) \mathbf{W}^{-1}(\mathbf{X}) \mathbf{X} (\delta \mathbf{X})^{-1} \mathbf{E}_o \quad (6.74)$$

identifying that

$$\mathcal{S}(\mathbf{X}) = d\mathbf{W}(\mathbf{X}) \mathbf{W}^{-1}(\mathbf{X}) \mathbf{X} (d\mathbf{X})^{-1} \quad (6.75)$$

This result is to be compared with the scalar sensitivity function defined in Equation 4.26, which can be put in the form

$$\mathcal{S}(x) = (\delta w) w^{-1} x (\delta x)^{-1} \quad (6.76)$$

6.6 Multiparameter Sensitivity

In this section, we derive formulas for the effect of change of \mathbf{X} on a scalar transfer function $w(\mathbf{X})$.

Let $x_k, k = 1, 2, \dots, pq$, be the elements of \mathbf{X} . The multivariable Taylor series expansion of $w(\mathbf{X})$ with respect to x_k is given by

$$\delta w = \sum_{k=1}^{pq} \frac{\partial w}{\partial x_k} \delta x_k + \sum_{j=1}^{pq} \sum_{k=1}^{pq} \frac{\partial^2 w}{\partial x_j \partial x_k} \frac{\delta x_j \delta x_k}{2!} + \dots \quad (6.77)$$

The first-order perturbation can then be written as

$$\delta w \approx \sum_{k=1}^{pq} \frac{\partial w}{\partial x_k} \delta x_k \quad (6.78)$$

Using Equation 4.26, we obtain

$$\frac{\delta w}{w} \approx \sum_{k=1}^{pq} \mathcal{S}(x_k) \frac{\delta x_k}{x_k} \quad (6.79)$$

This expression gives the fractional change of the transfer function w in terms of the scalar sensitivity functions $\mathcal{S}(x_k)$.

Refer to the fundamental matrix feedback-flow graph of Figure 6.3. If the amplifier has a single input and a single output from Equation 6.35, the overall transfer function $w(\mathbf{X})$ of the multiple-loop feedback amplifier becomes

$$w(\mathbf{X}) = D + \mathbf{C}\mathbf{X}(\mathbf{1}_p - \mathbf{A}\mathbf{X})^{-1}\mathbf{B} \quad (6.80)$$

When \mathbf{X} is perturbed to $\mathbf{X}^+ = \mathbf{X} + \delta\mathbf{X}$, the corresponding expression of Equation 6.80 is given by

$$w(\mathbf{X}) + \delta w(\mathbf{X}) = D + \mathbf{C}(\mathbf{X} + \delta\mathbf{X})(\mathbf{1}_p - \mathbf{A}\mathbf{X} - \mathbf{A}\delta\mathbf{X})^{-1}\mathbf{B} \quad (6.81)$$

or

$$\delta w(\mathbf{X}) = \mathbf{C}[(\mathbf{X} + \delta\mathbf{X})(\mathbf{1}_p - \mathbf{A}\mathbf{X} - \mathbf{A}\delta\mathbf{X})^{-1} - \mathbf{X}(\mathbf{1}_p - \mathbf{A}\mathbf{X})^{-1}]\mathbf{B} \quad (6.82)$$

As $\delta\mathbf{X}$ approaches zero, we obtain

$$\begin{aligned} \delta w(\mathbf{X}) &= \mathbf{C}[(\mathbf{X} + \delta\mathbf{X}) - \mathbf{X}(\mathbf{1}_p - \mathbf{A}\mathbf{X})^{-1}(\mathbf{1}_p - \mathbf{A}\mathbf{X} - \mathbf{A}\delta\mathbf{X})](\mathbf{1}_p - \mathbf{A}\mathbf{X} - \mathbf{A}\delta\mathbf{X})^{-1}\mathbf{B} \\ &= \mathbf{C}[\delta\mathbf{X} + \mathbf{X}(\mathbf{1}_p - \mathbf{A}\mathbf{X})^{-1}\mathbf{A}\delta\mathbf{X}](\mathbf{1}_p - \mathbf{A}\mathbf{X} - \mathbf{A}\delta\mathbf{X})^{-1}\mathbf{B} \\ &= \mathbf{C}(\mathbf{1}_q - \mathbf{X}\mathbf{A})^{-1}(\delta\mathbf{X})(\mathbf{1}_p - \mathbf{A}\mathbf{X} - \mathbf{A}\delta\mathbf{X})^{-1}\mathbf{B} \\ &\approx \mathbf{C}(\mathbf{1}_q - \mathbf{X}\mathbf{A})^{-1}(\delta\mathbf{X})(\mathbf{1}_p - \mathbf{A}\mathbf{X})^{-1}\mathbf{B} \end{aligned} \quad (6.83)$$

where \mathbf{C} is a row q vector and \mathbf{B} is a column p vector. Write

$$\mathbf{C} = [c_1 \ c_2 \ \cdots \ c_q] \quad (6.84a)$$

$$\mathbf{B}' = [b_1 \ b_2 \ \cdots \ b_p] \quad (6.84b)$$

$$\tilde{\mathbf{W}} = \mathbf{X}(\mathbf{1}_p - \mathbf{A}\mathbf{X})^{-1} = (\mathbf{1}_q - \mathbf{X}\mathbf{A})^{-1}\mathbf{X} = [\tilde{w}_{ij}] \quad (6.84c)$$

The increment $\delta w(\mathbf{X})$ can be expressed in terms of the elements of Equation 6.84 and those of \mathbf{X} . In the case where \mathbf{X} is diagonal with

$$\mathbf{X} = \text{diag}[x_1 \ x_2 \ \cdots \ x_p] \quad (6.85)$$

where $p = q$, the expression for $\delta w(\mathbf{X})$ can be succinctly written as

$$\begin{aligned} \delta w(\mathbf{X}) &= \sum_{i=1}^p \sum_{k=1}^p \sum_{j=1}^p c_i \left(\frac{\tilde{w}_{ik}}{x_k} \right) (\delta x_k) \left(\frac{\tilde{w}_{kj}}{x_k} \right) b_j \\ &= \sum_{i=1}^p \sum_{k=1}^p \sum_{j=1}^p \frac{c_i \tilde{w}_{ik} \tilde{w}_{kj} b_j}{x_k} \frac{\delta x_k}{x_k} \end{aligned} \quad (6.86)$$

Comparing this with Equation 6.79, we obtain an explicit form for the single-parameter sensitivity function as

$$\mathcal{S}(x_k) = \sum_{i=1}^p \sum_{j=1}^p \frac{c_i \tilde{w}_{ik} \tilde{w}_{kj} b_j}{x_k w(\mathbf{X})} \quad (6.87)$$

Thus, knowing Equations 6.84 and 6.85, we can calculate the multiparameter sensitivity function for the scalar transfer function $w(\mathbf{X})$ immediately.

Example 6.4

Consider again the voltage-series feedback amplifier of Figure 3.9, an equivalent network of which is shown in Figure 6.4. Assume that V_s is the input and V_{25} the output. The transfer function of interest is the amplifier voltage gain V_{25}/V_s . The elements of main concern are the two controlling parameters of the controlled sources. Thus, we let

$$\mathbf{x} = \begin{bmatrix} \tilde{\alpha}_1 & 0 \\ 0 & \tilde{\alpha}_2 \end{bmatrix} = \begin{bmatrix} 0.0455 & 0 \\ 0 & 0.0455 \end{bmatrix} \quad (6.88)$$

From Equation 6.27 we have

$$\mathbf{A} = \begin{bmatrix} -90.782 & 45.391 \\ -942.507 & 0 \end{bmatrix} \quad (6.89a)$$

$$\mathbf{B}' = [0.91748 \ 0] \quad (6.89b)$$

$$\mathbf{C} = [45.391 \ -2372.32] \quad (6.89c)$$

yielding

$$\tilde{\mathbf{W}} = \mathbf{X}(\mathbf{I}_2 - \mathbf{A}\mathbf{X})^{-1} = 10^{-4} \begin{bmatrix} 4.85600 & 10.02904 \\ -208.245 & 24.91407 \end{bmatrix} \quad (6.90)$$

Also, from Equation 6.13 we have

$$w(\mathbf{x}) = \frac{V_{25}}{V_s} = 45.387 \quad (6.91)$$

To compute the sensitivity functions with respect to $\tilde{\alpha}_1$ and $\tilde{\alpha}_2$, we apply Equation 6.87 and obtain

$$\begin{aligned} \mathcal{S}(\tilde{\alpha}_1) &= \sum_{i=1}^2 \sum_{j=1}^2 \frac{c_i \tilde{w}_{i1} \tilde{w}_{1j} b_j}{\tilde{\alpha}_1 w(\mathbf{x})} = \frac{c_1 \tilde{w}_{11} \tilde{w}_{11} b_1 + c_1 \tilde{w}_{11} \tilde{w}_{12} b_2 + c_2 \tilde{w}_{21} \tilde{w}_{11} b_1 + c_2 \tilde{w}_{21} \tilde{w}_{12} b_2}{\tilde{\alpha}_1 w} \\ &= 0.01066 \end{aligned} \quad (6.92a)$$

$$\mathcal{S}(\tilde{\alpha}_2) = \frac{c_1 \tilde{w}_{12} \tilde{w}_{21} b_1 + c_1 \tilde{w}_{12} \tilde{w}_{22} b_2 + c_2 \tilde{w}_{22} \tilde{w}_{21} b_1 + c_2 \tilde{w}_{22} \tilde{w}_{22} b_2}{\tilde{\alpha}_2 w} = 0.05426 \quad (6.92b)$$

As a check, we use Equation 4.30 to compute these sensitivities. From Equations 3.45 and 3.52, we have

$$F(\tilde{\alpha}_1) = 93.70 \quad (6.93a)$$

$$F(\tilde{\alpha}_2) = 18.26 \quad (6.93b)$$

$$\hat{F}(\tilde{\alpha}_1) = 103.07 \times 10^3 \quad (6.93c)$$

$$\hat{F}(\tilde{\alpha}_2) = 2018.70 \quad (6.93d)$$

Substituting these in Equation 4.30 the sensitivity functions are

$$\mathcal{S}(\tilde{\alpha}_1) = \frac{1}{F(\tilde{\alpha}_1)} - \frac{1}{\hat{F}(\tilde{\alpha}_1)} = 0.01066 \quad (6.94a)$$

$$\mathcal{F}(\tilde{\alpha}_2) = \frac{1}{F(\tilde{\alpha}_2)} - \frac{1}{\tilde{F}(\tilde{\alpha}_2)} = 0.05427 \quad (6.94b)$$

confirming Equation 6.92.

Suppose that $\tilde{\alpha}_1$ is changed by 4% and $\tilde{\alpha}_2$ by 6%. The fractional change of the voltage gain $w(\mathbf{X})$ is found from Equation 6.79 as

$$\frac{\delta w}{w} \approx \mathcal{F}(\tilde{\alpha}_1) \frac{\delta \tilde{\alpha}_1}{\tilde{\alpha}_1} + \mathcal{F}(\tilde{\alpha}_2) \frac{\delta \tilde{\alpha}_2}{\tilde{\alpha}_2} = 0.003683 \quad (6.95)$$

or 0.37%.

References

1. W.-K. Chen, *Active Network and Feedback Amplifier Theory*, New York: McGraw-Hill, 1980, Chaps. 2, 4, 5, 7.
2. W.-K. Chen, *Active Network and Analysis*, Singapore: World Scientific, 1991, Chaps. 2, 4, 5, 7.
3. J. B. Cruz Jr. and W. R. Perkins, A new approach to the sensitivity problem in multivariable feedback system design, *IEEE Trans. Autom. Control*, AC-9, 216–223, 1964.
4. E. S. Kuh and R. A. Rohrer, *Theory of Linear Active Networks*, San Francisco: Holden-Day, 1967.
5. I. W. Sandberg, On the theory of linear multi-loop feedback systems, *Bell Syst. Tech. J.*, 42, 355–382, 1963.

II

Nonlinear Circuits

Leon O. Chua

University of California, Berkeley

7	Qualitative Analysis <i>Martin Hasler</i>	7-1
	Introduction • Resistive Circuits • Autonomous Dynamic Circuits • Nonautonomous Dynamic Circuits • References	
8	Synthesis and Design of Nonlinear Circuits <i>Angel Rodríguez-Vázquez, Manuel Delgado-Restituto, Jose L. Huertas, and F. Vidal</i>	8-1
	Introduction • Approximation Issues • Aggregation, Scaling, and Transformation Circuits • Piecewise-Linear Circuitry • Polynomials, Rational, and Piecewise-Polynomial Functions • Sigmoids, Bells, and Collective Computation Circuits • Extension to Dynamic Systems • Appendix A: Catalog of Primitives • Appendix B: Value and Slope Hermite Basis Functions • References	
9	Representation, Approximation, and Identification <i>Guanrong Chen</i>	9-1
	Introduction • Representation • Approximation • Identification • References	
10	Transformation and Equivalence <i>Wolfgang Mathis</i>	10-1
	Transformation of Nonlinear Dynamical Circuit Equations • Normal Forms of Nonlinear Dynamical Circuit Equations • Dimensionless Forms of Circuit Equations • Equivalence of Nonlinear Resistive n -Ports • Equivalence of Nonlinear Dynamical n -Ports • Equivalence of Reciprocal Nonlinear Dynamic Circuits • References	
11	Piecewise-Linear Circuits and Piecewise-Linear Analysis <i>Joos Vandewalle and Lieven Vandenbergh</i>	11-1
	Introduction and Motivation • Hierarchy of Piecewise-Linear Models and Their Representations • Piecewise-Linear Models for Electronic Components • Structural Properties of Piecewise-Linear Resistive Circuits • Analysis of Piecewise-Linear Resistive Circuits • Piecewise-Linear Dynamic Circuits • Efficient Computer-Aided Analysis of PWL Circuits • Acknowledgment • References	
12	Simulation <i>Erik Lindberg</i>	12-1
	Numerical Solution of Nonlinear Algebraic Equations • Numerical Integration of Nonlinear Differential Equations • Use of Simulation Programs • References	

13 Cellular Neural Networks and Cellular Wave Computers	<i>Tamás Roska, Ákos Zarándy, and Csaba Rekeczky</i>	13-1
Introduction: Definition and Classification • Simple CNN Circuit Structure • Stored Program CNN Universal Machine and the Analogic Supercomputer Chip • Applications • Template Library: Analogical CNN Algorithms • Recent Advances • Recent Developments and Outlook • References		
14 Bifurcation and Chaos	<i>Michael Peter Kennedy</i>	14-1
Introduction to Chaos • Chua's Circuit: A Paradigm for Chaos • Chua's Oscillator • van der Pol Neon Bulb Oscillator • Synchronization of Chaotic Circuits • Applications of Chaos • References • Further Information		

7

Qualitative Analysis

7.1	Introduction	7-1
7.2	Resistive Circuits	7-1
	Number of Solutions of a Resistive Circuit • Bounds on Voltages and Currents • Monotonic Dependence	
7.3	Autonomous Dynamic Circuits.....	7-13
	Introduction • Convergence to DC-Operating Points	
7.4	Nonautonomous Dynamic Circuits.....	7-19
	Introduction • Boundedness of the Solutions • Unique Asymptotic Behavior	
	References.....	7-21

Martin Hasler

Swiss Federal Institute of Technology

7.1 Introduction

The main goal of circuit analysis is to determine the solution of the circuit, i.e., the voltages and the currents in the circuit, usually as functions of time. The advent of powerful computers and circuit analysis software has greatly simplified this task. Basically, the circuit to be analyzed is fed to the computer through some circuit description language, or it is analyzed graphically, and the software will produce the desired voltage or current waveforms. Progress has rendered the traditional paper-and-pencil methods obsolete, in which the engineer's skill and intuition led the way through series of clever approximations, until the circuits equations can be solved analytically.

A closer comparison of the numerical and the approximate analytical solution reveals, however, that the two are not quite equivalent. Although the former is precise, it only provides the solution of the circuit with given parameters, whereas the latter is an approximation, but the approximate solutions most often is given explicitly as a function of some circuit parameters. Therefore, it allows us to assess the influence of these parameters on the solution.

If we rely entirely on the numerical solution of a circuit, we never get a global picture of its behavior, unless we carry out a huge number of analyses. Thus, the numerical analysis should be complemented by a qualitative analysis, one that concentrates on general properties of the circuit, properties that do not depend on the particular set of circuit parameters.

7.2 Resistive Circuits

The term “resistive circuits” is not used, as one would imagine, for circuits that are composed solely of resistors. It admits all circuit elements that are not dynamic, i.e., whose constitutive relations do not involve time derivatives, integrals over time, or time delays, etc. Expressed positively, resistive circuit elements are described by constitutive relations that involve only currents and voltages at the same time instants.

Physical circuits can never be modeled in a satisfactory way by resistive circuits, but resistive circuits appear in many contexts as auxiliary constructs. The most important problem that leads to a resistive circuit is the determination of the equilibrium points, or, as is current use in electronics, the DC-operating points, of a dynamic circuit. The DC-operating points of a circuit correspond in a one-to-one fashion to the solutions of the resistive circuit obtained by removing the capacitors and by short circuiting the inductors. The resistive circuit associated with the state equations of a dynamic circuit is discussed in Ref. [1].

Among the resistive circuit elements we find, of course, the resistors. For the purposes of this introduction, we distinguish between, linear resistors, V -resistors, and I -resistors. V -resistors are voltage controlled, i.e., defined by constitutive relations of the form



FIGURE 7.1 Symbols of the V - and the I -resistor.

$$i = g(v) \quad (7.1)$$

In addition, we require that g is a continuous, increasing function of v , defined for all real v . Dually, an I -resistor is current controlled, i.e., defined by a constitutive relation of the form

$$v = h(i) \quad (7.2)$$

In addition, we require that h is a continuous, increasing function of i , defined for all real i . We use the symbols of Figure 7.1 for V - and I -resistor. Linear resistors are examples of both I - and V -resistors. An example of a V -resistor that is not an I -resistor is the junction diode, modeled by its usual exponential constitutive relation

$$i = I_s(e^{v/nV_T} - 1) \quad (7.3)$$

Although Equation 7.3 could be solved for v and thus the constitutive relation could be written in the form of Equation 7.2, the resulting function h would be defined only for currents between $-I_s$ and $+\infty$, which is not enough to qualify for an I -resistor. For the same reason, the static model for a Zener diode would be an I -resistor, but not a V -resistor. Indeed, the very nature of the Zener diode limits its voltages on the negative side.

A somewhat strange by-product of our definition of V - and I -resistors is that independent voltage sources are I -resistors and independent current sources are V -resistors. Indeed, a voltage source of value E has the constitutive relation

$$v = E \quad (7.4)$$

which clearly is of the form (Equation 7.2), with a constant function h , and a current source of value I has the form

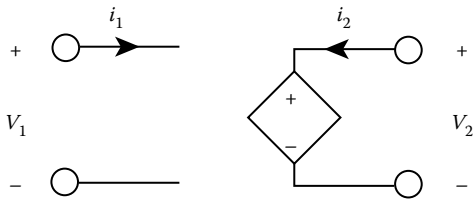
$$i = I \quad (7.5)$$

which is of the form (Equation 7.1) with a constant function g . Despite this, we shall treat the independent sources as a different type of element.

Another class of resistive elements is the controlled sources. We consider them to be two-ports, e.g., a voltage-controlled voltage source (VCVS). A VCVS is the two-port of Figure 7.2, where the constitutive relations are

$$v_1 = \alpha v_2 \quad (7.6)$$

$$i_1 = 0 \quad (7.7)$$



The other controlled sources have similar forms. Another useful resistive circuit element is the ideal operational amplifier. It is a two-port defined by the two constitutive relations

$$v_1 = 0 \tag{7.8}$$

$$i_1 = 0 \tag{7.9}$$

FIGURE 7.2 VCVS as a two-port.

This two-port can be decomposed into the juxtaposition of two singular one-ports, the nullator and the norator, as shown in Figure 7.3. The nullator has two constitutive relations:

$$v = 0, \quad i = 0 \tag{7.10}$$

whereas the norator has no constitutive relation.

For all practical purposes, the resistive circuit elements mentioned thus far are sufficient. By this we mean that all nonlinear resistive circuits encountered in practice possess an equivalent circuit composed of nonlinear resistors, independent and controlled sources, and nullator–norator pairs. Figure 7.4 illustrates this fact. Here, the equivalent circuit of the bipolar transistor is modeled by the Ebers–Moll equations:

$$\begin{pmatrix} i_1 \\ i_2 \end{pmatrix} = \begin{pmatrix} 1 + \frac{1}{\beta_F} & -1 \\ -1 & 1 + \frac{1}{\beta_R} \end{pmatrix} \begin{pmatrix} g(v_1) \\ g(v_2) \end{pmatrix} \tag{7.11}$$

The function g is given by the right-hand side of Equation 7.3.

Actually, the list of basic resistive circuit elements given so far is redundant, and the nullator–norator pairs render the controlled sources superfluous. An example of a substitution of controlled sources by nullator–norator pairs is given in Figure 7.4. Equivalent circuits exist for all four types of controlled sources with nullator–norator pairs. Figure 7.5 gives an equivalent circuit for a voltage-controlled current source (VCCS), where the input port is floating with respect to the output port.

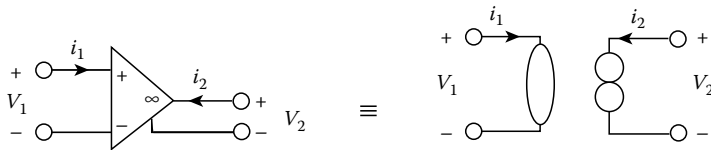


FIGURE 7.3 Operational amplifier as a juxtaposition of a nullator and a norator.

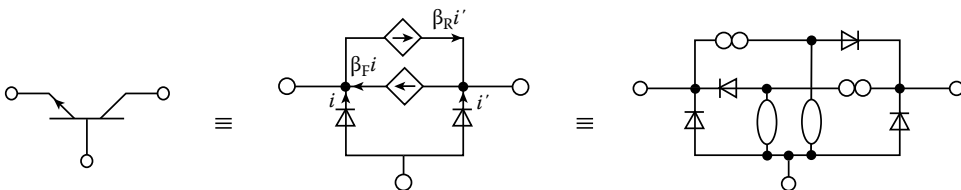


FIGURE 7.4 Equivalent circuit of a bipolar npn transistor.

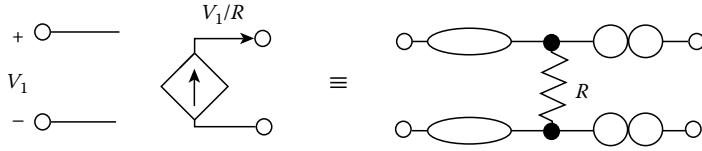


FIGURE 7.5 Equivalent circuit for a floating VCCS.

The system of equations that describes a resistive circuit is the collection of Kirchhoff equations and the constitutive relations of the circuit elements. It has the following form (if we limit ourselves to resistors, independent sources, nullators, and norators):

$$\mathbf{A}\mathbf{i} = \mathbf{0} \text{ (Kirchhoff's voltage law)} \tag{7.12}$$

$$\mathbf{B}\mathbf{v} = \mathbf{0} \text{ (Kirchhoff's voltage law)} \tag{7.13}$$

$$i_k = g(v_k) \text{ (V-resistor)} \tag{7.14}$$

$$v_k = h(i_k) \text{ (I-resistor)} \tag{7.15}$$

$$v_k = E_k \text{ (independent voltage source)} \tag{7.16}$$

$$i_k = I_k \text{ (independent current source)} \tag{7.17}$$

$$\begin{aligned} v_k &= 0 \\ i_k &= 0 \end{aligned} \text{ (nullators)} \tag{7.18}$$

In this system of equations, the unknowns are the branch voltages and the branch currents

$$\mathbf{v} = \begin{pmatrix} v_1 \\ v_2 \\ \vdots \\ v_b \end{pmatrix}, \quad \mathbf{i} = \begin{pmatrix} i_1 \\ i_2 \\ \vdots \\ i_b \end{pmatrix} \tag{7.19}$$

where the b is the number of branches. Because we have b linearly independent Kirchhoff equations [2], the system contains $2b$ equations and $2b$ unknowns. A solution $\xi = \begin{pmatrix} v \\ i \end{pmatrix}$ of the system is called a solution of the circuit. It is a collection of branch voltages and currents that satisfy Equations 7.12 through 7.19.

7.2.1 Number of Solutions of a Resistive Circuit

As we found earlier, the number of equations of a resistive circuit equals the number of unknowns. One may therefore expect a unique solution. This may be the norm, but it is far from being generally true. It is not even true for linear resistive circuits. In fact, the equations for a linear resistive circuit are of the form

$$\mathbf{H}\xi = \mathbf{e} \tag{7.20}$$

where the $2b \times 2b$ matrix \mathbf{H} contains the resistances and elements of value $0, \pm 1$, whereas the vector \mathbf{e} contains the source values and zeroes. The solution of Equation 7.20 is unique if the determinant of \mathbf{H} differs from zero. If it is zero, then the circuit has either infinitely many solutions or no solution at all. Is such a case realistic? The answer is yes and no. Consider two voltages sources connected as shown in Figure 7.6.

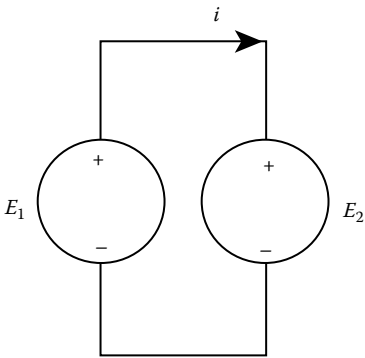


FIGURE 7.6 Circuit with zero or infinite solutions.

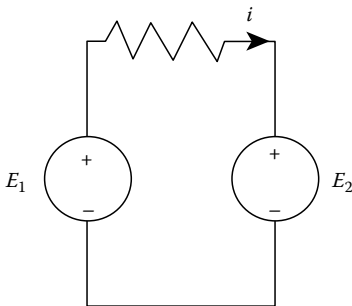


FIGURE 7.7 Circuit with exactly one solution.

resulting circuit is equivalent to the connection of a voltage source, a linear resistor, and the nonlinear resistor, as shown in Figure 7.10. Its solutions correspond to the intersections of the nonlinear resistor characteristic and the load line (Figure 7.9). Depending on the value of E , either one, two, or three solutions are available. Although we still need infinite precision to obtain two solutions, this is not the case for one or three solutions. Thus, more than one DC-operating point may be observed in electronic circuits. Indeed, for static memories, and multivibrators in general, multiple DC-operating points are an essential feature.

If $E_1 \neq E_2$, the constitutive relations of the sources are in contradiction with Kirchhoff's voltage law (KVL), and thus the circuit has no solution, whereas when $E_1 = E_2$, the current i in Figure 7.6 is not determined by the circuit equations, and thus the circuit has infinitely many solutions. One may object that the problem is purely academic, because in practice wires as connections have a small, but positive, resistance, and therefore one should instead consider the circuit of Figure 7.7, which has exactly one solution.

Examples of singular linear resistive circuits exist that are much more complicated. However, the introduction of parasitic elements always permits us to obtain a circuit with a single solution, and thus the special case in which the matrix \mathbf{H} in Equation 7.9 is singular can be disregarded. Within the framework of linear circuits, this attitude is perfectly justified. When a nonlinear circuit model is chosen, however, the situation changes. An example clarifies this point.

Consider the linear circuit of Figure 7.8. It is not difficult to see that it has exactly one solution, except when

$$R_1 R_3 = R_2 R_4 \tag{7.21}$$

In this case, the matrix \mathbf{H} in Equation 7.29 is singular and the circuit of Figure 7.8 has zero or infinitely many solutions, depending on whether E differs from zero. From the point of view of linear circuits, we can disregard this singular case because it arises only when Equation 7.21 is exactly satisfied with infinite precision.

Now, replace resistor R_4 by a nonlinear resistor, where the characteristic is represented by the bold line in Figure 7.9. The

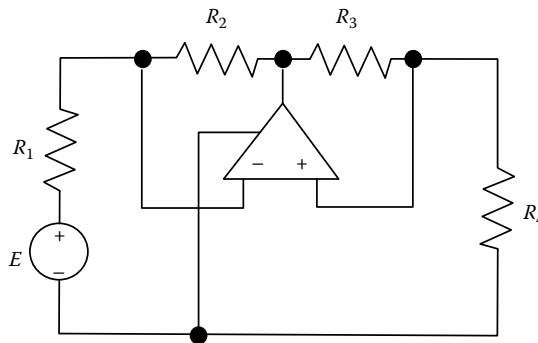


FIGURE 7.8 Circuit with one, zero, or infinite solutions.

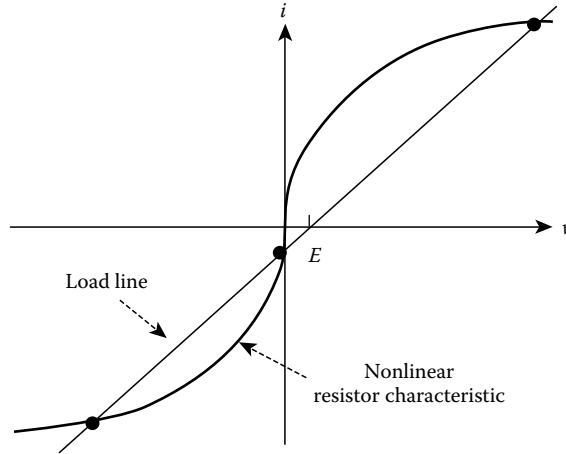


FIGURE 7.9 Characteristic of the nonlinear resistor and solutions of the circuit of Figure 7.10.

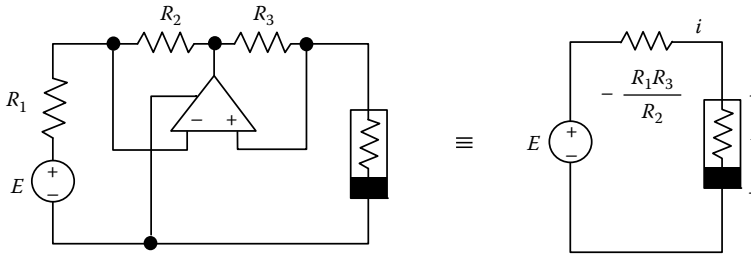


FIGURE 7.10 Circuit with one, two, or three solutions.

The example of Figure 7.10 shows an important aspect of the problem. The number of solutions depends on the parameter values of the circuit. In the example the value of E determines whether one, two, or three solutions are available. This is not always the case. An important class of nonlinear resistive circuits always has exactly one solutions, irrespective of circuit parameters. In fact, for many applications, e.g., amplification, signal shaping, logic operations, etc., it is necessary that a circuit has exactly one DC-operating point. Circuits that are designed for these functionalities should thus have a unique DC-operating point for any choice of element values.

If a resistive circuit contains only two-terminal resistors with increasing characteristics and sources, but no nonreciprocal element such as controlled sources, operational amplifiers, or transistors, the solution is usually unique. The following theorem gives a precise statement.

THEOREM 7.1

A circuit composed of independent voltage and current sources and strictly increasing resistors without loop of voltage sources and without cutset of current sources has at most one solution.

The interconnection condition concerning the sources is necessary. The circuit of Figure 7.6 is an illustration of this statement. Its solution is not unique because of the loop of voltage sources. The loop is

no longer present in the circuit of Figure 7.7, which satisfies the conditions of Theorem 7.1, and which indeed has a unique solution.

If the resistor characteristics are not *strictly* increasing but only increasing (i.e., if the v - i curves have horizontal or vertical portions), the theorem still holds, if we exclude loops of voltage sources and I -resistors, and cutsets of current sources and V -resistors.

Theorem 7.1 guarantees the uniqueness of the solution, but it cannot assure its existence. On the other hand, we do not need increasing resistor characteristics for the existence.

THEOREM 7.2

Let a circuit be composed of independent voltage and current sources and resistors whose characteristics are continuous and satisfy the following passivity condition at infinity:

$$v \rightarrow +\infty \Leftrightarrow i \rightarrow +\infty \quad \text{and} \quad v \rightarrow -\infty \Leftrightarrow i \rightarrow -\infty \quad (7.22)$$

If no loop of voltage sources and no cutset of current sources exist, then we have at least one solution of the circuit.

For refinements of this theorem, refer to Refs. [1,3].

If we admit nonreciprocal elements, neither Theorem 7.1 nor Theorem 7.2 remain valid. Indeed, the solution of the circuit of Figure 7.10 may be nonunique, even though the nonlinear resistor has a strictly increasing characteristic. In order to ensure the existence and uniqueness of a nonreciprocal nonlinear resistive circuit, nontrivial constraints on the interconnection of the elements must be observed. The theorems below give different, but basically equivalent, ways to formulate these constraints.

The first result is the culminating point of a series of papers by Sandberg and Wilson [3]. It is based on the following notion.

Definition 7.1:

- The connection of the two bipolar transistors shown in Figure 7.11 is called a feedback structure. The type of the transistors and the location of the collectors and emitters are arbitrary.
- A circuit composed of bipolar transistors, resistors, and independent sources contains a feedback structure, if it can be reduced to the circuit of Figure 7.11 by replacing each voltage source by a short circuit, each current source by an open circuit, each resistor and diode by an open or a short circuit, and each transistor by one of the five short-open circuit combinations represented in Figure 7.12.

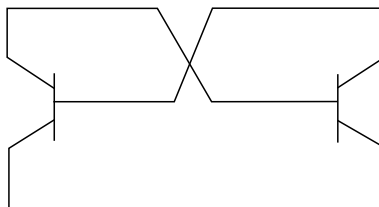


FIGURE 7.11 Feedback structure.

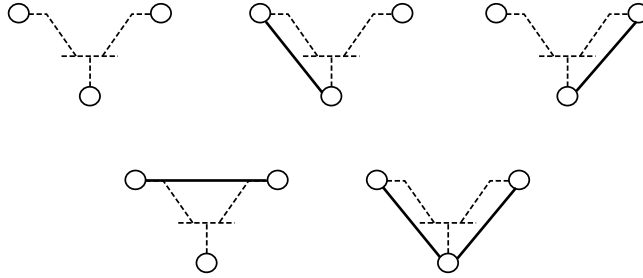


FIGURE 7.12 Short-open-circuit combinations for replacing the transistors.

THEOREM 7.3

Let a circuit be composed of bipolar transistors, described by the Ebers–Moll model, positive linear resistors, and independent sources. Suppose we have no loop of voltage sources and no cutset of current sources. If the circuit contains no feedback structure, it has exactly one solution.

This theorem [4] is extended in Ref. [5] to MOS transistors.

The second approach was developed by Nishi and Chua [6]. Instead of transistors, it admits controlled sources. In order to formulate the theorem, two notions must be introduced.

Definition 7.2: A circuit composed of controlled sources, resistors, and independent sources satisfies the interconnection condition, if the following conditions are satisfied:

- No loop is composed of voltage sources, output ports of (voltage or current) controlled voltage sources, and input ports of current-controlled (voltage or current) sources.
- No cutset is composed of current sources, outputs ports of (voltage or current) controlled current sources, and input ports of voltage-controlled (voltage or current) sources.

Definition 7.3: A circuit composed exclusively of controlled sources has a complementary tree structure if both the input and output ports each form a tree. The fundamental loop matrix of the input port tree has the form

$$B = [B_T | 1] \tag{7.23}$$

The circuit is said to have a positive (negative) complementary tree structure, if the determinant of B_T is positive (negative).

THEOREM 7.4

Suppose a circuit composed of controlled sources, strictly increasing resistors satisfying (Equation 7.22), and independent sources satisfies the interconnection condition. If, by replacing each resistor either by a short circuit or an open circuit, all independent and some dependent voltage sources by short circuits, and all independent and some dependent current sources by open circuits, one never obtains a negative complementary tree structure, the circuit has exactly one solution [6].

A similar theorem for circuits with operational amplifiers instead of controlled sources is proved in Ref. [7].

The third approach is that of Hasler [1,8]. The nonreciprocal elements here are nullator–norator pairs. Instead of reducing the circuit by some operations in order to obtain a certain structure, we must orient the resistors in certain way. Again, we must first introduce a new concept.

Definition 7.4: Let a circuit be composed of nullator–norator pairs, resistors, and independent voltage and current sources. A partial orientation of the resistors is uniform, if the following two conditions are satisfied:

- Every oriented resistor is part of an evenly directed loop composed only of oriented resistors and voltages sources.
- Every oriented resistor is part of an evenly directed cutset composed only of norators, oriented resistors, and voltage sources.

THEOREM 7.5

Let a circuit be composed of nullator–norator pairs, V- and I-resistors, and independent voltage and current sources. If the following conditions are satisfied, the circuit has exactly one solutions:

- *Norators, I-resistors, and voltage sources together form a tree.*
- *Nullators, I-resistors, and voltage sources together form a tree.*
- *Resistors have no uniform partial orientation, except for the trivial case, in which no resistor is oriented.*

We illustrate the conditions of this theorem with the example of Figure 7.10. In Figure 7.13 the resistors are specified as V- and I-resistors and a uniform orientation of the resistors is indicated. Note that the nonlinear resistor is a V-resistor, but not an I-resistor, because its current saturates. The linear resistors, however, are both V- and I-resistors. The choice in Figure 7.13 is made in order to satisfy the first two conditions of Theorem 7.5. Correspondingly, in Figures 7.14 and 7.15 the norator–I-resistor–voltage source tree and the nullator–I-resistor–voltage source tree are represented. Because the third condition is not satisfied, Theorem 7.5 cannot guarantee a unique solution. Indeed, as explained earlier, this circuit may have three solutions.

Theorem 7.5 has been generalized to controlled sources, to resistors that are increasing but neither voltage nor current controlled (e.g., the ideal diode), and to resistors that are decreasing instead of increasing [9].

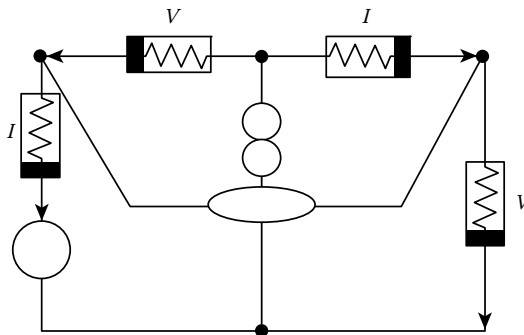


FIGURE 7.13 Circuit of Figure 7.10 with nullator and norator.

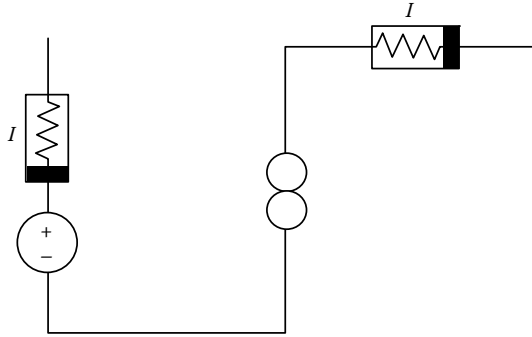


FIGURE 7.14 Norator- I -resistor-voltage source tree.

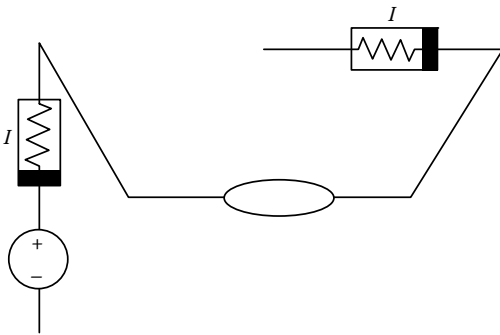


FIGURE 7.15 Nullator- I -resistor-voltage source tree.

Theorems 7.3, 7.4, and 7.5 have common features. Their conditions concern the circuit structure—the circuit graph that expresses the interconnection of the elements and the type of elements that occupy the branches of the graph, but not the element values. Therefore, the theorems guarantee the existence and uniqueness of the solution for whole classes of circuits, in which the individual circuits differ by their element values and parameters. In this sense the conditions are not only sufficient, but also necessary. This means, for example, in the case of Theorem 7.5 if all circuits with the same structure have exactly one solution, then the three conditions must be satisfied. However, by logical

contraposition, if one of the three conditions is not satisfied for a given circuit structure, a circuit with this structure exists which has either no solution or more than one solutions.

On the other hand, if we consider a specific circuit, the conditions are only sufficient. They permit us to prove that the solution exists and is unique, but some circuits do not satisfy the conditions and still have exactly one solution. However, if the parameters of such a circuit are varied, one eventually falls onto a circuit with no solution or more than one solution.

The main conditions of Theorems 7.3 and 7.4 have an evident intuitive meaning. The orientations to look for in Theorem 7.5 are linked to the sign of the currents and the voltages of the difference of two solutions. Because the resistors are increasing, these signs are the same for the voltage and current differences. If we extend the analysis of the signs of solutions or solution differences to other elements, we must differentiate between voltages and currents. This approach, in which two orientations for all branches are considered, one corresponding to the currents and one corresponding to the voltages, is pursued in Ref. [10].

The conditions of Theorems 7.3 through 7.5 can be verified by inspection for small circuits. For larger circuits, one must resort to combinatorial algorithms. Such algorithms are proposed in Refs. [11,12]. As can be expected from the nature of conditions, the algorithms grow exponentially with the number of resistors. It is not known whether algorithms of polynomial complexity exist.

Some circuits always have either no solution or an infinite number of solutions, irrespective of the element and parameter values. Figure 7.6 gives the simplest example. Such circuits clearly are not very useful in practice. The remaining circuits are those that may have a finite number $n > 1$ of solutions if the circuit parameters are chosen suitably. These are the circuits that are useful for static memories and for multivibrators in general. This class is characterized by the following theorem.

THEOREM 7.6

Let circuit be composed of nullator–norator pairs, V- and I-resistors, and independent voltage and current sources. If the following three conditions are satisfied, the circuit has more than one, but a finite number of solutions for a suitable choice of circuit parameters:

- Norators, I-resistors, and voltage sources together form a tree.
- Nullators, I-resistors, and voltage sources together form a tree.
- A nontrivial, uniform partial orientation of the resistors occurs.

Can we be more precise and formulate conditions on the circuit structure that guarantee four solutions, for example? This is not possible because changing the parameters of the circuit will lead to another number of solutions. Particularly with a circuit structure that satisfies the conditions of Theorem 7.6, there is a linear circuit that always has an infinite number of solutions. If we are more restrictive on the resistor characteristics, e.g., imposing convex or concave characteristics for certain resistors, it is possible to determine the maximum number of solutions. A method to determine an upper bound is given in Ref. [14], whereas the results of Ref. [15] allow us to determine the actual maximum number under certain conditions. Despite these results, however, the maximum number of solutions is still an open problem.

7.2.2 Bounds on Voltages and Currents

It is common sense for electrical engineers that in an electronic circuit all node voltages lie between zero and the power supply voltage, or between the positive and the negative power supply voltages, if both are present. Actually, this is only true for the DC-operating point, but can we prove it in this case? The following theorems give the answer. They are based on the notion of passivity.

Definition 7.5: A resistor is passive if it can only absorb, but never produce power. This means that for any point (v, i) on its characteristic we have

$$v \cdot i \geq 0 \quad (7.24)$$

A resistor is strictly passive, if in addition to Equation 7.24 it satisfies the condition

$$v \cdot i = 0 \rightarrow v = i = 0 \quad (7.25)$$

THEOREM 7.7

Let a circuit be composed of strictly passive resistors and independent voltage and current sources. Then, for every branch k of the circuit the following bounds can be given:

$$|v_k| \leq \sum_{\text{source branches } j} |v_j| \quad (7.26)$$

$$|i_k| \leq \sum_{\text{source branches } j} |i_j| \quad (7.27)$$

If, in addition, the circuit is connected and all sources have a common node, the ground node, then the maximum and the minimum node voltage are at a source terminal.

The theorem implies in particular that in a circuit with a single voltage source, all branch voltages are bounded by the source voltage in magnitude, and all node voltages lie between zero and the source voltage. Similarly, if a circuit has a single current source, all branch currents are bounded by the source current in magnitude. Finally, if several voltage sources are present that are all connected to ground and have positive value, then the node voltages lie between zero and the maximum source voltage. If some sources have positive values and others have negative values, then all node voltages lie between the maximum and the minimum source values.

This theorem and various generalizations can be found in Ref. [1]. The main drawback is that it does not admit nonreciprocal elements. A simple counterexample is the voltage amplifier of Figure 7.16. The voltage of the output node of the operational amplifier is

$$v = \frac{R_1 + R_2}{R_1} E \quad (7.28)$$

Thus, the output node voltage is higher than the source voltage. Of course, the reason is that the operational amplifier is an active element. It is realized by transistors and needs a positive and a negative voltage source as the power supply. The output voltage of the operational amplifier cannot exceed these supply voltages. This fact is not contained in the model of the ideal operational amplifier, but follows from the extension of Theorem 7.7 to bipolar transistors [1,16].

THEOREM 7.8

Let a circuit be composed of bipolar transistors modeled by the Ebers–Moll equations, of strictly passive resistors, and of independent voltage and current sources. Then, the conclusion of Theorem 7.7 hold.

At first glance, Theorem 7.8 appears to imply that it is impossible to build an amplifier with bipolar transistors. Indeed, it is impossible to build such an amplifier with a single source, the input signal. We need at least one power supply source that sets the limits of dynamic range of the voltages according to Theorem 7.8. The signal source necessarily has a smaller amplitude and the signal can be amplified roughly up to the limit set by the power supply source.

Theorem 7.8 can be extended to MOS transistors. The difficulty is that the nonlinear characteristics of the simplest model is not strictly increasing, and therefore some interconnection condition must be added to avoid parts with undetermined node voltages.

7.2.3 Monotonic Dependence

Instead of looking at single solutions of resistive circuits, as done earlier in the chapter, we consider here a solution as a function of a parameter. The simplest and at the same time the most important case is the dependence of a solution on the value of a voltage or current source. To have a well-defined situation, we suppose that the circuit satisfies the hypotheses of Theorem 7.5. In this case [1,8], the solution is a continuous function of the source values.

As an example, let us consider the circuit of Figure 7.17. We are interested in the dependence of the various currents on the source voltage E . Because the circuit contains only strictly increasing resistors, we

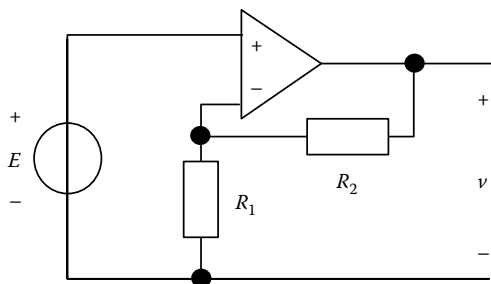


FIGURE 7.16 Voltage amplifier.

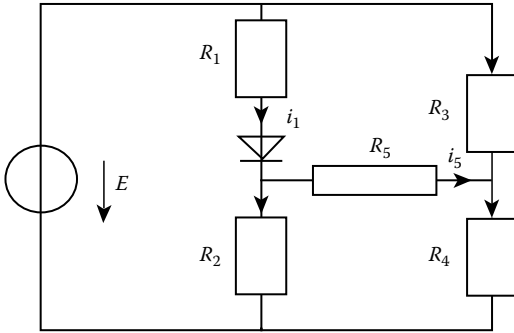


FIGURE 7.17 Circuit example for source dependence.

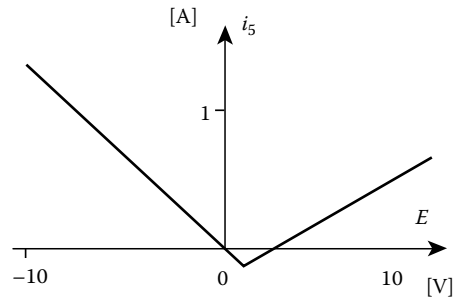


FIGURE 7.18 Nonmonotonic dependence.

expect all currents to be strictly monotonic functions of E . This is not true. In Figure 7.18, the current $i_5(E)$ is represented for $R_1 = R_2 = R_3 = 2R_4 = R_5 = 1 \Omega$ and for standard diode model parameters. Clearly, it is nonmonotonic.

7.3 Autonomous Dynamic Circuits

7.3.1 Introduction

This section adds to the resistive elements of Section 7.2—the capacitors and the inductors. A nonlinear capacitor is defined by the constitutive relation

$$v = h(q) \tag{7.29}$$

where the auxiliary variable q is the charge of the capacitor, which is linked to the current by

$$i = \frac{dq}{dt} \tag{7.30}$$

The dual element, the nonlinear inductor, is defined by

$$i = g(\varphi) \tag{7.31}$$

where the auxiliary variable φ , the flux, is linked to the voltage by

$$v = \frac{d\varphi}{dt} \tag{7.32}$$

The symbols of these two elements are represented in Figure 7.19.

The system of equations that describes an autonomous dynamic circuit is composed of Equations 7.12 through 7.17, completed with Equations 7.29 and 7.30 for capacitor branches and Equations 7.31 and 7.32 for inductor branches. Hence, it becomes a mixed differential–nondifferential system of equations. Its solutions are the voltages, currents, charges, and fluxes as functions of time. Because it contains differential equations, we have infinitely many solutions, each one determined by some set of initial conditions.



FIGURE 7.19 Symbols of the nonlinear capacitor and the nonlinear inductor.

If all variables except the charges and fluxes are eliminated from the system of equations, one obtains a reduced, purely differential system of equations

$$\frac{d\mathbf{q}}{dt} = \mathbf{f}(\mathbf{q}, \varphi) \quad (7.33)$$

$$\frac{d\varphi}{dt} = \mathbf{g}(\mathbf{q}, \varphi) \quad (7.34)$$

where \mathbf{q} and φ are the vectors composed of, respectively, the capacitor charges and the inductor fluxes. These are the state equations of the circuit. Under mild assumptions on the characteristics of the nonlinear elements (local Lipschitz continuity and eventual passivity), it can be shown that the solutions are uniquely determined by the initial values of the charges and fluxes at some time t_0 , $\mathbf{q}(t_0)$, and $\varphi(t_0)$, and that they exist for all times $t_0 \leq t < \infty$ [1,17].

It cannot be taken for granted, however, that the circuit equations actually can be reduced to that state Equations 7.33 and 7.34. On the one hand, the charges and fluxes may be dependent and thus their initial values cannot be chosen freely. However, the state equations may still exist, in terms of a subset of charges and fluxes. This means that only these charges and fluxes can be chosen independently as initial conditions. On the other hand, the reduction, even to some alternative set of state variables, may be simply impossible. This situation is likely to lead to impasse points, i.e., nonexistence of the solution at a finite time. We refer the reader to the discussion in Ref. [1]. In the sequel we suppose that the solutions exist from the initial time t_0 to $+\infty$ and that they are determined by the charges and fluxes at t_0 .

We are interested in the asymptotic behavior, i.e., the behavior of the solutions when the time t goes to infinity. If the dynamic circuit is linear and strictly stable, i.e., if all its natural frequencies are in the open left half of the complex plane, then all solutions converge to one and the same DC-operating (equilibrium) point. This property still holds for many nonlinear circuits, but not for all by far. In particular, the solutions may converge to different DC-operating points, depending on the initial conditions (static memories), they may converge to periodic solutions (free-running oscillators), or they may even show chaotic behavior (e.g., Chua's circuit). Here, we give conditions that guarantee the solutions converge to a unique solution or one among several DC-operating points.

7.3.2 Convergence to DC-Operating Points

The methods to prove convergence to one or more DC-operating points is based on Lyapunov functions. A Lyapunov function is a continuously differentiable function $W(\xi)$, where ξ is the vector composed of the circuit variables (the voltages, currents, charges, and fluxes). In the case of autonomous circuits, a Lyapunov function must have the following properties:

1. W is bounded below, i.e., there exists a constant W_0 such that

$$W(\xi) \geq W_0 \quad \text{for all } \xi \quad (7.35)$$

2. The set of voltages, currents, charges, and fluxes of the circuit such that $W(\xi) \leq E$ is bounded for any real E .
3. For any solution $\xi(t)$ of the circuit

$$\frac{d}{dt} W(\xi(t)) \leq 0 \quad (7.36)$$

4. If

$$\frac{d}{dt} W(\xi(t)) = 0 \quad (7.37)$$

then $\xi(t)$ is a DC-operating point.

If an autonomous circuit has a Lyapunov function and if it has at least one, but a finite number of DC-operating points, then every solution converges to a DC-operating point. The reason is that the Lyapunov function must decrease along each solution, and thus must result in a local minimum, a stable DC-operating point. If more than one DC-operating point exists, it may, as a mathematical exception that cannot occur in practice, end up in a saddle point, i.e., an unstable DC-operating point.

The problem with the Lyapunov function method is that it gives no indication as to how to find such a function. Basically, three methods are available to deal with this problem:

1. Some standard candidates for Lyapunov functions, e.g., the stored energy.
2. Use a certain kind of function and adjust the parameters in order to satisfy points 2 and 3 in the previous list. Often, quadratic functions are used.
3. Use an algorithm to generate Lyapunov functions [18–20].

The following theorems were obtained via approach 1, and we indicate which Lyapunov function was used to prove them. At first glance, this may seem irrelevant from an engineering point of view. However, if we are interested in designing circuits to solve optimization problems, we are likely to be interested in Lyapunov functions. Indeed, as mentioned previously, along any solution of the circuit, the Lyapunov function decreases and approaches a minimum of the function. Thus, the dynamics of the circuit solve a minimization problem. In this case, we look for a circuit with a given Lyapunov function, however, usually we look for a Lyapunov function for a given circuit.

THEOREM 7.9

Let a circuit be composed of capacitors and inductors with a strictly increasing characteristic, resistors with a strictly increasing characteristic, and independent voltage and current sources. Suppose the circuit has a DC-operating point $\bar{\xi}$. By Theorem 7.1, this DC-operating point is unique. Finally, suppose the circuit has no loop composed of capacitors, inductors, and voltage sources and no cutset composed of capacitors, inductors, and current sources. Then, all solutions of the circuit converge to $\bar{\xi}$.

The Lyapunov function of this circuit is given by a variant of the stored energy in the capacitors and the resistors, the stored energy with respect to $\bar{\xi}$ [1,17]. If the constitutive relations of the capacitors and the inductors are given by $v_k = h_k(q_k)$ and $i_k = g_k(v_k)$, respectively, then this Lyapunov function becomes

$$W(\xi) = \sum_{\substack{\text{capacitor} \\ \text{branches } k}} \int_{\bar{q}_k}^{q_k} (h_k(q) - h_k(\bar{q}_k))dq + \sum_{\substack{\text{inductor} \\ \text{branches } k}} \int_{\bar{\varphi}_k}^{\varphi_k} (g_k(\varphi) - g_k(\bar{\varphi}_k))d\varphi \tag{7.38}$$

The main condition (Equation 7.36) for a Lyapunov function follows from the fact that the derivative of the stored energy is the absorbed power, here in incremental form:

$$\frac{d}{dt} W(\xi) = \sum_{\substack{\text{capacitor} \\ \text{and inductor} \\ \text{branches } k}} \Delta v_k \Delta i_k = - \sum_{\substack{\text{resistor} \\ \text{branches } k}} \Delta v_k \Delta i_k \leq 0 \tag{7.39}$$

Various generalizations of Theorem 7.9 have been given. The condition “strictly increasing resistor characteristic” has been relaxed to a condition that depends on $\bar{\xi}$ in Refs. [1,17] and mutual inductances and capacitances have been admitted in Ref. [17].

Theorem 7.10 admits resistors with nonmonotonic characteristics. However, it does not allow for both inductors and capacitors.

THEOREM 7.10

Let a circuit be composed of capacitors with a strictly increasing characteristic, voltage-controlled resistors such that

$$v \rightarrow +\infty \Rightarrow i > I_+ > 0 \quad \text{and} \quad v \rightarrow -\infty \Rightarrow i < I_- < 0 \quad (7.40)$$

and independent voltage sources. Furthermore, suppose that the circuit has a finite number of DC-operating points. Then every solution of the circuit converges toward a DC-operating point.

This theorem is based on the then following Lyapunov function, called cocontent:

$$W(\xi(t)) = \sum_{\substack{\text{resistor} \\ \text{branches } k}} \int_0^{v_k} g_k(v) dv \quad (7.41)$$

where $i_k = g_k(v_k)$ is the constitutive relation of the resistor on branch k . The function W is decreasing along a solution of the circuit because

$$\begin{aligned} \frac{d}{dt} W(\xi(t)) &= \sum_{\substack{\text{resistor} \\ \text{branches } k}} \frac{dv_k}{dt} i_k = - \sum_{\substack{\text{capacitor} \\ \text{branches } k}} \frac{dv_k}{dt} i_k \\ &= - \sum_{\substack{\text{capacitor} \\ \text{branches } k}} \frac{dh_k}{dq} i_k^2 \leq 0 \end{aligned} \quad (7.42)$$

where $h_k(q_k)$ is the constitutive relation of the capacitor on branch k .

Theorem 7.10 has a dual version. It admits inductors instead of capacitors, current-controlled resistors, and current sources. The corresponding Lyapunov function is the content:

$$W(\xi) = \sum_{\substack{\text{resistor} \\ \text{branches } k}} \int_0^{i_k} h_k(i) di \quad (7.43)$$

where $v_k = h_k(i_k)$ is the constitutive relation of the resistor on branch k .

The main drawback of the two preceding theorems is that they do not admit nonreciprocal elements such as controlled sources, operational amplifiers, etc. In other words, no statement about the analog neural network of Figure 7.20 can be made. In this network the nonreciprocal element is the VCVS with the nonlinear characteristics $v_2 = \sigma(v_1)$. However, Theorem 7.10 can be generalized to a reciprocal voltage-controlled N -port resistor closed on capacitors and voltage sources. Such an N -port (Figure 7.21) is described by a constitutive relation of the form

$$i_k = g_k(v_1, \dots, v_N) \quad (7.44)$$

and it is reciprocal, if for all \mathbf{v} , and all k, j we have

$$\frac{\partial g_k}{\partial v_j}(\mathbf{v}) = \frac{\partial g_j}{\partial v_k}(\mathbf{v}) \quad (7.45)$$

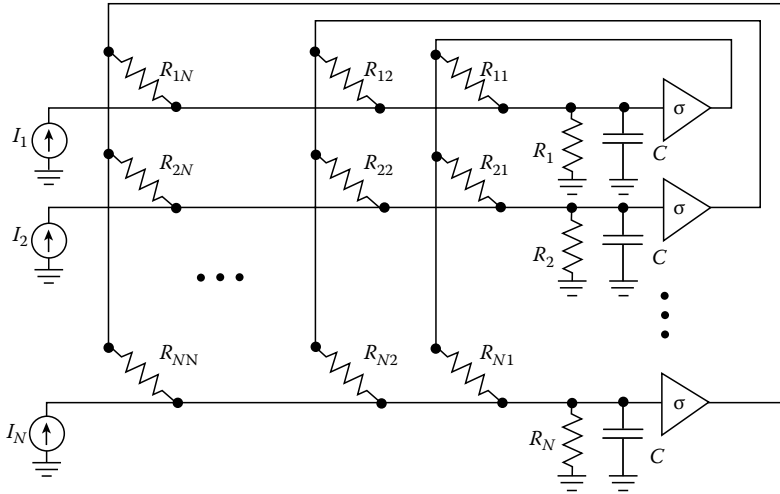


FIGURE 7.20 Analog neural network.

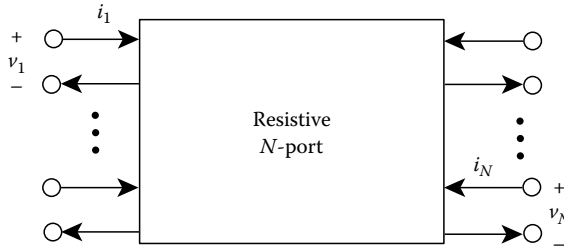


FIGURE 7.21 Resistive N -port.

THEOREM 7.11

Let a circuit be composed of charge-controlled capacitors with a strictly increasing characteristic and independent voltage sources that terminate a reciprocal voltage-controlled N -port with constitutive relation (Equation 7.42) so that we find constants V and $P > 0$ such that

$$\|\mathbf{v}\| \geq V \Rightarrow \mathbf{g} \cdot \mathbf{v} = \sum_{k=1}^N g_k(\mathbf{v})v_k \geq P \tag{7.46}$$

If the number of DC-operating points is finite, then all solutions converge toward a DC-operating point.

The proof of this theorem is based on the Lyapunov function $W(\mathbf{v})$ that satisfies

$$\frac{\partial W}{\partial v_k}(\mathbf{v}) = g_k(\mathbf{v}) \tag{7.47}$$

Thanks to Equation 7.45, function W exists. The first two conditions for a Lyapunov function are a consequence of Equation 7.46. Finally

$$\begin{aligned} \frac{d}{dt} W(\xi(t)) &= \sum_{\substack{\text{resistor} \\ \text{branches } k}} g_k(\mathbf{v}) \frac{dv_k}{dt} \\ &= \sum_{\substack{\text{resistor} \\ \text{branches } k}} i_k \frac{dv_k}{dt} \\ &= - \sum_{\substack{\text{capacitor} \\ \text{branches } k}} \frac{dh_k}{dq} i_k^2 \leq 0 \end{aligned} \quad (7.48)$$

where $h_k(q_k)$ is the constitutive relation of the capacitor on branch k .

To illustrate how Theorem 7.11 can be applied when Theorem 7.10 fails, consider the analog neural network of Figure 7.20. If the capacitor voltages are denoted by u_i and the voltages at the output of the voltage sources by v_j , the state equations for the network of Figure 7.1 become

$$-C_i \frac{du_i}{dt} = \frac{u_i}{R_i} + \sum_{j=1}^N \frac{u_i - v_j}{R_{ij}} + I_i \quad (7.49)$$

Suppose that the nonlinear characteristic $\sigma(u)$ is invertible. The state equations can be written in terms of the voltages v_i :

$$-C \frac{d\sigma^{-1}(v_i)}{dv} \frac{dv_i}{dt} = G_i \sigma^{-1}(v_i) - \sum_{j=1}^N \frac{v_j}{R_{ij}} + I_i \quad (7.50)$$

where

$$G_i = \frac{1}{R_i} + \sum_{j=1}^N \frac{1}{R_{ij}} \quad (7.51)$$

Equations 7.40 can be reinterpreted as the equations of a resistive N -port with the constitutive relations

$$g_i(\mathbf{v}) = G_i \sigma^{-1}(v_i) - \sum_{j=1}^N \frac{v_j}{R_{ij}} + I_i \quad (7.52)$$

closed on nonlinear capacitors with the constitutive relation

$$v = \sigma\left(\frac{q}{C}\right) \quad (7.53)$$

If σ is a sigmoidal function, as is most often supposed in this context (i.e., a strictly increasing function with $s(u) \rightarrow \pm 1$ for $u \rightarrow \pm\infty$), then the capacitors have a strictly increasing characteristic, as required by Theorem 7.11. Furthermore, the resistive N -port is reciprocal if for $i \neq j$

$$\frac{\partial g_i}{\partial v_j} = -\frac{1}{R_{ij}} = \frac{\partial g_j}{\partial v_i} = -\frac{1}{R_{ji}} \quad (7.54)$$

In other words, if for all i, j

$$R_{ij} = R_{ji} \quad (7.55)$$

On the other hand, inequality Equation 7.46 must be modified because the sigmoids have values only in the interval $[-1, +1]$ and thus Equation 7.50 are defined only on the invariant bounded set $S = \{\mathbf{v} \mid -1 < v_i < +1\}$. Therefore, inequality Equation 7.50 must be satisfied for vectors \mathbf{v} sufficiently close to the boundary of S . This is indeed the case, because $\sigma^{-1}(v) \rightarrow \pm\infty$ as $v \rightarrow \pm 1$, whereas the other terms of the right-hand side of Equation 7.52 remain bounded.

It follows that all solutions of the analog neural network of Figure 7.20 converge to a DC-operating point as $t \rightarrow \infty$, provided σ is a sigmoid function and the connection matrix R_{ij} (synaptic matrix) is symmetrical. The Lyapunov function can be given explicitly:

$$W(\mathbf{v}) = \sum_{i=1}^N G_i \int_0^{v_i} \sigma^{-1}(v) dv - \frac{1}{2} \sum_{i,j=1}^N \frac{v_i v_j}{R_{ij}} + \sum_{i=1}^N v_i I_i \quad (7.56)$$

7.4 Nonautonomous Dynamic Circuits

7.4.1 Introduction

This section is a consideration of circuits that contain elements where constitutive relations depend explicitly on time. However, we limit time dependence to the independent sources. For most practical purposes, this is sufficient. A time-dependent voltage source has a constitutive relation

$$v = e(t) \quad (7.57)$$

and a time-dependent current source

$$i = e(t) \quad (7.58)$$

where $e(t)$ is a given function of time which we suppose here to be continuous. In information processing circuits, $e(t)$ represents a signal that is injected into the circuit, whereas in energy transmission circuits $e(t)$ usually is a sinusoidal or nearly sinusoidal function related to a generator.

The time-dependent sources may drive the voltages and the currents to infinity, even if they only inject bounded signals into the circuit. Therefore, the discussion begins with the conditions that guarantee the boundedness of the solutions.

7.4.2 Boundedness of the Solutions

In electronic circuits, even active elements become passive when the voltages and currents grow large. This is the reason that solutions remain bounded.

Definition 7.6: A resistor is eventually passive if, for sufficiently large voltages and/or currents, it can only absorb power. More precisely, eventual passivity means that constants V and I exist such that, for all points (v, i) on the resistor characteristic with $|v| > V$ or $|i| > I$, we have

$$v \cdot i \geq 0 \quad (7.59)$$

Note that sources are not eventually passive, but as soon as an internal resistance of a source is taken into account, the source becomes eventually passive. The notion of eventual passivity can be extended to time-varying resistors.

Definition 7.7: A time-varying resistor is eventually passive if constants V and I are independent of time and are such that all points (v, i) , with $|v| > V$ or $|i| > I$ that at some time lie on the characteristic of the resistor, satisfy the passivity condition (Equation 7.59). According to this definition, time-dependent sources with internal resistance are eventually passive if the source signal remains bounded.

Eventual passivity allows us to deduce bounds for the solutions. These bounds are uniform in the sense that they do not depend on the particular solution. To be precise, this is true only asymptotically, as $t \rightarrow \infty$.

Definition 7.8: The solutions of a circuit are eventually uniformly bounded if there exist constants V, I, Q , and Φ such that, for any solution there exists a time T such that for any $t > T$, the voltages $v_k(t)$ are bounded by V , the currents $i_k(t)$ are bounded by I , the charges $q_k(t)$ are bounded by Q , and the fluxes $\varphi_k(t)$ are bounded by Φ .

Another manner of expressing the same property is to say that an attracting domain exists in state space [1].

THEOREM 7.12

A circuit composed of eventually passive resistors with $v \cdot i \rightarrow +\infty$ as $|v| \rightarrow \infty$ or $|i| \rightarrow \infty$, capacitors with $v \rightarrow \pm\infty$ as $q \rightarrow \neq\infty$, and inductors with $i \rightarrow \pm\infty$ as $\varphi \rightarrow \infty$ has eventually uniformly bounded solutions if no loop or cutset exists without a resistor [1,17].

Again, this theorem is proved by using a Lyapunov function, namely the stored energy

$$W(\xi) = \sum_{\substack{\text{capacitor} \\ \text{branches } k}} \int_0^{q_k} h_k(q) dq + \sum_{\substack{\text{capacitor} \\ \text{branches } k}} \int_0^{\varphi_k} g_k(\varphi) d\varphi \quad (7.60)$$

Inequality Equation 7.36 holds only outside of a bounded domain.

7.4.3 Unique Asymptotic Behavior

In the presence of signals with complicated waveforms that are injected into a circuit, we cannot expect simple waveforms for the voltages and the currents, not even asymptotically, as $t \rightarrow \infty$. However, we can hope that two solutions, starting from different initial conditions, but subject to the same source, have the same steady-state behavior. The latter term needs a more formal definition.

Definition 7.9: A circuit has unique asymptotic behavior if the following two conditions are satisfied:

1. All solutions are bounded.
2. For any two solutions $\xi_1(t)$ and $\xi_2(t)$

$$\|\xi_1(t) - \xi_2(t)\| \rightarrow_{t \rightarrow \infty} 0 \quad (7.61)$$

In order to prove unique asymptotic behavior, it is necessary to extend the notion of the Lyapunov function [1]. This does not lead very far, but at least it permits us to prove the following theorem.

THEOREM 7.13

Suppose a circuit is composed of resistors with a strictly increasing characteristic such that $v \cdot i \rightarrow \infty$ as $|v| \rightarrow \infty$ or $|i| \rightarrow \infty$, positive linear capacitors, positive linear inductors, time-dependent voltage (current) sources with bounded voltage (current) and a positive resistor in series (parallel). If no loop or cutset is composed exclusively of capacitors and inductors, the circuit has unique asymptotic behavior [1,17].

This theorem is unsatisfactory because linear reactances are required and real devices are never exactly linear. It has been shown that slight nonlinearities can be tolerated without losing the unique asymptotic behavior [21]. On the other hand, we cannot expect to get much stronger general results because nonautonomous nonlinear circuits may easily have multiple steady-state regimes and even more complicated dynamics, such as chaos, even if the characteristics of the nonlinear elements are all strictly increasing.

Another variant of Theorem 7.13 considers linear resistors and nonlinear reactances [17].

References

1. M. Hasler and J. Neiryneck, *Nonlinear Circuits*, Boston, MA: Artech House, 1986.
2. L.O. Chua, C.A. Desoer, and E.S. Kuh, *Linear and Nonlinear Circuits*, Electrical and Electronic Engineering Series, Singapore: McGraw-Hill International Editors, 1987.
3. A.N. Willson, Ed., *Nonlinear Networks: Theory and Analysis*, New York: IEEE Press, 1974.
4. R.O. Nielsen and A.N. Willson, A fundamental result concerning the topology of transistor circuits with multiple equilibria, *Proc. IEEE*, 68, 196–208, 1980.
5. A.N. Willson, On the topology of FET circuits and the uniqueness of their dc operating points, *IEEE Trans. Circuits Syst.*, 27, 1045–1051, 1980.
6. T. Nishi and L.O. Chua, Topological criteria for nonlinear resistive circuits containing controlled sources to have a unique solution, *IEEE Trans. Circuits Syst.*, 31, 722–741, Aug. 1984.
7. T. Nishi and L.O. Chua, Nonlinear op-amp circuits: Existence and uniqueness of solution by inspection, *Int. J. Circuit Theory Appl.*, 12, 145–173, 1984.
8. M. Hasler, Nonlinear nonreciprocal resistive circuits with a unique solution, *Int. J. Circuit Theory Appl.*, 14, 237–262, 1986.
9. M. Fosséprez, *Topologie et Comportement des Circuits non Linéaires non Réciproques*, Lausanne: Presses Polytechnique Romands, 1989.
10. M. Hasler, On the solution of nonlinear resistive networks, *J. Commun. (Budapest, Hungary)*, special issue on nonlinear circuits, July 1991.
11. T. Parker, M.P. Kennedy, Y. Lioa, and L.O. Chua, Qualitative analysis of nonlinear circuits using computers, *IEEE Trans. Circuits Syst.*, 33, 794–804, 1986.
12. M. Fosséprez and M. Hasler, Algorithms for the qualitative analysis of nonlinear resistive circuits, *IEEE ISCAS Proc.*, 2165–2168, May 1989.
13. M. Fosséprez and M. Hasler, Resistive circuit topologies that admit several solutions, *Int. J. Circuit Theory Appl.*, 18, 625–638, Nov. 1990.
14. M. Fosséprez, M. Hasler, and C. Schnetzler, On the number of solutions of piecewise linear circuits, *IEEE Trans. Circuits Syst.*, CAS-36, 393–402, March 1989.
15. T. Nishi and Y. Kawane, On the number of solutions of nonlinear resistive circuits, *IEEE Trans.*, E74, 479–487, 1991.
16. A.N. Willson, The no-gain property for networks containing three-terminal elements, *IEEE Trans. Circuits Syst.*, 22, 678–687, 1975.
17. L.O. Chua, Dynamic nonlinear networks: State of the art, *IEEE Trans. Circuits Syst.*, 27, 1059–1087, 1980.

18. R.K. Brayton and C.H. Tong, Stability of dynamical systems, *IEEE Trans. Circuits Syst.*, 26, 224–234, 1979.
19. R.K. Brayton and C.H. Tong, Constructive stability and asymptotic stability of dynamical systems, *IEEE Trans. Circuits Syst.*, 27, 1121–1130, 1980.
20. L. Vandenberghe and S. Boyd, A polynomial-time algorithm for determining quadratic Lyapunov functions for nonlinear systems, *Proc. ECCTD-93*, 1065–1068, 1993.
21. M. Hasler and Ph. Verburgh, Uniqueness of the steady state for small source amplitudes in nonlinear nonautonomous circuits, *Int. J. Circuit Theory Appl.*, 13, 3–17, 1985.

8

Synthesis and Design of Nonlinear Circuits

8.1	Introduction	8-1
8.2	Approximation Issues	8-3
	Unidimensional Functions • Piecewise-Linear and Piecewise-Polynomial Approximants • Gaussian and Bell-Shaped Basis Functions • Multidimensional Functions	
8.3	Aggregation, Scaling, and Transformation Circuits.....	8-11
	Transformation Circuits • Scaling and Aggregation Circuitry	
8.4	Piecewise-Linear Circuitry	8-18
	Current Transfer Piecewise-Linear Circuitry • Transresistance Piecewise-Linear Circuitry • Piecewise-Linear Shaping of Voltage-to-Charge Transfer Characteristics	
8.5	Polynomials, Rational, and Piecewise-Polynomial Functions	8-22
	Concepts and Techniques for Polynomic and Rational Functions • Multiplication Circuitry • Multipliers Based on Nonlinear Devices	
8.6	Sigmoids, Bells, and Collective Computation Circuits	8-29
	Sigmoidal Characteristics • Bell-Like Shapes • Collective Computation Circuitry	
8.7	Extension to Dynamic Systems	8-33
	Appendix A: Catalog of Primitives.....	8-34
	Appendix B: Value and Slope Hermite Basis Functions	8-35
	References.....	8-35

Angel Rodríguez-Vázquez
University of Seville

Manuel Delgado-Restituto
National Center of Microelectronics

Jose L. Huertas
National Center of Microelectronics

F. Vidal
University of Málaga

8.1 Introduction

Nonlinear synthesis and design can be informally defined as a constructive procedure to interconnect components from a catalog of available primitives, and to assign values to their constitutive parameters to meet a specific nonlinear relationship among electrical variables. This relationship is represented as an implicit integrodifferential operator, although we primarily focus on the synthesis of *explicit algebraic* functions,

$$y = f(\mathbf{x}) \tag{8.1}$$

where

- y is voltage or current
- $f(\cdot)$ is a nonlinear real-valued function
- \mathbf{x} is a vector with components that include voltages and currents

This synthesis problem is found in two different circuit-related areas: device modeling [8,76] and analog computation [26]. The former uses ideal circuit elements as primitives to build computer models of real circuits and devices (see Chapter 7). The latter uses real circuit components, available either off the shelf or integrable in a given fabrication technology, to realize hardware for nonlinear signal processing tasks. We focus on this second area, and intend to outline systematic approaches to devise electronic function generators. Synthesis relies upon hierarchical decomposition, conceptually shown in Figure 8.1, which encompasses several subproblems listed from top to bottom:

- Realization of nonlinear operators (multiplication, division, squaring, square rooting, logarithms, exponentials, sign, absolute value, etc.) through the interconnection of primitive components (transistors, diodes, operational amplifiers, etc.)
- Realization of elementary functions (polynomials, truncated polynomials, Gaussian functions, etc.) as the interconnection of the circuit blocks devised to build nonlinear operators
- Approximation of the target as a combination of elementary functions and its realization as the interconnection of the circuit blocks associated with these functions

Figure 8.1 illustrates this hierarchical decomposition of the synthesis problem through an example in which the function is approximated as a linear combination of truncated polynomials [30], where realization involves analog multipliers, built by exploiting the nonlinearities of bipolar junction transistors (BJTs) [63]. Also note that the subproblems cited above are closely interrelated and, depending on the availability of primitives and the nature of the nonlinear function, some of these phases can be bypassed. For instance, a logarithmic function can be realized exactly using BJTs [63], but requires approximation if our catalog includes only field-effect transistors whose nonlinearities are polymeric [44].

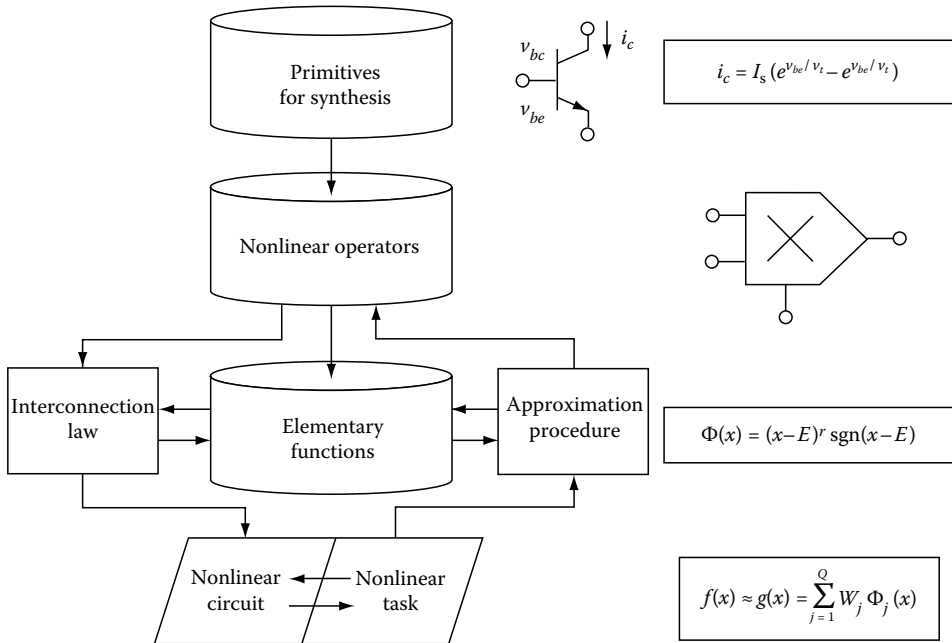


FIGURE 8.1 Hierarchical decomposition of the synthesis problem.

The technical literature contains excellent contributions to the solution of all these problems. These contributions can hardly be summarized or even quoted in just one section. Many authors follow a block-based approach which relies on the pervasive voltage operational amplifier (or op-amp), the rectification properties of junction diodes, and the availability of voltage multipliers, in the tradition of classical analog computation (e.g., Refs. [7,59,80]). Remarkable contributions have been made which focus on qualitative features such as negative resistance or hysteresis, rather than the realization of well-defined approximating functions [9,20,67]. Other contributions focus on the realization of nonlinear operators in the form of IC units. Translinear circuits, BJTs [23,62], and MOSFETs [79] are particularly well suited to realize algebraic functions in IC form. This IC orientation is shared by recent developments in analog VLSI computational and signal processing systems for neural networks [75], fuzzy logic [81], and other nonlinear signal processing paradigms [56,57,71].

This chapter is organized to fit the hierarchical approach in Figure 8.1. We review a wide range of approximation techniques and circuit design styles, for both discrete and monolithic circuits. It is based on the catalog of primitives shown in Appendix A. In addition to the classical op-amp-based continuous-time circuits, we include current-mode circuitry because nonlinear operators are realized simply and accurately by circuits that operate in *current domain* [23,57,62,79]. We also cover discrete-time circuits realized using analog dynamic techniques based on charge transfer, which is very significant for mixed-signal processing and computational microelectronic systems [27,72]. Section 8.2 is devoted to approximation issues and outlines different techniques for uni- and multidimensional functions, emphasizing hardware-oriented approaches. These techniques involve several nonlinear operators and the linear operations of scaling and aggregation (covered in Section 8.3, which also presents circuits to perform transformations among different kinds of characteristics). Sections 8.4 and 8.5 present circuits for piecewise-linear (PWL) and piecewise-polynomial (PWP) functions, Section 8.6 covers neural and fuzzy approximation techniques, and Section 8.7 outlines an extension to dynamic circuits.

8.2 Approximation Issues

8.2.1 Unidimensional Functions

Consider a target function, $f(x)$, given analytically or as a collection of measured data at discrete values of the independent variable. The approximation problem consists of finding a multiparameter function, $g(x, \mathbf{w})$, which yields proper fitting to the target, and implies solving two different subproblems: (1) which approximating functions to use, and (2) how to adjust the parameter vector, \mathbf{w} , to render optimum fitting. We only outline some issues related to this first point. Detailed coverage of both problems can be found in mathematics and optimization textbooks [73,78]. Other interesting views are found in circuit-related works [6,11,30], and the literature on neural and fuzzy networks [12,21,33,43,51].

An extended technique to design nonlinear electronic hardware for both discrete [63,80] and monolithic [35,62,79] design styles uses polynomial approximating functions,

$$g(x) = \sum_{j=0}^Q \alpha_j x^j \quad (8.2)$$

obtained through expansion by either Taylor series or orthogonal polynomials (Chebyshev, Legendre, or Laguerre) [26]. Other related approaches use rational functions,

$$g(x) = \frac{\sum_{j=0,Q} \alpha_j x^j}{\sum_{j=0,R} \beta_j x^j} \quad (8.3)$$

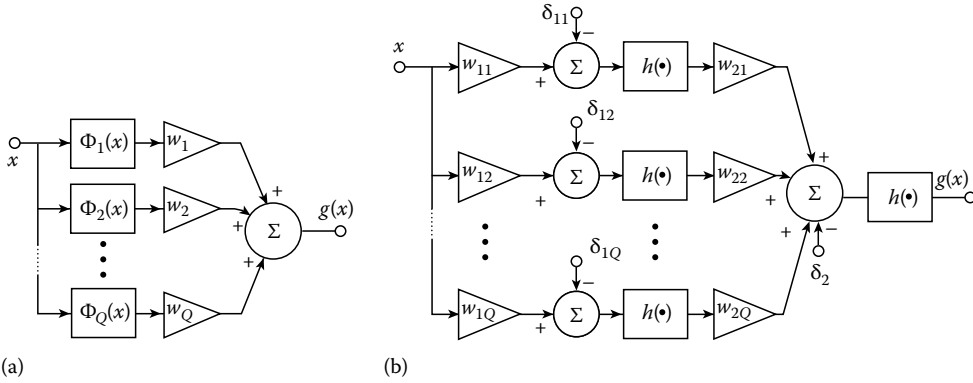


FIGURE 8.2 Block diagram for approximating function hardware. (a) Using linear combination of basis functions; (b) using two layers of nested sigmoids.

to improve accuracy in the approximation of certain classes of functions [14]. These can be realized by polynomial building blocks connected in feedback configuration [63]. In addition, Ref. [39] presents an elegant synthesis technique relying on linearly controlled resistors and conductors to take advantage of linear circuits synthesis methods (further extended in Ref. [28]).

From a more general point of view, hardware-oriented approximating functions can be classified into two major groups:

1. Those involving the linear combination of basis functions

$$g(x) = \sum_{j=1}^Q w_j \Phi_j(x) \tag{8.4}$$

which include polynomial expansions. PWL and PWP interpolation and radial basis functions (RBF). The hardware for these functions consists of two layers, as shown in Figure 8.2a. The first layer contains Q nonlinear processing nodes to evaluate the basis functions; the second layer scales the output of these nodes and aggregates these scaled signals in a summing node.

2. Those involving a multilayer of nested sigmoids [51]; for instance, in the case of two layers [82],

$$g(x) = h \left[\left\{ \sum_{j=1, Q} w_{2j} h(w_{1j}x - \delta_{1j}) \right\} - \delta_2 \right] \tag{8.5}$$

with the sigmoid function given by

$$h(x) = \frac{2}{1 + \exp(-\lambda x)} - 1 \tag{8.6}$$

where $\lambda > 0$ determines the steepness of the sigmoid. Figure 8.2b shows a hardware concept for this approximating function, also consisting of two layers.

8.2.2 Piecewise-Linear and Piecewise-Polynomial Approximants

A drawback of polynomial and rational approximants is that their behavior in a small region determines their behavior in the whole region of interest [78]. Consequently, they are not appropriate to fit functions

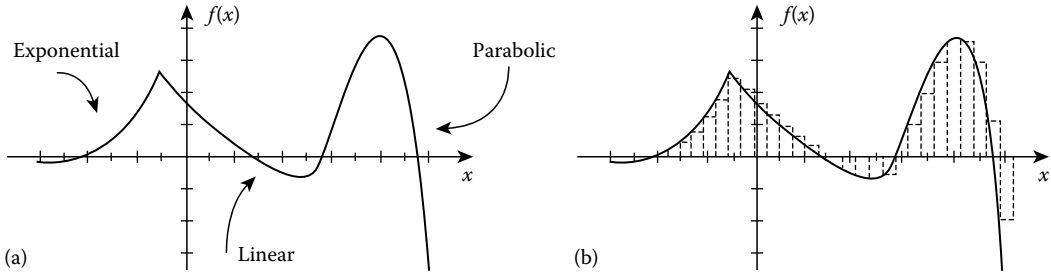


FIGURE 8.3 Example of nonuniform function. (a) A functions that is uniform throughout the whole region. (b) Interpolating the function by its samples associated to infinitely small subintervals.

that are uniform throughout the whole region (see Figure 8.3a). Another drawback is their lack of modularity, a consequence of the complicated dependence of each fitting parameter on multiple target data, which complicates the calculation of optimum parameter values. These drawbacks can be overcome by splitting the target definition interval into Q subintervals, and then expressing approximating function as a linear combination of basis functions, each having compact support over only one subinterval, i.e., zero value outside this subinterval. For the limiting case in which $Q \rightarrow \infty$, this corresponds to interpolating the function by its samples associated to infinitely small subintervals (Figure 8.3b). Such action is functionally equivalent to expressing a signal as its convolution with a delta of Dirac [10].

This splitting and subsequent approximation can be performed ad hoc, by using different functional dependences to fit each subregion. However, to support the systematic design of electronic hardware it is more convenient to rely on well-defined classes of approximating functions. In particular, Hermite PWP's provide large modularity by focusing on the interpolation of measured data taken from the target function. Any lack of flexibility as compared to the ad hoc approach may be absorbed in the splitting of the region.

Consider the more general case in which the function, $y = f(x)$, is defined inside a real interval $[\delta_0, \delta_{N+1}]$ and described as a collection of data measured at *knots* of a given interval partition, $\Delta = \{\delta_0, \delta_1, \delta_2, \dots, \delta_N, \delta_{N+1}\}$. These data may include the function values at these points, as well as their derivatives, up to the $(M - 1)$ th order,

$$f^{(k)}(\delta_i) = \left. \frac{d^k}{dx^k} f(x) \right|_{x=\delta_i} \quad i = 0, 1, 2, \dots, N, N + 1 \quad (8.7)$$

where k denotes the order of the derivative and is zero for the function itself. These data can be interpolated by a linear combination of basis polynomials of degree $2M - 1$,

$$g(x) = \sum_{i=0}^{N+1} \sum_{k=0}^{M-1} f^{(k)}(\delta_i) \Phi_{ik}(x) \quad (8.8)$$

where the expressions for these polynomials are derived from the interpolation data and continuity conditions [78]. Note that for a given basis function set and a given partition of the interval, each coefficient in Equation 8.8 corresponds to a single interpolation knot.

The simplest case uses linear basis functions to interpolate only the function values,

$$g(x) = \sum_{i=0}^{N+1} f(\delta_i) l_i(x) \quad (8.9)$$

with no function derivatives interpolated. Figure 8.4 shows the shape of the inner j th linear basis function, which equals 1 at δ_j and decreases to 0 at δ_{j-1} and δ_{j+1} . Figure 8.5a illustrates the representation

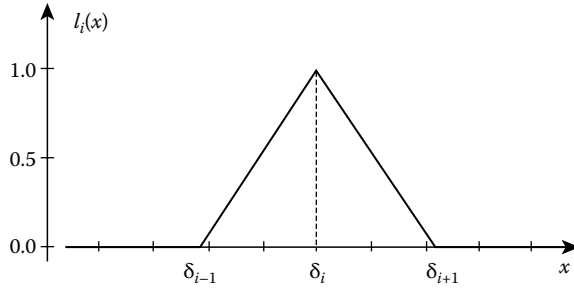


FIGURE 8.4 Hermite linear basis function.

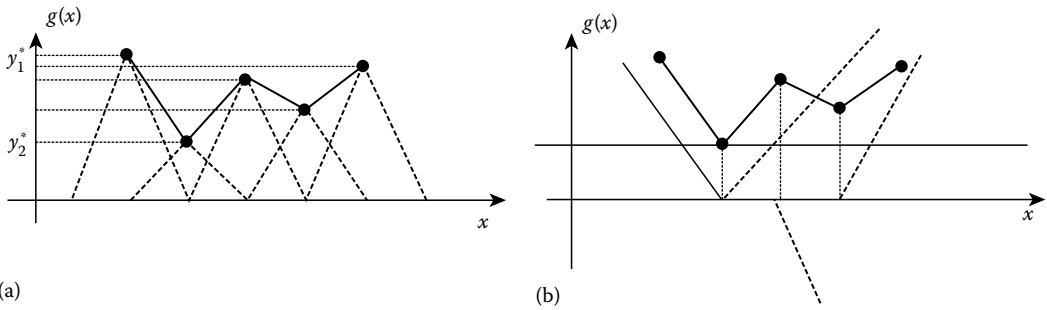


FIGURE 8.5 Decomposition of a PWL function using the extension operator. (a) Illustrating the representation in Equation 8.9. (b) Fitting some pieces from left to right and others from right to left.

in Equation 8.9. By increasing the degree of the polynomials, the function derivatives also can be interpolated. In particular, two sets of third-degree basis functions are needed to retain modularity in the interpolation of the function and its first derivative at the knots

$$g(x) = \sum_{i=0}^{N+1} f(\delta_i)v_i(x) + \sum_{i=0}^{N+1} f^{(1)}(\delta_i)s_i(x) \tag{8.10}$$

where Appendix B shows the shapes and expressions of the value, $v_i(x)$, and slope, $s_i(x)$, basis functions.

The modularity of Hermite polynomials is not free; their implementation is not cheapest in terms of components and, consequently, may not be optimal for application in which the target function is fixed. These applications are more conveniently handled by the so-called canonical representation of PWP functions. A key concept is the extension operator introduced in Ref. [6]; the basic idea behind this concept is to build the approximating function following an iterative procedure. At each iteration, the procedure starts from a function that fits the data on a subinterval, enclosing several pieces of the partition interval, and then adds new terms to also fit the data associated to the next piece. Generally, some pieces are fit from left to right and others from right to left, to yield

$$g(x) = g^0(x) + \sum_{i=1}^{N+} \Delta^+ g_i(x) + \sum_{i=-N_-}^{-1} \Delta^- g_i(x) \tag{8.11}$$

It is illustrated in Figure 8.5b. The functions in Equation 8.11 have the following general expressions

$$\begin{aligned} \Delta^+ g(x) &= wu_+(x - \delta) \equiv w(x - \delta)\text{sgn}(x - \delta) \\ \Delta^- g(x) &= wu_-(x - \delta) \equiv w(x - \delta)\text{sgn}(\delta - x) \\ g^0(x) &= ax + b \end{aligned} \tag{8.12}$$

where $\text{sgn}(\cdot)$ denotes the *sign* function, defined as an application of the real axis onto the discrete set $\{0,1\}$.

This representation, based on the extension operator, is elaborated in Ref. [6] to obtain the following canonical representation for unidimensional PWL functions:

$$g(x) = ax + b + \sum_{i=1}^N w_i |x - \delta_i| \tag{8.13}$$

which has the remarkable feature of involving only one nonlinearity: the absolute value function.

The extension operator concept was applied in Ref. [30] to obtain canonical representations for cubic Hermite polynomials and B-splines. Consequently, it demonstrates that a PWP function admits a global expression consisting of a linear combination of powers of the input variable, plus truncated powers of shifted versions of this variable. For instance, the following expression is found for a cubic B-spline:

$$g(x) = \sum_{r=0}^3 \alpha_r x^r + \sum_{i=1}^N \beta_i (x - \delta_i)^3 \text{sgn}(x - \delta_i) \tag{8.14}$$

with α_r and β_i obtainable through involved operations using the interpolation data. Other canonical PWP representations devised by these authors use

$$(x - \delta_i)^r \text{sgn}(x - \delta_i) = \frac{1}{2} \{ |x - \delta_i| + (x - \delta_i) \} (x - \delta_i)^{r-1} \tag{8.15}$$

to involve the absolute value, instead of the sign function, in the expression of the function.

8.2.3 Gaussian and Bell-Shaped Basis Functions

The Gaussian basis function belongs to the general class of RBF [51,52], and has the following expression:

$$\Phi(x) = \exp\left(-\frac{(x - \delta)^2}{2\sigma^2}\right) \tag{8.16}$$

plotted in Figure 8.6. The function value is significant only for a small region of the real axis centered around its center, δ , and its shape is controlled by the *variance* parameter, σ^2 . Thus, even though the

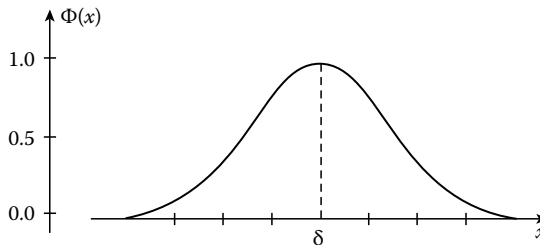


FIGURE 8.6 Gaussian basis function.

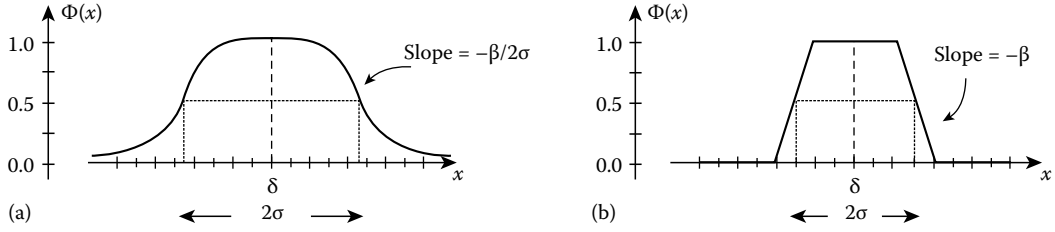


FIGURE 8.7 Fuzzy membership functions: (a) polynomial; (b) PWL.

support of Gaussian functions is not exactly compact, they are negligible except for well-defined local domains of the input values.

By linear combination of a proper number of Gaussians, and a proper choice of their centers and variances, as well as the weighting coefficients, it is possible to approximate nonlinear functions to any degree of accuracy [51]. Also, the local feature of these functions renders this adjustment process simpler than for multilayer networks composed of nested sigmoids, whose components are global [43,50].

A similar interpolation strategy arises in the framework of fuzzy reasoning, which is based on local membership functions whose shape resembles a Gaussian. For instance, in the ANFIS system proposed by Jang [33]

$$\Phi(x) = \frac{1}{1 + \left[\left(\frac{x-\delta}{\sigma} \right)^2 \right]^\beta} \tag{8.17}$$

as plotted in Figure 8.7a where the shape is controlled by β and σ , and the position is controlled by δ . Other authors, for instance, Yamakawa [81], use the PWL membership function shape of Figure 8.7b, which is similar to the Hermite linear basis function of Figure 8.4. From a more general point of view, cubic B-splines [78] used to build hardware [59] and for device modeling [76] also can be considered to be members of this class of functions.

8.2.4 Multidimensional Functions

Approximation techniques for multidimensional functions are informally classified into five groups:

1. Sectionwise PWP functions [6,30]
2. Canonical PWL representations [11]
3. Neurofuzzy interpolation [33,81]
4. Radial basis functions [51,52]
5. Multilayers of nested sigmoids [82]

8.2.4.1 Sectionwise Piecewise-Polynomial Functions

This technique reduces the multidimensional function to a sum of products of functions of only one variable:

$$g(\mathbf{x}) = \sum_{k_1=1}^{M_1} \sum_{k_2=1}^{M_2} \dots \sum_{k_p=1}^{M_p} \alpha(k_1, k_2, \dots, k_p) \prod_{j=1}^p \Phi_{k_j}(x_j) \tag{8.18}$$

where $\alpha(k_1, k_2, \dots, k_p)$ denotes a constant coefficient. These function representations were originally proposed by Chua and Kang for the PWL case [6] where

$$\begin{aligned} \Phi_1(x_j) &= 1 & \Phi_2(x_j) &= x_j & \Phi_3(x_j) &= |x_j - \delta_{j1}| \cdots \\ \Phi_{M_p}(x_j) &= |x_j - \delta_{jM_p-2}| \end{aligned} \tag{8.19}$$

Similar to the unidimensional case, the only nonlinearity involved in these basis functions is the absolute value. However, multidimensional functions not only require weighted summations, but also multiplications. The extension of Equation 8.18 to PWP functions was covered in Ref. [30], and involves the same kind of nonlinearities as Equations 8.14 and 8.15.

8.2.4.2 Canonical Piecewise Linear Representations

The canonical PWL representation of Equation 8.13 can be extended to the multidimensional case, based on the following representation:

$$g(\mathbf{x}) = \mathbf{a}^T \mathbf{x} + b + \sum_{i=1}^Q c_i |\mathbf{w}_i^T \mathbf{x} - \delta_i| \tag{8.20}$$

where

- \mathbf{a} and \mathbf{w}_i are P -vectors
- b , c_i , and δ_i are scalars

Q represents the number of hyperplanes that divide the whole space R^P into a finite number of polyhedral regions where $g(\cdot)$ can be expressed as an affine representation.

Note that Equation 8.20 avoids the use of multipliers. Thus, $g(\cdot)$ in Equation 8.20 can be realized through the block diagram of Figure 8.8, consisting of Q absolute value nonlinearities and weighted summers.

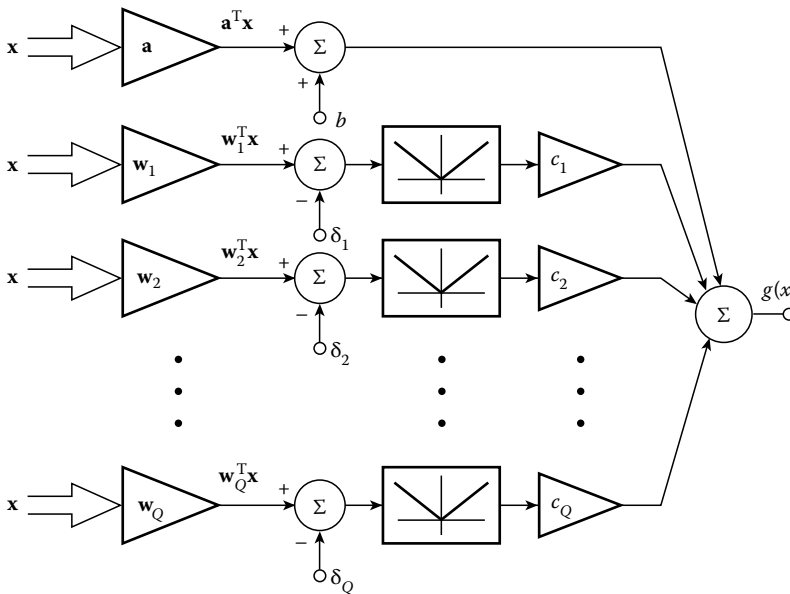


FIGURE 8.8 Canonical block diagram for a canonical PWL function.

8.2.4.3 Radial Basis Functions

The idea behind RBF expansion is to represent the function at each point of the input space as a linear combination of kernel functions whose arguments are the radial distance of the input point to a selected number of centers

$$g(\mathbf{x}) = \sum_{j=1}^Q w_j \Phi_j(\|\mathbf{x} - \delta_j\|) \tag{8.21}$$

where $\|\cdot\|$ denotes a norm imposed on R^P , usually assumed Euclidean. The most common basis function is a Gaussian kernel similar to Equation 8.16,

$$\Phi(\mathbf{x}) = \exp\left(-\frac{\|\mathbf{x} - \delta\|^2}{2\sigma^2}\right) \tag{8.22}$$

although many other alternatives are available [51], for instance,

$$\Phi(r) = (\sigma^2 + r^2)^{-\alpha}, \quad \Phi(r) = r, \quad \alpha \geq -1 \tag{8.23}$$

where r is the radial distance to the center of the basis function, $r \equiv \|\mathbf{x} - \delta\|$. Micchelli [42] demonstrated that any function where the first derivative is monotonic qualifies as a RBF. As an example, as Equation 8.23 displays, the identity function $\Phi(r) = r$ falls into this category, which enables connecting the representation by RBF to the canonical PWL representation [40]. Figure 8.9 is a block diagram for the hardware realization of the RBF model.

8.2.4.4 Neurofuzzy Interpolation

This technique exploits the interpolation capabilities of fuzzy inference, and can be viewed as the multidimensional extension of the use of linear combination of bell-shaped basis functions to approximate nonlinear functions of a single variable (see Equations 8.4 and 8.17). Apart from its connection to approximate reasoning and artificial intelligence, this extension exhibits features similar to the sectionwise PWP representation, namely, it relies on a well-defined class of unidimensional functions. However, neurofuzzy interpolation may be advantageous for hardware implementation because it requires easy-to-build collective computation operators instead of multiplications.

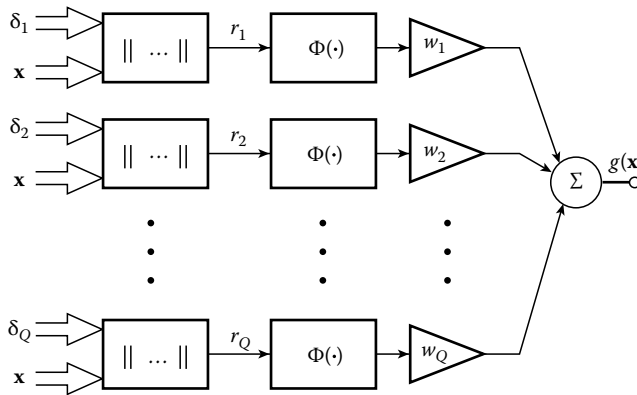


FIGURE 8.9 Concept of RBF hardware.

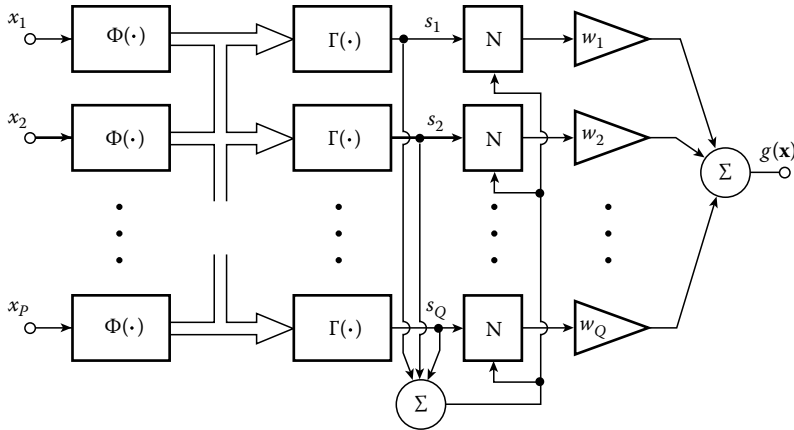


FIGURE 8.10 Conceptual architecture of a neurofuzzy interpolator.

Figure 8.10 depicts the block diagram of a neurofuzzy interpolator for the simplest case in which inference is performed using the singleton algorithm [33] to obtain

$$g(\mathbf{x}) = \sum_{j=1}^Q w_j \frac{s_j(\mathbf{x})}{\sum_{i=1, Q} s_i(\mathbf{x})} \tag{8.24}$$

where the functions $s_i(\mathbf{x})$, called activities of the fuzzy rules, are given as

$$s_j(\mathbf{x}) = \Gamma\{\Phi_{j1}(x_1), \Phi_{j2}(x_2), \dots, \Phi_{jp}(x_p)\} \tag{8.25}$$

where

- Γ(·) is any T-norm operator, for instance, the *minimum*
- Φ(·) has a bell-like shape (see Figure 8.7)

8.2.4.5 Multilayer Perceptron

Similar to Equation 8.5, but consists of the more general case of several layers, with the input to each nonlinear block given as a linear combination of the multidimensional input vector [82].

8.3 Aggregation, Scaling, and Transformation Circuits

The mathematical techniques presented in Section 8.2 require several nonlinear operators and the linear operators of scaling and aggregation (covered for completeness in this section). This section also covers transformation circuits. This is because in many practical situations we aim to exploit some nonlinear mechanism which intrinsically involves a particular kind of characteristics. For instance, a MOS transistor has inherent square-law transconductance, while a diode exhibits an exponential driving-point. Similarly, many nonlinear operators are naturally realized in current-mode domain and involve currents at both the input and the output. Thus, transformation circuits are needed to exploit these mechanisms for other types of characteristics.

8.3.1 Transformation Circuits

Two basic problems encountered in the design of transformation circuits are how to convert a voltage node into a current node and vice versa. We know no unique way to realize these functions. Instead, there

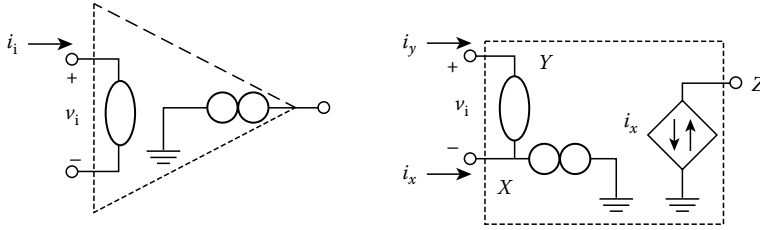


FIGURE 8.11 First-order models for voltage op-amps and CCIIs using nullators and norators.

are many alternatives which depend on which active component from Appendix A is used. The OTA can be represented to a first-order model as a voltage-controlled current source (VCCS) with linear transconductance parameter g_m . Regarding the op-amp and CCII, it is convenient to represent them by the first-order models of Figure 8.11, which contain nullators and norators.* A common appealing feature of both models is the virtual ground created by the input nullator. It enables us to sense the current drawn by nodes with fixed voltage—fully exploitable to design transformation circuits.

8.3.1.1 Voltage-to-Current Transformation

A straightforward technique for voltage-to-current conversion exploits the operation of the OTA as a VCCS (see Figure 8.12a) to obtain $i_o = g_m v_i$, where g_m is the OTA transconductance parameter [22]. A drawback is that its operation is linear only over a limited range of the input voltage. Also, the scaling factor is inaccurate and strongly dependent on temperature and technology. Consequently,

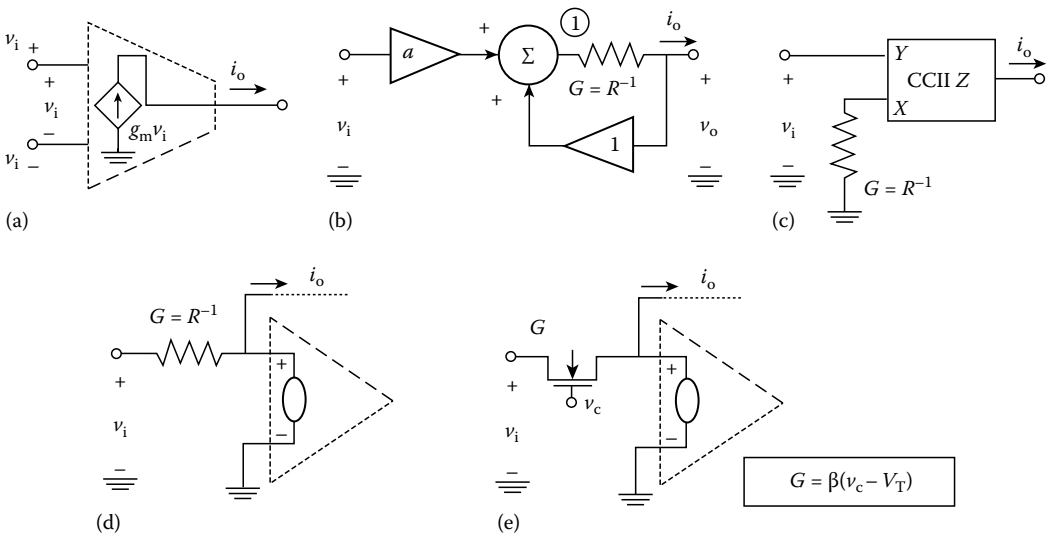


FIGURE 8.12 Voltage-to-current transformation: (a) using an OTA; (b) using voltage feedback; (c) using a current conveyor; (d) using virtual ground of an op-amp; (e) same as Figure 8.12d, but with active resistors.

* A nullator simultaneously yields a short circuit and an open circuit, while the voltage and the current at a norator are determined by the external circuitry. The use of a nullator to model the input port of an op amp is valid only if the component is embedded in a negative feedback configuration. With regard to the CCII, the required feedback is created by the internal circuitry.

voltage-to-current conversion using this approach requires circuit strategies to increase the OTA linear operation range [17,70], and tuning circuits to render the scaling parameter accurate and stable [70]. As counterparts, the value of the scaling factor is continuously adjustable through a bias voltage or current. Also, because the OTA operates in open loop, its operation speed is not restricted by feedback-induced pole displacements.

The use of feedback attenuates the linearity problem of Figure 8.12a by making the conversion rely on the constitutive equation of a passive resistor. Figure 8.12b illustrates a concept commonly found in op-amp-based voltage-mode circuits [29,59]. The idea is to make the voltage at node ① of the resistor change linearly with v_o , $v_1 = v_o + av_i$, and thus render the output current independent of v_o , to obtain $i_o = G(v_o + av_i - v_o) = aGv_i$. The summing node in Figure 8.12b is customarily realized using op-amps and resistors, which is very costly in the more general case in which the summing inputs have high impedance. The circuits of Figure 8.12c and d reduce this cost by direct exploitation of the virtual ground at the input of current conveyors (Figure 8.12c) and op-amps (Figure 8.12d). For both circuits, the virtual ground forces the input voltage v_i across the resistor. The resulting current is then sensed at the virtual ground node and routed to the output node of the conveyor, or made to circulate through the feedback circuitry of the op-amp, to obtain $i_o = Gv_i$.

Those implementations of Figure 8.12b through d that use off-the-shelf passive resistors overcome the accuracy problems of Figure 8.12a. However, the values of monolithic components are poorly controlled. Also, resistors may be problematic for standard VLSI technologies, where high-resistivity layers are not available and consequently, passive resistors occupy a large area. A common IC-oriented alternative uses the ohmic region of the MOS transistor to realize an active resistor [69] (Figure 8.12e). Tuning and linearity problems are similar to those for the OTA. Circuit strategies to overcome the latter are ground in Refs. [13,32,66,69].

8.3.1.2 Current-to-Voltage Transformation

The most straightforward strategy consists of a single resistor to draw the input current. It may be passive (Figure 8.13a) or active (Figure 8.13b). Its drawback is that the node impedance coincides with the resistor value, and thus makes difficult impedance matching to driving and loading stages. These matching problems are overcome by Figure 8.13c, which obtains low impedances at both the input and the output ports. On the other hand, Figure 8.13d obtains low impedance at only the input terminal, but maintains the output impedance equal to the resistor value. All circuits in Figure 8.13 obtain $v_o = Ri_i$, where $R = g_m^{-1}$ for the OTA.

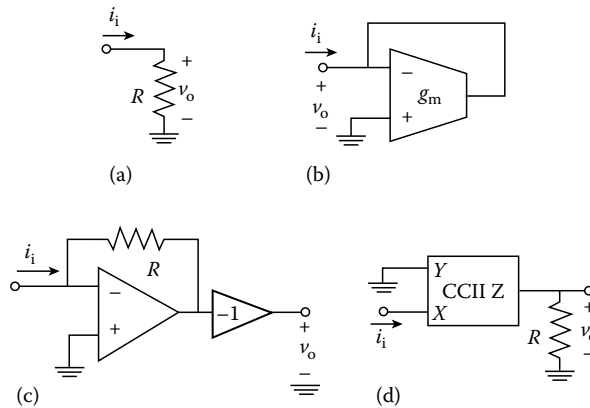


FIGURE 8.13 Current-to-voltage transformation: (a) using a resistor; (b) using a feedback OTA; (c) using op-amps; (d) using current conveyors.

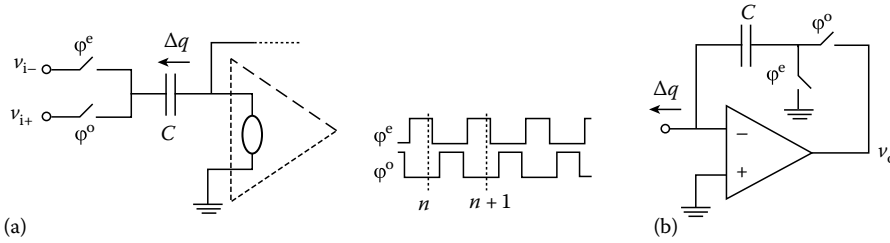


FIGURE 8.14 Transformations for sampled-data circuits: (a) voltage to charge; (b) charge to voltage.

8.3.1.3 Voltage/Charge Domain Transformations for Sampled-Data Circuits

The linearity and tuning problems of previous IC-related transformation approaches are overcome through the use of dynamic circuit design techniques based on switched-capacitors [72]. The price is that the operation is no longer asynchronous: relationships among variables are only valid for a discrete set of time instants. Variables involved are voltage and charge, instead of current, and the circuits use capacitors, switches, and op-amps.

Figure 8.14a is for voltage-to-charge transformation, while Figure 8.14b is for charge-to-voltage transformation. The switches in Figure 8.14a are controlled by nonoverlapping clock signals, so that the structure delivers the following incremental charge to the op-amp virtual ground node:

$$\Delta q^e = C(v_{i+} - v_{i-}) = -\Delta q^o \tag{8.26}$$

where the superscript denotes the clock phase during which the charge is delivered. Complementarily, the structure of Figure 8.14b initializes the capacitor during the even clock phase, and senses the incremental charge that circulates through the virtual ground of the op-amp during the odd clock phase. Thus, it obtains

$$v_o^o = C(\Delta q^o) \tag{8.27}$$

References [45,46,68] contain alternative circuits for the realization of the scaling function. Such circuits have superior performance in the presence of parasitics of actual monolithic op-amps and capacitors.

8.3.1.4 Transformation among Transfer Characteristics

Figure 8.15 depicts the general architecture needed to convert one kind of transfer characteristics, e.g., voltage transfer, into another, e.g., current transfer. Variables x' and y' of the original characteristics can be either voltage or current, and the same occurs for x and y of the converted characteristic. The figure depicts the more general case, which also involves a linear transformation of the characteristics themselves:

$$\begin{bmatrix} x \\ y \end{bmatrix} = \mathbf{A} \begin{bmatrix} x' \\ y' \end{bmatrix} = \begin{bmatrix} a_{11} & a_{12} \\ a_{21} & a_{22} \end{bmatrix} \begin{bmatrix} x' \\ y' \end{bmatrix} \tag{8.28}$$

For example, Figure 8.15 encloses the matrices to rotate the characteristics by an angle θ , and to reflect the characteristics with respect to an edge with angle θ . This concept of linear transformation converts and its applications in the synthesis of nonlinear networks was proposed initially by Chua [5] for driving-point characteristics, and further extended by Glover [24] and Huertas [29].

In the simplest case, in which the nondiagonal entries in Equation 8.28 are zero, the transformation performed over the characteristics is scaling, and the circuits of Figures 8.12 and 8.13 can be used directly

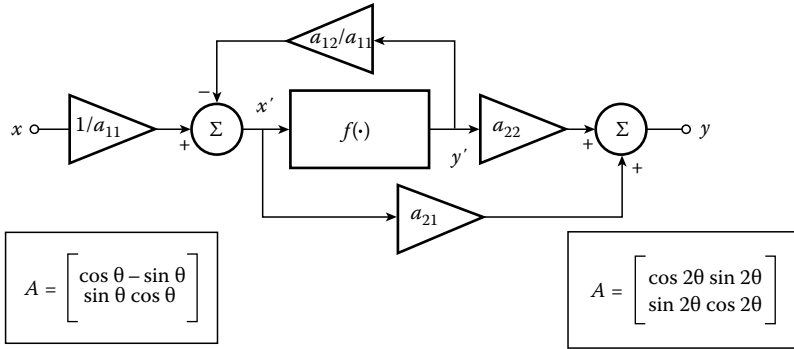


FIGURE 8.15 Concept of linear transformation converter for transfer characteristics: general architecture, and transformation matrices for rotation (left) and reflection (right).

to convert x into x' at the input front-end, and y' at the output front-end. Otherwise, aggregation operation is also required, which can be realized using the circuits described elsewhere.

8.3.1.5 From Driving Point to Transfer and Vice Versa

Figure 8.16 illustrates circuits to transform driving-point characteristics into related transfer characteristics. Figure 8.16a and b uses the same principle as Figure 8.12c and d to transform a voltage-controlled driving-point characteristic, $i_i = f(v_i)$, into a transconductance characteristics. On the other hand Figure 8.16c operates similarly to Figure 8.13c to transform a current-controlled driving-point characteristic, $v_i = f(i_i)$, into a transimpedance characteristic. If the resistance characteristics of the resistor in Figure 8.16a and b, or the conductance characteristic of the resistor in Figure 8.16c, is invertible, these circuits serve to invert nonlinear functions [63]. For instance, using a common base BJT in Figure 8.16c obtains a logarithmic function from the BJT exponential transconductance. Also, the use of a MOST operating in the ohmic region serves to realize a division operation.

Lastly, let us consider how to obtain driving-point characteristics from related transfer characteristics. Figure 8.17a and b corresponds to the common situation found in op-amp-based circuits, where the transfer is between voltages. Figure 8.17a is for the voltage-controlled case and Figure 8.17b is for the current-controlled case. They use feedback strategies similar to Figure 8.17b to render either the input voltage or the input current independent of the linear contributions of the other port variable. A general theory for this kind of transformation converter can be found in Ref. [29].

Note that these figures rely on a Thévenin representation. Similar concepts based on Norton representations allow us to transform current transfer characteristics into driving-point characteristics. However, careful design is needed to preserve the input current while sensing it.

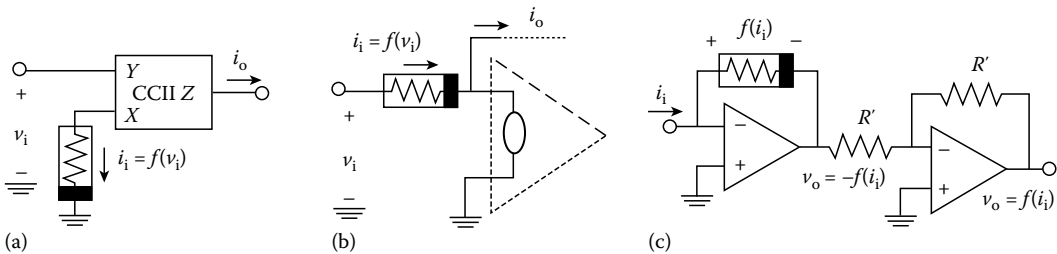


FIGURE 8.16 From driving point to transfer characteristics: (a) and (b) transconductance from voltage-controlled driving-point; (c) transimpedance from current-controlled driving-point.

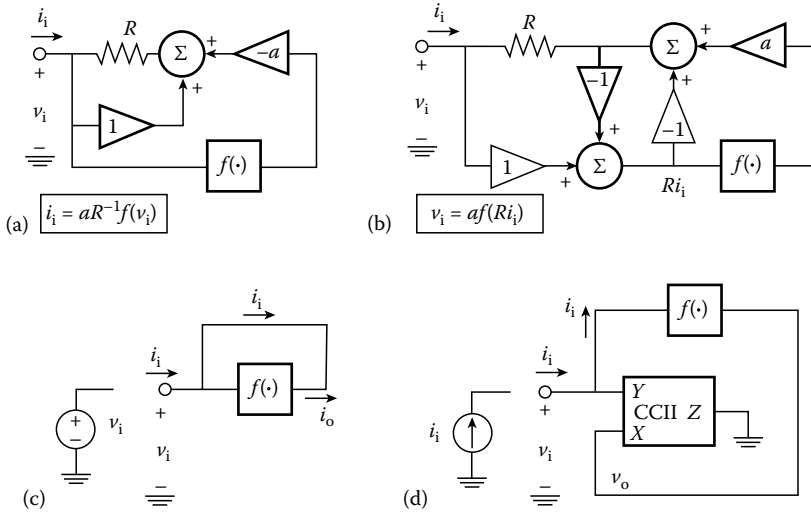


FIGURE 8.17 From transfer to driving-point characteristics. (a) Voltage-controlled case. (b) The current-controlled case. (c) A transconductor. (d) A current-controlled resistor.

Other interesting transformation circuits are depicted in Figure 8.17c and d. The block in Figure 8.17c is a transconductor that obtains $i_o = -f(v_i)$ with very large input impedance. Then, application of feedback around it obtains a voltage-controlled resistor, $i_o = f(v_i)$. Figure 8.17d obtains a current-controlled resistor, $v_i = f(i_i)$, using a current conveyor to sense the input current and feedback the output voltage of a transimpedance device with $v_o = f(i_i)$.

8.3.2 Scaling and Aggregation Circuitry

8.3.2.1 Scaling Operation

Whenever the weights are larger than unity, or are negatives, the operation of scaling requires active devices. Also, because any active device acts basically as a transconductor, the scaling of voltages is performed usually through the transformation of the input voltage into an intermediate current and the subsequent transformation of this current into the output voltage. Figure 8.18 illustrates this for an op-amp-based amplifier and an OTA-based amplifier. The input voltage is first scaled and transformed in i_o , and then this current is scaled again and transformed into the output voltage. Thus, the scaling factor depends on two design parameters. Extra control is achieved by also scaling the intermediate current.

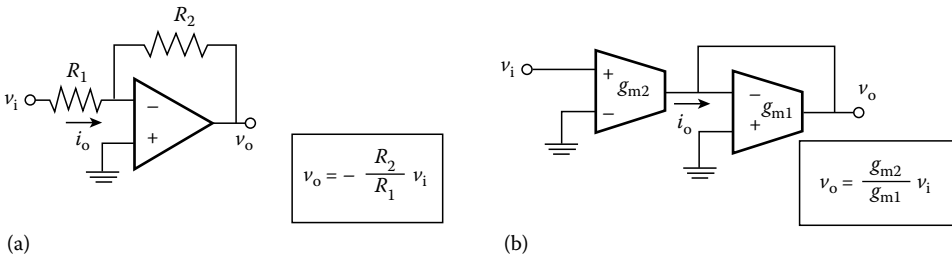


FIGURE 8.18 Mechanisms for voltage scaling. (a) An op-amp-based amplifier. (b) An OTA-based amplifier.

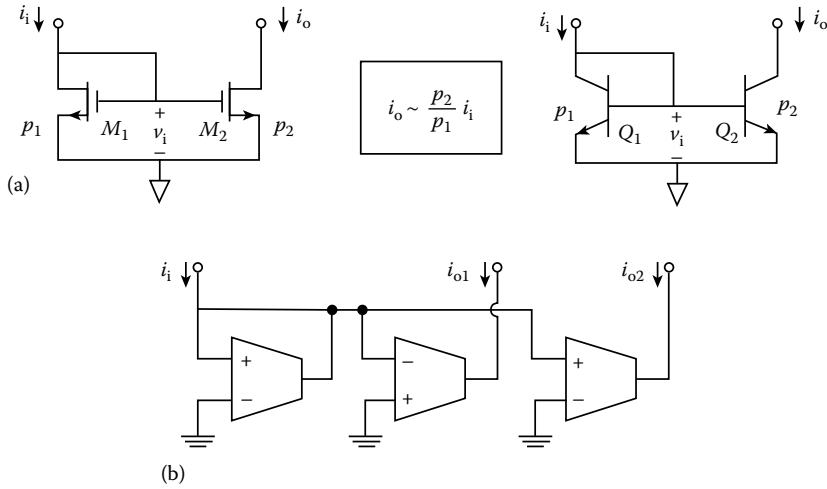


FIGURE 8.19 Current scaling using current mirrors. (a) Two matched transistors. (b) Noninverting amplification.

Let us now consider how to scale currents. The most convenient strategy uses a current mirror, whose simplest structure consists of two matched transistors connected as shown in Figure 8.19a [25]. Its operating principle relies on functional cancellation of the transistor nonlinearities to yield a linear relationship

$$i_o = p_2 f(v_i) = p_2 f \left[f^{-1} \left(\frac{i_i}{p_1} \right) \right] = \frac{p_2}{p_1} i_i \tag{8.29}$$

where p_1 and p_2 are parameters with value that can be designer controlled; for instance, β of the MOST or I_s of the BJT (see Appendix A and Ref. [44]). The input and output currents in Figure 8.19a must be positive. Driving the input and output nodes with bias currents I_B and $(p_2/p_1)I_B$, respectively, one obtains $i_i = i_i' + I_B$ and $i_o = i_o' + (p_2 + p_1)I_B$, and this enables bilateral operation on i_i' and i_o' .

In practical circuits, this simple design concept must be combined with circuit strategies to reduce errors due to nonnegligible input current of BJTs, DC voltage mismatch between input and output terminals, finite input resistance, and finite output resistance. Examples of these strategies can be found in Refs. [25,56,77]. On the other hand, sizing and layout strategies for other problems related to random mismatches between input and output devices are found in Ref. [41,48], which are applicable to most matching problems in MOS IC design.

The current mirror concept is extensible to any pair of matched transconductors, provided their transconductance characteristics are invertible and parameterized by a designer-controlled scale factor p , and that the dependence of the output current with the output voltage is negligible. In particular, the use of differential transconductors enables us to obtain bilateral operation simply, requiring no current-shifted biasing at the input and output nodes. It also simplifies achieving noninverting amplification (that is, positive scale factors), as Figure 8.19b illustrates. This figure also serves to illustrate the extension of the mirror concept to multiple current outputs. Note that except for loading considerations, no other limitations exist on the number of output transconductors that can share the input voltage. Also, because fan-out of a current source is strictly one, this replication capability is needed to enable several nodes to be excited by a common current. On the other hand, the fact that the different current output replicas can be scaled independently provides additional adjusting capability for circuit design.

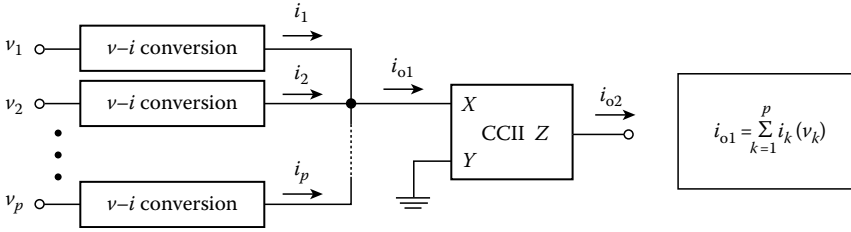


FIGURE 8.20 Aggregation of voltages through intermediate currents and current conveyor.

8.3.2.2 Signal Aggregation

As for the scaling operation, aggregation circuitry operates in current domain, based on Kirchhoff's current law (KCL). Thus, the aggregation of voltages requires that first they be transformed into currents (equivalently, charge packets in the switched-capacitor circuitry) and then added through KCL, while currents and incremental charges are added by routing all the components to a common node. If the number of components is large, the output impedance of the driving nodes is not large enough, and/or the input importance of the load is not small enough, this operation will encompass significant loading errors due to variations of the voltage at the summing node. This is overcome by clamping the voltage of this node using a virtual ground, which in practical circuits is realized by using either the input port of an op-amp, or terminals X and Y of a current conveyor. Figure 8.20 illustrates the current conveyor case.

8.4 Piecewise-Linear Circuitry

Consider the elementary PWL function that arise in connection with the different methods of representation covered in Section 8.2:

- Two-piece concave and convex characteristics (see Equation 8.12)
- Hermite linear basis function (see Figure 8.4 and Appendix B)
- Absolute value (see Equation 8.13)

where rectification is the only nonlinear operator involved. The circuit primitives in Appendix A exhibit several mechanisms which are exploitable in order to realize rectification:

- Cutoff of diodes and transistors—specifically, current through a diode negligible for negative voltage, output current of BJTs, and MOSTs negligible under proper biasing
- Very large resistance and zero offset voltage of an analog switch for negative biasing of the control terminal
- Digital encoding of the sign of a differential voltage signal using a comparator

Similar to scaling and aggregation operations, rectification is performed in current domain, using the mechanisms listed previously to make the current through a branch negligible under certain conditions. Three techniques are presented, which use current transfer in a transistor-based circuit, current-to-voltage transfer using diodes and op-amp, and charge transfer using switches and comparators, respectively.

8.4.1 Current Transfer Piecewise-Linear Circuitry

Figure 8.21a and b presents the simplest technique to rectify the current transferred from node ① to node ②. They exploit the feature of diodes and diode-connected transistors to support only positive

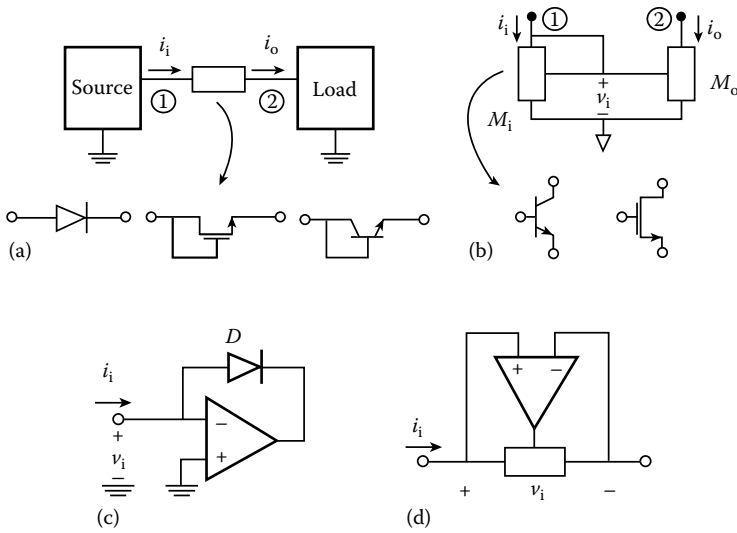


FIGURE 8.21 (a) and (b) Circuit techniques for current rectification; (c) and (d) superdiodes.

currents. Figure 8.21a operates by precluding negative currents to circulate from node ① to node ②, while Figure 8.21b also involves the nonlinear transconductance of the output transistor M_o ; negative currents driving the node ① force v_i to become smaller than the cut-in voltage and, consequently, the output current becomes negligible. A drawback to both circuits is that they do not provide a path for negative input currents, which accumulates spurious charge at the input node and forces the driving stage to operate outside its linear operating regime. Solutions to these problems can be found in Refs. [57,61]. Also, Figure 8.21a produces a voltage displacement equal to the cut-in voltage of the rectifying device, which may be problematic for applications in which the voltage at node ① bears information. A common strategy to reduce the voltage displacements uses feedback to create superdiodes (shown in Figure 8.21c for the grounded case and Figure 8.21d for the floating case), and where the reduction of the voltage displacement is proportional to the DC gain of the amplifier.

Figure 8.22a, called a current switch, provides paths for positive and negative currents entering node ①, and obtains both kinds of elementary PWL characteristics exploiting cutoff of either BJTs or MOSTs. It consists of two complementary devices: *npn* (top) and *pnp* BJTs, or *n*-channel (top) and *p*-channel MOSTs. Its operation is very simple: any positive input current increases the input voltage, turning the bottom device ON. Because both devices share the input voltage, the top device becomes OFF. Similarly, the input voltage decreases for negative input currents, so that the top device becomes ON and the bottom OFF. In sum, positive input currents are drawn to the bottom device, while negative currents are drawn to the top device.

An inconvenience of Figure 8.22a is the dead zone exhibited by its input driving-point characteristics, which is very wide for MOSTs. It may produce errors due to nonlinear loading of the circuitry that drives the input node. Figure 8.22b overcomes this by using a circuit strategy similar to that of the superdiodes. The virtual ground at the op-amp input renders the dead zone centered around the voltage level E , and its amplitude is reduced by a factor proportional to the amplifier DC gain. Some considerations related to the realization of this amplifier are found in Ref. [58].

Proper routing and scaling of the currents i_p and i_n in Figure 8.22a gives us the concave and convex basic characteristics with full control of the knot and position and the slope in the conducting region. Figure 8.22c is the associated circuit, in which the input bias current controls the knot position, and the slope in the conducting region is given by the gain of the current mirrors. Note that this circuit also obtains the absolute value characteristics, while Figure 8.22d obtains the Hermite linear basis function.

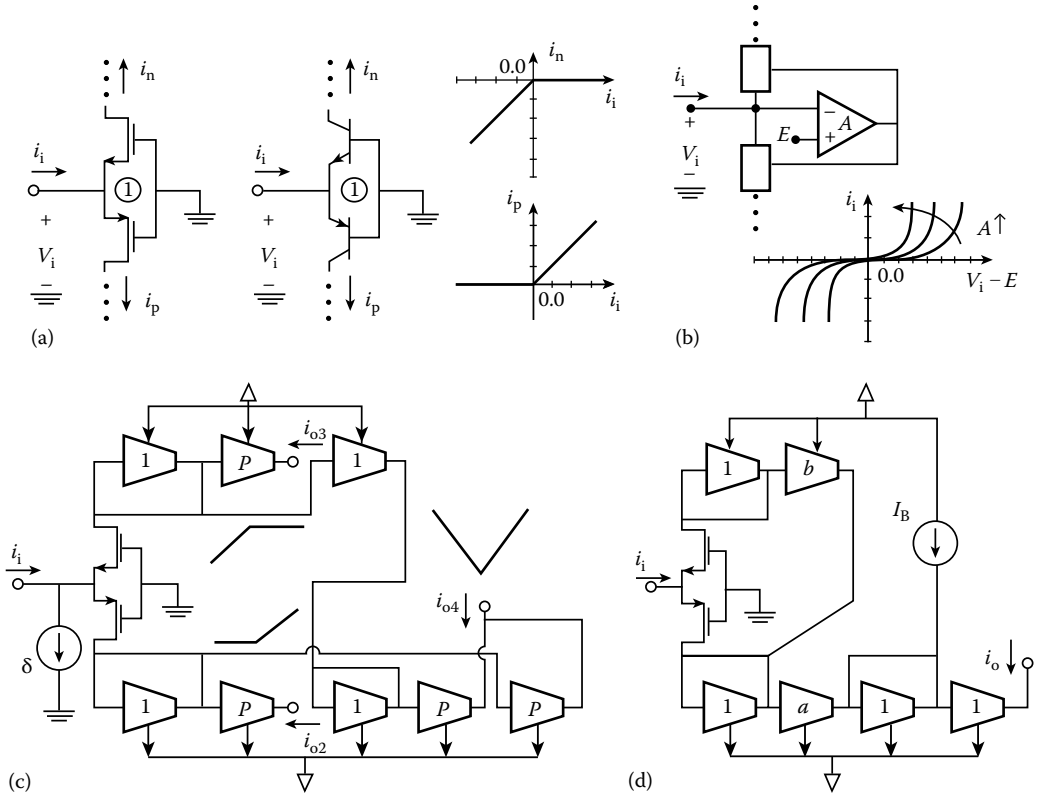


FIGURE 8.22 Current switch and its application for different basic PWL curves. (a) Dead zone exhibited by its input driving-point characteristics. (b) A circuit strategy similar to that of the superdiodes. (c) The associated circuit of (a). (d) A Hermite linear basis function circuit.

The way to obtain the PWL fuzzy membership function from this latter circuit is straightforward, and can be found in Ref. [58].

8.4.2 Transresistance Piecewise-Linear Circuitry

The circuit strategies involved in PWL current transfer can be combined in different ways with the transformation circuits discussed previously to obtain transconductance and voltage-transfer PWL circuits. In many cases design ingenuity enables optimum merging of the components and consequently, simpler circuits. Figure 8.23a depicts what constitutes the most extended strategy to realize the elementary PWL functions using off-the-shelf components [63,80]. The input current is split by the feedback circuitry around the op-amp to make negative currents circulate across D_n and positive currents circulate across D_p . Consequently, this feedback renders the input node of the op-amp a virtual ground and thus reduces errors due to finite diode cut-in voltage in the transresistance characteristics. Similar to Figure 8.22, the position of the knot in these elementary characteristics is directly controlled by an input bias current. Also note that the virtual ground can be exploited to achieve voltage-to-current transformation using the strategy of Figure 8.12d and thus, voltage-transfer operation.

Algebraic combination of the elementary curves provided by Figure 8.23a requires transforming the voltages v_{on} and v_{op} into currents and then aggregating these currents by KCL. For example, Figure 8.23b is the circuit for the absolute value and Figure 8.23c presents a possible implementation of the Hermite basis function.

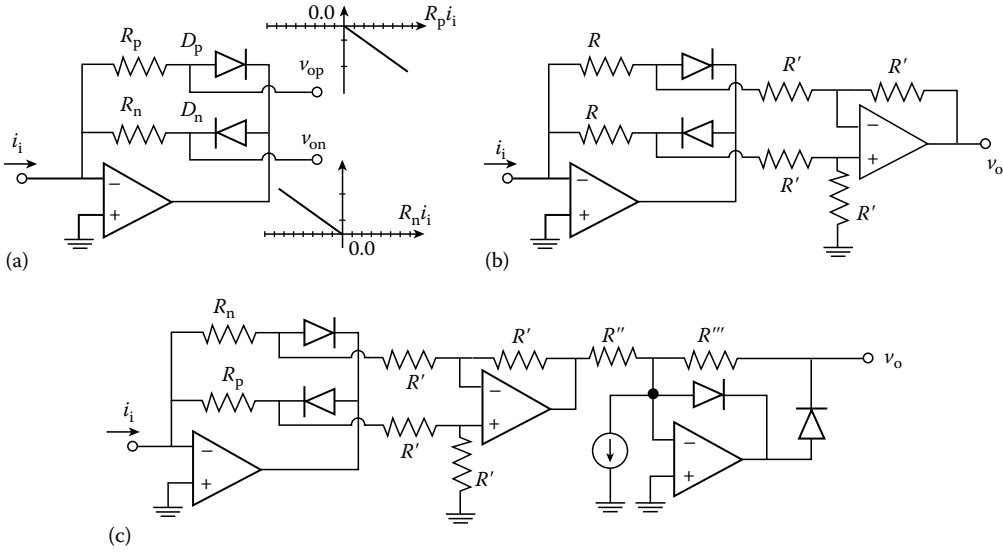


FIGURE 8.23 PWL transimpedance circuits. (a) Circuit for algebraic combination of the elementary curves. (b) Circuit for the absolute value. (c) Circuit for a possible implementation of the Hermite basis function.

Other related contributions found in the literature focus on the systematic realization of PWL driving-point resistors, and can be found in Refs. [7,10].

8.4.3 Piecewise-Linear Shaping of Voltage-to-Charge Transfer Characteristics

The realization of PWL relationships among sampled-data signals is based on nonlinear voltage-to-charge transfer and uses analog switches and comparators. Figure 8.24a is a circuit structure, where one of the capacitor terminals is connected to virtual ground and the other to a switching block. Assume that nodes ① and ② are both grounded. Note that for $(v - \delta) > 0$ the switch arrangement set node ④ to δ , while node ⑤ is set to v . For $(v - \delta) < 0$, nodes ④ and ⑤ are both grounded. Consequently, voltage at node ③ in this latter situation does not change from one clock phase to the next, and consequently, the incremental charge becomes null for $(v - \delta) < 0$. On the other hand, for $(v - \delta) > 0$, the voltage at node ③ changes from one clock phase to the next, and generates an incremental charge

$$\Delta q^e = C(v - \delta) = -\Delta q^o \tag{8.30}$$

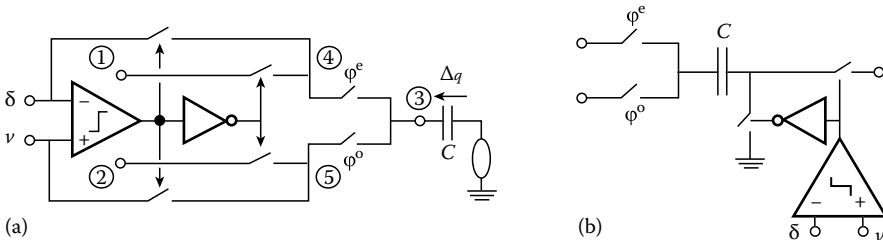


FIGURE 8.24 Circuits for rectification in voltage-to-charge domain. (a) Circuit structure where one of the capacitor terminals is connected to virtual ground and the other to a switching block. (b) Circuitry using series rectification of the circulating charge through a comparator-controlled switch.

which enables us to obtain negative and positive slopes using the same circuit, as shown in Figure 8.24a. To make the characteristics null for $(v - \delta) > 0$, it suffices to interchange the comparator inputs. Also, the technique is easily extended to the absolute value operation by connecting terminal ① to v , and terminal ② to δ . The realization of the Hermite linear basis function is straightforward and can be found in Ref. [55].

Other approaches to the realization of PWL switched-capacitor circuitry use series rectification of the circulating charge through a comparator-controlled switch (Figure 8.24b), and can be found in Refs. [16,31]. The latter also discusses exploitation of these switched-capacitor circuits to realize continuous-time driving-point characteristics, the associated transformation circuits, and the dynamic problematics.

8.5 Polynomials, Rational, and Piecewise-Polynomial Functions

These functions use rectification (required for truncation operation in the PWP case) and analog multiplication,

$$z = \frac{xy}{\alpha} \tag{8.31}$$

as basic nonlinear operators.* Joining the two inputs of the multiplier realizes the square function. Analog division is realized by applying feedback around a multiplier, illustrated at the conceptual level in Figure 8.25a; the multiplier obtains $e = (zy)/\alpha$, and for $A \rightarrow \infty$, the feedback forces $x = e$. Thus, if $y \neq 0$, the circuit obtains $z = \alpha(x/y)$. Joining y and z terminals, the circuit realizes the square root, $z = (\alpha x)^{1/2}$. This concept of division is applicable regardless of the physical nature of the variables involved. In the special case in which e and x are current and z is a voltage, the division can be accomplished using KCL to yield $x = e$. Figure 8.25b shows a circuit for the case in which the multiplication is in voltage domain, and Figure 8.25c is for the case in which multiplication is performed in transconductance domain. The transconductance gain for input z in the latter case must be negative to guarantee stability.

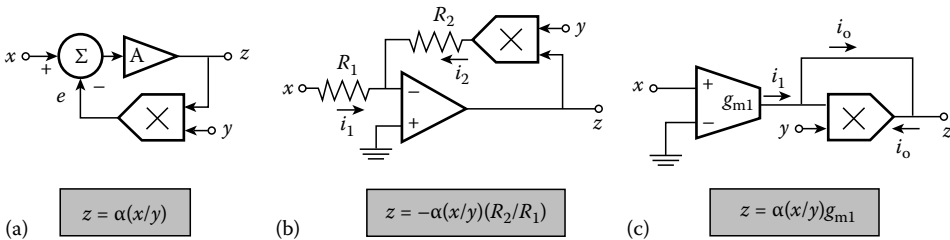


FIGURE 8.25 Division operator using a feedback multiplier: (a) concept; (b) with voltage multiplier and op-amp; (c) with transconductance multiplier and OTA.

* Scale factor α in Equation 1.31 must be chosen to guarantee linear operation in the full variation range of inputs and outputs.

8.5.1 Concepts and Techniques for Polynomial and Rational Functions

Figure 8.26 illustrates conceptual hardware for several polynomials up to the fifth degree. Any larger degree is realized similarly. Figure 8.27 uses polynomials and analog division to realize rational functions

$$g(x) = \frac{\sum_{i=0,Q} \alpha_j x^j}{\sum_{j=0,R} \beta_j x^j} \tag{8.32}$$

For simplicity, we have assumed that the internal scaling factors of the multipliers in Figures 8.26 and 8.27 equal one.

An alternative technique to realize rational functions is based on linearly controlled resistors, described as $v = (Lx)i$, and linearly controlled conductors, $i = (Cx)v$, where L and C are real parameters. This technique exploits the similarity between these characteristics and those which describe inductors and capacitors in the frequency domain, to take advantage of the synthesis techniques for rational transfer function in the s -plane through interconnection of these linear components [28,39] (Figure 8.28). As for the previous cases, realization of linearly controlled resistors and conductors require only multipliers and,

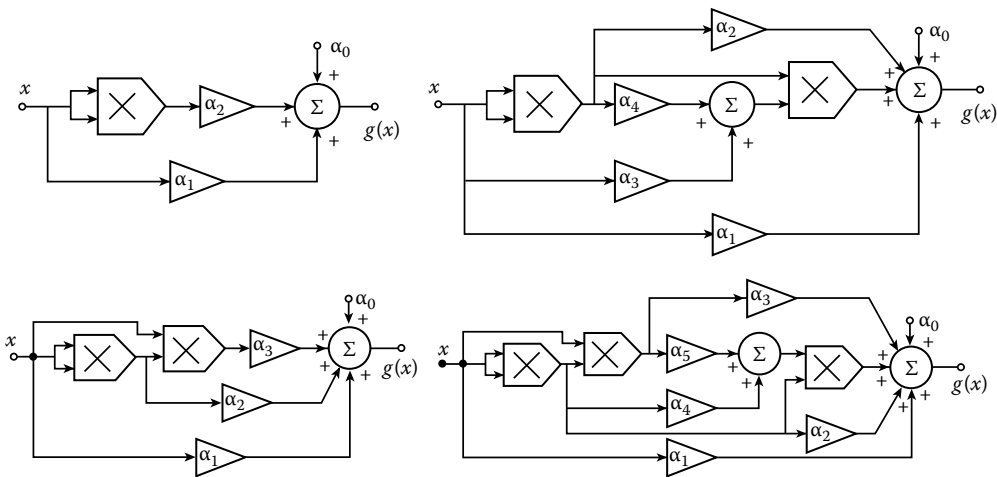


FIGURE 8.26 Conceptual hardware for polynomial functions.

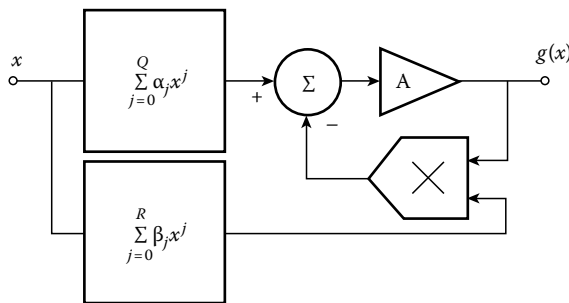


FIGURE 8.27 Rational function generation through feedback division.

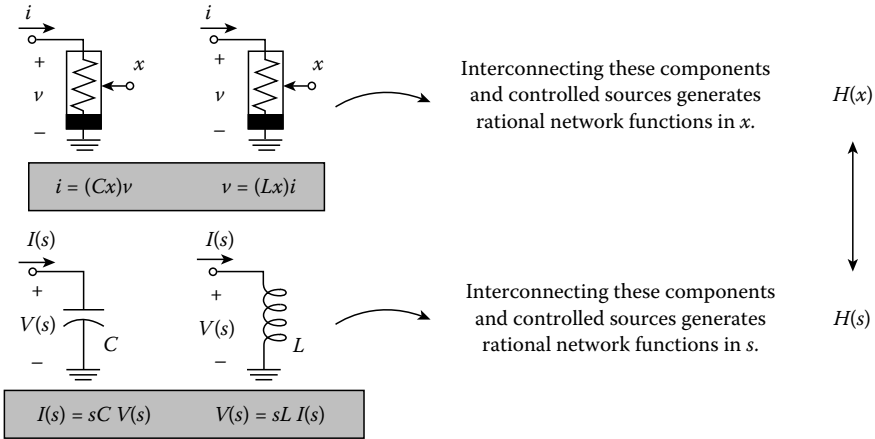


FIGURE 8.28 Usage of linearly controlled resistors to synthesize rational network functions.

depending upon the nature of the variables involved in the multipliers, voltage-to-current and current-to-voltage transformation circuits.

8.5.2 Multiplication Circuitry

Two basic strategies realize multiplication circuitry: using signal processing and exploiting some non-linear mechanism of the primitive components. Signal processing multipliers rely on the generation of a pulsed signal whose amplitude is determined by one of the multiplicands and its duty cycle by the other, so that the area is proportional to the result of the multiplication operation. Figure 8.29a presents an implementation concept based on averaging. This is performed by a low-pass filter where the input is a pulse train with amplitude proportional to x and duty cycle proportional to y . The latter proportionality is achieved through nonlinear sampling by comparing y with a time reference sawtooth signal. Thus, the

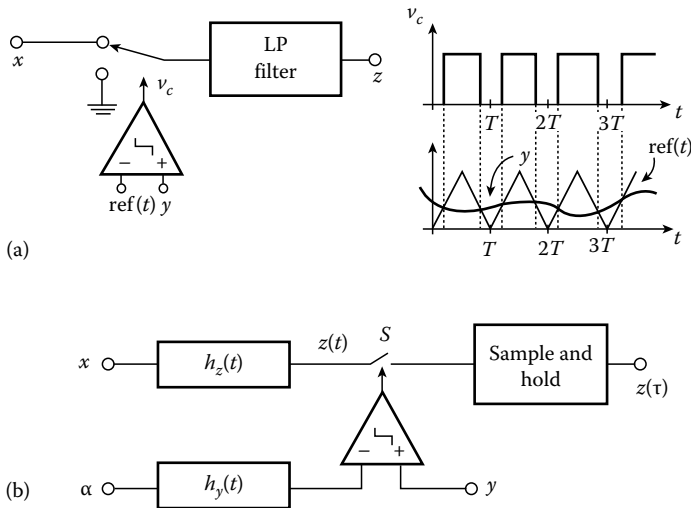


FIGURE 8.29 Signal processing multipliers by (a) averaging; (b) shaping in time domain.

area under each pulse in the train is the product of $x \times y$, extracted by the low-pass filter. This implementation concept is discussed in further detail in classical texts on analog computation [63], and applied more recently to analog VLSI signal processing [72].

Figure 8.29b is an alternative implementation concept based on signal shaping in the time domain. It uses two linear blocks with normalized unit step response given as $h_z(t)$ and $h_y(t)$. The first is driven by level x to obtain

$$z(t) = xh_z(t), \quad 0 \leq t < \tau \quad (8.33)$$

where τ denotes the duration of the time interval during which the switch S remains closed. The other is driven by a reference level α , to render τ given by

$$\tau = h_y^{-1}\left(\frac{y}{\alpha}\right) \quad (8.34)$$

Assuming both linear blocks are identical and the time function invertible, one obtains the steady-state value of z , $z(\tau)$, as the product of levels x and y .

The simplest implementation of Figure 8.29 uses integrators, i.e., $h(t) = t$, as linear blocks (see Figure 8.41b). Also note that the principle can be extended to the generation of powers of an input signal by higher-order shaping in time domain. In this case, both linear blocks are driven by reference levels. The block $h_y(t)$ consists of a single integrator, $\tau = y/\alpha$. The other consists of the cascade of P integrators, and obtains $z(t) = \beta t^P$. Thus, $z(t) = \beta(y/\alpha)^P$. Realizations suitable for integrated circuits are found in Refs. [34,55].

8.5.3 Multipliers Based on Nonlinear Devices

The primitives in Appendix A display several mechanisms that are exploitable to realize analog multipliers:

- Exponential functionals associated to the large-signal transconductance of BJTS, and the possibility of obtaining logarithmic dependencies using feedback inversion
- Square-law functionals associated to the large-signal transconductance of the MOS transistor operating in saturation region
- Small-signal transconductance of a BJT in active region as a linear function of collector current
- Small-signal transconductance of a MOST in saturation as a linear function of gate voltage
- Small-signal self-conductance of a MOS transistor in ohmic region as a linear function of gate voltage

These and related mechanisms have been explained in different ways and have resulted in a huge catalog of practical circuits. To quote all the related published material is beyond the scope of this section. The references listed at the end were selected because of their significance, and their cross-references contain a complete view of the state of the art. Also, many of the reported structures can be grouped according to the theory of *translinear circuits*, which provides a unified framework to realize nonlinear algebraic functions through circuits [23,62,79].

8.5.3.1 Log–Antilog Multipliers

Based on the exponential large-signal transconductance of the BJT, and the following relationships,

$$\begin{aligned} z' &= \ln(x) + \ln(y) = \ln(xy) \\ z &= e^{z'} = e^{\ln(xy)} = xy \end{aligned} \quad (8.35)$$

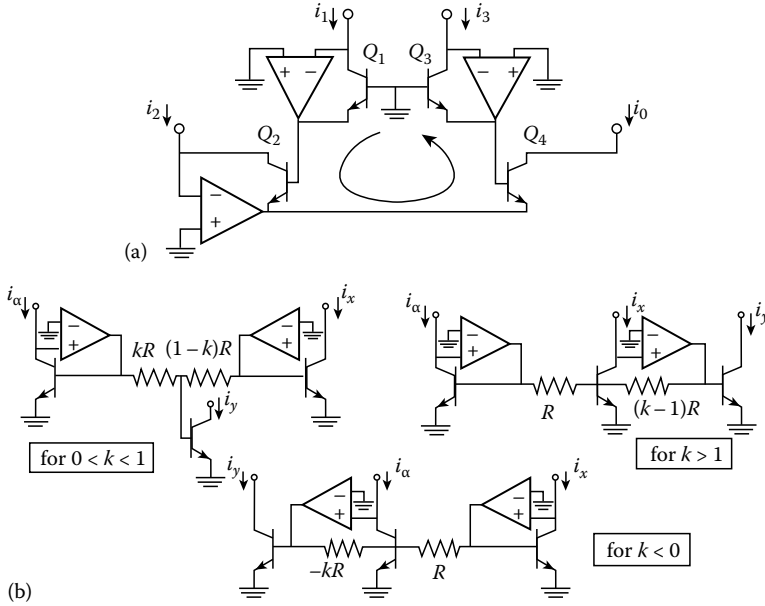


FIGURE 8.30 (a) Core block of a log-antilog multiplier; (b) circuits to elevate to a power.

which can be realized as illustrated in Figure 8.30a [65]. This circuit operates on positive terminal currents to obtain $i_0 = (i_1 i_2) / i_3$, which can be understood from translinear circuit principles by noting that the four base-to-emitter voltages define a translinear loop,

$$\begin{aligned}
 0 &= v_{be1} + v_{be2} - v_{be3} - v_{be4} \\
 &= \ln\left(\frac{i_1}{I_s}\right) + \ln\left(\frac{i_2}{I_s}\right) - \ln\left(\frac{i_3}{I_s}\right) - \ln\left(\frac{i_0}{I_s}\right)
 \end{aligned}
 \tag{8.36}$$

The circuit can be made to operate in four-quadrant mode, though restricted to currents larger than $-I_B$, by driving each terminal with a bias current source of value I_B . Also, because all input terminals are virtual ground the circuit can be made to operate on voltages by using the voltage-to-current transformation concept of Figure 8.12d. Similarly, the output current can be transformed into a voltage by using an extra op-amp and the current-to-voltage transformation concept of Figure 8.13c. Extension of this circuit structure to generate arbitrary powers is discussed in Ref. [23]. Figure 8.30b [1] uses similar techniques, based on introducing scaling factors in the translinear loop, to obtain

$$i_y = i_\alpha^{1-k} i_x^k
 \tag{8.37}$$

8.5.3.2 Square-Law Multipliers

Square-law multipliers are based on the algebraic properties of the square function, most typically

$$z = \frac{1}{4} [(x + y)^2 - (x - y)^2] = xy
 \tag{8.38}$$

shown conceptually in Figure 8.31a, and the possibility of obtaining the square of a signal using circuits, typically consisting of a few MOS transistors operating in saturation region. Figure 8.31b through f depict some squarer circuits reported in the literature.

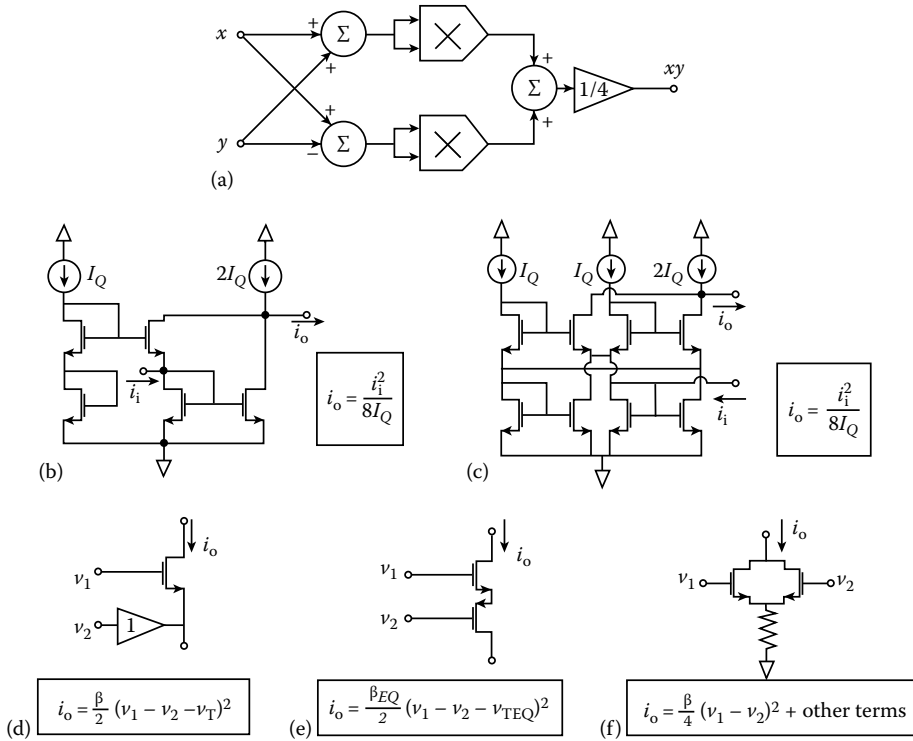


FIGURE 8.31 (a) Block diagram of the quarter-square multiplier; (b) current-mode squarer circuit in Ref. [3]; (c) current-mode squarer circuit in Ref. [79]; (d) voltage-mode squarer circuit in Ref. [36]; (e) voltage-mode squarer circuit in Ref. [60]; (f) voltage-mode squarer circuit in Ref. [49].

The completeness of square-law operators for the realization of nonlinear circuits was demonstrated from a more general point of view in Ref. [47], and their exploitation has evolved into systematic circuit design methodologies to perform both linear and nonlinear functions [3].

8.5.3.3 Transconductance Multipliers

A direct, straightforward technique to realize the multiplication function exploits the possibility of controlling the transconductance of transistors through an electrical variable (current or voltage). Although this feature is exhibited also by unilateral amplifiers, most practical realizations use differential amplifiers to reduce offset problems and enhance linearity [25]. Figure 8.32 presents a generic schematic for a differential amplifier, consisting of two identical three-terminal active devices with common bias current. The expressions on the right display its associated transconductance characteristics for *n*p*n*-BJTs and *n*-channel MOSTs, respectively [25]. These characteristics are approximated to a first-order model as

$$i_{z\text{BJT}} \approx \frac{i_y}{4U_t} v_x, \quad i_{z\text{MOST}} \approx (\sqrt{\beta i_y}) v_x \tag{8.39}$$

which clearly displays the multiplication operation, although restricted to a rather small linearity range. Practical circuits based on this idea focus mainly on increasing this range of linearity, and follow different design strategies. Figure 8.33 gives an example known as the Gilbert cell or Gilbert multiplier [23]. Corresponding realizations using MOS transistors are discussed in Refs. [2,53]. Sánchez-Sinencio et al. [61] present circuits to realize this multiplication function using OTA blocks. On the other

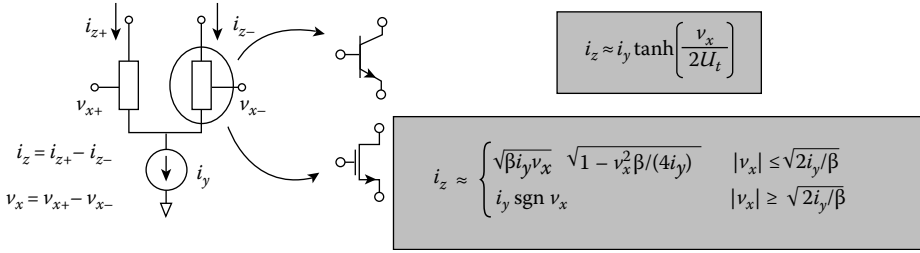


FIGURE 8.32 Differential amplifiers and their associated large-signal transconductances.

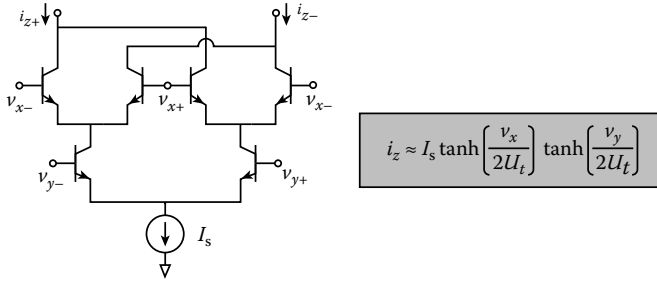


FIGURE 8.33 Bipolar Gilbert cell.

hand, Ref. [17] presents a tutorial discussion of different linearization techniques for MOS differential amplifiers.

8.5.3.4 Multiple Based in the Ohmic Region of MOS Transistors

The ohmic region of JFETs has been used to realize amplifiers with controllable gain for automatic gain control [54]. It is based on controlling the equivalent resistance of the JFET transistor in its ohmic region through a bias voltage. More recently, MOS transistors operating in the ohmic region were used to realize linear [69,70] and nonlinear [35] signal processing tasks in VLSI chips. There exist many ingenious circuits to eliminate second and higher-order nonlinearities in the equivalent resistance characteristics.

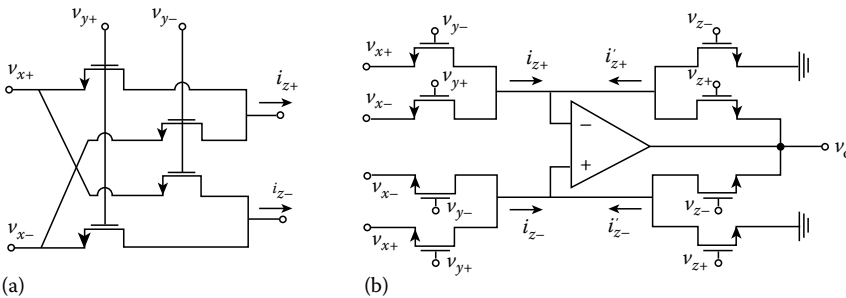


FIGURE 8.34 Four-quadrant multipliers based on MOS transistors in the ohmic region. (a) Circuit achieving very good nonlinear cancellation through cross-coupling and fully differential operation. (b) A more general view showing the conductance as well as the resistance of the MOS ohmic region used to obtain a versatile amplifier-divider building block.

The circuit in Figure 8.34a achieves very good nonlinearity cancellation through cross-coupling and fully differential operation, obtaining

$$i_{z+} - i_{z-} = 2\beta(v_{x+} - v_{x-})(v_{y+} - v_{y-}) \tag{8.40}$$

and its use in multiplication circuits is discussed in Refs. [35,66]. A more general view is presented in Figure 8.34b [35], where the conductance as well as the resistance of the MOS ohmic region are used to obtain a versatile amplifier-divider building block. Enomoto and Yasumoto [18] report another interesting multiplier that combines the ohmic region of the MOS transistor and sampled-data circuits.

8.6 Sigmoids, Bells, and Collective Computation Circuits

8.6.1 Sigmoidal Characteristics

As Equation 8.5 illustrates, approximating a nonlinear function through a multilayer perceptron requires the realization of sigmoidal functions, with arguments given as linear combinations of several variables. The exact shape of the sigmoidal is not critical for the approximation itself, although it may play an important role in fitting [82]. Figure 8.35 depicts two shapes used in practice. Figure 8.35a, the hard limiter, has an inner piece of large (ideally infinite) slope, while for Figure 8.35b, the soft limiter, this slope is smaller and can be used as a fitting parameter.

Most amplifiers have large-signal transfer characteristics whose shape is a sigmoid or an inverted sigmoid. We present only those circuits whose inputs are currents because this simplifies the circuitry needed to obtain these inputs as linear combinations of other variables. The op-amp circuit of Figure 8.36a realizes the soft limiter characteristics in transimpedance form. The center is set by the input bias current and the slope through the resistor ($\beta = R$). If the branch composed of the two Zener diodes is eliminated, the saturation levels E_+ and E_- are determined through the internal op-amp circuitry, inappropriate for accurate control. (Otherwise, they are determined through the Zener breakdown voltages.) On the other hand, Figure 8.36b also realizes the hard sigmoid in transimpedance domain [58]. The output saturation levels for this structure are $E_+ = V_{Tn}$ and $E_- = |V_{Tp}|$, where V_{Tn} and V_{Tp} are the threshold voltages of the NMOS transistor and the PMOS transistor, respectively. To obtain the output represented by a current, one can use voltage-to-current transformation circuits. References [15,57,58] discuss simpler alternatives operating directly in current domain. For instance, Figure 8.36c and d depicts circuits for the soft limiter characteristics and the hard limiter characteristics.

With regard to the calculation of the input to the sigmoid as a linear combination of variables, note that the input node of all circuits in Figure 8.36 is virtual ground. Consequently, the input current can be obtained as a linear combination of voltages or currents using the techniques for signal scaling and aggregation presented in Section 8.3.

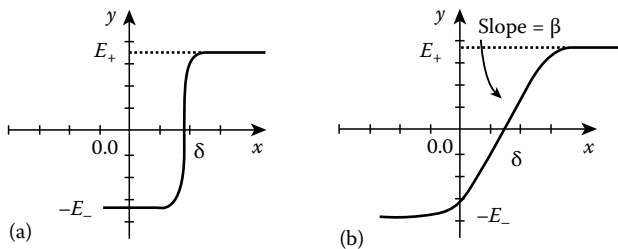


FIGURE 8.35 Typical sigmoidal shapes: (a) hard limiter; (b) soft limiter.

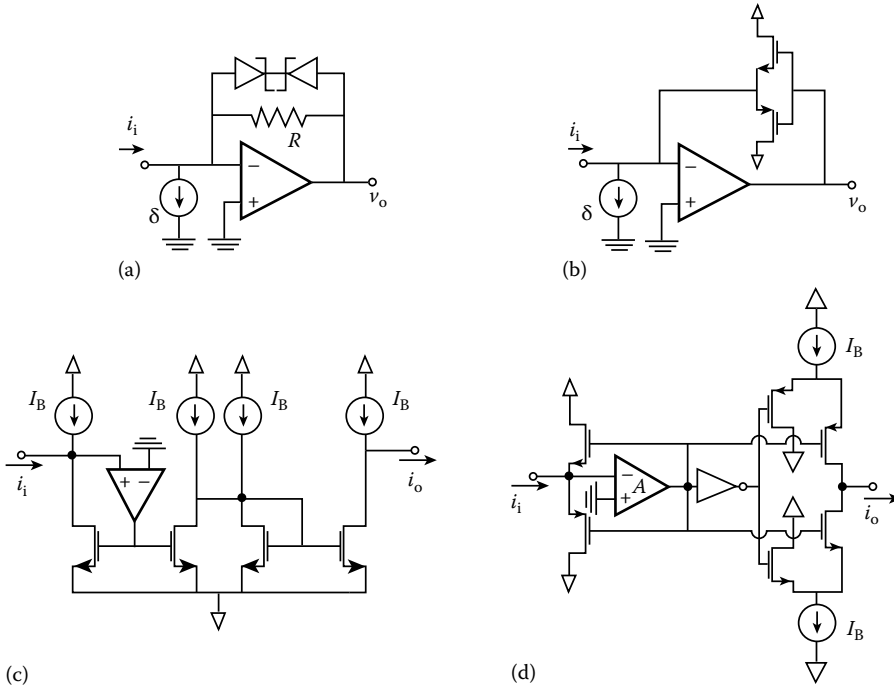


FIGURE 8.36 Realization of sigmoidal characteristics with input current: (a) transimpedance soft limiter; (b) transimpedance hard limiter; (c) and (d) soft and hard limiters in current transfer domain.

8.6.2 Bell-Like Shapes

The exact shapes of Equations 8.16 and 8.17 involve the interconnection of squarers, together with blocks to elevate to power, and exponential blocks—all realizable using techniques previously discussed in this chapter. However, these exact shapes are not required in many applications, and can be approximated using simpler circuits. Thus, let us consider the differential amplifier of Figure 8.32, and define $v_i = v_x$, $I_B = i_y$, and $i_o = i_z$ for convenience. The expressions for the large-signal transconductance displayed along with the figures show that they are sigmoids with saturation levels at I_B and $-I_B$. They are centered at $v_i = 0$, with the slope at this center point given by Equation 8.39. The center can be shifted by making $v_i = v_{x+}$ and $\delta = v_{x-}$.

Similar to the differential amplifier, most OTAs exhibit sigmoid-like characteristics under large-signal operation, exploitable to realize nonlinear functions [19,37,56,61,71]. This may rely on the mathematical techniques behind multilayer perceptrons, or on those behind RBF and fuzzy interpolation.

Figure 8.37a obtains a bell-shaped transconductance through a linear, KCL combination of the two sigmoidal characteristics, one of negative slope and the other of positive slope. The width and center of the bell (see Figure 8.7) are given respectively by

$$2\sigma = \delta_2 - \delta_1, \quad \delta = \frac{\delta_2 + \delta_1}{2} \tag{8.41}$$

controlled by the designer. The slope of the bell at the cross-over points is also controlled through the transconductance of the OTAs.

For simpler circuit realizations, this technique can be used directly with differential amplifiers, as shown in Figure 8.37b. The differential output current provided by the circuit can be transformed into a

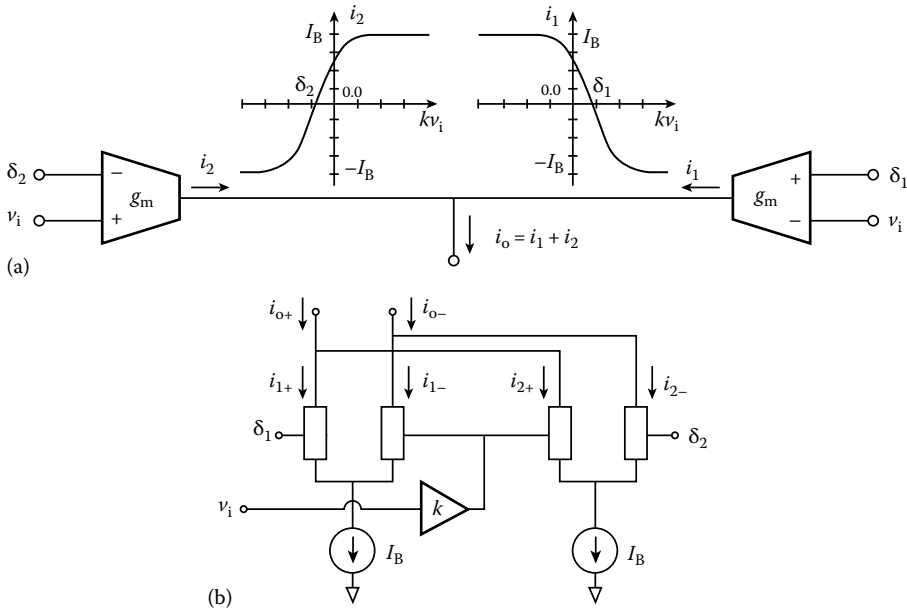


FIGURE 8.37 Transconductance circuits for bell-shaped function: (a) using OTAs; (b) using differential amplifiers.

unilateral one using a p -channel current mirror. Equation 8.41 also applies for this circuit, and the slope at the cross-overs is

$$\text{slope}_{\text{MOST}} = k\sqrt{\beta I_B}, \quad \text{slope}_{\text{BJT}} = \frac{kI_B}{4U_t} \tag{8.42}$$

Note that the control of this slope through the bias current changes the height of the bell. It motivates the use of a voltage gain block in Figure 8.37. Thus, the slope can be changed through its gain parameter k . The slope can also be changed through β for the MOSTs. Practical realizations of this concept are found in Refs. [4,71,74]. The voltage amplifier block can be realized using the techniques presented in this chapter. Simpler circuits based on MOS transistors are found in Ref. [53].

8.6.3 Collective Computation Circuitry

RBF and fuzzy inference require multidimensional operators to calculate radial distances in the case of RBF, and to normalize vectors and calculate T-norms in the case of fuzzy inference. These operators can be expressed as the interconnection of the nonlinear blocks discussed previously, or realized in a simpler manner through dedicated collective computation circuitry. Most of these circuits operate intrinsically in current domain and are worth mentioning because of this simplicity and relevance for parallel information processing systems.

8.6.3.1 Euclidean Distance

Figure 8.38 [38] presents a current-mode circuit to compute

$$i_y = \sqrt{\sum_{k=1,P} i_{xk}^2} \tag{8.43}$$

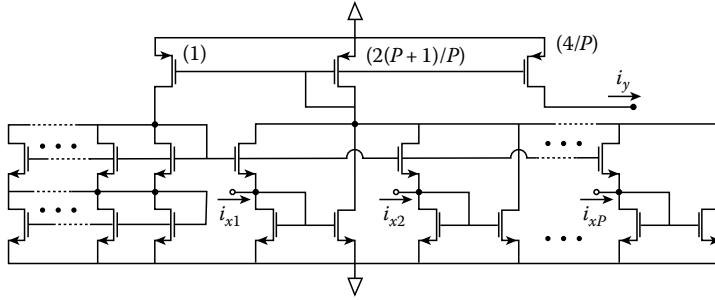


FIGURE 8.38 CMOS self-biased Euclidean distance circuit. (From Landolt, O., Vittoz, E., and Heim, P., *Electr. Lett.*, 28, 352, 1992. With permission.)

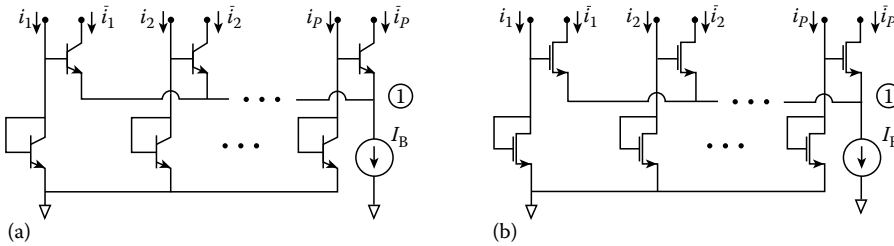


FIGURE 8.39 Current-mode normalization circuits: (a) BJT; (b) CMOS.

based on the square-law of MOS transistors in the saturation region. If the current i_k at each terminal is shifted through a bias current of value δ_k , the circuit serves to compute the Euclidean distance between the vector of input currents and the vector δ .

8.6.3.2 Normalization Operation

Figure 8.39 depicts circuits to normalize an input current vector, for the BJT [23] and the CMOS [74] cases, respectively. Their operation is based on KCL and the current mirror principle. Kirchhoff’s circuit law forces the sum of the output currents at node ① to be constant. On the other hand, the current mirror operation forces a functional dependency between each pair of input and output currents. Thus, they obtain

$$\bar{i}_k \approx \frac{i_k}{\sum_{j=1,P} i_j} \tag{8.44}$$

for each current component.

8.6.3.3 T-Norm Operator

The calculation of the minimum of an input vector \mathbf{x} is functionally equivalent to obtaining the complement of the maximum of the complements of its components. Figure 8.40a illustrates a classical approach used in analog computation to calculate the maximum of an input vector \mathbf{x} . It is based on the following steady-state equation:

$$-y + \sum_{k=1,P} u_{-1}(A(x_k - y)) = 0 \tag{8.45}$$

[26] and has integrators as key components. Figure 8.41b illustrates several integrator circuits. Combining these circuits with the circuitry for nonlinear functions provides systematic approaches to synthesize nonlinear dynamic systems based on the approximations presented in this chapter [56]. On the other hand, Rodríguez-Vázquez and Delgado-Restituto [57] discuss related techniques to synthesize nonlinear systems described by finite-difference equations.

Appendix A: Catalog of Primitives

Figure 8.42 outlines our catalog of primitive components, all of which are available off-the-shelf, and, depending on the fabrication technology, can be realized on a common semiconductor substrate [44]. Generally, the catalog differs between individual technologies; for instance, no *n*pn-BJT's are available in a CMOS *n*-well technology. The use of linear capacitors may appear surprising because we constrain ourselves to cover only static characteristics. However, we will not exploit their dynamic *i-v* relationship, but instead their constitutive equation in the charge-voltage plane, which is algebraic.

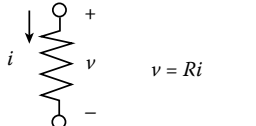
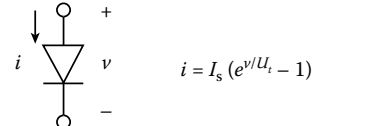
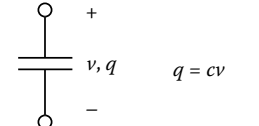
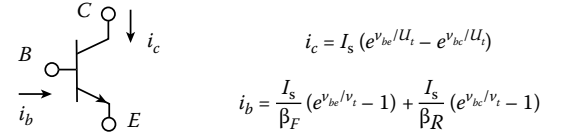
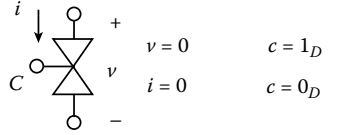
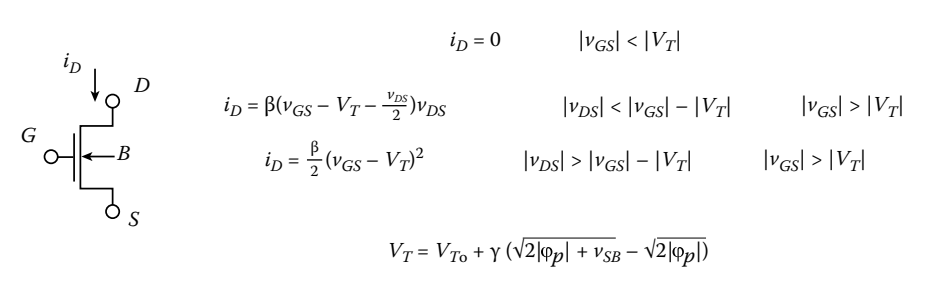
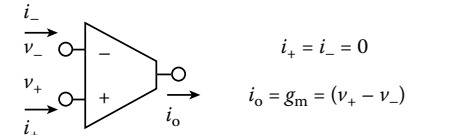
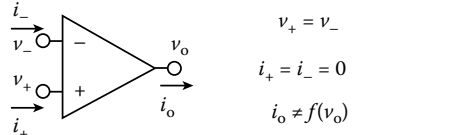
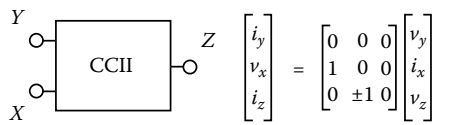
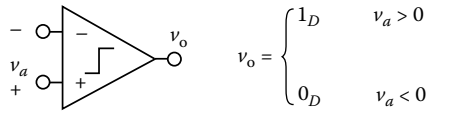
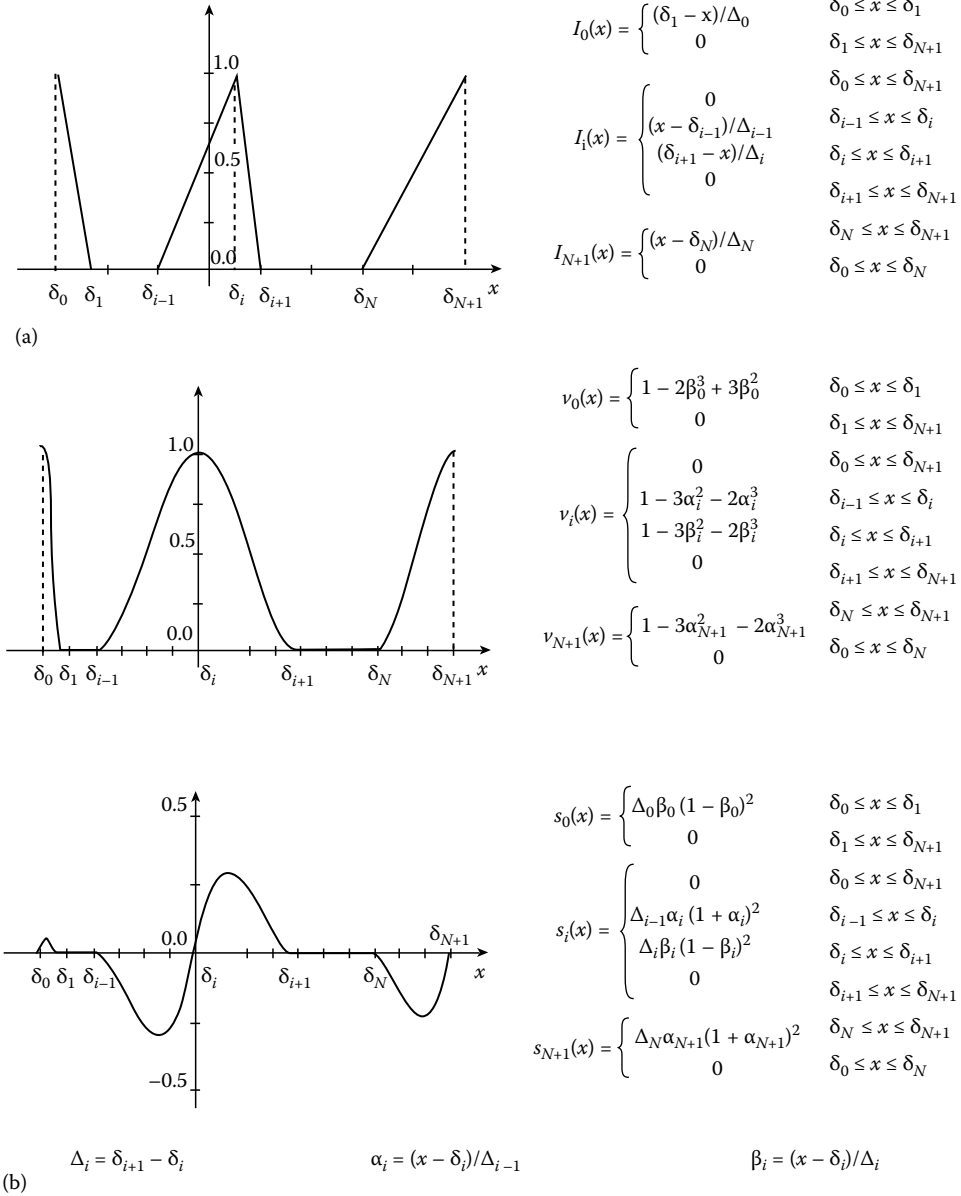
		
		
		
		
		

FIGURE 8.42 Section catalog of primitive circuit components.

Appendix B: Value and Slope Hermite Basis Functions



3. K. Bult and H. Wallinga, A class of analog CMOS circuits based on the square-law characteristics of an MOS transistor in saturation, *IEEE J. Solid-State Circuits*, 22, 357–365, 1987.
4. J. Choi, B. J. Sheu, and J. C. F. Change, A Gaussian synapse circuit for analog VLSI neural network, *IEEE Trans. Very Large Scale Integr. Syst.*, 2, 129–133, 1994.
5. L. O. Chua, The linear transformation converter and its applications to the synthesis of nonlinear networks, *IEEE Trans. Circuit Theory*, 17, 584–594, 1970.
6. L. O. Chua and S. M. Kang, Section-wise piecewise-linear functions: Canonical representation, properties and applications, *Proc. IEEE*, 67, 915–929, 1977.
7. L. O. Chua and S. Wong, Synthesis of piecewise-linear networks, *Elect. Circ. Syst.*, 2, 102–108, 1978.
8. L. O. Chua, Nonlinear circuits, *IEEE Trans. Circuits Syst.*, 31, 69–87, 1984.
9. L. O. Chua and G. Zhong, Negative resistance curve tracer, *IEEE Trans. Circuits Syst.*, 32, 569–582, 1985.
10. L. O. Chua, C. A. Desoer, and E. S. Kuh, *Linear and Nonlinear Circuits*, New York: McGraw-Hill, 1987.
11. L. O. Chua and A. C. Deng, Canonical piecewise linear representation, *IEEE Trans. Circuits Syst.*, 35, 101–111, 1988.
12. G. Cybenko, Approximation by superposition of a sigmoidal function, *Math. Control. Syst. Signals*, 2, 303–314, 1989.
13. Z. Czarnul, Modification of Banu–Tsvividis continuous-time integrator structure, *IEEE Trans. Circuits Syst.*, 33, 714–716, 1986.
14. R. W. Daniels, *Approximation Methods for Electronic Filter Design*, New York: McGraw-Hill, 1974.
15. M. Delgado-Restituto and A. Rodríguez-Vázquez, Switched-current chaotic neurons, *Electr. Lett.*, 30, 429–430, 1994.
16. M. Delgado-Restituto, A chaotic switched-capacitor circuit for $1/f$ noise generation, *IEEE Trans. Circuits Syst.*, 39, 325–328, 1992.
17. S. T. Dupuie and M. Ismail, High-frequency CMOS transconductors, in *Analogue IC Design: The Current-Mode Approach*, C. Toumazou, F. J. Lidgley, and D. G. Haigh, Eds., London: Peter Peregrinus Ltd., 1990.
18. T. Enomoto and M. Yasumoto, Integrated MOS four-quadrant analog multiplier using switched capacitor technology for analog signal processor IC's, *IEEE J. Solid-State Circuits*, 20, 852–859, 1985.
19. J. W. Fattaruso and R. G. Meyer, MOS analog function synthesis, *IEEE J. Solid-State Circuits*, 22, 1059–1063, 1987.
20. I. M. Filanovsky and H. Baltes, CMOS Schmitt trigger design, *IEEE Trans. Circuits Syst.*, 41, 46–49, 1994.
21. K. Funahashi, On the approximate realization of continuous mappings by neural networks, *Neural Networks*, 2, 183–192, 1989.
22. R. L. Geiger and E. Sánchez-Sinencio, Active filter design using operational transconductance amplifiers: A tutorial, *IEEE Circuits Devices Mag.*, 1, 20–32, 1985.
23. B. Gilbert, Current-mode circuits from a translinear view point: A tutorial, in *Analogue IC Design: The Current-Mode Approach*, C. Toumazou, F. J. Lidgley, and D. G. Haigh, Eds., London: Peter Peregrinus Ltd., 1990.
24. J. Glover, Basic T matrix patterns for 2-port linear transformation networks in the real domain, *IEEE Trans. Circuit Theory*, 10, 495–497, 1974.
25. P. R. Gray and R. G. Meyer, *Analysis and Design of Analog Integrated Circuits*, 3rd ed., New York: John Wiley & Sons, 1993.
26. A. Hausner, *Analog and Analog/Hybrid Computer Programming*, Englewood Cliffs, NJ: Prentice-Hall, 1971.
27. B. J. Hosticka, W. Brockherde, U. Kleine, and R. Schweer, Design of nonlinear analog switched-capacitor circuits using building blocks, *IEEE Trans. Circuits Syst.*, 31, 354–368, 1984.
28. J. L. Huertas, J. A. Acha, and A. Gago, Design of general voltage or current controlled resistive elements and their applications to the synthesis of nonlinear networks, *IEEE Trans. Circuits Syst.*, 27, 92–103, 1980.

29. J. L. Huertas, DT-adaptor: Applications to the design of nonlinear n -ports, *Int. J. Circuit Theory Appl.*, 8, 273–290, 1980.
30. J. L. Huertas and A. Rueda, Sectionwise piecewise polynomial function: Applications to the analysis and synthesis on nonlinear n -ports networks, *IEEE Trans. Circuits Syst.*, 31, 897–905, 1984.
31. J. L. Huertas, L. O. Chua, A. Rodríguez-Vázquez, and A. Rueda, Nonlinear switched-capacitor networks: Basic principles and piecewise-linear design, *IEEE Trans. Circuits Syst.*, 32, 305–319, 1985.
32. M. Ismail, Four-transistor continuous-time MOS transconductance, *Electr. Lett.*, 23, 1099–1100, 1987.
33. J. S. Jang, Neuro-fuzzy modeling: Architectures, analyses and applications, Ph. D. dissertation, University of California, Berkeley, CA, 1992.
34. C. Jansson, K. Chen, and C. Svensson, Linear, polynomial and exponential ramp generators with automatic slope adjustments, *IEEE Trans. Circuits Syst.*, 41, 181–185, 1994.
35. N. I. Khachab and M. Ismail, Linearization techniques for n th-order sensor models in MOS VLSI technology, *IEEE Trans. Circuits Syst.*, 38, 1439–1449, 1991.
36. Y. H. Kim and S. B. Park, Four-quadrant CMOS analog multiplier, *Electr. Lett.*, 28, 649–650, 1992.
37. K. Kimura, Some circuit design techniques using two cross-coupled, emitter-coupled pairs, *IEEE Trans. Circuits Syst.*, 41, 411–423, 1994.
38. O. Landolt, E. Vittoz, and P. Heim, CMOS self-biased Euclidean distance computing circuit with high dynamic range, *Electr. Lett.*, 28, 352–354, 1992.
39. N. R. Malik, G. L. Jackson, and Y. S. Kim, Theory and applications of resistor, linear controlled resistor, linear controlled conductor networks, *IEEE Trans. Circuits Syst.*, 31, 222–228, 1976.
40. A. I. Mees, M. F. Jackson, and L. O. Chua, Device modeling by radial basis functions, *IEEE Trans. Circuits Syst.*, 39, 19–27, 1992.
41. C. Michael and M. Ismail, *Statistical Modeling for Computer-Aided Design of MOS VLSI Circuits*, Boston, MA: Kluwer Academic, 1993.
42. C. A. Micchelli, Interpolation of scattered data: Distance matrices and conditionally positive definite functions, *Constr. Approx.*, 2, 11–22, 1986.
43. J. Moody and C. Darken, Fast learning in networks of locally-tuned processing units, *Neural Comput.*, 1, 281–294, 1989.
44. R. S. Muller and T. I. Kamins, *Device Electronics for Integrated Circuits*, New York: John Wiley & Sons, 1986.
45. K. Nagaraj, K. Singhal, T. R. Viswanathan, and J. Vlach, Reduction of finite-gain effect in switched-capacitor filters, *Electr. Lett.*, 21, 644–645, 1985.
46. K. Nagaraj, A parasitic-insensitive area-efficient approach to realizing very large time constants in switched-capacitor circuits, *IEEE Trans. Circuits Syst.*, 36, 1210–1216, 1989.
47. R. W. Newcomb, Nonlinear differential systems: A canonic multivariable theory, *Proc. IEEE*, 65, 930–935, 1977.
48. M. J. M. Pelgrom, A. C. J. Duijnmaijer, and A. P. G. Welbers, Matching properties of MOS transistors, *IEEE J. Solid-State Circuits*, 24, 1433–1440, 1989.
49. J. S. Peña-Finol and J. A. Connelly, A MOS four-quadrant analog multiplier using the quarter-square technique, *IEEE J. Solid-State Circuits*, 22, 1064–1073, 1987.
50. J. Platt, A resource allocating neural network for function interpolation, *Neural Comput.*, 3, 213–215, 1991.
51. T. Poggio and F. Girosi, Networks for approximation and learning, *Proc. IEEE*, 78, 1481–1497, 1990.
52. M. J. D. Powell, Radial basis functions for multivariate interpolation: A review, Rep 1985/NA12, Department Of Applied Mathematics and Theoretical Physics, Cambridge University, Cambridge, UK, 1985.
53. S. Qin and R. L. Geiger, A 5-V CMOS analog multiplier, *IEEE J. Solid-State Circuits*, 22, 1143–1146, 1987.
54. J. K. Roberge, *Operational Amplifiers: Theory and Practice*, New York: John Wiley, 1975.

55. A. Rodríguez-Vázquez, J. L. Huertas, and A. Rueda, Low-order polynomial curve fitting using switched-capacitor circuits, *Proc. IEEE Int. Symp. Circuits Syst.*, May, 40, 1123–1125, 1984.
56. A. Rodríguez-Vázquez and M. Delgado-Restituto, CMOS design of chaotic oscillators using state variables: A monolithic Chua's circuit, *IEEE Trans. Circuits Syst.*, 40, 596–613, 1993.
57. A. Rodríguez-Vázquez and M. Delgado-Restituto, Generation of chaotic signals using current-mode techniques, *J. Intell. Fuzzy Syst.*, 2, 15–37, 1994.
58. A. Rodríguez-Vázquez, R. Domínguez-Castro, F. Mederio, and M. Delgado-Restituto, High-resolution CMOS current comparators: Design and applications to current-mode functions generation, *Analog Integr. Circuits Signal Process.*, 7(2), 149–165, 1995.
59. A. Rueda, J. L. Huertas, and A. Rodríguez-Vázquez, Basic circuit structures for the synthesis of piecewise polynomial one-port resistors, *IEEE Proc.*, 132(Part G), 123–129, 1985.
60. S. Sakurai and M. Ismail, High frequency wide range CMOS analogue multiplier, *Electr. Lett.*, 28, 2228–2229, 1992.
61. E. Sánchez-Sinencio, J. Ramírez-Angulo, B. Linares-Barranco, and A. Rodríguez-Vázquez, Operational transconductance amplifier-based nonlinear function synthesis, *IEEE J. Solid-State Circuits*, 24, 1576–1586, 1989.
62. E. Seevinck, *Analysis and Synthesis of Translinear Integrated Circuits*, Amsterdam: Elsevier, 1988.
63. D. H. Sheingold, *Nonlinear Circuits Handbook*, Norwood, CA: Analog Devices Inc., 1976.
64. J. Silva-Martínez and E. Sánchez-Sinencio, Analog OTA multiplier without input voltage swing restrictions, and temperature compensated, *Electr. Lett.*, 22, 559–560, 1986.
65. S. Soclof, *Analog Integrated Circuits*, Englewood Cliffs, NJ: Prentice-Hall, 1985.
66. B. Song, CMOS RF circuits for data communication applications, *IEEE J. Solid-State Circuits*, 21, 310–317, 1986.
67. L. Strauss, *Wave Generation and Shaping*, New York: McGraw-Hill, 1970.
68. G. C. Temes and K. Haug, Improved offset compensation schemes for switched-capacitor circuits, *Electr. Lett.*, 20, 508–509, 1984.
69. Y. P. Tsvividis, M. Banu, and J. Khoury, Continuous-time MOSFET-C filters in VLSI, *IEEE J. Solid-State Circuits*, 21, 15–30, 1986.
70. Y. P. Tsvividis and J. O. Voorman, Eds., *Integrated Continuous-Time Filters*, New York: IEEE Press, 1993.
71. C. Turchetti and M. Conti, A general approach to nonlinear synthesis with MOS analog circuits, *IEEE Trans. Circuits Syst.*, 40, 608–612, 1993.
72. R. Unbehauen and A. Cichocki, *MOS Switched-Capacitor and Continuous-Time Integrated Circuits and Systems*, Berlin: Springer-Verlag, 1989.
73. G. N. Vanderplaats, *Numerical Optimization Techniques for Engineering Design: with Applications*, New York: McGraw-Hill, 1984.
74. F. Vidal and A. Rodríguez-Vázquez, A basic building block approach to CMOS design of analog neuro/fuzzy systems, *Proc. IEEE Int. Conf. Fuzzy Syst.*, 1, 118–123, 1994.
75. E. Vittoz, Analog VLSI signal processing why, where and how? *Analog Integr. Circuits Signal Process.*, 6, 27–44, 1994.
76. J. Vlach and K. Singhal, *Computer Methods for Circuit Analysis and Design*, 2nd ed., New York: Van Nostrand Reinhold, 1994.
77. Z. Wang, Analytical determination of output resistance and DC matching errors in MOS current mirrors, *IEEE Proc.*, 137(Part G), 397–404, 1990.
78. G. A. Watson, *Approximation Theory and Numerical Methods*, Chichester, UK: John Wiley & Sons, 1980.
79. R. Wiegierink, *Analysis and Synthesis of MOS Translinear Circuits*, Boston: Kluwer Academic, 1993.
80. Y. J. Wong and W. E. Ott, *Function Circuits; Design and Applications*, New York: McGraw-Hill, 1976.
81. T. Yamakawa, A fuzzy inference engineer in nonlinear analog mode and its application to fuzzy control, *IEEE Trans. Neural Networks*, 4, 496–522, 1993.
82. J. M. Zurada, *Introduction to Artificial Neural Systems*, St. Paul, MN: West Publishing, 1992.

9

Representation, Approximation, and Identification

9.1	Introduction	9-1
9.2	Representation	9-2
	Differential Equation and State-Space Representations • Input-Output Representation • Volterra Series Representation	
9.3	Approximation	9-10
	Best Approximation of Systems (Operators) • Best (Uniform) Approximation of Signals (Functions) • Best Approximation of Linear Functionals • Artificial Neural Network for Approximation	
9.4	Identification	9-26
	Linear Systems Identification • Nonlinear Systems Identification • Nonlinear Dynamic Systems Identification from Time Series	
	References	9-31

Guanrong Chen
City University of Hong Kong

9.1 Introduction

Representation, approximation, and identification of physical systems, linear or nonlinear, deterministic or random, or even chaotic, are three fundamental issues in systems theory and engineering. To describe a physical system, such as a circuit or a microprocessor, we need a mathematical formula or equation that can represent the system both qualitatively and quantitatively. Such a formulation is what we call a mathematical representation of the physical system. If the physical system is so simple that the mathematical formula or equation, or the like, can describe it perfectly without error, then the representation is ideal and ready to use for analysis, computation, and synthesis of the system. An ideal representation of a real system is generally impossible, so that system approximation becomes necessary in practice. Intuitively, approximation is always possible. However, the key issues are what kind of approximation is good, where the sense of “goodness” must first be defined, of course, and how to find such a good approximation. On the other hand, when looking for either an ideal or a approximate mathematical representation for a physical system, one must know the system structure (the form of the linearity or nonlinearity) and parameters (their values). If some of these are unknown, then one must identify them, leading to the problem of system identification.

This chapter is devoted to a brief description of mathematical representation, approximation, and identification of, in most cases, nonlinear systems. As usual, a linear system is considered to be a special case of a nonlinear system, but we do not focus on linear systems in this chapter on nonlinear circuits. It is

known that a signal, continuous or discrete, is represented by a function of time. Hence, a signal can be approximated by other functions and also may be identified using its sampled data. These are within the context of “representation, approximation, and identification,” but at a lower level—one is dealing with functions. A system, in contrast, transforms input signals to output signals, namely, maps functions to functions, and is therefore at a higher level—it can only be represented by an operator (i.e., a mapping). Hence, while talking about representation, approximation, and identification in this chapter, we essentially refer to operators. However, we notice that two systems are considered to be equivalent over a set of input signals if and only if (iff) they map the same input signal from the set to the same output signal, regardless of the distinct structures of the two systems. From this point of view, one system is a good approximation of the other if the same input produces outputs that are approximately the same under certain measure. For this reason, we also briefly discuss the classical function approximation theory in this chapter.

The issue of system representation is addressed in Section 9.2, while approximation (for both operators and functions) is discussed in Section 9.3, leaving the system identification problem to Section 9.4. Limited by space, we can discuss only deterministic systems. Topics on stochastic systems are hence referred to some standard textbooks [13,17].

It is impossible to cover all the important subjects and to mention many significant results in the field in this short and sketchy chapter. The selections made only touch upon the very elementary theories, commonly used methods, and basic results related to the central topics of the chapter, reflecting the author’s personal preference. In order to simplify the presentation, we elected to cite only those closely related references known to us, which may or may not be the original sources. From our citations, the reader should be able to find more references for further reading.

9.2 Representation

The scientific term “representation” as used here refers to a mathematical description of a physical system. The fundamental issue in representing a physical system by a mathematical formulation, called a mathematical model, is its correct symbolization, accurate quantization, and strong ability to illustrate and reproduce important properties of the original system.

A circuit consisting of some capacitor(s), inductor(s), and/or resistors(s), and possibly driven by a voltage source or a current source, is a physical system. In order to describe this system mathematically for the purpose of analysis, design, and/or synthesis, a mathematical model is needed. Any mathematical model, which can correctly describe the physical behavior of the circuit, is considered a mathematical representation of the circuit. A lower level mathematical representation of a circuit can, for instance, be a signal flow chart or a circuit diagram like the nonlinear Chua’s circuit shown in Figure 9.1, which is discussed next.

A circuit, such as that shown in Figure 9.1, can be used to describe a physical system, including its components and its internal as well as external connections. However, it is not convenient for carrying out theoretical analysis or numerical computations. This is because no qualitative or quantitative

description exists about the relations among the circuit elements and their dynamic behavior. Hence, a higher level mathematical model is needed to provide a qualitative and quantitative representation of the real physical circuit.

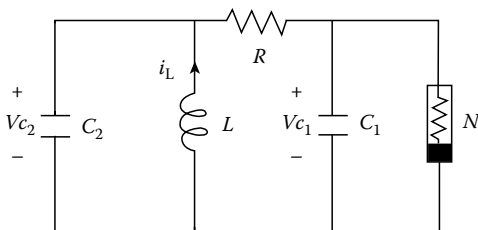


FIGURE 9.1 Chua’s circuit.

Among several commonly used mathematical modeling approaches for various physical systems, differential equations, state-space formulations, I–O mappings, and functional series (particularly, the Volterra series) are the most important and useful, which have been very popular in the field of circuits

and systems engineering. In the following, we introduce these mathematical representation methods, along with some brief discussions of other related issues. Limited by space, detailed derivations are omitted.

9.2.1 Differential Equation and State-Space Representations

Mathematical modeling via differential equations and via state-space descriptions are the most basic mathematical representation methods. We illustrate the concept of mathematical modeling and the two representation methods by a simple, yet representative example: the nonlinear circuit in Figure 9.1. This circuit consists of one inductor L , two capacitors C_1 and C_2 , one linear resistor R , and one nonlinear resistor, N , which is a nonlinear function of the voltage across its two terminals: $N = N(V_{C_1}(t))$. Let $i_L(t)$ be the current through the inductor L , and $V_{C_1}(t)$ and $V_{C_2}(t)$ be the voltages across C_1 and C_2 , respectively. For the time being, let us remove the nonlinear resistor N from Figure 9.1 and consider the remaining linear circuit. This nonlinear resistor N is readded to the circuit with detailed discussions in Equation 9.6.

For this linear circuit without the resistor N , it follows from Kirchhoff's laws that

$$C_1 \frac{d}{dt} V_{C_1}(t) = \frac{1}{R} [V_{C_2}(t) - V_{C_1}(t)] \quad (9.1)$$

$$C_2 \frac{d}{dt} V_{C_2}(t) = \frac{1}{R} [V_{C_1}(t) - V_{C_2}(t)] + i_L(t) \quad (9.2)$$

$$L \frac{d}{dt} i_L(t) = -V_{C_2}(t) \quad (9.3)$$

By simple calculation we can eliminate both $V_{C_2}(t)$ and i_L , leaving a single ordinary differential equation on the unknown voltage $V_{C_1}(t)$ as follows:

$$\frac{d^3}{dt^3} V_{C_1}(t) + \frac{1}{R} \left(\frac{1}{C_1} + \frac{1}{C_2} \right) \frac{d^2}{dt^2} V_{C_1}(t) + \frac{1}{C_2 L} \frac{d}{dt} V_{C_1}(t) + \frac{1}{C_1 C_2 R L} V_{C_1}(t) = 0 \quad (9.4)$$

Once $V_{C_1}(t)$ is obtained from Equation 9.4, based on certain initial conditions, the other two unknowns, $V_{C_2}(t)$ and i_L , can be obtained by using Equations 9.1 and 9.3, successively. Hence, this third-order ordinary differential equation describes both qualitatively and quantitatively the circuit shown in Figure 9.1 (without the nonlinear resistor N). For this reason, Equation 9.4 is considered to be a mathematical representation, called a differential equation representation, of the physical linear circuit.

Very often, a higher-order, single-variable ordinary differential equation similar to Equation 9.4 is not as convenient as a first-order multivariable system of ordinary differential equations as is the original system of Equations 9.1 through 9.3, even when an analytic formulation of the solution is desired. Hence, a more suitable way for modeling a physical system is to introduce the concept of system state variables, which leads to a first-order higher dimensional system of ordinary differential equations.

If we introduce three state variables in Equations 9.1 through 9.3:

$$x_1(t) = V_{C_1}(t), \quad x_2(t) = V_{C_2}(t), \quad x_3(t) = i_L(t)$$

then we can rewrite those equations in the following vector form:

$$\begin{cases} \dot{\mathbf{x}}(t) = \mathbf{A}\mathbf{x}(t) + \mathbf{B}\mathbf{u}(t), & t \geq 0 \\ \mathbf{x}(0) = \mathbf{x}_0 \end{cases} \quad (9.5)$$

with an initial value \mathbf{x}_0 (usually given), where

$$\mathbf{x}(t) = \begin{bmatrix} x_1(t) \\ x_2(t) \\ x_3(t) \end{bmatrix} \quad \text{and} \quad A = \begin{bmatrix} -\frac{1}{RC_1} & \frac{1}{RC_1} & 0 \\ \frac{1}{RC_2} & -\frac{1}{RC_2} & \frac{1}{C_2} \\ 0 & -\frac{1}{L} & 0 \end{bmatrix}$$

in which $\mathbf{x}(t)$ is called the state vector of the system. Here, to be more general and for convenience in the discussions following, we formally added the term $B\mathbf{u}(t)$ to the system, in which B is a constant matrix and $\mathbf{u}(t)$ is called the control input of the system. In the present case, of course, $\mathbf{u} = 0$ and it is not important to specify B . However, note that \mathbf{u} can be a nonzero external input to the circuit [19], which is discussed in more detail below.

This first-order, vector-valued linear ordinary differential equation is equivalent to the third-order differential equation representation (Equation 9.4) of the same physical circuit. A special feature of this state vector formulation is that with different initial state vectors and with zero control inputs, all the possible system state vectors together constitute a linear space of the same dimension [31]. Hence, Equation 9.5 is also called a linear state-space representation (or, a linear state-space description) for the circuit.

A few important remarks are in order. First, if the circuit is nonlinear, its state vectors do not constitute a linear space in general. Hence, its mathematical model in the state vector form should not be called a “state-space” representation. Note, however, that some of the linear system terminology such as state variables and state vectors usually make physical sense for nonlinear systems. Therefore, we use the term nonlinear state-variable representation to describe a first-order, vector-valued nonlinear ordinary differential equation of the form $\dot{\mathbf{x}}(t) = \mathbf{f}(\mathbf{x}(t), \mathbf{u}(t), t)$, where $\mathbf{f}(\cdot, \cdot, t)$ is generally a vector-valued nonlinear function. This is illustrated in more detail shortly.

Second, a linear state-space representation for a given physical system is not unique because one can choose different state variables. For example, in Equations 9.1 through 9.3 if we instead define $x_1 = V_{C_2}(t)$ and $x_2 = V_{C_1}(t)$, we arrive at a different linear state-space representation of the same circuit. However, we should note that if a linear nonsingular transformation of state vectors can map one state-space representation to another, then these two seemingly different representations are actually equivalent in the sense that the same initial values and control inputs will generate the same outputs (perhaps in different forms) through these two representations. Also worth noting is that not every circuit element can be used as a state variable, particularly for nonlinear systems. A basic requirement is that all the chosen state variables must be “linearly independent” in that the first-order, vector-valued ordinary differential equation has a unique solution (in terms of the control input) for any given initial values of the chosen state variables.

Finally, because A and B in the state-space representation (Equation 9.5) are both constant (independent of time), the representation is called a linear time-invariant system. If A or B is a matrix-valued function of time, then it will be called a linear time-varying system. Clearly, a time-invariant system is a special case of a time-varying system.

Now, let us return to the nonlinear circuit, with the nonlinear resistor N being connected to the circuit, as illustrated in Figure 9.1. Similar to Equations 9.1 through 9.3, we have the following circuit equations:

$$C_1 \frac{d}{dt} V_{C_1}(t) = \frac{1}{R} [V_{C_2}(t) - V_{C_1}(t)] - N(V_{C_1}(t)) \quad (9.6)$$

$$C_2 \frac{d}{dt} V_{C_2}(t) = \frac{1}{R} [V_{C_1}(t) - V_{C_2}(t)] + i_L(t) \quad (9.7)$$

$$L \frac{d}{dt} i_L(t) = -V_{C_2}(t) \quad (9.8)$$

Note that if the nonlinear resistor N is given by

$$\begin{aligned} N(V_{C_1}(t)) &= N(V_{C_1}(t); m_0, m_1) \\ &= m_0 V_{C_1}(t) + \frac{1}{2} (m_1 - m_0) \left(|V_{C_1}(t) + 1| - |V_{C_1}(t) - 1| \right) \end{aligned} \quad (9.9)$$

with $m_0 < 0$ and $m_1 < 0$ being two appropriately chosen constant parameters, then this nonlinear circuit is the well-known Chua's circuit [24].

It is clear that compared with the linear case, it would be rather difficult to eliminate two unknowns, particularly $V_{C_1}(t)$, in order to obtain a simple third-order, nonlinear differential equation that describes the nonlinear circuit. That is, it would often be inconvenient to use a higher-order, single-variable differential equation representation for a nonlinear physical system in general. By introducing suitable state variables, however, one can easily obtain a nonlinear state-variable representation in a first-order, vector-valued, nonlinear differential equation form. For instance, we may choose the following state variables:

$$x(\tau) = V_{C_1}(t), \quad y(\tau) = V_{C_2}(t), \quad \text{and} \quad z(\tau) = R i_L(t) \quad \text{with} \quad \tau = t/RC_2$$

where the new variable $z(\tau) = R i_L(t)$ and the rescaled time variable $\tau = t/RC_2$ are introduced to simplify the resulting representation of this particular circuit. Under this nonsingular linear transform, the previous circuit equations are converted to the following state-variable representation:

$$\begin{cases} \dot{x}(\tau) = p[-x(\tau) + y(\tau) - \tilde{N}(x(\tau))] \\ \dot{y}(\tau) = x(\tau) - y(\tau) + z(\tau) \\ \dot{z}(\tau) = -qy(\tau) \end{cases} \quad (9.10)$$

where

$$\begin{aligned} p &= C_2/C_1 \\ q &= R^2 C_2/L \end{aligned}$$

and

$$\begin{aligned} \tilde{N}(x(\tau)) &= N(x(\tau); \tilde{m}_0, \tilde{m}_1) \\ &= \tilde{m}_0 x(\tau) + \frac{1}{2} (\tilde{m}_1 - \tilde{m}_0) (|x(\tau) + 1| - |x(\tau) - 1|) \end{aligned} \quad (9.11)$$

with $\tilde{m}_0 = R m_0$ and $\tilde{m}_1 = R m_1$.

It is easy to see that this state-variable representation can be written as a special case in the following form, known as a canonical representation of Chua's circuit family:

$$\dot{\mathbf{x}}(\tau) = \mathbf{a} + A\mathbf{x}(\tau) + \sum_{i=1}^k |\mathbf{h}_i^T \mathbf{x}(\tau) - \beta_i| \mathbf{c}_i + B\mathbf{u}(\tau) \quad (9.12)$$

namely, with $\mathbf{a} = 0$, $k = 2$, $\mathbf{h}_1 = \mathbf{h}_2 = [1 \ 0 \ 0]^T$, $\beta_1 = -\beta_2 = -1$, $\mathbf{c}_1 = -\mathbf{c}_2 = \mathbf{H}(\tilde{m}_1 - \tilde{m}_0)$, $B\mathbf{u}(\tau)$ being a possible control input to the circuit [19], and

$$A = \begin{bmatrix} -\tilde{m}_0 - p & p & 0 \\ 1 & -1 & 1 \\ 0 & -q & 0 \end{bmatrix}$$

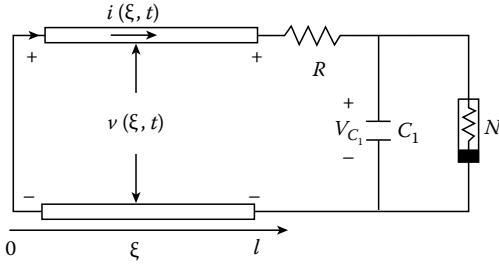


FIGURE 9.2 Time-delayed Chua's circuit.

The canonical (piecewise-linear) representation given by Equation 9.12 describes a large class of circuits that have very rich nonlinear dynamics [25,55].

Now, we return to Equations 9.6 through 9.8 and Figure 9.1. If we replace the $L - C_2$ part of Chua's circuit by a lossless transmission line (with the spatial variable ξ) of length l terminated on its left-hand side (at $\xi = 0$) by a short circuit, as depicted in Figure 9.2, then we obtain a time-delayed Chua's circuit [89]. This circuit has a partial differential equation representation of the form:

$$\begin{cases} \partial v / \partial \xi = -L \partial i(\xi, t) / \partial t \\ \partial i(\xi, t) / \partial \xi = -C_1 \partial v(\xi, t) / \partial t \\ v(0, t) = 0 \\ i(l, t) = N(v(l, t) - e - Ri(l, t)) + C_1 \partial [v(l, t) - Ri(l, t)] / \partial t \end{cases} \quad (9.13)$$

where $v(\xi, t)$ and $i(\xi, t)$ are the voltage and current, respectively, at the point $\xi \in [0, l]$ at time t , and $V_{c1} = e > 0$ is a constant, with the nonlinear resistor N satisfying

$$N(V_{C_1} - e) = \begin{cases} m_0(V_{C_1} - e) & |V_{C_1} - e| < 1 \\ m_1(V_{C_1} - e) - (m_1 - m_0)\text{sgn}(V_{C_1} - e) & |V_{C_1} - e| \geq 1 \end{cases}$$

In general, systems that are described by (linear or nonlinear) partial differential equations, with initial-boundary value conditions, are studied under a unified framework of (linear or nonlinear) operator semigroup theory, and are considered to have an infinite-dimensional system representation [7].

9.2.2 Input-Output Representation

A state-variable representation of a nonlinear physical system generally can be written as

$$\begin{cases} \dot{\mathbf{x}}(t) = \mathbf{f}(\mathbf{x}(t), \mathbf{u}(t), t), & t \geq 0 \\ \mathbf{x}(0) = \mathbf{x}_0 \end{cases} \quad (9.14)$$

where

- $\mathbf{f}(\cdot, \cdot, t)$ is a nonlinear, vector-valued function
- \mathbf{x}_0 is a (given) initial value for the state vector \mathbf{x} at $t = 0$
- \mathbf{u} is a control input to the system

Because not all state variables in the state vector \mathbf{x} can be measured (observed) in a physical system, let us suppose that what can be measured is only part of \mathbf{x} , or a mixture of its components, expressed by a vector-valued function of \mathbf{x} in the form

$$\mathbf{y}(t) = \mathbf{g}(\mathbf{x}(t), t), \quad t \geq 0 \quad (9.15)$$

where

- \mathbf{y} is called a (measurement or observation) output of the physical system
- \mathbf{g} is in general a lower dimensional vector-valued nonlinear function

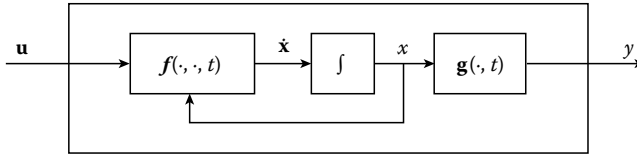


FIGURE 9.3 System I–O relationship.

As a particular case, \mathbf{g} can be linear or, even more so, be $\mathbf{g}(\mathbf{x}(t), t) = \mathbf{x}(t)$ when all the components of the state vector are directly measurable.

If both $\mathbf{f} = \mathbf{f}(\mathbf{x}(t), \mathbf{u}(t))$ and $\mathbf{g} = \mathbf{g}(\mathbf{x}(t))$ are not explicit functions of the independent time variable t , the corresponding state-variable representation (Equations 9.14 and 9.15) is said to be autonomous.

It is clear that with both the system input \mathbf{u} and output \mathbf{y} , one can simply represent the overall physical system by its input-output (I–O) relationship, as illustrated in Figure 9.3.

Now, under certain mild conditions on the nonlinear function \mathbf{f} , for a given control input \mathbf{u} , and an initial value \mathbf{x}_0 , the state-variable representation (Equation 9.14) has a unique solution, \mathbf{x} , which depends on both \mathbf{u} and \mathbf{x}_0 . If we denote the solution as

$$\mathbf{x}(t) = \mathcal{F}(t; \mathbf{u}(t), \mathbf{x}_0) \quad (9.16)$$

where \mathcal{F} is called an input-state mapping, then the overall I–O relationship shown in Figure 9.3 can be formulated as

$$\mathbf{y}(t) = \mathbf{g}(\mathcal{F}(t; \mathbf{u}(t), \mathbf{x}_0), t) \quad (9.17)$$

This is an I–O representation of the physical system having the state-variable representation (Equations 9.14 and 9.15).

As a simple example, let us consider the linear state-space representation (Equation 9.5), with a special linear measurement equation of the form $\mathbf{y}(t) = C\mathbf{x}(t)$, where C is a constant matrix. It is well known [31] that

$$\mathbf{y}(t) = C\mathcal{F}(t; \mathbf{u}(t), \mathbf{x}_0) = C \left\{ e^{tA} \mathbf{x}_0 + \int_0^t e^{(t-\tau)A} B \mathbf{u}(\tau) d\tau \right\}, \quad t \geq 0 \quad (9.18)$$

yielding an explicit representation formula for the I–O relationship of the linear circuit (together with the assumed measurement equation).

Note that because the state-variable representation (Equation 9.14) is not unique, as mentioned previously, this I–O representation is not unique in general. However, we note that if two state-variable representations are equivalent, then their corresponding I–O relationships also will be equivalent.

It is also important to note that although the above I–O relationship is formulated for a finite-dimensional open-loop system, it can also be applied to infinite-dimensional [7] and closed-loop systems [39]. In particular, similar to linear systems, many finite-dimensional, closed-loop nonlinear systems possess an elegant coprime factorization representation. The (left or right) coprime factorization representation of a nonlinear feedback system is a general I–O relationship that can be used as a fundamental framework, particularly suitable for studies of stabilization, tracking, and disturbance rejection. The problem is briefly described as follows. Let a nonlinear system (mapping) P be given, not necessarily stable, and assume that it has a right-coprime factorization $P = ND^{-1}$, where both N and D are stable (D^{-1} usually has the same stability as P). One is looking for two stable, nonlinear subsystems (mappings),

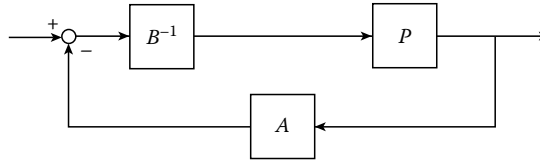


FIGURE 9.4 Right-coprime factorization of a nonlinear feedback system.

A and B^{-1} , representing feedback and feed-forward controllers, respectively, satisfying the Bezout identity

$$AN + BD = I$$

which are connected as shown in Figure 9.4, where B is also stable. If two controllers, A and B , can be found to satisfy such conditions, then even with an unstable P , the resulting closed-loop control system will be I–O, as well as internally, stable. In this sense, A and B together stabilize P .

For the left-coprime factorization, one simply uses formulas $P = D^{-1}N$ and $NA + DB = I$ instead and interchanges the two blocks of A and B^{-1} in Figure 9.4.

Taking into account causality and well-posedness of the overall closed-loop system, it is a technical issue as to how to construct the four subsystems A , B , D , and N , such that the preceding requirements can be satisfied. Some characterization results and construction methods are available in the literature [38,45,51,95].

9.2.3 Volterra Series Representation

Recall from the fundamental theory of ordinary differential equations that an explicit I–O representation of the overall system still can be found, even if the linear state-space representation (Equation 9.5) is time varying, via the state transition matrix $\Phi(t, \tau)$ determined by

$$\begin{cases} \frac{d}{dt} \Phi(t, \tau) = A(t)\Phi(t, \tau), & t \geq \tau \\ \Phi(\tau, \tau) = I \end{cases} \tag{9.19}$$

where I is the identity matrix. The formula, for the simple case $\mathbf{y}(t) = C(t)\mathbf{x}(t)$, is

$$\mathbf{y}(t) = C(t) \left\{ \Phi(t, 0)\mathbf{x}_0 + \int_0^t \Phi(t, \tau)B(\tau)\mathbf{u}(\tau)d\tau \right\}, \quad t \geq 0 \tag{9.20}$$

For linear time-invariant systems, we actually have $\Phi(t, \tau) = e^{(t-\tau)A}$, so that Equation 9.20 reduces to the explicit formula (Equation 9.18).

For a nonlinear system, a simple explicit I–O representation with a single integral of the form (Equation 9.18 or Equation 9.20) is generally impossible. A natural generalization of such an integral formulation is the Volterra series representation. For simplicity, let us consider the one-dimensional case in which $y(t) = g(x(t), t) = x(t)$ below. A Volterra series representation for a nonlinear I–O relationship $\mathcal{F}(\cdot)$, convergent in some measure, is an infinite sum of integrals in the following form:

$$\mathcal{F}(t, u(t)) = \phi_0(t; x_0) + \int_0^t \phi_1(t, \tau_1) u(\tau_1) d\tau_1 + \cdots + \int_0^t \cdots \int_0^{\tau_2} \phi_n(t, \tau_1, \dots, \tau_n) u(\tau_1) \cdots u(\tau_n) d\tau_1 \cdots d\tau_n + \cdots \quad (9.21)$$

where $\{\phi_n\}_{n=0}^\infty$ are called the Volterra kernels of the series. Here, we note that this Volterra series representation can be extended easily to higher-dimensional systems.

For some representations \mathcal{F} , the corresponding Volterra series may have only finitely many nonzero terms in the above infinite sum. In this case, it is called a Volterra polynomial, which does not have convergence problem for bounded inputs, provided that all the integrals exist. In particular, when \mathcal{F} is affine (or linear, if initial conditions are zero, so that $\phi_0 = 0$), its Volterra series has at most two nonzero terms, as given by Equations 9.18 and 9.20, and is called a first-order Volterra polynomial. In general, however, the Volterra series (Equation 9.21) is an infinite sum. Hence, the convergence of a Volterra series is a crucial issue in formulating such a representation for a given nonlinear I–O relationship [5,12,59,85].

In order to state a fundamental result about the convergence of a Volterra series, we must first recall that a mapping that takes a function to a (real or complex) value is called a functional and a mapping that takes a function to another function is called an operator. A functional may be considered to be a special operator if one views a value as a constant function in the image of the mapping. Clearly, the I–O relationship (Equation 9.17) and the Volterra series (Equation 9.21), including Volterra polynomials, are nonlinear operators. Recall also that an operator $\mathcal{T}: X \rightarrow Y$, where X and Y are normed linear spaces, is said to be continuous at $x \in X$ if $\|x_n - x\|_X \rightarrow 0$ implies $\|\mathcal{T}(x_n) - \mathcal{T}(x)\|_Y \rightarrow 0$ as $n \rightarrow \infty$. Note that for a linear operator, if it is continuous at a point, then it is also continuous on its entire domain [34], but this is not necessarily true for nonlinear operators.

As usual, we denote by $C[0, T]$ and $L_p[0, T]$, respectively, the space of continuous functions defined on $[0, T]$ and the space of measurable functions f satisfying $\int_0^T |f(t)|^p dt < \infty$ for $1 \leq p < \infty$ or $\sup_{t \in [0, T]} |f(t)| < \infty$ for $p = \infty$. The following result [5] is an extension of the classical Stone–Weierstrass theorem [22,36,40].

THEOREM 9.1

Let X be either $C[0, T]$ or $L_p[0, T]$, with $1 \leq p < \infty$, and Ω be a compact subset in X . Then, for any continuous operator $\mathcal{F}: \Omega \rightarrow L_q[0, T]$, where $(1/p) + (1/q) = 1$, and for any $\varepsilon > 0$, a Volterra polynomial $P_n(\cdot)$ exists, with n determined by ε , such that

$$\sup_{x \in \Omega} \|\mathcal{F}(x) - P_n(x)\|_{L_q} < \varepsilon$$

In other words, $P_n \rightarrow \mathcal{F}$ uniformly on the compact subset $\Omega \subset X$ as $n \rightarrow \infty$.

In the literature, many variants of this fundamental convergence theorem exist under various conditions in different forms, including the $L_\infty[0, T]$ case [45,59,84,85]. We may also find different methods for constructing the Volterra kernels $\{\phi_n\}_{n=0}^\infty$ for \mathcal{F} [83]. In addition, specially structured Volterra series representations abound for nonlinear systems, such as the Volterra series with finite memory [5], approximately finite memory [86], and fading memory [10].

Finally, it should be mentioned that in a more general manner, a few abstract functional series representations exist, including the generating power series representation for certain nonlinear systems [48], from which the Volterra series can be derived. Briefly, an important result is the following theorem [6,54,71,91].

THEOREM 9.2

Consider a nonlinear control system of the form

$$\begin{cases} \dot{x}(t) = g_0(x(t)) + \sum_{k=1}^m g_k(x(t))u_k(t), & t \in [0, T] \\ y(t) = h(x(t)) \end{cases}$$

where $h(\cdot)$ and $\{g_i(\cdot)\}_{i=0}^m$ are sufficiently smooth functionals, with an initial state x_0 . If the control inputs satisfy $\max_{0 \leq \tau \leq T} |u_k(\tau)| < 1$, then the corresponding output of this nonlinear system has a convergent functional series of the form

$$y(t) = h(x_0) + \sum_{i=0}^{\infty} \sum_{k_0, \dots, k_i=0}^m L_{g_{k_0}} \cdots L_{g_{k_i}} h(x_0) \int_0^t d\xi_{k_i} \cdots d\xi_{k_0} \quad (9.22)$$

where $L_g h(x_0) := [\partial h / \partial x] g(x)|_{x=x_0}$ and ξ_k are defined by

$$\xi_0(t) = t \quad \xi_k(t) = \int_0^t u_k(\tau) d\tau, \quad k = 1, \dots, m$$

with the notation

$$\int_0^t d\xi_{k_i} \cdots d\xi_{k_0} := \int_0^t d\xi_{k_i}(\tau) \int_0^{\tau} d\xi_{k_{i-1}} \cdots d\xi_{k_0}$$

Note that in order to guarantee the convergence of the functional series (Equation 9.22), in many cases it may be necessary for T to be sufficiently small.

Analogous to the classical Taylor series of smooth functions, a fairly general series representation for some nonlinear systems is still possible using polynomial operators, or the like [90]. As usual, however, the more general the presentation is, the less concrete the results. Moreover, a very general series expansion is likely to be very local, and its convergence is difficult to analyze.

9.3 Approximation

The mathematical term ‘‘approximation’’ used here refers to the theory and methodology of function (functional or operator) approximation. Mathematical approximation theory and techniques are important in engineering when one seeks to represent a set of discrete data by a continuous function, to replace a complicated signal by a simpler one, or to approximate an infinite-dimensional system by a finite-dimensional model, etc., under certain optimality criteria.

Approximation is widely used in system modeling, reduction, and identification, as well as in many other areas of control systems and signal processing [32]. A Volterra polynomial as a truncation of the infinite Volterra series (discussed earlier) serves as a good example of system (or operator) approximation, where the question ‘‘In what sense is this approximation good?’’ must be addressed further.

9.3.1 Best Approximation of Systems (Operators)

Intuitively, approximation is always possible. However, two key issues are the quality of the approximation and the efficiency of its computation (or implementation). Whenever possible, one would like to

have the best (or optimal) approximation, based on the available conditions and subject to all the requirements.

A commonly used criterion for best (or optimal) approximations is to achieve a minimum norm of the approximation error using a norm that is meaningful to the problem. Best approximations of systems (operators) include the familiar least-squares technique, and various other uniform approximations.

9.3.1.1 Least-Squares Approximation and Projections

Let us start with the most popular “best approximation” technique (the least-squares method), which can also be thought of as a projection, and a special min–max approximation discussed in the Section 9.3.1.2. Discrete data fitting by a continuous function is perhaps the best-known example of least-squares. The special structure of Hilbert space, a complete inner-product space of functions, provides a general and convenient framework for exploring the common feature of various least-squares approximation techniques. Because we are concerned with approximation of nonlinear systems rather than functions, a higher-level framework, the Hilbert space of operators, is needed. We illustrate such least-squares system (or operator) approximations with the following two examples.

First, we consider the linear space, H , of certain nonlinear systems that have a convergent Volterra series representation (Equation 9.21) mapping an input space X to an output space Y . Note that although a nontrivial Volterra series is a nonlinear operator, together they constitute a linear space just like nonlinear functions.

To form a Hilbert space, we first need an inner product between any two Volterra series. One way to introduce an inner product structure into this space is as follows. Suppose that all the Volterra series, $\mathcal{F}: X \rightarrow Y$, where both X and Y are Hilbert spaces of real-valued functions, have bounded admissible inputs from the set

$$\Omega = \{x \in X \mid \|x\|_X \leq \gamma < \infty\}$$

For any two convergent Volterra series of the form (Equation 9.21), say \mathcal{F} and \mathcal{G} , with the corresponding Volterra kernel sequences $\{\phi_n\}$ and $\{\psi_n\}$, respectively, we can define an inner product between them via the convergent series formulation

$$\langle \mathcal{F}, \mathcal{G} \rangle_H := \sum_{n=0}^{\infty} \frac{\rho_n}{n!} |\phi_n \psi_n|$$

with the induced norm $\|\mathcal{F}\|_H = \langle \mathcal{F}, \mathcal{F} \rangle_H^{1/2}$, where the weights $\{\rho_n\}$ satisfy

$$\sum_{n=0}^{\infty} \frac{1}{\rho_n} \frac{\gamma^{2n}}{n!} < \infty$$

Recall also that a reproducing kernel Hilbert space \tilde{H} is a Hilbert space (of real-valued functions or operators) defined on a set S , with a reproducing kernel $K(x, y)$, which belongs to \tilde{H} for each fixed x or y in S and has the property

$$\langle K(x, y), \mathcal{F}(y) \rangle_{\tilde{H}} = \mathcal{F}(x) \quad \forall \mathcal{F} \in \tilde{H} \text{ and } \forall x, y \in S$$

Using the notation defined above, the following useful result was established [43,45] and is useful for nonlinear systems identification (see Theorem 9.23).

THEOREM 9.3

The family of all the convergent Volterra series of the form (Equation 9.21) that maps the bounded input set Ω to Y constitutes a reproducing kernel Hilbert space with the reproducing kernel

$$K(x, y) = \sum_{n=0}^{\infty} \frac{1}{n!} \frac{1}{\rho_n} \langle x, y \rangle_X^n, \quad x, y \in \Omega \subset X \tag{9.23}$$

The reproducing kernel Hilbert space H defined above is called a generalized Fock space [46]. For the special case in which $\rho_n \equiv 1$, its reproducing kernel has a nice closed-form formula as an exponential operator $K(x, y) = e^{\langle xy \rangle}$.

Now, suppose that a nonlinear system \mathcal{F} is given, which has a convergent Volterra series representation (Equation 9.21) with infinitely many nonzero terms in the series. For a fixed integer $n \geq 0$, if we want to find an n th-order Volterra polynomial, denoted V_n^* , from the Hilbert space H such that

$$\|\mathcal{F} - V_n^*\|_H = \inf_{V_n \in H} \|\mathcal{F} - V_n\|_H \tag{9.24}$$

then we have a best approximation problem in the least-squares sense. To solve this optimization problem is to find the best Volterra kernels $\{\phi_k(t)\}_{k=0}^n$ over all the possible kernels that define the Volterra polynomial V_n , such that the minimization (Equation 9.24) is achieved.

Note that, if we view the optimal solution V_n^* as the projection of \mathcal{F} onto the $(n + 1)$ -dimensional subspace of H , then this least-squares minimization is indeed a projection approximation. It is then clear, even from the Hilbert space geometry (see Figure 9.5), that such an optimal solution, called a best approximant, always exists due to the norm-completeness of Hilbert space and is unique by the convexity of inner product space.

As a second example, let H be a Hilbert space consisting of all the linear and nonlinear systems that have an n th-order Taylor series representation of the form

$$P_n(\cdot) = \sum_{k=0}^n \alpha_k(t) M_k(\cdot) = \alpha_0(t) + \alpha_1(t)(\cdot)(t) + \dots + \alpha_n(t)(\cdot)^n(t) \tag{9.25}$$

where

$M_k(\cdot) := (\cdot)^k$ is the monomial operator of degree k

$\{\alpha_k\}_{k=0}^n$ are continuous real-valued functions satisfying certain conditions arising from some basic properties of both the domain and the range of the operator

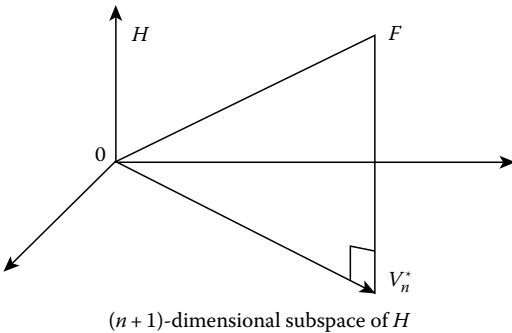


FIGURE 9.5 Projection in a Hilbert space.

Suppose that the monomial operators $\{M_k\}_{k=0}^{\infty}$ are orthogonal under the inner product of H . Given an l th-order polynomial operator P_l with $\alpha_l(t) \neq 0$ almost everywhere, if for a fixed integer $n < l$ we want to find an n th-order polynomial operator P_n^* of the form (Equation 9.25) from H , such that

$$\|P_l - P_n^*\|_H = \inf_{P_n \in H} \|P_l - P_n\|_H \tag{9.26}$$

then we have a best approximation problem in the least-squares sense. To solve this optimization problem is to find the best coefficient

functions $\{\alpha_k(t)\}_{k=0}^n$ over all possible functions that define the polynomial operator P_n . Again, because the optimal solution is the projection of P_l onto the $(n + 1)$ -dimensional subspace H of a Hilbert space to which P_l belongs, it always exists and is unique.

We now state a general result of least-squares approximation for systems, which is a straightforward generalization of the classical result of least-squares approximation for functions [22,36].

THEOREM 9.4

Let H be a Hilbert space of nonlinear operators, and let H_n be its n -dimensional subspace. Then, given an $\mathcal{F} \in H$, the least-squares approximation problem

$$\|\mathcal{F} - \mathcal{N}_n^*\|_H = \inf_{\mathcal{N}_n \in H_n} \|\mathcal{F} - \mathcal{N}_n\|_H$$

is always uniquely solvable, with the optimal solution given by

$$\mathcal{N}^*(\cdot) = \sum_{k=1}^n \langle \mathcal{F}, h_k \rangle_H h_k(\cdot)$$

where $\{h_k\}_{k=1}^n$ is an orthonormal basis of H_n .

A more general setting is to replace the Hilbert space H by a Banach space (a complete normed linear space, such as L_1 and L_∞ , which may not have an inner product structure). This extension includes the Hilbert space setting as a special case, but generally does not have so many special features. Even the existence and uniqueness of best approximants cannot be taken for granted in general—not even for the simpler case of best approximation of real-valued functions—if a Banach (non-Hilbert) space is considered [73]. Nevertheless, the following result is still convenient to use [22].

THEOREM 9.5

Let B be a uniformly convex Banach space and Ω be a closed convex set in B . Then, for any given $\mathcal{F} \in B$, the optimal approximation problem

$$\|\mathcal{F} - \omega^*\|_B = \inf_{\omega \in \Omega} \|\mathcal{F} - \omega\|_B$$

has a unique solution.

Here, a space (or subset) B is said to be uniformly convex if, for any $\varepsilon > 0$, there exists a $\delta > 0$ such that $\|f\|_B = \|g\|_B = 1$ and $\|1/2(f+g)\|_B > 1 - \delta$ together imply $\|f - g\|_B < \varepsilon$. Geometrically, a disk is uniformly convex while a triangle is only convex, but not uniformly so. It is then intuitively clear that for a given point outside (or inside) a disk, only a single point exists in the disk that has the shortest distance to the given point. However, this is not always true for a nonuniform case. In fact, a best approximation problem in the general Banach space setting has either a unique solution or has infinitely many solutions (if it is solvable), as can be seen from the next result [32].

THEOREM 9.6

Let Ω be a closed convex set in a Banach space B , and ω_1^* and ω_2^* be two optimal solutions of the best approximation problem

$$\left\| \mathcal{F} - \omega^* \right\|_B = \inf_{\omega \in \Omega} \left\| \mathcal{F} - \omega \right\|_B$$

Then, any convex combination of ω_1^* and ω_2^* in the form

$$\omega^* = a\omega_1^* + (1 - a)\omega_2^*, \quad 0 \leq a \leq 1$$

is also an optimal solution of the problem.

Usually, a best approximant (if it exists) for an optimal approximation problem in a Banach space is also called a (minimal) projection of the given operator from a higher-dimensional subspace onto a lower-dimensional subspace. In this extension, the projection has no simple geometric meaning of “orthonormality” due to the lack of an inner product structure. However, a projection operator with a unity norm in the Banach space setting is a natural generalization of the orthonormal projection in the Hilbert space framework.

9.3.1.2 Min–Max (Uniform) Approximation

It is clear from the least-squares approximation formulation that if the given nonlinear representation (operator) \mathcal{F} and the lower-order approximant (used to approximate \mathcal{F}) do not have the same structure (the same type of series), then the least-squares approximation cannot be applied directly or efficiently.

To introduce another approach, we first recall that for two given normed linear spaces X and Y and for a given bounded subset Ω of X , with $0 \in \Omega$, the operator norm of a nonlinear operator $\mathcal{N}: \Omega \rightarrow Y$ satisfying $\mathcal{N}(0) = 0$, can be defined as

$$\left\| \mathcal{N} \right\| = \sup_{\substack{x, y \in \Omega \\ x \neq y}} \frac{\left\| \mathcal{N}(x) - \mathcal{N}(y) \right\|_Y}{\left\| x - y \right\|_X} \quad (9.27)$$

Thus, given a norm-bounded nonlinear operator \mathcal{F} , representing a given physical system, we may consider the problem of finding another norm-bounded nonlinear operator \mathcal{N}^* from a certain class 1 of desired nonlinear operators (systems), not necessarily having the same structure as \mathcal{F} , to best approximate \mathcal{F} in the sense that

$$\left\| \mathcal{F} - \mathcal{N}^* \right\| = \inf_{\mathcal{N} \in \mathcal{N}} \left\| \mathcal{F} - \mathcal{N} \right\| \quad (9.28)$$

For example, \mathcal{N} can be the family of n th-order Volterra polynomials or n th-order polynomial operators discussed previously. Commonly used function spaces X and Y include the space of all continuous functions, the standard L_p space (or l_p for the discrete case), and the Hardy space H_p (for complex-variable functions [32]), with $1 \leq p \leq \infty$.

Because the nonlinear operator norm defined by Equation 9.27 is a sup (max) norm and this optimization is an inf (min) operation, the best approximation problem (Equation 9.28) is called a min–max approximation. Note also that because the nonlinear operator norm (Equation 9.27) is defined over all the bounded inputs in the set Ω , this approximation is uniform, and thus independent of each individual input function of the set Ω . For this reason, this approximation is also called a uniform approximation, indicating that the best approximant is the optimal solution over *all* input functions.

It should be noted that both existence and uniqueness of best approximation solutions to the min–max approximation problem (Equation 9.28) must be investigated according to the choice of the operator family N and the I–O spaces X and Y , which generally cannot be taken for granted, as previously discussed.

An important and useful class of nonlinear operators which can be put into a Banach space setting with great potential in systems and control engineering is the family of generalized Lipschitz operators [45]. To introduce this concept, we first need some notation. Let X be a Banach space of real-valued functions defined on $[0, \infty)$ and, for any $f \in X$ and any $T[0, \infty)$, define

$$[f]_T(t) = \begin{cases} f(t), & t < T \\ 0, & t > T \end{cases}$$

Then, form a normed linear space X^e , called the extended linear space associated with X , by

$$X^e = \left\{ f \in X \mid \left\| [f]_T \right\|_X < \infty, \forall T < \infty \right\}$$

For a subset $D \subseteq X^e$, any (linear or nonlinear) operator $\mathcal{G}: D \rightarrow Y^e$ satisfying

$$\left\| [\mathcal{G}(x_1)]_T - [\mathcal{G}(x_2)]_T \right\|_Y \leq L \left\| [x_1]_T - [x_2]_T \right\|_X, \quad \forall x_1, x_2 \in D, \quad \forall T \in [0, \infty)$$

for some constant $L < \infty$, is called a generalized Lipschitz operator defined on D . The least of such constants L is given by the seminorm of the operator \mathcal{G} :

$$\|\mathcal{G}\|: \sup_{T \in [0, \infty)} \sup_{\substack{x_1, x_2 \in D \\ [x_1]_T \neq [x_2]_T}} \frac{\left\| [\mathcal{G}(x_1)]_T - [\mathcal{G}(x_2)]_T \right\|_Y}{\left\| [x_1]_T - [x_2]_T \right\|_X}$$

and the operator norm of \mathcal{G} is defined via this seminorm by

$$\|\mathcal{G}\|_{\text{Lip}} = \|\mathcal{G}(x_0)\|_Y + \|\mathcal{G}\|$$

for an arbitrarily chosen and fixed $x_0 \in D$. The following result has been established [45].

THEOREM 9.7

The family of generalized Lipschitz operators

$$\text{Lip}(D, Y^e) = \{ \mathcal{G}: D \subseteq X^e \rightarrow Y^e \mid \|\mathcal{G}\|_{\text{Lip}} < \infty \text{ on } D \}$$

is a Banach space.

Based on this theorem, a best approximation problem for generalized Lipschitz operators can be similarly formulated, and many fundamental approximation results can be obtained. In addition, generalized Lipschitz operators provide a self-unified framework for both left and right coprime factorization representations of nonlinear feedback systems. Under this framework, the overall closed-loop system shown in Figure 9.4 can have a causal, stable, and well-posed coprime factorization representation, which can be applied to optimal designs such as tracking and disturbance rejection [45].

We now discuss briefly a different kind of min–max (uniform) approximation: the best Hankel norm approximation, where the norm (Equation 9.27) is replaced by the operator norm of a Hankel operator defined as follows [32,77]. Consider, for instance, the transfer function

$$H(z) = \alpha_0 + \alpha_1 z^{-1} + \alpha_2 z^{-2} + \dots$$

of a discrete time linear time-invariant system. The Hankel operator associated with this series is defined as the infinite matrix

$$\Gamma_\alpha := \left[\alpha_{|i-j|} \right] = \begin{bmatrix} \alpha_0 & \alpha_1 & \alpha_2 & \dots \\ \alpha_1 & \alpha_2 & \dots & \\ \alpha_2 & \dots & & \\ \vdots & & & \end{bmatrix}$$

which is a linear operator on a normed linear space of sequences. The operator norm of Γ_α over the l_2 space is called the Hankel norm of Γ_α .

One important feature of the Hankel operators is reflected in the following theorem [32,77].

THEOREM 9.8

An infinite Hankel matrix has a finite rank iff its corresponding functional series is rational (it sums up to a rational function); and this is true iff the rational series corresponds to a finite-dimensional bilinear system.

Another useful property of Hankel operators in system approximation is represented in the following theorem [28].

THEOREM 9.9

The family of compact Hankel operators is an M -ideal in the space of Hankel operators that are defined on a Hilbert space of real-valued functions.

Here, a compact operator is one that maps bounded sets to compact closures and an M -ideal is a closed subspace X of a Banach space Z such that X^\perp , the orthogonal complementary subspace of X in Z , is the range of the projection P from the dual space Z^* to X^\perp that has the property

$$\|f\| = \|P(f)\| + \|f - P(f)\| \quad \forall f \in Z^*$$

The importance of the M -ideal is that it is a proximal subspace with certain useful approximation characteristics, where the proximal property is defined as follows. Let $L(X)$ and $C(X)$ be the classes of bounded linear operators and compact operators, respectively, both defined on a Banach space X . If every $\mathcal{L} \in L(X)$ has at least one best approximant from $C(X)$, then $C(X)$ is said to be proximal in $L(X)$. A typical result would be the following: for any $1 < p < \infty$, $C(l_p)$ is proximal in $L(l_p)$. However, $C(X)$ is not proximal in $L(X)$ if $X = C[a, b]$, the space of continuous functions defined on $[a, b]$, or $X = L_p[a, b]$ for all $1 < p < \infty$ except $p = 2$.

9.3.2 Best (Uniform) Approximation of Signals (Functions)

Best approximations of signals for circuits and systems are also important. For example, two (different) systems (e.g., circuits) are considered to be equivalent over a set Ω of admissible input signals iff the same input from Ω yields the same outputs through the two systems. Thus, the problem of using a system to best approximate another may be converted, in many cases, to the best approximation problem for their output signals.

A signal is a function of time, usually real valued and one-dimensional. The most general formulation for best approximation of functions can be stated as follows. Let X be a normed linear space of real-valued functions and Ω be a subset of X . For a given f in X but not in Ω , find a $g^* \in \Omega$ such that

$$\|f - g^*\|_X = \inf_{g \in \Omega} \|f - g\|_X \quad (9.29)$$

In particular, if $X = L_\infty$, l_∞ , or H_∞ , the optimal solution is the best result for the worst case.

If such a g^* exists, then it is called a best approximant of f from the subset Ω . In particular, if $\Omega_1 \subset \Omega_2 \subset \dots$ is a sequence of subspaces in X , such that $\bigcup \Omega_n = X$, an important practical problem is to find a sequence of best approximants $g_n^* \in \Omega_n$ satisfying the requirement (Equation 9.29) for each $n = 1, 2, \dots$, such that $\|g_n^* - g^*\|_X \rightarrow 0$ as $n \rightarrow \infty$. In this way, for each n , one may be able to construct a simple approximant g_n^* for a complicated (even unknown) function f , which is optimal in the sense of the min-max approximation (Equation 9.29).

Existence of a solution is the first question about this best approximation. The fundamental result is the following [22,36].

THEOREM 9.10

For any $f \in X$, a best approximant g^ of f in Ω always exists, if Ω is a compact subset of X ; or Ω is a finite-dimensional subspace of X .*

Uniqueness of a solution is the second question in approximation theory, but it is not as important as the existence issue in engineering applications. Instead, characterization of a best approximant for a specific problem is significant in that it is often useful for constructing a best approximant.

As a special case, the preceding best approximation reduces to the least-squares approximation if X is a Hilbert space. The basic result is the following (compare it with Theorem 9.4, and see Figure 9.5).

THEOREM 9.11

Let H be a Hilbert space of real-valued functions, and let H_n be its n -dimensional subspace. Then, given an $f \in H$, the least-squares approximation problem

$$\|f - h_n^*\|_H = \inf_{h_n \in H_n} \|f - h_n\|_H$$

is always uniquely solvable, with the optimal solution given by

$$h_n^*(t) = \sum_{k=1}^n \langle f, h_k \rangle_H h_k(t)$$

where $\{h_k\}_{k=1}^n$ is an orthonormal basis of H_n .

Here, the orthonormal basis of H_n is a Chebyshev system, a system of functions which satisfy the Haar condition that the determinant of the matrix $[h_i(t_j)]$ is nonzero at n distinct points $t_1 < \dots < t_n$ in the domain. Chebyshev systems include many commonly used functions, such as algebraic and trigonometric polynomials, splines, and radial functions. Best approximation by these functions is discussed in more detail below.

We remark that the least-squares solution shown in Theorem 9.11 is very general, which includes the familiar truncations of the Fourier series [36] and the wavelet series [29] as best approximation.

9.3.2.1 Polynomial and Rational Approximations

Let π_n be the space of all algebraic polynomials $p_n(t)$ of degree not greater than n . For any continuous function $f(t)$ defined on $[a, b]$, one is typically looking for a best approximant $g_n^* p_n^* \in \pi_n$ for a fixed n , such that

$$\|f - p_n^*\|_{L_\infty[a,b]} = \min_{p_n \in \pi_n} \|f - p_n\|_{L_\infty[a,b]} \quad (9.30)$$

This is a best (min-max and uniform) algebraic polynomial approximation problem. Replacing the algebraic polynomials by the n th-order trigonometric polynomials of the form $\sum_{k=0}^n (a_k \cos(kt) + b_k \sin(kt))$ changes the problem to the best trigonometric polynomial approximation, in the same sense as the best algebraic polynomial approximation, for a given function $f \in C[-\pi, \pi]$. This can be much further extended to any Chebyshev system, such as the radial basis functions and polynomial spline functions, which are discussed later. According to the second part of Theorem 9.10, the best uniform polynomial approximation problem (Equation 9.30) always has a solution that, in this case, is unique. Moreover, this best approximant is characterized by the following important sign-alternation theorem. This theorem is also valid for the best uniform approximation from any other Chebyshev system [22,36].

THEOREM 9.12

The algebraic polynomial p_n^* is a best uniform approximant of $f \in C[a, b]$ from π_n iff there exist $n + 2$ points $a \leq t_0 < \dots < t_{n+1} \leq b$ such that

$$f(t_k) - p_n^*(t_k) = c(-1)^k \|f - p_n^*\|_{L_\infty[a,b]}, \quad k = 0, 1, \dots, n + 1$$

where $c = 1$ or -1 .

An efficient Remes (exchange) algorithm is available for constructing such a best approximant [79].

Another type of function is related to algebraic polynomials: the algebraic rational functions of the form $r_{n,m}(t) = p_n(t)/q_m(t)$, which has finite values on $[a, b]$ with coprime $p_n \in \pi_n$ and $q_m \in \pi_m$. We denote by $R_{n,m}$ the family of all such rational functions, or a subset of them, with fixed integers $n \geq 0$ and $m \geq 1$. Although $R_{n,m}$ is not a compact set or a linear space, the following result can be established [22].

THEOREM 9.13

For any given function $f \in C[a, b]$, there exists a unique $r_{n,m}^*(t) \in R_{n,m}$ such that

$$\|f - r_{n,m}^*\|_{L_\infty[a,b]} = \inf_{r_{n,m} \in R_{n,m}} \|f - r_{n,m}\|_{L_\infty[a,b]} \quad (9.31)$$

The optimal solution $r_{n,m}^*(t)$ of Equation 9.31 is called the best uniform rational approximant of $f(t)$ on $[a, b]$ from $R_{n,m}$.

Note that the unique best rational approximant may have different expressions unless it is coprime, as assumed previously. The following theorem [22] characterizes such a best approximant, in which we use $d(p_n)$ to denote the actual degree of p_n , $0 \leq d(p_n) \leq n$.

THEOREM 9.14

A rational function $r_{n,m}^* = p_n^*/q_m^*$ is a best uniform approximant of $f \in C[a, b]$ from $R_{n,m}$ iff there exist s points $a \leq t_1 < \dots < t_s \leq b$, with $s = 2 + \min\{n + d(q_m), m + d(p_n)\}$, such that

$$f(t_k) - r_{n,m}^*(t_k) = c(-1)^k \|f - r_{n,m}^*\|_{L_\infty[a,b]}, \quad k = 1, \dots, s$$

where $c = 1$ or -1 .

The Remes (exchange) algorithm [79] also can be used for constructing a best rational approximant.

An important type of function approximation, which utilizes rational functions, is the Padé approximation. Given a formal power series of the form

$$f(t) = c_0 + c_1 t + c_2 t^2 + \dots, \quad t \in [-1, 1]$$

not necessarily convergent, the question is to find a rational function $p_n(t)/q_m(t)$, where n and m are both fixed, to best approximate $f(t)$ on $[-1, 1]$, in the sense that

$$\left| f(t) - \frac{p_n(t)}{q_m(t)} \right| \leq c |t|^l, \quad t \in [-1, 1] \quad (9.32)$$

for a “largest possible” integer l . It turns out that normally the largest possible integer is $l = n + m + 1$. If such a rational function exists, it is called the $[n, m]$ th-order Padé approximant of $f(t)$ on $[-1, 1]$. The following result is important [22].

THEOREM 9.15

If $f(t)$ is $(n + m + 1)$ times continuously differentiable in a neighborhood of $t = 0$, then the $[n, m]$ th-order Padé approximant of $f(t)$ exists, with $l > n$. If $l \leq n + m + 1$, then the coefficients $\{a_k\}_{k=0}^n$ and $\{b_k\}_{k=0}^m$ of $p_n(t)$ and $q_m(t)$ are determined by the following linear system of algebraic equations:

$$\sum_{j=0}^i \frac{f^{(j)}(0)}{j!} b_{i-j} = a_i, \quad i = 0, 1, \dots, l - 1$$

with $a_{n+j} = b_{m+j} = 0$ for all $j = 1, 2, \dots$. Moreover, if p_n/q_m is the $[n, m]$ th-order Padé approximant of $f(t) = \sum_{k=0}^{\infty} \{a_k\}_{k=0}^n f_k t^k$, then the approximation error is given by

$$\left| f(t) - \frac{p_n(t)}{q_m(t)} \right| = \sum_{k=n+1}^{\infty} \left(\sum_{j=0}^m f_{k-j} b_j \right) \frac{t^k}{q_m(t)}, \quad t \in [-1, 1]$$

Padé approximation can be extended from algebraic polynomials to any other Chebyshev systems [22].

9.3.2.2 Approximation via Splines and Radial Functions

Roughly speaking, spline functions, or simply splines, are piecewise smooth functions that are structurally connected and satisfy some special properties. The most elementary and useful splines are polynomial splines, which are piecewise algebraic polynomials, usually continuous, with a certain degree of smoothness at the connections. More precisely, let

$$a = t_0 < t_1 < \cdots < t_n < t_{n+1} = b$$

be a partition of interval $[a, b]$. The polynomial spline of degree m with knots $\{t_k\}_{k=1}^n$ on $[a, b]$ is defined to be the piecewise polynomial $g_m(t)$ that is a regular algebraic polynomial of degree m on each subinterval $[t_k, t_{k+1}]$, $k=0, \dots, n$, and is $(m-1)$ times continuously differentiable at all knots [41,88]. We denote the family of these algebraic polynomial splines by $S_m(t_1, \dots, t_n)$, which is an $(n+m+1)$ -dimensional linear space.

Given a continuous function $f(t)$ on $[a, b]$, the best uniform spline approximation problem is to find a $g_m^* \in S_m(t_1, \dots, t_n)$ such that

$$\|f - g_m^*\|_{L_\infty[a,b]} = \inf_{g_m \in S_m} \|f - g_m\|_{L_\infty[a,b]} \quad (9.33)$$

According to the second part of Theorem 9.10, this best uniform approximation problem always has a solution. A best spline approximant can be characterized by the following sign-alteration theorem [72], which is a generalization of Theorem 9.12, from polynomials to polynomial splines.

THEOREM 9.16

The polynomial spline $g_m^(t)$ is a best uniform approximant of $f \in C[a, b]$ from $S_m(t_1, \dots, t_n)$ iff there exists a subinterval $[t_r, t_{r+s}] \subset [a, b]$, with integers r and $s \leq 1$, such that the maximal number γ of sign-alteration points on this subinterval $[t_r, t_{r+s}]$, namely,*

$$f(t_k) - g_m(t_k) = c(-1)^k \|f - g_m\|_{L_\infty[a,b]}, \quad t_k \in [t_r, t_{r+s}], \quad k = 1, \dots, \gamma$$

satisfies $\gamma \geq m + s + 1$, where $c = 1$ or -1 .

Polynomial splines can be used for least-squares approximation, just like regular polynomials, if the L_∞ -norm is replaced by the L_2 -norm in Equation 9.33. For example, B-splines, i.e., basic splines with a compact support, are very efficient in least-squares approximation. The spline quasi-interpolant provides another type of efficient approximation, which has the following structure

$$g_m(t) = \sum_k f(t_k) \phi_k^m(t) \quad (9.34)$$

and can achieve the optimal approximation order, where $\{\phi_k^m\}$ is a certain linear combination of B-splines of order m [18].

Spline functions have many variants and generalizations, including natural splines, perfect splines, various multivariate splines, and some generalized splines defined by linear ordinary or partial differential operators with initial-boundary conditions [27,41,42,44,88].

Splines are essentially local, in the sense of having compact supports, perhaps with the exception perhaps of the thin-plate splines [94], where the domains do not have a boundary.

Radial functions are global, with the property $\phi(r) \rightarrow \infty$ as $r \rightarrow \infty$ and, normally, $\phi(0) = 0$. Well-conditioned radial functions include $|r|^{2m+1}$, $r^{2m} \log(r)$, $(r^2 + a^2)^{\pm 1/2}$, $0 < a \ll 1$, etc. [80]. Many radial functions are good candidates for modeling nonlinear circuits and systems [63,64]. For example, for l distinct points $\mathbf{t}_1, \dots, \mathbf{t}_l$ in R^n , the radial functions $\{\phi(|\mathbf{t} - \mathbf{t}_k|)\}_{k=1}^l$ are linearly independent, and thus the minimization

$$\min_{\{c_k\}} \left| f(\mathbf{t}) - \sum_{k=1}^l c_k \phi(|\mathbf{t} - \mathbf{t}_k|) \right|^2 \quad (9.35)$$

at some scattered points can yield a best least-squares approximant for a given function $f(t)$, with some especially desirable features [81]. In particular, an affine plus radial function in the form

$$\mathbf{a} \cdot \mathbf{t} + b + \sum_{k=1}^l c_k \phi(|\mathbf{t} - \mathbf{t}_k|), \quad \mathbf{t} \in R^n \quad (9.36)$$

where \mathbf{a} , b , $\{c_k\}_{k=1}^l$ are constants, provides a good modeling framework for the canonical piecewise linear representation (Equation 9.12) of a nonlinear circuit [63].

9.3.2.3 Approximation by Means of Interpolation

Interpolation plays a central role in function approximation theory. The main theme of interpolation is this: suppose that an unknown function exists for which we are given some measurement data such as its function values, and perhaps some values of its derivatives, at some discrete points in the domain. How can we use this information to construct a new function that interpolates these values at the given points as an approximant of the unknown function, preferably in an optimal sense? Constructing such a function, called an interpolant, is usually not a difficult problem, but the technical issue that remains is what kind of functions should be used as the interpolant so that a certain meaningful and optimal objective is attained?

Algebraic polynomial interpolation is the simplest approach for the following Lagrange interpolation problem [22,36].

THEOREM 9.17

For arbitrarily given $n + 1$ distinct points $0 \leq t_0 < t_1 < \dots < t_n \leq 1$ and $n + 1$ real values v_0, v_1, \dots, v_n , there exists a unique polynomial $p_n(t)$ of degree n , which satisfies

$$p_n(t_k) = v_k, \quad k = 0, 1, \dots, n$$

This polynomial is given by

$$p_n(t) = \sum_{k=0}^n v_k L_k(t)$$

with the Lagrange basis polynomials

$$L_k(t) := \frac{(t - t_0) \cdots (t - t_{k-1})(t - t_{k+1})(t - t_n)}{(t_k - t_0) \cdots (t_k - t_{k-1})(t_k - t_{k+1})(t_k - t_n)}, \quad k = 0, \dots, n$$

Moreover, if $f(t)$ is l ($\leq n + 1$) times continuously differentiable on $[a, b]$, then the interpolation error is bounded by

$$\|f - p_n\|_{L_\infty[0,1]} \leq \frac{1}{n!} \|f^{(l)}\|_{L_\infty[0,1]} \|h\|_{L_\infty[0,1]}$$

where $h(t) = \prod_{k=0}^{n-1} (t - t_k)$, and $\|h\|_{L_\infty[0,1]}$ attains its minimum at the Chebyshev points $t_k = \cos(2k + 1)\pi/2(n + 1)$, $k = 0, 1, \dots, n$.

Note that the set $\{L_k(t)\}_{k=0}^n$ is a Chebyshev system on the interval $[t_0, t_n]$, which guarantees the existence and uniqueness of the solution. This set of basis functions can be replaced by any other Chebyshev system to obtain a unique interpolant.

If not only functional values, but also derivative values, are available and required to be interpolated by the polynomial,

$$p_n^{(i_k)}(t_k) = v_{k,i_k} \quad i_k = 0, \dots, m_k, \quad k = 0, 1, \dots, n$$

then we have a Hermite interpolation problem. An algebraic polynomial of degree $d = n + \sum_{k=0}^n m_k$ always exists as a Hermite interpolant. An explicit closed-form formula for the Hermite interpolant also can be constructed. For example, if only the functional values $\{v_k\}_{k=0}^n$ and the first derivative values $\{w_k\}_{k=0}^n$ are given and required to be interpolated, then the Hermite interpolant is given by

$$p_{2n}(t) = \sum_{k=0}^n \{v_k A_k(t) + w_k B_k(t)\}$$

where, with notation $L'_k(t_k) := (d/dt)L_k(t)|_{t=t_k}$,

$$A_k(t) = [1 - 2(t - t_k)L'_k(t_k)]L_k^2(t) \quad \text{and} \quad B_k(t) = (t - t_k)L_k^2(t)$$

in which $L_k(t)$ are Lagrange basis polynomials, $k = 0, 1, \dots, n$.

However, if those derivative values are not consecutively given, we have a Hermite–Birkhoff interpolation problem, which is not always uniquely solvable [61].

The preceding discussions did not take into consideration any optimality. The unique algebraic polynomial interpolant obtained previously may not be a good result in many cases. A well-known example is provided by Runge, in interpolating the continuous and smooth function $f(t) = 1/(1 + 25t^2)$ at $n + 1$ equally spaced points on the interval $[-1, 1]$. The polynomial interpolant $p_n(t)$ shows extremely high oscillations near the two end-points ($|t| > 0.726, \dots$). Hence, it is important to impose an additional optimality requirement (e.g., a uniform approximation requirement) on the interpolant. In this concern, the following result is useful [36].

THEOREM 9.18

Given a continuous function $f \in C[-1, 1]$, let $\{t_k\}_{k=1}^n$ be the Chebyshev points on $[-1, 1]$; namely, $t_k = \cos((2k - 1)\pi/(2n))$, $k = 1, \dots, n$. Let also $P_{2n-1}(t)$ be the polynomial of degree $2n - 1$ that satisfies the following special Hermite interpolation conditions: $P_{2n-1}(t_k) = f(t_k)$ and $P'_{2n-1}(t_k) = f'(t_k)$ and $P'_{2n-1}(t_k) = 0$, $k = 1, \dots, n$. Then, the interpolant $P_{2n}(t)$ has the uniform approximation property

$$\|f - P_{2n-1}\|_{L_\infty[-1,1]} \rightarrow 0 \quad \text{as} \quad n \rightarrow \infty$$

Because polynomial splines are piecewise algebraic polynomials, similar uniform approximation results for polynomial spline interpolants may be established [41,72,88].

Finally, a simultaneous interpolation and uniform approximation for a polynomial of a finite (and fixed) degree may be very desirable in engineering applications. The problem is that given and $f \in C[a, b]$ with $n + 1$ points $a \leq t_0 < t_1 < \dots < t_n \leq b$ and a given $\varepsilon > 0$, find a polynomial $p(t)$ of finite degree (usually, larger than n) that satisfies both

$$\|f - p\|_{L_\infty[a,b]} < \varepsilon \quad \text{and} \quad p(t_k) = f(t_k), \quad k = 0, 1, \dots, n$$

The answer to this question is the Walsh theorem, which states that this is always possible, even for complex polynomials [36]. Note that natural splines can also solve this simultaneous interpolation and uniform-approximation problem.

9.3.3 Best Approximation of Linear Functionals

As already mentioned, a functional is a mapping that maps functions to values. Definite integrals, derivatives evaluated at some points, and interpolation formulas are good examples of linear functionals.

The best approximation problem for a given bounded linear functional, L , by a linear combination of n independent and bounded linear functionals L_1, \dots, L_n , all defined on the same normed linear space X of functions, can be similarly stated as follows: determine n constant coefficients $\{a_k^*\}_{k=1}^n$ such that

$$\left\| L - \sum_{k=1}^n a_k^* L_k \right\|_{X^*} = \min_{\{a_k\}} \left\| L - \sum_{k=1}^n a_k L_k \right\|_{X^*} \quad (9.37)$$

where X^* is the dual space of X , which is also a normed linear space. A basic result is described by the following theorem [36].

THEOREM 9.19

If X is a Hilbert space, then the best approximation problem (Equation 9.37) is uniquely solvable. Moreover, if r and $\{r_k\}_{k=1}^n$, are the functional representors of L and $\{L_k\}_{k=1}^n$, respectively, then

$$\left\| r - \sum_{k=1}^n a_k r_k \right\|_{X^*} = \min \Rightarrow \left\| L - \sum_{k=1}^n a_k L_k \right\|_{X^*} = \min$$

It is important to note that for linear functionals, we have an interpolation problem: given bounded linear functionals L and $\{L_k\}_{k=1}^n$, all defined on a normed linear space X , where the last n functionals are linearly independent on X , and given also n points $x_k \in X$, $k = 1, \dots, n$, determine n constant coefficients $\{a_k\}_{k=1}^n$, such that

$$\sum_{k=1}^n a_k L_k(x_i) = L(x_i), \quad i = 1, \dots, n$$

Obviously, this problem is uniquely solvable. Depending on the specific formulation of the linear functionals, a bulk of the approximation formulas in the field of numerical analysis can be derived from this general interpolation formulation.

Finally, convergence problems also can be formulated and discussed for bounded linear functionals in a manner similar to interpolation and approximation of functions. The following result is significant [36].

THEOREM 9.20

Let L and $\{L_k\}_{k=1}^{\infty}$ be bounded linear functionals defined on a Banach space X . A necessary and sufficient condition for

$$\lim_{k \rightarrow \infty} \|L_k - L\|_{X^*} = 0$$

is that $\{L_k\}_{k=1}^{\infty}$ are uniformly bounded:

$$\|L_k\|_{X^*} \leq M < \infty \quad \forall k = 1, 2, \dots$$

and there is a convergent sequence $\{x_i\}_{i=1}^{\infty} \in X$, such that

$$\lim_{k \rightarrow \infty} L_k(x_i) = L(x_i) \quad \text{for each } i = 1, 2, \dots$$

9.3.4 Artificial Neural Network for Approximation

Artificial neural networks offer a useful framework for signal and system approximations, including approximation of continuous and smooth functions of multivariables. Due to its usually multilayered structure with many weights, an artificial neural network can be “trained,” and hence has a certain “learning” capability in data processing. For this reason, artificial neural networks can be very efficient in performing various approximations. The main concern with a large-scale artificial neural network is its demand on computational speed and computer memory.

Both parametrized and nonparametrized approaches to approximations use artificial neural networks. In the parametrized approach the activation function, basic function, and network topology are all predetermined; hence, the entire network structure is fixed, leaving only a set of parameters (weights) to be adjusted to best fit the available data. In this way, the network with optimal weights becomes a best approximant, usually in the least-squares sense, to a nonlinear system. Determining the weights from the data is called a training process. Back-propagation multilayered artificial neural networks are a typical example of the parametrized framework. The nonparametrized approach requires that the activation and/or basic functions also be determined, which turns out to be difficult in general.

To illustrate how an artificial neural network can be used as a system or signal approximant, we first describe the structure of a network. The term neuron used here refers to an operator or processing unit, which maps $R^n \rightarrow R$, with the mathematical expression

$$o_i = f_a(f_b(\mathbf{i}_i, \mathbf{w}_i)) \tag{9.38}$$

where $\mathbf{i}_i = [i_1, \dots, i_n]^T$ is the input vector, $\mathbf{w}_i = [w_{i1}, \dots, w_{in}]^T$ is the weight vector associated with the i th neuron, o_i the output of the i th neuron, f_a the activation function (usually sigmoidal or Gaussian), and

f_b the basic function (which can be linear, affine, or radial). For example, if an affine basic function is used, Equation 9.38 takes on the form

$$o_i = f_a(\mathbf{i}_i \cdot \mathbf{w}_i + b_i) \quad (9.39)$$

where b_i is a constant.

A fully connected feed-forward artificial neural network is generally a multi-input/multi-output network, where the output from each neuron of each layer is an input to each neuron of the next layer. Such a network, arranged in one input layer, multiple hidden layers, and one output layer, can be constructed as follows (see Figure 9.6). Suppose we have n -inputs, n_L -outputs and $L - 1$ hidden layers, and a linear basic function is used with a sigmoidal activation function $f_a(t) = \sigma(t)$:

$$\sigma(t) \rightarrow \begin{cases} 1 & \text{as } t \rightarrow +\infty \\ 0 & \text{as } t \rightarrow -\infty \end{cases}$$

Also, let $o_{l,i}$ be the output of the i th neuron at the l th layer and $w_{l,i} = [w_{l,i,1} \cdots w_{l,i,s}]^T$ be the weight vector associated with the same neuron connected to the neurons at the $(l - 1)$ st layer. Then, we have

$$o_{l,i} = \sigma \left(\sum_{j=1}^{n_l} o_{l-1,j} w_{l,i,j} + w_{l,i,0} \right) \quad (9.40)$$

Inductively, the output of the i th neuron in the last (the L th) layer is given by

$$o_{L,i} = \sigma \left(\sum_{j=1}^{n_{L-1}} w_{L,i,j} \left(\cdots \sigma \left(\sum_{q=1}^{n_i} w_{1,p,q} i_{n_0} + w_{1,p,0} \right) + w_{2,p,0} \right) + \cdots + w_{L,i,0} \right) \quad (9.41)$$

where $i = 1, \dots, n_L$.

The following best uniform approximation property of an artificial neural network is a fundamental result in neural-network approximation [35].

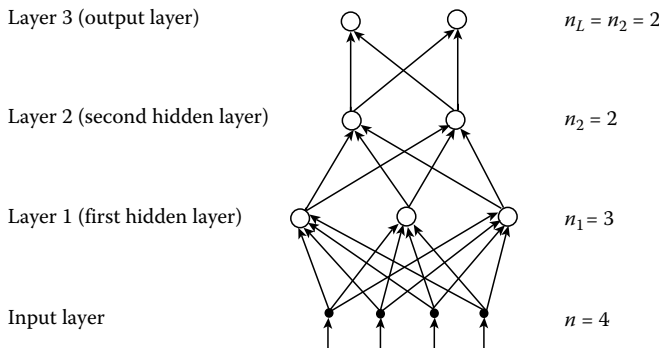


FIGURE 9.6 A two-hidden layer, feed-forward artificial neural network.

THEOREM 9.21

Let $f(t)$ be a continuous function defined on a compact subset $\Omega \subset R^n$. Then, for any $\varepsilon > 0$, there exists an integer $m \geq 1$ and real parameters $\{c_k, w_{ki}, b_k\}_{k=1}^m$ such that using any nonconstant, bounded, and monotonically increasing continuous function f_a as the activation function, the artificial neural network can uniformly approximate f on Ω , in the sense that

$$\|f - N\|_{L_\infty(\Omega)} < \varepsilon$$

where the network has the form

$$N(\mathbf{t}) = \sum_{k=1}^m c_k f_a \left(\sum_{i=1}^n w_{ki} t_i + b_k \right), \quad \mathbf{t} = [t_1 \cdots t_n]^T \in \Omega$$

Neural networks can also provide approximation for a mapping together with its derivatives [52]. On the other hand, neural networks can provide localized approximation, which is advantageous in that if a certain portion of the data is perturbed, only a few weights in the network need to be retrained. It was demonstrated that a single hidden layered network cannot provide localized approximation of continuous functions on any compact set of a Euclidean space with dimension higher than one; however, two hidden layers are sufficient for the purpose [33].

As mentioned previously, the basic function f_b in a network need not be linear. An artificial neural network, using a radial function for f_b , can also give very good approximation results [76]. Also, as a system approximation framework, stability of a network is very important [68]. Finally, a major issue that must be addressed in designing a large-scale network is the computer memory, which requires some special realization techniques [67].

9.4 Identification

System identification is a problem of finding a good mathematical model, preferably optimal in some sense, for an unknown physical system, using some available measurement data. These data usually include system outputs and sometimes also inputs. Very often, the available data are discrete, but the system to be identified is continuous [97].

A general formulation of the system identification problem can be described as follows. Let S be the family of systems under consideration (linear or nonlinear, deterministic or stochastic, or even chaotic), with input u and output γ , and let $R_{(u,\gamma)}$ be the set of I-O data. Define a mapping $M: S \rightarrow R_{(u,\gamma)}$. Then, a system $\mathcal{F} \in S$ is said to be (exactly) identifiable if the mapping M is invertible, and the problem is to find the $\mathcal{F} = M^{-1}(\tilde{u}, \tilde{\gamma})$ using the available data $(\tilde{u}, \tilde{\gamma}) \in R_{(u,\gamma)}$. Here, how to define the mapping M , linear or not, is the key to the identification problem. Usually, we also want M^{-1} to be causal for the implementation purpose.

The first question about system identification is of course the identifiability [82]. Not all systems, not even linear deterministic systems, are exactly identifiable [21]. Because many physical systems are not exactly identifiable, system identification in a weaker sense is more realistic.

Suppose that some inputs and their corresponding outputs of an unknown system, \mathcal{S}_1 , are given. We want to identify this unknown system by an approximate model, \mathcal{S}_2 , using the available I-O data, such that the corresponding outputs produced by any input through \mathcal{S}_1 and \mathcal{S}_2 , respectively, are “very close” under certain meaningful measure. If the structure of \mathcal{S}_1 (hence, \mathcal{S}_2) is known *a priori*, then what we need is to identify some system parameters. If the structure of \mathcal{S}_1 is not clear, the task becomes much more difficult because we must determine what kind of model to choose in approximating the unknown system [50]. This includes many crucial issues such as the linearity and dimension (or order) of the

model used. In particular, if the system is nonlinear and contains uncertainties, special techniques from set-valued mapping and differential inclusion theories may be needed [58].

Usually, the basic requirement is that \mathcal{S}_2 should be a best approximant of \mathcal{S}_1 from a desired class of simple and realizable models under a suitably chosen criterion. For example, the least-squares operator approximation discussed previously can be thought of as an identification scheme. For this reason, identification in the weak sense is traditionally considered to be one of the typical best approximation problems in mathematics. If a minimal, worst-case model-matching error bound is required, the approximation is known as the optimal recovery problem, for either functions or functionals [65,66], or for operators [15,45]. In system engineering it usually refers to system identification or reconstruction, with an emphasis on obtaining an identified model or a reconstruction scheme.

Generally speaking, system identification is a difficult problem, often leading to nonunique solutions when it is solvable. This is typically true for nonlinear circuits and systems. In systems and control engineering, an unknown system is identified by a desired model such that they can produce “close enough” outputs from the same input, measured by a norm in the signal space, such as L_p , l_p , or H_p ($1 \leq p \leq \infty$). For dynamic systems, however, this norm-measure is generally not a good choice because one is concerned with nonlinear dynamics of the unknown system, such as limit cycles, attractors, bifurcations, and chaos. Hence, it is preferable to have an identified model that preserves the same dynamic behavior. This is a very challenging research topic; its fundamental theories and methodologies are still open for further exploration.

9.4.1 Linear Systems Identification

Compared to nonlinear systems, linear systems, either autoregressive with moving-average (ARMA) or state-space models, can be relatively easily identified, especially when the system dimension (order) is fixed. The mainstream theory of linear system identification has the following characteristics [37]:

1. The model class consists of linear, causal, stable, finite-dimensional systems with constant parameters.
2. Both system inputs and their corresponding outputs are available as discrete or continuous data.
3. Noise, if any, is stationary and ergodic (usually with rational spectral densities), white and uncorrelated with state vectors in the past.
4. Criteria for measuring the closeness in model-matching are of least-squares type (in the deterministic case) or of maximum likelihood type (in the stochastic case).
5. Large-scale linear systems are decomposed into lower-dimensional subsystems, and nonlinear systems are decomposed into linear and simple (e.g., memoryless) nonlinear subsystems.

Because for linear systems, ARMA models and state-space models are equivalent under a nonsingular linear transformation [17,32], we discuss only ARMA models here.

An (n, m, l) th-order ARMAX model (an ARMA model with exogenous noisy inputs) has the general form

$$a(z^{-1})\mathbf{y}(t) = b(z^{-1})\mathbf{u}(t)c(z^{-1})\varepsilon(t), \quad t = \dots, -1, 0, 1, \dots \quad (9.42)$$

in which z^{-1} is the time-delay operator defined by $z^{-1}\mathbf{f}(t) = \mathbf{f}(t-l)$, and

$$a(z^{-1}) = \sum_{i=0}^n A_i z^{-i}, \quad b(z^{-1}) = \sum_{j=0}^m B_j z^{-j}, \quad c(z^{-1}) = \sum_{k=1}^l C_k z^{-k}$$

with constant coefficient matrices $\{A_i\}$, $\{B_j\}$, $\{C_k\}$ of appropriate dimensions, where $A_0 = I$ (or, is nonsingular). In the ARMAX model (Equation 9.42) $\mathbf{u}(t)$, $\mathbf{y}(t)$, and $\varepsilon(t)$ are considered to be system

input, output, and noise vectors, respectively, where the input can be either deterministic or random. In particular, if $l = 0$ and $n = 0$ (or $m = 0$), then Equation 9.42 reduces to a simple moving-average (MA) (or autoregressive, AR) model. Kolmogorov [56] proved that every linear system can be represented by an infinite-order AR model. It is also true that every nonlinear system with a Volterra series representation can be represented by a nonlinear AR model of infinite order [53].

The system identification problem for the ARMAX model (Equation 9.42) can now be described as follows. Given the system I–O data $(\mathbf{u}(t), \mathbf{y}(t))$ and the statistics of $\varepsilon(t)$, determine integers (n, m, l) (system-order determination) and constant coefficient matrices $\{A_i\}$, $\{B_j\}$, $\{C_k\}$ (system-parameter identification). While many successful methods exist for system parameter identification [3,23,49,60], system order determination is a difficult problem [47].

As already mentioned, the identifiability of an unknown ARMAX model using the given I–O data is a fundamental issue. We discuss the exact model identification problem here. The ARMAX model (Equation 9.42) is said to be exactly identifiable if $(\tilde{a}(z^{-1}), \tilde{b}(z^{-1}), \tilde{c}(z^{-1}))$ is an ARMAX model with $\tilde{n} \leq n$, $\tilde{m} \leq m$, and $\tilde{l} \leq l$, such that

$$\begin{cases} [\tilde{a}(z^{-1})]^{-1} \tilde{b}(z^{-1}) = [a(z^{-1})]^{-1} b(z^{-1}) \\ [\tilde{a}(z^{-1})]^{-1} \tilde{c}(z^{-1}) = [a(z^{-1})]^{-1} c(z^{-1}) \end{cases}$$

Note that not all ARMAX models are exactly identifiable in this sense. A basic result about this identifiability is the following [21].

THEOREM 9.22

The ARMAX model (Equation 9.42) (with $t \geq 0$) is exactly identifiable iff $a(z^{-1})$, $b(z^{-1})$, and $c(z^{-1})$ have no common left factor and the rank of the constant matrix $[A_n, B_m, C_l]$, consisting of the highest-order coefficient terms in $a(z^{-1})$, $b(z^{-1})$, $c(z^{-1})$, respectively, is equal to the dimension of the system output \mathbf{y} .

Even if an unknown system is exactly identifiable and its identification is unique, how to find the identified system is still a very technical issue. For simple AR models, the well-known Levinson–Durbin algorithm is a good scheme for constructing the identified model; for MA models, one can use Trench–Zohar and Berlekamp–Massey algorithms. There exist some generalizations of these algorithms in the literature [23]. For stochastic models with significant exogenous noise inputs, various statistical criteria and estimation techniques, under different conditions, are available [82]. Various recursive least-squares schemes, such as the least-mean-square (LMS) algorithm [96], and various stochastic searching methods, such as the stochastic gradient algorithm [49], are popular. Because of their simplicity and efficiency, the successful (standard and extended) Kalman filtering algorithms [16,30] have also been widely applied in parameters identification for stochastic systems [13,17,62], with many real-world applications [92].

Finally, for linear systems, a new framework, called the behavioral approach, is proposed for mathematical system modeling and some other related topics [2,98].

9.4.2 Nonlinear Systems Identification

Identifying a nonlinear system is much more difficult than identifying a linear system in general, whether it is in the exact or in the weak sense, as is commonly known and can be seen from its information-based complexity analysis [15,45].

For some nonlinear systems with simple Volterra series representations, the least-squares approximation technique can be employed for the purpose of identification in the weak sense [8]. As a simple

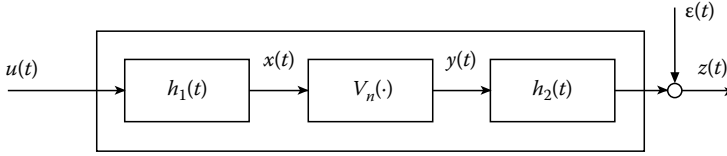


FIGURE 9.7 A cascaded linear–nonlinear system with noise input.

illustrative example, consider the cascaded nonlinear system with noise input shown in Figure 9.7. In this figure $h_1(t)$ and $h_2(t)$ are unit impulse responses of two linear subsystems, respectively, and $V_n(\cdot)$ is a memoryless nonlinear subsystem which is assumed to have an n th-order Volterra polynomial in the special form

$$y(t) = \sum_{k=1}^n c_k \int_0^t \cdots \int_0^t \phi_k(\tau_1, \dots, \tau_k) x(\tau_1) \cdots x(\tau_k) d\tau_1 \cdots d\tau_k \quad (9.43)$$

where all the Volterra kernels $\{\phi_k\}_{k=0}^n$ are assumed to be known, but the constant coefficients $\{c_k\}_{k=0}^n$ must be identified.

It is clear from Figure 9.7 that the output of the cascaded system can be expressed via convolution-type integrals as

$$z(t) = c_1 \left(\int h_2 \phi_1 h_1 u \right)(t) + \cdots + c_n \left(\int \cdots \int h_2 \phi_1 h_1 \cdots h_2 u \cdots u \right)(t) + \varepsilon(t) \quad (9.44)$$

Now, because all the integrals can be computed if the input function $u(t)$ is given, the standard least-squares technique can be used to determine the unknown constant coefficients $\{c_k\}_{k=0}^n$, using the measured system output $z(t)$.

A neural network implementation of Volterra series model identification is described in Ref. [1]. Neural network for system identification has been used in many different cases, as can also be seen from Ref. [70].

Finally, we consider one approach to nonlinear systems identification which combines the special structure of the generalized Fock space of Volterra series (Theorem 9.3) and the “training” idea from neural networks discussed previously (Theorem 9.21). For simplicity, consider the scalar nonlinear system

$$y(t) + f(y(t-1), y(t-2), \dots, y(t-n)) = u(t), \quad t = 0, 1, \dots \quad (9.45)$$

where n is a fixed integer, with the given initial conditions $y(-1) = y_1, \dots, y(-n) = y_n$. Introducing a simple notation

$$y^{t-1} = (y(t-1), \dots, y(t-n)) \quad (9.46)$$

we first rewrite this system as

$$\gamma(t) + f(\gamma^{t-1}) = u(t) \quad (9.47)$$

Then, we denote by E^n as the n -dimensional Euclidean space of continuous functions and let $u^1, \dots, u^m \in E^n$, called the domain training samples, be given data vectors that are componentwise nonzero and

distinct, namely, $u_i^k \neq u_j^k$ if $i \neq j$ for all $k = 1, \dots, m$, $1 \leq i, j \leq n$. Here, Equation 9.46 also has been used for these domain training samples. Also, let r_1, \dots, r_m be given real numbers, called the corresponding range training samples. The identification problem is to find an approximate system, $f^*(\cdot)$, among all Volterra series representations from the generalized Fock space formulated in Theorem 9.3, such that f^* maps all the domain training samples to their corresponding range training samples:

$$f^*(u^k) = r_k, \quad k = 1, \dots, m \quad (9.48)$$

and f^* has the minimum operator-norm among all such candidates. The following theorem provides an answer to this problem [45].

THEOREM 9.23

There is a unique element f^ of minimum norm in the generalized Fock space defined in Theorem 9.3, with the domain $\Omega = E^n$ therein, that satisfies the constraint (Equation 9.48). Moreover, f^* has the following expression:*

$$f^*(v) = \sum_{k=1}^m a_k K(u^k, v) \quad \forall v \in E^n$$

where $K(\cdot, \cdot)$ is the reproducing kernel defined in Theorem 9.3, and the system parameters are determined by

$$\begin{bmatrix} a_1 \\ \vdots \\ a_m \end{bmatrix} = \begin{bmatrix} K(u^1, u^1) & \cdots & K(u^1, u^m) \\ \vdots & & \vdots \\ K(u^m, u^1) & \cdots & K(u^m, u^m) \end{bmatrix}^{-1} \begin{bmatrix} r_1 \\ \vdots \\ r_m \end{bmatrix}$$

Here, it should be noted that because K is a reproducing kernel, the set of functions $\{K(u^k, \cdot)\}_{k=1}^m$ are linearly independent, so that the above inverse matrix exists.

Also, note that this system identification method can be applied to higher-dimensional systems and the continuous-time setting [45].

9.4.3 Nonlinear Dynamic Systems Identification from Time Series

Measurement (observation) data obtained from an unknown system are often available in the form of time series. There are some successful techniques for identification of linear and nonlinear systems from time series if the time series is generated from Gaussian white noise. For example, for linear systems we have the Box–Jenkins scheme and for nonlinear systems, a statistical method using a nonlinear filter [75].

Concerned with nonlinear dynamic systems, however, statistical methods and the commonly used norm-measure criterion may not be capable of identifying the system dynamics in general. This is because the main issue in this concern is the nonlinear dynamic behavior of the unknown system, such as limit cycles, attractors, bifurcations, and chaos. Hence, it is preferable that the identified model can preserve the nonlinear dynamics of the unknown system. This turns out to be a very challenging task; many fundamental theories and methodologies for this task remain to be developed.

When an unknown nonlinear dynamic system is measured to produce a set of continuous or discrete data (a time series), a natural approach for studying its dynamics from the available time series is to take an integral transform of the series, so as to convert the problem from the time domain to the frequency domain. Then, some well-developed engineering frequency domain methods can be applied to perform analysis and computation of the nonlinear dynamics [69].

One common approach formulated in the time domain is the (delay-coordinate) embedding method that can be applied to reconstruct (identify) an unknown nonlinear dynamic model from which only a set of discrete measurement data (a time series) is available.

Let us consider the problem of identifying a periodic trajectory of an unknown, nonlinear dynamic system using only an experimental time series measured from the system. Let $\{r_k\}$ be the available data. The embedding theory guarantees this can be done in the space R^m with the embedding dimension $m \geq 2n + 1$, where n is the dimension of the dynamic system [93], or $m \geq 2d_A$, where d_A is the dimension of the attractor [87]. A way to achieve this is to use the delay-coordinate technique, which approximates the unknown, nonlinear dynamics in R^m by introducing the embedding vector

$$\mathbf{r}_k = [r_k r_{k-\mu} \cdots r_{k-(m-1)\mu}]^T \quad (9.49)$$

where μ is the time-delay step. This embedding vector provides enough information to characterize the essence of the system dynamics and can be used to obtain an experimental Poincaré map, which helps in understanding the dynamics. For example, one may let the map be the equation of the first component of the vector being equal to a constant: $r_{k_i} = \text{constant}$. This procedure yields the successive points

$$\xi_i := [r_{k_i-\mu} \cdots r_{k_i-(m-1)\mu}]^T \quad (9.50)$$

at the i th piercing of the map by the trajectory (or the vector r_k), where k_i is the time index at the i th piercing. Then, one can locate the periodic trajectories of the unknown system using the experimental data [4,14]. In this approach, however, determining a reasonably good time-delay step size, i.e., the real number μ in Equation 9.49, remains an open technical problem.

Finally, we note that the embedding method discussed previously has been applied to the control of chaotic circuits and systems [19,20,74].

References

1. A. Abdulaziz and M. Farsi, Non-linear system identification and control based on neural and self-tuning control, *Int. J. Adapt. Control Signal Process.*, 7(4), 297–307, 1993.
2. A. C. Antoulas and J. C. Willems, A behavioral approach to linear exact modeling, *IEEE Trans. Autom. Control*, 38(12), 1776–1802, 1993.
3. K. J. Aström and P. Eykhoff, System identification: A survey, *Automatica*, 7, 123–162, 1971.
4. H. Atmanspacher, H. Scheingraber, and W. Voges, Attractor reconstruction and dimensional analysis of chaotic signals, in *Data Analysis in Astronomy III*, V. Di Gesù et al., Eds., New York: Plenum Press, 1988, pp. 3–19.
5. I. Baesler and I. K. Daugavet, Approximation of nonlinear operators by Volterra polynomials, *Am. Math. Soc. Transl.*, 155(2), 47–57, 1993.
6. S. P. Banks, *Mathematical Theories of Nonlinear Systems*, New York: Prentice-Hall, 1988.
7. A. Bensoussan, G. de Prado, M. C. Felfour, and S. K. Mitter, *Representation and Control of Infinite Dimensional Systems*, Boston: Birkhäuser, 1992.
8. S. A. Billings, Identification of nonlinear systems—a survey, *IEEE Proc., Pt. D*, 127, 272–285, 1980.

9. S. Boyd and L. O. Chua, Fading memory and the problem of approximating nonlinear operators with Volterra series, *IEEE Trans. Circuits Syst.*, 32(11), 1150–1161, 1985.
10. S. Boyd, L. O. Chua, and C. A. Desoer, Analytic foundations of Volterra series, *IMA J. Info. Control*, 1, 243–282, 1984.
11. D. Braess, *Nonlinear Approximation Theory*, New York: Springer-Verlag, 1986.
12. R. W. Brockett, Volterra series and geometric control theory, *Automatica*, 12, 167–176, 1976.
13. P. E. Caines, *Linear Stochastic Systems*, New York: John Wiley & Sons, 1988.
14. M. Casdagli, S. Eubank, J. D. Farmer, and J. Gibson, State space reconstruction in the presence of noise, *Physica D*, 51, 52–98, 1991.
15. G. Chen, Optimal recovery of certain nonlinear analytic mappings, *Optimal Recovery*, B. Bojanov and H. Wozniakowski, Eds., New York: Nova Science, 1992, pp. 141–144.
16. G. Chen, Ed., *Approximate Kalman Filtering*, New York: World Scientific, 1993.
17. G. Chen, G. Chen, and H. S. Hsu, *Linear Stochastic Control Systems*, Boca Raton, FL: CRC Press, 1995.
18. G. Chen, C. K. Chui, and M. J. Lai, Construction of real-time spline quasi-interpolation schemes, *Approx. Theory Appl.*, 4(4), 61–75, 1988.
19. G. Chen and X. Dong, *From Chaos to Order: Methodologies, Perspectives, and Applications*, Singapore: World Scientific, 1998.
20. G. Chen and J. Muiola, An overview of bifurcation, chaos and nonlinear dynamics in control systems, *The Franklin Institute Journal*, 331B, 819–858, 1994.
21. H. F. Chen and J. F. Zhang, On identifiability for multidimensional ARMAX model, *Acta Math. Appl. Sin.*, 9(1), 1–8, 1993.
22. E. W. Cheney, *Introduction to Approximation Theory*, New York: McGraw-Hill, 1966.
23. B. Choi, *ARMA Model Identification*, New York: Springer-Verlag, 1992.
24. L. O. Chua, The genesis of Chua's circuit, *AEU Int. J. Electr. Commun.*, 46, 187–257, 1992.
25. L. O. Chua and A. C. Deng, Canonical piecewise-linear modeling, *IEEE Trans. Circuits Syst.*, 33(5), 511–525, 1986.
26. L. O. Chua and A. C. Deng, Canonical piecewise-linear representation, *IEEE Trans. Circuits Syst.*, 35(1), 101–111, 1988.
27. C. K. Chui, *Multi-Variate Splines*, Philadelphia, PA: SIAM, 1988.
28. C. K. Chui, Approximations and expansions, in *Encyclopedia of Physical Science and Technology*, vol. 2, New York: Academic Press, 1992, pp. 1–29.
29. C. K. Chui, *An Introduction to Wavelets*, New York: Academic Press, 1992.
30. C. K. Chui and G. Chen, *Kalman Filtering with Real-Time Applications*, New York: Springer-Verlag, 1987.
31. C. K. Chui and G. Chen, *Linear Systems and Optimal Control*, New York: Springer-Verlag, 1989.
32. C. K. Chui and G. Chen, *Signal Processing and Systems Theory: Selected Topics*, New York: Springer-Verlag, 1992.
33. C. K. Chui, X. Li, and H. N. Mhaskar, Neural networks for localized approximation, *Math. Comput.*, 63, 607–623, 1994.
34. J. B. Conway, *A Course in Functional Analysis*, New York: Springer-Verlag, 1985.
35. G. Cybenko, Approximation by superposition of sigmoidal functions, *Math. Control, Signals Syst.*, 2, 303–314, 1989.
36. P. J. Davis, *Interpolation and Approximation*, New York: Dover, 1975.
37. M. Deistler, Identification of linear systems (a survey), in *Stochastic Theory and Adaptive Control*, T. E. Duncan and B. P. Duncan, Eds., New York: Springer-Verlag, 1991, pp. 127–141.
38. C. A. Desoer and M. G. Kabuli, Right factorizations of a class of time-varying nonlinear systems, *IEEE Trans. Autom. Control*, 33, 755–757, 1988.
39. C. A. Desoer and M. Vidyasagar, *Feedback Systems: Input–Output Properties*, New York: Academic Press, 1975.
40. R. A. DeVore and G. G. Lorentz, *Constructive Approximation*, New York: Springer-Verlag, 1993.

41. C. de Boor, *A Practical Guide to Splines*, New York: Springer-Verlag, 1978.
42. C. de Boor, K. Höllig, and S. Riemenschneider, *Box Splines*, New York: Springer-Verlag, 1993.
43. R. J. P. de Figueiredo and G. Chen, Optimal interpolation on a generalized Fock space of analytic functions, in *Approximation Theory VI*, C. K. Chui, L. L. Schumaker, and J. D. Ward, Eds., New York: Academic Press, 1989, pp. 247–250.
44. R. J. P. de Figueiredo and G. Chen, PDLG splines defined by partial differential operators with initial and boundary value conditions, *SIAM J. Numerical Anal.*, 27(2), 519–528, 1990.
45. R. J. P. de Figueiredo and G. Chen, *Nonlinear Feedback Control Systems: An Operator Theory Approach*, New York: Academic Press, 1993.
46. R. J. P. de Figueiredo and T. A. Dwyer, A best approximation framework and implementation for simulation of large scale nonlinear systems, *IEEE Trans. Circuits Syst.*, 27(11), 1005–1014, 1980.
47. J. G. de Gooijer, B. Abraham, A. Gould, and L. Robinson, Methods for determining the order of an autoregressive-moving average process: A survey, *Int. Statist. Rev.*, 53, 301–329, 1985.
48. M. Fliess, M. Lamnabhi, and F. L. Lagarrigue, An algebraic approach to nonlinear functional expansions, *IEEE Trans. Circuits Syst.*, 39(8), 554–570, 1983.
49. G. C. Goodwin and K. S. Sin, *Adaptive Filtering, Prediction and Control*, Englewood Cliffs, NJ: Prentice-Hall, 1984.
50. R. Haber and H. Unbehauen, Structure identification of nonlinear dynamic systems—a survey on input/output approaches, *Automatica*, 26(4), 651–677, 1990.
51. J. Hammer, Fraction representations of nonlinear systems: A simplified approach, *Int. J. Control*, 46, 455–472, 1987.
52. K. Hornik, M. Stinchcombe, and H. White, Universal approximation of an unknown mapping and its derivatives using multilayer feed-forward networks, *Neural Networks*, 3, 551–560, 1990.
53. L. R. Hunt, R. D. DeGroat, and D. A. Linebarger, Nonlinear AR modeling, *Circuits Syst. Signal Process.*, 14(5), 689–705, 1995.
54. A. Isidori, *Nonlinear Control Systems*, New York: Springer-Verlag, 1985.
55. C. Kahlert and L. O. Chua, A generalized canonical piecewise-linear representation, *IEEE Trans. Circuits Syst.*, 37(3), 373–383, 1990.
56. A. N. Kolmogorov, Interpolation and extrapolation von stationären zufälligen folgen, *Bull. Acad. Sci. USSR Ser. Math.*, 5, 3–14, 1941.
57. S. Y. Kung, *Digital Neural Networks*, Englewood Cliffs, NJ: Prentice-Hall, 1993.
58. A. B. Kurzhanski, Identification—a theory of guaranteed estimates, in *From Data to Model*, J. C. Willems, Ed., New York: Springer-Verlag, 1989, pp. 135–214.
59. C. Lesiak and A. J. Krener, The existence and uniqueness of Volterra series for nonlinear systems, *IEEE Trans. Autom. Control*, 23(6), 1090–1095, 1978.
60. L. Ljung, *System Identification: Theory for the User*, Englewood Cliffs, NJ: Prentice-Hall, 1987.
61. G. G. Lorentz, K. Jetter, and S. D. Riemenschneider, *Birkhoff Interpolation*, Reading, MA: Addison-Wesley, 1983.
62. H. Lütkepohl, *Introduction to Multiple Time Series Analysis*, New York: Springer-Verlag, 1991.
63. A. I. Mees, M. F. Jackson, and L. O. Chua, Device modeling by radial basis functions, *IEEE Trans. Circuits Syst.*, 39(11), 19–27, 1992.
64. A. I. Mees, Parsimonious dynamical reconstruction, *Int. J. Bifurcation Chaos*, 3(3), 669–675, 1993.
65. C. A. Micchelli and T. J. Rivlin, A survey of optimal recovery, in *Optimal Estimation in Approximation Theory*, C. A. Micchelli and T. J. Rivlin, Eds., New York: Plenum Press, 1977, pp. 1–54.
66. C. A. Micchelli and T. J. Rivlin, Lectures on optimal recovery, in *Numerical Analysis*, P. R. Turner, Ed., New York: Springer-Verlag, 1984, pp. 21–93.
67. A. N. Michel, J. A. Farrell, and W. Porod, Associative memories via artificial neural networks, *IEEE Control Syst. Mag.*, pp. 6–17, Apr. 1990.
68. A. N. Michel, J. A. Farrell, and W. Porod, Qualitative analysis of neural networks, *IEEE Trans. Circuits Syst.*, 36(2), 229–243, 1989.

69. J. L. Moiola and G. Chen, *Hopf Bifurcation Analysis: A Frequency Domain Approach*, Singapore: World Scientific, 1996.
70. K. S. Narendra and K. Parthasarathy, Identification and control of dynamic systems using neural networks, *IEEE Trans. Neural Networks*, 1(1), 4–27, 1990.
71. H. Nijmeijer and A. J. van der Schaft, *Nonlinear Dynamical Control Systems*, New York: Springer-Verlag, 1990.
72. G. Nürnberger, *Approximation by Spline Functions*, New York: Springer-Verlag, 1989.
73. W. Odyniec and G. Lewicki, *Minimal Projections in Banach Spaces*, New York: Springer-Verlag, 1990.
74. E. Ott, C. Grebogi, and J. A. Yorke, Controlling chaos, *Phys. Rev. Lett.*, 64, 1196–1199, 1990.
75. T. Ozaki, Identification of nonlinearities and non-Gaussianities in time series, in *New Directions in Time Series Analysis, Part I*, D. Brillinger et al., Eds., New York: Springer-Verlag, 1993, pp. 227–264.
76. J. Park and I. W. Sandberg, Approximation and radial-basis-function networks, *Neural Comput.*, 5, 305–316, 1993.
77. J. R. Partington, *An Introduction to Hankel Operators*, London: Cambridge University Press, 1988.
78. P. P. Petrushev and V. A. Popov, *Rational Approximation of Real Functions*, London: Cambridge University Press, 1987.
79. M. J. D. Powell, *Approximation Theory and Methods*, London: Cambridge University Press, 1981.
80. M. J. D. Powell, Radial basis functions for multi-variable interpolation: A review, *IMA Conference on Algorithms for Approximation of Functions and Data*, RMCS, Shrivenham, UK, 1985.
81. E. Quak, N. Sivakumar, and J. D. Ward, Least-squares approximation by radial functions, *SIAM J. Math. Anal.*, 24(4), 1043–1066, 1993.
82. B. L. S. P. Rao, *Identifiability in Stochastic Models*, New York: Academic Press, 1992.
83. W. J. Rugh, *Nonlinear Systems Theory: The Volterra/Wiener Approach*, Baltimore: Johns Hopkins University Press, 1981.
84. I. W. Sandberg, A perspective on system theory, *IEEE Trans. Circuits Syst.*, 31(1), 88–103, 1984.
85. I. W. Sandberg, Criteria for the global existence of functional expansions for input/output maps, *AT&T Tech. J.*, 64(7), 1639–1658, 1985.
86. I. W. Sandberg, Approximately finite memory and input–output maps, *IEEE Trans. Circuits Syst.*, 39(7), 549–556, 1992.
87. T. Sauer, J. A. Yorke, and M. Casdagli, Embedology, *J. Stat. Phys.*, 63(3–4), 579–616, 1991.
88. L. L. Schumaker, *Spline Functions: Basic Theory*, New York: John Wiley & Sons, 1981.
89. A. N. Sharkovsky, Chaos from a time-delayed Chua’s circuit, *IEEE Trans. Circuits Syst.*, 40(10), 781–783, 1993.
90. E. D. Sontag, *Polynomial Response Maps*, New York: Springer-Verlag, 1979.
91. E. D. Sontag, *Mathematical Control Theory*, New York: Springer-Verlag, 1990.
92. H. W. Sorenson, Ed., *Kalman Filtering: Theory and Applications*, New York: IEEE Press, 1985.
93. F. Takens, Detecting strange attractors in turbulence, in *Lecture Notes in Mathematics*, vol. 898, D. A. Rand and L. S. Yong, Eds., New York: Springer-Verlag, 1981, pp. 366–381.
94. F. I. Utreras, Positive thin plate splines, *J. Approx. Theory Appl.*, 1, 77–108, 1985.
95. M. S. Verma and L. R. Hunt, Right coprime factorizations and stabilization for nonlinear systems, *IEEE Trans. Autom. Control*, 38, 222–231, 1993.
96. B. Widrow and S. D. Stearns, *Adaptive Signal Processing*, Englewood Cliffs, NJ: Prentice-Hall, 1985.
97. J. C. Willems, Ed., *From Data to Model*, New York: Springer-Verlag, 1989.
98. J. C. Willems, Paradigms and puzzles in the theory of dynamical systems, *IEEE Trans. Autom. Control*, 36, 259–294, 1991.

10

Transformation and Equivalence

10.1	Transformation of Nonlinear Dynamical Circuit Equations	10-1
10.2	Normal Forms of Nonlinear Dynamical Circuit Equations	10-5
10.3	Dimensionless Forms of Circuit Equations	10-9
10.4	Equivalence of Nonlinear Resistive n -Ports	10-16
10.5	Equivalence of Nonlinear Dynamical n -Ports	10-17
10.6	Equivalence of Reciprocal Nonlinear Dynamic Circuits	10-18
	References	10-23

Wolfgang Mathis
University of Hanover

10.1 Transformation of Nonlinear Dynamical Circuit Equations

One of the basic problems in studying linear and nonlinear dynamical electrical circuits is the analysis of the underlying descriptive equations and their solution manifold. In the case of linear or affine circuits, the constitutive relations of circuit elements are restricted to classes of linear or affine functions and, therefore, possess rather restricted types of solutions. In contrast, the solution manifold of nonlinear networks may consist of many different types. Naturally, it is useful to decompose nonlinear networks into classes that possess certain similarities. One approach, for example, is to consider the solution manifold and to decompose solutions into similar classes. Furthermore, if the descriptive differential equations of dynamic networks are considered to be mathematical sets, their decompositions will be of interest.

The technique of equivalence relations is the preferred method used to decompose a set of mathematical objects into certain classes. A well-known approach to define equivalence relations uses transformation groups. For example, real symmetric $n \times n$ matrices $\mathbb{R}_s^{n \times n}$ can be decomposed into equivalence classes by using the general linear transformation group $GL(n; \mathbb{R})$, and by applying the following similarity transformation:

$$\mathbf{M} \rightarrow \mathbf{U}^{-1}\mathbf{M}\mathbf{U}, \quad (10.1)$$

where $\mathbf{U} \in GL(n; \mathbb{R})$. By applying $GL(n; \mathbb{R})$, the set $\mathbb{R}_s^{n \times n}$ is decomposed into similarity classes that are characterized by their eigenvalues. Furthermore, each class of $\mathbb{R}_s^{n \times n}$ contains a diagonal matrix \mathbf{D} with these eigenvalues on the main diagonal [35]. These eigenvalues are invariants of the group and characterize different classes. These and other related results can be applied to classify linear and affine dynamical networks [20]. Thus, properties of the \mathbf{A} -matrix of the state-space equations are used for the classification. Note that each linear and affine dynamical network can be described in state-space form.

We discuss the theory of equivalence of linear and affine dynamical networks only as special cases of nonlinear networks. An interesting reformulation of the classical material of the decomposition of real matrices by using similarity transformations in the framework of one-parameter groups in $GL(n; \mathbb{R})$ is given by Ref. [21].

A classification of the vector fields is needed in order to classify differential equations of the type $\dot{\mathbf{x}} = \mathbf{f}(\mathbf{x})$, where $\mathbf{x} \in \mathbb{R}^n$ and $\mathbf{f}: \mathbb{R}^n \rightarrow \mathbb{R}^n$ is a vector field on \mathbb{R}^n . A first concept is established by a k -times differentiable change of coordinates that transforms a differentiable equation $\dot{\mathbf{x}} = \mathbf{f}(\mathbf{x})$ into $\dot{\mathbf{y}} = \mathbf{g}(\mathbf{y})$ by a function $\mathbf{h} \in C^k$. C^k is the set of k -times continuously differentiable functions $\mathbf{h}: \mathbb{R}^n \rightarrow \mathbb{R}^n$. In other words, two vector fields are called C^k -conjugate if there exists a C^k -diffeomorphism \mathbf{h} ($k \geq 1$) such that $\mathbf{h} \circ \mathbf{f} = \mathbf{g} \circ \mathbf{h}$. An equivalent formulation uses the concept of flows associated with differential equations $\dot{\mathbf{x}} = \mathbf{f}(\mathbf{x})$. A flow is a continuously differentiable function $\varphi: \mathbb{R} \times \mathbb{R}^n \rightarrow \mathbb{R}^n$ such that, for each $t \in \mathbb{R}$, the restriction $\varphi(t, \cdot) =: \varphi_t(\cdot)$ satisfies $\varphi_0 = \text{id}_{\mathbb{R}^n}$ and $\varphi_t \circ \varphi_s = \varphi_{t+s}$ for all $t, s \in \mathbb{R}$. The relationship to a associated differential equation is given by

$$\mathbf{f}(\mathbf{x}) := \left. \frac{d\varphi_t}{dt}(\mathbf{x}) \right|_{t=0} = \lim_{\varepsilon \rightarrow 0} \left\{ \frac{\varphi(\varepsilon, \mathbf{x}) - \varphi(0, \mathbf{x})}{\varepsilon} \right\}. \tag{10.2}$$

For more details see, for example, Ref. [13]. Two flows φ_t and Ψ_t (associated with \mathbf{f} and \mathbf{g} , respectively) are called C^k -conjugate, if there exists a C^k -diffeomorphism \mathbf{h} ($k \geq 1$) such that $\mathbf{h} \circ \varphi_t = \Psi_t \circ \mathbf{h}$. In the case that $k=0$, the term C^k -conjugate needs to be replaced by C^0 or topological conjugate and \mathbf{h} is a homeomorphism. Clearly, differential equations, vector fields, and flows are only alternative ways of presenting the same dynamics.

By the previous definitions, equivalence relations can be generated and the set of differential equations $\dot{\mathbf{x}} = \mathbf{f}(\mathbf{x})$ (as well as vector fields and flows) can be decomposed in certain classes of inequivalent differential equations and so on with different behavior (with respect to the equivalence relation). Although C^k -conjugate seems to be a natural concept for classifying differential equations, vector fields, and flows, this approach leads to a very refined classification (up to a diffeomorphism). In other words, too many systems become inequivalent. We consider two examples for illustrating this statement. Consider the nonlinear dynamical circuit (see Figure 10.1) with the descriptive equations (in a dimensionless form):

$$C \frac{dv_C}{dt} = i(v_C, i_L) - i_L, \tag{10.3}$$

$$L \frac{di_L}{dt} = v_C + v(v_C, i_L), \tag{10.4}$$

where the nonlinear functions $i: \mathbb{R}^2 \rightarrow \mathbb{R}$ and $v: \mathbb{R}^2 \rightarrow \mathbb{R}$ characterize the nonlinear controlled sources. If these controlled sources are given in the following form:

$$i = i(v_C, i_L) := -\frac{1}{2} \left(\sqrt{v_C^2 + i_L^2} - 1 \right) v_C, \tag{10.5}$$

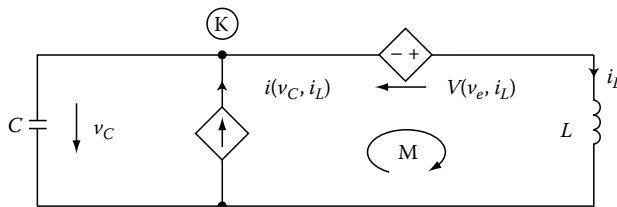


FIGURE 10.1 Circuit with nonlinear controlled sources.

$$v = v(v_C, i_L) = -\frac{1}{2} \left(\sqrt{v_C^2 + i_L^2 - 1} \right) i_L, \quad (10.6)$$

we obtain the following concrete descriptive equations for the circuits

$$C \frac{dv_C}{dt} = -\frac{1}{2} \left(\sqrt{v_C^2 + i_L^2 - 1} \right) v_C - i_L, \quad (10.7)$$

$$L \frac{di_L}{dt} = v_C - \frac{1}{2} \left(\sqrt{v_C^2 + i_L^2 - 1} \right) i_L. \quad (10.8)$$

These equations can be transformed into the following form if we use polar coordinates (r, ϕ) by $v_C := r \cos(\phi t)$ and $i_L := r \sin(\phi t)$:

$$\frac{dr}{dt} = \frac{1}{2}(1-r)r, \quad \dot{\phi} = 1, \quad (10.9)$$

where $C=1$ and $L=1$. If we consider the same circuit with the parameters $C=1/2$ and $L=1/2$ we obtain the slightly different descriptive equations:

$$\frac{dr}{dt} = \frac{1}{2}(1-r)r, \quad \dot{\phi} = 2. \quad (10.10)$$

Note that both differential equations differ only by a time rescaling $t \rightarrow 2t$. The question arises whether these two sets of equations are C^1 conjugate.

It can be demonstrated (see Refs. [2,29]) that if a diffeomorphism converts a singular point of a vector field into a singular point of another vector field, then the derivative of the diffeomorphism converts the Jacobian matrix of the first vector field at its singular point into the Jacobian matrix of the second field at its singular point. Consequently, these two Jacobian matrices are in the same similarity class and therefore, have the same eigenvalues. In other words, the eigenvalues of the Jacobian matrices are invariants with respect to a diffeomorphism, and the corresponding decomposition of the set of vector fields (differential equations and flows) is continuous rather than discrete. Obviously, the eigenvalues of Equations 10.9 and 10.10 ($\lambda_1=1/2$, $\lambda_2=1$ and $\tilde{\lambda}_1=1$, $\tilde{\lambda}_2=2$, respectively) are different and, in conclusion, the two vector fields are not C^1 conjugate. Moreover, these two vector fields are not topologically or C^0 conjugate. A more ‘‘coarse’’ equivalence relation is needed in order to classify these vector fields, differential equations, and flows. As mentioned above, a time rescaling transforms the differential equations (Equations 10.9 and 10.10) into one another and therefore it should be no essential difference between these two differential equations. This motivates the following definition.

Definition 10.1: Two flows φ_t and ψ_t are called C^k equivalent ($k \geq 1$) if there exists a C^k diffeomorphism \mathbf{h} that takes each orbit of φ_t into an orbit of ψ_t , preserving their orientation. In the case of $k=0$, the flows are called C^0 or topologically equivalent.

Because C^k equivalence preserves the orientation of orbits, the relation $\mathbf{h}(\varphi_t(\mathbf{x})) = \varphi_{\tau_y}(\mathbf{y})$ with $\mathbf{y} = \mathbf{h}(\mathbf{x})$ between φ_t and ψ_t is allowed, where τ_y is an increasing function of t for every \mathbf{y} .

It can be demonstrated (see Ref. [29]) that the eigenvalues of the Jacobian matrices of the two vector fields must be in the same ratio if a monotonic time rescaling is allowed. Therefore, the two vector fields (Equations 10.9 and 10.10) are C^1 equivalent. However, the two linear vector fields of the equations

$$\begin{pmatrix} \dot{x} \\ \dot{y} \end{pmatrix} = \begin{pmatrix} 1 & 0 \\ 0 & 1 \end{pmatrix} \begin{pmatrix} x \\ y \end{pmatrix}, \quad \begin{pmatrix} \dot{x} \\ \dot{y} \end{pmatrix} = \begin{pmatrix} 1 & 0 \\ 0 & 1 + \varepsilon \end{pmatrix} \begin{pmatrix} x \\ y \end{pmatrix} \quad (10.11)$$

are not C^1 equivalent for any $\varepsilon \neq 0$, although the solutions of the differential equations are very close for small ε in a finite time interval. In conclusion, topological equivalence is the appropriate setting for classifying differential equations, vector fields, and flows. Note, that the decomposition of the set of linear vector fields into equivalence classes using the topological equivalence does not distinguish between nodes, improper nodes, and foci, but does distinguish between sinks, saddles, and sources. This suggests the following theorem [3]:

THEOREM 10.1

Let $\dot{\mathbf{x}} = \mathbf{Ax}$ ($\mathbf{x} \in \mathbb{R}^n$ and $\mathbf{A} \in \mathbb{R}^{n \times n}$) define a hyperbolic flow on \mathbb{R}^n , e.g., the eigenvalues of \mathbf{A} have only nonzero parts, with n_s eigenvalues with a negative real part. Then, $\dot{\mathbf{x}} = \mathbf{Ax}$ is topological equivalent to the system ($n_u := n - n_s$):

$$\dot{\mathbf{x}}_s = -x_s, \quad \mathbf{x}_s \in \mathbb{R}^{n_s}, \quad (10.12)$$

$$\dot{\mathbf{x}}_u = +x_u, \quad \mathbf{x}_u \in \mathbb{R}^{n_u}. \quad (10.13)$$

Therefore, it follows that hyperbolic linear flows can be classified in a finite number of types using topological equivalence.

A local generalization of this theorem to nonlinear differential equations is known as the theorem of Hartmann and Grobman; see, e.g., Ref. [3].

THEOREM 10.2

Let \mathbf{x}^* be a hyperbolic fixed point of $\dot{\mathbf{x}} = \mathbf{f}(\mathbf{x})$ with the flow $\varphi_t: U \subseteq \mathbb{R}^n \rightarrow \mathbb{R}^n$, i.e., the eigenvalues of the Jacobian matrix $\mathbf{J}_f(\mathbf{x}^*)$ have only nonzero real parts. Then, there is a neighborhood N of \mathbf{x}^* on which $\dot{\mathbf{x}} = \mathbf{f}(\mathbf{x})$ is topologically equivalent to $\dot{\mathbf{x}} = \mathbf{J}_f(\mathbf{x}^*) \mathbf{x}$.

The combination of the two theorems implies that a very large set of differential equations can be classified in an isolated hyperbolic fixed point by a finite number of types (namely, n_s (or n_u)). The reason behind this interesting result is that the theorem of Hartman and Grobman, based on homeomorphisms, leads to a coarse decomposition of the set of vector fields under consideration.

As a consequence of the preceding theorems, the behavior of nonlinear differential equations near hyperbolic fixed points is equivalent up to a homeomorphism to the behavior of a simple system of linear differential equations. In the theory of nonlinear circuits, these mathematical results can be interpreted in the following way: The behavior of nonlinear circuits near an operational point where the Jacobian matrix of the descriptive equations (in statespace form) has only eigenvalues with nonzero real parts is “similar” to that of a corresponding linear dynamical circuit. Therefore, the analysis of these nonlinear circuits can be decomposed into two steps: (1) calculation of the operational points and the eigenvalues of

their Jacobian matrix and (2) restricting to the hyperbolic operational points we consider the behavior of the dynamics near these operational points; that is called small-signal behavior.

In the following section, we discuss more general methods for the analysis of vector fields that have at least one nonhyperbolic fixed point.

10.2 Normal Forms of Nonlinear Dynamical Circuit Equations

In Section 10.1, we present theorems useful for classifying the “local” behavior of nonlinear differential equations near hyperbolic fixed points by using “global” results from the theory of linear differential equations. An essential remaining problem is to calculate a homeomorphic transformation \mathbf{h} in concrete cases. An alternative way to circumvent some of the difficulties is to apply the theory of normal forms that goes back to the beginning of the twentieth century and is based on classical ideas of Poincaré and Dulac. Detailed investigations of this subject are beyond the scope of this section and, therefore, an interested reader should consult the monographs of Refs. [2,3,10] as well as Ref. [29], where also further references of the theory of normal forms can be found. In this section, we present only the main ideas to illustrate its areas of applications.

In contrast to the theory described in Section 10.1, which is dedicated to hyperbolic cases, the theory of normal forms applies diffeomorphisms instead of homeomorphisms. This is necessary in order to distinguish the dynamical behavior of differential equations in more detail. To classify the topological types of fixed points of nonlinear differential equations $\dot{\mathbf{x}} = \mathbf{f}(\mathbf{x})$ one proceeds in two steps:

1. Construction of a “normal form” in which the nonlinear terms of the vector field \mathbf{f} take their “most simple” form
2. Determination of the topological type of the fixed point (under consideration) from the normal form

We present the main aspects of this “algorithm” without a proof. First, we suppose that the vector field $\mathbf{f}(\mathbf{x})$ of the nonlinear differential equation $\dot{\mathbf{x}} = \mathbf{f}(\mathbf{x})$ satisfies $\mathbf{f}(\mathbf{0}) = \mathbf{0}$ (otherwise, using a suitable transformation) and that it is represented by a formal Taylor expansion:

$$\mathbf{f}(\mathbf{x}) = \mathbf{A}\mathbf{x} + \tilde{\mathbf{f}}(\mathbf{x}), \quad (10.14)$$

where

$$\begin{aligned} \mathbf{A} &= \mathbf{J}_f(\mathbf{x}) \\ \tilde{\mathbf{f}}(\mathbf{x}) &= O(\|\mathbf{x}\|^2) \text{ is of class } C^r \end{aligned}$$

Power (Taylor) series with no assumptions about convergence are called *formal series*. In practice, we begin with the formal series and then we determine the corresponding region of convergence (if available). Otherwise we use the framework of the theory of the so-called asymptotic series where a convergence in a strict sense is not necessary. In perturbation theory of differential equations most of the power series have to be considered as asymptotic series since a convergence in a strict sense is not available. More details about asymptotic series and perturbation theory can be, e.g., found in Refs. [28,45,57].

If a power series representation is derived, we apply a diffeomorphic C^r change of coordinates $\mathbf{h}: \mathbb{R}^n \rightarrow \mathbb{R}^n$ with $\mathbf{y} \mapsto \mathbf{x} = \mathbf{h}(\mathbf{y})$ ($\mathbf{h}(\mathbf{0}) = \mathbf{0}$) in the form of a near identity transformation:

$$\mathbf{h}(\mathbf{y}) := \mathbf{y} + \mathbf{h}^k(\mathbf{y}), \quad (10.15)$$

where $\mathbf{h}^k(\mathbf{y})$ is a homogeneous polynomial of order k in \mathbf{y} ($k \geq 2$). The result of the transformation is

$$\dot{\mathbf{y}} = \{id + \mathbf{J}_h(\mathbf{y})\}^{-1} \mathbf{A}(\mathbf{y} + \mathbf{h}^k(\mathbf{y})) + \{id + \mathbf{J}_h(\mathbf{y})\}^{-1} \tilde{\mathbf{f}}(\mathbf{y} + \mathbf{h}^k(\mathbf{y})) \quad (10.16)$$

$$= \mathbf{A}\mathbf{y} + \mathbf{g}(\mathbf{y}) \quad (10.17)$$

where

$\mathbf{J}_h(\mathbf{y})$ is the Jacobian matrix of \mathbf{h}^k with respect to \mathbf{y}
 $\mathbf{g}(\mathbf{h}) = O(\|\mathbf{y}\|^2)$ is a class C^r

For the following discussion it is useful to define \mathbf{f}_T^k of a sufficient differentiable function $\mathbf{f}: \mathbb{R}^n \rightarrow \mathbb{R}^n$ as the “truncated” Taylor series in $\mathbf{0}$ expansion that have a degree less or equal k ; the i th-order term of the Taylor series of \mathbf{f} is denoted by \mathbf{f}_i . In a more abstract setting these “truncated” Taylor series are called k -jets; see Ref. [38] for more details. The set of \mathbf{f}_T^k 's forms a real vector space of functions and is denoted by H_k^n where the components are homogeneous polynomials in n variables of degree k . Using the k -jet notation and expanding \mathbf{g} into a (formal) Taylor series, Equation 10.17 can be reformulated as

$$\dot{\mathbf{y}} = \mathbf{g}_T^{k-1}(\mathbf{y}) + \mathbf{g}_R^k(\mathbf{y}), \quad (10.18)$$

where \mathbf{g}_R^k contains all terms of degree k or higher.

Expanding $\tilde{\mathbf{f}}$ of Equation 10.14 into a Taylor series

$$\tilde{\mathbf{f}} = \tilde{\mathbf{f}}_2 + \tilde{\mathbf{f}}_3 + \cdots \quad (10.19)$$

and using it to represent \mathbf{g}_R^k of Equation 10.18 we can get

$$\dot{\mathbf{y}} = \mathbf{g}_T^{k-1}(\mathbf{y}) + \{\mathbf{f}_k - [\mathbf{A}\mathbf{y}, \mathbf{h}^k]\} + O(\|\mathbf{y}\|^{k+1}), \quad (10.20)$$

where in the sense of Equation 10.17 the so-called Lie bracket $[\mathbf{A}\mathbf{y}, \mathbf{h}^k]$ of the linear vector field $\mathbf{A}\mathbf{y}$ and of $\mathbf{h}^k(\mathbf{y})$ is introduced by

$$[\mathbf{A}\mathbf{y}, \mathbf{h}^k](\mathbf{y}) := \mathbf{J}_h(\mathbf{y})\mathbf{A}\mathbf{y} - \mathbf{A}\mathbf{h}^k(\mathbf{y}). \quad (10.21)$$

Now we define the linear operator $L_A^k: H_k^n \rightarrow H_k^n$ by

$$L_A^k \mathbf{h}^k: \mathbf{y} \rightarrow [\mathbf{A}\mathbf{y}, \mathbf{h}^k](\mathbf{y}) \quad (10.22)$$

with the range \mathcal{R}_k , and let C_k be any complementary subspace to \mathcal{R}_k in H_k^n , i.e., $H_k^n = \mathcal{R}_k \oplus C_k$ ($k \geq 2$). Then, the following theorem implies a simplification of a nonlinear differential equation $\dot{\mathbf{x}} = \mathbf{f}(\mathbf{x})$, which can be interpreted as an equivalent representation of the associated dynamical circuit equations.

THEOREM 10.3

Let $\mathbf{f}: \mathbb{R}^n \rightarrow \mathbb{R}^n$ be a C^r vector field with $\mathbf{f}(\mathbf{0}) = \mathbf{0}$ and $\mathbf{A} \in \mathbb{R}^{n \times n}$, and let the decomposition $\mathcal{R}_k \oplus C_k$ of H_k^n be given. Then, there exists a series of near identity transformations $\mathbf{x} = \mathbf{y} + \mathbf{h}^k(\mathbf{y}) \in \Omega$ for $k = 2, 3, \dots, r$, where $\Omega \subset \mathbb{R}^n$ is a neighborhood of the origin and $\mathbf{h}^k \in H_k^n$, such that the equation $\dot{\mathbf{x}} = \mathbf{f}(\mathbf{x})$ is transformed to

$$\dot{\mathbf{y}} = \mathbf{A}\mathbf{y} + \mathbf{g}_2(\mathbf{y}) + \mathbf{g}_3(\mathbf{y}) + \cdots + \mathbf{g}_k(\mathbf{y}) + O(\|\mathbf{y}\|^{r+1}), \quad \mathbf{y} \in \Omega, \quad (10.23)$$

where $\mathbf{g}_k \in C_k$ for $k = 2, 3, \dots$

A proof of this theorem and the following definition can be found in, e.g., Ref. [4].

Definition 10.2: Let $\mathcal{R}_k \oplus C_k$ be decompositions of H_k^n for $k=2, 3, \dots, r$. The “truncated” equation of (Equation 10.23)

$$\dot{\mathbf{y}} = \mathbf{A}\mathbf{y} + \mathbf{g}_2(\mathbf{y}) + \mathbf{g}_3(\mathbf{y}) + \dots + \mathbf{g}_k(\mathbf{y}), \quad (10.24)$$

where $\mathbf{g}_k \in C_k$ ($k=2, 3, \dots, r$) is called normal form of $\dot{\mathbf{x}} = \mathbf{A}\mathbf{x} + \tilde{\mathbf{f}}(\mathbf{x})$ associated with matrix \mathbf{A} up to order $r \geq 2$ (with respect to the decomposition where $\mathbf{g}_k \in C_k$ for $k=2, 3, \dots, \mathcal{R}_k \oplus C_k$).

Theorem 10.3 suggests an equivalence relation in the set of vector fields \mathbf{f} that decomposes the set into equivalence classes. Each class can be represented by using the definition of normal forms. Because a concrete normal form depends on the choice of complementary subspaces C_k , it is not unique. In practical problems a constructive method of finding these subspaces is needed. An elegant way to find these subspaces is to start with the introduction of a suitable inner product $\langle \cdot | \cdot \rangle_n$ in H_k^n that is needed to define the adjoint operator $(L_A^k)^*$ of L_A^k (in a sense of linear algebra) by

$$\langle \eta | L_A^k(\xi) \rangle_n := \langle (L_A^k)^*(\eta) | \xi \rangle_n, \quad \text{for all } \eta, \xi \in H_k^n. \quad (10.25)$$

It can be shown that $(L_A^k)^* = L_{A^*}^k$ where $\mathbf{A}^* = \mathbf{A}^T$ is the transposed matrix of the matrix \mathbf{A} . The desired construction is available as an application of the following theorem.

THEOREM 10.4

Vector space $\ker \{L_{A^*}^k\}$ that is the solution space of the equation $L_{A^*}^k \xi = 0$ is a complementary subspace of \mathcal{R}_k in H_k^n , i.e.,

$$H_k^n = \mathcal{R}_k \oplus \ker \{L_{A^*}^k\}. \quad (10.26)$$

The interesting reader is referred to Ref. [4] for a detailed discussion of this subject. As a consequence, finding a normal form in the above sense up to the order r requires solving the partial differential equation $L_{A^*}^k \xi = 0$ with definition (Equation 10.22). From an algebraic point of view this means that a base of $\ker \{L_{A^*}^k\}$ has to be chosen, but this can be done, again, with some degrees of freedom. For example, the two sets of differential equations are distinct normal form of $\dot{\mathbf{x}} = \mathbf{A}\mathbf{x} - \tilde{\mathbf{f}}(\mathbf{x})$ associated with the same matrix \mathbf{A} (see Ref. [4]):

$$\frac{d}{dt} \begin{pmatrix} x_1 \\ x_2 \end{pmatrix} = \begin{pmatrix} 0 & 1 \\ 0 & 0 \end{pmatrix} \begin{pmatrix} x_1 \\ x_2 \end{pmatrix} + \begin{pmatrix} ax_1^2 \\ bx_2^2 + ax_1x_2 \end{pmatrix}, \quad (10.27)$$

$$\frac{d}{dt} \begin{pmatrix} x_1 \\ x_2 \end{pmatrix} = \begin{pmatrix} 0 & 1 \\ 0 & 0 \end{pmatrix} \begin{pmatrix} x_1 \\ x_2 \end{pmatrix} + \begin{pmatrix} 0 \\ bx_1^2 + bx_1x_2 \end{pmatrix}. \quad (10.28)$$

To reduce the number of nonlinear monomials in the normal forms, a more useful base of C_k must be determined. If a nonlinear differential equation of the form $\dot{\mathbf{x}} = \mathbf{A}\mathbf{x} - \tilde{\mathbf{f}}(\mathbf{x})$ is given with an arbitrary matrix \mathbf{A} , several partial differential equations need to be solved. This, in general, is not an easy task. If \mathbf{A} is diagonal or has an upper triangular form, methods for constructing a base are available. For this purpose we introduce the following definition:

Definition 10.3: Let $\mathbf{A} \in \mathbb{R}^{n \times n}$ possesses the eigenvalues $\lambda_1, \dots, \lambda_n$ and let $x_1^{\alpha_1} x_1^{\alpha_2} \dots x_1^{\alpha_n} \mathbf{e}_j$ be a monomial in n variables. It is called a resonant monomial if the so-called resonant condition:

$$\alpha \cdot \lambda - \lambda_j = 0 \quad (10.29)$$

is satisfied ($\alpha^T := (\alpha_1, \dots, \alpha_n)$, $\lambda^T := (\lambda_1, \dots, \lambda_n)$). If the resonant condition holds for some $\sqrt{\alpha^T \alpha} \geq 2$ and some $j \in \{1, \dots, n\}$, we say that \mathbf{A} has a resonant set of eigenvalues.

The importance of this definition is that the following statement can be shown: a monomial $x_1^{\alpha_1} x_1^{\alpha_2} \cdots x_1^{\alpha_n} \mathbf{e}_j$ is an element of $\ker \{L_{A^*}^k\}$ if and only if $\alpha^T \cdot \lambda - \lambda_j = 0$ [4]. The next theorem proves that if \mathbf{A} is diagonal, a minimal normal form exists (in certain sense).

THEOREM 10.5

Let $\mathbf{A} = \text{diag}(\lambda_1, \dots, \lambda_n)$. Then an A -normal form equation up to order r can be chosen to contain all resonant monomials up to order r .

If some eigenvalues of \mathbf{A} are complex, a linear change to complex coordinates is needed to apply this theorem. Furthermore, theorems and definitions need to be modified to such complex cases. In the case of differential equation:

$$\frac{d}{dt} \begin{pmatrix} x_1 \\ x_2 \end{pmatrix} = \begin{pmatrix} 0 & -1 \\ +1 & 0 \end{pmatrix} \begin{pmatrix} x_1 \\ x_2 \end{pmatrix} + O(\|\mathbf{x}\|^2) \quad (10.30)$$

that can be used to describe oscillator circuits, the coordinates are transformed to

$$\dot{z}_1 := x_1 + jx_2, \quad (10.31)$$

$$\dot{z}_2 := x_1 - jx_2 \quad (10.32)$$

with the resonant set of eigenvalues $\{-j, +j\}$ that can be written in a complex normal form (z represents z_1 and z_2 , respectively):

$$\dot{z} = j + a_1 |z|^2 z + \cdots + a_k |z|^{2k} z. \quad (10.33)$$

This normal form equation—Poincaré normal form—is used intensively in the theory of the Poincaré–Andronov–Hopf bifurcation. The monograph of Hale and Kočak [30] is worth reading for the illustration of this phenomenon in nonlinear dynamical systems. A detailed proof of the Poincaré–Andronov–Hopf theorem can be found, e.g., in Ref. [32]. These authors emphasize that further preparation of the system of differential equations is needed before the normal form theorem is applicable. In general, the linearized part of $\dot{\mathbf{x}} = \mathbf{A}\mathbf{x} + \tilde{\mathbf{f}}(\mathbf{x})$ (in a certain fixed point of the vector field \mathbf{f}) has two classes of eigenvalues: (a) *central* eigenvalues $\lambda_i \in j\mathbb{R} \subset \mathbb{C}$ and (b) *noncentral* eigenvalues $\lambda_i \in \mathbb{C} \setminus j\mathbb{R}$. The dynamic behavior of a system associated with the noncentral eigenvalues is governed by the theorem of Grobman and Hartman (see Section 10.1) and therefore it is oriented in generic sense at the exponential behavior of linear systems. If a system has no central eigenvalues it is called a *hyperbolic system*. In circuit applications network, models with a hyperbolic behavior are related to, e.g., amplifiers and active filters; see, e.g., Ref. [44].

A more complex behavior is only possible if the theorem of Grobman and Hartman cannot be applied, i.e., we have systems with central eigenvalues see Ref. [49]. Therefore in the design of oscillator circuits we have to derive conditions to get central eigenvalues, e.g., Barkhausen criterion. The noncentral eigenvalues in these systems are related with the relaxation behavior and should be eliminated if we are interested in the dominant asymptotic behavior. A systematic procedure to eliminate noncentral eigenvalues from the system is based on the so-called center manifold theorem (see Ref. [11]) that is used also in the paper of Hassard and Wan [32]. A numerical algorithm is presented by Hassard et al. [31]. A more detailed discussion of this essential theorem goes beyond the scope of this section; however, more about the theory of normal forms of vector fields and its applications in circuit analysis can be found

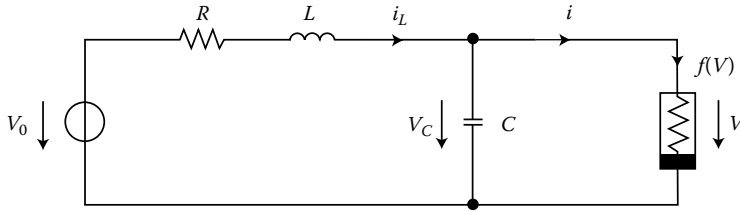


FIGURE 10.2 Nonlinear circuit with tunnel diode.

in Refs. [21,22]. Until now, we have discussed differential equations of the type $\dot{\mathbf{x}} = \mathbf{f}(\mathbf{x})$. Descriptive equations of circuits consist, in general, of linear and nonlinear algebraic equations, as well as differential equations. Therefore, the so-called constrained differential equations need to be considered for applications in circuit theory. A typical example is the well-known circuit shown in Figure 10.2, containing a model of a tunnel diode (see Refs. [9,53]). Circuit equations can be written as

$$C \frac{dv_C}{dt} = i_L - f(v_C), \quad (10.34)$$

$$L \frac{di_L}{dt} = -v_C - Ri_L + V_0, \quad (10.35)$$

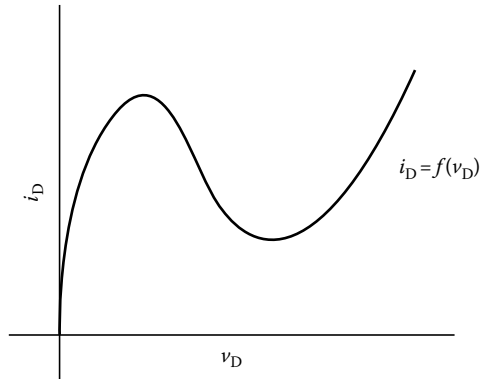


FIGURE 10.3 Characteristic of a tunnel diode.

where $i_D = f(v_D)$ is the characteristic of the tunnel diode (see Figure 10.3).

If the behavior of the circuit is considered with respect to the timescale $\tau := RC$, then the differential equations (Equations 10.34 and 10.35) can be reformulated as

$$\frac{dv}{d\theta} = i - F(v), \quad (10.36)$$

$$\varepsilon \frac{di}{d\theta} = -v - i + 1, \quad (10.37)$$

where

$$\theta : t/\tau$$

$$i := (R/V_0) i_L$$

$$v := v_C/V_0$$

$$\varepsilon : L/(CR^2)$$

$$F(v) := (R/V_0) f(V_0 \cdot v)$$

The behavior of the idealized circuit, where $\varepsilon = 0$ is often of interest. These types of descriptive equations are called constrained equations or differential-algebraic equations (DAEs). The above discussed theory of normal forms for vector fields cannot be applied directly to DAEs; however, a generalized theory is available, as presented (with applications) in Refs. [24,25].

10.3 Dimensionless Forms of Circuit Equations

In Section 10.1, the problem of equivalence is considered in a rather complex manner by adopting the mathematical point of view of dynamical systems. We use this approach in Section 10.6 to classify a

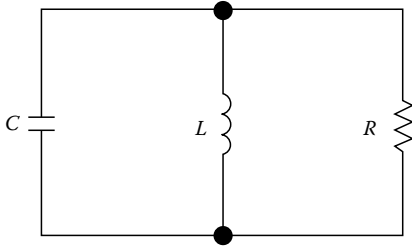


FIGURE 10.4 LCR circuit.

special class of nonlinear dynamical circuits. In contrast to this approach, another kind of equivalence of descriptive equations for linear time-invariant circuits and for certain nonlinear circuits is well known. It is illustrated by means of a simple example. The RLC parallel circuit in Figure 10.4, analyzed in the frequency domain, can be described by its impedance

$$Z(j\omega) = \frac{1}{1/R + j(\omega C - \frac{1}{\omega L})}. \quad (10.38)$$

In the case of small damping, this formula can be simplified using the so-called Q -factor that is defined as the ratio of the current flowing through L (or C) to the current flowing through the whole circuit in the case of resonance. The case of small damping is characterized by the condition $R/(2L) \ll \omega_0$, where $\omega_0 := 1/\sqrt{LC}$ (Thompson's formula for LC circuits with $R=0$). The Q -factor is given by $Q := 1/(\omega_0\sqrt{RC})$. Simple calculations lead to a so-called normalized impedance

$$\tilde{Z} := \frac{Z}{R} = \left[1 - jQ^{-1} \left(\frac{\omega}{\omega_0} - \frac{\omega_0}{\omega} \right) \right]^{-1} \quad (10.39)$$

that contains only two instead of three parameters. By using this method, a whole class of RLC circuits may be described by the same normalized impedance and which can be “de-normalized” at a certain frequency if a special filter application is considered. Therefore, an equivalence relation is defined in this manner. Handbooks of filter design written for practical electrical engineers contain diagrams of those and similar frequency curves of normalized impedances as well as admittances. Nor that the formula (Equation 10.39) is exact, although the interpretation of the parameters Q and ω_0 depends on the condition $R/(2L) \ll \omega_0$.

Methods for normalizing descriptive equations of circuits and for reducing the number of parameters are known in linear and nonlinear circuit theory; see, e.g., Ref. [20]. Unfortunately, these methods are stated without a presentation of their mathematisch reasoning. The main ideas for justification of normalization procedures are based on the so-called dimensional analysis. Their first applications in physics and the development of their mathematical foundations can be traced to the end of the nineteenth century. In this section, we discuss only a few aspects of this subject. Interested readers may find more details about the theory and applications of dimensional analysis as well as further references in a paper of Mathis and Chua [50]. In this paper they demonstrated that for a complete mathematical discussion of physical quantities, several algebraic concepts (e.g., Lie groups, etc.) are needed. In this section, a concise introduction into dimensional analysis is preferred and therefore, an intuitive introduction based on multiparameter Lie groups is presented. We use main ideas from the monograph of Ovsiannikov [55].

For describing physical systems, suitable descriptive physical quantities are required that can be measured. To perform a physical measurement of one of these quantities, we need at least one measuring instrument that provides us with corresponding measuring values on its scale. This scale is calibrated with respect to a standard cell. Therefore, an intuitive mathematical model of a physical quantity ϕ consists of two parts: a real number $|\phi|$ that characterizes its value, and a symbol E_ϕ that is due to the standard cell. In general, a measuring instrument is composed of elementary measuring instruments to evaluate, e.g., time or frequency, length, voltage, and charge. Each elementary instrument is calibrated with a corresponding standard cell and, therefore, associated to the instrument. Entirely, an arbitrary physical quantity ϕ is defined by

$$\phi := |\phi| E_1^{\lambda_1} E_2^{\lambda_2} \cdots E_r^{\lambda_r}, \quad (10.40)$$

where

r is the number of elementary instruments for measuring ϕ

λ_k determine how many times an elementary instrument have to be applied and whether the value on the scale needs to multiplied or divided

The dimensionality of a physical quantity ϕ is defined by

$$[\phi] := E_1^{\lambda_1} E_2^{\lambda_2} \cdots E_r^{\lambda_r}, \quad (10.41)$$

where $r \geq n$ such that a physical quantities is fully described by $\phi = |\phi| [\phi]$.

A physical quantity ϕ is called dimensionless if its dimensionality is null, that is if $\lambda_1 = 0, \lambda_2 = 0, \dots, \lambda_r = 0$. Moreover, a set of n physical quantities $\phi_1, \phi_2, \dots, \phi_n$ is called dependent (in the sense of their dimensionality) if there exist integers $\chi_1, \chi_2, \dots, \chi_n$ (not all equal zero) such that the product of these quantities

$$\phi_1^{\chi_1} \phi_2^{\chi_2} \cdots \phi_n^{\chi_n} \quad (10.42)$$

is dimensionless. Otherwise $\phi_1 \phi_2 \cdots \phi_n$ are called independent.

The main problem of (physical) dimension theory is to determine how many independent physical quantities are included in a set of n describing quantities, to find them, and then express the other quantities in the set in terms of these independent quantities. As an application, a systematic procedure to normalize physical descriptive equations can be given—instead a intuitive manner as considered above.

In order to solve the main problem, the change of measuring instruments and measuring scales needs to be introduced and modeled in a mathematical manner. Obviously, in terms of modeling physical quantities, the same ϕ can be represented in different ways. Using two sets of measuring instruments, denoted by E_1, E_2, \dots, E_r and $\tilde{E}_1, \tilde{E}_2, \dots, \tilde{E}_r$, respectively, ϕ is given by

$$|\phi| E_1^{\lambda_1} E_2^{\lambda_2} \cdots E_r^{\lambda_r} = |\tilde{\phi}| \tilde{E}_1^{\tilde{\lambda}_1} \tilde{E}_2^{\tilde{\lambda}_2} \cdots \tilde{E}_r^{\tilde{\lambda}_r}, \quad (10.43)$$

where in general $r \neq p$. This suggests the so-called analogy transformation (see Ref. [50]):

$$E_k = a_1^{\alpha_1} \cdots a_k^{\alpha_k} \tilde{E}_1^{\alpha_1} \cdots \tilde{E}_k^{\alpha_k}, \quad k = 1, \dots, r. \quad (10.44)$$

Transformations of the scales of measuring instruments—in the following denoted as *scale transformations*—are special analogy transformations:

$$E_k = a_k \tilde{E}_k, \quad k = 1, \dots, r. \quad (10.45)$$

It can be demonstrated that analogy transformations of dimension theory are special cases of the so-called extension groups. These groups belong to the r -parameter Lie groups and, subsequently, all results of dimension theory can be interpreted by theorems from this mathematical theory. Further details are contained in Ref. [55]. To introduce the main ideas, we consider only scale transformations in this section.

Let $\mathcal{Z} := \mathbb{R}^n \times \mathbb{R}^m$ be the Cartesian product of the set of n -column vectors \mathbf{x} and m -column vectors \mathbf{y} , and let $\{\mathbf{e}_1, \dots, \mathbf{e}_n\}$ and $\{\mathbf{f}_1, \dots, \mathbf{f}_m\}$, be, respectively, arbitrary (but fixed) bases of these vector spaces. Endowing \mathcal{Z} with the structure of a direct sum $\mathbb{R}^n \oplus \mathbb{R}^m$, each $z \in \mathcal{Z}$ can be represented by (with respect to these bases)

$$z = \sum_{i=1}^n x^i \mathbf{e}_i + \sum_{k=1}^m y^k \mathbf{f}_k. \quad (10.46)$$

An extension of \mathcal{Z} (with respect to these bases) is defined by the transformation:

$$h: z \rightarrow \sum_{i=1}^n c^i x^i \mathbf{e}_i + \sum_{k=1}^m d^k y^k \mathbf{f}_k \quad (c^i >, d^k > 0). \quad (10.47)$$

Obviously, the set of all extensions generates an Abelian group of transformations on \mathcal{Z} that is an $(n+m)$ -parameter Lie group. this group is denoted by $\text{diag}\{\mathbf{e}_i, \mathbf{f}_k\}$. Any subgroup $H \subset \text{diag}\{\mathbf{e}_i, \mathbf{f}_k\}$ is called an extension group of \mathcal{Z} . We now consider extension groups H^r , with $0 < r \leq n+m$.

Ovsiannikov [55] demonstrated that extensions of H^r can be represented, choosing a parametric group, in the form:

$$\tilde{x}^i = x^i \prod_{\alpha=1}^r (a_\alpha)^{\lambda_\alpha^i}, \quad \tilde{y}^k = y^k \prod_{\alpha=1}^r (a_\alpha)^{\mu_\alpha^k}, \quad (10.48)$$

where

$$\begin{aligned} i &= 1, \dots, n \\ k &= 1, \dots, m \end{aligned}$$

The main property of transformation groups is that they induce equivalence relations decomposing the subjects on which the group acts into equivalence classes. If h_p acts on elements $x \in X$, and let $\mathbf{p} \in \mathbb{R}^p$ the vector of parameters, an *orbit* $U(x)$ of a point $x \in X$ is defined by the set $U(x) := \{\xi \in X | \xi = h_p(x, \mathbf{p}), \text{ for all } \mathbf{p} \in \mathbb{R}^p\}$. In this sense, the points of an orbit can be identified by a transformation group. A transformation group acts transitive on X if there exists an orbit $U(x)$ that is an open subset of X , with $\bar{U} = X$.

To study the so-called local Lie groups with actions that are defined near a null neighborhood of the parameter space (including the vector $\mathbf{0}$), we can discuss the Lie algebra that characterizes the local behavior of the associated local Lie group. In finite dimensional parameter spaces, a Lie algebra is generated by certain partial differential operators. Using the representations (Equation 10.48) of H^r , the operators are of the form:

$$\sum_{i=1}^n \lambda_\alpha^i x^i \frac{\partial}{\partial x^i} + \sum_{k=1}^m \mu_\alpha^k y^k \frac{\partial}{\partial y^k}, \quad (10.49)$$

where

$$\begin{aligned} i &= 1, \dots, n \\ k &= 1, \dots, m \end{aligned}$$

These operators can be represented in a matrix form:

$$\mathbf{M}(z) := \mathbf{M}_1 \circ \text{diag}\{x^1, \dots, x^n, y^1, \dots, y^m\}, \quad (10.50)$$

where

$$\mathbf{M}_1 := \begin{pmatrix} \lambda_1^1 & \cdots & \lambda_1^n, \mu_1^1 & \cdots & \mu_1^m \\ \vdots & \cdots & \vdots & \cdots & \vdots \\ \lambda_r^1 & \cdots & \lambda_r^n, \mu_r^1 & \cdots & \mu_r^m \end{pmatrix}. \quad (10.51)$$

Obviously, H^r is not transitive if $r < n+m$.

In order to solve the main problem of dimension theory, we need to introduce invariants of a Lie group. Let $F : X \rightarrow Y$ be a function on X and let transformations h_p of a transformation group act on X , then F is an invariant of the group if $F(h_p(x)) = F(x)$ holds for any $x \in X$ and $\mathbf{p} \in \mathbb{R}^p$. The invariant $J : X \rightarrow Y$ is called a universal invariant if there exists, for any invariant $F : X \rightarrow Y$ of the group, a function Φ such that $F = \Phi \circ J$. The following main theorem can be proved for the extension group [55].

THEOREM 10.6

For the extension group H^r on Z , there exists a universal invariant $J : Z \rightarrow \mathbb{R}^{n+m-r}$ if the condition $r < n + m$ is satisfied. The independent components of J have the monomial form:

$$J^\tau(Z) = \prod_{i=1}^n (x^i)^{\theta_k^\tau} \cdot \prod_{k=1}^m (y^k)^{\sigma_k^\tau}, \quad (10.52)$$

where $\tau = 1, \dots, n + m - r$.

If dimensional analysis considers only scale transformations (Equation 10.45), this theorem contains the essential result of the so-called *Pi-theorem*. For this purpose we present a connection between the dimensionalities and the extension group H^r (see Ref. [55]). The group H^r of the space \mathbb{R}^n , defined only by the dimensions of the physical quantities ϕ_k with respect to the set of symbols $\{E_\alpha\}$, has a one-to-one correspondence with every finite set $\{\phi_k\}$ of n physical quantities, which can be measured in the system of symbols $\{E_\alpha\}$ consisting of r independent measurement units; see Equation 10.43. The transformations belonging to the group H^r give the rule of change in the form

$$|\tilde{\phi}| = |\phi| \prod_{\alpha=1}^r (a^\alpha)^{\lambda_\alpha} \quad (10.53)$$

of the numerical values $|\phi_k|$ as a result of the transition from the units $\{E_\alpha\}$ to $\{\tilde{E}_\alpha\}$ by means of Equation 10.45.

As a consequence of this relationship, a quantity ϕ is dimensionless if and only if its numerical value is an invariant of the group H^r . Thus, the problem to determine the independent physical quantities of a given set of quantities is solved by the construction of a universal invariant of H^r stated by the Pi-theorem; see also Ref. [7]. Normalization as well as the popular method of dimension comparison, are consequences of the invariance of physical equations with respect to the group of analogy (scale) transformations. In applications of dimensional theory, a normal form that has certain advantageous properties is desired. For example, it is useful to reduce the number of parameters in physical equations. Normal forms of this type are used very often in practical calculations, but with no clarification of their mathematical foundations.

Circuit equations, similar to other physical equations, contain numerous parameters. In applications, it is often desired to suppress some of these parameters and moreover, they should be replaced by the numerical value 1.

For this purpose, Desloge [26] chooses a new system of units $\{E_\alpha\}$. A theory of Desloge's method, based on analogy transformation (Equation 10.44) instead of scale transformation (Equation 10.45), was presented by Mathis and Chua [50]. The main idea behind this method is that, beside the foundation units time $[T]$, voltage $[E]$, and charge $[Q]$ that are useful in circuit theory, the units of other parameters are considered as foundational units. We denote the units by $[A_\alpha]$ instead of E_α . For example, in the case of the tunnel-diode circuit (see Figure 10.2), $[T]$, $[E]$, and $[Q]$, as well as $[R]$, $[C]$, and $[L]$, need to be

discussed. As a consequence of Desloge's method, three of the four parameters can be suppressed and the other variables will be normalized. The method works in the case of linear as well as nonlinear circuits.

The method is illustrated using the tunnel-diode circuit equations (Equations 10.34 and 10.35). At first, the dimensional matrix is determined by

$$\begin{array}{c} [T] \quad [E] \quad [Q] \\ [R] \begin{pmatrix} 1 & 1 & -1 \\ 2 & 1 & -1 \\ 0 & -1 & 1 \end{pmatrix} \\ [L] \\ [C] \end{array} \quad (10.54)$$

that characterizes the relation between the dimensions of t , v , q , R , C , and L .

Now, Desloge considers another set of power independent dimensional scalars A_1 , A_2 , and A_3 with

$$[A_i] = [T]^{a_i^1} [E]^{a_i^2} [Q]^{a_i^3}, \quad i = 1, 2, 3. \quad (10.55)$$

These relations are interpreted as an analogy transformation (Equation 10.44). Applying the map $L(\cdot)$ that has the same properties as the logarithmic function (see Ref. [50]) to Equation 10.55, the symbols $L([A_1])$, $L([A_2])$, and $L([A_3])$ are represented by linear combinations of $L([T])$, $L([E])$, $L([Q])$. The coefficient matrix in Equation 10.55 is regular and contains the exponents. Solving these linear equations using "antilog," the $[T]$, $[E]$, and $[Q]$ are products of powers of $[A_1]$, $[A_2]$, and $[A_3]$. In this manner, dimensionless versions of differential equations of the tunnel-diode circuit can be derived.

By using the independent units $A_1 := L$, $A_2 := C$, and $A_3 := V_0$ to replace their values $|V_0|$, $|L|$, and $|C|$ by 1 (with respect to the new units), the following equation is derived by Desloge's approach sketched previously

$$\begin{array}{c} [T] \quad [E] \quad [Q] \\ [V_0] \begin{pmatrix} 0 & 1 & 0 \\ 2 & 1 & -1 \\ 0 & -1 & 1 \end{pmatrix} \begin{pmatrix} \ln([T]) \\ \ln([E]) \\ \ln([Q]) \end{pmatrix} = \begin{pmatrix} \ln([V_0]) \\ \ln([L]) \\ \ln([C]) \end{pmatrix}. \\ [L] \\ [C] \end{array} \quad (10.56)$$

Multiplying Equation 10.56 by the inverse of the dimensional matrix

$$\begin{array}{c} [V_0] \quad [L] \quad [C] \\ [T] \begin{pmatrix} 0 & 1/2 & 1/2 \\ 1 & 0 & 0 \\ 1 & 0 & 1 \end{pmatrix} \\ [E] \\ [Q] \end{array} \quad (10.57)$$

and applying "antilog" to the result, we obtain

$$[T] = [L]^{1/2} [C]^{-1/2}, \quad [E] = [V_0], \quad [Q] = [V_0] [C]. \quad (10.58)$$

From these equations, the relations between the old and new units can be derived; see Ref. [50]. T , E , and Q are expressed by the new units L , C , and V_0 and the parameters and variables in Equations 10.34 and 10.35 can be reformulated if the numerical values of V_0 , L , and C are added

$$T = |L|^{-1/2} |C|^{-1/2} L^{1/2} C^{1/2}, \quad E = |V_0|^{-1} V_0, \quad Q = |V_0|^{-1} |C|^{-1} V_0 C. \quad (10.59)$$

These relations represent parameters and variables of the tunnel-diode circuit with respect to the new quantities

$$R = \frac{|R||C|^{1/2}}{|L|^{1/2}} L^{1/2} C^{-1/2}, \quad V_0 = 1 \cdot V_0, \quad L = 1 \cdot L, \quad C = 1 \cdot C, \quad (10.60)$$

$$i_L = \frac{|i_L||L|^{1/2}}{|V_0||C|^{1/2}} V_0 L^{-1/2} C^{1/2}, \quad v_C = \frac{|v_C|}{|V_0|} V_0, \quad t = \frac{|t|}{|L|^{1/2}|C|^{1/2}} L^{1/2} C^{1/2}. \quad (10.61)$$

The dimensional exponents for these quantities can be found by using the inverse dimensional matrix (Equation 10.57):

1. T, E, Q : their exponents correspond the associated rows of Equation 10.57
2. V_0, L, C, R : premultiply Equation 10.57 with the corresponding row of Equation 10.54

For example, taking $[C] \triangleq (0 - 11)$ results in

$$[C] \begin{pmatrix} [T] & [E] & [Q] \\ 0 & -1 & 1 \end{pmatrix} \begin{pmatrix} [T] \\ [E] \\ [Q] \end{pmatrix} \begin{pmatrix} [V_0] & [L] & [C] \\ 0 & 1/2 & 1/2 \\ 1 & 0 & 0 \\ 1 & 0 & 1 \end{pmatrix} = [C] \begin{pmatrix} [V_0] & [L] & [C] \\ 0 & 0 & 1 \end{pmatrix} \quad (10.62)$$

or with the corresponding row $[R] \triangleq (11 - 1)$ of Equation 10.54

$$[R] \begin{pmatrix} [T] & [E] & [Q] \\ 1 & 1 & -1 \end{pmatrix} \begin{pmatrix} [T] \\ [E] \\ [Q] \end{pmatrix} \begin{pmatrix} [V_0] & [L] & [C] \\ 0 & 1/2 & 1/2 \\ 1 & 0 & 0 \\ 1 & 0 & 1 \end{pmatrix} = [R] \begin{pmatrix} [V_0] & [L] & [C] \\ 0 & 1/2 & -1/2 \end{pmatrix}. \quad (10.63)$$

With these representations of the dimensional quantities, we can obtain a dimensionless representation of Equations 10.34 and 10.35

$$\frac{d\bar{v}_C}{d\bar{t}} = \bar{i}_L - \bar{f}(\bar{v}_C), \quad (10.64)$$

$$\frac{d\bar{i}_L}{d\bar{t}} = 1 - \sqrt{\varepsilon} \bar{i}_L - \bar{v}_C, \quad (10.65)$$

where

$$\bar{v}_C := \frac{|v_C|}{|V_0|}, \quad \bar{t} := \frac{|t|}{\sqrt{|L||C|}}, \quad \sqrt{\varepsilon} := \frac{|R||C|^{1/2}}{|L|^{1/2}}, \quad \bar{i}_L := \frac{|i_L||L|^{1/2}}{|V_0||C|^{1/2}}. \quad (10.66)$$

Furthermore, the dimensionless tunnel-diode current \bar{f} is defined by

$$\bar{f}(\bar{v}_C) := V_0^{-1} L^{1/2} C^{-1/2} f(V_0 \bar{v}_C). \quad (10.67)$$

The associated dimensionless form of Equations 10.36 and 10.37 can be derived by another scaling of the current $\hat{i}_L := \sqrt{\varepsilon} \bar{i}_L$. Obviously, the dimensionless normal form is not unique.

The classical dimensional analysis shows that $R^2 C/L$ is the only dimensionless constant of the quantities in Equations 10.34 and 10.35. Because the describing equations of the parallel LCR circuit

include the same variables constants, the results of the previous dimensional analysis of the tunnel-diode circuit can be used to normalize Equation 10.38.

Further interesting applications of Desloge's approach of suppressing superfluous parameters in the describing equations can be found in the theory of singular perturbation analysis. The reader is referred, e.g., to the monograph of Smith [57] for further details. Miranker [53] demonstrated that the differential equations of the tunnel-diode circuit can be studied on three timescales $\tau_1 := L/R$, $\tau_2 := RC$, and $\tau_3 := \sqrt{LC}$ where different phenomena arise. If these phenomena are known, corresponding timescales can be written down. However, since all dimensionless equations can be derived in a systematic manner using Desloge's approach also the corresponding timescales result. In this way, e.g., all normalized differential equations describing Chua's circuit (see Ref. [42]) can be obtained but other representations of these differential are possible using dimensional analysis.

10.4 Equivalence of Nonlinear Resistive n -Ports

In this section, we only consider equivalence of nonlinear resistive n -ports; however, resistive circuits without accessible ports will not be included in the discussion. Although the explanations that follow are restricted to resistive n -ports, this theory can be easily extended to pure capacitive and inductive n -ports; see Ref. [23]. In Section 10.5, we give a definition of those n -ports.

At first, we consider linear resistive 1-ports that contain Ohmic resistors described by $v_k = R_k i_k$ or/and $i_k = G_k u_k$, and independent current and voltage sources $v_k = V_0^k$ and $i_k = I_0^k$. We can use Helmholtz–Thevenin's or Mayer–Norton's theorem [40,51] to compare any two of those 1-ports and reduce a complex 1-port to a more simple "normal" form. Therefore, two of those 1-ports are called equivalent if they have the same Helmholtz–Thevenin or Mayer–Norton resistor-source 1-port representation. Clearly, by this approach, an equivalence relation is defined in the set of linear resistive 1-ports and it is decomposed into "rich" classes of 1-ports. To calculate these normal forms, Δ -Y and/or Y- Δ transformations are needed; see Refs. [20,51]. It is known that this approach is not applicable to nonlinear resistive networks because, e.g., Δ -Y and/or Y- Δ transformations generally do not exist for nonlinear networks. This was observed by Millar [52] for the first time. Certain circuits where these transformations can be performed were presented by Chua [14]. More recently, Boyd and Chua [5,6] clarified the reasons behind this difficulty from the point of view of Volterra series. As a conclusion, the set of nonlinear resistive 1-ports can be decomposed into equivalence classes, but no reasonable large classes of equivalent 1-ports exist. More general studies of this subject are based on the well-known substitution theorem, which can be used successfully in a certain class of nonlinear circuits. A detailed discussion of the classical substitution theorem can be found in Refs. [27,57] and in an abstract setting in Refs. [33,56]. Some results applicable to 1-ports can be generalized to linear resistive n -ports (extraction of independent sources), but this point of view is not suited for nonlinear resistive n -ports.

Better understanding of nonlinear resistive n -ports and the problem of equivalence cannot be based on the "operational" approach mentioned earlier. Instead, a geometrical approach that was developed by Brayton and Moser [9] is more useful. These authors (see also Ref. [8]) characterize a resistive n -port in a generic manner by n independent relations between the $2n$ port variables, n -port currents i_1, \dots, i_n , and n -port voltages u_1, \dots, u_n . Geometrically, this means that in the $2n$ -dimensional space of port variables, the external behavior of a resistive n -port can be represented generically by an n -dimensional surface. The classical approach formulates a system of equations by

$$\begin{aligned} y_1 - f_1(x_1, \dots, x_n) &= 0, \\ &\vdots \\ y_n - f_n(x_1, \dots, x_n) &= 0, \end{aligned} \tag{10.68}$$

where x 's and y 's are the port variables. The zero set of equations (Equation 10.69) corresponds to the n -dimensional surface. Therefore, two n -ports are called equivalent if they are different parametrizations of the same n -port surface. As an application of this point of view, Brayton and Moser [9] demonstrated that a 2-port consisting of a Y-circuit and a circuit consisting of a Δ -circuit cannot be equivalent, in general. For example, they proved by means of Legendre transformations that a Y-circuit with two Ohmic resistors and a third resistor can be equivalent to a Δ -circuit if and only if the third resistor is also linear. Therefore, the operational approach is not a very useful equivalence concept for nonlinear n -ports.

The subject of synthesizing a prescribed input-output behavior of nonlinear resistive n -ports is closely related to the problem of equivalence. Several results were published in this area using ideal diodes, resistors with a concave and convex characteristic, dc voltage and current sources, ideal op-amps, and controlled sources. Therefore, we give a short review of some of these results. On the other hand we do not consider the synthesis of resistive n -ports.

Although the synthesis of nonlinear resistive n -ports was of interest to many circuit designers since the beginning of twentieth century, the first systematic studies of this subject based on previous studies of Millar [52] were published by Chua [13,14]; see, e.g., Itoh [37] for more recent aspects of nonlinear circuit synthesis. Chua's synthesis approach based on the introduction of new linear 2-ports (R -rotators, R -reflectors, and scalors) as well as their electronic realizations. Now, curves in the i - v space of port current i and port voltage v that characterize a (nonlinear) resistive 1-port can be reflected and scaled in a certain manner. Chua suggested that a prescribed behavior of an active or passive nonlinear resistive 1-port can be reduced essentially to the realization of passive i - v curves. Piecewise-linear approximations of characteristics of different types of diodes, as well as the previously mentioned 2-ports, are used to realize a piecewise-linear approximation of any prescribed passive i - v curve. In another article, Chua [15] discussed a unified procedure to synthesize a nonlinear dc circuit mode that represents a prescribed family of input and output curves of any strongly passive 3-terminal device (e.g., a transistor). It was assumed that the desired curves are piecewise-linear. Since then, this research area has grown very rapidly and piecewise-linear synthesis and modeling has become an essential tool in the simulation of nonlinear circuits; see Refs. [19,34,39,41].

10.5 Equivalence of Nonlinear Dynamical n -Ports

In this section, we consider more general n -ports that can be used for device modeling; see Ref. [16]. Although many different *lumped* multiterminal and multiport circuits are used, a decomposition into two mutually exclusive classes is possible: algebraic and dynamic multiterminal and multiports. Adopting the definition of Chua [16], an $(n + 1)$ -terminal of n -port circuit is called an algebraic element if and only if its constitutive relations can be expressed symbolically by algebraic relationships involving at most two dynamically independent variables for each port. In the case of an 1-port, a so-called memristor is described by flux and charge, a resistor by voltage and current, an inductor by flux and current, and a capacitor by voltage and charge. An element is called a dynamic element if and only if it is not an algebraic element.

Despite the fact that the class of all dynamic elements is much larger than that of algebraic ones, the following theorem of Chua [16] suggests that resistive multiports are essential for dynamic elements, too.

THEOREM 10.7

Every lumped $(n + 1)$ -terminal or n -port element can be synthesized using only a finite number n of linear 2-terminal capacitors (or inductors) and one (generally nonlinear) $(n + m)$ -port resistor with n accessible ports and m ports for the capacitors.

This theorem demonstrates that any n -port made of lumped multiterminal and/or multiport elements is equivalent to a multiterminal network where all of its nonlinear elements are *memoryless*. This fact offers a possibility to classify $(n + 1)$ -terminal and n -port elements in an operational manner.

The proof of this theorem provides the answer of a fundamental question: what constitutes a minimal set of network elements from which all lumped elements can be synthesized?

THEOREM 10.8

The following set \mathcal{M} of network elements constitutes the minimal basic building blocks in the senses that any lumped multiterminal or multiport element described by a continuous constitutive relation on any closed and bounded set can be synthesized using only a finite number of elements of \mathcal{M} , and that this statement is false if even one element is deleted from \mathcal{M} :

1. Linear 2-terminal capacitors (or inductors)
2. Nonlinear 2-terminal resistors
3. Linear 2-port current-controlled voltage sources (CCVS) defined by $v_1 = 0$ and $v_2 = ki_1$
4. Linear 2-port current-controlled current sources (CCCS) defined by $i_1 = 0$ and $i_2 = \tilde{k}v_1$

The proof of Theorem 10.8 (see Ref. [16]) is based on a remarkable theorem of Kolmogoroff, which asserts that a continuous function $f: \mathbb{R}^n \rightarrow \mathbb{R}$ can always be decomposed over the unit cube of \mathbb{R}^n into a certain sum of functions of a single variable. Although the proof of Theorem 10.8 is constructive, it is mainly of theoretical interest since the number of controlled sources needed in the realization is often excessive.

10.6 Equivalence of Reciprocal Nonlinear Dynamic Circuits

As already mentioned in Section 10.1, a certain set of circuits can be decomposed into classes of equivalent circuits by some type of equivalence relation. Such equivalence relations are introduced in a direct manner with respect to the descriptive equations, using a transformation group of classifying the behavior of the solution of the descriptive equations. In the last few sections, several useful ideas for defining equivalence relations were discussed that can be suitable for circuit theory. In this section equivalent dynamical circuits are considered in more detail. It should be emphasized again that equivalence has a different meaning depending of the applied equivalence relation.

As the so-called state-space equations in circuit and system theory arose in the early 1960s, a first type of equivalence was defined because various circuits can be described by the same state-space equations. Of course, from this observation an equivalence relation is induced; see Ref. [61] for further references. Although this approach is interesting, in some cases different choices of variables for describing nonlinear circuits exist that need not lead to equivalent state-space equations; see, e.g., Ref [17]. In other words, the transformations of coordinates are not well conditioned. This approach was applied also to nonlinear input–output systems.

If we consider nonlinear reciprocal circuits, the Brayton–Moser approach [9] to formulate the describing equations for this class of circuits is very suitable; see also Ref. [48]. In order to formulate a generalized type of state-space equations, Brayton and Moser used a so-called mixed-potential function P . P depends on the capacitor voltages \mathbf{v} and the inductor currents \mathbf{i} where the vector field of the circuit equations can be derived by partial derivatives. The Brayton–Moser equations can be formulated in the following manner:

$$\mathbf{C}(\mathbf{v}) \frac{d\mathbf{v}}{dt} = -\frac{\partial P}{\partial \mathbf{v}}(\mathbf{v}, \mathbf{i}), \quad -\mathbf{L}(\mathbf{i}) \frac{d\mathbf{i}}{dt} = -\frac{\partial P}{\partial \mathbf{i}}(\mathbf{v}, \mathbf{i}). \quad (10.69)$$

A discussion of the Brayton–Moser equations from a point of view of constrained differential equation in a differential geometric setting can be found in Ref. [46]. A very general concept of constructing mixed-potential functions is presented by Weiss et al. [60]. In the following, we consider the equivalence concept for reciprocal nonlinear dynamical circuits based in Brayton–Moser equations where Varaiya and Verma [58] included external ports (input–output description). For this purpose they use a more compact form of the Brayton–Moser where the generalized state vector $\mathbf{x} := (\mathbf{v}, \mathbf{i})$ and the coefficient matrix $\mathbf{A} := \text{diag}(\mathbf{C}(\mathbf{v}), -\mathbf{L}(\mathbf{i}))$ is introduced. It should be noted that another geometric approach for nonlinear dynamical input–output circuits is available based on Hamiltonian equations with external ports—the so-called port Hamiltonian equations—where a so-called Dirac structure is used for energy preserving interconnections. With respect to this concept, the reader is referred to the literature; see recent publications of Maschke [47] and can der Schaft [12]) and the cited older publications.

The input–output circuit description of Verma [59] is formulated in the following manner: Let $\mathbf{x} \in \mathbb{R}^n$ the state-space vector, $\mathbf{u} \in \mathbb{R}^m$ the input vector, and $\mathbf{e} \in \mathbb{R}^m$ the output vector, then the Brayton–Moser type state-space equations can be generated by a matrix-valued function $\mathbf{A}(\mathbf{x}): \mathbb{R}^n \rightarrow \mathbb{R}^{n \times n}$ and a real-valued function $P: \mathbb{R}^n \times \mathbb{R}^m \rightarrow \mathbb{R}$

$$\mathbf{A}(\mathbf{x}) \frac{d\mathbf{x}}{dt} = - \frac{\partial P}{\partial \mathbf{x}}(\mathbf{x}, \mathbf{u}), \quad (10.70)$$

$$\mathbf{e} = \frac{\partial P}{\partial \mathbf{u}}(\mathbf{x}, \mathbf{u}). \quad (10.71)$$

For two such circuits $N_1 = \{\mathbf{A}_1, P_1\}$ and $N_2 = \{\mathbf{A}_2, P_2\}$, Varaiya and Verma [58] defined the following equivalence concept.

Definition 10.4: *Two Brayton–Moser type circuits N_1 and N_2 with the outputs $\mathbf{e}_1 = \partial P_1 / \partial \mathbf{u}$ and $\mathbf{e}_2 = \partial P_2 / \partial \mathbf{u}$ are input–output equivalent if there exists a diffeomorphism Θ with $\mathbf{y} = \Theta(\mathbf{x})$, such that for all $\mathbf{x}_0 \in \mathbb{R}^n$, all input functions \mathbf{u} , and all $t \geq 0$ the following assumptions are satisfied*

1. $\Theta(x(t, \mathbf{x}_0, \mathbf{u})) = \mathbf{y}(t, \Theta(\mathbf{x}_0), \mathbf{u})$
2. $\mathbf{e}_1(t, \mathbf{x}_0, \mathbf{u}) = \mathbf{e}_2(t, \Theta(\mathbf{x}_0), \mathbf{u})$

The diffeomorphism Θ is called the equivalence map.

Thus, two circuits are equivalent if their external behavior is identical, i.e., if for the same input and corresponding states they yield the same output. It is clear that this definition results an equivalence relation on the set of all dynamical circuits under consideration. In their paper, Varaiya and Verma [58] showed that, under the additional assumption of controllability, the diffeomorphism Θ establishes an isometry between the manifold with the (local) pseudo-Riemannian metric $\langle d\mathbf{x}, d\mathbf{x} \rangle := \langle d\mathbf{x}, \mathbf{A}_1 d\mathbf{x} \rangle$ and the manifold with the (local) pseudo-Riemannian metric $\langle d\mathbf{y}, d\mathbf{y} \rangle := \langle d\mathbf{y}, \mathbf{A}_2 d\mathbf{y} \rangle$ in many interesting cases of nonlinear reciprocal circuits. This statement has an interesting interpretation in the circuit context. It can be proven that Θ must relate the reactive parts of the circuits N_1 and N_2 in such a way that, if N_1 is in the state \mathbf{x} and N_2 is in the state $\mathbf{y} = \Theta(\mathbf{x})$, and if the input \mathbf{u} is applied, then

$$\left\langle \frac{d\mathbf{i}}{dt}, \mathbf{L}(\mathbf{i}) \frac{d\mathbf{i}}{dt} \right\rangle - \left\langle \frac{d\mathbf{v}}{dt}, \mathbf{C}(\mathbf{v}) \frac{d\mathbf{v}}{dt} \right\rangle = \left\langle \frac{d\tilde{\mathbf{i}}}{dt}, \tilde{\mathbf{L}}(\tilde{\mathbf{i}}) \frac{d\tilde{\mathbf{i}}}{dt} \right\rangle - \left\langle \frac{d\tilde{\mathbf{v}}}{dt}, \tilde{\mathbf{C}}(\tilde{\mathbf{v}}) \frac{d\tilde{\mathbf{v}}}{dt} \right\rangle. \quad (10.72)$$

The concept of equivalence defined in a certain subset of nonlinear dynamic circuits with input and output terminals given by Varaiya and Verma [58] is based on diffeomorphic coordinate transformations

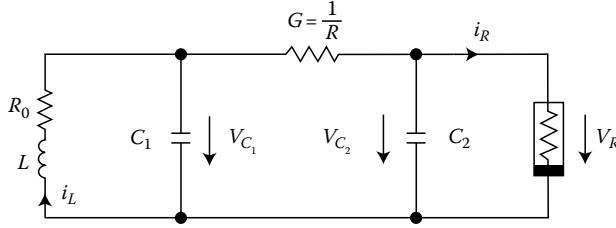


FIGURE 10.5 Modified Chua's circuit.

(the transformation group of diffeomorphisms). Unfortunately, the authors present no ideas about the kind of “coarse graining” produced in this set of circuits by their equivalence relation. However, a comparison to C^k conjugacy or C^k equivalence of vector fields in Section 10.1 implies that input–output equivalence leads to a “fine” decomposition in the set of Brayton–Moser input–output circuits. To classify the main features of the dynamics of circuits, the concept of topological equivalence (the transformation group of homeomorphisms) is useful. On the other hand, in the case of circuits with nonhyperbolic fixed points, the group of diffeomorphisms is needed to distinguish the interesting features. An interesting application of C^1 equivalence of vector fields is given by Chua [18]. To compare nonlinear circuits that generate chaotic signals, Chua applied the concept of equivalence relation and concluded that the class of circuits and systems that are C^1 equivalent to Chua's circuit (see Figure 10.5) is relative small. The nonlinearity in this circuit is described by a piecewise-linear i - v characteristic; see Ref. [42] for further details. The equations describing Chua's circuit are

$$\frac{dv_{C_1}}{dt} = \frac{1}{C_1} [G(v_{C_2} - v_{C_1}) - f(v_{C_1})], \tag{10.73}$$

$$\frac{dv_{C_2}}{dt} = \frac{1}{C_2} [G(v_{C_1} - v_{C_2}) + i_L], \tag{10.74}$$

$$\frac{di_L}{dt} = \frac{1}{L} [v_{C_2} - R_0 i_L], \tag{10.75}$$

where $R_0 = 0$ and the piecewise-linear function is defined by (G_a, G_b, E suitable constants)

$$f(v_{C_1}) := G_b v_{C_1} + \frac{1}{2} (G_a - G_b) (|v_{C_1} + E| - |v_{C_1} - E|). \tag{10.76}$$

Chua's extended approach to study the set of the piecewise-linear circuits that includes Chua's circuit introduces the concept of global unfoldings. This concept can be considered as an analogy to the theory of “local unfoldings” of nonhyperbolic systems in a small neighborhood of singularities [3,30]. Heuristically, a minimum number of parameters in a given nonhyperbolic system is obtained. Chua demonstrated that Chua's circuit with arbitrary $R_0 \neq 0$ can be considered as an “unfolding” of the original circuit. Furthermore, he proved that a class of circuits that can be described without any loss of generality by

$$\dot{\mathbf{x}} = \mathbf{Ax} + \mathbf{b}, \quad x_1 \leq -1 \tag{10.77}$$

$$= \mathbf{Ax}, \quad -1 \leq x_1 \leq +1 \tag{10.78}$$

$$= \mathbf{Ax} + \mathbf{b}, \quad x_1 \geq +1 \tag{10.79}$$

is equivalent to the unfolded Chua’s circuit if certain conditions are satisfied. In the associated parameter space, these conditions defined a set of measure zero. The proof of this theorem as well as some applications are included in Ref. [18].

The ideas of normal forms presented in Section 10.2 can be applied to nonlinear circuits with hyperbolic and nonhyperbolic fixed points. A similar theory of normal forms of maps can be used to study limit cycles, but this subject is beyond our scope; see Ref. [3] for further details. In any case the vector field has to be reduced to lower dimensions and that can be achieved by the application of the so-called center manifold theorem. Altman [1] illustrated this approach by calculating the center manifold of Chua’s circuit equations and its normal form in a tutorial style. To perform the analytical computations the piecewise nonlinearity (Equation 10.78) is replaced by a cubic function $f(x) = c_0x + c_1x^3$. Based on this normal form, Altman studied bifurcations of Chua’s circuits.

In the following, we describe applications of normal form theory from Section 10.2 to decompose nonlinear dynamical circuits at an arbitrary fixed point into nondynamical and dynamical parts; a sketch of this concept is presented by Keidies and Mathis [43]. In this section we restrict ourself to nonlinear dynamical circuits with constant sources where the describing equations are formulated in a state-space form:

$$\dot{\mathbf{x}} = \mathbf{f}(\mathbf{x}), \quad \mathbf{f}: \mathbf{R}^n \rightarrow \mathbf{R}^n, \tag{10.80}$$

where all nonlinear reactances are replaced by linear reactances, nonlinear resistors, and linear controlled sources; see, e.g., Ref. [20]. It is assumed that all nonlinearities are polynomial functions and can be interpreted as nonlinear controlled sources. It can be assumed that the circuit is decomposed into a linear part that consists of linear reactances and resistive elements, and the nonlinear controlled sources. In other words, the RHS \mathbf{f} of Equation 10.82 can be reformulated in the form $\mathbf{f}(\mathbf{x}) = \mathbf{A}\mathbf{x} + \tilde{\mathbf{f}}(\mathbf{x})$; a block diagram is shown in Figure 10.6. Now, the normal form theorem is applied to transform the nonlinear controlled sources to the input. It is known from Section 10.2 that all nonresonant parts of $\tilde{\mathbf{f}}(\mathbf{x})$ can be eliminated until a prescribed order k if the associated homological equation is satisfied. Therefore, after a nearly identity transformation (Equation 10.15) the normal form of the nonresonant part can be described by (see Figure 10.6)

$$\dot{\mathbf{y}} = \mathbf{A}\mathbf{y}, \quad \mathbf{x} = \mathbf{y} + \mathbf{h}(\mathbf{y}). \tag{10.81}$$

For this decomposition we have to define the nonresonant and resonant terms of the vector field where the eigenvalues of the linear part \mathbf{A} of \mathbf{f} and the degree of the polynomial nonlinearities must be studied.

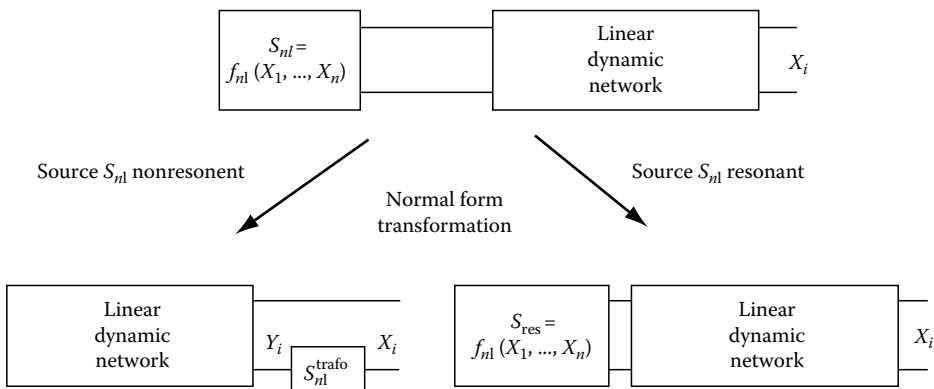


FIGURE 10.6 Decomposition of nonlinear dynamic circuits.

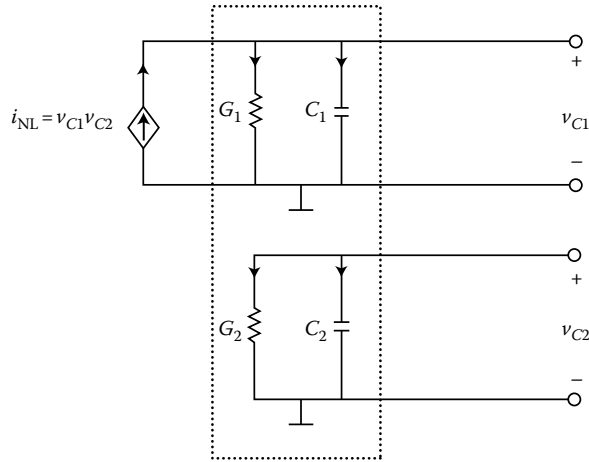


FIGURE 10.7 Decomposition of a simple nonlinear dynamic circuits.

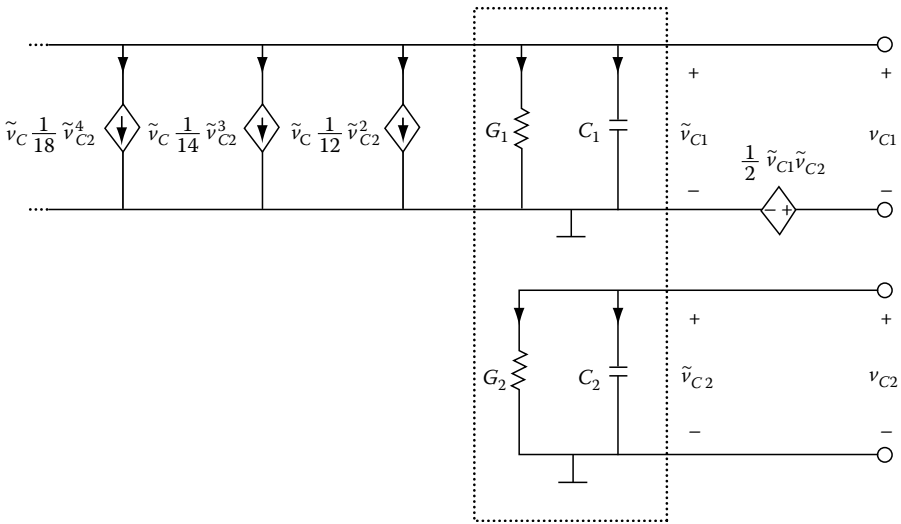


FIGURE 10.8 Decomposition

Under certain conditions, a finite recursive process exists, such that all nonlinear controlled sources can be transformed to the input of the linear part of the circuit under consideration. In these cases, the circuits are described by Equation 10.83 and the corresponding block diagram is shown on the left-hand side in Figure 10.6. If resonant terms occur, a number of additional sources are generated by means of a recursive process. In these cases the controlled cannot transform to the input what is shown on the right-hand side of Figure 10.6. In order to illustrate these statements, a simple example is presented in Figure 10.7. After a nearly identity transformation, a reduction of the nonresonant terms, and the recursive process with respect to the resonant terms, the decomposed circuit is shown in Figure 10.8. Therefore, this application of normal form theorems in circuit analysis can be interpreted as a kind of extraction of nonlinear controlled sources from a nonlinear dynamic circuit. Finally it should be mentioned that this decomposition based on the normal form theorem is related in a certain sense to the so-called exact linearization that is studied in the theory of nonlinear control systems; see, e.g., Refs. [36,54].

References

1. E. J. Altman Bifurcations analysis of Chua's circuit with application for low-level visual sensing, in: R. N. Madan (Ed.), *Chua's Circuit: A Paradigm for Chaos*, Singapore: World Scientific, 1993.
2. V. I. Arnold, *Geometrical Methods in the Theory of Ordinary Differential Equations*, Berlin-New York: Springer-Verlag, 1983.
3. D. K. Arrowsmith and C. M. Place, *An introduction to Dynamical Systems*, Cambridge: Cambridge University Press, 1993.
4. M. Ashkenazi and S.-N. Chow, Normal forms near critical points for differential equations and maps, *IEEE Trans. Circuits Syst.*, 35, 850–862, 1988.
5. S. Boyd and L. O. Chua, Uniqueness of a basic nonlinear structure, *IEEE Trans. Circuits Syst.*, 30, 648–651, 1983.
6. S. Boyd and L. O. Chua, Uniqueness of circuits and systems containing one nonlinearity, *IEEE Trans. Autom. Control*, 30, 674–681, 1985.
7. G. W. Bluman and S. Kumei, *Symmetries and Differential Equations*, New York: Springer-Verlag, 1989.
8. R. K. Brayton, Nonlinear reciprocal networks, in: H. S. Wilf and F. Harary (Eds.), *Mathematical Aspects of Electrical Network Analysis*, Providence, RI: AMS, 1971.
9. R. K. Brayton and J. K. Moser, Nonlinear networks, I, II, *Quart. Appl. Math.*, 23, 1–33, 81–104, 1964.
10. A. D. Bruno, *Local Methods in Nonlinear Differential Equations*, Berlin-New York: Springer-Verlag, 1981.
11. J. Carr, *Applications of Center Manifold Theorem*, Berlin-New York: Springer-Verlag, 1981.
12. J. Cervera, A. J. van der Schaft, and A. Banos, Interconnection of port-Hamiltonian systems and composition of Dirac structures, *Automatica*, 43, 212–225, 2007.
13. L. O. Chua, The rotator—A new network element, *Proc. IEEE*, 55, 1566–1577, 1967.
14. L. O. Chua, Synthesis of new nonlinear network elements, *Proc. IEEE*, 56, 1325–1340, 1968.
15. L. O. Chua, Modelling of three terminals devices: A black box approach, *IEEE Trans. Circuit Theory*, 19, 555–562, 1972.
16. L. O. Chua, Device modeling via basic nonlinear circuit elements, *IEEE Trans. Circuits Syst.*, 27, 1014–1044, 1980.
17. L. O. Chua, Dynamical nonlinear networks: State of the Art, *IEEE Trans. Circuits Syst.*, 27, 1059–1087, 1980.
18. L. O. Chua, Global unfolding of Chua's circuit, *IEEE Trans. Fundam. E76-A*, 704–734, 1993.
19. L. O. Chua and A. C. Deng, Canonical piecewise linear representation, *IEEE Trans. Circuits Syst.*, 33, 101–111, 1988.
20. L. O. Chua, C. A. Desoer, and E. S. Kuh, *Linear and Nonlinear Circuits*, New York: McGraw-Hill, 1987.
21. L. O. Chua and H. Kokukbo, Normal forms for nonlinear vector fields—Part I: Theory and algorithms, *IEEE Trans. Circuits Syst.*, 35, 863–880, 1988.
22. L. O. Chua and H. Kokukbo, Normal forms for nonlinear vector fields—Part II: Applications, *IEEE Trans. Circuits Syst.*, 36, 51–70, 1989.
23. L. O. Chua and Y.-F. Lam, A theory of algebraic n -ports, *IEEE Trans. Circuit Theory*, 20, 370–382, 1973.
24. L. O. Chua and H. Oka, Normal forms of constrained nonlinear differential equations—Part I: Theory and algorithm", *IEEE Trans. Circuits Syst.*, 35, 881–901, 1988.
25. L. O. Chua and H. Oka, Normal forms of constrained nonlinear differential equations—Part II: Bifurcations, *IEEE Trans. Circuits Syst.*, 36, 71–88, 1989.
26. E. A. Desloge, Suppression and restoration of constants in physical equations, *Am J. Phys.*, 52, 312–316, 1984.
27. C. A. Desoer and E. S. Kuh, *Basic Circuit Theory*, New York: McGraw-Hill, 1969.

28. N. Fenichel, Geometric singular perturbation theory for ordinary differential equations, *J. Diff. Eq.*, 31, 5398, 1979.
29. J. Guckenheimer and P. Holmes, *Nonlinear Oscillations, Dynamical Systems, and Bifurcations of Vector Fields*, Berlin-New York: Springer-Verlag 1990.
30. S. Hale and H. Koçak, *Dynamics and Bifurcation*, Berlin-New York: Springer-Verlag, 1991.
31. B. D. Hassard, N. D. Kazarinoff, and Y.-H. Wan, *Theory and Applications of the Hopf Bifurcation*, Cambridge: Cambridge University Press, 1980.
32. B. D. Hassard and Y.-H. Wan, Bifurcation formulae derived from center manifold theorem, *J. Math. Anal. Appl.*, 63, 297–312, 1978.
33. J. Haase, On generalizations and applications of the substitution theorems, *Proc. ECCTD'85*, Praha, Czech., Sept. 2–6, 1985. pp. 220–223.
34. W. P. M. H. Heemels, M. K. Camlibel, and J. M. H. Schumacher, On the dynamic analysis of piecewise-linear networks, *IEEE Trans. Circuits Syst. -I: Fundamental Theory and Applications*, 49, 315–327, 2002.
35. R. A. Horn and C. R. Johnson, *Matrix Analysis*, Cambridge: Cambridge University Press, 1992.
36. A. Isidori, *Nonlinear Control Systems*, Berlin-New York: Springer-Verlag, 1989.
37. M. Itoh, Synthesis of electronic circuits for simulating nonlinear dynamcis, *International Journal of Bifurcation and Chaos*, 11(3), 605–653, 2001.
38. V. G. Ivancevic and T. T. Ivancevic, *Geometric Dynamics of Complex Systems*, Dordrecht, The Netherlands: Springer-Verlag 2006.
39. J. Jess, Piecewise linear models for nonlinear dynamic systems, *Frequenz*, 42, 71–78, 1988.
40. D. H. Johnson, Scanning our past—Origins of the equivalent circuit concept: The current-source equivalent, *Proc. IEEE*, 91, 817–821, 2003.
41. T. A. M. Kevenaar and D. M. W. Leenaerts, A comparison of piecewise-linear model descriptions, *IEEE Trans. Circuits Syst. I*, 39, 996–1004, 1992.
42. R. N. Madan, Ed., *Chua's Circuit: A Paradigm for Chaos*, Singapore: World Scientific, 1993.
43. C. Keidies and W. Mathis, Applications of normal forms to the analysis of nonlinear circuits, *Proc. 1993 Int. Symp. Nonlinear Theory and Its Appl. (NOLTA)*, Hawaii, pp. 853–858, Dec. 1993.
44. G. M. Maggio, O. De Feo, and M. P. Kennedy, A general method to predict the amplitude of oscillation in nearly-sinusoidal oscillators, *IEEE Trans. Circuits Sys. I*, 5(8), 1586–1595, Aug 2004.
45. J. Kevorkian and J. D. Cole, *Multiple Scale and Singular Perturbation Methods*, Berlin-New York: Springer-Verlag, 1996.
46. W. Marten, W. Mathis, and L. O. Chua, On the geometrical meaning of pseudo hybrid content and mixed potential, *Int. J. Electronics Communications (AEÜ)*, 46 (4), 305–309, 1992.
47. C. Valentin, M. Magos, and B. Maschke, A port-Hamiltonian formulation of physical switching systems with varying constraints, *Automatica*, 43, 1125–1133, 2007.
48. W. Mathis, *Theory of Nonlinear Networks (in German)*, Berlin-Heidelberg: Springer-Verlag, 1987.
49. W. Mathis, Nonlinear electronic circuits—An overview, *Proc. MIXDES 2000*, Gdynia, Poland, 2000, p. 1517.
50. W. Mathis and L. O. Chua, Applications of dimensional analysis to network theory, *Proc. ECCTD'91*, Copenhagen Denmark, pp. 1243–1252, Sept. 4–6, 1991.
51. W. Mathis and R. Pauli, Network theorems, in: J. G. Webster (Ed.), *Encyclopedia of Electrical and Electronics Engineering*, New York: John Wiley& Sons, Inc., Vol. 14, 1999, pp. 227–240.
52. W. Millar, The nonlinear resistive 3-pole: Some general concepts, *Proc. Symp. Nonlinear Circuit Anal.*, Institute of Brooklyn, New York: Interscience, 1957.
53. W. L. Miranker, *Numerical Methods for Stiff Equations and Singular Perturbation Problems*, Dordrecht: D. Reidel, 1981.
54. H. Nijmeijer and A. van der Schaft, *Nonlinear Dynamical Control Systems*, New York: Springer-Verlag, 1990.

55. L. V. Ovsianikov, *Group Analysis of Differential Equations*, New York: Academic Press, 1982.
56. A. Reibiger, W. Mathis, T. Nähring, and Lj. Trajkovic, Mathematical foundations of the TC-method for computing multiple DC-operating points, *Int. J. Appl. Electromagn. Mech.*, 17, 169–191, 2003.
57. D. R. Smith, *Singular-Perturbation Theory*, Cambridge: Cambridge University Press, 1985.
58. P. P. Varaiya and J. P. Verma, Equivalence of nonlinear reciprocal networks, *IEEE Trans. Circuit Theory*, 18, 214–217, 1971.
59. J. P. Verma, Equivalence of nonlinear networks, Ph.D. dissertation, University of California, Berkeley, 1969.
60. L. Weiss, W. Mathis, and L. Trajković, A generalization of Brayton-Moser's mixed potential function, *IEEE Trans. Circuits Syst. I: Fundamental Theory and Applications*, 45, 423–427, 1998.
61. A. N. Willson, Jr., *Nonlinear Networks: Theory and Analysis*, New York: IEEE, 1975.

11

Piecewise-Linear Circuits and Piecewise- Linear Analysis

11.1	Introduction and Motivation	11-1
11.2	Hierarchy of Piecewise-Linear Models and Their Representations	11-3
11.3	Piecewise-Linear Models for Electronic Components...	11-8
11.4	Structural Properties of Piecewise-Linear Resistive Circuits.....	11-14
11.5	Analysis of Piecewise-Linear Resistive Circuits.....	11-15
	Theorem Canonical PWL (Tableau Analysis) • Algorithm	
11.6	Piecewise-Linear Dynamic Circuits	11-18
11.7	Efficient Computer-Aided Analysis of PWL Circuits	11-19
	Acknowledgment	11-20
	References.....	11-20

Joos Vandewalle
Catholic University of Leuven

Lieven Vandenberghe
University of California, Los Angeles

11.1 Introduction and Motivation

In this chapter, we present a comprehensive description of the use of piecewise-linear (PWL) methods in modeling, analysis, and structural properties of nonlinear circuits. The main advantages of piecewise-linear circuits are fourfold. (1) Piecewise-linear circuits are the easiest in the class of nonlinear circuits to analyze exactly, because many methods for linear circuits can still be used. (2) The piecewise-linear approximation is an adequate approximation for most applications. Moreover, certain operational amplifier (op-amp), operational transconductance amplifier (OTA), diode and switch circuits are essentially piecewise linear. (3) Quite a number of methods exist to analyze piecewise-linear circuits. (4) Last, but not least, piecewise-linear circuits exhibit most of the phenomena of nonlinear circuits while still being manageable. Hence, PWL circuits provide unique insight in nonlinear circuits.

This chapter is divided into six sections. First, the piecewise-linear models will be presented and interrelated. A complete hierarchy of models and representations of models is presented. Rather than proving many relations, simple examples are given. Second, the piecewise-linear models for several important electronic components are presented. Third, since many PWL properties are preserved by interconnection, a short discussion on the structural properties of piecewise-linear circuits is given in Section 11.4. Fourth, analysis methods of PWL circuits are presented, ranging from the Katzenelson algorithm to the linear complementarity methods and the homotopy methods. Fifth, we discuss PWL dynamic circuits, such as the famous Chua circuit, which produces chaos. Finally, in Section 11.7, efficient

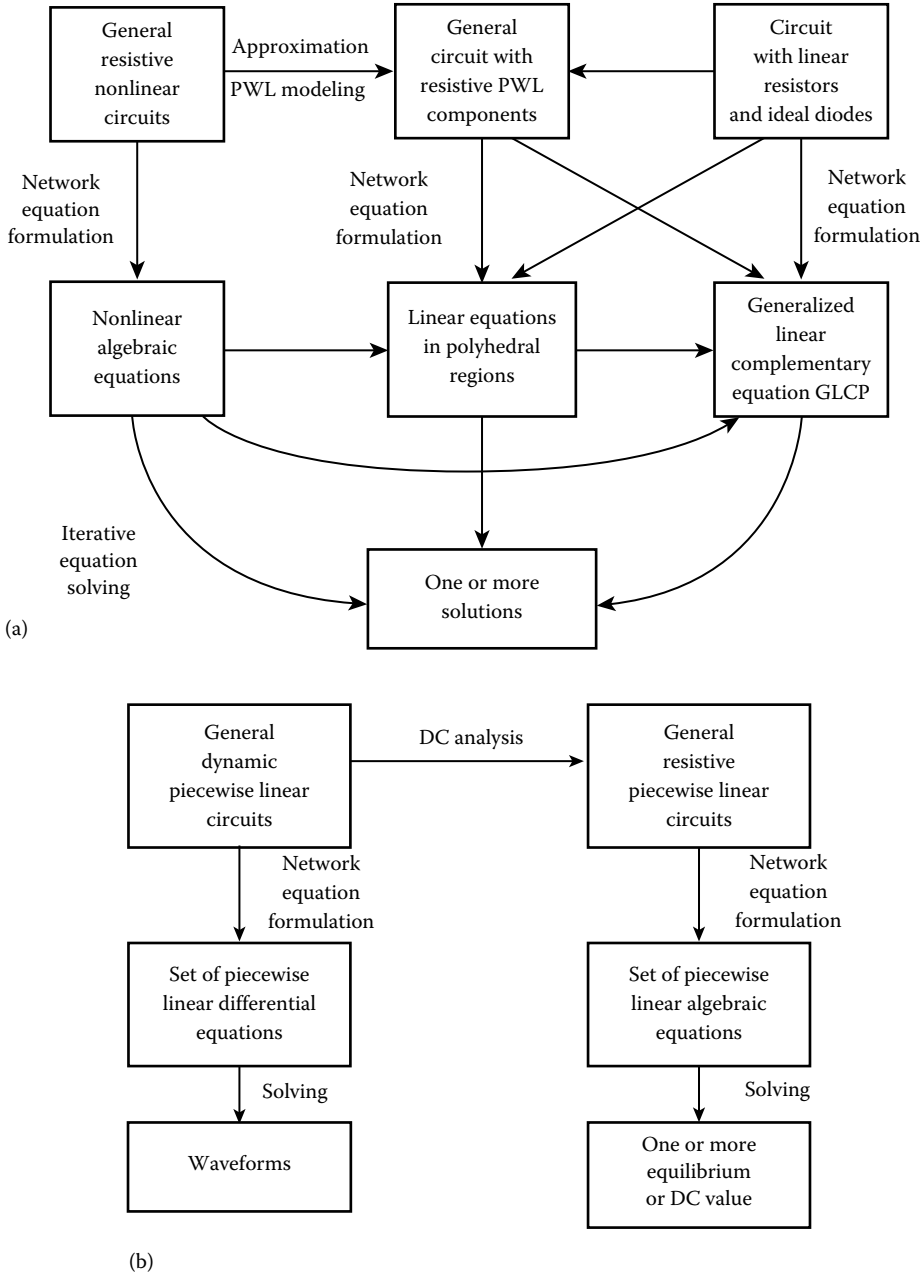


FIGURE 11.1 Interrelation of PWL circuit analysis methods: (a) resistive and (b) dynamic nonlinear circuits.

computer-aided analysis of PWL circuits and the hierarchical mixed-mode PWL analysis are described. A comprehensive reference list is included. For the synthesis of PWL circuits, we refer to Chapter 8.

In order to situate these subjects in the general framework of nonlinear circuits, it is instructive to interrelate the PWL circuit analysis methods (Figure 11.1). In the horizontal direction of the diagrams, one does the PWL approximation of the dc analysis from left to right. In the vertical direction, we show the conversion from a circuit to a set of equations by network equation formulation and the conversion

from equations to solutions (waveforms or dc values) by solution methods. The specific methods and names used in the figure are described in detail in the different parts.

11.2 Hierarchy of Piecewise-Linear Models and Their Representations

In the past 25 years, much progress has been achieved in the representations of piecewise-linear resistive multiports and their relationships (see Refs. [1,2]). From a practical point of view, a clear trade-off exists between the efficiency of a representation in terms of the number of parameters and the ease of evaluation (explicit versus implicit models) on the one hand and the generality or accuracy on the other hand. Here, we go from the easiest and most efficient to the most general representations.

We define here a resistive multiport (Figure 11.2) as an n -port whose port variables (the vector of port currents $i = [i_1, \dots, i_n]^T$ and the vector of port voltages $v = [v_1, \dots, v_n]^T$) are related by m algebraic equations called constitutive equations

$$\phi(i, v) = 0 \tag{11.1}$$

where $i, v \in \mathbb{R}^n$ and $\phi(\cdot, \cdot)$ maps \mathbb{R}^{2n} into \mathbb{R}^m .

For example, for a bipolar transistor (Figure 11.3), one obtains the explicit form $i_1 = f_1(v_1, v_2)$ and $i_2 = f_2(v_1, v_2)$, and $i = [i_1, i_2]^T$ and $v = [v_1, v_2]^T$. These relations can be measured with a curve tracer as dc characteristic curves. Clearly, here $\phi(\cdot, \cdot)$ is a map from $\mathbb{R}^4 \rightarrow \mathbb{R}^2$ in the form

$$i_1 - f_1(v_1, v_2) = 0 \tag{11.2}$$

$$i_2 - f_2(v_1, v_2) = 0 \tag{11.3}$$

It is easy to see that a complete table of these relationships would require an excessive amount of computer storage already for a transistor. Hence, it is quite natural to describe a resistive n -port with a piecewise-linear map f over polyhedral regions P_k by

$$v = f(i) = a_k + B_k i, \quad i \in P_k, \quad k \in \{0, 1, \dots, 2^l - 1\} \tag{11.4}$$

where the Jacobian $B_k \in \mathbb{R}^{n \times n}$ and the offset vector $a_k \in \mathbb{R}^n$ are defined over the polyhedral region P_k , separated by hyperplanes $c_i^T x - d_i = 0, i = 1, \dots, l$ and defined by

$$P_k = \left\{ x \in \mathbb{R}^n \mid c_j^T x - d_j \geq 0, j \in I_k, c_j^T x - d_j \leq 0, j \notin I_k \right\} \tag{11.5}$$

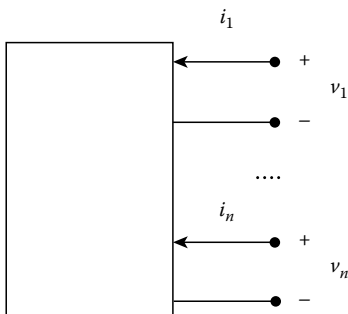


FIGURE 11.2 Resistive n -port.

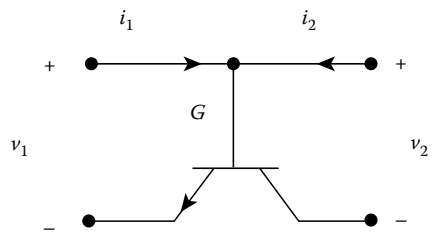


FIGURE 11.3 Two-port configuration of a bipolar transistor.

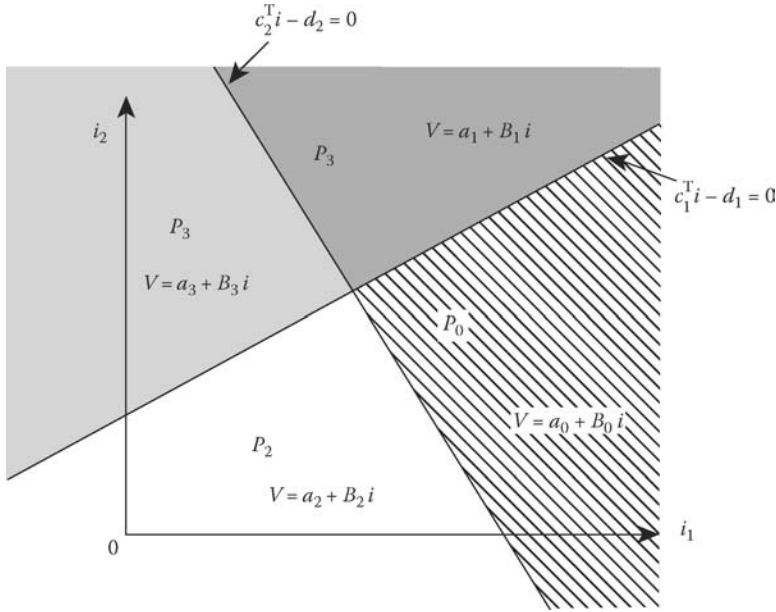


FIGURE 11.4 PWL function defined in four polyhedral regions in \mathbb{R}^n defined by $c_1^T i - d_1 \leq 0$ and $c_2^T i \geq d_2 > 0$.

where

$$\begin{aligned}
 k &= \sum_{j \in I_k} 2^{j-1} \\
 I_k &\subseteq \{1, 2, \dots, l\} \\
 c_j &\in \mathbb{R}^n, d_j \in \mathbb{R}^n
 \end{aligned}$$

In other words, the hyperplanes $c_i^T x - d_i = 0, i = 1, \dots, l$ separate the space \mathbb{R}^n into 2^l polyhedral regions P_k (see Figure 11.4) where the constitutive equations are linear.

The computer storage requirements for this representation is still quite large, especially for large multiports. A more fundamental problem with this rather intuitive representation is that it is not necessarily continuous at the boundaries between two polyhedral regions. In fact, the continuity of the nonlinear map is usually desirable for physical reasons and also in order to avoid problems in the analysis.

The canonical PWL representation [6] is a very simple, attractive, and explicit description for a resistive multiport that solves both problems:

$$v = f(i) = a + Bi + \sum_{j=1}^l e_j |c_j^T i - d_j| \tag{11.6}$$

One can easily understand this equation by looking at the wedge form of the modulus map (see Figure 11.5). It has two linear regions: in the first $x \geq 0$ and $y = x$, while in the second $x \leq 0$ and $y = -x$. At the boundary the function is clearly continuous. Equation 11.6 is hence also continuous and is linear in each of the polyhedral regions P_k described by Equation 11.5. If l modulus terms are in Equation 11.6, there are 2^l polyhedral regions where the map Equation 11.6

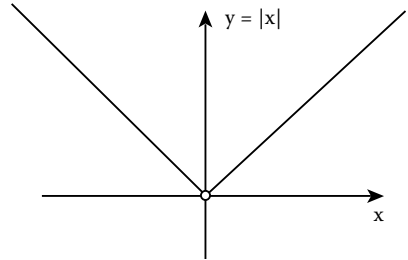


FIGURE 11.5 Absolute value function $y = |x|$.

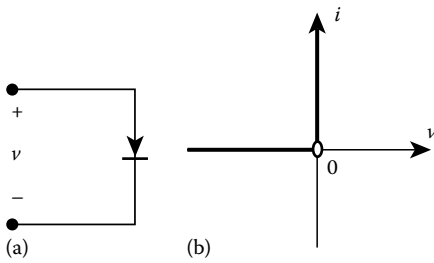


FIGURE 11.6 (a) The ideal diode and (b) the $(i-v)$ relation of an ideal diode.

is linear. Because the map is represented canonically with $n + n^2 + l(n + 1)$ real parameters, this is a very compact and explicit representation.

Several examples of canonical PWL models for components are given in Section 11.3.

From Figure 11.5, it should be clear that the right and left derivative of $y = |x|$ at 0 are different, their difference being 2. Hence, the Jacobian J_+ and J_- of Equation 11.6 will be different on the boundary between the two neighboring polyhedral regions where $(c_j i - d_j) \geq 0$ and $(c_j i - d_j) \leq 0$.

$$J_+ - J_- = 2e_j c_j^T \tag{11.7}$$

Observe that this difference is a rank 1 matrix, which is also called a dyadic or outer vector product of e_j and c_j . Moreover, this difference is independent of the location of the independent variable i on the boundary. This important observation is made in Ref. [24], and is called the consistent variation property [10] and essentially says that the variation of the Jacobian of a canonical PWL representation is independent of the place where the hyperplane $c_j i - d_j = 0$ is crossed. Of course, this implies that the canonical PWL representation (Equation 11.6) is not the most general description for a continuous explicit PWL map. In Refs. [26,29] two more general representations, which include nested absolute values, are presented. These are too complicated for our discussion.

Clearly, the canonical PWL representation (Equation 11.6) is valid only for single-valued functions. It can clearly not be used for an important component: the ideal diode (Figure 11.6) characterized by the multivalued (i, v) relation. It can be presented analytically by introducing a real scalar parameter ρ [31].

$$i = \frac{1}{2}(\rho + |\rho|) \tag{11.8}$$

$$v = \frac{1}{2}(\rho - |\rho|) \tag{11.9}$$

This parametric description can easily be seen to correspond to Figure 11.6b because $i = \rho$ and $v = 0$ for $\rho \geq 0$, while $i = 0$ and $v = \rho$ when $\rho \leq 0$. Such a parametric description $i = f(\rho)$ and $v = g(\rho)$ with f and g PWL can be obtained for a whole class of unicursal curves [6].

When we allow implicit representations between v and i for a multiport, we obtain a linear complementarity problem (LCP) model Equations 5.10 through 5.12 with an interesting state space like form [55]:

$$v = Ai + Bu + f \tag{11.10}$$

$$s = Ci + Du + g \tag{11.11}$$

$$u \geq 0, \quad s \geq 0, \quad u^T s = 0 \tag{11.12}$$

where $A \in \mathbb{R}^{n \times n}$, $B \in \mathbb{R}^{n \times l}$, $f \in \mathbb{R}^{n \times n}$, $c \in \mathbb{R}^{l \times n}$, $D \in \mathbb{R}^{l \times l}$ are the parameters that characterize the relationship between v and i . In the model, u and s are called the state vectors and we say that $u \geq 0$ when all its components are nonnegative. Clearly, Equation 11.12 dictates that all components of u and s should be nonnegative and that, whenever a component u_j satisfies $u_j > 0$, then $s_j = 0$ and, vice versa, when $s_j > 0$, then $u_j = 0$. This is called the linear complementarity property, which we have seen already in the ideal diode equation (Equations 11.8 and 11.9) where $i \geq 0$, $v \geq 0$ and $iv = 0$. Hence, an implicit or LCP model for the ideal diode equation (Equations 11.8 and 11.9) is

$$v = u \tag{11.13}$$

$$s = i \tag{11.14}$$

$$u \geq 0, \quad s \geq 0, \quad us = 0 \tag{11.15}$$

In order to understand that the general equations (Equations 11.10 through 11.12) describe a PWL relation such as Equations 11.4 and 11.5 between i and v over polyhedral regions, one should observe first that $v = Ai + f$ is linear when $u = 0$ and $s = Ci + g \geq 0$. Hence, the relation is linear in the polyhedral region determined by $Ci + g \geq 0$. In general, one can consider 2^l possibilities for u and s according to

$$(u_j \geq 0 \text{ and } s_j = 0) \text{ or } (u_j = 0 \text{ and } s_j \geq 0) \quad \text{for } j = 1, 2, \dots, l$$

Denote sets of indexes U and S for certain values of u and s satisfying Equation 11.12

$$U = \{j | u_j \geq 0 \text{ and } s_j = 0\} \tag{11.16}$$

$$S = \{j | u_j = 0 \text{ and } s_j \geq 0\} \tag{11.17}$$

then, clearly, U and S are complementary subsets of $\{1, 2, \dots, l\}$ when for any j , u_j and s_j cannot be both zero. Clearly, each of these 2^l possibilities corresponds to a polyhedral region P_U in \mathbb{R}^n , which can be determined from

$$u_j \geq 0 \quad (Ci + Du + g)_j = 0 \quad \text{for } j \in U \tag{11.18}$$

$$u_j = 0 \quad (Ci + Du + g)_j \geq 0 \quad \text{for } j \in S \tag{11.19}$$

The PWL map in region P_U is determined by solving the u_j for $j \in U$ from Equation 11.18 and substituting these along with $u_j = 0$ for $j \in S$ into Equation 11.10. This generates, of course, a map that is linear in the region P_U .

When Equation 11.11 is replaced by the implicit equation

$$Es + Ci + Du + g\alpha = 0, \quad \alpha \geq 0$$

in Equations 11.10 through 11.13, we call the problem a generalized linear complementarity problem (GLCP).

A nontrivial example of an implicit PWL relation (LCP model) is the hysteresis one port resistor (see Figure 11.7). Its equations are

$$v = -i + [-\mathbf{1} \ \mathbf{1}] \begin{bmatrix} u_1 \\ u_2 \end{bmatrix} + 1 \tag{11.20}$$

$$\begin{bmatrix} s_1 \\ s_2 \end{bmatrix} = \begin{bmatrix} -1 \\ 1 \end{bmatrix} i + \begin{bmatrix} -1 & 1 \\ 1 & -1 \end{bmatrix} \begin{bmatrix} u_1 \\ u_2 \end{bmatrix} + \begin{bmatrix} 1 \\ 0 \end{bmatrix} \tag{11.21}$$

$$\begin{aligned} s_1 \geq 0, \quad s_2 \geq 0, \quad u_1 \geq 0, \quad u_2 \geq 0, \\ u_1 s_1 + u_2 s_2 = 0 \end{aligned} \tag{11.22}$$

In the first region P , we have

$$\begin{aligned} s_1 = -i + 1 \geq 0, \quad s_2 = i \geq 0, \quad \text{and} \\ v = -i + 1 \end{aligned} \tag{11.23}$$

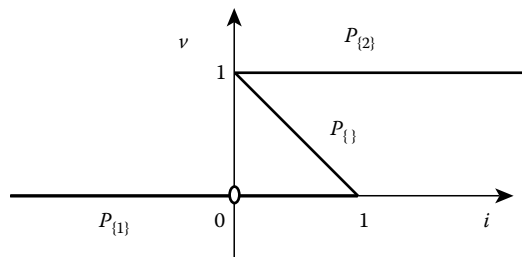


FIGURE 11.7 Hysteresis nonlinear resistor.

The region $P_{\{1,2\}}$, on the other hand, is empty because the following set of equations are contradictory:

$$\begin{aligned} s_1 = s_2 = 0, \quad -i - u_1 + u_2 + 1 = 0, \\ i + u_1 - u_2 = 0 \end{aligned} \tag{11.24}$$

The region $P_{[1]}$ is

$$u_1 \geq 0, \quad s_1 = -i - u_1 + 1 = 0, \quad u_2 = 0, \quad s_2 = i + u_1 \geq 0 \tag{11.25}$$

Hence, $u_1 = -i + 1$ and $s_2 = 1$ and $v = -i + i - 1 + 1 = 0$, while $i \leq 1$.

Finally, the region $P_{[2]}$ is

$$u_1 \geq 0, \quad s_1 = -i + u_2 + 1 \geq 0, \quad u_2 \geq 0, \quad s_2 = i - u_2 = 0$$

Hence

$$u_2 = i \quad \text{and} \quad s_1 = 1 \quad \text{and} \quad v = -i + i + 1 = 1, \quad \text{while} \quad i \geq 0 \tag{11.26}$$

It is now easy to show in general that the canonical PWL representation is a special case of the LCP model. Just choose $u_j \geq 0$ and $s_j \geq 0$ for all j as follows:

$$|c_j^T i - d_j| = \frac{1}{2}(u_j + s_j) \tag{11.27}$$

$$c_j^T i - d_j = \frac{1}{2}(u_j - s_j) \tag{11.28}$$

then, u and s are complementary vectors, i.e.,

$$u \geq 0, \quad s \geq 0, \quad u^T s = 0$$

Observe that the moduli in Equation 11.6 can be eliminated with Equation 11.27 to produce an equation of the form (Equation 11.10) and that (Equation 11.28) produces an equation of the form (Equation 11.11).

More generally, it has been proven [36] that the implicit model includes all explicit models. Because it also includes the parametric models, one obtains the general hierarchy of models as depicted in Figure 11.8.

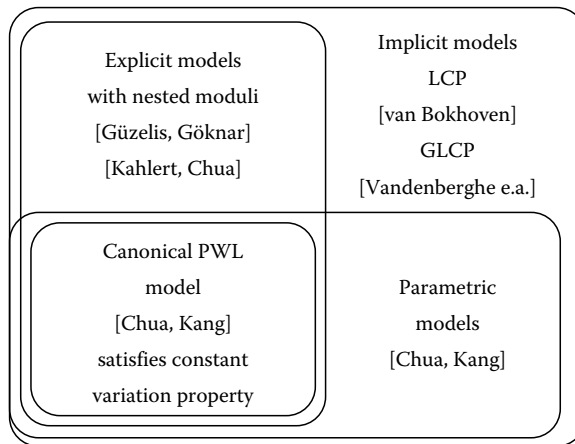


FIGURE 11.8 Interrelation of the PWL models.

A general remark should be made about all models that have been presented until now. Although the models have been given for resistive multiports where the voltages v at the ports are expressed in terms of the currents i , analogous equations can be given for the currents i in terms of the voltages, or hybrid variables. It can even be adapted for piecewise-linear capacitors, inductors, or memristors, where the variables are, respectively, q, v for capacitors, φ, i for inductors, and q, φ for memristors.

11.3 Piecewise-Linear Models for Electronic Components

In order to simulate nonlinear networks with a circuit or network simulator, the nonlinear behavior of the components must be modeled first. During this modeling phase, properties of the component that are not considered important for the behavior of the system may be neglected. The nonlinear behavior is often important, therefore, nonlinear models have to be used. In typical simulators such as SPICE, nonlinear models often involve polynomials and transcendental functions for bipolar and MOS transistors. These consume a large part of the simulation time, so table lookup methods have been worked out. However, the table lookup methods need much storage for an accurate description of multiports and complex components.

The piecewise-linear models constitute an attractive alternative that is both efficient in memory use and in computation time. We discuss here the most important components. The derivation of a model usually requires two steps: first, the PWL approximation of constitutive equations, and second, the algebraic representation.

Two PWL models for an ideal diode (Figure 11.6) have been derived, that is, a parametric model (Equations 11.8 and 11.9) and an implicit model (Equations 11.13 through 11.15, while a canonical PWL model does not exist.

The piecewise-linear models for op-amps and OTAs are also simple and frequently used. The piecewise-linear approximation of op-amps and OTAs of Figure 11.9 is quite accurate. It leads to the

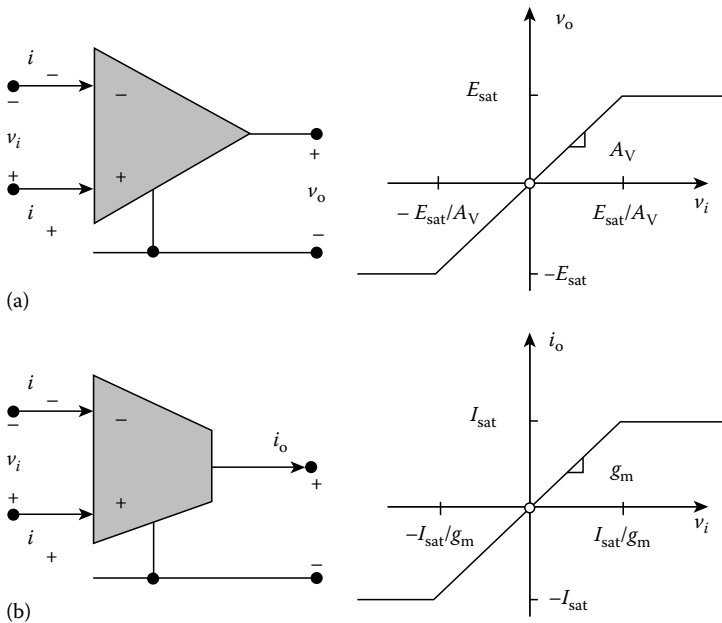


FIGURE 11.9 (a) Op-amp and PWL model and (b) OTA and PWL model.

following representation for the op-amp, which is in the linear region for $-E_{\text{sat}} \leq v_0 \leq E_{\text{sat}}$ with voltage amplification A_v and positive and negative saturation E_{sat} and $-E_{\text{sat}}$

$$v_0 = \frac{A_v}{2} \left(\left| v_i + \frac{E_{\text{sat}}}{A_v} \right| - \left| v_i - \frac{E_{\text{sat}}}{A_v} \right| \right) \quad (11.29)$$

$$i_- = i_+ = 0 \quad (11.30)$$

This is called the op-amp finite-gain model. In each of the three regions, the op-amp can be replaced by a linear circuit.

For the OTA, we have similarly in the linear region for $-I_{\text{sat}} \leq i_0 \leq I_{\text{sat}}$ with transconductance gain g_m and positive and negative saturation I_{sat} and $-I_{\text{sat}}$

$$i_0 = \frac{g_m}{2} \left(\left| v_i + \frac{I_{\text{sat}}}{g_m} \right| - \left| v_i - \frac{I_{\text{sat}}}{g_m} \right| \right) \quad (11.31)$$

$$i_- = i_+ = 0 \quad (11.32)$$

Next, for a tunnel diode, one can perform a piecewise-linear approximation for the tunnel-diode characteristic as shown in Figure 11.10. It clearly has three regions with conductances g_1 , g_2 , and g_3 . This PWL characteristic can be realized by three components (Figure 11.10b) with conductances, voltage sources, and diodes. The three parameters G_0 , G_1 , and G_2 of Figure 11.10b must satisfy

$$\text{In Region 1: } G_0 = g_1 \quad (11.33)$$

$$\text{In Region 2: } G_0 + G_1 = g_2 \quad (11.34)$$

$$\text{In Region 3: } G_0 + G_1 + G_2 = g_3 \quad (11.35)$$

Thus, $G_0 = g_1$, $G_1 = -g_1 + g_2$, and $G_2 = -g_2 + g_3$. We can derive the canonical PWL representation as follows:

$$i = -\frac{1}{2}(G_1 E_1 + G_2 E_2) + \left(G_0 + \frac{1}{2}G_1 + \frac{1}{2}G_2 \right) v + \frac{1}{2}G_1 |v - E_1| + \frac{1}{2}G_2 |v - E_2| \quad (11.36)$$

Next, we present a canonical piecewise-linear bipolar transistor model [12]. Assume a *npn*-bipolar transistor is connected in the common base configuration with $v_1 = v_{BE}$, $v_2 = v_{BC}$, $i_1 = i_E$, and $i_2 = i_C$, as shown in Figure 11.3. We consider data points in a square region defined by $0.4 \leq v_1 \leq 0.7$ and $0.4 \leq v_2 \leq 0.7$, and assume the terminal behavior of the transistor follows the Ebers-Moll equation; namely,

$$i_1 = \frac{I_s}{\alpha_f} \left(e^{v_1/V_T} - 1 \right) - I_s \left(e^{v_2/V_T} - 1 \right) \quad (11.37)$$

$$i_2 = \frac{I_s}{\alpha_r} \left(e^{v_2/V_T} - 1 \right) - I_s \left(e^{v_1/V_T} - 1 \right) \quad (11.38)$$

with $I_s = 10^{-14}$ A, $V_T = 26$ mV, $\alpha_f = 0.99$, and $\alpha_r = 0.5$. In Ref. [12], the following canonical piecewise-linear model is obtained, which optimally fits the data points (Figure 11.11)

$$\begin{aligned} \begin{bmatrix} i_1 \\ i_2 \end{bmatrix} &= \begin{bmatrix} a_1 \\ a_2 \end{bmatrix} + \begin{bmatrix} b_{11} & b_{21} \\ b_{12} & b_{22} \end{bmatrix} \begin{bmatrix} v_1 \\ v_2 \end{bmatrix} + \begin{bmatrix} c_{11} \\ c_{21} \end{bmatrix} |m_1 v_1 - v_2 + t_1| \\ &+ \begin{bmatrix} c_{12} \\ c_{22} \end{bmatrix} |m_2 v_1 - v_2 + t_2| + \begin{bmatrix} c_{13} \\ c_{23} \end{bmatrix} |m_3 v_1 - v_2 + t_3| \end{aligned} \quad (11.39)$$

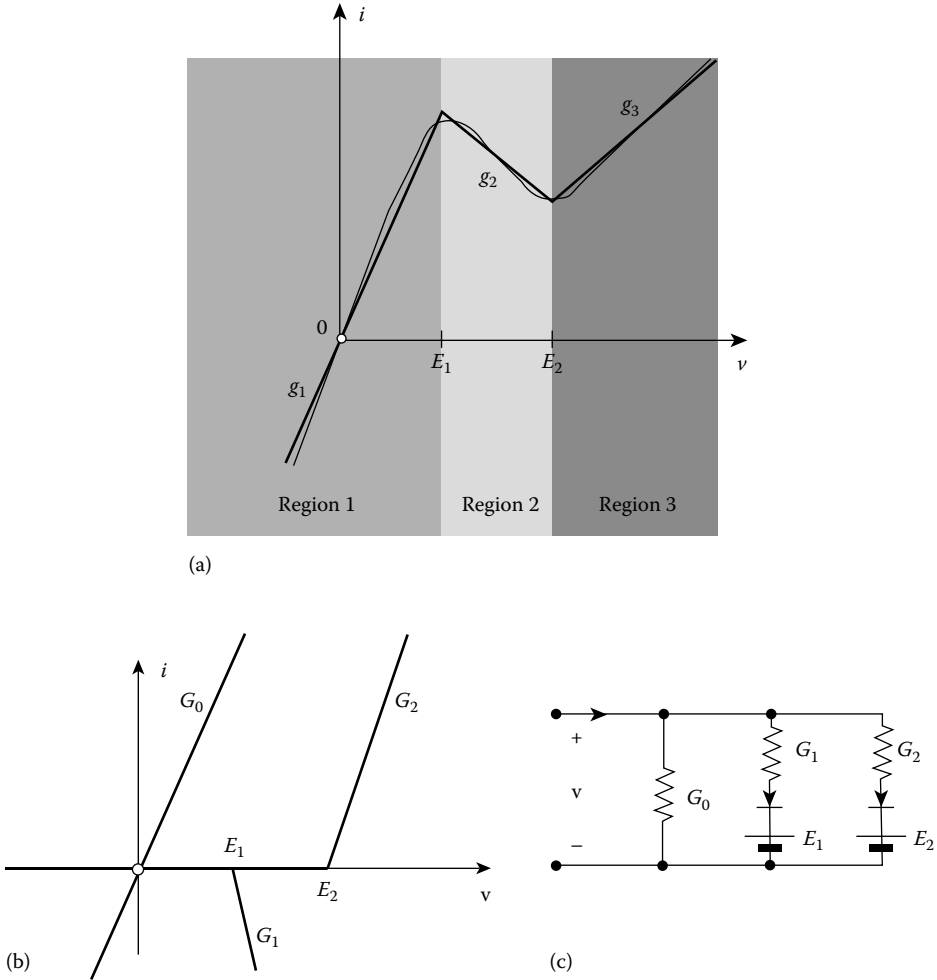


FIGURE 11.10 (a) Piecewise-linear approximation of the tunnel-diode characteristic. The three-segment approximation defines the three regions indicated. (b) Decomposition of the piecewise-linear characteristic (a) into three components, and (c) the corresponding circuit.

where

$$\begin{aligned}
 \begin{bmatrix} a_1 \\ a_2 \end{bmatrix} &= \begin{bmatrix} 5.8722 \times 10^{-3} \\ -3.2652 \times 10^{-2} \end{bmatrix} & \begin{bmatrix} b_{11} \\ b_{21} \end{bmatrix} &= \begin{bmatrix} 3.2392 \times 10^{-2} \\ -3.2067 \times 10^{-2} \end{bmatrix} \\
 \begin{bmatrix} b_{12} \\ b_{22} \end{bmatrix} &= \begin{bmatrix} -4.0897 \times 10^{-2} \\ 8.1793 \times 10^{-2} \end{bmatrix} & \begin{bmatrix} c_{11} \\ c_{21} \end{bmatrix} &= \begin{bmatrix} 3.1095 \times 10^{-6} \\ -3.0784 \times 10^{-6} \end{bmatrix} \\
 \begin{bmatrix} c_{12} \\ c_{22} \end{bmatrix} &= \begin{bmatrix} -9.9342 \times 10^{-3} \\ 1.9868 \times 10^{-2} \end{bmatrix} & \begin{bmatrix} c_{13} \\ c_{23} \end{bmatrix} &= \begin{bmatrix} -3.0471 \times 10^{-2} \\ 6.0943 \times 10^{-2} \end{bmatrix} \\
 \begin{bmatrix} m_1 \\ m_2 \\ m_3 \end{bmatrix} &= \begin{bmatrix} 1.002 \times 10^4 \\ -1.4 \times 10^{-4} \\ 1.574 \times 10^{-6} \end{bmatrix} & \begin{bmatrix} t_1 \\ t_2 \\ t_3 \end{bmatrix} &= \begin{bmatrix} -6472 \\ 0.61714 \\ 0.66355 \end{bmatrix}
 \end{aligned}$$

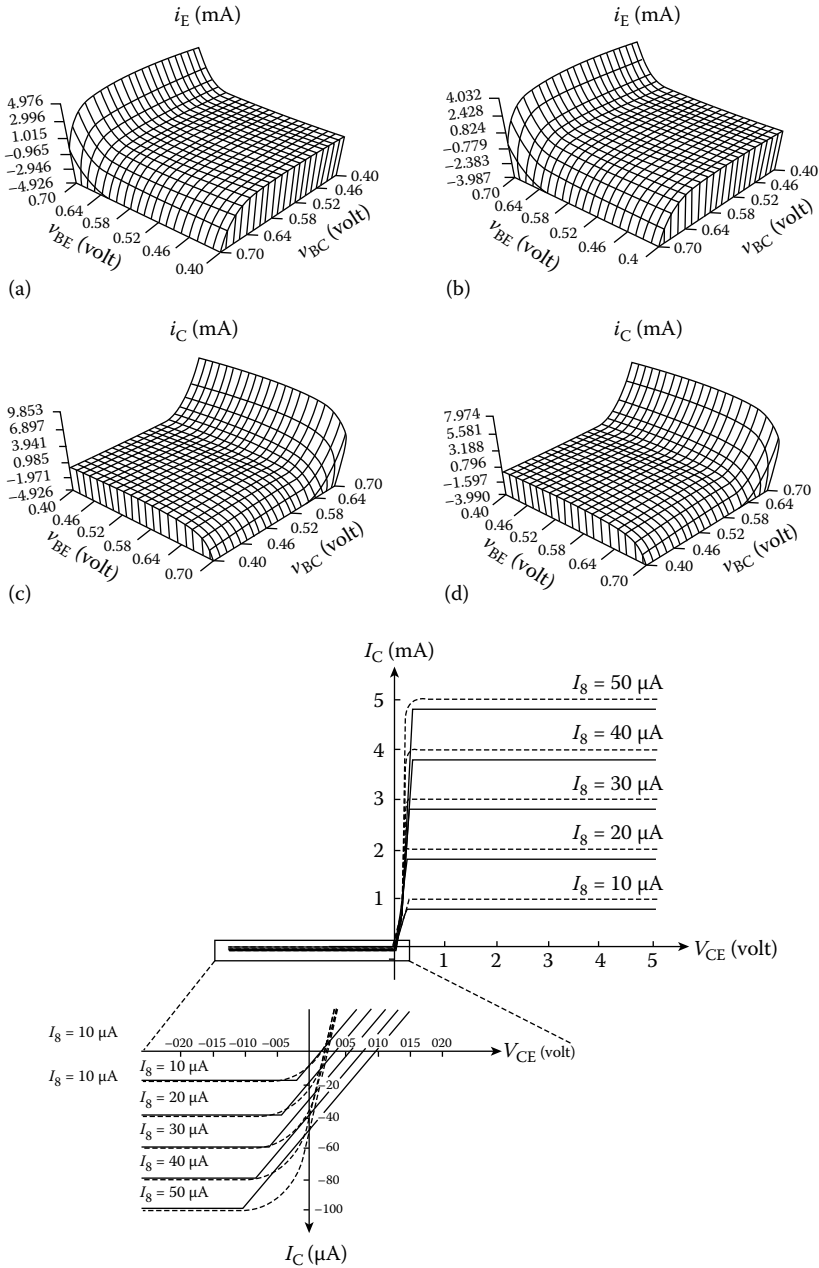


FIGURE 11.11 Three-dimensional plots for the emitter current in the Ebers–Moll model given by Equations 11.37 and 11.38. (b) Three-dimensional plot for the emitter current in the canonical piecewise-linear model given by Ref. [10, (B.1)] (low-voltage version). (c) Three-dimensional plot for the collector current in the Ebers–Moll model given by Equations 11.37 and 11.38. (d) Three-dimensional plot for the collector current in the canonical piecewise-linear model given by Ref. [10, (B.1)] (low-voltage version). (e) Comparison between the family of collector currents in the Ebers–Moll model (dashed line) and the canonical piecewise-linear model (solid line). (From Chua, L.O. and Deng, A., *IEEE Trans. Circuits Syst.*, CAS-33, 519, 1986. With permission.)

Next, a canonical piecewise-linear MOS transistor model is presented. Assume the MOS transistor is connected in the common source configuration with $v_1 = v_{GS}$, $v_2 = v_{DS}$, $i_1 = i_G$, and $i_2 = i_D$, as illustrated, in Figure 11.12, where both v_1, v_2 are in volts, and i_1, i_2 are in microamperes. The data points are uniformly spaced in a grid within a rectangular region defined by $0 \leq v_1 \leq 5$, and $0 \leq v_2 \leq 5$. We assume the data points follow the Shichman–Hodges model, namely,

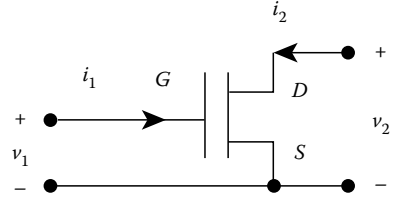


FIGURE 11.12 Two-port configuration of the MOSFET.

$$\begin{aligned} i_1 &= 0 \\ i_2 &= k[(v_1 - V_t)v_2 - 0.5v_2^2], \quad \text{if } v_1 - V_t \geq v_2 \end{aligned}$$

or

$$i_2 = 0.5k(v_1 - V_t)^2[1 + \lambda(v_2 - v_1 + V_t)], \quad \text{if } v_1 - V_t < v_2 \quad (11.40)$$

with $k = 50 \mu\text{A}/\text{V}^2$, $V_t = 1 \text{ V}$, $\lambda = 0.02 \text{ V}^{-1}$. Applying the optimization algorithm of Ref. [11], we obtain the following canonical piecewise-linear model (see Figure 11.13):

$$\begin{aligned} i_2 &= a_2 + b_{21}v_1 + b_{22}v_2 + c_{21}|m_1v_1 - v_2 + t_1| \\ &\quad + c_{22}|m_2v_1 - v_2 + t_2| + c_{23}|m_3v_1 - v_2 + t_3| \end{aligned} \quad (11.41)$$

where

$$\begin{aligned} a_2 &= -61.167, & b_{21} &= 30.242, & b_{22} &= 72.7925 \\ c_{21} &= -49.718, & c_{22} &= -21.027, & c_{23} &= 2.0348 \\ m_1 &= 0.8175, & m_2 &= 1.0171, & m_3 &= -23.406 \\ t_1 &= -2.1052, & t_2 &= -1.4652, & t_3 &= 69 \end{aligned}$$

Finally, a canonical piecewise-linear model of GaAs FET is presented. The GaAs FET has become increasingly important in the development of microwave circuits and high-speed digital IC's due to its fast switching speed.

$$\begin{aligned} i_2 &= a_2 + b_{21}v_1 + b_{22}v_2 + c_{21}|m_1v_1 - v_2 + t_1| \\ &\quad + c_{22}|m_2v_1 - v_2 + t_2| + c_{23}|m_3v_1 - v_2 + t_3| \end{aligned} \quad (11.42)$$

where $v_1 = v_{GS}$ (V), $v_2 = v_{DS}$ (V), $i_2 = i_D$ (mA), and

$$\begin{aligned} a_2 &= 6.3645, & b_{21} &= 2.4961, & b_{22} &= 32.339 \\ c_{21} &= 0.6008, & c_{22} &= 0.9819, & c_{23} &= -29.507 \\ m_1 &= -19.594, & m_2 &= -6.0736, & m_3 &= 0.6473 \\ t_1 &= -44.551, & t_2 &= -8.9962, & t_3 &= 1.3738 \end{aligned}$$

Observe that this model requires only three absolute-value functions and 12 numerical coefficients and compares rather well to the analytical model (Figure 11.14).

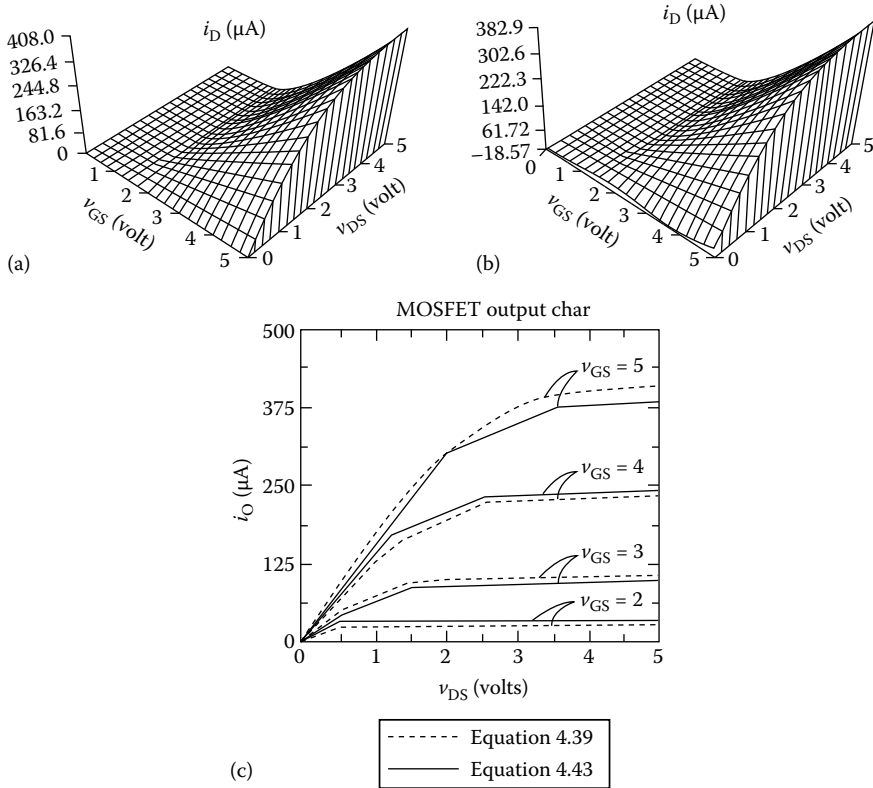


FIGURE 11.13 (a) Three-dimensional plot of drain current from the Shichman–Hodges model. (b) Three-dimensional plot of the drain current from the canonical piecewise-linear model. (c) Family of drain currents modeled by Equations 11.40 (dashed line) and 11.41 (solid line). (From Chua, L.O. and Deng, A., *IEEE Trans. Circuits Syst.*, CAS-33, 520, 1986. With permission.)

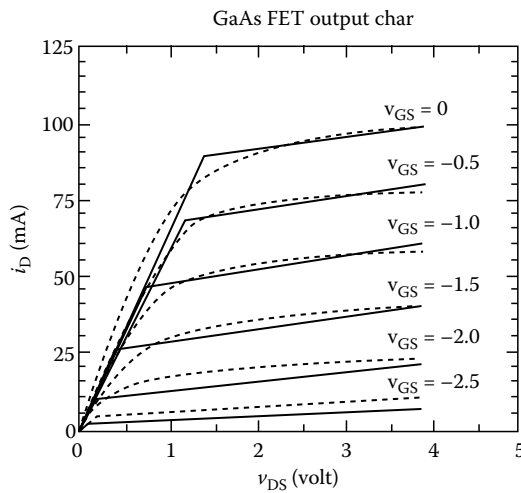


FIGURE 11.14 Comparison of the canonical piecewise linear described by Equation 11.42 (solid line) and the analytical model (dashed line) for the ion-implanted GaAs FET. (From Chua, L.O. and Deng, A., *IEEE Trans. Circuits Syst.*, CAS-33, 522, 1986. With permission.)

More piecewise-linear models for timing analysis of logic circuits can be found in Ref. [21]. In the context of analog computer design, even PWL models of other nonlinear relationships have been derived in Ref. [51].

11.4 Structural Properties of Piecewise-Linear Resistive Circuits

When considering interconnections of PWL resistors (components), it follows from the linearity of KVL and KCL that the resulting multiport is also a piecewise-linear resistor. However, if the components have a canonical PWL representation, the resulting multiport may not have a canonical PWL representation. This can be illustrated by graphically deriving the equivalent one port of the series connection of two tunnel diodes [3] (Figure 11.15). Both resistors have the same current, so we have to add the corresponding voltages $v = v_1 + v_2$ and obtain an $i-v$ plot with two unconnected parts. Values of i correspond to three values of v_1 for R_1 and three values of v_2 for R_2 , and hence to nine values of the equivalent resistor (Figure 11.15d). This illustrates once more that nonlinear circuits may have more solutions than expected at first sight. Although the two tunnel diodes R_1 and R_2 have a canonical PWL representation, the equivalent one port of their series connection has neither a canonical PWL voltage description, nor a current one. It, however, has a GLCP description because KVL, KCL, and the LCP of R_1 and R_2 constitute a GLCP. If the $v-i$ PWL relation is monotonic, the inverse $i-v$ function exists and then some uniqueness properties hold.

These observations are, of course, also valid for the parallel connection of two PWL resistors and for more complicated interconnections.

In Section 11.3, we illustrated with an example how a PWL one-port resistor can be realized with linear resistors and ideal diodes. This can be proven in general. One essentially needs a diode for each breakpoint in the PWL characteristic. Conversely, each one port with diodes and resistors is a PWL one port resistor.

This brings us to an interesting class of circuits composed of linear resistors, independent sources, linear controlled sources, and ideal diodes. These circuits belong to the general class of circuits with PWL

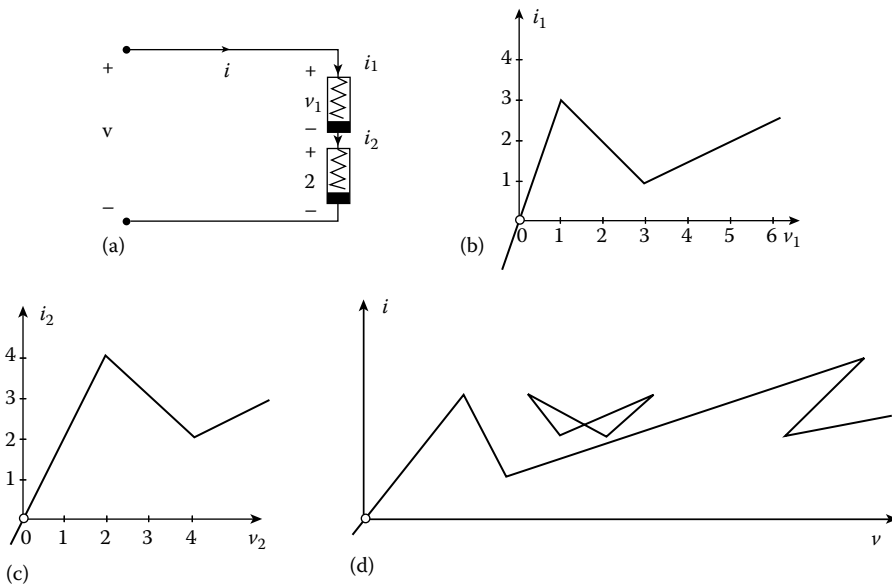


FIGURE 11.15 (a) The series connection of two tunnel diodes, (b) and (c), their $i-v$ characteristics, and (d) the composite $i-v$ plot, which consists of two unconnected parts.

components (see Figure 11.1a) and can be described by GLCP equations. Such networks have not only shown their importance in analysis but also in the topologic study of the number of solutions and more general qualitative properties. When only short-circuit and open-circuit branches are present, one independent voltage source with internal resistance and ideal diodes, an interesting loop cut set exclusion property holds that is also called the colored branch theorem or the arc coloring theorem (see Section 1.7 of *Fundamentals of Circuits and Filters*). It says that the voltage source either forms a conducting loop with forward-oriented diodes and some short circuits or there is a cut set of the voltage source, some open circuits, and blocking diodes. Such arguments have been used to obtain [23] topologic criteria for upper bounds of the number of solutions of PWL resistive circuits. In fact, diode resistor circuits have been used extensively in PWL function generators for analog computers [51]. These electrical analogs can also be used for mathematical programming problems (similar to linear programming) and have reappeared in the neural network literature.

11.5 Analysis of Piecewise-Linear Resistive Circuits

It is first demonstrated that all conventional network formulation methods (nodal, cut, set, hybrid, modified nodal, and tableau) can be used for PWL resistive circuits where the components are described with canonical or with LCP equations. These network equations may have one or more solutions. In order to find solutions, one can either search through all the polyhedral regions P_k by solving the linear equations for that region or by checking whether its solution is located inside that region P_k .

Because many regions often exist, this is a time-consuming method, but several methods can be used to reduce the search [28,61]. If one is interested in only one solution, one can use solution tracing methods, also called continuation methods or homotopy methods, of which the Katzenelson method is best known. If one is interested in all solutions, the problem is more complicated, but some algorithms exist.

11.5.1 Theorem Canonical PWL (Tableau Analysis)

Consider a connected resistive circuit N containing only linear two-terminal resistors, dc-independent sources, current-controlled and voltage-controlled piecewise-linear two-terminal resistors, linear- and piecewise-linear-controlled sources (all four types) and any linear multiterminal resistive elements. A composite branch of this circuit is given in Figure 11.16. If each piecewise-linear function is represented in the canonical form (Equation 11.6), then the *tableau formulation* also has the canonical PWL form

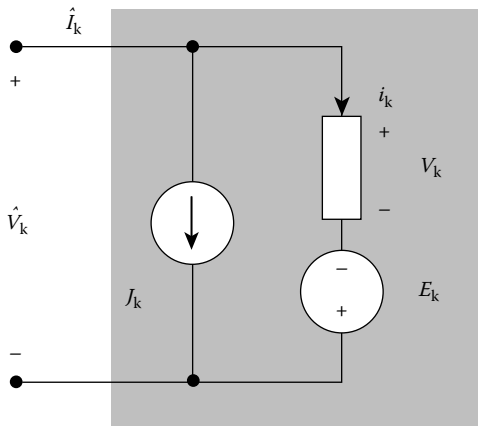


FIGURE 11.16 A composite branch.

$$f(x) = a + Bx + \sum_{i=1}^p c_i |\alpha_i^T x - \beta_i| = 0 \quad (11.43)$$

where $x = [i^T, v^T, v_n^T]^T$ and i , respectively v , is the branch current voltage vector (Figure 11.16) and v_n is the node-to-datum voltage vector.

PROOF. Let A be the reduced incidence matrix of N relative to some datum node, then KCL, KVL, and element constitutive relations give

$$Ai = AJ \quad (11.44)$$

$$v = A^T v_n + E \quad (11.45)$$

$$f_1(i) + f_v(v) = S \quad (11.46)$$

where we can express $f_i(\cdot)$ and $f_v(\cdot)$ in the canonical form (Equation 11.6)

$$f_i(i) = a_i + B_i i + C_i \text{abs}(D_i^T e - e_1) \quad (11.47)$$

$$f_v(v) = a_v + B_v v + C_v \text{abs}(D_v^T v - e_v) \quad (11.48)$$

Substituting Equations 11.47 and 11.48 into Equation 11.46, we obtain

$$\begin{aligned} \begin{bmatrix} -AJ \\ -E \\ a_I + a_v - S \end{bmatrix} + \begin{bmatrix} A & 0 & 0 \\ 0 & 1 & A^T \\ B_I & B_v & 0 \end{bmatrix} \begin{bmatrix} i \\ v \\ v_n \end{bmatrix} &= \begin{bmatrix} 0 & 0 & 0 \\ 0 & 0 & 0 \\ C_I & C_v & 0 \end{bmatrix} \\ \text{abs} \left[\begin{bmatrix} D_I & 0 & 0 \\ 0 & D_v & 0 \\ 0 & 0 & 0 \end{bmatrix} \begin{bmatrix} i \\ v \\ v_n \end{bmatrix} - \begin{bmatrix} e_1 \\ e_v \\ 0 \end{bmatrix} \right] &= 0 \end{aligned} \quad (11.49)$$

Clearly, Equation 11.49 is in the canonical form of Equation 11.43.

Of course, an analogous theorem can be given when the PWL resistors are given in LCP form. Then the tableau constitute a GLCP. Moreover, completely in line with the section on circuit analysis (see Chapter 23 of *Fundamentals of Circuits and Filters*), one can derive nodal, cut set, loop, hybrid, and modified nodal analysis from the tableau analysis by eliminating certain variables. Alternatively, one can also directly derive these equations.

Whatever the description for the PWL components may be, one can always formulate the network equations as linear equations

$$0 = f(x) = a_k + B_k x, \quad x \in P_k \quad (11.50)$$

in the polyhedral region P_k defined by Equation 11.50. The map f is a continuous PWL map. A solution x of Equation 11.50 can then be computed in a finite number of steps with the Katzenelson algorithm [4,33], by tracing the map f from an initial point $(x^{(1)}, y^{(1)})$ to a value $(x^*, 0)$ (see Figure 11.18).

11.5.2 Algorithm

STEP 1. Choose an initial point $x^{(1)}$ and determine its polyhedral region $P^{(1)}$, and compute

$$y^{(1)} = f(x^{(1)}) = a^{(1)} + B^{(1)}x \text{ and set } j = 1$$

STEP 2. Compute

$$\hat{x} = x^{(j)} + (B^{(j)})^{-1}(0 - y^{(j)}) \quad (11.51)$$

STEP 3. If $\hat{x} \in P^{(j)}$, we have obtained a solution \hat{x} of $f(\hat{x}) = 0$. Stop.

STEP 4. Otherwise, compute

$$x^{(j+1)} = x^{(j)} + \lambda^{(j)}(\hat{x} - x^{(j)}) \quad (11.52)$$

where $\lambda^{(j)}$ is the largest number such that $x^{(j+1)} \in P^{(j)}$, i.e., $x^{(j+1)}$ is on the boundary between $P^{(j)}$ and $P^{(j+1)}$ (see Figure 11.17).

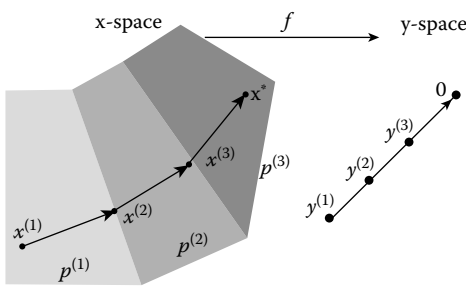


FIGURE 11.17 Iteration in the Katzenelson algorithm for solving $y=f(x)=0$.

STEP 5. Identify $P^{(j+1)}$ and the linear map $y = a^{(j+1)} + B^{(j+1)} x$ in the polyhedral region $P^{(j+1)}$ and compute

$$y^{(j+1)} = y^{(j)} + \lambda^{(j)}(y^* - y^{(j)}) \tag{11.53}$$

Set $j = j + 1$. Go to step 2.

This algorithm converges to a solution in a finite number of steps if the determinants of all matrices $B^{(j)}$ have the same sign. This condition is satisfied when the i - v curves for the PWL one port resistors are monotonic. The Katzenelson algorithm was extended in Ref. [45] by taking the sign of the determinants into

account in Equations 11.52 and 11.53. This requires the PWL resistors to be globally coercive. If by accident in the iteration the point $x^{(j+1)}$ is not on a single boundary and instead is located on a corner, the region $P^{(j+1)}$ is not uniquely defined. However, with a small perturbation [1], one can avoid this corner and still be guaranteed to converge.

This algorithm was adapted to the canonical PWL Equation 11.49 in Ref. [8]. It can also be adapted to the GLCP. However, there exist circuits where this algorithm fails to converge. For the LCP problem, one can then use other algorithms [20,40,56]. One can also use other homotopy methods [43,57,60], which can be shown to converge based on eventual passivity arguments. In fact, this algorithm extends the rather natural method of source stepping, where the PWL circuit is solved by first making all sources zero and then tracing the solution for increasing (stepping up) the sources. It is instructive to observe here that these methods can be used successfully in another sequence of the steps in Figure 11.1a. Until now, we always first performed the horizontal step of PWL approximation or modeling and then the vertical step of network equation formulation. With these methods, one can first perform the network equation formulation and then the PWL approximation. The advantage is that one can use a coarser grid in the simplicial subdivision far away from the solution, and hence dynamically adapt the accuracy of the PWL approximation.

In any case, if all solutions are requested, all these homotopy-based methods are not adequate, because not all solutions can be found even if the homotopy method is started with many different $x^{(1)}$. Hence, special methods have been designed. It is beyond the scope of this text to give a complete algorithm [39,59], but the solution of the GLCP basically involves two parts. First, calculate the solution set of all nonnegative solutions to Equations 11.10 and 11.11. This is a polyhedral cone where extremal rays can be easily determined [44,54]. Second, this solution set is intersected with a hyperplane and the complementarity condition $u^T s = 0$ implies the elimination of vertices (respectively, convex combinations) where these complementarity (respectively, cross complementarity) is not satisfied. This has allowed to systematically obtain the complete solution set for the circuit of Figure 11.15 and for circuits with infinitely many solutions.

A more recent method [46] covers the PWL i - v characteristic with a union of polyhedra and hierarchically solves the circuit with finer and finer polyhedra.

An important improvement in efficiency for the methods is possible when the PWL function $f(\cdot)$ is separable, i.e., there exist $f^i : \mathbb{R}^+ \rightarrow \mathbb{R}^n$ $i = 1, 2, \dots, n$ such that

$$f(x) = \sum_{i=1}^n f^i(x_i) \tag{11.54}$$

This happens when there are only two terminal PWL resistors, linear resistors, and independent sources, and if the bipolar transistors are modeled by the Ebers–Moll model (see Equation 11.39). Then, the subdivision for x is rectangular and each rectangle is subdivided into simplices (see Figure 11.18). This

property can be used to eliminate certain polyhedral regions without solutions [62] and also to speed up the Katzenelson-type algorithm [60,62]. If there are MOS transistors, the map f is not separable but one can apply the extended concept of pairwise separable map [62].

11.6 Piecewise-Linear Dynamic Circuits

As mentioned at the end of Section 11.2, the piecewise-linear descriptions of Section 11.2 can be used also for PWL capacitors, respectively, inductors and memristors, by replacing the port voltages v and currents i by q, v , respectively, φ, i and φ, q . Whenever we have a network obtained by interconnecting linear and/or PWL resistors, inductors, capacitors, and memristors, we have a dynamic piecewise-linear circuits. Of course, such networks are often encountered because it includes the networks with linear R, L, C , and linear-dependent sources, diodes, switches, op-amps, and components such as bipolar and MOS transistors, and GaAs FETs with PWL resistive models. This includes several important and famous nonlinear circuits such as Chua’s circuit [18,19], and the cellular neural networks (CNNs) [48], which are discussed in Chapter 13 and Section 14.2.

Of course, PWL dynamic circuits are much more interesting and much more complicated and can exhibit a much more complex behavior than resistive circuits and hence this subject is much less explored. It is clear from the definition of a PWL dynamic circuit that it can be described by linear differential equations over polyhedral regions. Hence, it can exhibit many different types of behavior. They may have many equilibria, which can essentially be determined by solving the resistive network (see Section 11.5 and Figure 11.1) obtained by opening the capacitive ports and short circuiting the inductive ports (dc analysis). When there is no input waveform, the circuit is said to be autonomous and has transients. Some transients may be periodic and are called limit cycles but they may also show chaotic behavior. Next, one may be interested in the behavior of the circuit for certain input waveforms (transient analysis). This can be performed by using integration rules in simulations.

For the analysis of limit cycles, chaos, and transients, one can of course use the general methods for nonlinear circuits, but some improvements can be made based on the PWL nature of the nonlinearities. Here, we only describe the methods briefly. If one is interested in the periodic behavior of a PWL dynamic circuit (autonomous or with a periodic input), then one can, for each PWL nonlinearity, make some approximations.

First, consider the case that one is only interested in the dc and fundamental sinusoidal contributions in all signals of the form $i(t) = A_0 + A_1 \cos \omega t$. The widely used describing function method [6] for PWL resistors $v = f(i)$ consists of approximating this resistor by an approximate resistor where $\hat{v}(t) = D_0 + D_1 \cos \omega t$ has only the dc and fundamental contribution of $v(t)$. This is often a good approximation since the remainder of the circuit often filters out all higher harmonics anyway. Using a Fourier series, one can then find D_0 and D_1 as

$$D_0(A_0, A_1) = \frac{1}{2\pi} \int_0^{2\pi} f(A_0 + A_1 \cos \phi) d\phi$$

$$D_1(A_0, A_1) = \frac{1}{\pi A_1} \int_0^{2\pi} f(A_0 + A_1 \cos \phi) d\phi$$

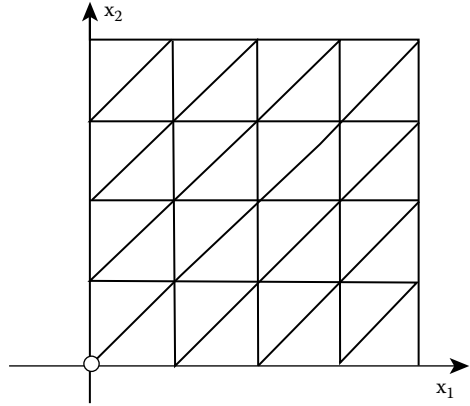


FIGURE 11.18 Simplicial subdivision.

By replacing all PWL components by their describing functions, one can use linear methods to set up the network equations in the Laplace–Fourier domain. When this approximation is not sufficient, one can include more harmonics. Then, one obtains the famous harmonic balance method, because one is balancing more harmonic components.

Alternatively, one can calculate the periodic solution by simulating the circuit with a certain initial condition and considering the map $F: x_0 \rightarrow x_1$ from the initial condition x_0 to the state x_1 one period later. Of course, a fixed point $x^* = F(x^*)$ of the map corresponds to a periodic solution. It has been demonstrated [27] that the map F is differentiable for PWL circuits. This is very useful in setting up an efficient iterative search for a fixed point of F . This map is also useful in studying the eventual chaotic behavior and is then called the Poincaré return map.

In transient analysis of PWL circuits, one is often interested in the sensitivity of the solution to certain parameters in order to optimize the behavior. As a natural extension of the adjoint network for linear circuits in Ref. [22], the adjoint PWL circuit is defined and used to determine simple sensitivity calculations for transient analysis.

Another important issue is whether the PWL approximation of a nonlinear characteristic in a dynamic circuit has a serious impact on the transient behavior. In Ref. [63], error bounds were obtained on the differences of the waveforms.

11.7 Efficient Computer-Aided Analysis of PWL Circuits

Transient analysis and timing verification is an essential part of the VLSI system design process. The most reliable way of analyzing the timing performance of a design is to use analog circuit analysis methods. Here as well, a set of algebraic-differential equations has to be solved. This can be done by using implicit integration formulas that convert these equations into a set of algebraic equations, which can be solved by iterative techniques like Newton–Raphson (see Chapter 12). The computation time then becomes excessive for large circuits. It mainly consists of linearizations of the nonlinear component models and the solution of the linear equations. In addition, the design process can be facilitated substantially if this simulation tool can be used at many different levels from the top level of specifications over the logic and switch level to the circuit level. Such a hierarchical simulator can support the design from top to bottom and allow for mixtures of these levels. In limited space, we describe here the main simulation methods for improving the efficiency and supporting the hierarchy of models with pieewise-linear methods. We refer the reader to Chapter 8, *Computer Aided Design and Design Automation* for general simulation of VLSI circuits and to the literature for more details on the methods and for more descriptions on complete simulators.

It is clear from our previous discussion that PWL models and circuit descriptions can be used at many different levels. An op-amp, for example, can be described by the finite gain model (see Figure 11.9 and Equations 11.29 and 11.30), but when it is designed with a transistor circuit it can be described by PWL circuit equations as in Section 11.5. Hence, it is attractive to use a simulator that can support this top-down design process [35]. One can then even incorporate logic gates into the PWL models. One can organize the topological equations of the network hierarchically, so that it is easy to change the network topology. The separation between topological equations and model descriptions allows for an efficient updating of the model when moving from one polyhedral region into another. Several other efficiency issues can be built into a hierarchical PWL simulator.

An important reduction in computation time needed for solving the network equations can be obtained by using the consistent variation property. In fact, only a rank one difference exists between the matrices of two neighboring polyhedral regions, and hence, one inverse can be easily derived from the other [8,35]. In the same spirit, one can at the circuit level take advantage of the PWL transistor models (see Ref. [62] and separability discussion in Section 8.5). In Ref. [53], the circuit is partitioned dynamically into subcircuits during the solution process, depending on the transistor region of operation. Then, the subcircuits are dynamically ordered and solved with block Gauss–Seidel for minimal or no coupling among them.

Interesting savings can be obtained [34] by solving the linear differential equations in a polyhedral region with Laplace transformations and by partitioning the equations. However, the computation of the intersection between trajectories in neighboring polyhedral regions can be a disadvantage of this method.

Acknowledgment

This work was supported by the Research Council Kuleuven Project MEFISTO666GOA.

References

1. M. J. Chien, Piecewise-linear homeomorphic resistive networks, *IEEE Trans. Circuits Syst.*, CAS-24, 118–127, Mar. 1977.
2. M. J. Chien and E. S. Kuh, Solving nonlinear resistive network using piecewise-linear analysis and simplicial subdivision, *IEEE Trans. Circuits Syst.*, CAS-24, 305–317, 1977.
3. L. O. Chua, Analysis and synthesis of multivalued memoryless nonlinear networks, *IEEE Trans. Circuits Theory*, CT-14, 192–209, June 1967.
4. L. O. Chua and P. M. Lin, *Computer-Aided Analysis of Electronic Circuits: Algorithms and Computational Techniques*, Englewood Cliffs, NJ: Prentice-Hall, 1975.
5. L. O. Chua and P. M. Lin, A switching-parameter algorithm for finding multiple solutions of nonlinear resistive circuits, *Int. J. Circuit Theory Appl.*, 4, 215–239, 1976.
6. L. O. Chua and S. M. Kang, Section-wise piecewise-linear functions: Canonical representation properties and applications, *Proc. IEEE*, 65, 915–929, June 1977.
7. L. O. Chua and D. J. Curtin, Reciprocal n -port resistor represented by continuous n -dimensional piecewise-linear function realized by circuit with 2-terminal piecewise-linear resistor and $p + g$ port transformer, *IEEE Trans. Circuits Syst.*, CAS-27, 367–380, May 1980.
8. L. O. Chua and R. L. P. Ying, Finding all solutions of piecewise-linear circuits, *Int. J. Circuit Theory Appl.*, 10, 201–229, 1982.
9. L. O. Chua and R. L. P. Ying, Canonical piecewise-linear analysis, *IEEE Trans. Circuits Syst.*, CAS-30, 125–140, 1983.
10. L. O. Chua and A. C. Deng, Canonical piecewise-linear analysis—Part II: Tracing driving-point and transfer characteristics, *IEEE Trans. Circuits Syst.*, CAS-32, 417–444, May 1985.
11. L. O. Chua and A. C. Deng, Canonical piecewise-linear modeling, unified parameter optimization algorithm: Application to pn junctions, bipolar transistors, MOSFETs, and GaAs FETs, *IEEE Trans. Circuits Syst.*, CAS-33, 511–525, May 1986.
12. L. O. Chua and A. C. Deng, Canonical piecewise linear modeling, *IEEE Trans. Circuits Syst.*, CAS-33, 511–525, May 1986.
13. L. O. Chua and A. C. Deng, Canonical piecewise linear analysis: Generalized breakpoint hopping algorithm, *Int. J. Circuit Theory Appl.*, 14, 35–52, 1986.
14. L. O. Chua and A. C. Deng, Canonical piecewise linear representation, *IEEE Trans. Circuits Syst.*, 35, 101–111, Jan. 1988.
15. L. O. Chua and A. C. Deng, Canonical piecewise-linear modeling, ERL Memo. UCB/ERL M85/35, University of California, Berkeley, Apr. 26, 1985.
16. L. O. Chua and G. Lin, Canonical realization of Chua's circuit family, *IEEE Trans. Circuits Syst.*, 37, 885–902, July 1990.
17. L. O. Chua and G. Lin, Intermittency in piecewise-linear circuit, *IEEE Trans. Circuits Syst.*, 38, 510–520, May 1991.
18. L. O. Chua, The genesis of Chua's circuit, *Archiv Elektronik Übertragungstechnik*, 46(4), 250–257, 1992.
19. L. O. Chua, C.-W. Wu, A.-S. Huang, and G.-Q. Zhong, A universal circuit for studying and generating chaos, *IEEE Trans. Circuits Syst. I*, 40(10), 732–744, 745–761, Oct. 1993.

20. R. Cottle, J.-S. Pang, and R. Stone, *The Linear Complementarity Problem*, New York: Academic Press, 1992.
21. A. C. Deng, Piecewise-linear timing model for digital CMOS circuits, *IEEE Trans. Circuits Syst.*, 35, 1330–1334, Oct. 1988.
22. Y. Elcherif and P. Lin, Transient analysis and sensitivity computation in piecewise-linear circuits, *IEEE Trans. Circuits Syst.*, 36, 1525–1533, Dec. 1988.
23. M. Fossepréz, M. J. Hasler, and C. Schnetzler, On the number of solutions of piecewise-linear resistive circuits, *IEEE Trans. Circuits Syst.*, 36, 393–402, Mar. 1989.
24. T. Fujisawa and E. S. Kuh, Piecewise-linear theory of nonlinear networks, *SIAM J. Appl. Math.*, 22(2), 307–328, Mar. 1972.
25. T. Fujisawa, E. S. Kuh, and T. Ohtsuki, A sparse matrix method for analysis of piecewise-linear resistive circuits, *IEEE Trans. Circuit Theory*, 19, 571–584, Nov. 1972.
26. G. Güzelis and I. Gökner, A canonical representation for piecewise affine maps and its applications to circuit analysis, *IEEE Trans. Circuits Syst.*, 38, 1342–1354, Nov. 1991.
27. I. N. Hajj and S. Skelboe, Dynamic systems: Steady-state analysis, *IEEE Trans. Circuits Syst.*, CAS-28, 234–242, March 1981.
28. Q. Huang and R. W. Liu, A simple algorithm for finding all solutions of piecewise-linear networks, *IEEE Trans. Circuits Syst.*, 36, 600–609, Apr. 1989.
29. C. Kahlert and L. O. Chua, A generalized canonical piecewise-linear representation, *IEEE Trans. Circuits Syst.*, 37, 373–383, Mar. 1990.
30. C. Kahlert and L. O. Chua, Completed canonical piecewise-linear representation: Geometry of domain space, *IEEE Trans. Circuits Syst.*, 39, 222–236, Mar. 1992.
31. S. M. Kang and L. O. Chua, A global representation of multidimensional piecewise-linear functions with linear partitions, *IEEE Trans. Circuits Syst.*, CAS-25, 938–940, Nov. 1978.
32. S. Karamardian, The complementarity problem, *Mathemat. Program.*, 2, 107–129, 1972.
33. S. Karamardian and J. Katzenelson, An algorithm for solving nonlinear resistive networks, *Bell Syst. Tech. J.*, 44, 1605–1620, 1965.
34. R. J. Kaye and A. Sangiovanni-Vincentelli, Solution of piecewise-linear ordinary differential equations using waveform relaxation and Laplace transforms, *IEEE Trans. Circuits Syst.*, CAS-30, 353–357, June 1983.
35. T. A. M. Kevenaer and D. M. W. Leenaerts, A flexible hierarchical piecewise-linear simulator, *Integrat. VLSI J.*, 12, 211–235, 1991.
36. T. A. M. Kevenaer and D. M. W. Leenaerts, A comparison of piecewise-linear model descriptions, *IEEE Trans. Circuits Syst.*, 39, 996–1004, Dec. 1992.
37. M. Kojima and Y. Yamamoto, Variable dimension algorithms: Basic theory, interpretations and extensions of some existing methods, *Mathemat. Program.*, 24, 177–215, 1982.
38. S. Lee and K. Chao, Multiple solution of piecewise-linear resistive networks, *IEEE Trans. Circuits Syst.*, CAS-30, 84–89, Feb. 1983.
39. D. M. W. Leenaerts and J. A. Hegt, Finding all solutions of piecewise-linear functions and the application to circuits design, *Int. J. Circuit Theory Appl.*, 19, 107–123, 1991.
40. C. E. Lemke, On complementary pivot theory, in *Nonlinear Programming*, J. B. Rosen, O. L. Mangasarian, and K. Ritten, Eds., New York: Academic Press, 1968, pp. 349–384.
41. J. Lin and R. Unbehauen, Canonical piecewise-linear approximations, *IEEE Trans. Circuits Syst.*, 39, 697–699, Aug. 1992.
42. R. Lum and L. O. Chua, Generic properties of continuous piecewise-linear vector fields in 2-D space, *IEEE Trans. Circuits Syst.*, 38, 1043–1066, Sep. 1991.
43. R. Melville, L. Trajkovic, S.-C. Fang, and L. Watson, Artificial homotopy methods for the DC operating point problem, *IEEE Trans. Comput.-Aided Design Integrat. Circuits Syst.*, 12, 861–877, June 1993.

44. T. S. Motzkin, H. Raiffa, G. L. Thompson, and R. M. Thrall, The double description method, in *Contributions to the Theory of Games Ann. Mathemat. Studies*, H. W. Kuhn and A. W. Tucker, Eds., Princeton: Princeton University Press, 1953, pp. 51–73.
45. T. Ohtsuki, T. Fujisawa, and S. Kumagai, Existence theorem and a solution algorithm for piecewise-linear resistor circuits, *SIAM J. Math. Anal.*, 8(1), 69–99, 1977.
46. S. Pastore and A. Premoli, Polyhedral elements: A new algorithm for capturing all the equilibrium points of piecewise-linear circuits, *IEEE Trans. Circuits Syst. I.*, 40, 124–132, Feb. 1993.
47. V. C. Prasad and V. P. Prakash, Homeomorphic piecewise-linear resistive networks, *IEEE Trans. Circuits Syst.*, 35, 251–253, Feb. 1988.
48. T. Roska and J. Vandewalle, *Cellular Neural Networks*, New York: John Wiley & Sons, 1993.
49. I. W. Sandberg, A note on the operating-point equations of semiconductor-device networks, *IEEE Trans. Circuits Syst.*, 37, 966, July 1990.
50. A. S. Solodovnikov, *System of Linear Inequalities*, translated by L. M. Glasser and T. P. Branson, Chicago: University of Chicago, 1980.
51. T. E. Stern, *Theory of Nonlinear Networks and Systems: An Introduction*, Reading, MA: Addison-Wesley, 1965.
52. S. Stevens and P.-M. Lin, Analysis of piecewise-linear resistive networks using complementary pivot theory, *IEEE Trans Circuits Syst.*, CAS-28, 429–441, May 1981.
53. O. Tejayadi and I. N. Hajj, Dynamic partitioning method for piecewise-linear VLSI circuit simulation, *Int. J. Circuit Theory Appl.*, 16, 457–472, 1988.
54. S. N. Tschernikow, *Lineare Ungleichungen*. Berlin: VEB Deutscher Verlag der Wissenschaften, 1971; translation from H. Weinert and H. Hollatz, *Lineinye Neravenstva*, 1968, into German.
55. W. M. G. van Bokhoven, *Piecewise-Linear Modelling and Analysis*. Deventer: Kluwer Academic, 1980.
56. C. Van de Panne, A complementary variant of Lemke's method for the linear complementary problem, *Mathemat. Program.*, 7, 283–310, 1974.
57. L. Vandenberghe and J. Vandewalle, Variable dimension algorithms for solving resistive circuits, *Int. J. Circuit Theory Appl.*, 18, 443–474, 1990.
58. L. Vandenberghe and J. Vandewalle, A continuous deformation algorithm for DC-analysis of active nonlinear circuits, *J. Circuits Syst. Comput.*, 1, 327–351, 1991.
59. L. Vandenberghe, B. L. De Moor, and J. Vandewalle, The generalized linear complementarity problem applied to the complete analysis of resistive piecewise-linear circuits, *IEEE Trans. Circuits Syst.*, 36, 1382–1391, 1989.
60. K. Yamamura and K. Horiuchi, A globally and quadratically convergent algorithm for solving resistive nonlinear resistive networks, *IEEE Trans. Comput.-Aided Design Integrat. Circuits Syst.*, 9, 487–499, May 1990.
61. K. Yamamura and M. Ochiai, Efficient algorithm for finding all solutions of piecewise-linear resistive circuits, *IEEE Trans. Circuits Syst.*, 39, 213–221, Mar. 1992.
62. K. Yamamura, Piecewise-linear approximation of nonlinear mappings containing Gummel-Poon models or Shichman-Hodges models, *IEEE Trans. Circuits Syst.*, 39, 694–697, Aug. 1992.
63. M. E. Zaghloul and P. R. Bryant, Nonlinear network elements: Error bounds, *IEEE Trans. Circuits Syst.*, CAS-27, 20–29, Jan. 1980.

12

Simulation

12.1	Numerical Solution of Nonlinear Algebraic Equations	12-2
12.2	Numerical Integration of Nonlinear Differential Equations.....	12-3
12.3	Use of Simulation Programs	12-4
	SPICE • APLAC • NAP2 • ESACAP • DYNAST	
	References.....	12-18

Erik Lindberg

Technical University of Denmark

This chapter deals with the simulation or analysis of a nonlinear electrical circuit by means of a computer program. The program creates and solves the differential-algebraic equations of a model of the circuit. The basic tools in the solution process are *linearization*, *difference approximation*, and *the solution of a set of linear equations*. The output of the analysis may consist of (1) all node and branch voltages and all branch currents of a bias point (dc analysis), (2) a linear small-signal model of a bias point that may be used for analysis in the frequency domain (ac analysis), or (3) all voltages and currents as functions of time in a certain time range for a certain excitation (transient analysis). A model is satisfactory if there is good agreement between measurements and simulation results. In this case, simulation may be used instead of measurement for obtaining a better understanding of the nature and abilities of the circuit. The crucial point is to set up a model that is as simple as possible, in order to obtain a fast and inexpensive simulation, but sufficiently detailed to give the proper answer to the questions concerning the behavior of the circuit under study. Modeling is the bottleneck of simulation.

The model is an equivalent scheme—"schematics-capture"—or a branch table—"net-list"—describing the basic components (n -terminal elements) of the circuit and their connection. It is always possible to model an n -terminal element by means of a number of 2-terminals (branches). These internal 2-terminals may be coupled. By pairing the terminals of an n -terminal element, a port description may be obtained. The branches are either admittance branches or impedance branches. All branches may be interpreted as controlled sources. An admittance branch is a current source primarily controlled by its own voltage or primarily controlled by the voltage or current of another branch (transadmittance). An impedance branch is a voltage source primarily controlled by its own current or primarily controlled by the current or voltage of another branch (transimpedance). Control by signal (voltage or current) and control by time-derivative of signal are allowed. Control by several variables is allowed. Examples of admittance branches are (1) the conductor is a current source controlled by its own voltage, (2) the capacitor is a current source controlled by the time-derivative of its own voltage, and (3) the open circuit is a zero-valued current source (a conductor with value zero). Examples of impedance branches are (1) the resistor is a voltage source controlled by its own current, (2) the inductor is a voltage source controlled by the time-derivative of its own current, and (3) the short circuit is a zero-valued voltage source (a resistor with value zero)

A component may often be modeled in different ways. A diode, for example, is normally modeled as a current source controlled by its own voltage such that the model can be linearized into a dynamic conductor in parallel with a current source during the iterative process of finding the bias point of the diode. The diode may also be modeled as (1) a voltage source controlled by its own current (a dynamic resistor in series with a voltage source), (2) a static conductor being a function of the voltage across the diode, or (3) a static resistor being a function of the current through the diode. Note that in the case where a small-signal model is wanted, for frequency analysis, only the dynamic model is appropriate.

The primary variables of the model are the currents of the impedance branches and the node potentials. The current law of Kirchhoff (the sum of all the currents leaving a node is zero) and the current–voltage relations of the impedance branches are used for the creation of the equations describing the relations between the primary variables of the model. The contributions to the equations from the branches are taken one branch at a time based on the question: Will this branch add new primary variables? If yes, then a new column (variables) and a new row (equations) must be created and updated, or else the columns and rows corresponding to the existing primary variables of the branch must be updated. This approach to equation formulation is called the extended nodal approach or the modified nodal approach (MNA).

In the following, some algorithms for solving a set of nonlinear algebraic equations and nonlinear differential equations are briefly described. Because we are dealing with physical systems and because we are responsible for the models, we assume that at least one solution is possible. The zero solution is, of course, always a solution. It might happen that our models become invalid if we, for example, increase the amplitudes of the exciting signals, diminish the risetime of the exciting signals, or by mistake create unstable models. It is important to define the range of validity for our models. What are the consequences of our assumptions? Can we believe in our models?

12.1 Numerical Solution of Nonlinear Algebraic Equations

Let the equation system to be solved be $f(x, u) = 0$, where x is the vector of primary variables and u is the excitation vector. Denote the solution by x_s . Then, if we define a new function $g(x) = \alpha(f(x, u)) + x$, where α may be some function of $f(x, u)$, which is zero for $f(x, u) = 0$, then we can define an iterative scheme where $g(x)$ converges to the solution x_s by means of the iteration: $x_{k+1} = g(x_k) = \alpha(f(x_k, u)) + x_k$ where k is the iteration counter.

If for all x in the interval $[x_a, x_b]$ the condition $\|g(x_a) - g(x_b)\| \leq L^* \|x_a - x_b\|$ for some $L < 1$ is satisfied, the iteration is called a contraction mapping. The condition is called a Lipschitz condition. Note that a function is a contraction if it has a derivative less than 1.

For $\alpha = -1$, the iterative formula becomes $x_{k+1} = g(x_k) = -f(x_k, u) + x_k$. This scheme is called the Picard method, the functional method, or the contraction mapping algorithm. At each step, each nonlinear component is replaced by a linear static component corresponding to the solution x_k . A nonlinear conductor, for example, is replaced by a linear conductor defined by the straight line through the origin and the solution point. Each iterative solution is calculated by solving a set of linear equations. All components are updated and the next iteration is made. When two consecutive solutions are within a prescribed tolerance, the solution point is accepted.

For $\alpha = -1/(df/dx)$, the iterative formula becomes $x_{k+1} = g(x_k) = -f(x_k, u)/(df(x_k, u)/dx) + x_k$. This scheme is called the Newton–Raphson method or the derivative method. At each step, each nonlinear component is replaced by a linear dynamic component plus an independent source corresponding to the solution x_k . A nonlinear conductor, for example, is replaced by a linear conductor defined by the derivative of the branch current with respect to the branch voltage (the slope of the nonlinearity) in parallel with a current source corresponding to the branch voltage of the previous solution. A new solution is then calculated by solving a set of linear equations. The components are updated and the next iteration is made. When the solutions converge within a prescribed tolerance, the solution point is accepted.

It may, of course, happen that the previously mentioned iterative schemes do not converge before the iteration limit k_{\max} is reached. One reason may be that the nonlinearity $f(x)$ changes very rapidly for a small change in x . Another reason could be that $f(x)$ possess some kind of symmetry that causes cycles in the Newton–Raphson iteration scheme. If convergence problems are detected, the iteration scheme can be *modified* by introducing a limiting of the actual step size. Another approach may be to change the modeling of the nonlinear branches from voltage control to current control or vice versa. Often, the user of a circuit analysis program may be able to solve convergence problems by means of proper modeling and adjustment of the program options [1–5].

12.2 Numerical Integration of Nonlinear Differential Equations

The dynamics of a nonlinear electronic circuit may be described by a set of coupled first-order differential equations–algebraic equations of the form: $dx/dt = f(x, y, t)$ and $g(x, y, t) = 0$, where x is the vector of primary variables (node potentials and impedance branch currents), y is the vector of variables that cannot be explicitly eliminated, and f and g are nonlinear vector functions. It is always possible to express y as a function of x and t by inverting the function g and inserting it into the differential equations such that the general differential equation form $dx/dt = f(x, t)$ is obtained. The task is then to obtain a solution $x(t)$ when an initial value of x is given. The usual methods for solving differential equations reduce to the solution of difference equations, with either the derivatives or the integrals expressed *approximately* in terms of finite differences.

Assume, at a given time t_0 , we have a known solution point $x_0 = x(t_0)$. At this point, the function f can be expanded in Taylor series: $dx/dt = f(x_0, t) + A(x_0)(x - x_0) + \dots$ where $A(x_0)$ is the Jacobian of f evaluated at x_0 . Truncating the series, we obtain a linearization of the equations such that the small-signal behavior of the circuit in the neighborhood of x_0 is described by $dx/dt = A * x + k$, where A is a constant matrix equal to the Jacobian and k is a constant vector.

The most simple scheme for the approximate solution of the differential equation $dx/dt = f(x, t) = Ax + k$ is the forward Euler formula $x(t) = x(t_0) + hA(t_0)$ where $h = t - t_0$ is the integration time step. From the actual solution point at time t_0 , the next solution point at time t is found along the tangent of the solution curve. It is obvious that we will rapidly leave the vicinity of the exact solution curve if the integration step is too large. To guarantee stability of the computation, the time step h must be smaller than $2/|\lambda|$ where λ is the largest eigenvalue of the Jacobian A . Typically, h must not exceed $0.2/|\lambda|$.

The forward Euler formula is a linear *explicit* formula based on forward Taylor expansion from t_0 . If we make backward Taylor expansion from t we arrive at the backward Euler formula: $x(t) = x(t_0) + hA(t)$. Because the unknown appears on both sides of the equation, it must in general be found by iteration so the formula is a linear *implicit* formula. From a stability point of view, the backward Euler formula has a much larger stability region than the forward Euler formula. The truncation error for the Euler formulas is of order h^2 .

The two Euler formulas can be thought of as polynomials of degree 1 that approximate $x(t)$ in the interval $[t_0, t]$. If we compute $x(t)$ from a second-order polynomial $p(t)$ that matches the conditions that $p(t_0) = x(t_0)$, $dp/dt(t_0) = dx/dt(t_0)$ and $dp/dt(t) = dx/dt(t)$, we arrive at the trapezoidal rule: $x(t) = x(t_0) + 0.5hA(t_0) + 0.5hA(t)$. In this case, the truncation error is of order h^3 .

At each integration step, the size of the local truncation error can be estimated. If it is too large, the step size must be reduced. An explicit formula such as the forward Euler may be used as a predictor giving a starting point for an implicit formula like the trapezoidal, which in turn is used as a corrector. The use of a predictor–corrector pair provides the base for the estimate of the local truncation error. The trapezoidal formula with varying integration step size is the main formula used in the Simulation Program with Integrated Circuit Emphasis (SPICE) program.

The two Euler formulas and the trapezoidal formula are special cases of a general linear multistep formula $\Sigma(a_i x_{n-i} + b_i h(dx/dt)_{n-i})$, where i goes from -1 to $m - 1$ and m is the degree of the polynomial

used for the approximation of the solution curve. The trapezoidal rule, for example, is obtained by setting $a_{-1} = -1$, $a_0 = +1$, and $b_{-1} = b_0 = 0.5$, all other coefficients being zero. The formula can be regarded as being derived from a polynomial of degree r which matches $r + 1$ of the solution points x_{n-i} and their derivatives $(dx/dt)_{n-i}$.

Very fast transients often occur together with very slow transients in electronic circuits. We observe widely different time constants. The large spread in component values, for example, from large decoupling capacitors to small parasitic capacitors, implies a large spread in the modules of the eigenvalues. We say that the circuits are stiff. A family of implicit multistep methods suitable for stiff differential equations has been proposed by C.W. Gear. The methods are stable up to the polynomial of order 6. For example, the second-order Gear formula for fixed integration step size h may be stated as $x_{n+1} = -(1/3)x_{n-1} + (4/3)x_n + (2/3)h(dx/dt)_{n+1}$.

By changing both the *order* of the approximating polynomial and the integration *step size*, the methods adapt themselves dynamically to the performance of the solution curve. The family of Gear formulas is modified into a “stiff-stable variable-order variable-step predictor–corrector” method based on implicit approximation by means of backward difference formulas (BDFs). The resulting set of nonlinear equations is solved by modified Newton–Raphson iteration. Note that numerical integration, in a sense, is a kind of low-pass filtering defined by means of the minimum integration step [1–5].

12.3 Use of Simulation Programs

Since 1960, a large number of circuit-simulation programs have been developed by universities, industrial companies, and commercial software companies. In particular, the SPICE program has become a standard simulator both in the industry and in academia. Here, only a few programs, which together cover a very large number of simulation possibilities, are presented. Due to competition, there is a tendency to develop programs that are supposed to cover any kind of analysis so that only one program should be sufficient (the Swiss Army Knife Approach). Unfortunately this implies that the programs become very large and complex to use. Also, it may be difficult to judge the correctness and accuracy of the results of the simulation having only one program at your disposal. If you try to make the same analysis of the same model with different programs, you will frequently see that the results from the programs may not agree completely. By comparing the results, you may obtain a better feel for the correctness and accuracy of the simulation. The programs SPICE and Analysis Program for Linear Active Circuits (APLAC) supplemented with the programs Nonlinear Analysis Program version 2 (NAP2), Engineering System and Circuit Analysis (ESACAP), and DYNAMIC Simulation Tool (DYNAST) have proven to be a good choice in the case where a large number of different kinds of circuits and systems are to be modeled and simulated (the Tool Box Approach). The programs are available in inexpensive evaluation versions running on IBM compatible personal computers. The “net-list” input languages are very close, making it possible to transfer input data easily between the programs. In order to make the programs more “user-friendly” graphics interphase language “schematics-capture,” where you draw the circuit on the screen, has been introduced. Unfortunately, this approach makes it a little more difficult for the user to transfer data between the programs. In the following, short descriptions of the programs are given and a small circuit is simulated in order to give the reader an idea of the capabilities of the programs.

12.3.1 SPICE

The first versions of SPICE (Simulation Program with Integrated Circuit Emphasis version 2), based on the MNA, were developed in 1975 at the Electronics Research Laboratory, College of Engineering, University of California, Berkeley, CA.

SPICE is a general-purpose circuit analysis program. Circuit models may contain resistors, capacitors, inductors, mutual inductors, independent sources, controlled sources, transmission lines, and the

most common semiconductor devices: diodes, bipolar junction transistors, and field effect transistors. SPICE has very detailed built-in models for the semiconductor devices, which may be described by about 50 parameters. Besides the normal dc, ac, and transient analyses, the program can make sensitivity, noise, and distortion analysis and analysis at different temperatures. In the various commercial versions of the program many other possibilities have been added; for example, analog behavior modeling (poles and zeros) and statistical analysis.

In order to give an impression of the “net-list” input language, the syntax of the statements describing controlled sources is the following:

```
Voltage Controlled Current Source: Gxxx N+ N- NC+ NC- VALUE
Voltage Controlled Voltage Source: Exxx N+ N- NC+ NC- VALUE
Current Controlled Current Source: Fxxx N+ N- VNAM VALUE
Current Controlled Voltage Source: Hxxx N+ N- VNAM VALUE
```

where the initial characters of the branch name G, E, F, and H indicate the type of the branch; $N+$ and $N-$ are integers (node numbers) indicating the placement and orientation of the branch, respectively; $NC+$, $NC-$, and $VNAM$ indicate from where the control comes ($VNAM$ is a dummy dc voltage source with value 0 inserted as an ammeter!); and $VALUE$ specifies the numerical value of the control, which may be a constant or a polynomial expression in case of nonlinear dependent sources. Independent sources are specified with $Ixxx$ for current and $Vxxx$ for voltage sources.

The following input file describes an analysis of the Chua oscillator circuit. It is a simple harmonic oscillator with losses ($C2$, $L2$, and $RL2$) loaded with a linear resistor ($R61$) in series with a capacitor ($C1$) in parallel with a nonlinear resistor. The circuit is influenced by a sinusoidal voltage source VRS through a coil $L1$. Comments may be specified either as lines starting with an asterisk “*” or by means of a semicolon “;” after the statement on a line. A statement may continue by means of a plus “+” as the first character on the following line.

```
PSpice input file CRC-CHUA.CIR, first line, title line :
* *: The Chua Oscillator, sinusoidal excitation, F=150mV > :
* : RL2=1 ohm, RL1=0 ohm f=1286.336389 Hz :
* : ref. K. Murali and M. Lakshmanan, :
* : Effect of Sinusoidal Excitation on the Chua's Circuit, :
* : IEEE Transactions on Circuits and Systems-1: :
* : Fundamental Theory and Applications, :
* : vol.39, No.4, April 1992, pp. 264-270 :
* : input source; :-----:
VRS 7 0 sin(0 150m 1.2863363889332e+3 0 0) :
* : choke :
L1 6 17 80e-3 ; mH :
VRL1 17 7 DC 0 ; ammeter for measure of IL1 :
* : harmonic oscillator; :-----:
L2 6 16 13m :
RL2 16 0 1 :
C2 6 0 1.250u :
* : load; :-----:
r61 6 10 1310 :
vrrC1 10 11 DC 0 :
C1 11 0 0.017u :
* i(vrr10)=current of nonlinear resistor :
vrr10 10 1 DC 0 :
```

```
* : non-linear circuit; :-----:
.model n4148 d (is=0.1p rs=16 n=1); vt=n*k*T/q :
d13 1 3 n4148 :
d21 2 1 n4148 :
rm9 2 22 47k :
vrm9 22 0 DC -9 ; negative power supply :
rp9 3 33 47k :
vrp9 33 0 DC +9 :
r20 2 0 3.3k :
r30 3 0 3.3k :
* : ideal op. amp.; :-----:
evop 4 0 1 5 1e+20 :
r14 1 4 290 :
r54 5 4 290 :
r50 5 0 1.2k :
* :-----:
.TRAN 0.05m 200m 0 0.018m UIC :
.plot tran v(11) :
.probe :
.options acct nopage opts gmin=1e-15 reltol=1e-3 :
+ abstol=1e-12 vntol=1e-12 tnom=25 itl5=0 :
+ limpts=15000 :
.end :
```

The analysis is controlled by means of the statements: .TRAN, where, for example, the maximum integration step is fixed to 18 μ s, and .OPTIONS, where, for example, the relative truncation error is set to 1e-3. The result of the analysis is presented in Figure 12.1. It is seen that transition from chaotic behavior to a period 5 limit cycle takes place at about 100 ms. A very important observation is that the result of the analysis may depend on (1) the choice of the control parameters and (2) the order of the branches in the “net-list,” for example, if the truncation error is set to 1e-6 instead of 1e-3 previously, the result becomes quite different. This observation is valid for all programs [5-11].

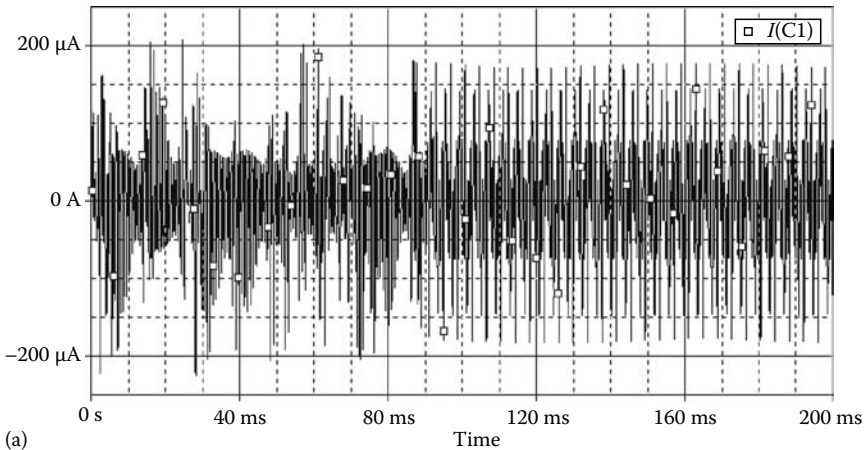


FIGURE 12.1 (a) PSPICE analysis. The current of C1: $I(C1)$ as function of time in the interval 0–200 ms.

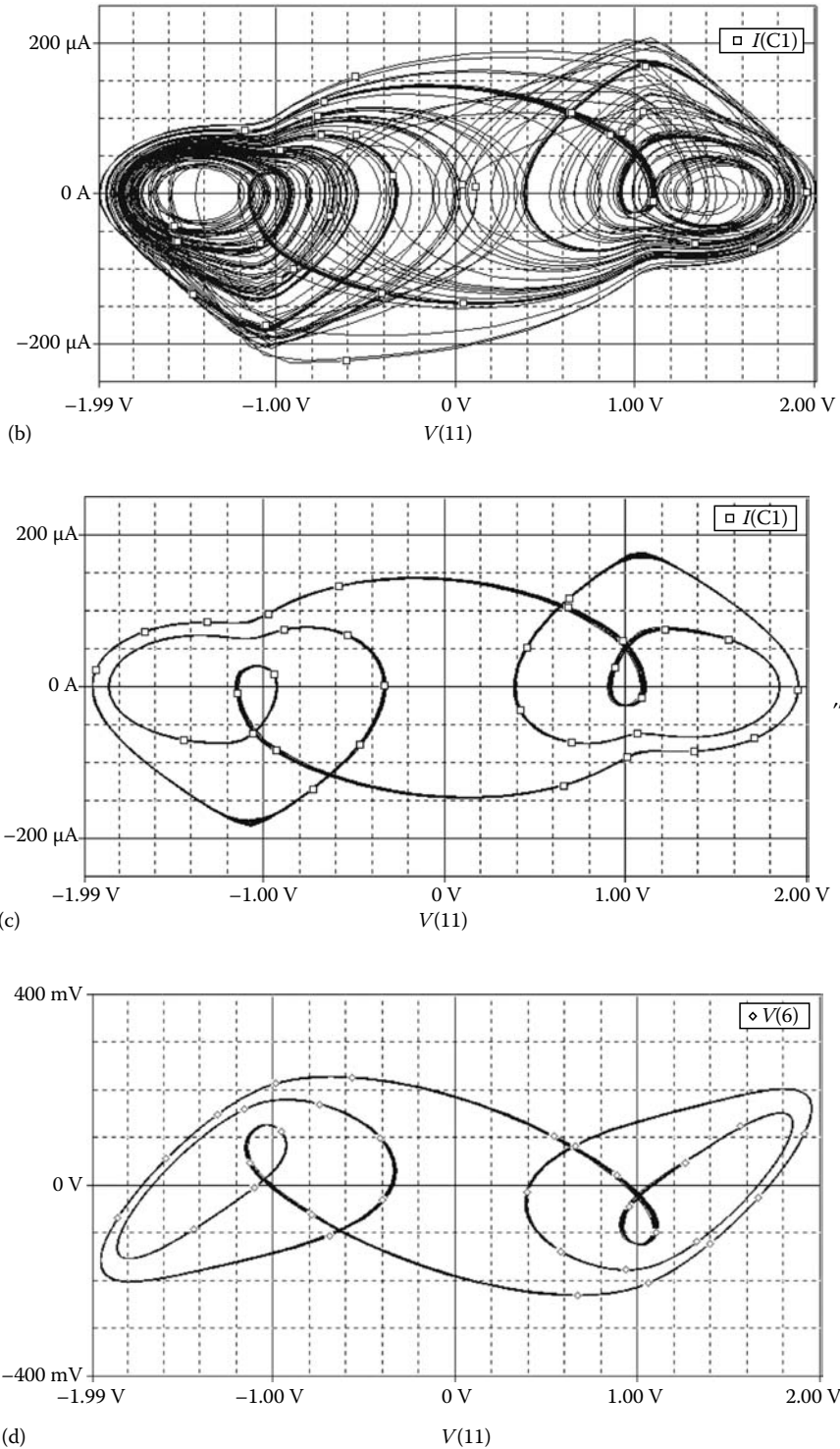


FIGURE 12.1 (continued) (b) The current of C1: $I(C1)$ as function of the voltage of C1: $V(11)$. (c) The current of C1: $I(C1)$ as function of the voltage of C1: $V(11)$ in the time interval 100–200 ms. (d) The voltage of C2: $V(6)$ as function of the voltage of C1: $V(11)$ in the time interval 100–200 ms.


```

+ I = I_VRL1
  Ind L2 6 16 13m
  Res RL2 16 0 1
  Cap C2 6 0 1.250u
  Res r61 6 10 1310
$ Not implemented
$ vrrC1 10 11 DC 0
  Volt vrrC1 10 11 DC = {vrrC1 = 0}
+ I = IC1
  Cap C1 11 0 0.017u
$ Not implemented
$ vrr10 10 1 DC 0
  Volt vrr10 10 1 DC = {vrr10 = 0}
+ I = IRNL
* $: non-linear circuit$; $:-----$
  Diode d13 1 3 MODEL = "n4148"
  Diode d21 2 1 MODEL = "n4148"
  Res rm9 2 22 47k
  Volt vrm9 22 0 DC = {vrm9 = -9} $ $; negative power supply
+ I = I_vrm9
  Res rp9 3 33 47k
$ Not implemented
$ vrp9 33 0 DC +9
  Volt vrp9 33 0 DC = {vrp9 = 9} $ +9 must be 9
  Res r20 2 0 3.3k
  Res r30 3 0 3.3k
  VCVS evop 4 0 1 1 5 [1e+20] LINEAR
  Res r14 1 4 290
  Res r54 5 4 290
  Res r50 5 0 1.2k
$$ Analysis commands
$$ .TRAN 0.05m 200m 0 0.018m UIC
$ Sweep "TRAN Analysis 1"
$+ LOOP (1+(200m-(0))/(0.05m)) TIME LIN 0 200m TMAX=0.018m
$+ NW=1 $ UIC
$$ .plot tran v(11)
$ Show Y Vtran(11) $
$ EndSweep
$ the following lines are added and the sweep above is commented
Sweep "TRAN Analysis 2"
+ LOOP (4001) TIME LIN 0 200m TMAX=0.018m
$+ NW=1 $ UIC
$ .plot tran v(11)
Show Y Itran(IC1) X Vtran(11) $
EndSweep
$.probe

```

The result of the analysis is presented in Figure 12.2. It is observed that limit cycle behavior is not obtained in the APLAC analysis in the time interval from 0 to 200 ms.

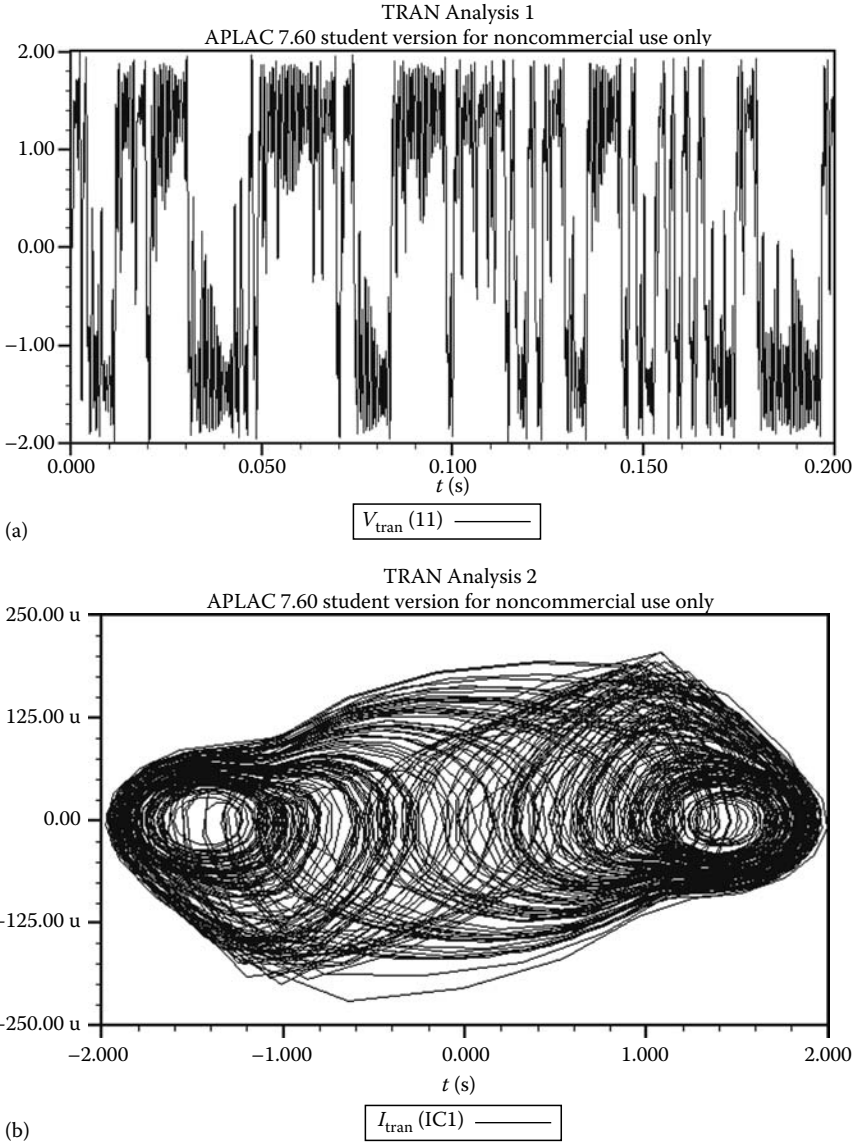


FIGURE 12.2 (a) The voltage of C1: $V(11)$ as function of time in the interval 0–200 ms. (b) The current of C1: $I(C1)$ as function of the voltage of C1: $V(11)$.

12.3.3 NAP2

The first versions of NAP2 (Nonlinear Analysis Program version 2) [10], based on the extended nodal equation formulation were developed in 1973 at the Institute of Circuit Theory and Telecommunication, Technical University of Denmark, Lyngby, Denmark.

NAP2 is a general-purpose circuit analysis program. Circuit models may contain resistors, conductors, capacitors, inductors, mutual inductors, ideal operational amplifiers, independent sources, controlled sources, and the most common semiconductor devices: diodes, bipolar junction transistors, and field effect transistors. NAP2 has only simple built-in models for the semiconductor devices, which require about 15 parameters. Besides the normal dc, ac, and transient analyses, the program can make parameter

variation analysis. Any parameter (e.g., component value or temperature) may be varied over a range in an arbitrary way and dc, ac, or transient analysis may be performed for each value of the parameter. Optimization of dc bias point (given: voltages, find: resistors) is possible. Event detection is included so that it is possible to interrupt the analysis when a certain signal, for example, goes from a positive to a negative value. The results may be combined into one output plot. It is also possible to calculate the poles and zeros of driving point and transfer functions for the linearized model in a certain bias point. Eigenvalue technique (based on the QR algorithm by J.G.F. Francis) is the method behind the calculation of poles and zeros. Group delay (i.e., the derivative of the phase with respect to the angular frequency) is calculated from the poles and zeros. This part of the program is available as an independent program named ANP3 (Analytical Network Program version 3).

In order to give an impression of the “net-list” input language, the syntax of the statements describing controlled sources is as follows:

```
Voltage Controlled Current Source: Ixxx N+ N- VALUE VByyy
Voltage Controlled Voltage Source: Vxxx N+ N- VALUE VByyy
Current Controlled Current Source: Ixxx N+ N- VALUE IByyy
Current Controlled Voltage Source: Vxxx N+ N- VALUE Ibyyy
```

where the initial characters of the branch name I and V indicate the type of the branch; $N+$ and $N-$ are integers (node numbers) indicating the placement and orientation of the branch, respectively; and VALUE specifies the numerical value of the control, which may be a constant or an arbitrary functional expression in case of nonlinear control. IB and VB refer to the current or voltage of the branch, respectively, from where the control comes. If the control is the time derivative of the branch signal, SI or SV may be specified. Independent sources must be connected to a resistor R or a conductor G as follows: $Rxxx N+ N- VALUE E = VALUE$ and $Gxxx N+ N- VALUE J = VALUE$, where VALUE may be any function of time, temperature, and components.

The input file “net-list” below describes the same analysis of the Chua oscillator circuit as performed by means of SPICE and APLAC. The circuit is a simple harmonic oscillator with losses (C2, L2, and RL2) loaded with a linear resistor (R61) in series with a capacitor (C1) in parallel with a nonlinear resistor. The circuit is excited by a sinusoidal voltage source through a coil L1. The frequency is specified as angular frequency in rps. It is possible to specify more than one statement on one line. Colon “:” indicate start of a comment statement and semicolon “;” indicates end of a statement. The greater than character “>” indicates continuation of a statement on the following line. It is observed that most of the lines are comment lines with the PSPICE input statements.

```
*circuit; *list 2, 9; : file CRC-CHUA.NAP
*: PSpice input file CRC-CHUA.CIR, first line, title line > :
: translated into NAP2 input file
: The Chua Oscillator, sinusoidal excitation, F=150mV > :
: RL2 = 1 ohm, RL1 = 0 ohm f = 1286.336389 Hz :
: ref. K. Murali and M. Lakshmanan, :
: Effect of Sinusoidal Excitation on the Chua's Circuit, :
: IEEE Transactions on Circuits and Systems - 1: :
: Fundamental Theory and Applications, :
: vol.39, No.4, April 1992, pp. 264-270 :
: input source; : -----
: VRS 7 0 sin(0 150m 1.2863363889332e+3 0 0) :
: sin/sin/; Rs 7 0 0 e=150m*sin(8.0822898994674e+3*time) :
: choke ; L1 6 17 80mH; RL1 17 7 0 :
: L1 6 17 80e-3 ;:mH :
```

```

: VRL1 17 7 DC 0 ;:ammeter for measure of IL1 :
: -----:
: harmonic oscillator; L2 6 16 13mH; RL2 16 0 1 :
: C2 6 0 1.250uF :
: L2 6 16 13m :
: RL2 16 0 1 :
: C2 6 0 1.250u :
: -----:
: load; r61 6 10 1310; rrc1 10 11 0; c1 11 0 0.017uF :
: rrr10 10 1 0: irr10=current of nonlinear resistor :
: r61 6 10 1310 :
: vrrC1 10 11 DC 0 :
: C1 11 0 0.017u :
: i(vrr10)=current of nonlinear resistor :
: vrr10 10 1 DC 0 :
: non-linear circuit; :-----:
: .model n4148 d (is=0.1p rs=16 n=1); vt=n*k*T/q :
: n4148 /diode/ is=0.1p gs=62.5m vt=25mV; :
: td13 13 n4148; td21 2 1 n4148; :
: d13 1 3 n4148 :
: d21 2 1 n4148 :
: rm9 2 0 47k e=-9; rp9 3 0 47k E=+9; :
: rm9 2 22 47k :
: vrm9 22 0 DC -9; negative power supply :
: rp9 3 33 47k :
: vrp9 33 0 DC +9 :
: r20 2 0 3.3k; r30 3 0 3.3k; :
: r20 2 0 3.3k :
: r30 3 0 3.3k :
: ideal op. amp.; :-----:
: gop 1 5 0; vop 4 0 vgap: no value means infinite value;:
: evop 4 0 1 5 1e+20 :
: r14 1 4 290; r54 5 4 290; r50 5 0 1.2k; :
: r14 1 4 290 :
: r54 5 4 290 :
: r50 5 0 1.2k :
: -----:
: *time time 0 200m : variable order, variable step:
: .TRAN 0.05m 200m 0 0.018m UIC:
: *tr vnull *plot(50 v6) v1 *probe:
: .plot tran v(11) :
: .probe :
: *run cycle=15000 minstep=1e-20 > :
: trunc=1e-3 step=50n:
: .options acct nopage opts gmin=1e-15 reltol=1e-3 :
: + abstol=1e-12 vntol=1e-12 tnom=25 itl5=0 :
: + limpts=15000 :
: .end :
: *end :

```

The program options are set by means of the statement *RUN, where, for example, the minimum integration step is set to $1e-20$ s and the relative truncation error is set to $1e-6$. The result of the analysis is presented in Figure 12.3. It can be observed that transition from chaotic behavior to a period 5 limit cycle takes place at about 50 ms. If we compare to the results obtained above by means of SPICE and APLAC,

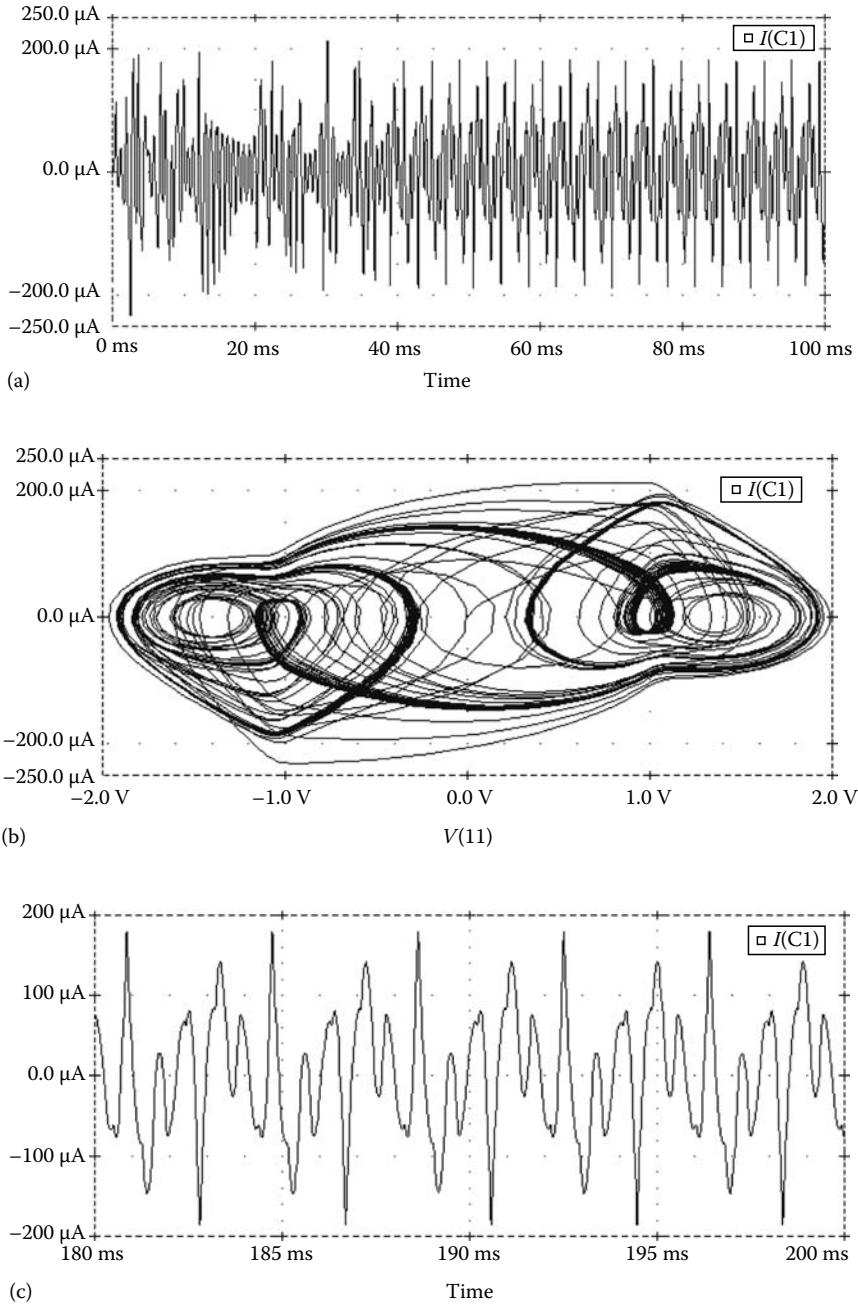


FIGURE 12.3 (a) NAP2 analysis. The current of C1: $I(C1)$ as function of time in the interval 0–100 ms. (b) The current of C1: $I(C1)$ as function of the voltage of C1: $V(11)$ in the time interval 0–100 ms. (c) The current of C1: $I(C1)$ as function of time in the interval 180–200 ms.

(continued)

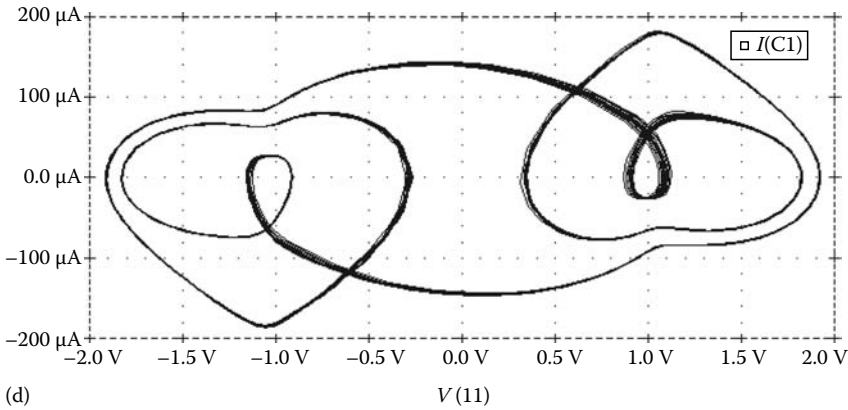


FIGURE 12.3 (continued) (d) The current of C1: $I(C1)$ as function of the voltage of C1: $V(11)$ in the time interval 100–200 ms.

we see that although the three programs are “modeled and set” the same way, for example, with the same relative tolerance $1e-3$, the results are different due to the chaotic nature of the circuit and possibly also due to the different strategies of equation formulation and solution used in the three programs. For example, SPICE uses the trapezoidal integration method with variable step; APLAC and NAP2 use the Gear integration methods with variable order and variable step.

12.3.4 ESACAP

The first versions of ESACAP program based on the extended nodal equation formulation were developed in 1979 at Elektronik Centralen, Hoersholm, Denmark, for the European Space Agency as a result of a strong need for a simulation language capable of handling interdisciplinary problems (e.g., coupled electrical and thermal phenomena). ESACAP was therefore born with facilities that have only recently been implemented in other simulation programs (e.g., facilities referred to as behavioral or functional modeling).

ESACAP carries out analyses on nonlinear systems in dc and in the time domain. The nonlinear equations are solved by a hybrid method combining the robustness of the gradient method with the good convergence properties of the Newton–Raphson method. The derivatives required by the Jacobian matrix are symbolically evaluated from arbitrarily complex arithmetic expressions and are therefore exact. The symbolic evaluation of derivatives was available in the very first version of ESACAP. It has now become a general numerical discipline known as automatic differentiation. The time-domain solution is found by numerical integration implemented as BDFs of variable step and orders 1 through 6 (modified Gear method). An efficient extrapolation method (the epsilon algorithm) accelerates the asymptotic solution in the periodic steady-state case.

Frequency-domain analyses may be carried out on linear or linearized systems (e.g., after a dc analysis). Besides complex transfer functions, special outputs such as group delay and poles/zeros are available. The group delay is computed as the sum of the frequency sensitivities of all the reactive components in the system. Poles and zeros are found by a numerical interpolation of transfer functions evaluated on a circle in the complex frequency plane. ESACAP also includes a complex number postprocessor by means of which any function of the basic outputs can be generated (e.g., stability factor, s -parameters, complex ratios).

Sensitivities of all outputs with respect to all parameters are available in all analysis modes. The automatic differentiation combined with the adjoint network provides exact partial derivatives in the frequency domain. In the time domain, integration of a sensitivity network (using the already LUfactorized Jacobian) provides the partial derivatives as functions of time.

The ESACAP language combines procedural facilities, such as if-then-else, assignment statements, and do-loops, with the usual description by structure (nodes/branches). Arbitrary expressions containing system variables and their derivatives are allowed for specifying branch values thereby establishing any type of nonlinearity. System variables of nonpotential and noncurrent type may be defined and used everywhere in the description (e.g., for defining power, charge). The language also accepts the specification of nonlinear differential equations. Besides all the standard functions known from high-level computer languages, ESACAP provides a number of useful functions. One of the most important of these functions is the delay function. The delay function returns one of its arguments delayed by a specified value, which in turn may depend on system variables. Another important function is the threshold switch—the ZEROREF function—used in if-then-else constructs for triggering discontinuities. The ZEROREF function interacts with the integration algorithm that may be reinitialized at the exact threshold crossing. The ZEROREF function is an efficient means for separating cause and action in physical models thereby eliminating many types of causality problems. Causality problems are typical examples of bad modeling techniques and the most frequent reason for divergence in the simulation of dynamic systems.

Typical ESACAP applications include electronics as well as thermal and hydraulic systems. The frequency domain facilities have been a powerful tool for designing stable control systems including nonelectronics engineering disciplines.

In order to give an idea of the input language, the syntax of the statements describing sources is as follows:

```
Current Source: Jxxx (N+, N-) = VALUE;
Voltage Source: Exxx (N+, N-) = VALUE;
```

where the initial characters of the branch name: J and E indicate the type of the branch; $N+$ and $N-$ are node identifiers (character strings), which, as a special case, may be integer numbers (node numbers). The node identifiers indicate the placement and orientation of the branch. The VALUE specifies the numerical value of the source, which may be an arbitrary function of time, temperature, and parameters as well as system variables (including their time derivatives). Adding an apostrophe references the time derivative of a system variable. $V(N1,N2)'$, for example, is the time derivative of the voltage drop from node $N1$ to node $N2$.

The next input file—actually, a small program written in the ESACAP language—describes an analysis of a tapered transmission line. The example shows some of the powerful tools available in the ESACAP language such as (1) the delay function, (2) the do-loop, and (3) the sensitivity calculation. The description language of ESACAP is a genuine simulation and modeling language. However, for describing simple systems, the input language is just slightly more complicated than the languages of SPICE, APLAC, and NAP2. Data are specified in a number of blocks (“chapters” and “sections”) starting with \$\$ and \$. Note how the line model is specified in a do-loop where ESACAP creates nodes and branches of a ladder network [11].

```
Example.155 Tapered line in the time domain.
# Calculation of sensitivities.
# This example shows the use of a do-loop for the discretization of a
# tapered transmission line into a chain of short line segments. The
# example also demonstrates how to specify partial derivatives of any
# parameter for sensitivity calculations.
$$DESCRIPTION # chapter - - - - -
$CON: n_sections=60; END; # section- - - - -
# n_sections is defined as a globally available constant.
# Only this constant needs to be modified in order to change
# the resolution of discretization
```

```

# Transmission line specified by characteristic impedance and length.
# Modelled by the ESACAP delay function (DEL) .
$MODEL: LineCell(in,out): Z0,length;
  delay=length/3e8;
  J_reverse(0,in)=DEL(2*V(out)/Z0-I(J_forward), delay);
  J_forward(0,out)=DEL(2*V(in)/Z0-I(J_reverse), delay);
  G1(in,0)=1/Z0; G2(out,0)=1/Z0;
END; # end of section-----
# Tapered line specified by input and output impedance and length
# This model calls LineCell n_sections times in a do-loop.
$MODEL: TaperedLine(in,out): Z1,Z2,length;
  ALIAS_NODE(in,1); # Let node in and 1 be the same.
  ALIAS_NODE(out,[n_sections+1]); # Let node out and n_sections+1 be
  # the same.
# Notice that values in square brackets become part of an identifier
FOR (i=1, n_sections) DO
X[i]([i],[i+1])=LineCell(Z1+i*(Z2-Z1)/n_sections, length/n_sections);
ENDDO;
END; # end of section -----
# Main network calls the model of the tapered line and terminates
# it by a 50 ohm source and 100 ohm load.
$NETWORK: # section-----
IF (TIME.LT.1n) THEN
  Esource(source,0)=0;
ELSE
  Esource(source,0)=1;
ENDIF;
# Esource(source,0)=TABLE(TIME,(0,0),(1n,0),(1.001n,1),(10n,1));
Rsource(source,in)=50;
Rload(out,0)=100;
Z1=50; Z2=100; length=1;
X1(in,out)=TaperedLine(Z1,Z2,length);
END; # end of section -----
# Time-domain analysis
$$TRANSIENT # chapter-----
# Analysis parameters
$PARAMETERS: # section-----
  TIME=0,20n; # Total time sweep
  HMAX=2p; # Max integration step
END; # end of section-----
# Specification of desired results. Adding an exclamation mark (!) to an
# output will show the value on the ESACAP real-time graphics display.
$DUMP: # section-----
  FILE=<dump.155>; TIME=0,20n,20p;
  TIME; V(in)!; V(out)!;
  (V(in),DER(Z1))!; # Partial derivatives with respect
  (V(out),DER(Z1))!; # to Z1
END; # end of section -----
$$STOP # chapter-----

```

The result of the analysis is presented in Figure 12.4.

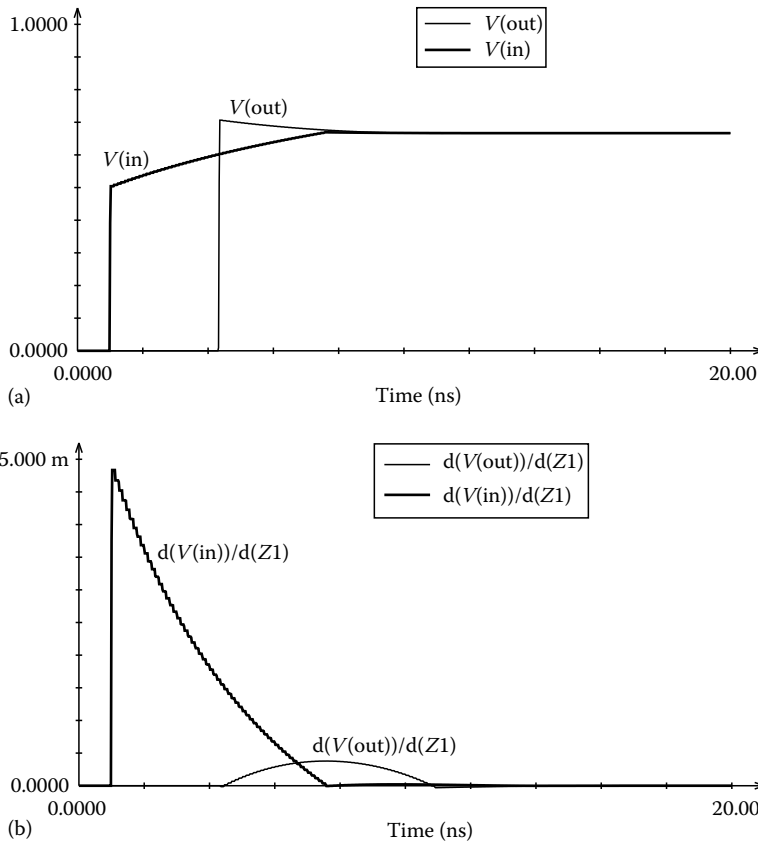


FIGURE 12.4 (a) ESACAP analysis. The input voltage of the tapered line: $V(\text{in})$ and the output voltage of the tapered line: $V(\text{out})$ as functions of time in the interval from 0 to 20 ns. (b) The sensitivities of $V(\text{in})$ and $V(\text{out})$ with respect to $Z1$.

12.3.5 DYNAST

DYNAST [7] was developed in 1992 in a joint venture between the Czech Technical University, Prague, the Czech Republic and Katholieke Universiteit Leuven, Heverlee, Belgium. The program was developed as an interdisciplinary simulation and design tool in the field of “mechatronics” (mixed mechanical/electrical systems).

The main purpose of DYNAST is to simulate dynamic systems decomposed into subsystems defined independently of the system structure. The structure can be hierarchical. DYNAST is a versatile software tool for modeling, simulation, and analysis of general linear as well as nonlinear dynamic systems, both in time and frequency domain. Semisymbolic analysis is possible (poles and zeros of network functions, inverse Laplace transformation using closed-form formulas).

Three types of subsystem models are available in DYNAST. The program admits systems descriptions in the form of (1) a multipole diagram respecting physical laws, (2) a causal or an acausal block diagram, (3) a set of equations, or (4) in a form combining the above approaches.

1. In DYNAST the physical-level modeling of dynamic systems is based on subsystem multipole models or multiterminal models. These models respect the continuity and compatibility postulates that apply to all physical energy-domains. (The former postulate corresponds to the laws of conservation of energy, mass, electrical charge, etc.; the latter is a consequence of the system

connectedness.) The multipole poles correspond directly to those subsystem locations in which the actual energetic interactions between the subsystems take place (such as shafts, electrical terminals, pipe inlets, etc.). The interactions are expressed in terms of products of complementary physical quantity pairs: the through variables flowing into the multipoles via the individual terminals, and the across variables identified between the terminals.

2. The causal blocks, specified by explicit functional expressions or transfer functions, are typical for any simulation program. But the variety of basic blocks is very poor in DYNAST, as its language permits definition of the block behavior in a very flexible way. Besides the built-in basic blocks, user specified multi-input multi-output macroblocks are available as well. The causal block interconnections are restricted by the rule that only one block output may be connected to one or several block inputs. In the DYNAST block variety, however, causal blocks are also available with no restrictions imposed on their interconnections, as they are defined by implicit-form expressions.
3. DYNAST can also be used as an equation solver for systems of nonlinear first-order algebro-differential and algebraic equations in the implicit form. The equations can be submitted in a natural way (without converting them into block diagrams) using a rich variety of functions including the Boolean, event-dependent, and tabular ones. The equations, as well as any other input data, are directly interpreted by the program without any compilation.

The equation formulation approach used for both multipoles and block diagrams evolved from the extended method of nodal voltages (MNA) developed for electrical systems. Because all the equations of the diagrams are formulated simultaneously, no problems occur with the *algebraic loops*. As the formulated equations are in the implicit form, it does not create any problems with the *causality* of the physical models.

The integration method used to solve the nonlinear algebro-differential and algebraic equations is based on a stiff-stable implicit backward-differentiation formula (a modified Gear method). During the integration, the step length as well as the order of the method is varied continuously to minimize the computational time while respecting the admissible computational error. Jacobians necessary for the integration are computed by symbolic differentiation. Their evaluation as well as their LU decomposition, however, is not performed at each iteration step if the convergence is fast enough. Considerable savings of computational time and memory are achieved by a consistent matrix sparsity exploitation.

To accelerate the computation of periodic responses of weakly damped dynamic systems, the iterative epsilon-algorithm is utilized. Also, fast-Fourier transformation is available for spectral analysis of the periodic steady-state responses.

DYNAST runs under DOS- or WINDOWS-control on IBM-compatible PCs. Because it is coded in FORTRAN 77 and C-languages, it is easily implemented on other platforms. It is accompanied by a menu-driven *graphical environment*. The block and multiport diagrams can be submitted in a graphical form by a schematic capture editor. DYNAST can be easily augmented by various pre- and postprocessors because all its input and output data are available in the ASCII code. Free "net-list" access to DYNAST is possible by means of e-mail or online over the Internet [7].

References

1. Calahan, D. A., *Computer-Aided Network Design*. New York: McGraw-Hill, 1972.
2. Chua, L. O. and P. M. Lin, *Computer-Aided Analysis of Electronic Circuits*. Englewood Cliffs, NJ: Prentice Hall, 1975.
3. Dertouzos, M. L. et al., *Systems, Networks, and Computation: Basic Concepts*. New York: McGraw-Hill, 1972.
4. Ostrowski, A. M., *Solution of Equations and Systems of Equations*. New York: Academic Press, 1966.

5. Valtonen, M. et al., *APLAC—An Object-Oriented Analog Circuit Simulator and Design Tool*. Espoo, Finland: Circuit Theory Lab., Helsinki University of Technology and Nokia Corporation Research Center, 1992, <http://www.aplac.hut.fi/aplac/general.html>, <http://www.aplac.com/>
6. Intusoft, *IsSpice3—ICAPS System Packages*. San Pedro, CA: Intusoft, 1994, <http://www.intusoft.com/>
7. Mann, H., *DYNAST—A Multipurpose Engineering Simulation Tool*. Prague, Czech Republic: The Czech Technical University, 1994, <http://www.it.dtu.dk/ecs/teacher.htm>, <http://icosym.cvut.cz/cacsd/msa/onlinetools.html>, <http://icosym.cvut.cz/dyn/download/public/>
8. Meta-Software, *HSPICE User's Manual H9001*. Campbell, CA: Meta-Software, 1990.
9. MicroSim, *PSpice—The Design Center*. Irvine, CA: MicroSim, 1994, <http://www.cadencepcb.com> and <http://www.pspice.com/>
10. Rübner-Petersen, T., *NAP2—A Nonlinear Analysis Program for Electronic Circuits*, Version 2, Users Manual 16/5-73, Report IT-63, ISSN-0105-8541. Lyngby, Denmark: Institute of Circuit Theory and Telecommunication, Technical University of Denmark, 1973, <http://www.it.dtu.dk/ecs/programs.htm#nnn>, <http://www.it.dtu.dk/ecs/napanp.htm>
11. Stangerup, P., *ESACAP User's Manual*. Nivaa, Denmark: StanSim Research Aps., 1990, <http://www.it.dtu.dk/ecs/esacap.htm>
12. Vlach, J. and K. Singhal, *Computer Methods for Circuit Analysis and Design*. New York: Van Nostrand Reinhold, 1983.
13. Funk, D. G. and D. Christiansen (Eds.), *Electronic Engineers' Handbook*, 3rd ed. New York: McGraw-Hill, 1989.

13

Cellular Neural Networks and Cellular Wave Computers

Tamás Roska

*Hungarian Academy of Sciences and
Pázmány Péter Catholic University*

Ákos Zarándy

*Hungarian Academy of Sciences and
Pázmány Péter Catholic University*

Csaba Rekeczky

*Eutecus Inc. and Pázmány Péter
Catholic University*

13.1	Introduction: Definition and Classification	13-1
	Typical CNN Models	
13.2	Simple CNN Circuit Structure	13-3
13.3	Stored Program CNN Universal Machine and the Analogic Supercomputer Chip	13-6
13.4	Applications	13-8
	Image Processing—Form, Motion, Color, and Depth • Partial Differential Equations • Relation to Biology	
13.5	Template Library: Analogical CNN Algorithms	13-11
13.6	Recent Advances	13-16
13.7	Recent Developments and Outlook.....	13-17
	References.....	13-18

13.1 Introduction: Definition and Classification

Current very-large-scale integration (VLSI) technologies provide for the fabrication of chips with several million transistors. With these technologies a single chip may contain one powerful digital processor, a huge memory containing millions of very simple units placed in a regular structure, and other complex functions. A powerful combination of a simple logic processor placed in a regular structure is the cellular automaton invented by John von Neumann. The cellular automaton is a highly parallel computer architecture. Although many living neural circuits resemble this architecture, the neurons do not function in a simple logical mode: they are analog “devices.” The cellular neural network architecture, invented by Chua and his graduate student Yang [1], has both the properties: the cell units are nonlinear continuous-time dynamic elements placed in a cellular array. Of course, the resulting nonlinear dynamics in space could be extremely complex. The inventors, however, showed that these networks can be designed and used for a variety of engineering purposes, while maintaining stability and keeping the dynamic range within well-designed limits. Subsequent developments have uncovered the many inherent capabilities of this architecture (IEEE conferences: CNNA-90, CNNA-92, CNNA-94, 96, 98, 00, 02; Special issues: *International Journal of Circuit Theory and Applications*, 1993, 1996, 1998, 2002; and *IEEE Transactions on Circuits and Systems, I and II*, 1993, 1999, etc.). In the circuit implementation, unlike analog computers or general neural networks, the cellular neural/nonlinear network (CNN) cells are not the ubiquitous high-gain operational amplifiers. In most practical cases, they are either simple unity-gain amplifiers or simple second- or third-order simple dynamic circuits with one to two simple nonlinear components. Tractability

in the design and the possibility for exploiting the complex nonlinear dynamic phenomena in space, as well as the trillion operations per second (TeraOPS) computing speed in a single chip are but some of the many attractive properties of cellular neural networks. The trade-off is in the accuracy; however, in many cases, the accuracy achieved with current technologies is enough to solve a lot of real-life problems.

The CNN is a new paradigm for multidimensional, nonlinear, dynamic processor arrays [1,2]. The mainly uniform processing elements, called cells or artificial neurons, are placed on a regular geometric grid (with a square, hexagonal, or other pattern). This grid may consist of several two-dimensional (2-D) layers packed upon each other (Figure 13.1). Each processing element or cell is an analog dynamical system, the state (x), the input (u), and the output (y) signals are analog (real-valued) functions of time (both continuous-time and discrete-time signals are allowed). The interconnection and interaction pattern assumed at each cell is mainly local within a neighborhood N_r , where N_r denotes the first “ r ” circular layers of surrounding cells. Figure 13.2 shows a 2-D layer with a square grid of interconnection

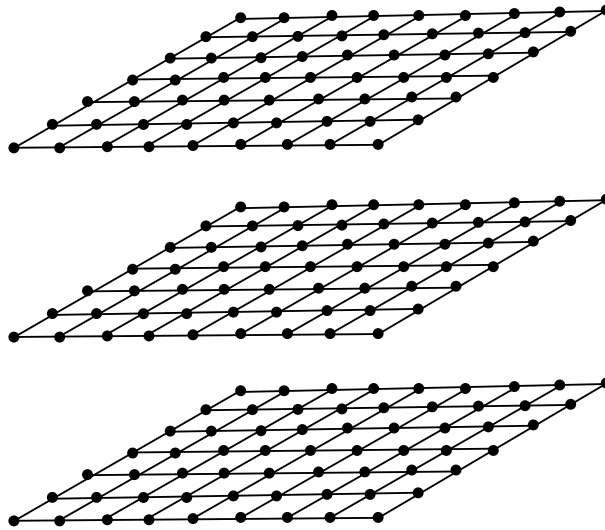


FIGURE 13.1 CNN grid structure with the processing elements (cells) located at the vertices.

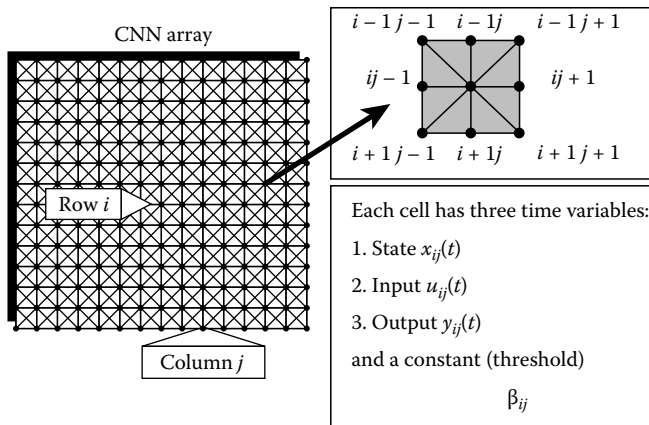


FIGURE 13.2 A single, 2-D CNN layer and a magnified cell with its neighbor cells with the normal neighborhood radius $r = 1$.

radius of 1 (nearest neighborhood). Each vertex contains a cell and the edges represent the interconnections between the cells. The pattern of interaction strengths between each cell and its neighbors is the “program” of the CNN array. It is called a cloning template (or just template).

Depending on the types of grids, processors (cells), interactions, and modes of operation, several classes of CNN architectures and models have been introduced. Although the summary below is not complete, it gives an impression of vast diversities.

13.1.1 Typical CNN Models

1. Grid type
 - Square
 - Hexagonal
 - Planar
 - Circular
 - Equidistant
 - Logarithmic
2. Processor type
 - Linear
 - Sigmoid
 - First-order
 - Second-order
 - Third-order
3. Interaction type
 - Linear memoryless
 - Nonlinear
 - Dynamic
 - Delay-type
4. Mode of operation
 - Continuous-time
 - Discrete-time
 - Equilibrium
 - Oscillating
 - Chaotic

13.2 Simple CNN Circuit Structure

The simplest first-order dynamic CNN cell used in the seminal paper [1] is illustrated in Figure 13.3. It is placed on the grid in the position ij (row i and column j). It consists of a single state capacitor with a parallel resistor and an amplifier $[f(x_{ij})]$. This amplifier is a voltage-controlled current source (VCCS), where the controlling voltage is the state capacitor voltage. To make the amplifier model self-contained, a parallel resistor of unit value is assumed to be connected across the output port. Hence, the voltage transfer characteristic of this amplifier is also equal to $f(\cdot)$. In its simplest form this amplifier has a unity-gain saturation characteristic (see Figure 13.7 for more details).

The aggregate feedforward and feedback interactions are represented by the current sources i_{input} and i_{output} , respectively. Figure 13.4 shows these interactions in more detail. In fact, the feedforward interaction term i_{input} is a weighted sum of the input voltages (u_{kl}) of all cells in the neighborhood (N_r). Hence, the feedforward template, the so-called \mathbf{B} template, is a small matrix of size $(2r+1) \times (2r+1)$ containing the template elements b_{kl} , which can be implemented by an array of linear VCCSs. The controlling voltages of these controlled sources are the input voltages of the cells within the neighborhood of radius r . This means, for example, that b_{12} is the VCCS controlled by the input voltage of the cell lying

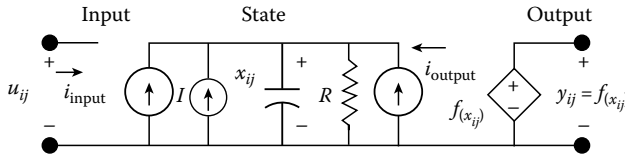


FIGURE 13.3 Simple first-order CNN cell.

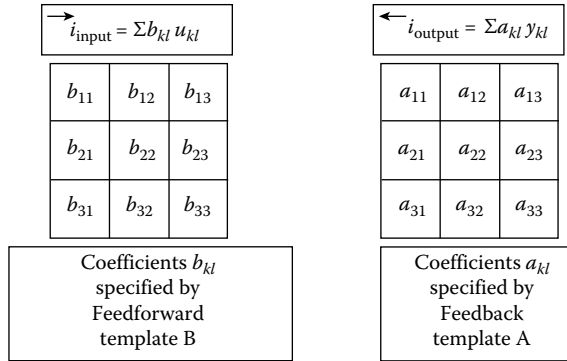


FIGURE 13.4 The 19 numbers (a program) that govern the CNN array (the 19th number is the constant bias term I , but it is not shown in the figure) define the cloning template (A , B , and I).

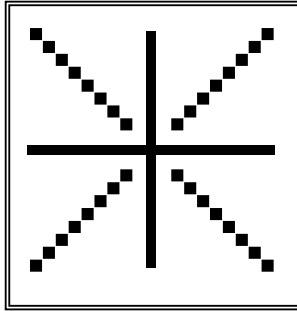
north from the cell ij . In most practical cases the B template is translation invariant, i.e., the interaction pattern (the B template) is the same for all cells. Hence, the chip layout will be very regular (as in memories or PLAs). The feedback interaction term i_{output} is a weighted sum of the output voltages (y_{kl}) of all cells in the neighborhood (N_r). The weights are the elements of a small matrix A called the A template (or feedback template). Similar arguments apply for the A template as for the B template discussed previously. If the constant threshold term is translation invariant as denoted by the constant current source I , then in the case of $r = 1$, the complete cloning template contains only 19 numbers (A and B and I , i.e., $9 + 9 + 1$ terms), irrespective of the size of the CNN array. These 19 numbers define the task which the CNN array can solve.

What kind of tasks are we talking about? The simplest, and perhaps the most important, are image-processing tasks. In the CNN array computer, the input and output images are coded as follows. For each picture element (called pixel) in the image, a single cell is assigned in the CNN. This means that a one-to-one correspondence exists between the pixels and the CNN cells. Voltages in the CNN cells code the grayscale values of the pixels. Black is coded by $+1$ V, white is -1 V, and the grayscale values are in between. Two independent input images can be defined pixel-by-pixel: the input voltages u_{ij} and the initial voltage values of the capacitors x_{ij} (0) (cell-by-cell). Placing these input images onto the cell array and starting the transient, the steady-state outputs y_{ij} will encode the output image. The computing time is equal to the settling time of the CNN array. This time is below $1 \mu\text{s}$ using a CNN chip made with a $1.0\text{--}1.5 \mu\text{m}$ technology containing thousands of CNN processing elements, i.e., pixels, in an area of about 2 cm^2 . This translates to a computing power of several 100 billion operations per second (GXPS). The first tested CNN chip [3] was followed by several others implementing a discrete-time CNN model [4] and chips with on-chip photosensors in each cell [5].

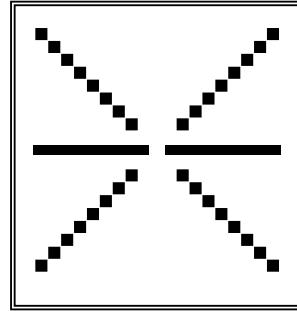
For example, if we place the array of voltage values defined by the image shown in Figure 13.5b as the input voltage and the initial state capacitor voltage values in the CNN array with the cloning template shown in Figure 13.5a, then after the transients have settled down, the output voltages will encode the output image of Figure 13.5c. Observe that the vertical line has been deleted. Since the image

$$A = \begin{bmatrix} 0 & 0 & 0 \\ 0 & 2 & 0 \\ 0 & 0 & 0 \end{bmatrix}, \quad B = \begin{bmatrix} 0 & -0.25 & 0 \\ 0 & 0 & 0 \\ 0 & -0.25 & 0 \end{bmatrix}, \quad I = -1.5$$

(a)



(b)



(c)

FIGURE 13.5 An input and output image where the vertical line was deleted.

contains 40×40 pixels, the CNN array contains 40×40 cells. It is quite interesting that if we had more than one vertical line, the computing time would be the same. Moreover, if we had an array of 100×100 cells on the chip, the computing time would remain the same as well. This remarkable result is due to the fully parallel nonlinear dynamics of the CNN computer. Some propagating-type templates induce wavelike phenomena. Their settling times increase with the size of the array.

For other image-processing tasks, processing form, motion, color, and depth, more than 100 cloning templates have been developed to date and the library of new templates is growing rapidly. Using the Cellular Neural Network Workstation Tool Kit [6], they can be called in from a CNN template library (CTL). New templates are being developed and published continually.

The dynamics of the CNN array is described by the following set of differential equations:

$$\begin{aligned} dx_{ij}/dt &= -x_{ij} + I + i_{\text{output}} + i_{\text{input}} \\ y_{ij} &= f(x_{ij}) \\ i &= 1, 2, \dots, N \quad \text{and} \quad j = 1, 2, \dots, M \quad (\text{the array has } N \times M \text{ cells}) \end{aligned}$$

where the last two terms in the state equation are given by the sums shown in Figure 13.4.

We can generalize the domain covered by the original CNN defined via linear and time-invariant templates by introducing the “nonlinear” templates (denoted by “ \wedge ”) and the “delay” templates (indicated by τ in the superscript) as well, to obtain the generalized state equation shown below. The unity-gain nonlinear sigmoid characteristics f are depicted in Figure 13.6.

$$\begin{aligned} \frac{dvx_{ij}}{dt} &= -vx_{ij} + I_{ij} + \sum_{kl \in N_r(ij)} \hat{A}_{ij;kl} (vy_{kl}(t), vy_{ij}(t)) + \sum_{kl \in N_c(ij)} \hat{B}_{ij;kl} (vu_{kl}(t), vu_{ij}(t)) \\ &+ \sum_{kl \in N_r(ij)} A_{ij;kl}^\tau vy_{kl}(t - \tau) + \sum_{kl \in N_c(ij)} B_{ij;kl}^\tau vu_{kl}(t - \tau) \end{aligned}$$

Several strong results have been proved that assure stable and reliable operations. If the A template is symmetric, then the CNN is stable. Several other results have extended this condition [4,7]. The sum of the absolute values of all the 19 template elements plus 1 defines the dynamic range within which the

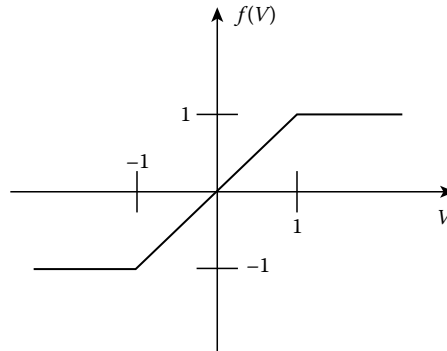


FIGURE 13.6 The simple unity-gain sigmoid characteristics.

- 1-, 2-, 3-, or n -dimensional *array* of mainly identical *dynamical systems*, called cells or processor units, which satisfies two properties:
 - Most *interactions are local* within a finite radius r
 - All *state variables are continuous valued* signals

FIGURE 13.7 CNN definition.

state voltage remains bounded during the entire transient, if the input and initial state signals are <1 V in absolute value [1].

In a broader sense, the CNN is defined [8] as shown in Figure 13.7, see also Ref. [32].

13.3 Stored Program CNN Universal Machine and the Analogic Supercomputer Chip

For different tasks, say image-processing, we need different cloning templates. If we want to implement them in hardware, we would need different chips. This is inefficient except for dedicated, mass-production applications.

The invention of the CNN universal machine [9] has overcome the problem above. It is the first stored-program array computer with analog nonlinear array dynamics. One CNN operation, for example, solving thousands of nonlinear differential equations in a microsecond, is just one single instruction. In addition, a single instruction is represented by just a few analog (real) values (numbers). In the case when the nearest neighborhood is used, only 19 numbers are generated. When combining several CNN templates, for example, extracting first contours in a grayscale image, then detecting those areas where the contour has holes, etc., we have to design a flowchart logic that satisfies the correct sequence of the different templates. The simple flowchart for the previous example is shown in Figure 13.8. One key point is that, in order to exploit the high speed of the CNN chips, we have to store the intermediate results cell-by-cell (pixel-by-pixel). Therefore, we need a local analog memory (LAM). By combining several template actions we can write more complex flowcharts for implementing almost any analogic algorithms. The name analogic is an acronym for “analog and logic.” It is important to realize that analogic computation is completely different from hybrid computing. To cite just one point, among others, no A/D or D/A conversions occur during the computation of an analogic program. As with digital microprocessors, to control the execution of an analogic algorithm, we need a global programming unit. The global architecture of the CNN universal machine is shown in Figure 13.9.

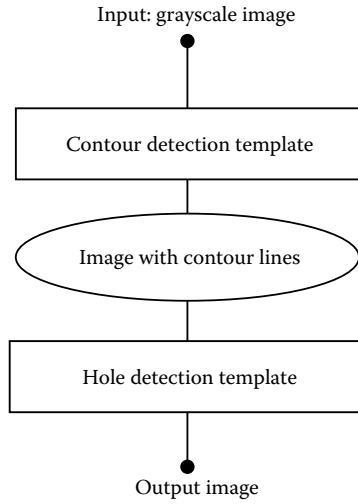


FIGURE 13.8 Flowchart representing the logic sequence of two templates.

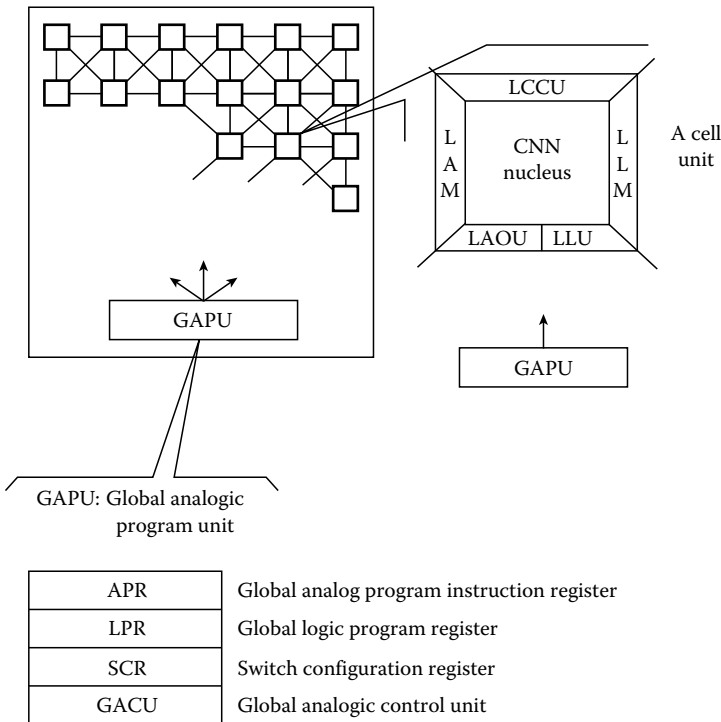


FIGURE 13.9 Global architecture of the CNN universal machine.

As we can see from this figure, the CNN nucleus described in Section 13.2 has been generalized to include several crucial functions depicted in the periphery. We have already discussed the role of the LAM that provides the local (on-chip) storage of intermediate analog results. Because the results of many detection tasks in applications involve only black-and-white logic values, adding a local logic memory (LLM) in each cell is crucial. After applying several templates in a sequence, it is often necessary to combine their results. For example, to analyze motion, consecutive snapshots processed by CNN templates are compared. The local analog output unit (LAOU) and the local logic unit (LLU) perform these tasks, both on the local analog (gray scale) and the logical (black-and-white) values. The local communication and control unit (LCCU) of each cell decodes the various instructions coming from the global analogic program unit (GAPU).

The global control of each cell is provided by the GAPU. It consists of four parts:

1. Analog program (instruction) register (APR) stores the CNN template values (19 values for each CNN template instruction in the case of nearest interconnection). The templates stored here will be used during the run of the prescribed analogical algorithm.
2. Global logic program register (LPR) stores the code for the LLUs.
3. Flexibility of the extended CNN cells is provided by embedding controllable switches in each cell. By changing the switch configurations of each cell simultaneously, we can execute many tasks using the same cell. For example, the CNN program starts by loading a given template, storing the results of this template action in the LAM, placing this intermediate result back on the input to prepare the cell, starting the action with another template, etc. The switch configurations of the cells are coded in the switch configuration register (SCR).
4. Finally, the heart of the GAPU is the global analogic control unit (GACU), which contains the physical machine code of the logic sequence of analogical algorithm. It is important to emphasize that here the control code is digital; hence, although its internal operation is analog and logical, a CNN universal chip can be programmed with the same flexibility and ease as a digital microprocessor—except the language is much simpler. Indeed, a high-level language, a compiler, an operating system, and an algorithm development system are available for CNN universal chip architectures. Moreover, by fabricating optical sensors cell-by-cell on the chip [5], the image input is directly interfaced.

The CNN universal chip is called supercomputer chip because the execution speed of an analogic algorithm falls in the same range as the computing power of today's average digital supercomputers (a TeraOPS). Another reason for this enormous computing power is that the reprogramming time of a new analog instruction (template) is of the same order, or less, than the analog array execution time (less than a microsecond). This is about 1 million times faster than some fully interconnected analog chips.

Based on the previously mentioned novel characteristics, the CNN universal chip can be considered to be an analogic microprocessor.

13.4 Applications

In view of its flexibility and its very high speed in image-processing tasks, the CNN universal machine is ideal for many applications. In the following, we briefly describe three areas. For more applications, the reader should consult the references at the end of this chapter.

13.4.1 Image Processing—Form, Motion, Color, and Depth

Image processing is currently the most popular application of CNN. Of the more than 100 different templates currently available, the vast majority are for image-processing tasks. Eventually, we will have templates for almost all conceivable local image-processing operations. Form (shape), motion, color, and depth can all be ideally processed via CNN. The interested reader can find many examples and

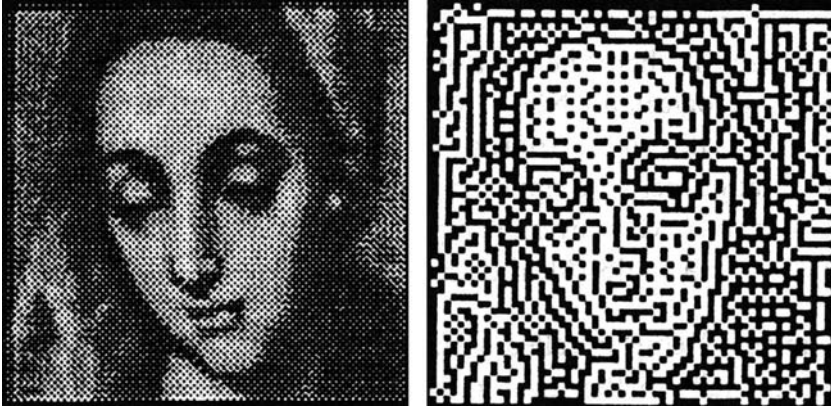


FIGURE 13.10 Halftoning: an original grayscale image (LHS) and its halftoned version (RHS). A low resolution is deliberately chosen in (b) in order to reveal the differing dot densities at various regions of the image.

applications in the references. CNN handles analog pixel values, so grayscale images are processed directly.

Many templates detect simple features like different types of edges, convex or concave corners, lines with a prescribed orientation, etc. Other templates detect semiglobal features like holes, groups of objects within a given size of area, or delete objects smaller than a given size. There are also many CNN global operations like calculating the shadow, histogram, etc. Halftoning is commonly used in fax machines, laser printers, and newspapers. In this case, the local gray level is represented by black dots of identical size, whose density varies in accordance with the gray level. CNN templates can do this job as well. A simple example is shown in Figure 13.10. The original grayscale image is shown on the left-hand side, the halftoned image is shown on the right-hand side. The “smoothing” function of our eye completes the image-processing task.

More complex templates detect patterns defined within the neighborhood of interaction. In this case, the patterns of the **A** and **B** templates somehow reflect the pattern of the object to be detected.

Because the simplest templates are translation invariant, the detection or pattern recognition is translation invariant as well. By clever design, however, some rotationally invariant detection procedures have been developed as well.

Combining several templates according to some prescribed logic sequence, more complex pattern detection tasks can be performed, e.g., halftoning.

Color-processing CNN arrays represent the three basis colors by single layers via a multilayer CNN. For example, using the red-green-blue (RGB) representation in a three-layer CNN, simple color-processing operations can be performed. Combining them with logic, conversions between various color representations are possible.

One of the most complex tasks that has been undertaken by an analogic CNN algorithm is the recognition of bank notes. Recognition of bank notes in a few milliseconds is becoming more and more important. Recent advances in the copy machine industry have made currency counterfeiting easier. Therefore, automatic bank note detection is a pressing need. Figure 13.11 shows a part of this process (which involves color processing as well). The dollar bill shown in the foreground is analyzed and the circles of a given size are detected (colors are not shown). The “color cube” means that each color intensity is within prescribed lower and upper limit values.

Motion detection can be achieved by CNN in many ways. One approach to process motion is to apply two consecutive snapshots to the input and the initial state of the CNN cell. The CNN array calculates the various combinations between the two snapshots. The simplest case is just taking the difference to detect

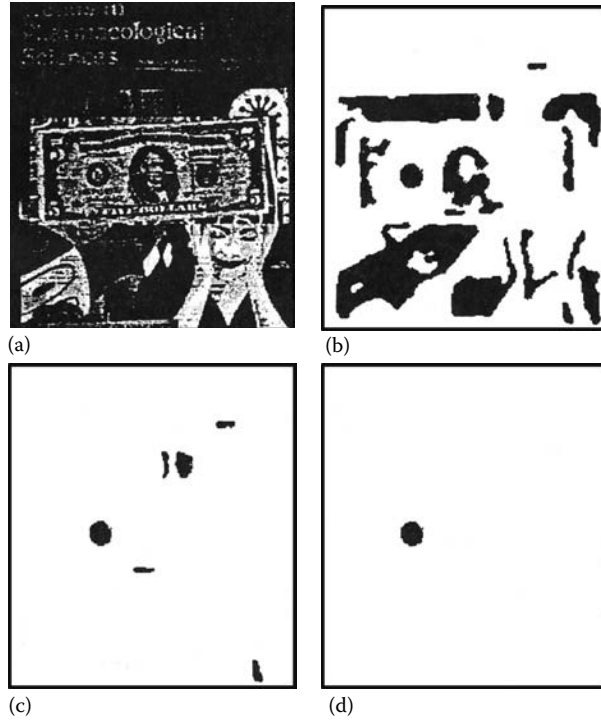


FIGURE 13.11 Some intermediate steps in the dollar bill recognition process. An input image (a) shown here in single color results in the “color cube” (b), the convex objects (c), and the size classification (d).* (From Zarándy, A., Werblin, F., Roska, T., Chua, L.O., and Novel type of analogical CNN algorithms for recognizing bank notes, Memorandum UCB/ERL, M94/29 1994, Electronics Research Laboratory, University of California, Berkeley, CA, 1994. With permission.)

motion. Detecting direction, shape, etc. of moving objects are only the simplest problems that can be solved via CNN. In fact, even depth detection can be included as well.

13.4.2 Partial Differential Equations

As noted in the original paper [1], even the simple-cell CNN with the linear template

$$A = \begin{bmatrix} 0 & 1 & 0 \\ 1 & -3 & 1 \\ 0 & 1 & 0 \end{bmatrix}, \quad B = 0, \quad I = 0$$

can approximate the solution of a diffusion-type partial differential equation (PDE) on a discrete spatial grid. This solution maintains continuity in time, a nice property not possible in digital computers.

By adding just a simple capacitor to the output, i.e., by placing a parallel RC circuit across the output port of the cell of Figure 13.3, the following wave equation will be represented in a discrete space grid:

$$d^2p(t)/dt^2 = \Delta p$$

* Figure 13.11 shows a part of this process [31] (which involves color processing as well). The dollar bill shown in the foreground is analyzed and the circles of a given size are detected (colors are not shown).

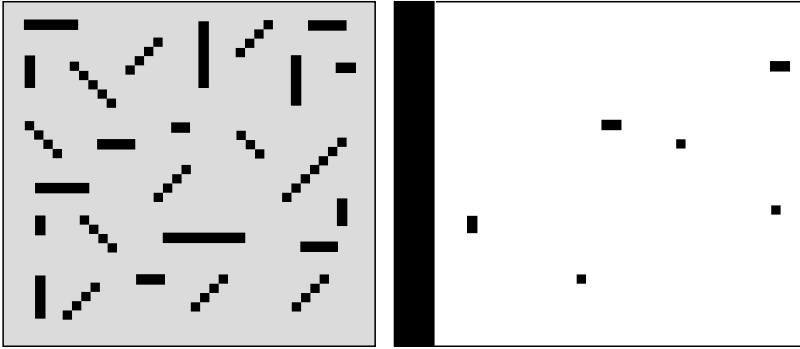


FIGURE 13.12 The length tuning effect. The input image on the LHS contains bars of different lengths. The out image on the RHS contains only those that are smaller than a given length. (From Roska, T., Hámori, J., Lábos, E., Lotz, K., Takács, J., Venetianer, P., Vidnyánszki, Z., and Zarándy, A., *IEEE Trans. Circuits Syst. I*, 40, 182, 1993. With permission.)

where

$p(t) = P(x, y, t)$ is the state (intensity) variable on a 2-D plane (x, y)

Δ is the Laplacian operator (the sum of the second derivatives related to x and y)

In some cases, it is useful to use a cell circuit that is chaotic. Using the canonical Chua's circuit, other types of PDEs can be modeled, generating effects like autowaves, spiral waves, Turing patterns, and so on (e.g., Perez-Munuzuri et al. in Ref. [7]).

13.4.3 Relation to Biology

Many topographical sensory organs have processing neural-cell structures very similar to the CNN model. Local connectivity in a few sheets of regularly situated neurons is very typical. Vision, especially the retina, reflects these properties strikingly. It is not surprising that, based on standard neurobiological models, CNN models have been applied to the modeling of the subcortical visual pathway [10]. Moreover, a new method has been devised to use the CNN universal machine for combining retina models of different species in a programmed way. Modalities from other sensory organs can be modeled similarly and combined with the retina models [11]. This has been called bionic eye.

Many of these models are neuromorphic. This means that there is a one-to-one correspondence between the neuroanatomy and the CNN structure. Moreover, the CNN template reflects the interconnection pattern of the neurons (called receptive field organizations). Length tuning is such an example. A corresponding input and output picture of the neuromorphic length tuning model is shown in Figure 13.12. Those bars that have lengths smaller than or equal to three pixels are detected.

13.5 Template Library: Analogical CNN Algorithms

During the last few years, after the invention of the cellular neural network paradigm and the CNN universal machine, many new cloning templates have been discovered. In addition, the number of innovative analogical CNN algorithms, combining both analog cloning templates and local as well as global logic, is presently steadily increasing at a rapid rate.

As an illustration, let us choose a couple of cloning templates from the CNN library [1,12]. In each case, a name, a short description of the function, the cloning templates, and a representative input-output image pair are shown. With regard to the inputs, the default case means that the input and initial state are the same. If $\mathbf{B} = 0$, then the input picture is chosen as the initial state.

Name: AVERAGE

Function. Spatial averaging of pixel intensities over the $r = 1$ convolutional window.

$$A = \begin{bmatrix} 0 & 1 & 0 \\ 1 & 2 & 1 \\ 0 & 1 & 0 \end{bmatrix}, \quad B = \begin{bmatrix} 0 & 0 & 0 \\ 0 & 0 & 0 \\ 0 & 0 & 0 \end{bmatrix}, \quad I = 0$$

Example. Input and output picture.

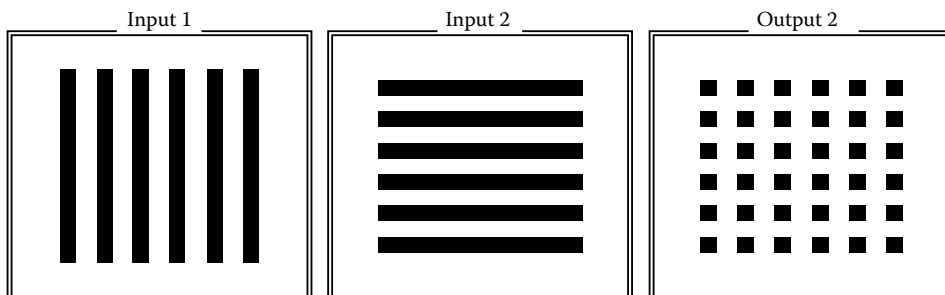


Name: AND

Function. Logical “AND” function of the input and the initial state pictures.

$$A = \begin{bmatrix} 0 & 0 & 0 \\ 0 & 1.5 & 0 \\ 0 & 0 & 0 \end{bmatrix}, \quad B = \begin{bmatrix} 0 & 0 & 0 \\ 0 & 1.5 & 0 \\ 0 & 0 & 0 \end{bmatrix}, \quad I = -1$$

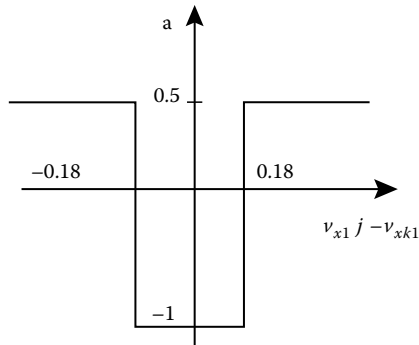
Example. Input, initial state, and output picture.



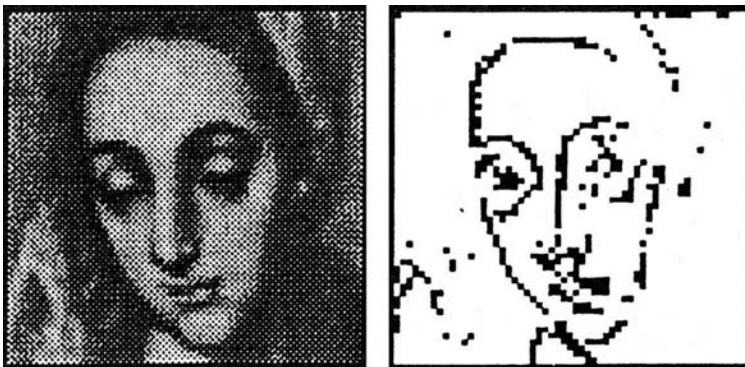
Name: CONTOUR

Function. Grayscale contour detector.

$$A = \begin{bmatrix} 0 & 0 & 0 \\ 0 & 2 & 0 \\ 0 & 0 & 0 \end{bmatrix}, \quad B = \begin{bmatrix} a & a & a \\ a & a & a \\ a & a & a \end{bmatrix}, \quad I = 0.7$$



Example. Input and output picture.

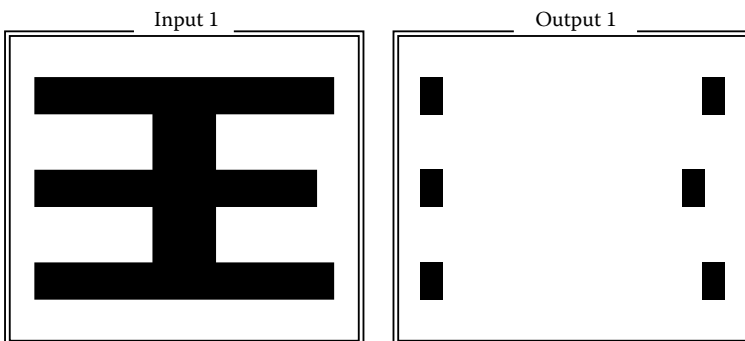


Name: CORNER

Function. Convex corner detector.

$$A = \begin{bmatrix} 0 & 0 & 0 \\ 0 & 2 & 0 \\ 0 & 0 & 0 \end{bmatrix}, \quad B = \begin{bmatrix} -0.25 & -0.25 & -0.25 \\ -0.25 & 2 & -0.25 \\ -0.25 & -0.25 & -0.25 \end{bmatrix}, \quad I = -3$$

Example. Input and output picture.

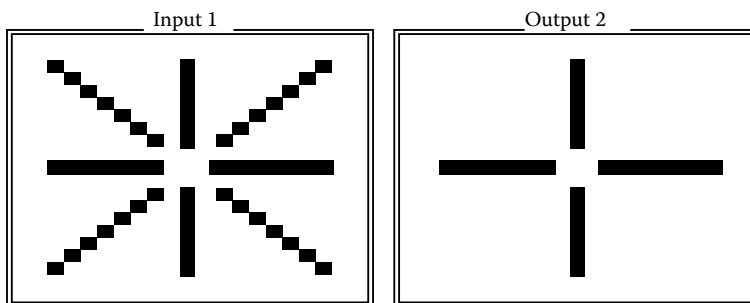


Name: DELDIAG1

Function. Deletes one pixel wide diagonal lines (5).

$$A = \begin{bmatrix} 0 & 0 & 0 \\ 0 & 2 & 0 \\ 0 & 0 & 0 \end{bmatrix}, \quad B = \begin{bmatrix} -0.25 & 0 & -0.25 \\ 0 & 0 & 0 \\ -0.25 & 0 & -0.25 \end{bmatrix}, \quad I = -2$$

Example. Input and output picture.

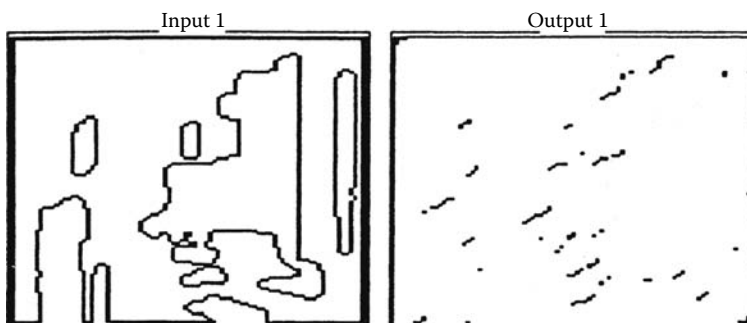


Name: DIAG

Function. Deletes the diagonal lines.

$$A = \begin{bmatrix} 0 & 0 & 0 & 0 & 0 \\ 0 & 0 & 0 & 0 & 0 \\ 0 & 0 & 2 & 0 & 0 \\ 0 & 0 & 0 & 0 & 0 \\ 0 & 0 & 0 & 0 & 0 \end{bmatrix}, \quad B = \begin{bmatrix} -1 & -1 & -0.5 & 0.5 & 1 \\ -1 & -0.5 & 1 & 1 & 0.5 \\ -0.5 & 1 & 5 & 1 & -0.5 \\ 0.5 & 1 & 1 & -0.5 & -1 \\ 1 & 0.5 & -0.5 & -1 & -1 \end{bmatrix}, \quad I = -9$$

Example. Input and output picture.

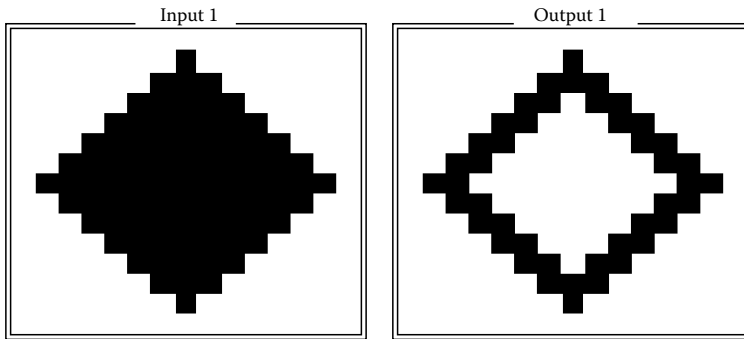


Name: EDGE

Function. Black-and-white edge detector.

$$A = \begin{bmatrix} 0 & 0 & 0 \\ 0 & 2 & 0 \\ 0 & 0 & 0 \end{bmatrix}, \quad B = \begin{bmatrix} -0.25 & -0.25 & -0.25 \\ -0.25 & 2 & -0.25 \\ -0.25 & -0.25 & -0.25 \end{bmatrix}, \quad I = -1.5$$

Example. Input and output picture.



Name: MATCH

Function. Detects 3×3 patterns matching exactly the one prescribed by the template B , namely, having a black/white pixel where the template value is ± 1 , respectively.

$$A = \begin{bmatrix} 0 & 0 & 0 \\ 0 & 1 & 0 \\ 0 & 0 & 0 \end{bmatrix}, \quad B = \begin{bmatrix} v & v & v \\ v & v & v \\ v & v & v \end{bmatrix}, \quad I = -N + 0.5$$

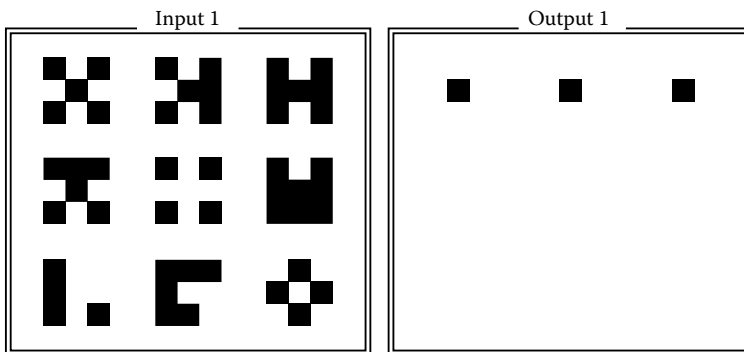
where

- $v = +1$, if corresponding pixel is required to be black
- $v = 0$, if corresponding pixel is don't care
- $v = -1$, if corresponding pixel is required to be white

N = number of pixels required to be either black or white, i.e., the number of nonzero values in the B template

Example. Input and output picture, using the following values:

$$A = \begin{bmatrix} 0 & 0 & 0 \\ 0 & 1 & 0 \\ 0 & 0 & 0 \end{bmatrix}, \quad B = \begin{bmatrix} 1 & -1 & 1 \\ 0 & 1 & 0 \\ 1 & -1 & 1 \end{bmatrix}, \quad I = -6.5$$

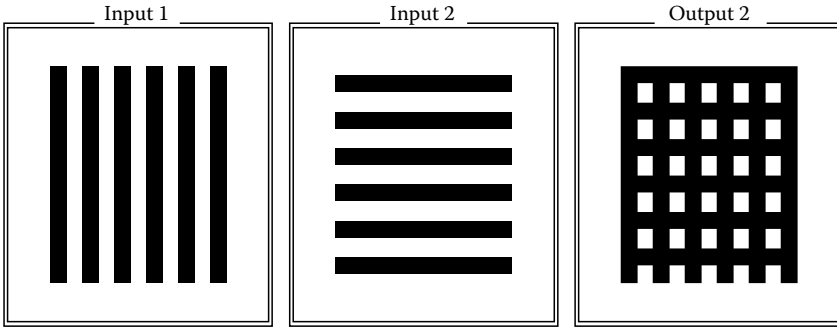


Name: OR

Function. Logical “OR” function of the input and the initial state.

$$A = \begin{bmatrix} 0 & 0 & 0 \\ 0 & 3 & 0 \\ 0 & 0 & 0 \end{bmatrix}, \quad B = \begin{bmatrix} 0 & 0 & 0 \\ 0 & 3 & 0 \\ 0 & 0 & 0 \end{bmatrix}, \quad I = 2$$

Example. Input, initial state, and output picture.

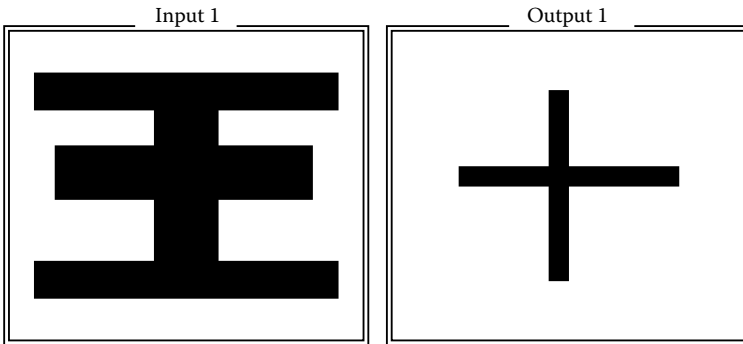


Name: PEELPIX

Function. Peels one pixel from all directions.

$$A = \begin{bmatrix} 0 & 0.4 & 0 \\ 0.4 & 1.4 & 0.4 \\ 0 & 0.4 & 0 \end{bmatrix}, \quad B = \begin{bmatrix} 4.6 & -2.8 & 4.6 \\ -2.8 & 1 & -2.8 \\ 4.6 & -2.8 & 4.6 \end{bmatrix}, \quad I = -7.2$$

Example. Input and output picture.



13.6 Recent Advances

After the first few integrated circuit implementations of the basic CNN circuits, stored programmable analogic CNN universal machine chips have been fabricated. Indeed, a full-fledged version of them [13] is the first visual microprocessor, all the 4096 cell processors of it contain an optical sensor right on the surface of the chip (a focal plane). This implementation represents, at the same time, the most complex operational, stored programmable analog CMOS integrated circuit ever reported, in terms of the number of transistors operating in analog mode (about 1 million). The equivalent digital computing power of this

visual microprocessor is about a few TeraOPS. It processes grayscale input images and has a grayscale output. A 128×128 processor version has recently been fabricated. A binary input/output CNN universal machine chip with 48×48 cell processors has a higher cell density [14], and another circuit design strategy [15] is aiming to implement 5×5 or even higher neighborhood templates.

These chips are the first examples of a new, analogic, topographic (spatial-temporal) computing technology. Its computational infrastructure (high-level language, called Alpha, compiler, operating system, etc.) has also been developed [16], and the industrial applications have been started in a couple of companies worldwide. Moreover, a key application area of this technology is sensor computing [17]. Integrating 2-D topographic sensor arrays with the CNN universal machine on a single chip, providing a direct, dynamic interaction with tuning of the sensors, this is a capability no other technology offers with comparable computational power.

Recently, it has been shown that PDE-based techniques, the most advanced methods for complex image-processing problems, could solve tasks intractable with other methods. Their only drawback is the excessive digital computing power they need. In our cellular computing technology, however, the elementary instruction could be a solution of a PDE. It has been shown that, in addition to the simple diffusion PDE implementation described previously, almost all PDEs can be implemented by CNN [18]. Indeed, active waves [2] have been successfully applied using operational analogic CNN universal machine chips with 4096 cell processors, manifesting at least three orders of magnitude speed advantage compared to fully digital chips of comparable IC technology feature size.

Following the first steps in modeling living sensory modalities, especially vision, motivated especially by a breakthrough in understanding the neurobiological constructs of the mammalian retina [19], new models and a modeling framework [20] have been developed based on CNNs. Their implementation in complex cell CNN universal machines [21] is under construction.

Studies on complexity related to CNN models and implementations have been emerging recently. Following the groundbreaking theoretical studies of Turing on the morphogenesis of CNN-like coupled nonlinear units [22] and a few experimental case studies of the well-publicized “complex systems,” as well as many exotic waves generated by coupled A template CNNs, the root of complexity in pattern formation at the edge of chaos has been discovered [23]. As far as the computational complexity is concerned, the study of a new quality of computational complexity has been explored [24], showing qualitatively different properties compared to the classical digital complexity theory as well as the complexity on reals [25].

To further explore the vast amount of literature on CNN technology and analogic cellular computing, the interested reader could consult the bibliography at the website of the technical committee on Cellular Neural Networks and Array Computing of the IEEE Circuits and Systems Society (<http://www.ieee-cas.org/~cnnactc>), some recent monographs [26–28], and an undergraduate textbook [29].

13.7 Recent Developments and Outlook

During the last few years, CNN technology, as well as its offsprings and generalizations, has generated several significant results and the first few companies have entered into the market. The main events are as follows.

The appearance of the first commercially available, stored programmable, visual microprocessor, the Q-Eye (with 176×144 cell processors and on-chip optical sensors, 10,000 frame per second, and <300 mW), embedded in the self-contained Eye-RIS system, both are from AnaFocus Ltd., Seville (www.anafocus.com). A new version of the Bi-i camera-computer, using emulated digital cellular array architecture, has also been developed, and applied in some mission critical tasks (Eutecus Inc., Berkeley, California, www.eutecus.com).

Several algorithmic and theoretical results as well as application case studies have been published. A new type of algorithmic thinking is emerging that is based on spatial-temporal waves as elementary instructions.

The CNN universal machine, with some extensions and diverse physical implementations became a general computational platform: the cellular wave computer. This has been happening in parallel with a dramatic new trend in microprocessor architecture development, namely the multi- and many core architectures on a single chip. The other side of the story is the cellular supercomputer development.

The essence of this new trend is that processor arrays on a single chip are becoming the next main direction in CMOS technology, when saturating the clock frequency due to the power dissipation constraints. Today, products are already on the market with about 100 processors and the trend is continuing, including the latest FPGAs. Hence, the cellular many-core processor arrays are becoming the major trend in computing in general, and in sensory computing, in particular. Since the wire delay is becoming greater than the gate delay, the communication speed is reduced dramatically far from a given processor. Hence, the mainly (not exclusively) locally connected cellular processor array architectures on a single chip become a physical necessity. Interestingly, the high-end supercomputers are also following this lead (the highest speed Blue Gene of IBM has a 3-D toroidal cellular architecture).

This new development has made the cellular wave computer architecture a must in many applications. As an example, a very efficient PDE implementation was made by using CNN models on an FPGA and on a CELL Multiprocessor (IBM, Sony, Toshiba) developed for a game console, as well.

Interestingly, the circuit hardware implementation issues (now at a 45 nm CMOS technology) are forcing the conversion of the computing architectures. The details can be found in a recent review article [30]. It seems that the cellular wave computer might become a prototype architecture, although the cell processors are of different forms and implementations (digital, analog, mixed mode, optical, etc.), and the spatial-temporal, mainly locally and sparsely globally connected communication framework is necessary. Interestingly, many different sensory organs, uncovered recently by neurobiologists, are following this architecture.

References

1. L. O. Chua and L. Yang, Cellular neural networks: Theory, *IEEE Trans. Circuits Syst.*, 35, 1257–1272, 1988.
2. Cs. Rekeczky and L. O. Chua, Computing with front propagation-active contours and skeleton models in continuous-time CNN, *J. VLSI Signal Process. Syst.*, 23, 373–402, 1999.
3. J. Cruz and L. O. Chua, A CNN chip for connected component detection, *IEEE Trans. Circuits Syst.*, 38, 812–817, 1991.
4. H. Harrer, J. A. Nossek, and R. Stelzl, An analog implementation of discrete-time cellular neural networks, *IEEE Trans. Neural Networks*, 3, 466–476, 1992.
5. R. Dominguez-Castro, S. Espejo, A. Rodriguez-Vazquez, and R. Carmona, A CNN universal chip in CMOS technology, *Proceedings of the IEEE Third International Workshop on CNN and Applications (CNNA-94)*, Rome, Italy, pp. 91–96, 1994.
6. T. Roska and J. Vandewalle, Eds., *Cellular Neural Networks*, Chichester, Wiley, 1993.
7. J. A. Nossek and T. Roska, Eds., Special issues on cellular neural networks, *IEEE Trans. Circuits Syst. I*, 40, Mar. 1993; Special issue on cellular neural networks, *IEEE Trans. Circuits Syst. II*, 40, Mar. 1993.
8. L. O. Chua and L. Yang, Cellular neural networks: Applications, *IEEE Trans. Circuits Syst.*, 35, 1273–1290, 1988.
9. T. Roska and L. O. Chua, The CNN universal machine: An analogic array computer, *IEEE Trans. Circuits Syst. II*, 40, 163–173, 1993.
10. T. Roska, J. Hamori, E. Labos, K. Lotz, K. Takacs, P. Venetianer, Z. Vidnyanszki, and A. Zarandy, The use of CNN models in the subcortical visual pathway, *IEEE Trans. Circuits Syst. I*, 40, 182–195, 1993.
11. F. Werblin, T. Roska, and L. O. Chua, The analogic cellular neural network as a bionic eye, *Int. J. Circuit Theory Appl. (CTA)*, 23(6), 541–569, 1995.

12. CNN Analogic Nonlinear Dynamics (CANDY) Simulator, guide and program (student version), Available at <http://lab.analogic.sztaki.hu>
13. G. Linán, S. Espejo, R. Dominguez-Castro, E. Roca, and A. Rodriguez-Vázquez, CNNUC3: A mixed signal 64×64 CNN Universal Chip, *Proceedings of IEEE MicroNeuro*, Granada, Spain, pp. 61–68, 1999.
14. A. Paasio, A. Davidzuk, K. Halonen, and V. Porra, Minimum-size 0.5 micron CMOS programmable 48×48 test chip, *Proceedings of the European Conference on Circuit Theory and Design ECCTD'97*, Vol. I, Budapest, Hungary, pp. 154–156, 1997.
15. W. C. Yen and C. Y. Wu, The design of neuron-bipolar junction transistor (vBJT) cellular neural network (CNN) structure with multi-neighborhood-layer templates, *Proceedings of 6th IEEE International Workshop on Cellular Neural Networks and Their Applications (CNNA'2000)*, 23–25 May, Catania University, Catania, Italy, pp. 195–200, 2000.
16. T. Roska, Á. Zarándy, S. Zöld, P. Földesy, and P. Szolgay, The computational infrastructure of analogic CNN computing—Part I: The CNN-UM chip prototyping system, *IEEE Trans. Circuits Syst. I: Special issue on bio-inspired processors and cellular neural networks for vision (CAS-I Special Issue)*, 46(2), 261–268, 1999.
17. T. Roska, Computer-sensors: Spatial-temporal computers for analog array signals, dynamically integrated with sensors, *J. VLSI Signal Process. Syst.*, 23, 221–238, 1999.
18. T. Roska, L. O. Chua, D. Wolf, T. Kozek, R. Tetzlaff, and F. Puffer, Simulating nonlinear waves and partial differential equations via CNN, *IEEE Trans. Circuits Syst. I*, 42, 807–815, 1995.
19. B. Roska and F. S. Werblin, Vertical interactions across ten parallel, stacked representations in the mammalian retina, *Nature*, 410, 583–587, Mar. 29, 2001.
20. F. Werblin, B. Roska, D. Bálya, Cs. Rekeczky, and T. Roska, Implementing a retinal visual language in CNN: A neuromorphic case study, *Proceedings of the IEEE ISCAS 2001*, Vol. III, Sydney, pp. 333–336, 2001.
21. Cs. Rekeczky, T. Serrano, T. Roska, and Á. Rodríguez-Vázquez, A stored program 2nd order/3-layer complex cell CNN-UM, *Proceedings of 6th IEEE International Workshop on Cellular Neural Networks and Their Applications (CNNA-2000)*, 23–25 May, Catania University, Catania, Italy, pp. 15–20, 2000.
22. A. M. Turing, The chemical basis of morphogenesis, *Philos. Trans. R. Soc. London*, B237, 37–72, 1952.
23. L. O. Chua, *CNN: A Paradigm for Complexity*, World Scientific, Singapore, 1998.
24. T. Roska, AnaLogic wave computers—wave-type algorithms: Canonical description, computer classes, and computational complexity, *Proceedings of IEEE ISCAS 2001*, Sydney, Australia, Vol. III, pp. 41–44, 2001.
25. L. Blum, F. Cucker, M. Shub, and S. Smale, *Complexity and Real Computation*, Springer, New York, 1998.
26. G. Manganaro, P. Arena, and L. Fortuna, *Cellular Neural Networks—Chaos, Complexity and VLSI Processing*, Springer, Berlin, 1999.
27. M. Hänggi and G. Moschitz, *Cellular Neural Networks—Analysis, Design and Optimization*, Kluwer Academic, Boston, MA, 2000.
28. T. Roska and Á. Rodríguez-Vázquez, Eds., *Towards the Visual Microprocessor—VLSI Design and the Use of Cellular Neural Network Universal Machine*, Wiley, New York, 2001.
29. L. O. Chua and T. Roska, *Cellular Neural Network and Visual Computing—Foundations and Applications*, Cambridge University Press, New York, 2002.
30. T. Roska, Circuits, computers, and beyond Boolean logic, *Int. J. Circuit Theory Appl.*, Sept.–Oct., 2007.
31. Zarándy, A., Werblin, F., Roska, T., Chua, L. O., and Novel type of analogical CNN algorithms for recognizing bank notes, Memorandum UCB/ERL, M94/29 1994, Electronics Research Laboratory, University of California, Berkeley, CA, 1994.
32. L. O. Chua and T. Roska, The CNN paradigm, *IEEE Trans. Circuits Syst. I*, 40, 147–156, 1993.

14

Bifurcation and Chaos

14.1	Introduction to Chaos	14-1
	Electrical and Electronic Circuits as Dynamical Systems • Classification and Uniqueness of Steady-State Behaviors • Stability of Steady-State Trajectories • Horseshoes and Chaos • Structural Stability and Bifurcations	
14.2	Chua's Circuit: A Paradigm for Chaos.....	14-27
	Dynamics of Chua's Circuit • Chaos in Chua's Circuit • Steady-States and Bifurcations in Chua's Circuit • Manifestations of Chaos • Practical Realization of Chua's Circuit • Experimental Steady-State Solutions • Simulation of Chua's Circuit • Dimensionless Coordinates and the α - β Parameter-Space Diagram	
14.3	Chua's Oscillator.....	14-43
	State Equations • Topological Conjugacy • Eigenvalues-to-Parameters Mapping Algorithm for Chua's Oscillator	
14.4	van der Pol Neon Bulb Oscillator.....	14-48
	Winding Numbers • Circle Map • Experimental Observations of Mode-Locking and Chaos in van der Pol's Neon Bulb Circuit • Circuit Model	
14.5	Synchronization of Chaotic Circuits	14-56
	Linear Mutual Coupling • Pecora-Carroll Drive-Response Concept	
14.6	Applications of Chaos	14-64
	Pseudorandom Sequence Generation • Communicating with Chaos	
	References.....	14-71
	Further Information.....	14-72

Michael Peter Kennedy
University College Cork

14.1 Introduction to Chaos

14.1.1 Electrical and Electronic Circuits as Dynamical Systems

A system is something having parts that may be perceived as a single entity. A dynamical system is one that changes with time; what changes is the state of the system. Mathematically, a dynamical system consists of a space of states (called the state space or phase space) and a rule, called the dynamic, for determining which state corresponds at a given future time to a given present state [8]. A deterministic dynamical system is one where the state, at any time, is completely determined by its initial state and dynamic. In this section, we consider only deterministic dynamical systems.

A deterministic dynamical system may have a continuous or discrete state space and a continuous-time or discrete-time dynamic.

A lumped* circuit containing resistive elements (resistors, voltage and current sources) and energy-storage elements (capacitors and inductors) may be modeled as a continuous-time deterministic dynamical system in \mathbb{R}^n . The evolution of the state of the circuit is described by a system of ordinary differential equations (ODEs) called state equations.

Discrete-time deterministic dynamical systems occur in electrical engineering as models of switched-capacitor (SC) and digital filters, sampled phase-locked loops, and sigma-delta modulators. Discrete-time dynamical systems also arise when analyzing the stability of steady-state solutions of continuous-time systems. The evolution of a discrete-time dynamical system is described by a system of *difference equations*.

14.1.1.1 Continuous-Time Dynamical Systems

THEOREM 14.1 (Existence and Uniqueness of Solution for a Differential Equation)

Consider a continuous-time deterministic dynamical system defined by a system of ordinary differential equations of the form

$$\dot{\mathbf{X}}(t) = \mathbf{F}(\mathbf{X}(t), t) \quad (14.1)$$

where $\mathbf{X}(t) \in \mathbb{R}^n$ is called the state, $\dot{\mathbf{X}}(t)$ denotes the derivative of $\mathbf{X}(t)$ with respect to time, $\mathbf{X}(t_0) = \mathbf{X}_0$ is called the initial condition, and the map $\mathbf{F}(\cdot, \cdot): \mathbb{R}^n \times \mathbb{R}_+ \rightarrow \mathbb{R}^n$ is (1) continuous almost everywhere[†] on $\mathbb{R}^n \times \mathbb{R}_+$ and (2) globally Lipschitz[‡] in \mathbf{X} . Then, for each $(\mathbf{X}_0, t_0) \in \mathbb{R}^n \times \mathbb{R}_+$, there exists a continuous function $\phi(\cdot; \mathbf{X}_0, t_0): \mathbb{R}_+ \rightarrow \mathbb{R}^n$ such that

$$\phi(t_0; \mathbf{X}_0, t_0) = \mathbf{X}_0$$

and

$$\dot{\phi}(t; \mathbf{X}_0, t_0) = \mathbf{F}(\phi(t; \mathbf{X}_0, t_0), t) \quad (14.2)$$

Furthermore, this function is unique.

The function $\phi(\cdot; \mathbf{X}_0, t_0)$ is called the solution or trajectory (\mathbf{X}_0, t_0) of the differential Equation 14.1.

The image $\{\phi(t; \mathbf{X}_0, t_0) \in \mathbb{R}^n | t \in \mathbb{R}_+\}$ of the trajectory through (\mathbf{X}_0, t_0) is a continuous curve in \mathbb{R}^n called the orbit through (\mathbf{X}_0, t_0) .

$\mathbf{F}(\cdot, \cdot)$ is called the vector field of Equation 14.1 because its image $\mathbf{F}(\mathbf{X}, t)$ is a vector that defines the direction and speed of the trajectory through \mathbf{X} at time t .

The vector field \mathbf{F} generates the flow ϕ , where $\phi(\cdot; \cdot, \cdot): \mathbb{R}_+ \times \mathbb{R}^n \times \mathbb{R}_+ \rightarrow \mathbb{R}^n$ is a collection of continuous maps $\{\phi(t; \cdot, \cdot): \mathbb{R}^n \times \mathbb{R}_+ \rightarrow \mathbb{R}^n | t \in \mathbb{R}_+\}$.

In particular, a point $\mathbf{X}_0 \in \mathbb{R}^n$ at t_0 is mapped by the flow into $\mathbf{X}(t) = \phi_t(t; \mathbf{X}_0, t_0)$ at time t .

* A lumped circuit is one with physical dimensions that are small compared with the wavelengths of its voltage and current waveforms [2].

† By continuous almost everywhere, we mean the following: let D be a set in \mathbb{R}_+ that contains a countable number of discontinuities and for each $\mathbf{X} \in \mathbb{R}^n$, assume that the function $t \in \mathbb{R}_+ \setminus D \rightarrow \mathbf{F}(\mathbf{X}, t) \in \mathbb{R}^n$ is continuous and for any $\tau \in D$ the left-hand and right-hand limits $\mathbf{F}(\mathbf{X}, \tau)$ and $\mathbf{F}(\mathbf{X}, \tau_+)$, respectively, are finite in \mathbb{R}^n [1]. This condition includes circuits that contain switches and/or squarewave voltage and current sources.

‡ There is a piecewise continuous function $k(\cdot): \mathbb{R}_+ \rightarrow \mathbb{R}_+$ such that $\|\mathbf{F}(\mathbf{X}, t) - \mathbf{F}(\mathbf{X}', t)\| \leq k(t) \|\mathbf{X} - \mathbf{X}'\|$, $\forall t \in \mathbb{R}_+$, $\forall \mathbf{X}, \mathbf{X}' \in \mathbb{R}^n$.

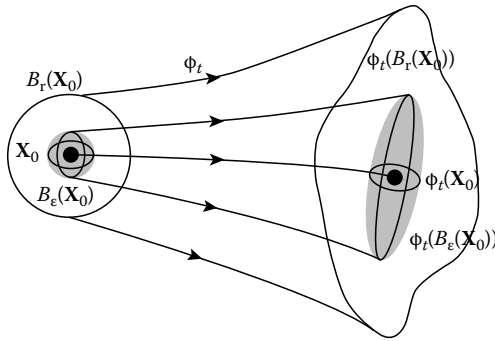


FIGURE 14.1 Vector field F of an autonomous continuous-time dynamical system generates a flow ϕ that maps a point \mathbf{X}_0 in the state space to its image $\phi_t(\mathbf{X}_0)$ t seconds later. A volume of state space $B_r(\mathbf{X}_0)$ evolves under the flow into a region $\phi_t[B_r(\mathbf{X}_0)]$. Sufficiently close to the trajectory $\phi_t(\mathbf{X}_0)$, the linearized flow maps a sphere of radius ε into an ellipsoid.

14.1.1.2 Autonomous Continuous-Time Dynamical Systems

If the vector field of a continuous-time deterministic dynamical system depends only on the state and is *independent* of time t , then the system is said to be *autonomous* and may be written as

$$\dot{\mathbf{X}}(t) = \mathbf{F}[\mathbf{X}(t)]$$

or simply

$$\dot{\mathbf{X}} = \mathbf{F}(\mathbf{X}) \tag{14.3}$$

If, in addition, the vector field $\mathbf{F}(\cdot): \mathbb{R}^n \rightarrow \mathbb{R}^n$ is *Lipschitz*,* then there is a *unique* continuous function $\phi(\cdot, \mathbf{X}_0): \mathbb{R}_+ \rightarrow \mathbb{R}^n$ (called the trajectory through \mathbf{X}_0), which satisfies,

$$\dot{\phi}(t, \mathbf{X}_0) = \mathbf{F}[\phi(t, \mathbf{X}_0)], \quad \phi(t_0, \mathbf{X}_0) = \mathbf{X}_0 \tag{14.4}$$

Because the vector field is independent of time, we choose $t_0 \equiv 0$. For shorthand, we denote the flow by ϕ and the map $\phi(t, \cdot): \mathbb{R}^n \rightarrow \mathbb{R}^n$ by ϕ_t .

The t -advance map ϕ_t takes a state $\mathbf{X}_0 \in \mathbb{R}^n$ to state $\mathbf{X}(t) = \phi_t(\mathbf{X}_0)$ t seconds later. In particular, ϕ_0 is the identity mapping. Furthermore, $\phi_{t+s} = \phi_t \phi_s$, because the state $\mathbf{Y} = \phi_s(\mathbf{X})$ to which \mathbf{X} evolves after time s evolves after an additional time t into the same state \mathbf{Z} as that to which \mathbf{X} evolves after time $t + s$:

$$\mathbf{Z} = \phi_t(\mathbf{Y}) = \phi_t[\phi_s(\mathbf{X})] = \phi_{t+s}(\mathbf{X})$$

A bundle of trajectories emanating from a ball $B_r(\mathbf{X}_0)$ of radius r centered at \mathbf{X}_0 is mapped by the flow into some region $\phi_t[B_r(\mathbf{X}_0)]$ after t seconds (see Figure 14.1). Consider a short segment of the trajectory $\phi_t(\mathbf{X}_0)$ along which the flow is differentiable with respect to \mathbf{X} : in a sufficiently small neighborhood of this trajectory, the flow is almost linear, so the ball $B_\varepsilon(\mathbf{X}_0)$ of radius ε about \mathbf{X}_0 evolves into an ellipsoid $\phi_t[B_\varepsilon(\mathbf{X}_0)]$, as shown.

An important consequence of Lipschitz continuity in an autonomous vector field and the resulting uniqueness of solution of Equation 14.3 is that a trajectory of the dynamical system cannot go through the same point twice in two different directions. In particular, no two trajectories may cross each other; this is called the noncrossing property [18].

14.1.1.3 Nonautonomous Dynamical Systems

A nonautonomous, n -dimensional, continuous-time dynamical system may be transformed to an $(n + 1)$ -dimensional autonomous system by appending time as an additional state variable and writing

$$\begin{aligned} \dot{\mathbf{X}}(t) &= \mathbf{F}[\mathbf{X}(t), X_{n+1}(t)] \\ \dot{X}_{n+1}(t) &= 1 \end{aligned} \tag{14.5}$$

* There exists a finite $k \in \mathbb{R}^n$ such that $\|\mathbf{F}(\mathbf{X}) - \mathbf{F}(\mathbf{X}')\| \leq k \|\mathbf{X} - \mathbf{X}'\|, \forall \mathbf{X}, \mathbf{X}' \in \mathbb{R}^n$.

In the special case where the vector field is periodic with period T , as for example in the case of an oscillator with sinusoidal forcing, the periodically forced system Equation 14.5 is equivalent to the $(n + 1)$ th-order autonomous system

$$\begin{aligned}\dot{\mathbf{X}}(t) &= \mathbf{F}(\mathbf{X}(t), \theta(t)T) \\ \dot{\theta}(t) &= \frac{1}{T}\end{aligned}\tag{14.6}$$

where $\theta(t) = X_{n+1}/T$.

By identifying the n -dimensional hyperplanes corresponding to $\theta = 0$ and $\theta = 1$, the state space may be transformed from $\mathbb{R}^n \times \mathbb{R}_+$ into an equivalent cylindrical state space $\mathbb{R}^n \times S^1$, where S^1 denotes the circle. In the new coordinate system, the solution through (\mathbf{X}_0, t_0) of Equation 14.6 is

$$\begin{pmatrix} \mathbf{X}(t) \\ \theta_{S^1}(t) \end{pmatrix} = \begin{pmatrix} \phi_t(\mathbf{X}_0, t_0) \\ t/T \bmod 1 \end{pmatrix}$$

where $\theta(t) \in \mathbb{R}_+$ is identified with a point on S^1 (which has normalized angular coordinate $\theta_{S^1}(t) \in [0, 1)$) via the transformation $\theta_{S^1}^1(t) = \theta(t) \bmod 1$. Using this technique, periodically forced nonautonomous systems can be treated like autonomous systems.

14.1.1.4 Discrete-Time Dynamical Systems

Consider a discrete-time deterministic dynamical system defined by a system of difference equations of the form

$$\mathbf{X}(k + 1) = \mathbf{G}(\mathbf{X}(k), k)\tag{14.7}$$

where

$\mathbf{X}(k) \in \mathbb{R}^n$ is called the state

$\mathbf{X}(k_0) = \mathbf{X}_0$ is the initial condition

$\mathbf{G}(\cdot, \cdot): \mathbb{R}^n \times \mathbb{Z}_+ \rightarrow \mathbb{R}^n$ maps the current state $\mathbf{X}(k)$ into the next state $\mathbf{X}(k + 1)$, where $k_0 \in \mathbb{Z}_+$

By analogy with the continuous-time case, there exists a function $\phi(\cdot, \mathbf{X}_0, k_0): \mathbb{Z}_+ \rightarrow \mathbb{R}^n$ such that

$$\phi(k_0; \mathbf{X}_0, k_0) = \mathbf{X}_0$$

and

$$\phi(k + 1; \mathbf{X}_0, k_0) = \mathbf{G}(\phi(k; \mathbf{X}_0, k_0), k)$$

The function $\phi(\cdot; \mathbf{X}_0, k_0): \mathbb{Z}_+ \rightarrow \mathbb{R}^n$ is called the solution or trajectory through (\mathbf{X}_0, k_0) of the difference Equation 14.7.

The image $\{\phi(k; \mathbf{X}_0, k_0) \in \mathbb{R}^n \mid k \in \mathbb{Z}_+\}$ in \mathbb{R}^n of the trajectory through (\mathbf{X}_0, k_0) is called an orbit through (\mathbf{X}_0, k_0) .

If the map $\mathbf{G}(\cdot, \cdot)$ of a discrete-time dynamical system depends only on the state $\mathbf{X}(k)$ and is independent of k then the system is said to be autonomous and may be written more simply as

$$\mathbf{X}_{k+1} = \mathbf{G}(\mathbf{X}_k)\tag{14.8}$$

where \mathbf{X}_k is shorthand for $\mathbf{X}(k)$ and the initial iterate k_0 is chosen, without loss of generality, to be zero. Using this notation, \mathbf{X}_k is the image \mathbf{X}_0 after k iterations of the map $\mathbf{G}(\cdot): \mathbb{R}^n \rightarrow \mathbb{R}^n$.

Example: Nonlinear Parallel RLC Circuit

Consider the parallel RLC circuit in Figure 14.2. This circuit contains a linear inductor L , a linear capacitor C_2 , and a nonlinear resistor N'_R , where the continuous piecewise-linear driving-point (DP) characteristic (see Figure 14.3) has slope G'_a for $|V'_R| \leq E$ and slope G'_b for $|V'_R| > E$. The DP characteristic of N'_R may be written explicitly

$$I'_R(V'_R) = G'_b V'_R + \frac{1}{2}(G'_a - G'_b)(|V'_R + E| - |V'_R - E|)$$

This circuit may be described by a pair of ODEs and is therefore a second-order, continuous-time dynamical system. Choosing I_3 and V_2 as state variables, we write

$$\begin{aligned} \frac{dI_3}{dt} &= -\frac{1}{L}V_2 \\ \frac{dV_2}{dt} &= \frac{1}{C_2}I_3 - \frac{1}{C_2}I'_R(V_2) \end{aligned}$$

with $I_3(0) = I_{3_0}$ and $V_2(0) = V_{2_0}$.

We illustrate the vector field by drawing vectors at uniformly spaced points in the two-dimensional state space defined by (I_3, V_2) . Starting from a given initial condition (I_{3_0}, V_{2_0}) , a solution curve in state space is the locus of points plotted out by the state as it moves through the vector field, following the direction of the arrow at every point. Figure 14.4 illustrates typical vector fields and trajectories of the circuit.

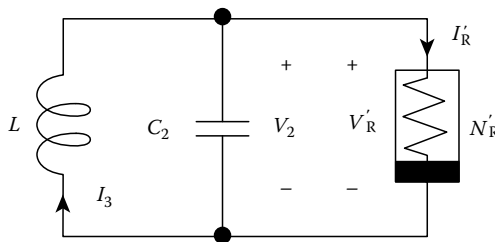


FIGURE 14.2 Parallel RLC circuit where the nonlinear resistor N'_R has a DP characteristic as illustrated in Figure 14.3. By Kirchhoff's voltage law, $V'_R = V_2$.

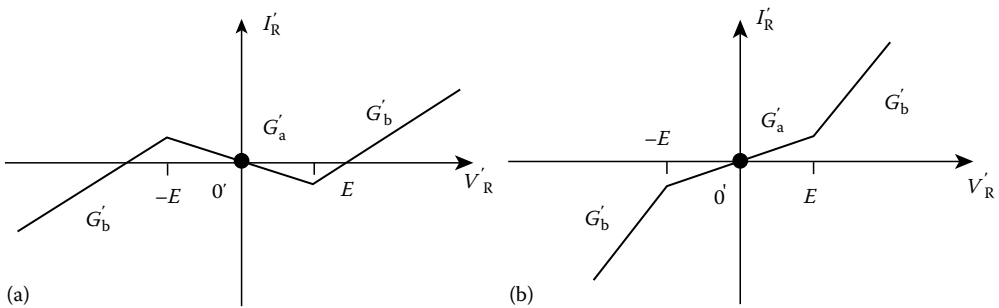


FIGURE 14.3 DP characteristic of N'_R in Figure 14.2 when (a) $G'_a < 0$ and (b) $G'_a > 0$.

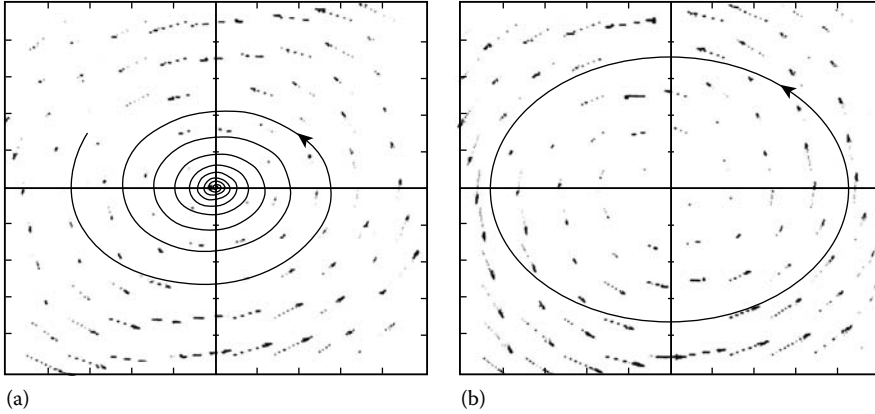


FIGURE 14.4 Vector fields for the nonlinear RLC circuit in Figure 14.2. $L = 18$ mH, $C_2 = 100$ nF, $E = 0.47$ V. (a) $G'_a = 242.424 \mu\text{S}$, $G'_b = 1045.455 \mu\text{S}$: all trajectories converge to the origin. (b) $G'_a = -257.576 \mu\text{S}$, $G'_b = 545.455 \mu\text{S}$: the unique steady-state solution is a limit cycle. Horizontal axis: I_3 , 400 $\mu\text{A}/\text{div}$; vertical axis: V_2 , 200 mV/div. (From Kennedy, M. P., *IEEE Trans. Circuits Syst. I Fundam. Theory Appl.*, 40, 647, Oct. 1993. With permission.)

If L , C_2 , and G'_b are positive, the steady-state behavior of the circuit depends on the sign of G'_a . When $G'_a > 0$, the circuit is dissipative everywhere and all trajectories collapse toward the origin. The unique steady-state solution of the circuit is the stable dc equilibrium condition $I_3 = V_2 = 0$.

If $G'_a > 0$, N'_r looks like a negative resistor close to the origin and injects energy into the circuit, pushing trajectories away. Further out, where the characteristic has positive slope, trajectories are pulled in by the dissipative vector field. The resulting balance of forces produces a steady-state orbit called a *limit cycle*, which is approached asymptotically by all initial conditions of this circuit.

This limit cycle is said to be *attracting* because nearby trajectories move toward it and it is structurally stable in the sense that, for almost all values of G'_a , a small change in the parameters of the circuit has little effect on it. In the special case when $G'_a \equiv 0$, a perturbation of G'_a causes the steady-state behavior to change from an equilibrium point to a limit cycle; this is called a *bifurcation*.

In the following sections, we consider in detail steady-state behaviors, stability, structural stability, and bifurcations.

14.1.2 Classification and Uniqueness of Steady-State Behaviors

A trajectory of a dynamical system from an initial state \mathbf{X}_0 settles, possibly after some transient, onto a set of points called a *limit set*. The ω -limit set corresponds to the asymptotic behavior of the system as $t \rightarrow +\infty$ and is called the steady-state response. We use the idea of recurrent states to determine when the system has reached steady state.

A state \mathbf{X} of a dynamical system is called recurrent under the flow ϕ if, for every neighborhood $B_\epsilon(\mathbf{X})$ of \mathbf{X} and for every $T > 0$, there is a time $t > T$ such that $\phi_t(\mathbf{X}) \cap B_\epsilon(\mathbf{X}) \neq \emptyset$. Thus, a state \mathbf{X} is recurrent if, by waiting long enough, the trajectory through \mathbf{X} repeatedly returns arbitrarily close to \mathbf{X} [7].

Wandering points correspond to transient behavior, while steady-state or asymptotic behavior corresponds to orbits of recurrent states.

A point \mathbf{X}_ω is an ω -limit point of \mathbf{X}_0 if and only if $\lim_{k \rightarrow +\infty} \phi_{t_k}(\mathbf{X}_0) = (\mathbf{X}_\omega)$ for some sequence $\{t_k | k \in \mathbb{Z}_+\}$ such that $t_k \rightarrow +\infty$. The set $L(\mathbf{X}_0)$ of ω -limit points of \mathbf{X}_0 is called ω -limit set of \mathbf{X}_0 .*

A limit set L is called attracting if there exists a neighborhood U of L such that $L(\mathbf{X})_0 = L$ for all $\mathbf{X}_0 \in U$. Thus, nearby trajectories converge toward an attracting limit set as $t \rightarrow \infty$.

* The set of points to which trajectories converge from \mathbf{X}_0 as $t \rightarrow -\infty$ is called the α -limit set of \mathbf{X}_0 . We consider only positive time, therefore, by *limit set*, we mean the ω -limit set.

An attracting set \mathcal{A} that contains at least one orbit that comes arbitrarily close to every point in \mathcal{A} is called an attractor [7].

In an asymptotically stable linear system the limit set is independent of the initial condition and unique so it makes sense to talk of the steady-state behavior. By contrast, a nonlinear system may possess several different limit sets and therefore may exhibit a variety of steady-state behaviors, depending on the initial condition.

The set of all points in the state space that converge to a particular limit set L is called the basin of attraction of L .

Because nonattracting limit sets cannot be observed in physical systems, the asymptotic or steady-state behavior of a real electronic circuit corresponds to motion on an attracting limit set.

14.1.2.1 Equilibrium Point

The simplest steady-state behavior of a dynamical system is an equilibrium point. An equilibrium point or stationary point of Equation 14.3 is a state \mathbf{X}_Q at which the vector field is zero. Thus, $\mathbf{F}(\mathbf{X}_Q) = \mathbf{0}$ and $\phi_t(\mathbf{X}_Q) = \mathbf{X}_Q$; a trajectory starting from an equilibrium point remains indefinitely at that point.

In state space, the limit set consists of a single nonwandering point \mathbf{X}_Q . A point is a zero-dimensional object. Thus, an equilibrium point is said to have dimension zero.

In the time domain, an equilibrium point of an equilibrium circuit is simply a dc solution or operating point.

An equilibrium point or fixed point of a discrete-time dynamical system is a point \mathbf{X}_Q that satisfies

$$\mathbf{G}(\mathbf{X}_Q) = \mathbf{X}_Q$$

Example: Nonlinear Parallel RLC Circuit

The nonlinear RLC circuit shown in Figure 14.2 has just one equilibrium point $(I_{3Q}, V_{2Q}) = (0, 0)$. When G'_a is positive, a trajectory originating at any point in the state converges to this attracting dc steady-state (as shown in Figure 14.4a). The basin of attraction of the origin is the entire state space.

All trajectories, and not just those that start close to it, converge to the origin, so this equilibrium point is said to be a global attractor.

When $G'_a < 0$, the circuit possesses two steady-state solutions: the equilibrium point at the origin, and the limit cycle Γ . The equilibrium point is unstable in this case. All trajectories, except that which starts at the origin, are attracted to Γ .

14.1.2.2 Periodic Steady-State

A state \mathbf{X} is called periodic if there exists $T > 0$ such that $\phi_T(\mathbf{X}) = \mathbf{X}$. A periodic orbit which is not a stationary point is called a cycle.

A limit cycle Γ is an isolated periodic orbit of a dynamical system (see Figure 14.5b). The limit cycle trajectory visits every point on the simple closed curve Γ with period T . Indeed, $\phi_t(\mathbf{X}) = \phi_{t+T}(\mathbf{X}) \forall \mathbf{X} \in \Gamma$. Thus, every point on the limit cycle Γ is a nonwandering point.

A limit cycle is said to have dimension one because a small piece of it looks like a one-dimensional object: a line. Then, n components $X_i(t)$ of a limit cycle trajectory $\mathbf{X}(t) = [X_1(t), X_2(t), \dots, X_n(t)]^T$ in \mathbb{R}^n are periodic time waveforms with period T .

Every periodic signal $X(t)$ may be decomposed into a Fourier series—a weighted sum of sinusoids at integer multiples of a fundamental frequency. Thus, a periodic signal appears in the frequency domain as a set of spikes at integer multiples (harmonics) of the fundamental frequency. The amplitudes of these spikes correspond to the coefficient in the Fourier series expansion of $X(t)$. The Fourier transform is an extension of these ideas to aperiodic signals; one considers the distribution of the signal's power over a continuum of frequencies rather than on a discrete set of harmonics.

The distribution of power in a signal $X(t)$ is most commonly quantified by means of the power density spectrum, often simply called the power spectrum. The simplest estimator of the power spectrum is the periodogram [17] which, given N uniformly spaced samples $X(k/f_s)$, $k = 0, 1, \dots, N - 1$ of $X(t)$, yields $N/2 + 1$ numbers $P(nf_s/N)$, $n = 0, 1, \dots, N/2$, where f_s is the sampling frequency.

If one considers the signal $X(t)$ as being composed of sinusoidal components at discrete frequencies, then $P(nf_s/N)$ is an estimate of the power in the component at frequency nf_s/N . By Parseval's theorem, the sum of the power in each of these components equals the mean-squared amplitude of the N samples of $X(t)$ [17].

If $X(t)$ is periodic with period T , then its power will be concentrated in a dc component, a fundamental frequency component $1/T$, and harmonics. In practice, the discrete nature of the sampling process causes power to "leak" between adjacent frequency components; this leakage may be reduced by "windowing" the measured data before calculating the periodogram [17].

Example: Periodic Steady-State Solution

Figure 14.5b depicts a state-space orbit, time waveform, and power spectrum of a periodic steady-state solution of a third-order, autonomous, continuous-time dynamical system.

The orbit in state space is an asymmetric closed curve consisting of four loops. In the time domain, the waveform has four crests per period and a dc offset. In the power spectrum, the dc offset manifests itself as a spike at zero frequency. The period of approximately 270 Hz produces a fundamental component at that frequency. Notice that the fourth harmonic (arising from "four crests per period") has the largest magnitude. This power spectrum is reminiscent of subharmonic mode locking in a forced oscillator.

14.1.2.3 Subharmonic Periodic Steady-State

A subharmonic periodic solution or period- K orbit of a discrete-time dynamical system is a set of K points $\{\mathbf{X}_1, \mathbf{X}_2, \dots, \mathbf{X}_K\}$ that satisfy

$$\mathbf{X}_2 = \mathbf{G}(\mathbf{X}_1), \quad \mathbf{X}_3 = \mathbf{G}(\mathbf{X}_2) \cdots \mathbf{X}_K = \mathbf{G}(\mathbf{X}_{K-1}), \quad \mathbf{X}_1 = \mathbf{G}(\mathbf{X}_K)$$

More succinctly, we may write $\mathbf{X}_i = \mathbf{G}^{(K)}(\mathbf{X}_i)$, where $\mathbf{G}^{(K)} = \mathbf{G}[\mathbf{G}(\cdots[\mathbf{G}(\cdot)]\cdots)]$ denotes \mathbf{G} applied K times to the argument of the map; this is called the K th iterate of \mathbf{G} .

Subharmonic periodic solutions occur in systems that contain two or more competing frequencies, such as forced oscillators or sampled-data circuits. Subharmonic solutions also arise following period-doubling bifurcations (see Section 14.1.5).

14.1.2.4 Quasiperiodic Steady-State

The next most complicated form of steady-state behavior is called quasiperiodicity. In state space, this corresponds to a *torus* (see Figure 14.5a). Although a small piece of a limit cycle in \mathbb{R}^3 looks like a line, a small section of two-torus looks like a plane; a two-torus has dimension two.

A quasiperiodic function is one that may be expressed as a countable sum of periodic functions with incommensurate frequencies, i.e., frequencies that are not rationally related. For example, $X(t) = \sin(t) + \sin(2\pi t)$ is a quasiperiodic signal. In the time domain, a quasiperiodic signal may look like an amplitude-or phase-modulated waveform.

Although the Fourier spectrum of a periodic signal consists of a discrete set of spikes at integer multiples of a fundamental frequency, that of a quasiperiodic solution comprises a discrete set of spikes at incommensurate frequencies, as presented in Figure 14.5a.

In principle, a quasiperiodic signal may be distinguished from a periodic one by determining whether the frequency spikes in the Fourier spectrum are harmonically related. In practice, it is impossible to

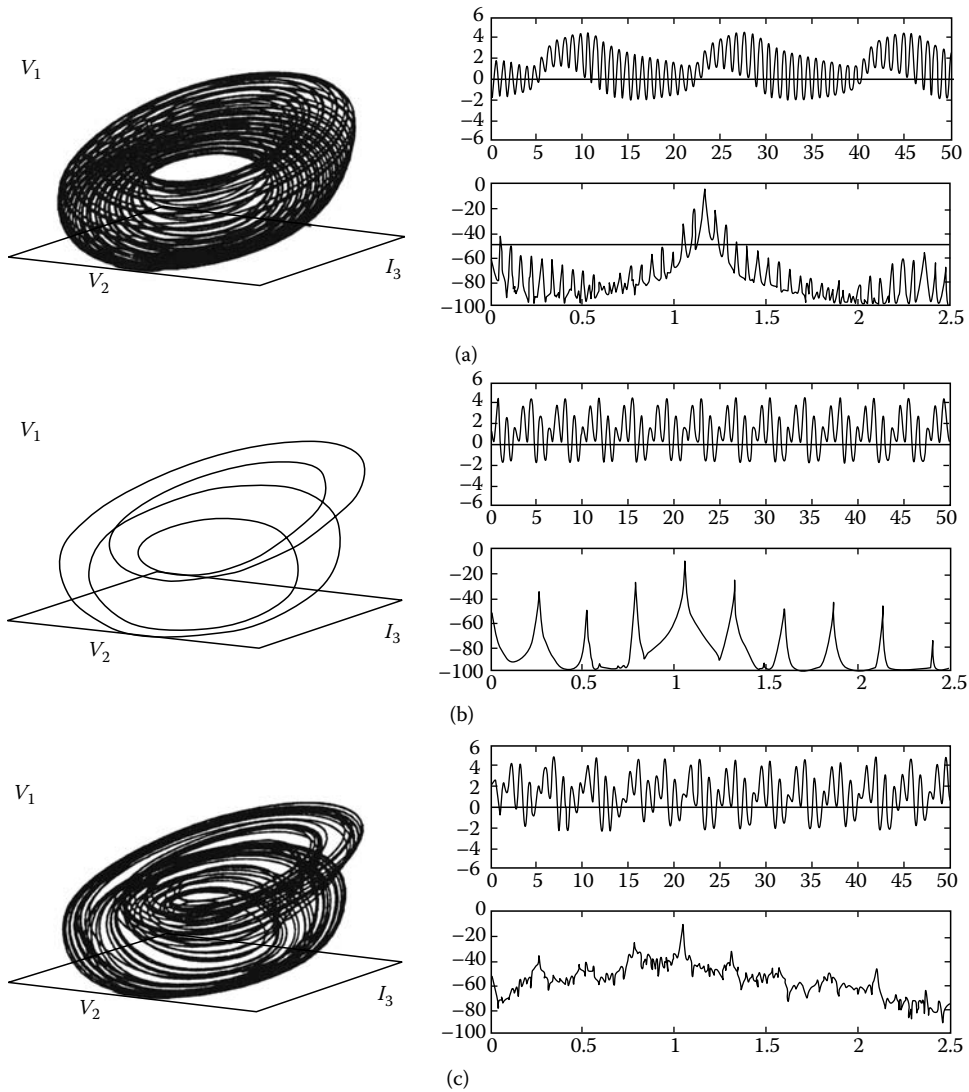


FIGURE 14.5 Quasiperiodicity (torus breakdown) route to chaos in Chua's oscillator. Simulated state-space trajectories, time waveforms $V_1(t)$, and power spectra of $V_2(t)$. (a) Quasiperiodic steady-state—the signal is characterized by a discrete power spectrum with incommensurate frequency components; (b) periodic window—all spikes in the power spectrum are harmonically related to the fundamental frequency; (c) chaotic steady-state following breakdown of the torus—the waveform has a broadband power spectrum. Time plots; horizontal axis— t (ms); vertical axis— V_1 (V). Power spectra: horizontal axis—frequency (kHz); vertical axis—power (mean-squared amplitude) of $V_2(t)$ (dB).

determine whether a measured number is rational or irrational; therefore, any spectrum that appears to be quasiperiodic may simply be periodic with an extremely long period.

A two-torus in a three-dimensional state space looks like a doughnut. Quasiperiodic behavior on a higher dimensional torus is more difficult to visualize in state space but appears in the power spectrum as a set of discrete components at incommensurate frequencies. A K -torus has dimension K .

Quasiperiodic behavior occurs in discrete-time systems where two incommensurate frequencies are present. A periodically forced or discrete-time dynamical system has a frequency associated with

the period of the forcing or sampling interval of the system; if a second frequency is introduced that is not rationally related to the period of the forcing or the sampling interval, then quasiperiodicity may occur.

Example: Discrete Torus

Consider a map from the circle S^1 onto itself. In polar coordinates, a point on the circle is parameterized by an angle θ . Assume that θ has been normalized so that one complete revolution of the circle corresponds to a change in θ of 1. The state of this system is determined by the normalized angle θ and the dynamics by

$$\theta_{k+1} = (\theta_k + \Omega) \bmod 1$$

If Ω is a rational number (of the form J/K where $J, K \in \mathbb{Z}_+$), then the steady-state solution is a period- K (subharmonic) orbit. If Ω is irrational, we obtain quasiperiodic behavior.

14.1.2.5 Chaotic Steady-State

DC equilibrium periodic as well as quasiperiodic steady-state behaviors have been correctly identified and classified since the pioneering days of electronics in the 1920s. By contrast, the existence of more exotic steady-state behaviors in electronic circuits has been acknowledged only in the past 30 years. Although the notion of chaotic behavior in dynamical systems has existed in the mathematics literature since the turn of the century, unusual behaviors in the physical sciences as recently as the 1960s were described as “strange.” Today, we classify as *chaos* the recurrent* motion in a deterministic dynamical system, which is characterized by a positive Lyapunov exponent (LE).

From an experimentalist’s point of view, chaos may be defined as bounded steady-state behavior in a deterministic dynamical system that is not an equilibrium point, nor periodic, and not quasiperiodic [15].

Chaos is characterized by repeated stretching and folding of bundles of trajectories in state space. Two trajectories started from almost identical initial conditions diverge and soon become uncorrelated; this is called sensitive dependence on initial conditions and gives rise to long-term unpredictability.

In the time domain, a chaotic trajectory is neither periodic nor quasiperiodic, but looks “random.” This “randomness” manifests itself in the frequency domain as a broad “noise-like” Fourier spectrum, as presented in Figure 14.5c.

Although an equilibrium point, a limit cycle, and a K -torus each have integer dimension, the repeated stretching and folding of trajectories in a chaotic steady-state gives the limit set a more complicated structure that, for three-dimensional continuous-time circuits, is something more than a surface but not quite a volume.

14.1.2.6 Dimension

The structure of a limit set $L \subset \mathbb{R}^n$ of a dynamical system may be quantified using a generalized notion of dimension that considers not just the geometrical structure of the set, but also the time evolution of trajectories on L .

Capacity (D_0 Dimension)

The simplest notion of dimension, called capacity (or D_0 dimension), considers a limit set simply as set of points, without reference to the dynamical system that produced it.

* Because a chaotic steady-state does not settle down onto a single well-defined trajectory, the definition of recurrent states must be used to identify posttransient behavior.

To estimate the capacity of L , cover the set with n -dimensional cubes having side length ϵ . If L is a D_0 -dimensional object, then the minimum number $N(\epsilon)$ of cubes required to cover L is proportional to ϵ^{-D_0} . Thus, $N(\epsilon) \propto \epsilon^{-D_0}$.

The D_0 dimension is given by

$$D_0 = \lim_{\epsilon \rightarrow 0} - \frac{\ln N(\epsilon)}{\ln \epsilon}$$

When this definition is applied to a point, a limit cycle (or line), or a two-torus (or surface) \mathbb{R}^3 , the calculated dimensions are 0, 1, and 2, respectively, as expected. When applied to the set of nonwandering points that comprise a chaotic steady-state, the D_0 dimension is typically noninteger. An object that has noninteger dimension is called a fractal.

Example: The Middle-Third Cantor Set

Consider the set of points that is obtained by repeatedly deleting the middle third of an interval, as indicated in Figure 14.6a. At the first iteration, the unit interval is divided into 2^1 pieces of length $1/3$ each; after k iterations, the set is covered by 2^k pieces of length $1/3^k$. By contrast, the set that is obtained by dividing the intervals into thirds but not throwing away the middle third each time (Figure 14.6b) is covered at the k th step by 3^k pieces of length $1/3^k$.

Applying the definition of capacity, the dimension of the unit interval is

$$\lim_{k \rightarrow \infty} \frac{k \ln 3}{k \ln 3} = 1.00$$

By contrast, the middle-third Cantor set has dimension

$$\lim_{k \rightarrow \infty} \frac{k \ln 2}{k \ln 3} \approx 0.63$$

The set is something more than a zero-dimensional object (a point) but not quite one-dimensional (like a line segment); it is a fractal.

Correlation (D_2) Dimension

The D_2 dimension considers not just the geometry of a limit set, but also the time evolution of trajectories on the set.

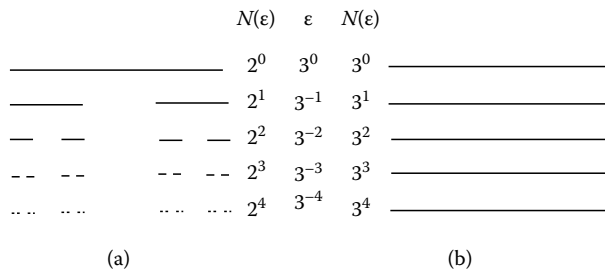


FIGURE 14.6 (a) The Middle-third Cantor set is obtained by recursively removing the central portion of an interval. At the k th step, the set consists of $N(\epsilon) = 2^k$ pieces of length $\epsilon = 3^{-k}$. The limit set has capacity 0.63. (b) By contrast, the unit interval is covered by 3^k pieces of length 3^{-k} . The unit interval has dimension 1.00.

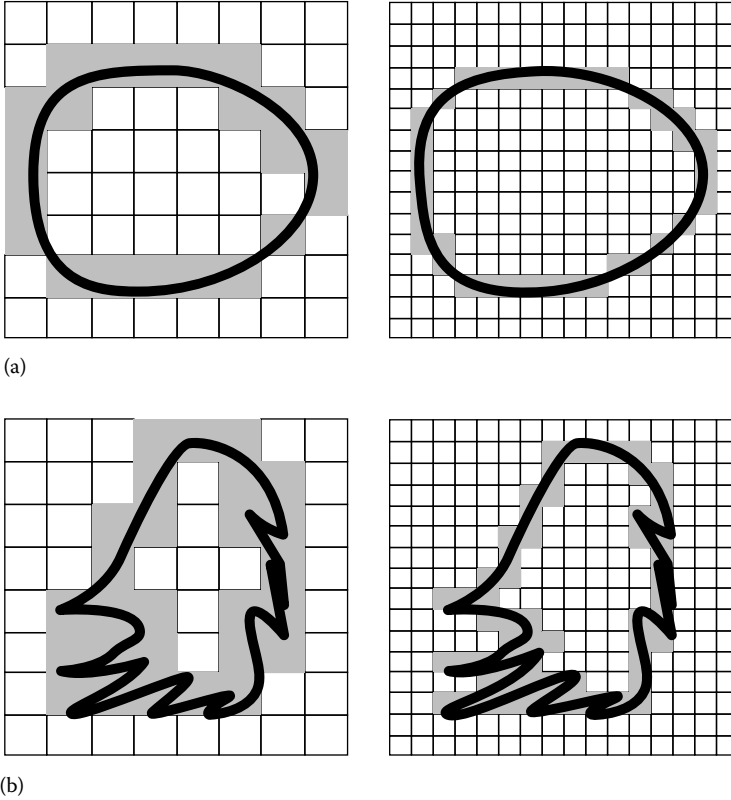


FIGURE 14.7 Coverings of two limit sets L_a (a) and L_b (b) with squares of side length ϵ_0 and $\epsilon_0/2$, respectively.

Consider the two limit sets L_a and L_b in \mathbb{R}^2 shown in Figure 14.7a and b, respectively. The D_0 dimension of these sets may be determined by iteratively covering them with squares (two-dimensional “cubes”) of side length $\epsilon = \epsilon_0/2^k, k = 0, 1, 2, \dots$, counting the required number of squares $N(\epsilon)$ for each ϵ , and evaluating the limit

$$D_0 = \lim_{k \rightarrow \infty} - \frac{\ln N(\epsilon)}{\ln(\epsilon)}$$

For the smooth curve L_a , the number of squares required to cover the set grows linearly with $1/\epsilon$; hence $D_0 = 1.0$. By contrast, if the kinks and folds in set L_b are present at all scales, then the growth of $N(\epsilon)$ versus $1/\epsilon$ is superlinear and the object has a noninteger D_0 dimension between 1.0 and 2.0.

Imagine now that L_a and L_b are not simply static geometrical objects but are orbits of discrete-time dynamical systems. In this case, a steady-state trajectory corresponds to a sequence of points moving around the limit set.

Cover the limit set with the minimum number $N(\epsilon)$ of “cubes” with side length ϵ , and label the boxes $1, 2, \dots, i, \dots, N(\epsilon)$. Count the number of times $n_i(N, \epsilon)$ that a typical steady-state trajectory of length N visits box i and define

$$p_i = \lim_{N \rightarrow \infty} \frac{n_i(N, \epsilon)}{N}$$

where p_i is the relative frequency with which a trajectory visits the i th cube. The D_2 dimension is defined as

$$D_2 = \lim_{\epsilon \rightarrow 0} \frac{\ln \sum_{i=1}^{N(\epsilon)} p_i^2}{\ln \epsilon}$$

In general, $D_2 \leq D_0$ with equality when a typical trajectory visits all $N(\epsilon)$ cubes with the same relative frequency $p = 1/N(\epsilon)$. In this special case,

$$\begin{aligned} D_2 &= \lim_{\epsilon \rightarrow 0} \frac{\ln \sum_{i=1}^{N(\epsilon)} \frac{1}{N(\epsilon)^2}}{\ln \epsilon} \\ &= \lim_{\epsilon \rightarrow 0} -\frac{\ln N(\epsilon)}{\ln \epsilon} \\ &= D_0 \end{aligned}$$

An efficient algorithm (developed by Grassberger and Procaccia) for estimating D_2 is based on the approximation $\sum_{i=1}^{N(\epsilon)} p_i^2 \approx C(\epsilon)$ [15], where $C(\epsilon) = \lim_{N \rightarrow 0} \frac{1}{N^2}$ (the number of pairs of points (X_i, X_j) such that $\|X_i - X_j\| < \epsilon$) is called the correlation. The D_2 or correlation dimension is given by

$$D_2 = \lim_{\epsilon \rightarrow 0} \frac{\ln C(\epsilon)}{\ln \epsilon}$$

Example: Correlation (D_2) Dimension

The correlation dimension of the chaotic attractor in Figure 14.5c, estimated using INSITE, is 2.1, while D_2 for the uniformly covered torus in Figure 14.5a is 2.0.

14.1.3 Stability of Steady-State Trajectories

Consider once more the nonlinear RLC circuit in Figure 14.2. If G'_a is negative, this circuit settles to a periodic steady-state from almost every initial condition. However, a trajectory started from the origin will, in principle, remain indefinitely at the origin since this is an equilibrium point. The circuit has two possible steady-state solutions. Experimentally, only the limit cycle will be observed. Why?

If trajectories starting from states close to a limit set converge to that steady state, the limit set is called an attracting limit set. If, in addition, the attracting limit set contains at least one trajectory that comes arbitrarily close to every point in the set, then it is an attractor. If nearby points diverge from the limit set, it is called a repellor.

In the nonlinear RLC circuit with $G'_a < 0$, the equilibrium point is a repellor and the limit cycle is an attractor.

14.1.3.1 Stability of Equilibrium Points

Qualitatively, an equilibrium point is said to be stable if trajectories starting close to it remain nearby for all future time and unstable otherwise. Stability is a local concept, dealing with trajectories in a small neighborhood of the equilibrium point.

To analyze the behavior of the vector field in the vicinity of an equilibrium point \mathbf{X}_Q , we write $\mathbf{X} = \mathbf{X}_Q + \mathbf{x}$ and substitute into Equation 14.3 to obtain

$$\begin{aligned}\dot{\mathbf{X}}_Q + \dot{\mathbf{x}} &= \mathbf{F}(\mathbf{X}_Q + \mathbf{x}) \\ \mathbf{F}(\mathbf{X}_Q) + \dot{\mathbf{x}} &\approx \mathbf{F}(\mathbf{X}_Q) + \mathbf{D}_x\mathbf{F}(\mathbf{X}_Q)\mathbf{x}\end{aligned}\quad (14.9)$$

where we have kept just the first two terms of the Taylor series expansion of $\mathbf{F}(\mathbf{X})$ about \mathbf{X}_Q . The Jacobian matrix $\mathbf{D}_x\mathbf{F}(\mathbf{X})$ is the matrix of partial derivatives of $\mathbf{F}(\mathbf{X})$ with respect to \mathbf{X} :

$$\mathbf{D}_x\mathbf{F}(\mathbf{X}) = \begin{bmatrix} \frac{\partial F_1(\mathbf{X})}{\partial X_1} & \frac{\partial F_1(\mathbf{X})}{\partial X_2} & \cdots & \frac{\partial F_1(\mathbf{X})}{\partial X_n} \\ \frac{\partial F_2(\mathbf{X})}{\partial X_1} & \frac{\partial F_2(\mathbf{X})}{\partial X_2} & \cdots & \frac{\partial F_2(\mathbf{X})}{\partial X_n} \\ \vdots & \vdots & \ddots & \vdots \\ \frac{\partial F_n(\mathbf{X})}{\partial X_1} & \frac{\partial F_n(\mathbf{X})}{\partial X_2} & \cdots & \frac{\partial F_n(\mathbf{X})}{\partial X_n} \end{bmatrix}$$

Subtracting $\mathbf{F}(\mathbf{X}_Q)$ from both sides of Equation 14.9 we obtain the linear system

$$\dot{\mathbf{x}} = \mathbf{D}_x\mathbf{F}(\mathbf{X}_Q)\mathbf{x}$$

where the Jacobian matrix is evaluated at \mathbf{X}_Q . This linearization describes the behavior of the circuit in the vicinity of \mathbf{X}_Q ; we call this the local behavior.

Note that the linearization is simply the small-signal equivalent circuit at the operating point \mathbf{X}_Q . In general, the local behavior of a circuit depends explicitly on the operating point \mathbf{X}_Q . For example, a pn -junction diode exhibits a small incremental resistance under forward bias, but a large small-signal resistance under reverse bias.

14.1.3.2 Eigenvalues

If \mathbf{X}_Q is an equilibrium point of Equation 14.3, a complete description of its stability is contained in the eigenvalues of the linearization of Equation 14.3 about \mathbf{X}_Q . These are defined as the roots λ of the characteristic equation

$$\det[\lambda\mathbf{I} - \mathbf{D}_x\mathbf{F}(\mathbf{X}_Q)] = 0 \quad (14.10)$$

where \mathbf{I} is the identity matrix.

If the real parts of all of the eigenvalues $\mathbf{D}_x\mathbf{F}(\mathbf{X}_Q)$ are strictly negative, then the equilibrium point \mathbf{X}_Q is asymptotically stable and is called a sink because all nearby trajectories converge toward it.

If any of the eigenvalues has a positive real part, the equilibrium point is unstable; if all of the eigenvalues have positive real parts, the equilibrium point is called a source. An equilibrium point that has eigenvalues with both negative and positive real parts is called a saddle. A saddle is unstable.

An equilibrium point is said to be hyperbolic if all the eigenvalues of $\mathbf{D}_x\mathbf{F}(\mathbf{X}_Q)$ have nonzero real parts. All hyperbolic equilibrium points are either unstable or asymptotically stable.

14.1.3.3 Discrete-Time Systems

The stability of a fixed point \mathbf{X}_Q of a discrete-time dynamical system

$$\mathbf{X}_{k+1} = \mathbf{G}(\mathbf{X}_k)$$

is determined by the eigenvalues of the linearization $\mathbf{D}_x\mathbf{G}(\mathbf{X}_Q)$ of the vector field \mathbf{G} , evaluated at \mathbf{X}_Q .

The equilibrium point is classified as stable if all of the eigenvalues of $\mathbf{D}_x\mathbf{G}(\mathbf{X}_Q)$ are strictly less than unity in modulus, and unstable if any has modulus greater than unity.

14.1.3.4 Eigenvectors, Eigenspaces, Stable and Unstable Manifolds

Associated with each distinct eigenvalue λ of the Jacobian matrix $D_{\mathbf{x}}\mathbf{F}(\mathbf{X}_{\mathbf{Q}})$ is an eigenvector \vec{v} defined by

$$D_{\mathbf{x}}\mathbf{F}(\mathbf{X}_{\mathbf{Q}})\vec{v} = \lambda\vec{v}$$

A real eigenvalue γ has a real eigenvector $\vec{\eta}$. Complex eigenvalues of a real matrix occur in pairs of the form $\sigma \pm j\omega$. The real and imaginary parts of the associated eigenvectors $\vec{\eta}_r \pm j\vec{\eta}_c$ span a plane called a complex eigenplane.

The n_s -dimensional subspace of \mathbb{R}^n associated with the stable eigenvalues of the Jacobian matrix is called the stable eigenspace, denoted $E^s(\mathbf{X}_{\mathbf{Q}})$. The n_u -dimensional subspace corresponding to the unstable eigenvalues is called the unstable eigenspace, denoted $E^u(\mathbf{X}_{\mathbf{Q}})$.

The analogs of the stable and unstable eigenspaces for a general nonlinear system are called the local stable and unstable manifolds* $W^s(\mathbf{X}_{\mathbf{Q}})$ and $W^u(\mathbf{X}_{\mathbf{Q}})$.

The stable manifold $W^s(\mathbf{X}_{\mathbf{Q}})$ is defined as the set of all states from which trajectories remain in the manifold and converge under the flow to $\mathbf{X}_{\mathbf{Q}}$. The unstable manifold $W^u(\mathbf{X}_{\mathbf{Q}})$ is defined as the set of all states from which trajectories remain in the manifold and diverge under the flow from $\mathbf{X}_{\mathbf{Q}}$.

By definition, the stable and unstable manifolds are invariant under the flow (if $\mathbf{X} \in W^s$, then $\phi_t(\mathbf{X}) \in W^s$). Furthermore, the n_s - and n_u -dimensional tangent spaces to W^s and W^u at $\mathbf{X}_{\mathbf{Q}}$ are E^s and E^u (as shown in Figure 14.8). In the special case of a linear or affine vector field \mathbf{F} , the stable and unstable manifolds are simply the eigenspaces E^s and E^u .

Chaos is associated with two characteristic connections of the stable and unstable manifolds. A homoclinic orbit (see Figure 14.9a) joins an isolated equilibrium point $\mathbf{X}_{\mathbf{Q}}$ to itself along its stable and unstable manifolds. A heteroclinic orbit

(Figure 14.9b) joins two distinct equilibrium points, $\mathbf{X}_{\mathbf{Q}1}$ and $\mathbf{X}_{\mathbf{Q}2}$, along the unstable manifold of one and the stable manifold of the other.

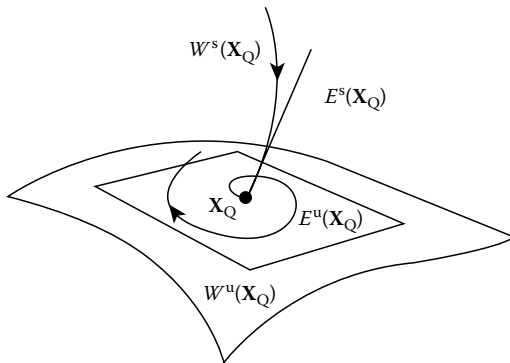


FIGURE 14.8 Stable and unstable manifolds $W^s(\mathbf{X}_{\mathbf{Q}})$ and $W^u(\mathbf{X}_{\mathbf{Q}})$ of an equilibrium point $\mathbf{X}_{\mathbf{Q}}$. The stable and unstable eigenspaces $E^s(\mathbf{X}_{\mathbf{Q}})$ and $E^u(\mathbf{X}_{\mathbf{Q}})$ derived from the linearization of the vector field at $\mathbf{X}_{\mathbf{Q}}$ are tangent to the corresponding manifolds W^s and W^u at $\mathbf{X}_{\mathbf{Q}}$. A trajectory approaching the equilibrium point along the stable manifold is tangential to $E^s(\mathbf{X}_{\mathbf{Q}})$ at $\mathbf{X}_{\mathbf{Q}}$; a trajectory leaving $\mathbf{X}_{\mathbf{Q}}$ along the unstable manifold is tangential to $E^u(\mathbf{X}_{\mathbf{Q}})$ at $\mathbf{X}_{\mathbf{Q}}$.

14.1.3.5 Stability of Limit Cycles

Although the stability of an equilibrium point may be determined by considering the eigenvalues of the linearization of the vector field near the point, how does one study the stability of a limit cycle, torus, or chaotic steady-state trajectory?

The idea introduced by Poincaré is to convert a continuous-time dynamical system into an equivalent discrete-time dynamical system by taking a transverse slice through the flow. Intersections of trajectories with this so-called Poincaré section define a Poincaré map from the section to themselves. Since the limit cycle is a fixed point $\mathbf{X}_{\mathbf{Q}}$ of the associated discrete-time dynamical system, its stability may be determined by examining the eigenvalues of the linearization of the Poincaré map at $\mathbf{X}_{\mathbf{Q}}$.

* An m -dimensional manifold is a geometrical object every small section of which looks like \mathbb{R}^m . More precisely, M is an m -dimensional manifold if, for every $x \in M$, there exists an open neighborhood U of x and a smooth invertible map which takes U to some open neighborhood of \mathbb{R}^m . For example, a limit cycle of a continuous-time dynamical system is a one-dimensional manifold.

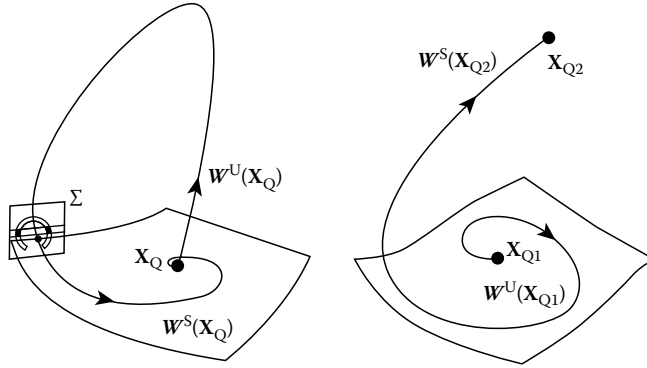


FIGURE 14.9 (a) Homoclinic orbit joins an isolated equilibrium point X_Q to itself along its stable and unstable manifolds. (b) A heteroclinic orbit joins two distinct equilibrium points, X_{Q1} and X_{Q2} , along the unstable manifolds of one and the stable manifold of the other.

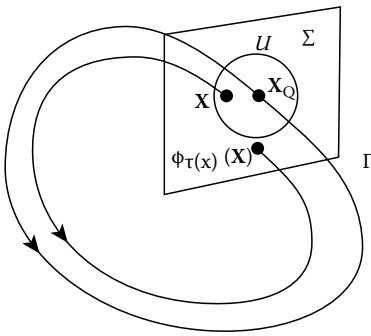


FIGURE 14.10 Transverse Poincaré section Σ through the flow of a dynamical system induces a discrete Poincaré map from a neighborhood U of the point of intersection X_Q to Σ .

14.1.3.6 Poincaré Sections

A Poincaré section of an n -dimensional autonomous continuous-time dynamical system is an $(n - 1)$ -dimensional hyperplane Σ in the state space that is intersected transversally* by the flow.

Let Γ be a closed orbit of the flow of a smooth vector field F , and let X_Q be a point of intersection of Γ with Σ . If T is the period of Γ and $X \in \Sigma$ is sufficiently close to X_Q , then the trajectory $\phi_t(X)$ through X will return to Σ after a time $\tau(X) \approx T$ and intersect the hyperplane at a point $\phi_{\tau(X)}(X)$, as illustrated in Figure 14.10.

This construction implicitly defines a function (called a Poincaré map or first return map) $G: U \rightarrow \Sigma$

$$G(X) = \phi_{\tau(X)}(X)$$

where U is a small region of Σ close to X_Q . The corresponding discrete-time dynamical system

$$X_{k+1} = G(X_k)$$

has a fixed point at X_Q .

The stability of the limit cycle is determined by the eigenvalues of the linearization $D_X G(X_Q)$ of G at X_Q . If all of the eigenvalues of $D_X G(X_Q)$ have modulus less than unity, the limit cycle is asymptotically stable; if any has modulus greater than unity, the limit cycle is unstable.

Note that the stability of the limit cycle is independent of the position and orientation of the Poincaré plane, provided that the intersection is chosen *transverse* to the flow. For a nonautonomous system with periodic forcing, a natural choice for the hyperplane is at a fixed phase θ_0 of the forcing.

* A *transverse* intersection of manifolds in \mathbb{R}^n is an intersection of manifolds such that, from any point in the intersection, all directions in \mathbb{R}^n can be generated by linear combinations of vectors tangent to the manifolds.

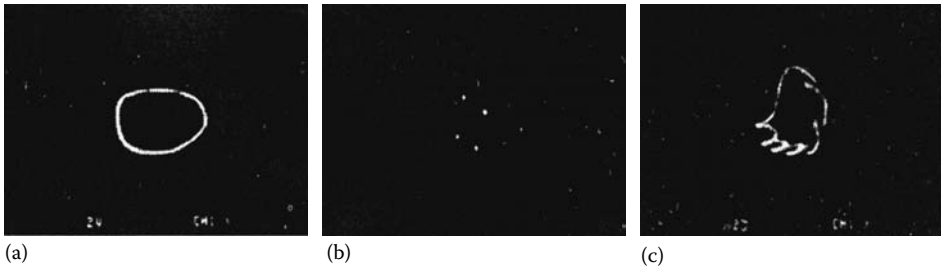


FIGURE 14.11 Experimental Poincaré sections corresponding to a torus breakdown sequence in Chua's oscillator. (a) Torus, (b) period-four orbit, (c) chaotic attractor resulting from torus breakdown. (From Chua, L.O., Wu, C.W., Hung, A., and Zhong, G.-Q., *IEEE Trans. Circuits Syst.*, 40, 738, Oct. 1993. With permission.)

In the Poincaré section, a limit cycle looks like a fixed point. A period- K subharmonic of a non-autonomous system with periodic forcing appears as a period- K orbit of the corresponding map (see Figure 14.11b).

The Poincaré section of a quasiperiodic attractor consisting of two incommensurate frequencies looks like a closed curve—a transverse cut through a two-torus (Figure 14.11a).

The Poincaré section of chaotic attractor has fractal structure, as depicted in Figure 14.11c.

14.1.4 Horseshoes and Chaos

Chaotic behavior is characterized by sensitive dependence on initial conditions. This phrase emphasizes the fact that small differences in initial conditions are persistently magnified by the dynamics of the system so that trajectories starting from nearby initial conditions reach totally different states in a finite time.

Trajectories of the nonlinear RLC circuit in Figure 14.2 that originate near the equilibrium point are initially stretched apart exponentially by the locally negative resistance in the case $G'_a < 0$. Eventually, however, they are squeezed together onto a limit cycle, so the stretching is not persistent. This is a consequence of the noncrossing property and eventual passivity.

Although perhaps locally active, every physical resistor is eventually passive meaning that, for a large enough voltage across its terminals, it dissipates power. This in turn limits the maximum values of the voltages and currents in the circuit giving a bounded steady-state solution. All physical systems are bounded, so how can small differences be magnified persistently in a real circuit?

14.1.4.1 Chaos in the Sense of Shil'nikov

Consider a flow ϕ in \mathbb{R}^3 that has an equilibrium point at the origin with a real eigenvalue $\gamma > 0$ and a pair of complex conjugate eigenvalues $\sigma \pm j\omega$ with $\sigma < 0$ and $\omega \neq 0$. Assume that the flow has a homoclinic orbit Γ through the origin.

One may define a Poincaré map for this system by taking a transverse section through the homoclinic orbit, as illustrated in Figure 14.9a.

THEOREM 14.2 (Shil'nikov)

If $|\sigma/\gamma| < 1$, the flow ϕ can be perturbed to ϕ' such that ϕ' has a homoclinic orbit Γ' near Γ and the Poincaré map of ϕ' defined in a neighborhood of Γ' has a countable number of horseshoes in its discrete dynamics.

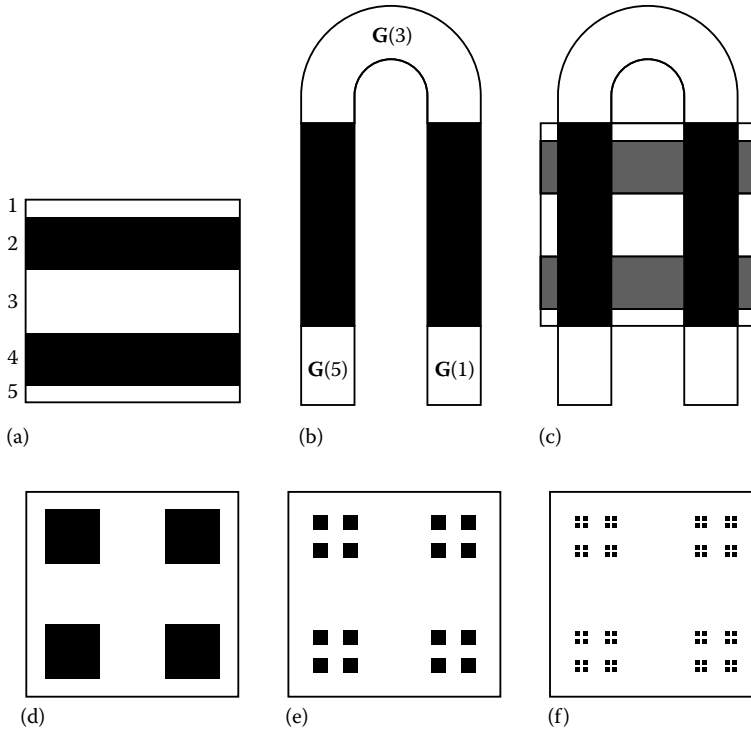


FIGURE 14.12 The Smale horseshoe map stretches the unit square (a), folds it into a horseshoe (b), and lays it back on itself (c), so that only points lying in bands 2 and 4 of (a) are mapped into the square. At the next iteration, only those points in $(G(2) \cup G(4)) \cap (2 \cup 4)$ (d) are mapped back to the square. Repeated iterations of the map (d)–(f) remove all points from the square except an invariant (fractal) set of fixed points.

The characteristic horseshoe shape in the Poincaré map stretches and folds trajectories repeatedly (see Figure 14.12). The resulting dynamics exhibit extreme sensitivity to initial conditions [7].

The presence of horseshoes in the flow of a continuous-time system that satisfies the assumptions of Shil'nikov's theorem implies the existence of countable numbers of unstable periodic orbits of arbitrarily long period as well as an uncountable number of complicated bounded nonperiodic chaotic solutions [7].

Horseshoes

The action of the Smale horseshoe map is to take the unit square (Figure 14.12a), stretch it, fold it into a horseshoe shape (Figure 14.12b), and lay it down on itself (Figure 14.12c). Under the action of this map, only four regions of the unit square are returned to the square.

Successive iterations of the horseshoe map return smaller and smaller regions of square to itself, as shown in Figure 14.12d through f. If the map is iterated *ad infinitum*, the unit square is ultimately mapped onto a set of points. These points form an invariant (fractal) limit set L that contains a countable set of periodic orbits of arbitrarily long periods, an uncountable set of bounded nonperiodic orbits, and at least one orbit that comes arbitrarily close to every point in L .

The properties of the map still hold if the horseshoe is distorted by a perturbation of small size but arbitrary shape. Thus, the dynamical behavior of the horseshoe map is structurally stable.*

Although the invariant limit set of a horseshoe map consists of nonwandering points, it is not attracting. Therefore, the existence of a horseshoe in the flow of a third-order system does not imply

* *Structural stability* is discussed in more detail in Section 14.1.5.

that the system will exhibit chaotic steady-state behavior. However if a typical trajectory in the Poincaré map remains in a neighborhood of the invariant set, then the system may exhibit chaos. Thus, although Shil'nikov's theorem is a strong indicator of chaos, it does not provide definitive proof that a system is chaotic.

Example: Chaos in a Piecewise-Linear System

Although we have stated it for the case $\sigma < 0$, $\gamma > 0$, Shil'nikov's theorem also applies when the equilibrium point at the origin has an unstable pair of complex conjugate eigenvalues and a stable real eigenvalue. In that case, it is somewhat easier to visualize the stretching and folding of bundles of trajectories close to a homoclinic orbit.

Consider the trajectory in a three-region piecewise-linear vector field in Figure 14.13. We assume that the equilibrium point P_- has a stable real eigenvalue γ_1 (where the eigenvector is $E^r(P_-)$) and an unstable complex conjugate pair of eigenvalues $\sigma_1 \pm j\omega_1$, the real and imaginary parts of whose eigenvectors span the plane $E^c(P_-)$ [2], as illustrated. A trajectory originating from a point \mathbf{X}_0 on $E^c(P_-)$ spirals away from the equilibrium point along $E^c(P_-)$ until it enters the D_0 region, where it is folded back into D_{-1} . Upon reentering D_{-1} , the trajectory is pulled toward P_- roughly in the direction of the real eigenvector $E^r(P_-)$, as illustrated.

Now imagine what would happen if the trajectory entering D_{-1} from D_0 were in precisely the direction $E^r(P_-)$. Such a trajectory would follow $E^r(P_-)$ toward P_- , reaching the equilibrium point asymptotically as $t \rightarrow \infty$. Similarly, if we were to follow this trajectory backward in time through D_0 and back onto $E^c(P_-)$ in D_{-1} , it would then spiral toward P_- , reaching it asymptotically as $t \rightarrow -\infty$. The closed curve thus formed would be a homoclinic orbit, reaching the same equilibrium point P_- asymptotically in forward and reverse time.

Although the homoclinic orbit itself is not structurally stable, and therefore cannot be observed experimentally, horseshoes are structurally stable. A flow ϕ that satisfies the assumptions of Shil'nikov's theorem contains a countable infinity of horseshoes; for sufficiently small perturbations ϕ' of the flow, finitely many of the horseshoes will persist. Thus, both the original flow and the perturbed flow exhibit chaos in the sense of Shil'nikov.

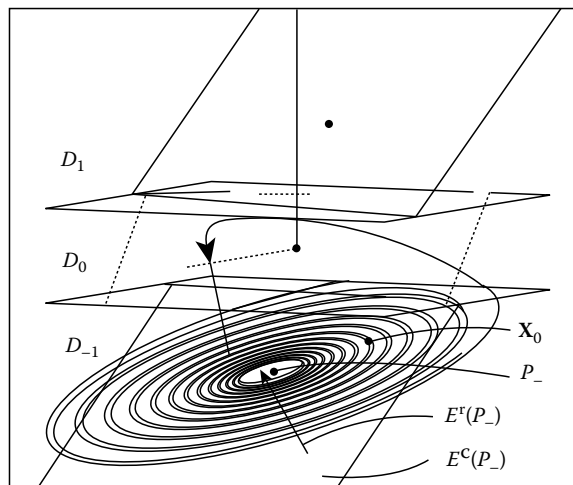


FIGURE 14.13 Stretching and folding mechanism of chaos generation in Chua's circuit. A trajectory spirals away from the equilibrium point P_- along the eigenplane $E^c(P_-)$ until it enters the D_0 region, where it is folded back into D_{-1} and returns to the unstable eigenplane $E^c(P_-)$ close to P_- . (From Kennedy, M.P., *IEEE Trans. Circuits Syst. I Fundam. Theory Appl.*, 40, 657, Oct. 1993. With permission.)

In Figure 14.13, we see that a trajectory lying close to a homoclinic orbit exhibits similar qualitative behavior: it spirals away from P_- along the unstable complex plane $E^c(P_-)$, is folded in D_0 , reenters D_{-1} above $E^c(P_-)$, and is pulled back toward $E^c(P_-)$, only to be spun away from P_- once more.

Thus, two trajectories starting from distinct initial states close to P_- on $E^c(P_-)$ are stretched apart exponentially along the unstable eigenplane before being folded in D_1 and reinjected close to P_- ; this gives rise to sensitive dependence on initial conditions. The recurrent stretching and folding continues *ad infinitum*, producing a chaotic steady-state solution.

14.1.4.2 Lyapunov Exponents

The notion of sensitive dependence on initial conditions may be made more precise through the concept of LEs. LEs quantify the average exponential rates of separation of trajectories along the flow.

The flow in a neighborhood of asymptotically stable trajectory is contracting so the LEs are zero or negative.* Sensitive dependence on initial conditions results from a positive LE.

To determine the stability of an equilibrium point, we consider the eigenvalues of the linearization of the vector field in the vicinity of equilibrium trajectory. This idea can be generalized to any trajectory of the flow.

The local behavior of the vector field along a trajectory $\phi_t(\mathbf{X}_0)$ of an autonomous continuous-time dynamical system (Equation 14.3) is governed by the linearized dynamics

$$\begin{aligned} \dot{\mathbf{x}} &= \mathbf{D}_X \mathbf{F}(\mathbf{X})\mathbf{x}, \quad \mathbf{x}(0) = \mathbf{x}_0 \\ &= \mathbf{D}_X \mathbf{F}[\phi_t(\mathbf{X}_0)]\mathbf{x} \end{aligned}$$

This is a linear time-varying system where the state transition matrix, $\Phi_t(\mathbf{X}_0)$, maps a point \mathbf{x}_0 into $\mathbf{x}(t)$. Thus

$$\mathbf{x}(t) = \Phi_t(\mathbf{X}_0)\mathbf{x}_0$$

Note that Φ_t is a linear operator. Therefore, a ball $B_\varepsilon(\mathbf{X}_0)$ of radius ε about \mathbf{X}_0 is mapped into an ellipsoid, as presented in Figure 14.1. The principal axes of the ellipsoid are determined by the singular values of Φ_t .

The singular values $\sigma_1(t), \sigma_2(t), \dots, \sigma_n(t)$ of Φ_t are defined as the square roots of the eigenvalues of $\Phi_t^H \Phi_t$, where Φ_t^H is the complex conjugate transpose of Φ_t . The singular values are ordered so that $\sigma_1(t) > \sigma_2(t) > \dots > \sigma_n(t)$.

In particular, a ball of radius ε is mapped by the linearized flow into an ellipsoid (see Figure 14.1), the maximum and minimum radii of which are bounded by $\sigma_1(t)\varepsilon$ and $\sigma_n(t)\varepsilon$, respectively.

The stability of a steady-state orbit is governed by the average local rates of expansion and contraction of volumes of state space close to the orbit. The LEs λ_i are defined by

$$\lambda_i = \lim_{t \rightarrow \infty} \frac{1}{t} \ln \sigma_i(t)$$

whenever this limit exists. The LEs quantify the average exponential rates of separation of trajectories along the flow.

The LEs are a property of a steady-state trajectory. Any transient effect is averaged out by taking the limit as $t \rightarrow \infty$. Furthermore, the LEs are global quantities of an attracting set that depend on the local stability properties of a trajectory within the set.

* A continuous flow that has a bounded trajectory not tending to an equilibrium point has a zero LE (in the direction of flow).

The set $\{\lambda_i, i = 1, 2, \dots, n\}$ is called the Lyapunov spectrum. An attractor has the property that the sum of its LEs is negative.

Lyapunov Exponents of Discrete-Time Systems

The local behavior along an orbit of the autonomous discrete-time dynamical system (Equation 14.8) is governed by the linearized dynamics

$$\mathbf{x}_{k+1} = \mathbf{D}_x \mathbf{G}(\mathbf{x}_k) \mathbf{x}_k, \quad k = 0, 1, 2, \dots$$

where the state transition matrix, $\Phi_k(\mathbf{X}_0)$, maps a point \mathbf{x}_0 into \mathbf{x}_k . Thus,

$$\mathbf{x}_k = \Phi_k(\mathbf{X}_0) \mathbf{x}_0$$

The LEs λ_i for the discrete-time dynamical system (Equation 14.8) are defined by

$$\lambda_i = \lim_{t \rightarrow \infty} \frac{1}{k} \ln \sigma_i(k)$$

whenever this limit exists. $\sigma_i(k)$ denotes the i th singular value of $\Phi_k^H \Phi_k$.

Lyapunov Exponents of Steady-State Solutions

Consider once more the continuous-time dynamical system (Equation 14.3). If $\mathbf{D}_x \mathbf{F}$ were constant along the flow, with n distinct eigenvalues $\tilde{\lambda}_i$,

$i = 1, 2, \dots, n$, then

$$\Phi_t = \begin{pmatrix} \exp(\tilde{\lambda}_1 t) & 0 & \cdots & 0 \\ 0 & \exp(\tilde{\lambda}_2 t) & \cdots & 0 \\ \vdots & \vdots & \ddots & \vdots \\ 0 & 0 & \cdots & \exp(\tilde{\lambda}_n t) \end{pmatrix}$$

and

$$\Phi_t^H \Phi_t = \begin{pmatrix} \exp(2\text{Re}(\tilde{\lambda}_1)t) & 0 & \cdots & 0 \\ 0 & \exp(2\text{Re}(\tilde{\lambda}_2)t) & \cdots & 0 \\ \vdots & \vdots & \ddots & \vdots \\ 0 & 0 & \cdots & \exp(2\text{Re}(\tilde{\lambda}_n)t) \end{pmatrix}$$

giving $\sigma_i(t) = \exp(\text{Re}(\tilde{\lambda}_i)t)$ and

$$\begin{aligned} \lambda_i &= \lim_{t \rightarrow \infty} \frac{1}{t} \ln(\exp[\text{Re}(\tilde{\lambda}_i)t]) \\ &= \text{Re}(\tilde{\lambda}_i) \end{aligned}$$

In this case, the LEs are simply the real parts of the eigenvalues of $\mathbf{D}_x \mathbf{F}$.

All the eigenvalues of a stable equilibrium point have negative real parts and therefore the largest LE of an attracting equilibrium point is negative.

Trajectories close to a stable limit cycle converge onto the limit cycle. Therefore, the largest LE of a periodic steady-state is zero (corresponding to motion along the limit cycle [15]), and all its other LEs are negative.

TABLE 14.1 Classification of Steady-State Behaviors according to Their Limit Sets, Power Spectra, LEs, and Dimension

Steady State	Limit Set	Spectrum	LEs	Dimension
DC	Fixed point	Spike at DC	$0 > \lambda_1 \geq \dots \geq \lambda_n$	0
Periodic	Closed curve	Fundamental plus	$\lambda_1 = 0$	1
		Integer harmonics	$0 > \lambda_2 \geq \dots \geq \lambda_n$	
Quasiperiodic	K -torus	Incommensurate	$\lambda_1 = \dots = \lambda_K = 0$	K
		Frequencies	$0 > \lambda_{K+1} \geq \dots \geq \lambda_n$	
Chaotic	Fractal	Broad spectrum	$\lambda_1 > 0$	Noninteger
			$\sum_{i=1}^n \lambda_i < 0$	

A quasiperiodic K -torus has K zero LEs because the flow is locally neither contracting nor expanding along the surface of the K -torus.

A chaotic trajectory is locally unstable and therefore has a positive LE; this produces sensitive dependence on initial conditions. Nevertheless, in the case of a chaotic attractor, this locally unstable chaotic trajectory belongs to an attracting limit set to which nearby trajectories converge.

The steady-state behavior of a four-dimensional continuous-time dynamical system which has two positive, one zero, and one negative LE is called hyperchaos.

The Lyapunov spectrum may be used to identify attractors, as summarized in Table 14.1.

14.1.5 Structural Stability and Bifurcations

Structural stability refers to the sensitivity of a phenomenon to small changes in the parameter of a system. A structurally stable vector field \mathbf{F} is one for which sufficiently close vector fields \mathbf{F}' have equivalent* dynamics [18].

The behavior of a typical circuit depends on a set of parameters one or more of which may be varied in order to optimize some performance criteria. In particular, one may think of a one-parameter family of systems

$$\dot{\mathbf{X}} = \mathbf{F}_\mu(\mathbf{X}) \tag{14.11}$$

where the vector field is parametrized by a control parameter μ . A value μ_0 of Equation 14.11 for which the flow of Equation 14.11 is not structurally stable is a bifurcation value of μ [7].

The dynamics in the state space may be qualitatively very different from one value of μ to another. In the nonlinear RLC circuit example, the steady-state solution is a limit cycle if the control parameter G'_a is negative and an equilibrium point if G'_a is positive. If G'_a is identically equal to zero, trajectories starting from $I_{30} = 0$, $V_{20} < E$ yield sinusoidal solutions. These sinusoidal solutions are not structurally stable because the slightest perturbation of G'_a will cause the oscillation to decay to zero or converge to the limit cycle, depending on whether G'_a is made slightly larger or smaller than zero.

If we think of this circuit as being parametrized by G'_a , then its vector field is not structurally stable at $G'_a \equiv 0$. We say that the equilibrium point undergoes a bifurcation (from stability to instability) as the value of the bifurcation parameter G'_a is reduced through the bifurcation point $G'_a = 0$.

* Equivalent means that there exists a continuous invertible function h that transforms \mathbf{F} into \mathbf{F}' .

14.1.5.1 Bifurcation Types

In this section, we consider three types of local bifurcation: the Hopf bifurcation, the saddle-node bifurcation, and the period-doubling bifurcation [18]. These bifurcations are called local because they may be understood by linearizing the system close to an equilibrium point or limit cycle.

Hopf Bifurcation

A Hopf bifurcation occurs in a continuous-time dynamical system (Equation 14.3) when a simple pair of complex conjugate eigenvalues of the linearization $\mathbf{D}_x\mathbf{F}(\mathbf{X}_Q)$ of the vector field at an equilibrium point \mathbf{X}_Q crosses the imaginary axis.

Typically, the equilibrium point changes stability from stable to unstable and a stable limit cycle is born. The bifurcation at $G'_a \equiv 0$ in the nonlinear *RLC* circuit is Hopf-like.*

When an equilibrium point undergoes a Hopf bifurcation, a limit cycle is born. When a limit cycle undergoes a Hopf bifurcation, motion on a two-torus results.

Saddle-Node Bifurcation

A saddle-node bifurcation occurs when a stable and an unstable equilibrium point merge and disappear; this typically manifests itself as the abrupt disappearance of an attractor.

A common example of a saddle-node bifurcation in electronic circuits is switching between equilibrium states in a Schmitt trigger. At the threshold for switching, a stable equilibrium point corresponding to the “high” saturated state merges with the high-gain region’s unstable saddle-type equilibrium point and disappears. After a switching transient, the trajectory settles to the other stable equilibrium point, which corresponds to the “low” state.

A saddle-node bifurcation may also manifest itself as a switch between periodic attractors of different sizes between a periodic attractor and a chaotic attractor, or between a limit cycle at one frequency and a limit cycle at another frequency.

Period-Doubling Bifurcation

A period-doubling bifurcation occurs in a discrete-time dynamical system (Equation 14.8) when a real eigenvalue of the linearization $\mathbf{D}_x\mathbf{G}(\mathbf{X}_Q)$ of the map \mathbf{G} at an equilibrium point crosses the unit circle at -1 [7].

In a continuous-time system, a period-doubling bifurcation occurs only from a periodic solution (an equilibrium point of the Poincaré map). At the bifurcation point, a periodic orbit with period T changes smoothly into one with period $2T$, as illustrated in Figure 14.14a and b.

Blue Sky Catastrophe

A blue sky catastrophe is a global bifurcation that occurs when an attractor disappears “into the blue,” usually because of a collision with a saddle-type limit set. Hysteresis involving a chaotic attractor is often caused by a blue sky catastrophe [18].

14.1.5.2 Routes to Chaos

Each of the three local bifurcations may give rise to a distinct route to chaos, and all three have been reported in electronic circuits. These routes are important because it is often difficult to conclude from experimental data alone whether irregular behavior is due to measurement noise or to underlying chaotic dynamics. If, upon adjusting a control parameter, one of the three prototype routes is observed, this indicates that the dynamics might be chaotic.

* Note that the Hopf bifurcation theorem is proven for sufficiently smooth systems and does not strictly apply to piecewise-linear systems. However, a physical implementation of a piecewise-linear characteristic, such as that of N_R , is always smooth.

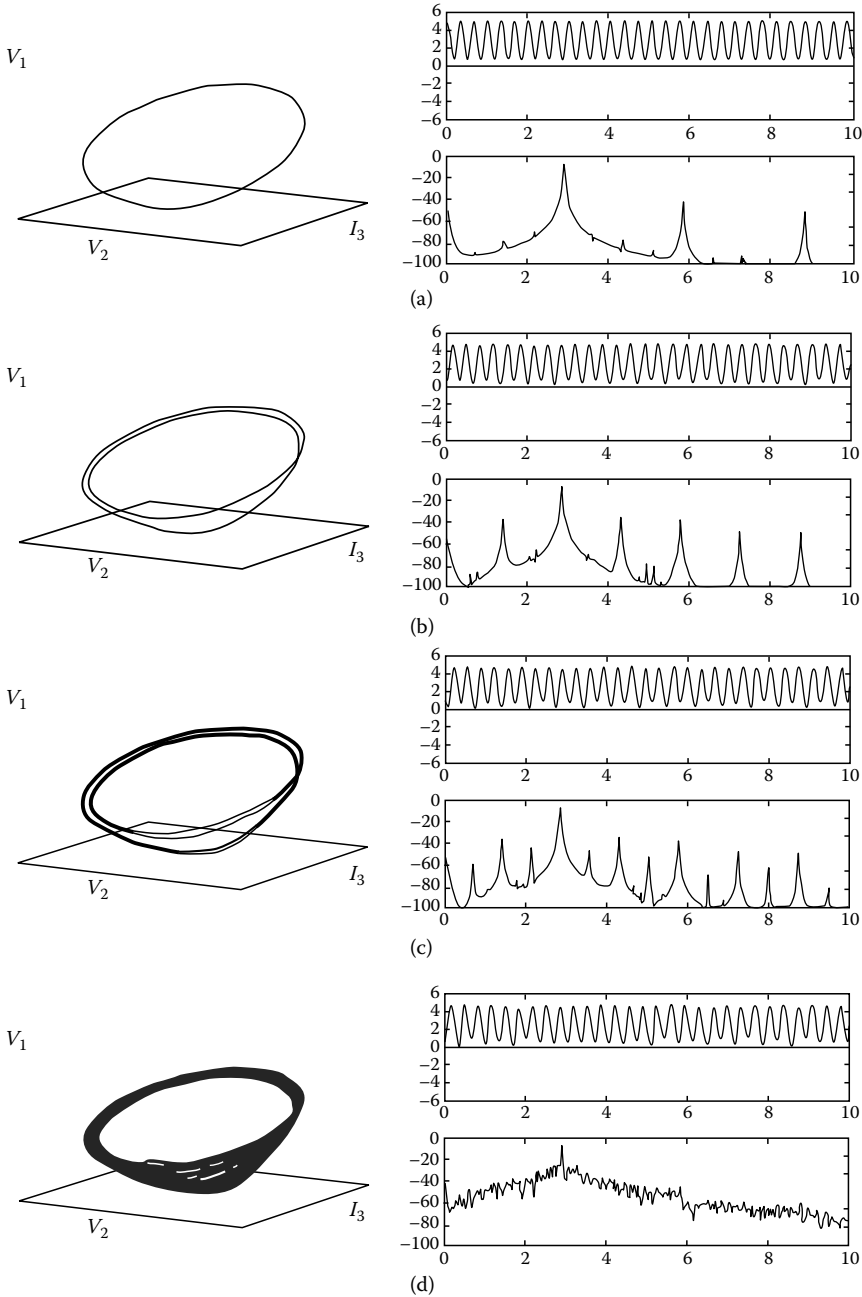


FIGURE 14.14 Period-doubling route to chaos in Chua's oscillator. Simulated state-space trajectories, time waveforms $V_1(t)$, and power spectra of $V_2(t)$ (a) $G = 530 \mu\text{S}$: periodic steady-state—the signal is characterized by a discrete power spectrum with energy at integer multiples of the fundamental frequency f_0 ; (b) $G = 537 \mu\text{S}$: period-two—after a period-doubling bifurcation, the period of the signal is approximately twice that of (a). In the power spectrum, a spike appears at the new fundamental frequency $\approx f_0/2$. (c) $G = 539 \mu\text{S}$: period-four—a second period-doubling bifurcation gives rise to a fundamental frequency of $\approx f_0/4$; (d) $G = 541 \mu\text{S}$: spiral Chua's attractor—a cascade of period doublings results in a chaotic attractor that has a broadband power spectrum. Time plots: horizontal axis— t (ms); vertical axis— V_1 (V). Power spectra: horizontal axis—frequency (kHz); vertical axis—power (mean-squared amplitude of $V_2(t)$) (dB).

Periodic-Doubling Route to Chaos

The period-doubling route to chaos is characterized by a cascade of period-doubling bifurcations. Each period-doubling transforms a limit cycle into one at half the frequency, spreading the energy of the system over a wider range of frequencies. An infinite cascade of such doublings results in a chaotic trajectory of infinite period and a broad frequency spectrum that contains energy at all frequencies. Figure 14.14 is a set of snapshots of the period-doubling route to chaos in Chua's oscillator.

An infinite number of period-doubling bifurcations to chaos can occur over a finite range of the bifurcation parameter because of a geometric relationship between the intervals over which the control parameter must be moved to cause successive bifurcations. Period-doubling is governed by a universal scaling law that holds in the vicinity of the bifurcation point to chaos μ_∞ .

Define the ratio δ_k of successive intervals μ , in each of which there is a constant period of oscillation, as follows,

$$\delta_k = \frac{\mu_{2^k} - \mu_{2^{k-1}}}{\mu_{2^{k+1}} - \mu_{2^k}}$$

where μ_{2^k} is the bifurcation point for the period from $2^k T$ to $2^{k+1} T$. In the limit as $k \rightarrow \infty$, a universal constant called the Feigenbaum number δ is obtained:

$$\lim_{k \rightarrow \infty} \delta_k = \delta = 4.6692 \dots$$

The period-doubling route to chaos is readily identified from a state-space plot, time series, power spectrum, or a Poincaré map.

Intermittency Route to Chaos

The route to chaos caused by saddle-node bifurcations comes in different forms, the common feature of which is direct transition from regular motion to chaos. The most common type is the intermittency route and results from a single saddle-node bifurcation. This is a route and not just a jump because, straight after the bifurcation, the trajectory is characterized by long intervals of almost regular motion (called laminar phases) and short bursts of irregular motion. The period of the oscillations is approximately equal to that of the system just before the bifurcation. This is illustrated in Figure 14.15.

As the parameter passes through the critical value μ_c at the bifurcation point into the chaotic region, the laminar phases become shorter and the bursts become more frequent, until the regular intervals disappear altogether. The scaling law for the average interval of the laminar phases depends on $|\mu - \mu_c|$, so chaos is not fully developed until some distance from the bifurcation point [13].

Intermittency is best characterized in the time domain because its scaling law depends on the length of the laminar phases.

Another type of bifurcation to chaos associated with saddle-nodes is the direct transition from a regular attractor (fixed point or limit cycle) to a coexisting chaotic one, without the phenomenon of intermittency.

Quasiperiodic (Torus Breakdown) Route to Chaos

The quasiperiodic route to chaos results from a sequence of Hopf bifurcations. Starting from a fixed point, the three-torus generated after three Hopf bifurcations is not stable in the sense that there exists an arbitrarily small perturbation of the system (in terms of parameters) for which the three-torus gives way to chaos.

A quasiperiodic-periodic-chaotic sequence corresponding to torus breakdown in Chua's oscillator is given in Figure 14.5.

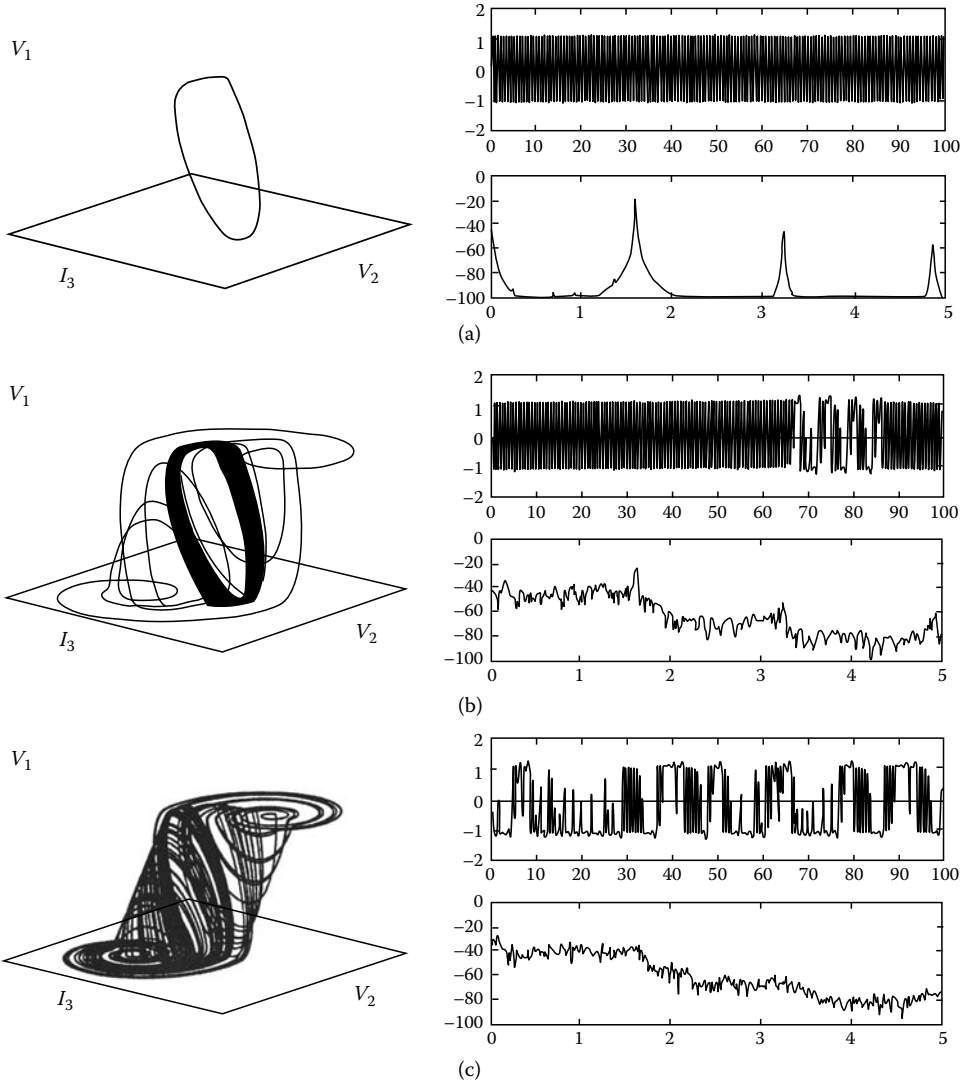


FIGURE 14.15 Intermittency route to chaos in Chua’s oscillator. Simulated state-space trajectories, time waveforms $V_1(t)$ and power spectra of $V_2(t)$ (a) Periodic steady-state—the signal is characterized by a discrete power spectrum with energy at integer multiples of the fundamental frequency; (b) onset of intermittency—the time signal contains long regular laminar phases and occasional bursts of irregular motion—in the frequency domain, intermittency manifests itself as a raising of the noise floor; (c) fully developed chaos—laminar phases are infrequent and the power spectrum is broad. Time plots: horizontal axis— t (ms); vertical axis— V_1 (V). Power spectra: horizontal axis—frequency (kHz); vertical axis—power (mean-squared amplitude of $V_2(t)$) (dB).

Quasiperiodicity is difficult to detect from a time series; it is more readily identified by means of a power spectrum or Poincaré map (see Figure 14.11).

14.1.5.3 Bifurcation Diagrams and Parameter Space Diagrams

Although state-space, time- and frequency-domain measurements are useful for characterizing steady-state behaviors, nonlinear dynamics offers several other tools for summarizing qualitative information concerning bifurcations.

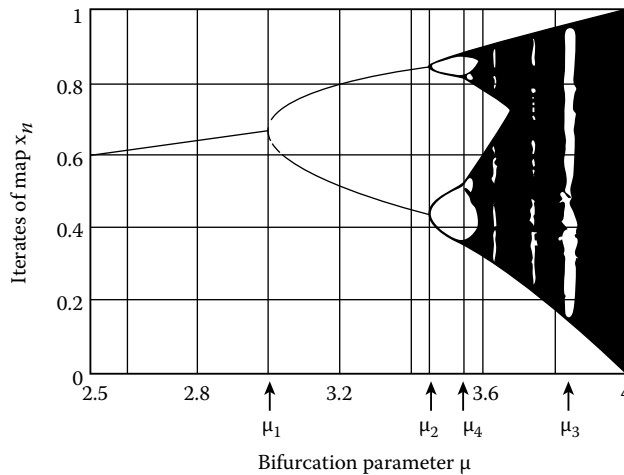


FIGURE 14.16 Bifurcation diagram for the logistic map: $X_{k+1} = \mu X_k(1 - X_k)$. The first period-doubling bifurcation occurs at $\mu = \mu_1$, the second at μ_2 , and the third at μ_4 . μ_3 corresponds to a period-three window. When $\mu = 4$, the entire interval $(0, 1)$ is visited by a chaotic orbit $\{X_k, k = 0, 1, \dots\}$. (From Wu, C.W. and Rul'kov, N.R., *IEEE Trans. Circuits Syst. I Fundam. Theory Appl.*, 40, 708, Oct. 1993. With permission.)

A bifurcation diagram is a plot of the attracting sets of a system versus a control parameter. Typically, one chooses a state variable and plots this against a single control parameter. In discrete systems, one simply plots successive values of a state variable. In the continuous-time case, some type of discretization is needed, typically by means of a Poincaré section.

Figure 14.16 is a bifurcation diagram of the logistic map $X_{k+1} = \mu X_k(1 - X_k)$ for $\mu \in [2.5, 4]$ and $X_k \in [0, 1]$. Period doubling from period-one to period-two occurs at μ_2 ; the next two doublings in the period-doubling cascade occur at μ_2 and μ_4 , respectively. A periodic window in the chaotic region is indicated by μ_3 . The map becomes chaotic by the period-doubling route if μ is increased from μ_3 and by the intermittency route if μ is reduced out of the window.

When more than one control parameter is present in a system, the steady-state behavior may be summarized in a series of bifurcation diagrams, where one parameter is chosen as the control parameter, with the others held fixed, and only changed from one diagram to the next. This provides a complete but cumbersome representation of the dynamics [13].

A clearer picture of the global behavior is obtained by partitioning the parameter space by means of bifurcation curves, and labeling the regions according to the observed steady-state behaviors within these regions. Such a picture is called a parameter space diagram.

14.2 Chua's Circuit: A Paradigm for Chaos

Chaos is characterized by a stretching and folding mechanism; nearby trajectories of a dynamical system are repeatedly pulled apart exponentially and folded back together.

In order to exhibit chaos, an autonomous circuit consisting of resistors, capacitors, and inductors must contain (1) at least one locally active resistor, (2) at least one nonlinear element, and (3) at least three energy-storage elements. The active resistor supplies energy to separate trajectories, the nonlinearity provides folding, and the three-dimensional state space permits persistent stretching and folding in a bounded region without violating the noncrossing property of trajectories.

Chua's circuit (see Figure 14.17) is the simplest electronic circuit that satisfies these criteria. It consists of a linear inductor, a linear resistor, two linear capacitors, and a single nonlinear resistor N_R . The circuit is readily constructed at low cost using standard electronic components and exhibits a rich variety of bifurcations and chaos [10].

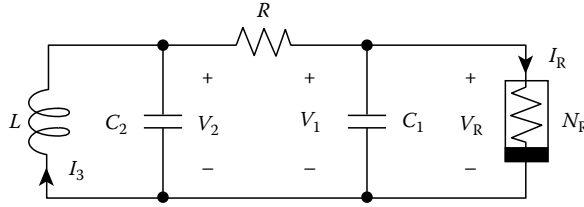


FIGURE 14.17 Chua’s circuit consists of a linear inductor L , two linear capacitors (C_2, C_1), a linear resistor R , and a voltage-controlled nonlinear resistor N_R .

14.2.1 Dynamics of Chua’s Circuit

14.2.1.1 State Equations

Chua’s circuit may be described by three ODEs. Choosing V_1, V_2 , and I_3 as state variables, we write

$$\begin{aligned} \frac{dV_1}{dt} &= \frac{G}{C_1}(V_2 - V_1) - \frac{1}{C_1}f(V_1) \\ \frac{dV_2}{dt} &= \frac{G}{C_2}(V_1 - V_2) + \frac{1}{C_2}I_3 \\ \frac{dI_3}{dt} &= -\frac{1}{L}V_2 \end{aligned} \tag{14.12}$$

where $G = 1/R$ and $f(V_R) = G_b V_R + 1/2(G_a + G_b) (|V_R + E| - |V_R - E|)$, as depicted in Figure 14.18.

Because of the piecewise-linear nature of N_R , the vector field of Chua’s circuit may be decomposed into three distinct affine regions: $V_1 < -E$, $|V_1| \leq E$, and $V_1 > E$. We call these the D_{-1}, D_0 , and D_1 regions, respectively. The global dynamics may be determined by considering separately the behavior in each of the three regions (D_{-1}, D_0 , and D_1) and then gluing the pieces together along the boundary planes U_{-1} and U_1 .

14.2.1.2 Piecewise-Linear Dynamics

In each region, the circuit is governed by a three-dimensional autonomous affine dynamical system of the form

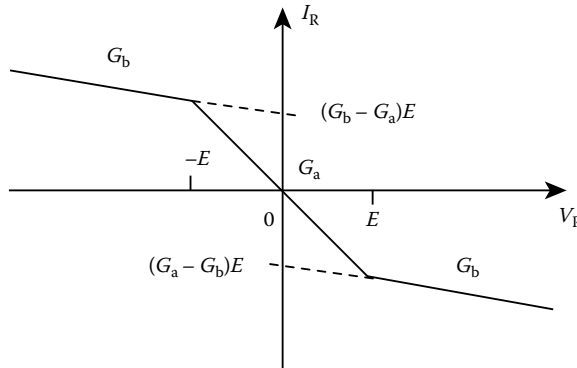


FIGURE 14.18 The DP characteristic of the nonlinear resistor N_R in Chua’s circuit has breakpoints at $\pm E$ and slopes G_a and G_b in the inner and outer regions, respectively.

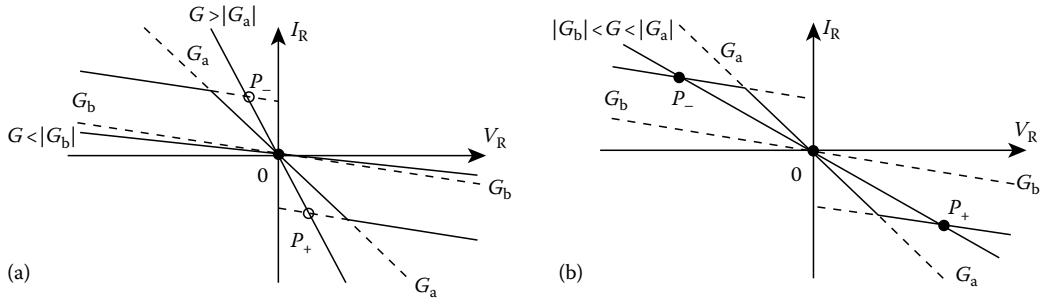


FIGURE 14.19 DC equilibrium points of Figure 14.17 may be determined graphically by intersecting the load line $I_R = -GV_R$ with the DP characteristic of N_R . (a) If $G > |G_a|$ or $G < |G_b|$, the circuit has a unique equilibrium point at the origin (P_- and P_+ are virtual equilibria in this case). (b) When $|G_b| < G < |G_a|$, the circuit has three equilibrium points at P_- , 0 and P_+ .

$$\dot{\mathbf{X}} = \mathbf{A}\mathbf{X} + \mathbf{b} \tag{14.13}$$

where

- \mathbf{A} is the (constant) system matrix
- \mathbf{b} is a constant vector

The equilibrium points of the circuit may be determined graphically by intersecting the load line $I_R = -GV_R$ with the DP characteristic $I_R = f(V_R)$ of the nonlinear resistor N_R , as presented in Figure 14.19 [2]. When $G > |G_a|$ or $G > |G_b|$, the circuit has a unique equilibrium point at the origin (and two virtual equilibria P_- and P_+); otherwise, it has three equilibrium points at P_- , 0, and P_+ .

The dynamics close to an equilibrium point \mathbf{X}_Q are governed locally by the linear system

$$\dot{\mathbf{x}} = \mathbf{A}\mathbf{x} \tag{14.14}$$

If the eigenvalues λ_1 , λ_2 , and λ_3 of \mathbf{A} are distinct, then every solution $\mathbf{x}(t)$ of Equation 14.14 may be expressed in the form

$$\mathbf{x}(t) = c_1 \exp(\lambda_1 t) \vec{\xi}_1 + c_2 \exp(\lambda_2 t) \vec{\xi}_2 + c_3 \exp(\lambda_3 t) \vec{\xi}_3$$

where

- $\vec{\xi}_1$, $\vec{\xi}_2$, and $\vec{\xi}_3$ are the (possibly complex) eigenvectors associated with the eigenvalues λ_1 , λ_2 , and λ_3 , respectively
- c_k 's are (possibly complex) constants that depend on the initial state \mathbf{X}_0

In the special case when \mathbf{A} has one real eigenvalue γ and a complex conjugate pair of eigenvalues $\sigma \pm j\omega$, the solution of Equation 14.14 has the form

$$\mathbf{x}(t) = c_r \exp(\gamma t) \vec{\xi}_\gamma + 2c_c \exp(\sigma t) [\cos(\omega t + \phi_c) \vec{\eta}_r - \sin(\omega t + \phi_c) \vec{\eta}_i]$$

where

- $\vec{\eta}_r$ and $\vec{\eta}_i$ are the real and imaginary parts of the eigenvectors associated with the complex conjugate pair of eigenvalues
- $\vec{\xi}_\gamma$ is the eigenvector defined by $\mathbf{A}\vec{\xi}_\gamma = \gamma \vec{\xi}_\gamma$
- c_r , c_c , and ϕ_c are real constants that are determined by the initial conditions

Let us relabel the real eigenvector E^r , and define E^c as the complex eigenplane spanned by $\vec{\eta}_r$ and $\vec{\eta}_i$.

We can think of the solution $\mathbf{x}(t)$ of Equation 14.14 as being the sum of two distinct components $\mathbf{x}_r(t) \in E^r$ and $\mathbf{x}_c(t) \in E^c$:

$$\begin{aligned}\mathbf{x}_r(t) &= c_r \exp(\gamma t) \vec{\xi}_\gamma \\ \mathbf{x}_c(t) &= 2c_c \exp(\sigma t) [\cos(\omega t + \phi_c) \vec{\eta}_r - \sin(\omega t + \phi_c) \vec{\eta}_i]\end{aligned}$$

The complete solution $\mathbf{X}(t)$ of Equation 14.13 may be found by translating the origin of the linearized coordinate system to the equilibrium point \mathbf{X}_Q . Thus,

$$\begin{aligned}\mathbf{X}(t) &= \mathbf{X}_Q + \mathbf{x}(t) \\ &= \mathbf{X}_Q + \mathbf{x}_r(t) + \mathbf{x}_c(t)\end{aligned}$$

We can determine the qualitative behavior of the complete solution $\mathbf{X}(t)$ by considering separately the components $\mathbf{x}_r(t)$ and $\mathbf{x}_c(t)$ along E^r and E^c , respectively.

If $\gamma > 0$, $\mathbf{x}_r(t)$ grows exponentially in the direction of E^r ; if $\gamma < 0$ the component $\mathbf{x}_r(t)$ tends asymptotically to zero. When $\sigma > 0$ and $\omega \neq 0$, $\mathbf{x}_c(t)$ spirals away from \mathbf{X}_Q along the complex eigenplane E^c , and if $\sigma < 0$, $\mathbf{x}_c(t)$ spirals toward \mathbf{X}_Q and E^c .

We remark that the vector E^r and plane E^c are invariant under the flow of Equation 14.13: if $\mathbf{X}(0) \in E^r$, then $\mathbf{X}(t) \in E^r$ for all t ; if $\mathbf{X}(0) \in E^c$ then $\mathbf{X}(t) \in E^c$ for all t . An important consequence of this is that a trajectory $\mathbf{X}(t)$ cannot cross through the complex eigenspace E^c ; suppose $\mathbf{X}(t_0) \in E^c$ at some time t_0 , then $\mathbf{X}(t) \in E^c$ for all $t > t_0$.

14.2.2 Chaos in Chua's Circuit

In the following discussion, we consider a fixed set of component values: $L = 18$ mH, $C_2 = 100$ nF, $C_1 = 10$ nF, $G_a = -50/66$ mS = -757.576 μ S, $G_b = -9/22$ mS = -409.091 μ S, and $E = 1$ V. When $G = 550$ μ S, three equilibrium points occur at P_+ , 0 , and P_- . The equilibrium point at the origin (0) has one unstable real eigenvalue γ_0 and a stable complex pair $\sigma_0 \pm j\omega_0$. The outer equilibria (P_- and P_+) each have a stable real eigenvalue γ_1 and an unstable complex pair $\sigma_0 \pm j\omega_1$.

14.2.2.1 Dynamics of D_0

A trajectory starting from some initial state \mathbf{X}_0 in the D_0 region may be decomposed into its components along the complex eigenplane $E^c(0)$ and along the eigenvector $E^r(0)$. When $\gamma_0 > 0$ and $\sigma_0 < 0$, the component along $E^c(0)$ spirals toward the origin along this plane while the component in the direction $E^r(0)$ grows exponentially. Adding the two components, we see that a trajectory starting slightly above the stable complex eigenplane $E^c(0)$ spirals toward the origin along the $E^c(0)$ direction, all the while being pushing away from $E^c(0)$ along the unstable direction $E^r(0)$. As the (stable) component along $E^c(0)$ shrinks in magnitude, the (unstable) component grows exponentially, and the trajectory follows a helix of exponentially decreasing radius whose axis lies in the direction of $E^r(0)$; this is illustrated in Figure 14.20.

14.2.2.2 Dynamics of D_{-1} and D_1

The eigenvector $E^r(P_+)$ is associated with the stable real eigenvalue γ_1 in the D_1 region. The real and imaginary parts of the complex eigenvectors associated with $\sigma_1 \pm j\omega_1$ define a complex eigenplane $E^c(P_+)$.

A trajectory starting from some initial state \mathbf{X}_0 in the D_1 region may be decomposed into its components along the complex eigenplane $E^c(P_+)$ and the eigenvector $E^r(P_+)$. When $\gamma_1 < 0$ and $\sigma_1 > 0$, the component on $E^c(P_+)$ spirals away from P_+ along this plane while the component in the direction of $E^r(0)$ tends asymptotically toward P_+ . Adding the two components, we see that a trajectory starting close to the stable real eigenvector $E^r(P_+)$ above the complex eigenplane moves toward $E^c(P_+)$

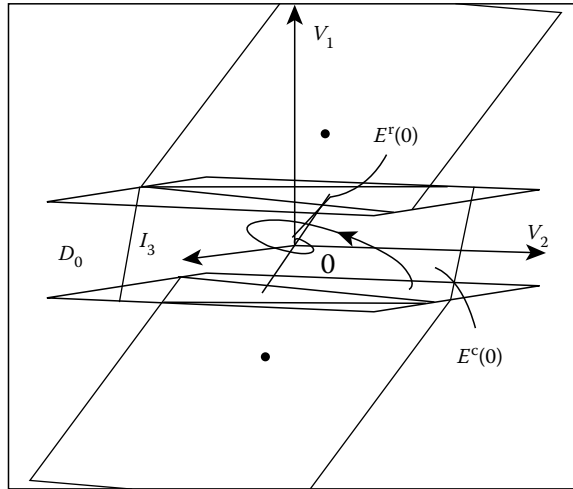


FIGURE 14.20 Dynamics of the D_0 region. A trajectory starting slightly above the stable complex eigenplane $E^c(0)$ spirals toward the origin along this plane and is repelled close to 0 in the direction of the unstable eigenvector $E^r(0)$. (From Kennedy, M.P., *IEEE Trans. Circuits Syst. I Fundam. Theory Appl.*, 40, 660, Oct. 1993. With permission.)

along a helix of exponentially increasing radius. Because the component along $E^r(P_+)$ shrinks exponentially in magnitude and the component on $E^c(P_+)$ grows exponentially, the trajectory is quickly flattened onto $E^c(P_+)$, where it spirals away from P_+ along the complex eigenplane; this is illustrated in Figure 14.21.

By symmetry, the equilibrium point P_- in the D_{-1} region has three eigenvalues: γ_1 and $\sigma_1 \pm j\omega_1$. The eigenvector $E^r(P_-)$ is associated with the stable real eigenvalue γ_1 ; the real and imaginary parts of the eigenvectors associated with the unstable complex pair $\sigma_1 \pm j\omega_1$ define an eigenplane $E^c(P_-)$, along which trajectories spiral away from P_- .

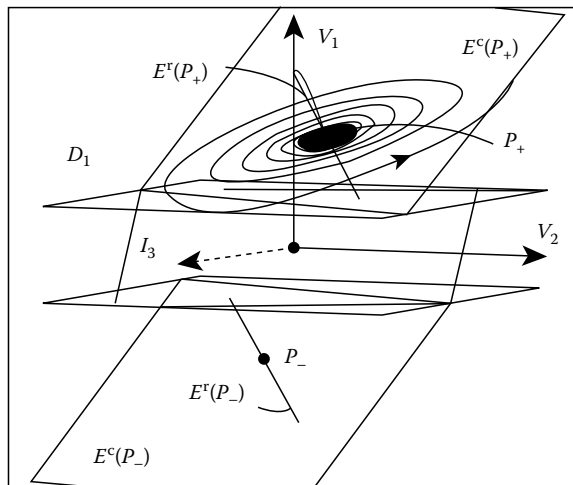


FIGURE 14.21 Dynamics of the D_1 region. A trajectory starting above the unstable complex eigenplane $E^c(P_+)$ close to the eigenvector $E^r(P_+)$ moves toward the plane and spirals away from P_+ along $E^c(P_+)$. By symmetry, the D_{-1} region has equivalent dynamics. (From Kennedy, M.P., *IEEE Trans. Circuits Syst.*, 40, 662, Oct. 1993. With permission.)

14.2.2.3 Global Dynamics

With the given set of parameter values, the equilibrium point at the origin has an unstable real eigenvalue and a stable pair of complex conjugate eigenvalues; the outer equilibrium point P_- has a stable real eigenvalue and an unstable complex pair.

In particular, P_- has a pair of unstable complex conjugate eigenvalues $\sigma_1 \pm \omega_1$ ($\sigma_1 > 0$, $\omega_1 \neq 0$) and a stable real eigenvalue γ_1 , where $|\sigma_1| < |\omega_1|$. In order to prove that the circuit is chaotic in the sense of Shil'nikov, it is necessary to show that it possesses a homoclinic orbit for this set of parameter values.

A trajectory starting on the eigenvector $E^c(0)$ close to 0 moves away from the equilibrium point until it crosses the boundary U_1 and enters D_1 , as illustrated in Figure 14.20. If this trajectory is folded back into D_0 by the dynamics of the outer region, and reinjected toward 0 along the stable complex eigenplane $E^c(0)$ then a homoclinic orbit is produced.

That Chua's circuit is chaotic in the sense of Shil'nikov was first proven by Chua et al. [21] in 1985. Since then, there has been an intensive effort to understand every aspect of the dynamics of this circuit with a view to developing it as a paradigm for learning, understanding, and teaching about nonlinear dynamics and chaos [3].

14.2.3 Steady-States and Bifurcations in Chua's Circuit

In the following discussion, we consider the global behavior of the circuit using our chosen set of parameters with R in the range $0 \leq R \leq 2000 \Omega$ ($500 \mu\text{S} \leq G < \infty\text{S}$).

Figure 14.14 is a series of simulations of the equivalent circuit in Figure 14.26 with the following parameter values: $L = 18 \text{ mH}$, $C_2 = 100 \text{ nF}$, $C_1 = 10 \text{ nF}$, $G_a = -50/66 \text{ mS} = -757.576 \mu\text{S}$, $G_b = -9/22 \text{ mS} = -409.091 \mu\text{S}$, and $E = 1 \text{ V}$. $R_0 = 12.5 \Omega$, the parasitic series resistance of a real inductor. R is the bifurcation parameter.

14.2.3.1 Equilibrium Point and Hopf Bifurcation

When R is large (2000Ω), the outer equilibrium points P_- and P_+ are stable ($\gamma_1 < 0$ and $\sigma_1 < 0$, $\omega_1 \neq 0$); the inner equilibrium point 0 is unstable ($\gamma_0 > 0$ and $\sigma_0 < 0$, $\omega_0 \neq 0$).

Depending on the initial state of the circuit, the system remains at one outer equilibrium point or the other. Let us assume that we start at P_+ in the D_1 region. This equilibrium point has one negative real eigenvalue and a complex pair with negative real parts. The action of the negative real eigenvalue γ_1 is to squeeze trajectories down onto the complex eigenplane $E^c(P_+)$, where they spiral toward the equilibrium point P_+ .

As the resistance R is decreased, the real part of the complex pair of eigenvalues changes sign and becomes positive. Correspondingly, the outer equilibrium points become unstable as σ_1 passes through 0; this is a Hopf-like bifurcation.* The real eigenvalue of P_+ remains negative so trajectories in the D_1 region converge toward the complex eigenplane $E^c(P_+)$. However, they spiral away from the equilibrium point P_+ along $E^c(P_+)$ until they reach the dividing plane U_1 (defined by $V_1 + E$) and enter the D_0 region.

The equilibrium point at the origin in the D_0 region has a stable complex pair of eigenvalues and an unstable real eigenvalue. Trajectories that enter the D_0 region on the complex eigenplane $E^c(0)$ are attracted to the origin along this plane. Trajectories that enter D_0 from D_1 below or above the eigenplane either cross-over to D_{-1} or are turned back toward D_1 , respectively. For R sufficiently large, trajectories that spiral away from P_+ along $E^c(P_+)$ and enter D_0 above $E^c(0)$ are returned to D_1 , producing a stable period-one limit cycle. This is illustrated in Figure 14.14a.

* Recall that the Hopf bifurcation theorem strictly applies only for sufficiently smooth systems, but that physical implementations of piecewise-linear characteristics are typically smooth.

14.2.3.2 Period-Doubling Cascade

As the resistance R is decreased further, a period-doubling bifurcation occurs. The limit cycle now closes on itself after encircling P_+ twice; this is called a period-two cycle because a trajectory takes approximately twice the time to complete this closed orbit as to complete the preceding period-one orbit (see Figure 14.14b).

Decreasing the resistance R still further produces a cascade of period-doubling bifurcations to period-four (Figure 14.14c), period-eight, period-sixteen, and so on until an orbit of infinite period is reached, beyond which we have chaos (see Figure 14.14d). This is a spiral Chua's chaotic attractor.

The spiral Chua's attractor in Figure 14.14d looks like a ribbon or band that is smoothly folded on itself; this folded band is the simplest type of chaotic attractor [18]. A trajectory from an initial condition \mathbf{X}_0 winds around the strip repeatedly, returning close to \mathbf{X}_0 , but never closing on itself.

14.2.3.3 Periodic Windows

Between the chaotic regions in the parameter space of Chua's circuit, there exist ranges of the bifurcation parameter R over which stable periodic motion occurs. These regions of periodicity are called periodic windows and are similar to those that exist in the bifurcation diagram of the logistic map (see Figure 14.16).

Periodic windows of periods three and five are readily found in Chua's circuit. These limit cycles undergo period-doubling bifurcations to chaos as the resistance R is decreased.

For certain sets of parameters, Chua's circuit follows the intermittency route to chaos as R is increased out of the period-three window.

14.2.3.4 Spiral Chua's Attractor

Figure 14.22 outlines three views of another simulated spiral Chua's chaotic attractor. Figure 14.22b is a view along the edge of the outer complex eigenplanes $E^c(P_+)$ and $E^c(P_-)$; notice how trajectories in the D_1 region are compressed toward the complex eigenplane $E^c(P_+)$ along the direction of the stable real eigenvector $E^s(P_+)$ and they spiral away from the equilibrium point P_+ along $E^c(P_+)$.

When a trajectory enters the D_0 region through U_1 from D_1 , it is twisted around the unstable real eigenvector $E^u(0)$ and returned to D_1 .

Figure 14.22c illustrates clearly that when the trajectory enters D_0 from D_1 , it crosses U_1 above the eigenplane $E^c(0)$. The trajectory cannot cross through this eigenplane and therefore it must return to the D_1 region.

14.2.3.5 Double-Scroll Chua's Attractor

Because we chose a nonlinear resistor with a symmetric nonlinearity, every attractor that exists in the D_1 and D_0 regions has a counterpart (mirror image) in the D_{-1} and D_0 regions. As the coupling resistance R is decreased further, the spiral Chua's attractor "collides" with its mirror image and the two merge to form a single compound attractor called a double-scroll Chua's chaotic attractor [10], as presented in Figure 14.23.

Once more, we show three views of this attractor in order to illustrate its geometrical structure. Figure 14.23b is a view of the attractor along the edge of the outer complex eigenplanes $E^c(P_+)$ and $E^c(P_-)$. Upon entering the D_1 region from D_0 , the trajectory collapses onto $E^c(P_+)$ and spirals away from P_+ along this plane.

Figure 14.23c is a view of the attractor along the edge of the complex eigenplane $E^c(0)$ in the inner region. Notice once more that when the trajectory crosses U_1 into D_0 above $E^c(0)$, it must remain above $E^c(0)$ and so returns to D_1 . Similarly, if the trajectory crosses U_1 below $E^c(0)$, it must remain below $E^c(0)$ and therefore crosses over to the D_{-1} region. Thus, $E^c(0)$ presents a knife-edge to the trajectory as it crosses U_1 into the D_0 region, forcing it back toward D_1 or across D_0 to D_{-1} .

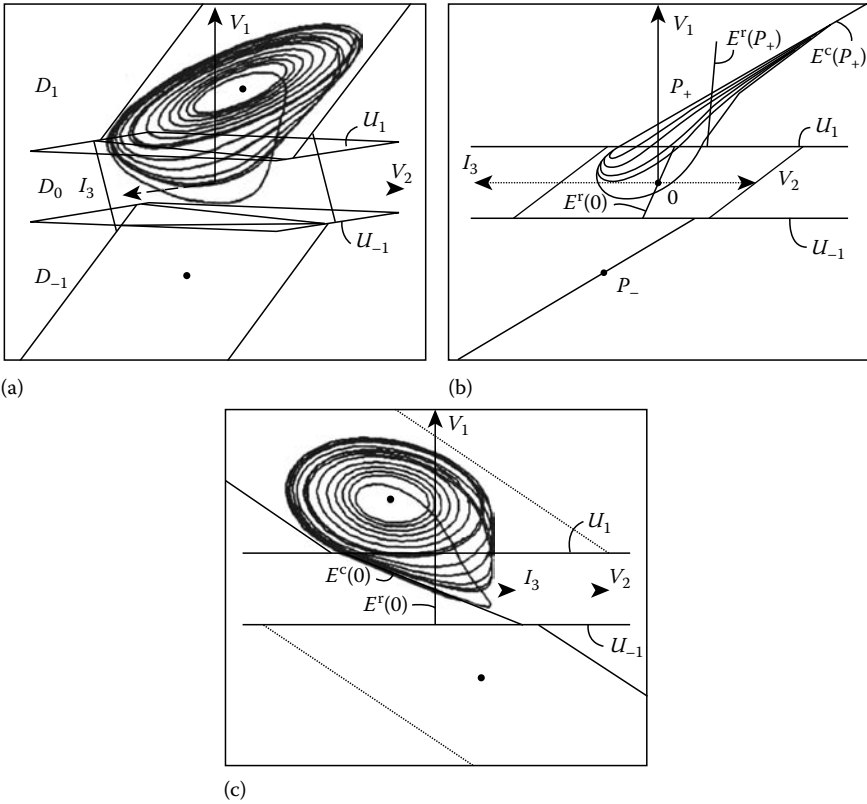


FIGURE 14.22 Three views of a simulated spiral Chua’s attractor in Chua’s oscillator with $G = 550 \mu\text{S}$. (a) Reference view (compare with Figure 14.14d). (b) View of the edge of the outer complex eigenplanes $E^c(P_+)$ and $E^c(P_-)$; note how trajectory in D_1 is flattened onto $E^c(P_+)$. (c) View along the edge of the complex eigenplane $E^c(0)$; trajectories cannot cross this plane. (From Kennedy, M.P., *IEEE Trans. Circuits Syst. I Fundam. Theory Appl.*, 40, 664, Oct. 1993. With permission.)

14.2.3.6 Boundary Crisis

Reducing the resistance R still further produces more regions of chaos, interspersed with periodic windows. Eventually, for a sufficiently small value of R , the unstable saddle trajectory that normally resides outside the stable steady-state solution collides with the double-scroll Chua’s attractor and a blue sky catastrophe called a boundary crisis [10] occurs. After this, all trajectories become unbounded.

14.2.4 Manifestations of Chaos

14.2.4.1 Sensitive Dependence on Initial Conditions

Consider once more the double-scroll Chua’s attractor shown in Figure 14.23. Two trajectories starting from distinct but almost identical initial states in D_1 will remain “close together” until they reach the separating plane U_1 . Imagine that the trajectories are still “close” at the knife-edge, but that one trajectory crosses into D_0 slightly above $E^c(0)$ and the other slightly below $E^c(0)$. The former trajectory returns to D_1 and the latter crosses over to D_{-1} ; their “closeness” is lost.

The time-domain waveforms $V_1(t)$ for two such trajectories are shown in Figure 14.24. These are solutions of Chua’s oscillator with the same parameters as in Figure 14.23; the initial conditions are $(I_3, V_2, V_1) = (1.810 \text{ mA}, 222.014 \text{ mV}, -2.286 \text{ V})$ [solid curve] and $(I_3, V_2, V_1) = (1.810 \text{ mA},$

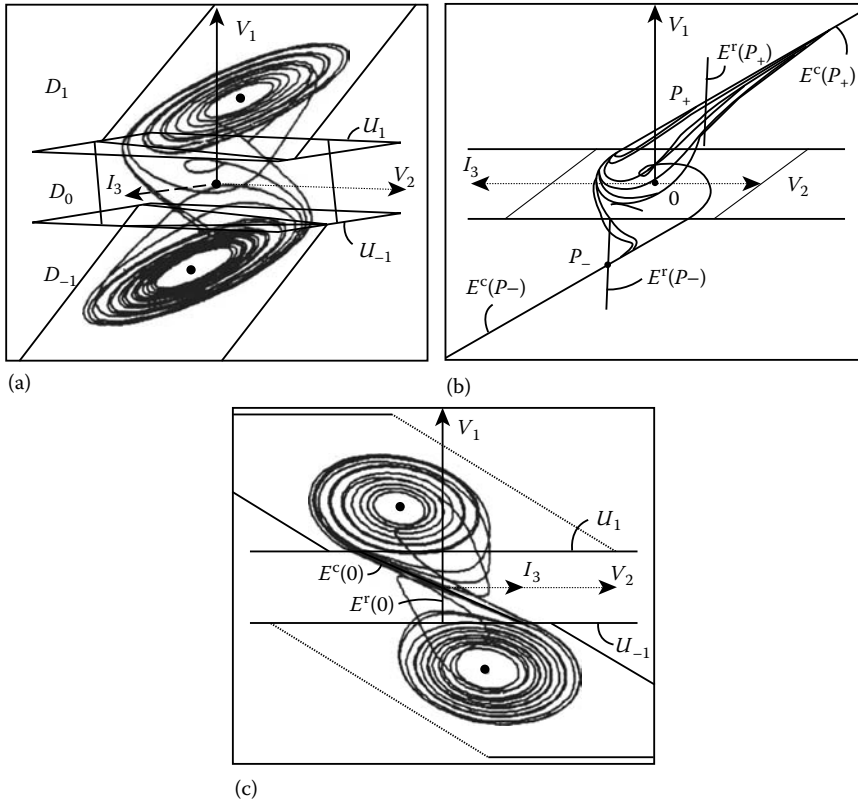


FIGURE 14.23 Three views of a simulated double-scroll Chua's attractor in Chua's oscillator with $G = 565 \mu\text{S}$. (a) Reference view (compare with Figure 14.14d). (b) View along the edge of the outer complex eigenplanes $E^c(P_+)$ and $E^c(P_-)$; note how the trajectory in D_1 is flattened onto $E^c(P_+)$ and onto $E^c(P_-)$ in D_{-1} . (c) View along the edge of the complex eigenplane $E^c(0)$; a trajectory entering D_0 from D_1 above this plane returns to D_1 while one entering D_0 below $E^c(0)$ crosses to D_{-1} . (From Kennedy, M.P., *IEEE Trans. Circuits Syst. I Fundam. Theory Appl.*, 40, 665, Oct. 1993. With permission.)

222.000 mV, -2.286 V) [dashed curve]. Although the initial conditions differ by less than 0.01% in just one component (V_2), the trajectories diverge and become uncorrelated within 5 ms because one crosses the knife-edge before the other.

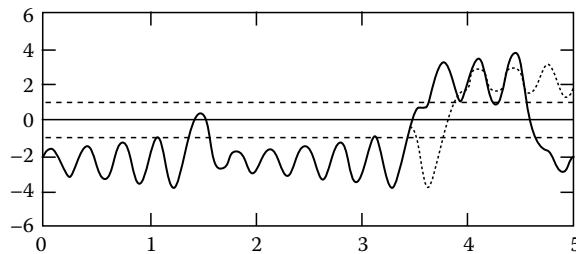


FIGURE 14.24 Sensitive dependence on initial conditions. Two time waveforms $V_1(t)$ from Chua's oscillator with $G = 550 \mu\text{S}$, starting from $(I_3, V_2, V_1) = (1.810 \text{ mA}, 222.01 \text{ mV}, -2.286 \text{ V})$ [solid line] and $(I_3, V_2, V_1) = (1.810 \text{ mA}, 222.000 \text{ mV}, -2.286 \text{ V})$ [dashed line]. Note that the trajectories diverge within 5 ms. Horizontal axis: t (ms); vertical axis: V_1 (V). Compare with Figure 14.23.

This rapid decorrelation of trajectories that originate in nearby initial states, commonly called sensitive dependence on initial conditions, is a generic property of chaotic systems. It gives rise to an apparent randomness in the output of the system and long-term unpredictability of the state.

14.2.4.2 “Randomness” in the Time Domain

Figures 14.14a through d show the state-space trajectories of period-one, period-two, and period-four periodic attractors, a spiral Chua’s chaotic attractor, respectively, and the corresponding voltage waveforms $V_1(t)$.

The “period-one” waveform is periodic; it looks like a slightly distorted sinusoid. The “period-two” waveform is also periodic. It differs qualitatively from the “period-one” in that the pattern of a large peak followed by a small peak repeats approximately once every two cycles of the period-one signal; that is why it is called period-two.

In contrast with these periodic time waveforms, $V_1(t)$ for the spiral Chua’s attractor is quite irregular and does not appear to repeat itself in any observation period of finite length. Although it is produced by a third-order deterministic differential equation, the solution looks “random.”

14.2.4.3 Broadband “Noise-Like” Power Spectrum

In the following discussion, we consider 8192 samples of $V_2(t)$ recorded at 200 kHz; leakage in the power spectrum is controlled by applying a Welch window [17] to the data.

We remarked earlier that the period-one time waveform corresponding to the attractor in Figure 14.14a, is almost sinusoidal; we expect, therefore, that most of its power should be concentrated at the fundamental frequency. The power spectrum of the period-one waveform $V_2(t)$ shown in Figure 14.14a consists of a sharp spike at approximately 3 kHz and higher harmonic components that are over 30 dB below the fundamental.

Because the period-two waveform repeats roughly once every 0.67 ms, this periodic signal has a fundamental frequency component at approximately 1.5 kHz (see Figure 14.14b). Notice, however, that most of the power in the signal is concentrated close to 3 kHz.

The period-four waveform repeats roughly once every 1.34 ms, corresponding to a fundamental frequency component at approximately 750 Hz (see Figure 14.14c). Note once more that most of the power in the signal is still concentrated close to 3 kHz.

The spiral Chua’s attractor is qualitatively different from these periodic signals. The aperiodic nature of its time-domain waveforms is reflected in the broadband noise-like power spectrum (Figure 14.14d). No longer is the power of the signal concentrated in a small number of frequency components; rather, it is distributed over a broad range of frequencies. This broadband structure of the power spectrum persists even if the spectral resolution is increased by sampling at a higher frequency f_s . Notice that the spectrum still contains a peak at approximately 3 kHz that corresponds to the average frequency of rotation of the trajectory about the fixed point.

14.2.5 Practical Realization of Chua’s Circuit

Chua’s circuit can be realized in a variety of ways using standard or custom-made electronic components. All the linear elements (capacitor, resistor, and inductor) are readily available as two-terminal devices. A nonlinear resistor N_R with the prescribed DP characteristic (called a Chua diode [10]) may be implemented by connecting two negative resistance converters in parallel as outlined in Figure 14.25. A complete list of components is given in Table 14.2.

The op-amp subcircuit consisting of A_1 , A_2 , and R_1 – R_6 functions as a negative resistance converter N_R with DP characteristic as shown in Figure 14.28b. Using two 9 V batteries to power the op-amps gives $V^+ = 9$ V and $V^- = -9$ V. From measurements of the saturation levels of the AD712 outputs, $E_{\text{sat}} \approx 8.3$ V, giving $E \approx 1$ V. With $R_2 = R_3$ and $R_5 = R_6$, the nonlinear characteristic is defined by $G_a = -1/R_1 - 1/R_4 = -50/66$ mS, $G_b = 1/R_3 - 1/R_4 = -9/22$ mS, and $E = R_1 E_{\text{sat}} / (R_1 + R_2) \approx 1$ V [10].

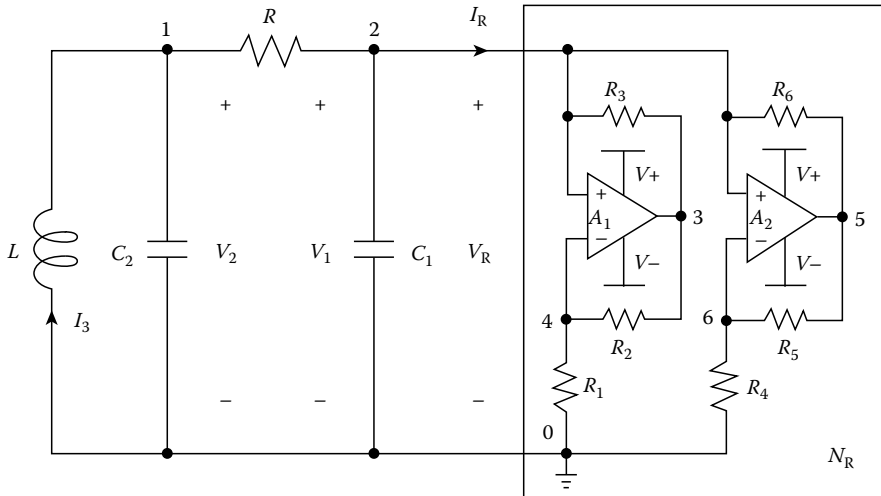


FIGURE 14.25 Practical implementation of Chua’s circuit using two op-amps and six resistors to realize the Chua diode. Component values are listed in Table 14.2. (From Kennedy, M.P., *IEEE Trans. Circuits Syst. I Fundam. Theory Appl.*, 40, 640–656, 657–674, Oct. 1993. With permission.)

TABLE 14.2 Component List for the Practical Implementation of Chua’s Circuit, Depicted in Figure 14.25

Element	Description	Value	Tolerance (%)
A_1	Op-amp ($\frac{1}{2}$ AD712, TL082, or equivalent)	—	—
A_2	Op-amp ($\frac{1}{2}$ AD712, TL082, or equivalent)	—	—
C_1	Capacitor	10 nF	± 5
C_2	Capacitor	100 nF	± 5
R	Potentiometer	2 k Ω	—
R_1	$\frac{1}{4}$ W resistor	3.3 k Ω	± 5
R_2	$\frac{1}{4}$ W resistor	22 k Ω	± 5
R_3	$\frac{1}{4}$ W resistor	22 k Ω	± 5
R_4	$\frac{1}{4}$ W resistor	2.2 k Ω	± 5
R_5	$\frac{1}{4}$ W resistor	220 Ω	± 5
R_6	$\frac{1}{4}$ W resistor	220 Ω	± 5
L	Inductor (TOKO-type 10 RB, or equivalent)	118 mH	± 10

The equivalent circuit of Figure 14.25 is presented in Figure 14.26, where the real inductor is modeled as a series connection of an ideal linear inductor L and a linear resistor R_0 . When the inductor’s resistance is modeled explicitly in this way, the circuit is called Chua’s oscillator [5].

14.2.6 Experimental Steady-State Solutions

A two-dimensional projection of the steady-state attractor in Chua’s circuit may be obtained by connecting V_2 and V_1 to the X and Y channels, respectively, of an oscilloscope in X - Y mode.

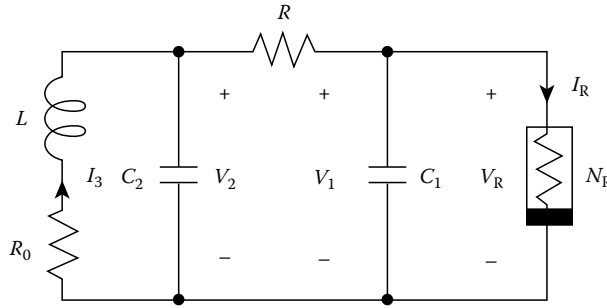


FIGURE 14.26 Chua’s oscillator.

14.2.6.1 Bifurcation Sequence with R as Control Parameter

By reducing the variable resistor R in Figure 14.25 from $2000\ \Omega$ to 0 , Chua’s circuit exhibits a Hopf bifurcation from dc equilibrium, a sequence of period-doubling bifurcations to a spiral Chua’s attractor, periodic windows, a double-scroll Chua’s chaotic attractor, and a boundary crisis, as illustrated in Figure 14.27.

Notice that varying R in this way causes the size of the attractors to change: the period-one orbit is large, period-two is smaller, the spiral Chua’s attractor is smaller again, and the double-scroll Chua’s attractor shrinks considerably before it dies. This shrinking is due to the equilibrium points P_+ and P_- moving closer toward the origin as R is decreased. Consider the load line in Figure 14.19b: as R is decreased, the slope G increases, and the equilibrium points P_- and P_+ move toward the origin. Compare also the positions of P_+ in Figures 14.22a and 14.23a.

14.2.6.2 Outer Limit Cycle

No physical system can have unbounded trajectories. In particular, any physical realization of a Chua diode is eventually passive, meaning simply that for a large enough voltage across its terminals, the instantaneous power $P_R(t) [= V_R(t)I_R(t)]$ consumed by the device is positive.

Hence, the DP characteristic of a real Chua diode must include at least two outer segments with positive slopes which return the characteristic to the first and third quadrants (see Figure 14.28b). From a practical point of view, as long as the voltages and currents on the attractor are restricted to the negative resistance region of the characteristic, these outer segments will not affect the circuit’s behavior.

The DP characteristic of the op-amp-based Chua diode differs from the desired piecewise-linear characteristic depicted in Figure 14.28a in that it has five segments, the outer two of which have positive slopes $G_c = 1/R_5 = 1/220\ \text{S}$.

The “unbounded” trajectories that follow the boundary crisis in the ideal three-region system are limited in amplitude by these dissipative outer segments and a large limit cycle results, as illustrated in Figure 14.27i. This effect could, of course, be simulated by using a five-segment DP characteristic for N_R as illustrated in Figure 14.28b.

The parameter value at which the double-scroll Chua’s attractor disappears and the outer limit cycle appears is different from that at which the outer limit cycle disappears and the chaotic attractor reappears. This “hysteresis” in parameter space is the characteristic of a blue sky catastrophe.

14.2.7 Simulation of Chua’s Circuit

Our experimental observations and qualitative descriptive description of the global dynamics of Chua’s circuit may be confirmed by simulation using a general purpose ODE solver such as MATLAB[®] [22] or by employing a customized simulator such as “ABC++” [23].

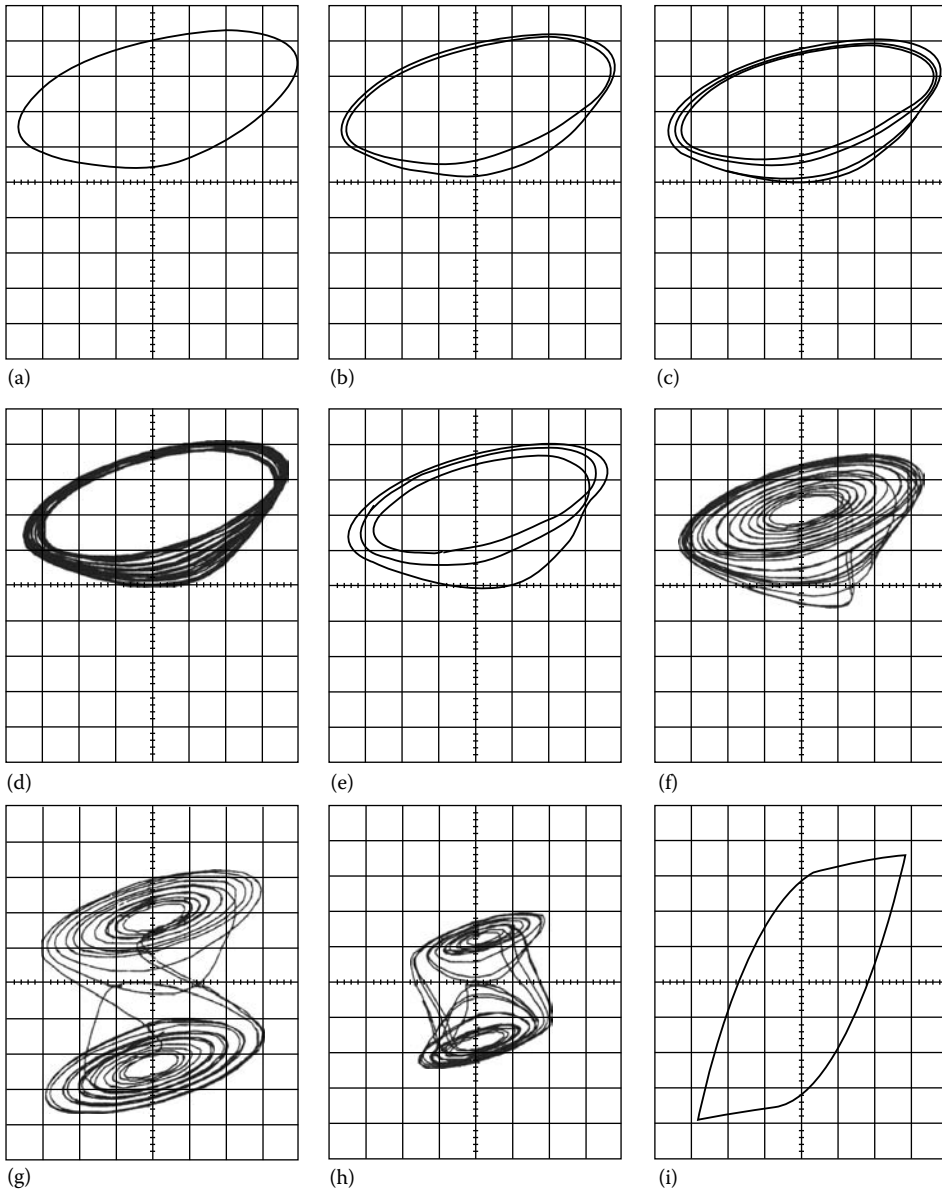


FIGURE 14.27 Typical experimental bifurcation sequence in Chua's circuit (component values as in Table 14.2) recorded using a digital storage oscilloscope. Horizontal axis V_2 (a)–(h) 200 mV/div, (i) 2 V/div; vertical axis V_1 (a)–(h) 1 V/div, (i) 2 V/div. (a) $R = 1.83 \text{ k}\Omega$, period-one; (b) $R = 1.82 \text{ k}\Omega$, period-two; (c) $R = 1.81 \text{ k}\Omega$, period-four; (d) $R = 1.80 \text{ k}\Omega$, spiral Chua's attractor; (e) $R = 1.797 \text{ k}\Omega$, period-three window; (f) $R = 1.76 \text{ k}\Omega$, spiral Chua's attractor; (g) $R = 1.73 \text{ k}\Omega$, double-scroll Chua's attractor; (h) $R = 1.52 \text{ k}\Omega$, double-scroll Chua's attractor; (i) $R = 1.42 \text{ k}\Omega$, large limit cycle corresponding to the outer segments of the Chua diode's DP characteristic. (From Kennedy, M.P., *IEEE Trans. Circuits Syst. I Fundam. Theory Appl.*, 40, 669, Oct. 1993. With permission.)

For electrical engineers who are familiar with the SPICE circuit simulator but perhaps not with chaos, we present a net-list and simulation results for a robust op-amp-based implementation of Chua's circuit. The AD712 op-amps in this realization of the circuit are modeled using Analog Devices' AD712 macromodel. The TOKO 10RB inductor has a nonzero series resistance that we have included in the

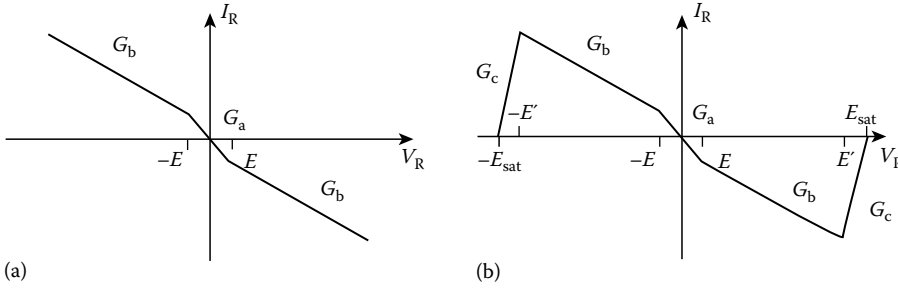


FIGURE 14.28 (a) Required three-segment piecewise-linear DP characteristic for the Chua diode in Figure 14.17. (b) Every physically realizable nonlinear resistor N_R is eventually passive—the outermost segments (while not necessarily linear as presented here) must lie completely within the first and third quadrants of the $V_R - I_R$ plane for sufficiently large $|V_R|$ and $|I_R|$.

SPICE net-list; a typical value of RO for this inductor is 12.5Ω . Node numbers are as Figure 14.25: the power rails are 111 and 222; 10 is the “internal” node of the physical inductor, where its series inductance is connected to its series resistance.

A double-scroll Chua’s attractor results from a PSPICE simulation using the input deck shown in Figure 14.29; this attractor is plotted in Figure 14.30.

14.2.8 Dimensionless Coordinates and the α - β Parameter-Space Diagram

Thus far, we have discussed Chua’s circuit equations in terms of seven parameters: $L, C_2, G, C_1, E, G_a,$ and G_b . We can reduce the number of parameters by normalizing the nonlinear resistor such that its breakpoints are at ± 1 V instead of $\pm E$ V. Furthermore, we may write Chua’s circuit Equation 14.12 in normalized dimensionless form by making the following change of variables: $X_1 = V_1/E, X_2 = V_2/E, X_3 = I_3/(EG),$ and $\tau = tG/C_2$. The resulting state equations are

$$\begin{aligned} \frac{dX_1}{d\tau} &= \alpha[X_2 - X_1 - f(X_1)] \\ \frac{dX_2}{d\tau} &= X_1 - X_2 + X_3 \\ \frac{dX_3}{d\tau} &= -\beta X_2 \end{aligned} \tag{14.15}$$

where $\alpha = C_2/C_1, \beta = C_2/(LG^2),$ and $f(X) = bX + 1/2(a - b)(|X + 1| - |X - 1|); a = G_a/G$ and $b = G_b/G$. Thus, each set of seven circuit parameters has an equivalent set of four normalized dimensionless parameters $\{\alpha, \beta, a, b\}$. If we fix the values of a and b (which correspond to the slopes G_a and G_b of the Chua diode), we can summarize the steady-state dynamical behavior of Chua’s circuit by means of a two-dimensional parameter-space diagram.

Figure 14.31 presents the (α, β) parameter-space diagram with $a = -8/7$ and $b = -5/7$. In this diagram, each region denotes a particular type of steady-state behavior: for example, an equilibrium point, period-one orbit, period-two, spiral Chua’s attractor, double-scroll Chua’s attractor. Typical state-space behaviors are shown in the insets. For clarity, we show chaotic regions in a single shade; it should be noted that these chaotic regions are further partitioned by periodic windows and “islands” of periodic behavior.

To interpret the α - β diagram, imagine fixing the value of $\beta = C_2/(LG^2)$ and increasing $\alpha = C_2/C_1$ from a positive value to the left of the curve labeled “Hopf at P^\pm ”; experimentally, this corresponds to fixing the parameters $L, C_2, G, E, G_a,$ and $G_b,$ and reducing the value of C_1 —this is called a “ C_1 bifurcation sequence.”